Project No. 09-778

Materials, Turbomachinery and Heat Exchangers for Supercritical CO2 Systems

Reactor Concepts RD&D

Dr. Mark Anderson
University of Wisconsin - Madison

In collaboration with:
Sandia National Laboratory

Piyush Sabharwall, Technical POC
Carl Sink, Federal POC

NEUP Nuclear Energy University Programs
U.S. Department of Energy

FINAL REPORT

Project Title: Materials, Turbomachinery and heat exchangers for supercritical CO2 systems
Covering Period Nov 1, 2009 to Oct 30, 2012
Date of Report: Oct 30, 2012
Recipient: University of Wisconsin – Madison
Department of Engineering Physics
1500 Engineering Drive
Madison, WI, 53706
Award Number: 88234
Project Number: 09-778
Principal Investigators:

Anderson, Mark
608-263-2802
manderson@engr.wisc.edu

Nellis, Greg
608-265-6626
gfnellis@engr.wisc.edu

Corradini, Mike
608-263-1648
Corradini@engr.wisc.edu

Project Objective: The objective of the proposed activity is to produce the data that is necessary data to evaluate the performance of the Supercritical carbon dioxide cycle. This includes a study of the materials compatibility at high temperatures of various alloys, the heat transfer and pressure drop in compact heat exchanger units and turbomachinery issues, primarily leakage rates through dynamic seals. This experimental work will serve as a test bed for model development, design calculations and help define further tests necessary to develop high efficiency power conversion cycles for use on a variety of reactor designs, including the SFR and VHTR.

Table of Contents

1 Background

The increasing importance of improved efficiency and reduced capital cost has lead to significant work in studying advanced Brayton cycles for high temperature energy conversion. Research conducted by Dostal et. al. 2006 has shown that the supercritical CO_2 (S-CO_2) cycle using recompression is more efficient than other cycle alternatives when operating at moderate temperatures. The turbomachinery components required by the cycle are highly compact, resulting in significant power densities and leading to a cost benefit based on decreased equipment costs. Wright et. al. 2008 has begun testing of supercritical CO_2 compressors and turbines with promising initial results. However there are several areas in which additional research is needed in order to make the supercritical CO_2 cycle commercially viable. These include detailed materials studies, thermal and hydraulic performance characterization of the supercritical fluid (i.e., heat transfer and pressure drop measurements for heat exchange passages), and study of the behavior of dynamic seals operating under the two-phase and choked flow conditions required by the S-CO_2 turbomachine. This proposal intends to address several of these areas, making use of existing facilities and infrastructure. This work will be accomplished in collaboration with researchers at SNL and will leverage previous expertise working with supercritical fluids.

1.1 Approach

The proposed research has been broken down into three separate tasks. The first task deals with the analysis of materials related to the high temperature S-CO_2 Brayton cycle. The most taxing materials issues with regard to the cycle are associated with the high temperatures in the reactor side heat exchanger or in the high temperature turbine. The system could experience pressures that are as high as 20MPa and temperatures as high as 650 C.

The second task deals with optimization of the heat exchangers required by the S-CO_2 cycle; the S-CO_2 flow passages in these heat exchangers are required whether the cycle is coupled with a high temperature gas reactor (VHTR) or a sodium fast reactor. At least three heat exchangers will be required; the pre-cooler before compression, the recuperator, and the heat exchanger that interfaces with the reactor coolant. Each of these heat exchangers is unique and must be optimized separately. However it is possible that each of these heat exchangers could be of the formed or etched plate compact heat exchanger design with a unique channel design specifically optimized to maximize heat transfer while minimizing pressure drop under the operating conditions that exist within the component. The most challenging heat exchanger is likely the pre-cooler. In the pre-cooler there exists only about a 40^{o}C temperature change. However, the pre-cooler operates close to the critical point of the CO_2 and therefore there are substantial changes in the properties. For example, the density is nearly six times higher at the outlet than the inlet and the specific heat varies by a factor of 10. This research will focus on this most challenging component.

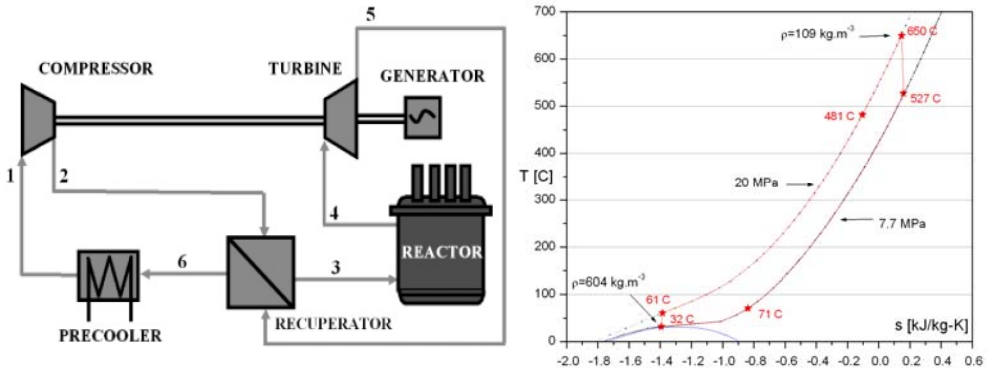

Figure 1: Simple CO2 Brayton cycle and T-s diagram showing temperature and pressure variations. (Dostal 2006)

The third task examines seal leakage through various dynamic seal designs under the conditions that are expected in the S-CO_2 cycle; these include supercritical as well as choked and two-phase flow conditions. Seal leakage is likely to be a primary consideration in the design of a S-CO_2 system because (1) high partial evacuation of much of the turbomachine envelope, (2) the high density of S-CO_2, and (3) the large pressures associated with S-CO_2 lead to large pressure differences across the seals. The test facility will be flexible relative to operating condition and seal geometry and will provide experimental measurements of leakage flow for a variety of seal geometries (labyrinth, brush, etc.) over a range of conditions. Empirical and semi-empirical models of the leakage flow will be developed using these data in order to facilitate seal design and optimization and also enable cycle models to more precisely include the impact of seal leakage on performance.

2 Task 1 - Materials testing of alloys in S-CO2

Ten different alloys with six samples of each alloy resulting in 60 samples were tested in the facility described below with research grade CO_2 at a temperature of 650^{o}C for a total duration of 3000 hours. Every 500 hours the system was shut down and one sample of each alloy was removed for analysis.

Research grade 99.9998% CO_2 was used to charge the system and was flowed through the system during testing to ensure low O_2 levels below the desired 200ppm as measured with the RGA. A series of three heater tapes controlled by SCR circuits and a LabView^{TM} PID control system based on the center test section CO_2 temperature were used to maintain the temperature at 650°C +/- 2°C. An autoclave temperature uniformity less than 2°C is was achieved for the duration of the 3000 hour tests. A series of NIST traceable, calibrated K-type thermocouples were used to record the temperature as a function of time at several locations in the system including three key measurements in the autoclave Inconel 625 tube; one at the entrance of the autoclave, one in the center of the sample holder and one at the exit of the autoclave. Temperature measurements at each location were acquired at a rate of 0.01Hz. A flowing system was used to ensure constantly refreshed and uniform conditions throughout the autoclave. The incoming CO_2 was heated to within 5°C of the test section temperature before injection into the autoclave and the temperature was monitored by a thermocouple inserted into a high pressure compression fitting tee near the entrance of the autoclave. Preheating of the CO_2 flow was achieved by flowing the CO_2 through a 0.055 in. I.D. Hastealoy C-276 wrapped with nichrome wire. The exiting stream of CO_2 with a flow rate from 0-5 ml/min (sufficient to replace the autoclave volume every 2 hours) was used to

control the pressure within the autoclave to within 1% of the nominal 20MPa by matching the exiting CO_2 flow with a PID controlled (based on pressure) CO_2-SFC-24 double piston pump (10000 psi, 0-24 ml/min). Pressure in the test section was recorded with a Siemens SITRANS pressure gauge at a rate of 0.01Hz (accuracy 0.1% FS).
Each sample was carefully weighed on a Sartorius CPA26P six place (0.002mg) balance to record the weight change of the alloy after each of the 500-hour exposures. Initial SEM analysis of a select number of samples was also performed to examine the surface oxide layer.

2.1 Facility description

Figure 2 shows a schematic of the S-CO_2 autoclave system constructed at the University of Wisconsin-Madison for exposure of sample alloys to high pressure and high temperature CO_2 environments . Figure 3 shows the PID diagram used for the LabView DAQ control. The facility is comprised of eight different components which will be discussed below in detail; 1) gas supply system, 2) high pressure CO_2 pumping system 3) CO_2 pre-heat, 4) Inconel 625 temperature and pressure controlled autoclave, 5) CO_2 pre-cooler, 6) pressure controlled flow and gas sampling system, 7) sample holder, and 8) computer control and acquisition system. The facility was designed to operate at pressures up to 25MPa (3925 psi) at temperatures of 650^o C. It can achieve higher pressures at lower temperatures and was pressure tested with water at room temperature up to 63.7MPa (10,000 psi) before operation. The facility was designed to accommodate a large number of samples in a horizontal configuration (the current test used 60 samples) with a slight gas flow through the system to maintain gas purity levels. The entire facility has a foot print area 76.2 x 182.9 cm and is 198 cm tall and is positioned in a steel structure. The facility requires high purity CO_2 gas input, water cooling, exhaust gas system, and approximately 100 amps at 240 volts single phase AC for various heaters and 20 amps at 120 volts single phase AC for control computers and low voltage power supplies. Figure 4 is a photograph of the entire system located in the basement of the Computer-Aided Engineering building in the Engineering Campus of the University of Wisconsin- Madison.

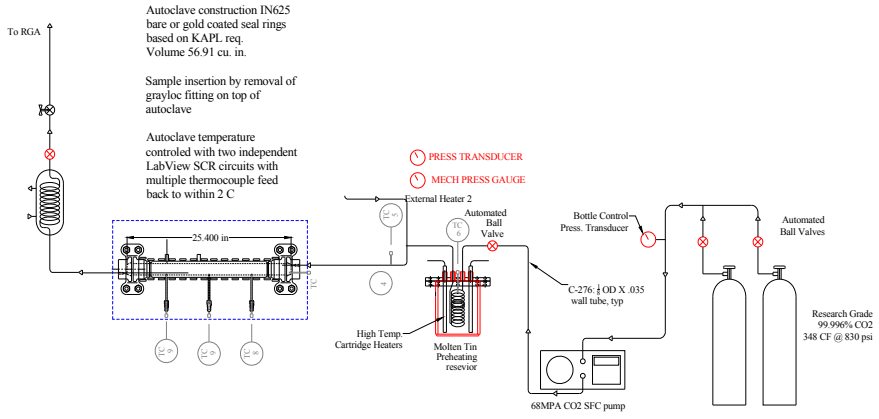

Figure 2 Supercritical carbon dioxide corrosion system diagram

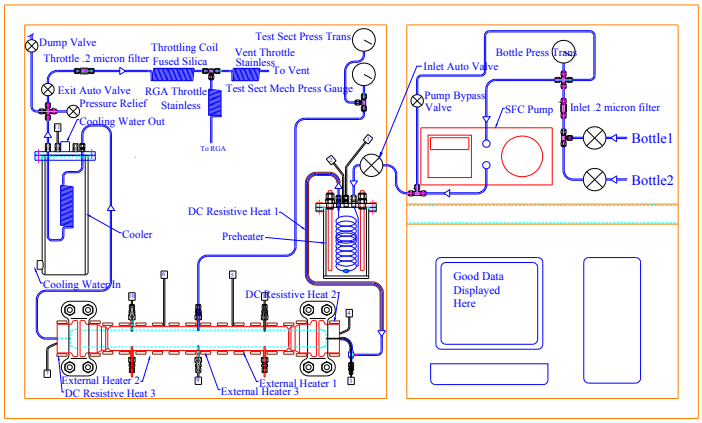

Figure 3 Labview control drawing for operation of the autoclave system showing key components

Figure 4 Photograph of the S-CO_2 autoclave exposure facility at the University of Wisconsin (designed and constructed by Mark Anderson and Paul Brooks)

2.1.1 Gas supply system

The gas supply system consisted of two high purity research grade bottles of CO_2 analyzed to be of 99.9998% purty. The gas was supplied by Linde Company. The bottles used were siphon bottles with the feed tube penetrating to the bottom of the bottle. The bottles were situated on a scale so that the weight change of the bottle could be monitored during the course of testing. The two bottles were attached to a manifold with isolation valves for each bottle. The manifold was also connected to a Siemens SITRANS pressure gauge to monitor the bottle pressure throughout the course of the experiments. Two bottles were used based on calculations of the estimated flow rate and the inventory of the CO_2 such that more than enough gas was available for the individual 500-hour test runs. They were filled with 80 lbs of CO_2 and at a flow rate of 7 ml/min. The manifold system however allowed the possibility of replacing a bottle during a test by isolating one bottle and replacing it, and then purging the line before the bottle was brought on line. This however was not necessary during the course of the 500-hour test. To ensure high enough back pressure for the pumping system and to maintain the high gas purity the bottles not more than 45lbs of CO_2 were used from an individual bottle. This corresponded to a backpressure of about 600 psi.

2.1.2 Pumping system

The high purity CO_2 gas bottle manifold was connected to a dual piston peltier cooled liquid CO_2 chromatography pump manufactured by Lab Alliance. This pump was capable of pumping up to 20 ml/min at pressures up to 10,000 psi. The high purity gas was fed directly from the manifold to the pumping system however valves were located on each side in case of a pump failure. The down stream valve was a computer-controlled pneumatic valve that could be shut down in the case of a pump fault to isolate the autoclave. The pump shown in Figure 5 has two sapphire pistons and a pulse dampener to smooth out the flow. The pump was controlled with LabView through an RS232 connection on the back. This allowed feed back from the autoclave pressure transducer to control the pumping speed with a PID algorithm programmed within the LabView software. The output flow rate indicated by the pump in addition to the internal pump pressure output was recorded in the LabView data files and monitored throughout the experiment to ensure proper operation. The outlet of the pump was also fitted with a one-way flow valve to prevent back flow in the event of a pump malfunction.

Figure 5 Photograph of the Lab Alliance high pressure CO_2 pump

2.1.3 Pre-Heater

Two different pre-heater systems were used. The first consisted of a 20 foot section of Hastaloy 276 stainless tube 1/8 inch OD wrapped into a coil and inserted into a stainless steel can filled with high thermal conductivity copper powder surrounding and six 1000 W immersion heaters. The CO_2 flowed through the tube and was heated to the controlled temperature of the copper powder. The second pre-heater was installed after the first pre-heater can. This consisted of the same 1/8 inch OD Hastaloy tube with nicrhrome wire wrapped around it insulated by high temperature ceramic tape. A DC power supply was used to control the heating rate in the tube and a thermocouple located at the entrance of the autoclave were used to ensure the incoming CO_2 was at the desired temperature. During testing it was found that the second pre-heater was sufficient to heat the fluid to the desired temperature and was robust enough for each of the 500-hour tests.

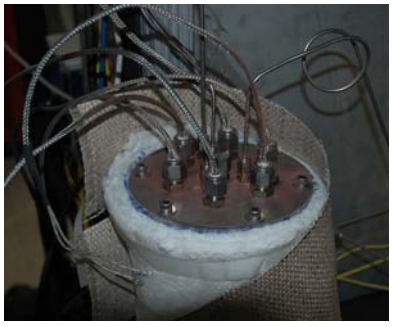

Figure 6 Image of pre-heat can with heaters and S-CO2 tubing immersed in a copper powder matrix

2.1.4 Autoclave

The autoclave system was constructed out of 2 inch schedule 160 Inconel 625 alloy to provide the high temperature strength and corrosion resistance. This same tube was used for previous SCW loops and showed good corrosion resistance. Figure 8 shows a side view of the autoclave pipe

with the different heater tape sections used to control the temperature. Each of the three heated zones was wrapped with HTS/Amtec ceramic-coated heater tapes (see appendix for details). This image also shows the thermocouple ports used to measure the interior temperature of the autoclave. A series of K-type thermocouples were welded to the outside of the pipe and three omega 1/8" calibrated (see appendix for calibration data) thermocouples were inserted into the autoclave through the ¼" OD tubing and compression fittings. This extension tubing was used to create the pressure seal away from the main heating coils and allowed the thermocouples to extend a ¼" inside the autoclave piping. The three thermocouples that were installed within the autoclave controlled the temperature of their respective heater zones to within 1°C. Zone 1 is on the right and controlled by thermocouple 8, Zone 2 is in on the left side and controlled by thermocouple 10 and zone 3 is in the center of the autoclave and controlled by thermocouple 9. Opposite thermocouple 9 is a pressure tap that monitors and controls the pressure of the autoclave by feedback to the LabView code and the HPLC pumping system. The ends of the autoclave were also heated but these were heated with nichrome wire wrapped around the Grayloc fitting. These temperatures were monitored and controlled by thermocouples 4 and 7 (see PID drawing Figure 2). In an effort to monitor the incoming temperature a tee system was used in the inlet line and a thermocouple 3 was inserted and snaked into the entrance area of the autoclave. The remaining compression fitting on the left side of the autoclave was used to hold the sample holder in place and keep it from turning. The last compression fitting was an extra and was capped off for the entire duration of the testing. Figure 7 shows a photo of the end of the autoclave where the samples were inserted. In this photograph the lower heat shield is also seen.

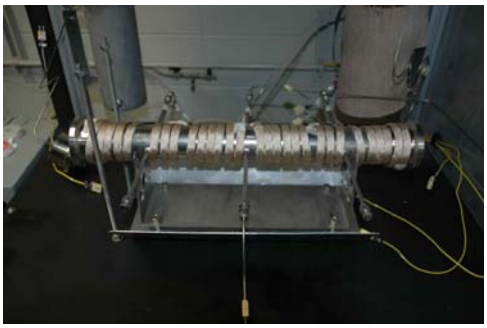

Figure 7 Photograph of the end of the autoclave system where the samples are inserted

Figure 7 shows a photograph of the autoclave with the insulation. Two layers of 1 inch thick made of high temperature alumina wool insulation were used along with a layer of high temperature alumina fiber blanket was used to keep the system temperature constant and limit heat loss. This insulation was wired to the autoclave. Insulation caps were also used on the Grayloc end fittings and only a small layer was used around the bolts to limit the thermal expansion in order to maintain the high-pressure seal. Figure 2.8 shows a photograph of the silver coated Grayloc seal used in the end caps to maintain the pressure of 3000 psig.

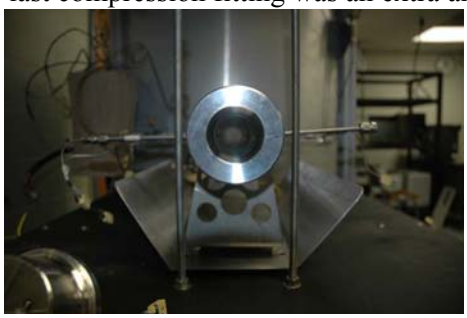

Figure 8 Photo of the autoclave before insulation

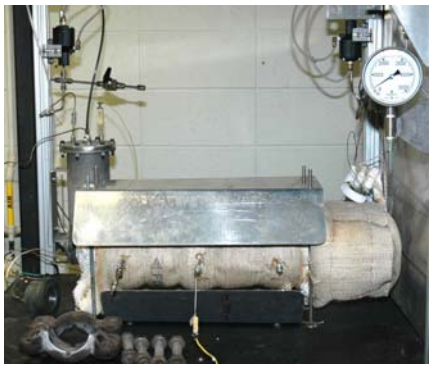

Figure 9 (Left) Photograhp of the insulated autoclave with one end of the Grayloc fittings removed for sample insertion. Figure 2.8 (Right) Photograph of seal ring for Grayloc end cap

2.1.5 Cooler

The S- CO_2 fluid flow exited the autoclave to the left through a 1/8" tube welded into a Grayloc end cap (very similar to the inlet). After the fluid exited the autoclave it was cooled down in a cooling can to room temperature. This was necessary in order to pass the fluid through a capillary tube to control the pressure and to allow online RGA system to analysis. The cooling can consisted of a 20-foot piece of 1/8 Hastaloy 276 tubing inserted into a can circulated with building cooling water. Figure 10 shows a photograph of this system. Water entered through a 1/4-inch line on the top of the can and exited from a fitting welded to the bottom of the can. The S-CO_2 entered through the 1/8-inch uninsulated line. The temperature of the S- CO_2 reduced significantly just due to convective heat transfer to ambient before entering the cooler. The CO_2 then exited through the second 1/8 port on the top of the can passed through a valve and was connected to a 2 meter 50 micron ID quartz capillary tube to reduce the pressure to ambient and provide back pressure such that the system could be held at pressure. This capillary tube length was determined by pretests at the desired flow rate of the pumping system. The longer the tube, the lower the flow rate.

Figure 10Photograph of CO2 Cooling canister

2.1.6 Gas sampling

It was desired to measure the exiting gas purity for the duration of the test. This was achieved by the use of a RGA (Residual Gas Analyzer) mass spectrometer (Pfeiffer prisma QMS422) and sampling gas through the capillary tube. A tee was attached to the capillary tube with a 1/16 inch OD line going to a variable leak valve which could be adjusted to operate at the desired inlet pressure to the quadruple mass spec of 5e-6 mbar. The other leg of the tee was attached to another small section of 100-micron capillary tube to allow gas to gas to exit. This allowed a continuous stream of gas to be sampled with the RGA. Charge to mass ratio intensity spectra (proportional to the partial pressure) of each of the research grade CO_2 cylinders from

Figure 11 RGA mass spectrometer used to measure gas purity

Airgas were analyzed prior to testing and saved to compare the outlet gas. During each of the 500 hour tests a little less than 2 bottles were needed for the desired flow rate. The bottle number used at the different times was recorded in the Quadstar^{TM} program along with the spectrum from the exiting gas. Figure 11is a photograph of the gas sampling system. The system was calibrated with 4 test gases discussed in the appendix.

2.1.7 Sample holder

The samples were mounted in an alumina (Al_2O_3) boat and then inserted into the autoclave through the end fitting. The alumina boat was designed to hold all 70 samples at one time. An inconel -625 holder was fabricated to hold the alumina boat in the proper orientation and position within the autoclave. Figure 12shows a photograph of the sample boat and the inconel holder. The holder has two tabs on the backside of the system and a little finger in the front to keep the sample holder in place. The two tabs at the back are used to position the holder within the autoclave. The hole in the tabs aligns with an inconel 625 1/8-diameter rod that enters through one of the compression fittings on the autoclave. The samples were loaded and held on a 1/8th inch diameter alumina rod with alumina spacers between each of the samples tested. The samples were codified and engraved with a number to facilitate identification.

Figure 12 Sample boat in the inconel holder with the samples. The top photo shows the holeson the tabs used to lock the holder inplace. Alumina washers separate the samples.

.

2.1.8 Computer control system

The entire facility was controlled by a PC running a LabView code that controlled the temperatures and pressures to within specifications. A diagram of the LabView control system is shown in Figure 3. This PC also recorded the entire temperature and pressure history during the runs. A second computer was attached to the RGA mass spectrometer to record spectra at a rate of one every 30 minutes. All the data is contained in the accompanying DVD including all calibrations, pictures and analysis. The computer systems were installed to a battery back up system to momentary power disruptions. If a disruption occurred or a parameter was significantly out of specification an emergency e-mail message would be sent to the operator. In addition status e-mails were sent every 2 hours to an operator to check the conditions of the test.

2.2 Testing procedure

Prior to loading the samples and running the system initial shake down tests were conducted with the facility to determine the heat -up and cool down times and to determine any operational issues. Based on these tests it took approximately 4 hours to increase the temperature from room temperature to 650^{o}C and achieve a steady temperature and pressure with very little overshoot.

The sample holder and tubing were cleaned with alcohol after construction and the system was conditioned at temperature with S-CO_2 for approximately 48 hours prior to loading the samples. The samples were loaded on to the holder in a clean environment with clean gloves and plastic tweezers to ensure no contamination of the samples. The samples holder was set in the autoclave and locked into position with the 1/8th inch dowel-retaining rod. Before the system was sealed CO_2 was flowed through the system for about 5 minutes. The grayloc fitting was then installed and sealed. CO_2 from the research grade bottle was again flowed through the system and out of the depressurization valve located after the cooler for approximately 30 minutes to flush the system of any air. Once the system was sufficiently flushed the valve was closed and the autoclave was filled to 800-psig or bottle pressure with CO_2. The heaters were then turned on and ramped to 300^{o}C; occasional venting through the exit valve was necessary to keep the pressure below 3000 psi. Once 300^{o}C was achieved the system temperature was increased to 650^{o}C. When the system was at temperature the pressure was brought up to 3000 psig with the pump and then the auto control was initiated to allow control of the system pressure with the LabView code controlling the pumping speed. The input to the PID for the pump was the Siemens pressure transducer connected to the center of the autoclave. Once the system reached a reasonable steady state, determined by a less than 1^{o}C temperature and less than 5-psig-pressure variation, the 500-hour clock was started. At this point the Data acquisition system was set to record temperature, pressure and flow rates every 100 seconds and the mass spectrometer was set to record spectra every 30 minutes. After 500 hours the pumping system was shut down and the heaters were switched off. It took approximately 5 hours to cool from 650^{o}C down to 50^{o}C at which time the insulation could be removed and the system pressure released.

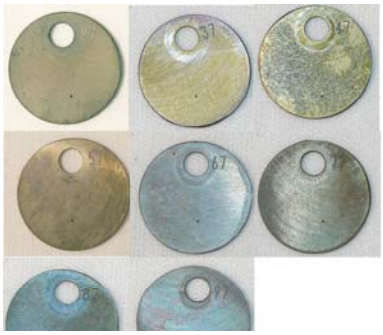

Figure 13 Compiled photo of samples after 500 hours of testing

Once the system was sufficiently cooled, typically the next day the left side Grayloc fitting was removed and the sample holder was taken out of the autoclave. The samples were then weighed with a precision 6 place Sartarious CPA26P balance. Prior to weighing each sample a calibrated 0.5 gram weight was used to ensure calibration of the scale. This was done by weighing the calibrated source 10 times before each sample weight (the calibrated source was kept in a closed environmentally controlled cabinet during the entire 6 month testing period and never touched with anything other than a plastic tweezers). Weighing was done by placing the sample on the scale closing the door to the scale and then waiting for a stable reading to appear. Then the sample was removed and the procedure repeated 10 times. The data was recorded in the laboratory notebook and then transferred to an Excel spread sheet after all the data was collected for the run.

The samples were then individually photographed with a Nikon D70 SLR camera with a 150mm micro lens and with a 36mm extension tube. Figure 13 shows an example of the photographs of the samples taken. In this figure the individual images were complied for each of the 7 series samples into one image.

After photographing all except the lowest number samples were reloaded into the sample holder and the next 500-hour test was started following the same procedure discussed above.

2.2.1 Observations during testing

After the first 500-hour test significant oxidation was observed on the F91 and HCM12A samples along with significant weight changes. ***Error! Reference source not found.***and Figure 14 show photographs of these samples. Based on the physical condition of the samples and the severe weight change (Figure 2.15) it was determined that significant oxidation and spallation occurred.

Figure 15 F91 samples after 500 hour exposure to s-CO2 at 3000 psig

Figure 14 HCM12A samples after 500 hour exposure to s-CO2 at 3000 psig

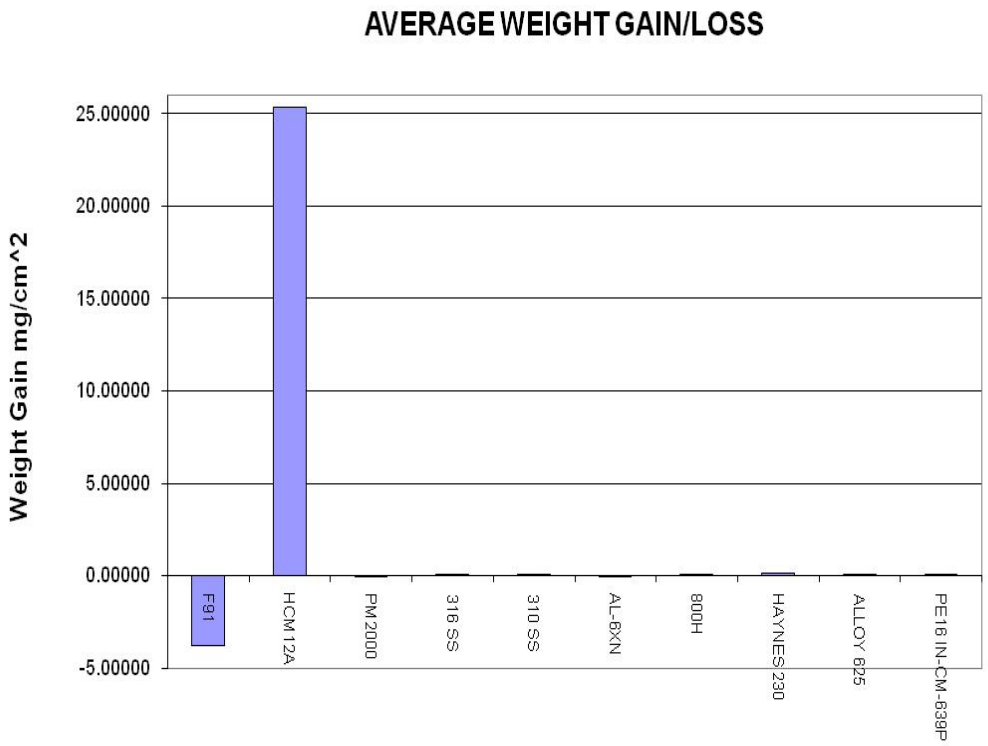

Figure 16 Sample weight change after 500 hour exposure to s-CO2 at 3000 psig and 650C

Also evident was some debris on the alumina sample holder. That appeared to come from the F91 and HCM12A. Figure 17 is a photograph of the samples after they were removed from the autoclave. The dark bands on the alumina crucible are thought to have come from the spallation of oxides from the two ferritic steels.

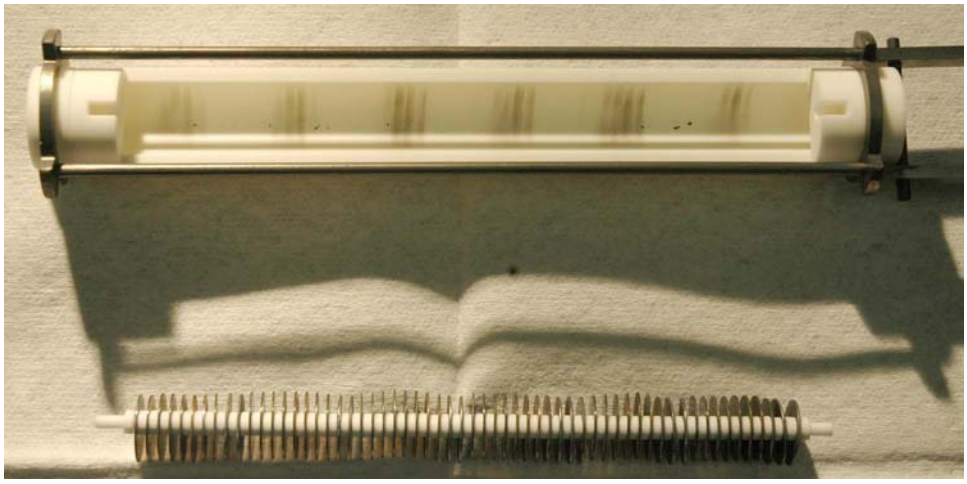

Figure 17 Debris on sample holder after 500 hour testing

Based on these results it was decided to remove both the F91 and the HCM12A samples for the remainder of the test. The sample holder was scrubbed with alcohol and sonically cleaned with distilled water to remove the traces of the oxide debris. The sample holder was then baked in the autoclave under CO_2 gas at 650^{o}C for 24 hours prior to reloading the remaining samples.
Throughout the remainder of the testing no other significant spallation of the other alloys was observed that might have caused an influence on the other samples. Figure 18shows the last set of sample alloys that were exposed to the entire 3000-hour time at temperature and pressure. Details of the weight change measurements and analysis are described in a subsequent section.

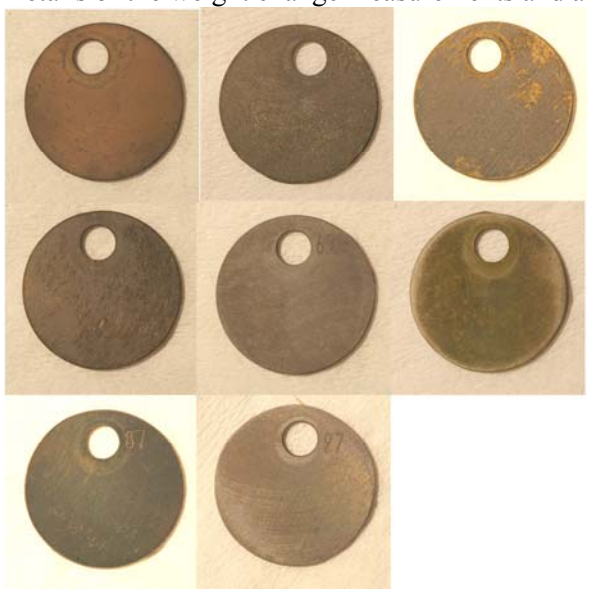

Figure 18 Alloy samples exposed to 3000 hours in an enviornment of s-CO2 at a pressure of 3000 psig and a tempeature of 650C

.

2.3 Detailed test information

During the entire 3000-hour test there were a few temperature excursions and pressure excursions as shown in the plots below. All the data has been provided in the DVD and the summary data is presented in the appendix here only T9 is shown (center of autoclave temperatures) since there was less than 2°C difference between this and T8 and T10 (the other two internal autoclave temperatures). In the 500-hour test there was a 3 pressure drops that lasted a total of less than a total 5 hours. This occurred due to a break in the capillary tube resulting in the system decreasing to bottle pressure. In all cases no temperature excursion resulted and no the gas composition was not compromised. During this short transient the flow rate increased to try to compensate for the leak.

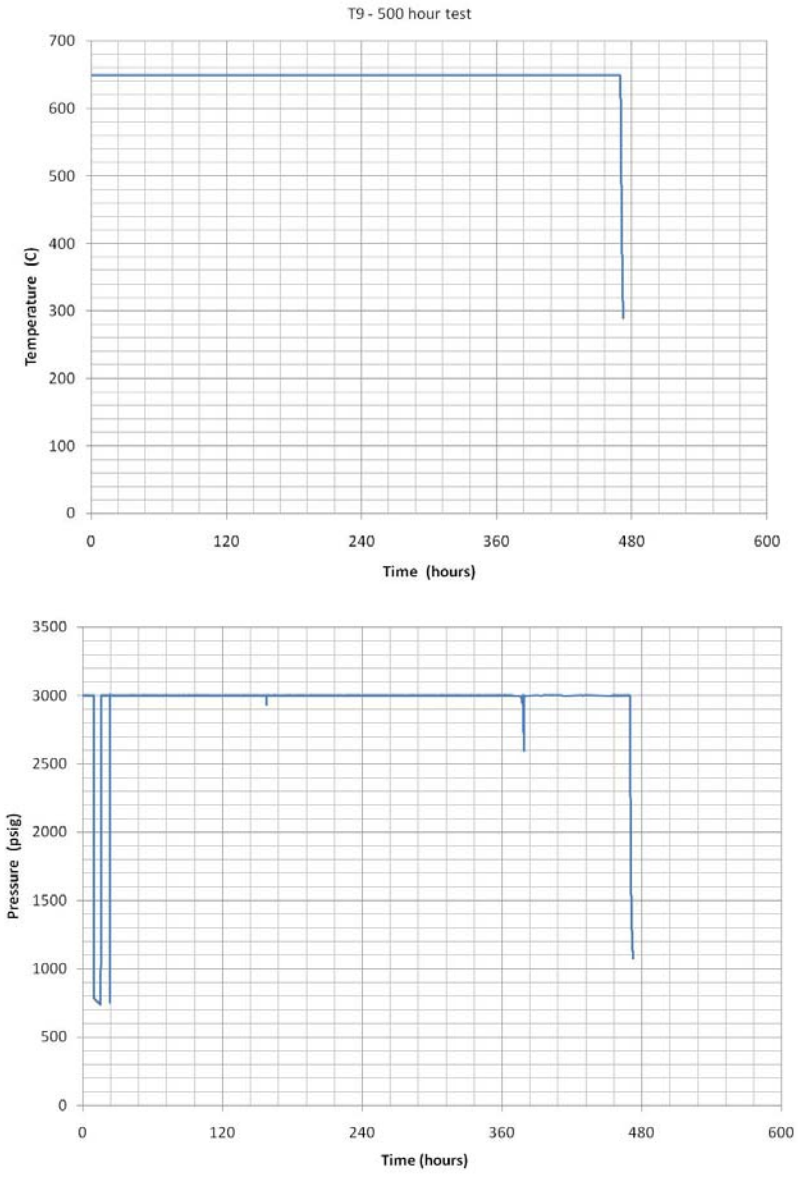

Figure 19Temperature and pressure history for the first 500 hour test duration

During the time period of 500-1000 hours no temperature excursions were recorded, however 5 small pressure excursions occurred for a total duration of less than 1 hour as shown in the figures

below. Again these were due to issues with the capillary tube and the gas composition was not compromised.

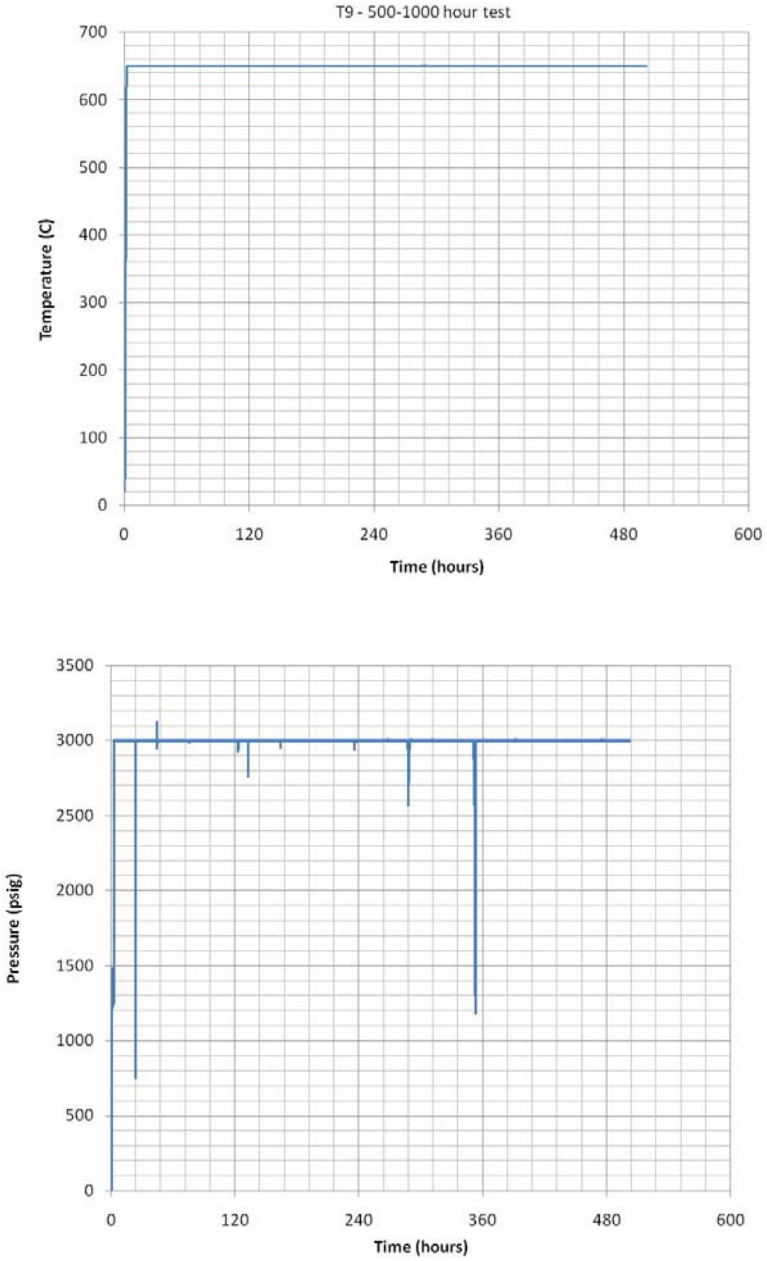

Figure 20Temperature and pressure history for the 500-1000 hour test duration

During the time period of 1000-1500 hours no temperature excursions were recorded, however 4 small pressure excursions occurred for a total duration of less than 8 hours total as shown in the figures below. Again these were due to issues with the capillary tube and the gas composition was not compromised and this is not thought to affect the test in any significant way.

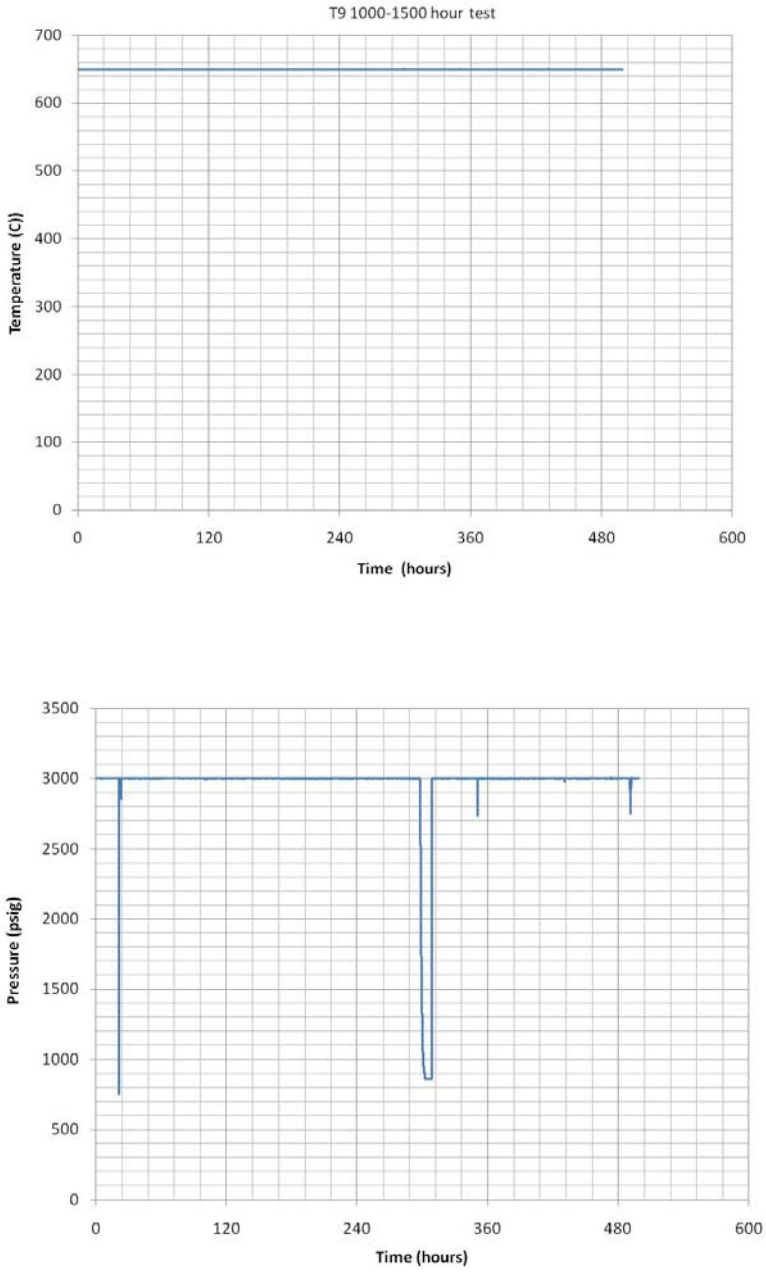

Figure 21 Temperature and pressure history for the 1000-1500 hour test duration

During the test time period 1500-2000 hours no temperature or pressure excursions were recorded Figure 22.

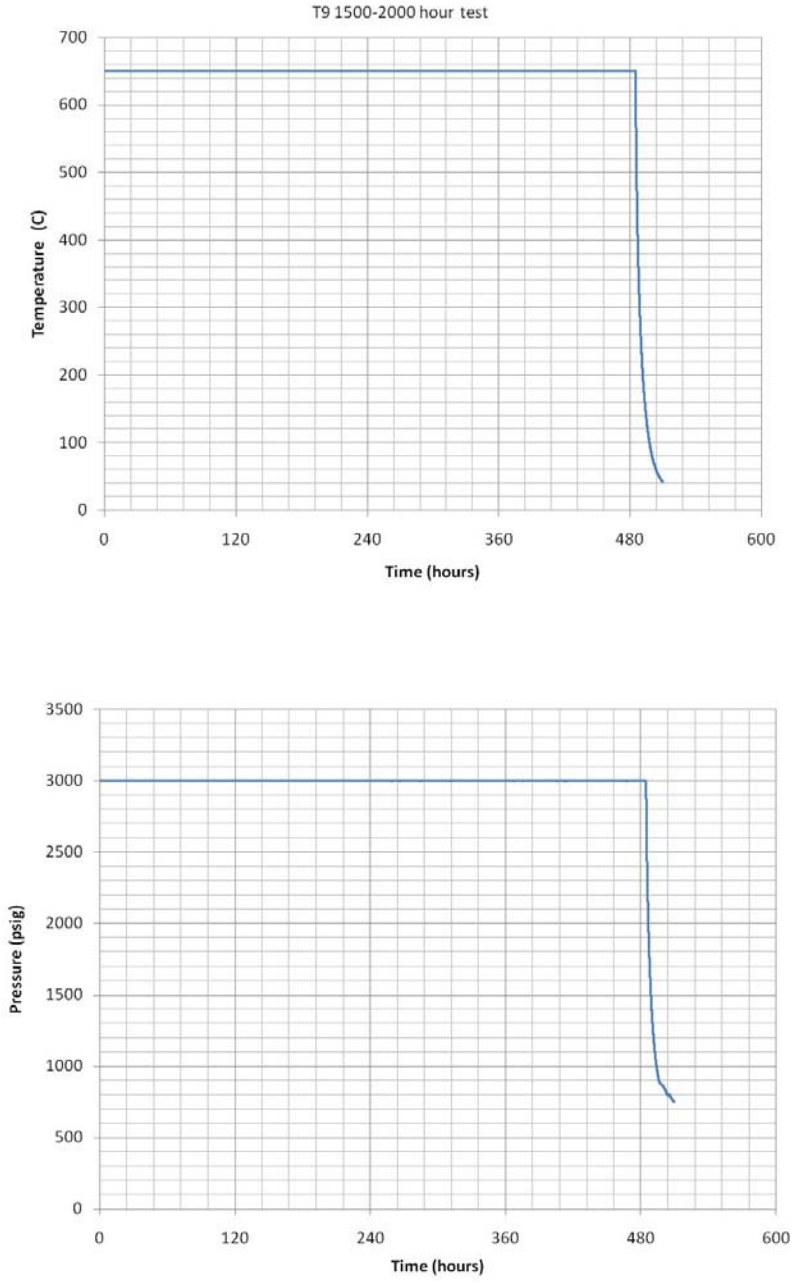

Figure 22 Temperature and pressure history for the 1500-2000 hour test duration

During the time period of 2000-2500 hours a slight temperature excursion was recorded at the same time that a large pressure change occurred (Figure 23). This was a result in a fault in the HPLC pump which got stuck on the maximum flow rate. Unfortunately this event lasted for several hours but since the fluid was still in the supercritical state it is thought that there was little effect to the materials. It was possible to fix the problem without a shut down and the system was returned to the desired pressure.

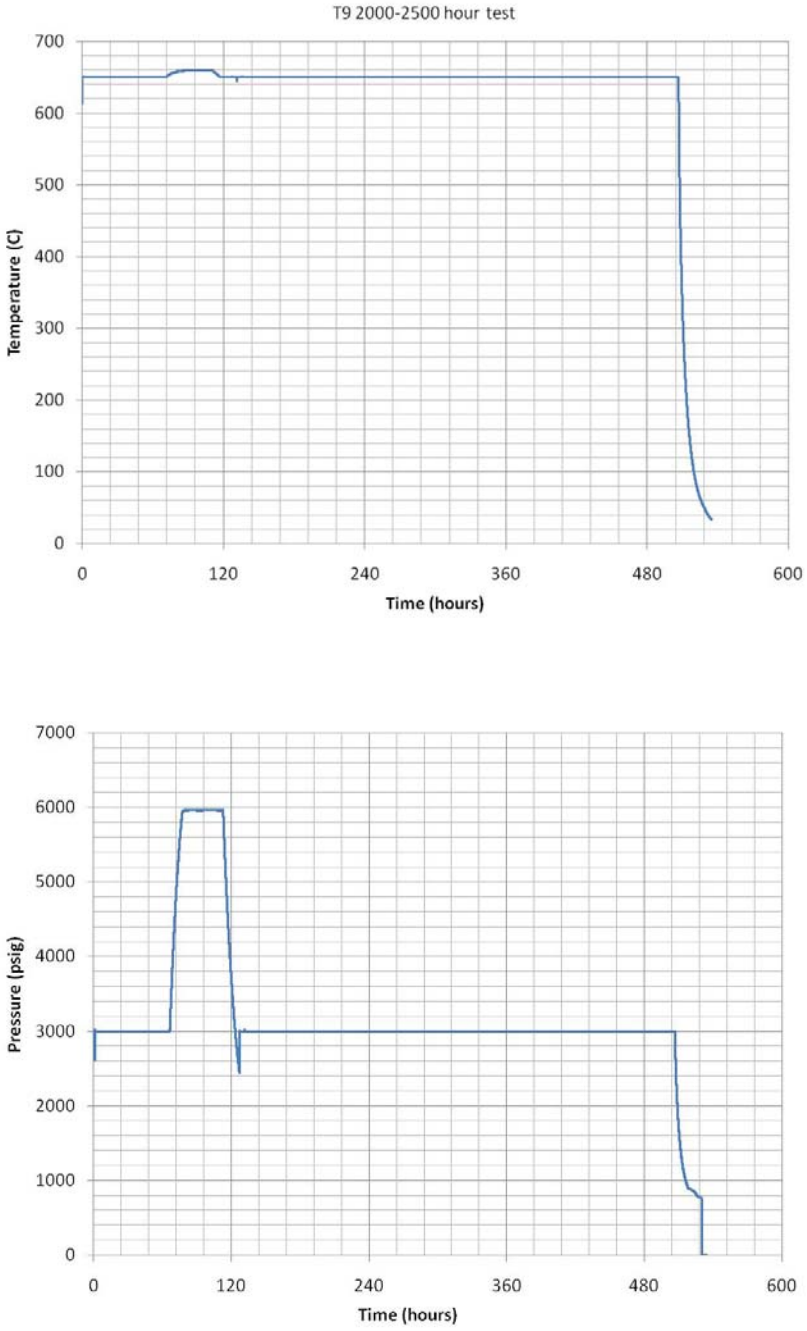

Figure 23 Temperature and pressure history for the 2000-2500 hour test duration

During the time period of 2500-3000 hour test a small temperature excursions was recorded along with an accompanying slight pressure drop (Figure 24). The temperature excursion was a result of a small power fluctuation that resulted in an error in the code, which fired the SCR controlling the autoclave temperature at full power. The pressure was manually dropped while the temperature problem was fixed. Although relatively short about 15 minutes this resulted in a peak temperature of 800^{o}C. Due to the short duration it is felt that this did not significantly affect

the corrosion rates, however the temperature plays a larger role then the pressure on the corrosion. Overall during the entire 3000-hour test period there were very little significant pressure or temperature fluctuations and the system ran reasonably well.

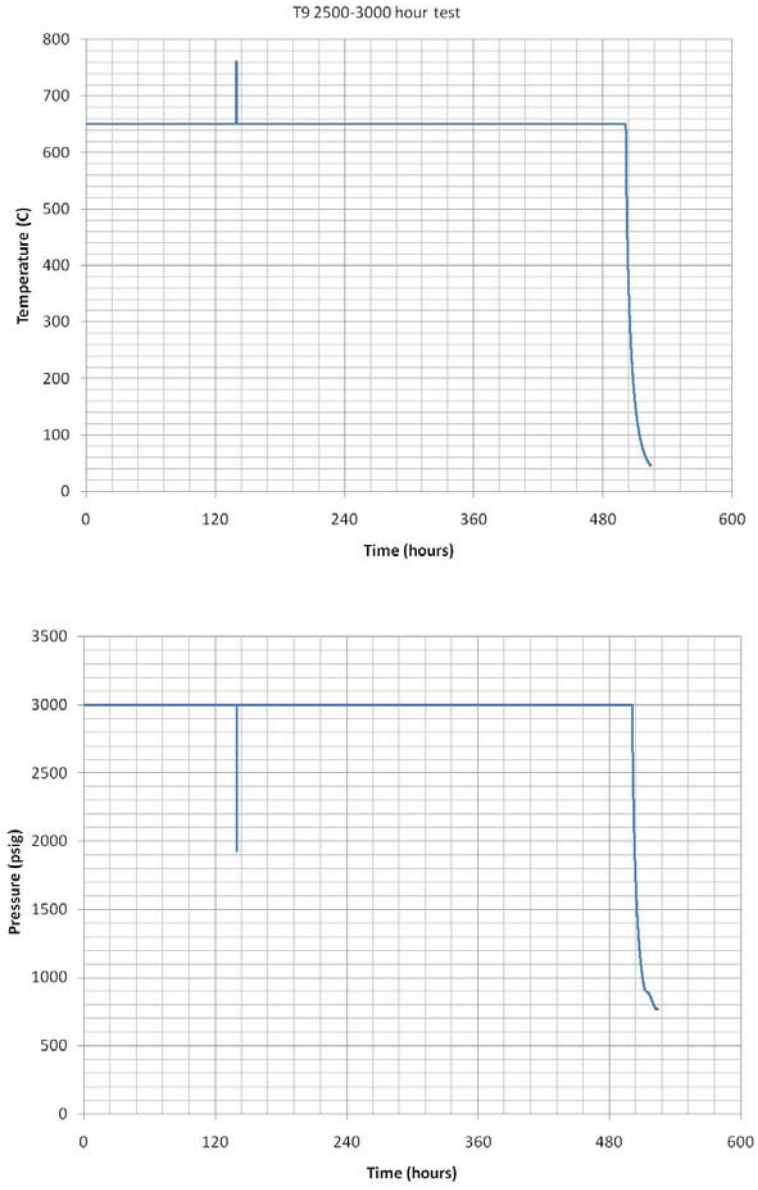

Figure 24 Temperature and pressure history for the 2500-3000 hour test duration

2.3.1 Gas purity

During the entire test period no detectable difference between the bottle gas and the exiting gas stream was observed indicating that the samples were exposed to 99.9998% CO_2 throughout the 3000 hour testing period. This is also true during the few pressure and temperature fluctuations. Most of the pressure fluctuations occurred with the capillary tube down stream, which affected the Mass spec readings, but there is no reason to suspect any change in the gas composition within the autoclave.

2.3.2 Weight change analysis

Disk samples of 10 alloys were exposed to S-CO_2 at 650°C and 20.7 MPa with a flow rate of ~0.3 g/min for a variety of times up to 3000 hours. They are austenitic steels including 316 stainless steel, 310 stainless steel, AL-6XN, and Incoloy alloy 800H, ferritic-martensitic steels including F91, HCM12A, and PM 2000 (a powder metallurgy alloy), and Ni-base alloys including Haynes alloy 230, Inconel 625, and Nimonic alloy PE16. Their typical chemical compositions are listed in Table 1.

Table 1: Typical chemical compostion (wt%) of the tested austenitic (A) steels and Ni alloys; F/M) ferritic or ferritic-martensitic steels.

Alloy		Fe	Cr	Ni	Mn	Si	Mo	Co	Nb	W	Ti	Al	Cu	V	C	N	Extra
A (Fe-base)	316SS	64.3[a]	17.4	13.3	1.7	.43	2.7	-	-	-	-	-	-	-	.045	.044	P,S
	310SS	54.3[a]	24.8	19.1	.99	.72	-	-	-	-	-	-	-	-	.04	-	P,S
	AL-6XN	47.9[a]	20.5	24.0	.4	.4	6.2		-	-	-	-	.2	-	.02	.22	P,S
	800H	45.3[a]	20.4	31.6	.76	.13	-	-	-	-	.57	.50	.42	-	.07	-	P,S
A (Ni-base)	Haynes230	3*	22	57[a]	.5	.4	2	5*	-	14	-	.3	-	-	.10	-	B,La
	Alloy625	4.4	21.9	61.2[a]	.08	.11	8.4	.05	3.17	-	.21	.2	.19	.014	.01	-	Ta,Mg,S
	PE16	34.2	16.2	43.5[a]	.05	.05	3.3	.05	-	-	1.24	1.18	-	-	.046	-	Zr,B
F/M	PM2000	74.5[a]	19	-	-	-	-	-	-	-	.5	5.5	-	-	-	-	Y_2O_3:.5
	F91	89.1[a]	8.4	.21	.45	.28	.9	-	.076	-	-	.022	.17	.22	.10	.048	P,S
	HCM12A	84.2[a]	10.8	.39	.64	.27	.3	-	.054	1.89	-	.001	1.02	.19	.11	.063	P,S,B

[a] As Balance *Maximum

Table 2: Weight gains of the samples exposed to the S-CO2 for a variety of times

Alloy	Exposure Time (hour)					
	500	1000	1500	2000	2500	3000
F91	8.1812±1.2352	-	-	-	-	-
HCM12A	13.7989±3.4522	-	-	-	-	-
316SS	0.0480±0.0090	0.9707±0.0877	1.3550±0.0334	1.5911±0.0992	1.7616±0.0917	1.8366
310SS	0.0795±0.0160	0.2172±0.0411	0.2319±0.0307	0.2277±0.0356	0.2190±0.0419	0.2006
AL-6XN	0.0374±0.0173	0.2104±0.0257	0.2104±0.0217	0.2234±0.0159	0.2332±0.0149	0.2334
800H	0.0591±0.0111	0.1349±0.0185	0.1488±0.0177	0.1529±0.0366	0.1624±0.0452	0.1526
Haynes230	0.1007±0.0108	0.1193±0.0081	0.1301±0.0076	0.1385±0.0069	0.1442±0.0071	0.1474
Alloy625	0.0890±0.0193	0.1172±0.0212	0.1232±0.0237	0.1311±0.0178	0.1541±0.0010	0.1769
PE16	0.0900±0.0211	0.1062±0.0348	0.1279±0.0367	0.1454±0.0531	0.1255±0.0265	0.1678
PM2000	0.0385±0.0029	0.0467±0.0054	0.0468±0.0065	0.0567±0.0014	0.0642±0.0020	0.0716
# Samples	6	5	4	3	2	1

The weight of the samples prior to and after successive 500-hour exposures was measured by a precision Sartprois CPA26P weighing balance with a readability of 2 µg. The results are summarized in Table 2. Significant weight gain was observed for the ferritic-martensitic steels F91 (8.18 ± 1.24 mg/cm^2) and HCM12A (13.80 ± 3.45 mg/cm^2) based on the data of 6 samples per steel exposed to the S-CO_2 for 500 hours. Distinct oxide scale exfoliation was observed on both steels to different degrees. Due to the excessive exfoliation these alloys were removed for the longer-term study.

The weight change as a function of exposure time of all the alloys tested (minus P91 and HCM12A) are plotted in various forms in Figure 25*,* Figure 26*, and 4.0.3.* Weight gain was observed on all the samples. The alloys can be divided into 4 groups according based on their weight gain levels. The 316SS, group (I) as labeled in Figure 25, showed a small weight gain after 500 hours exposure, which is similar to the other alloys. However, the weight gains significantly increased with exposure times differentiating it from the other alloys.

The detailed weight gains of the other alloys in group (II) - (IV) are shown in Figure 27 The ferritic steel PM2000, group (IV), showed the smallest weight gain as a function of exposure time. Similar weight gains were observed for the alloys 310SS and AL-6XN, group (II). Unlike the relatively constant weight gain of the alloy AL-6XN, the alloy 310SS showed a maximum weight gain after exposure for ~1500 hours, suggesting the possibility of exfoliation. The alloys 800H, Haynes 230, Inconel 625, and Nimonic PE16, as group (III), showed similar weight gains, which are smaller than the weight gain of group (II) but larger than that of group (IV).

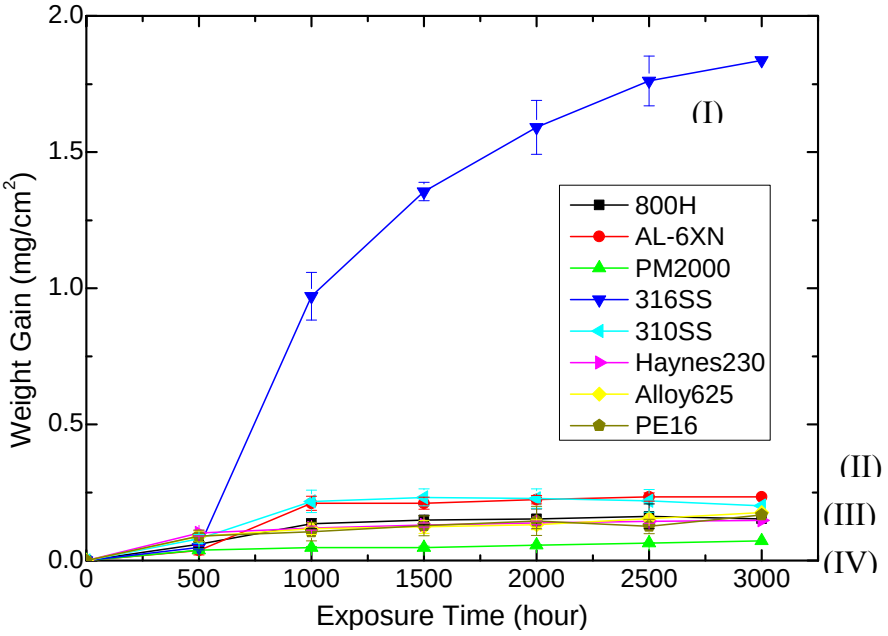

Figure 25: Weight gain of the samples exposed to the s-CO2 at 650C

.

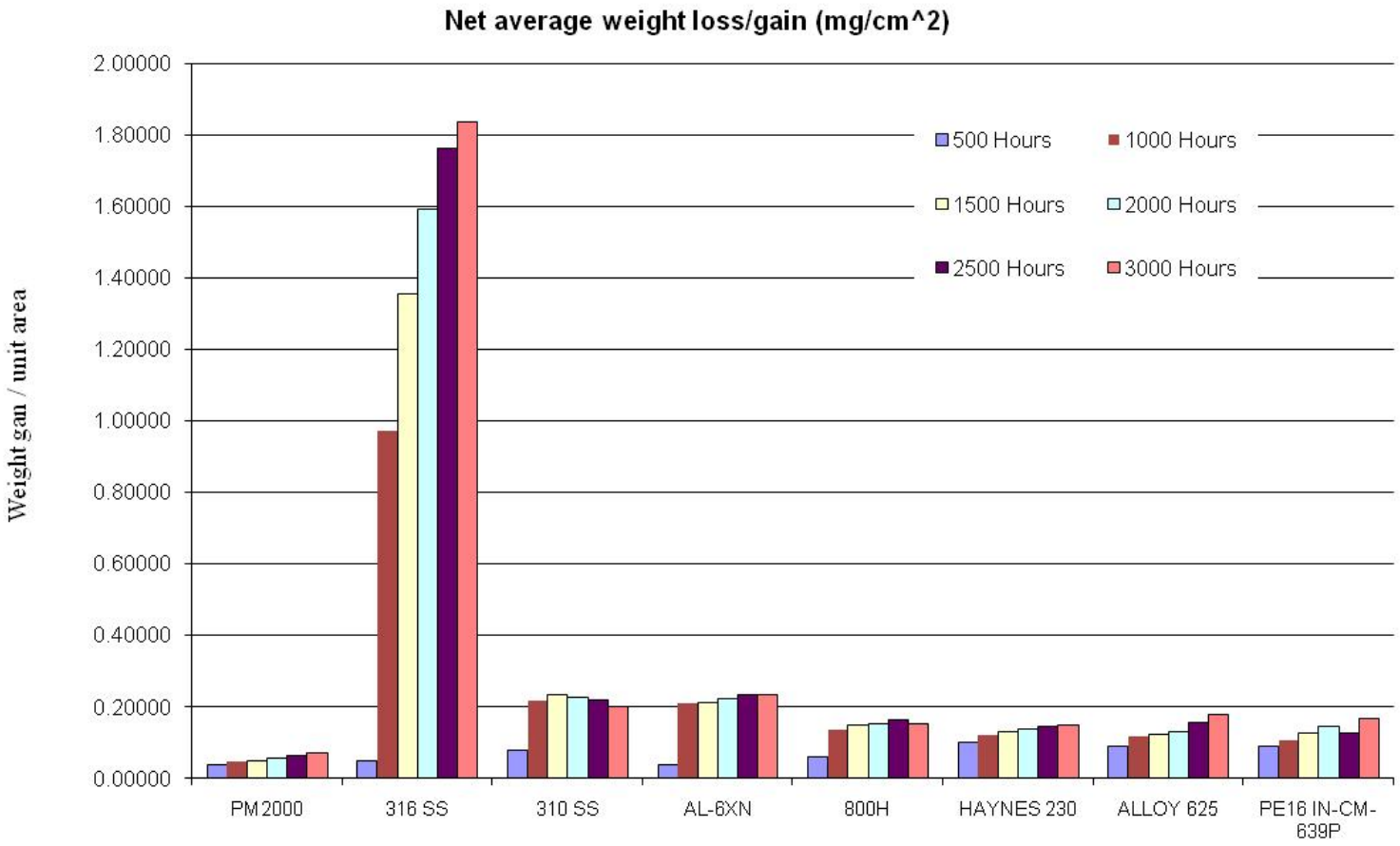

Figure 26: Bar graph of sample weights per unit exposed area

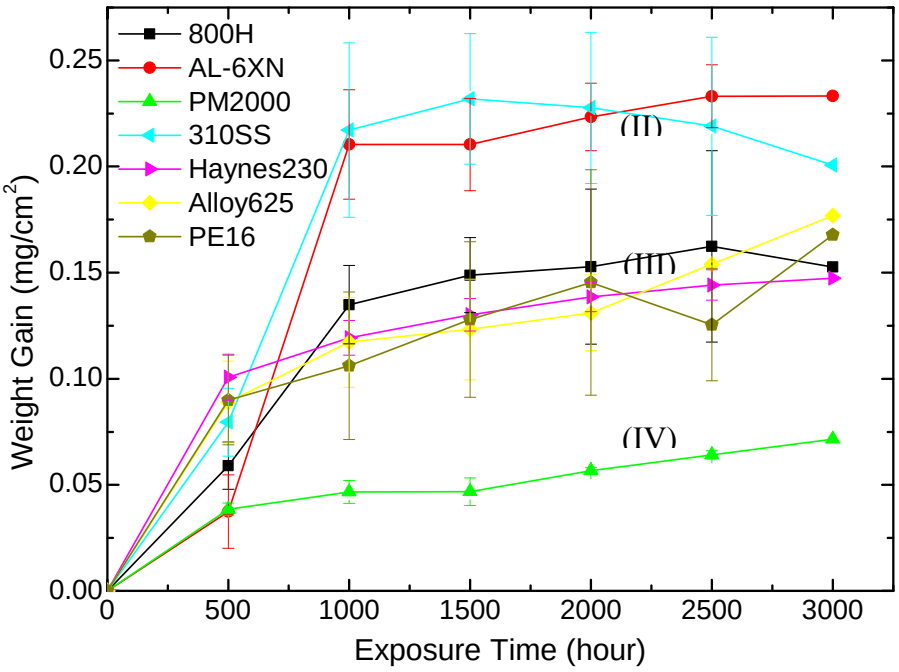

Figure 27: Weight gain of the samples exposed to the s-co2 at 650C

The weight gain data of the alloys as shown in Figure 25 and Figure 27 are fitted with $w^a = k \times t$, where w, t, a, and k are weight gain (mg/cm^2), exposure time (hour), oxide growth kinetics, and oxide growth rate constant. The fitting parameters (a and k) and fitting quality (R^2) of the alloys are listed in Table 3. Only the data of alloys Haynes 230, Inconel 625, and PM2000 showed good fitting results with the equation. The data of the Haynes 230 has the best fitting result indicating an approximately quintic growth rate law (~4.7) of the oxide scale. The oxide scale of the alloys Inconel 625 and PM2000 followed a similar approximately cubic growth rate law (~2.7). The superior corrosion resistance ferritic steel PM2000 compared to the ferritic steels P91 and HCM12A is indicative of the importance of Al in imparting corrosion resistance in the S-CO_2 at 650^{o}C.

Table 3: Results of the weight gain (w) as a function of exposure time (t) of the austenitic steels. Fitting parameters a and k denote the law of oxide growth kinetics and corresponding rate constant, respectively. The correlation coefficient (R^2) approaching 1indicates good fitting quality

Group	Alloy	Fitting Equation: $w^a = k \times t$		
		a	k	R^2
(I)	316SS	1.25	7.98×10^{-4}	0.87
(II)	310SS	3.34	2.78×10^{-6}	0.47
	AL-6XN	2.04	2.13×10^{-5}	0.66
(III)	800H	2.68	2.92×10^{-6}	0.74
	Haynes230	4.72	4.25×10^{-8}	0.99
	Alloy625	2.71	2.59×10^{-6}	0.93
	PE16	3.14	9.65×10^{-7}	0.82
(IV)	PM2000	2.72	2.21×10^{-7}	0.92

2.4 Microscopic Analysis

After corrosion tests, all alloys were examined with scanning electron microscopy (SEM, both plan and cross-sectional views) with energy dispersive X-ray spectroscopy (EDS) capabilities. Select samples were investigated by X-ray diffraction (XRD) and X-ray photoelectron spectroscopy (XPS).

2.4.1 Alloys Inconel 625, Haynes 230, PM2000 and PE16, 310SS, 316SS

The plan view of Alloy 625 after exposure to SCO_2 for 1500 hours is shown in Figure 28 A surface oxide was clearly observed and there was evidence of sporadic spallation (<5%). Figure 29shows the x-ray diffraction of the surface of Alloy 625 after exposure to SCO_2 for 1500 hours. A variety of surface oxides were observed including, $NiCr_2O_4$, Al_2O_3, FeO, NiO, and Cr_2O_3. Because x-ray diffraction was taken with the x-ray beam impinging the surface of the oxidized sample it is not possible to tell the location of each specific oxide along the depth of this multi-layered oxide structure. Figure 30shows the cross-sectional SEM image of the oxide layer formed on Alloy 625 after exposure to SCO_2 for 1500 hours and the corresponding EDS compositional line scan. The oxide layer was approximately 0.6□m thick and consists predominantly of a Cr-rich oxide.

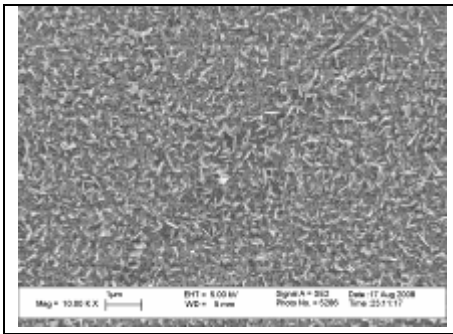

(a)

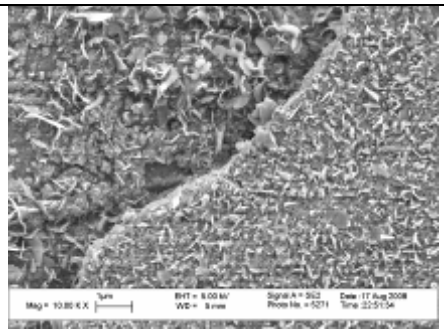

(b)

Figure 28: Surface morphology of alloy 625 after 1500 hours exposure (a) typical structure, and (b) sporadic spallation (<5%)

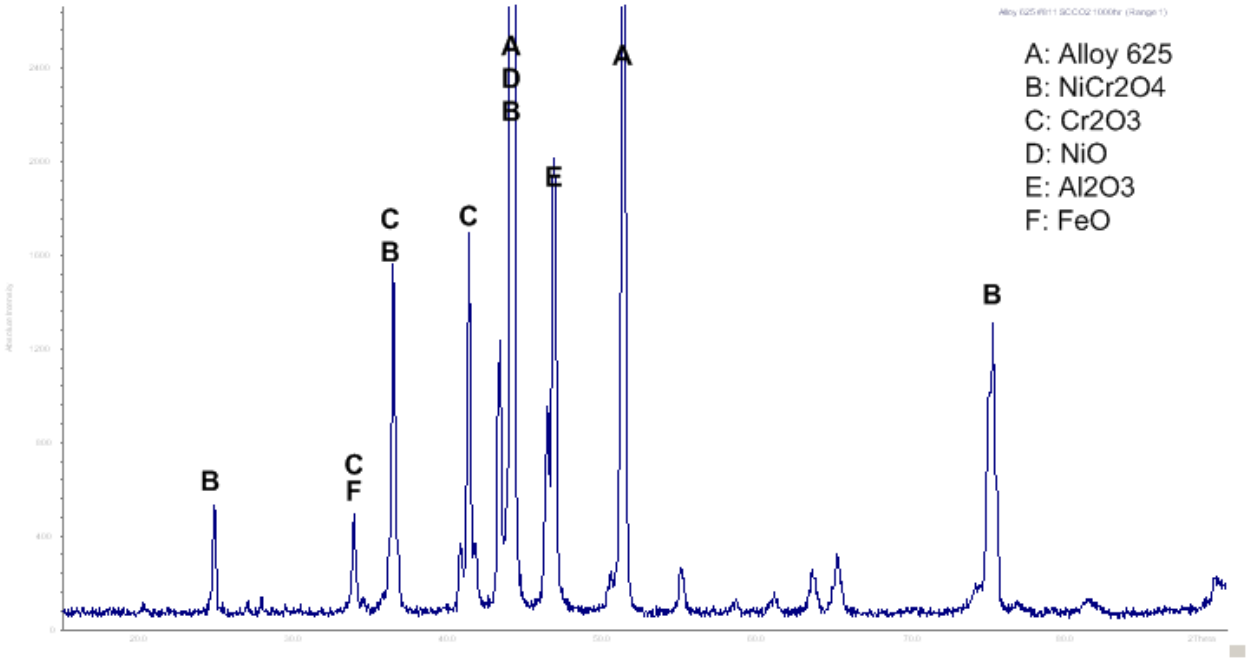

Figure 29: X-ray diffraction pattern of the surface oxide formed on Alloy 625 after 1500 hours exposure (a) typical structure, and (b) sporadic spallation (<5%)

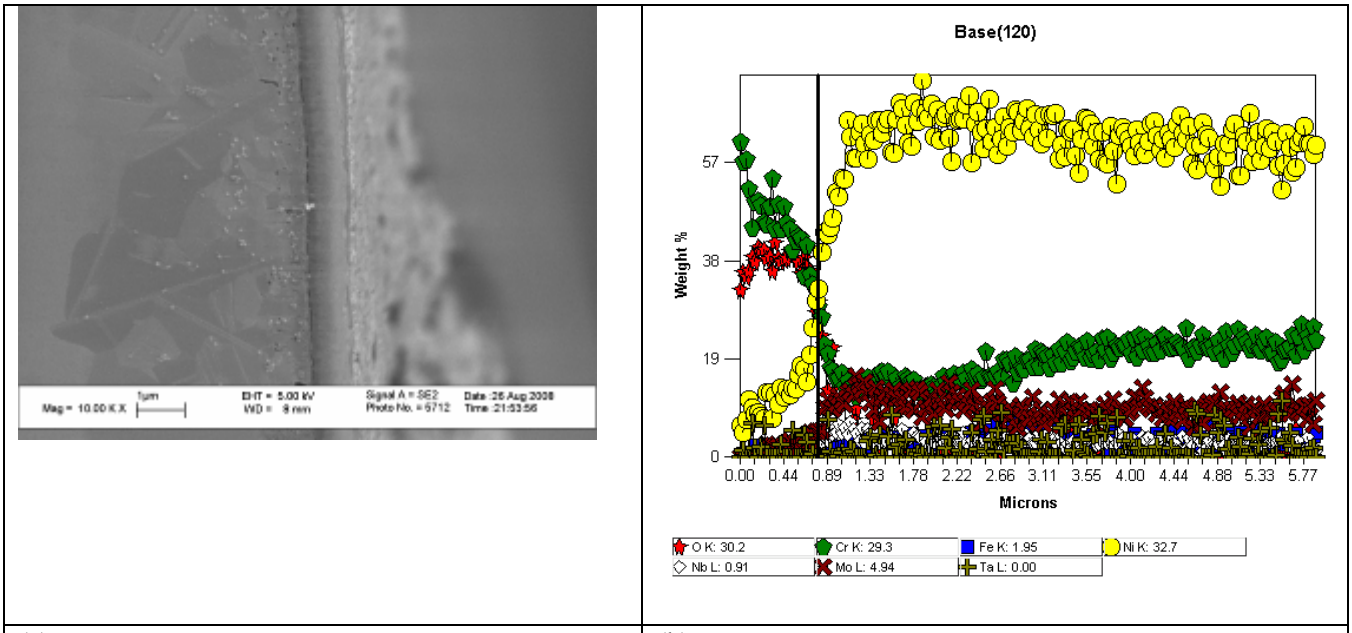

(a) (b)

Figure 30: (a) SEM cross-sectional image of the oxide layer formed on Alloy 625 after 1500 hours exposure and (b) the corresponding EDS compositional line-scan

The oxide layer structure and thickness formed on Haynes 230 was very similar to that observed on Alloy 625. Figure 31 shows SEM plan and cross-sectional image views of the oxide layer formed on Haynes 230 after exposure for 1500 hours, as well as elemental x-ray mapping and EDS line-scan of the oxide layer.

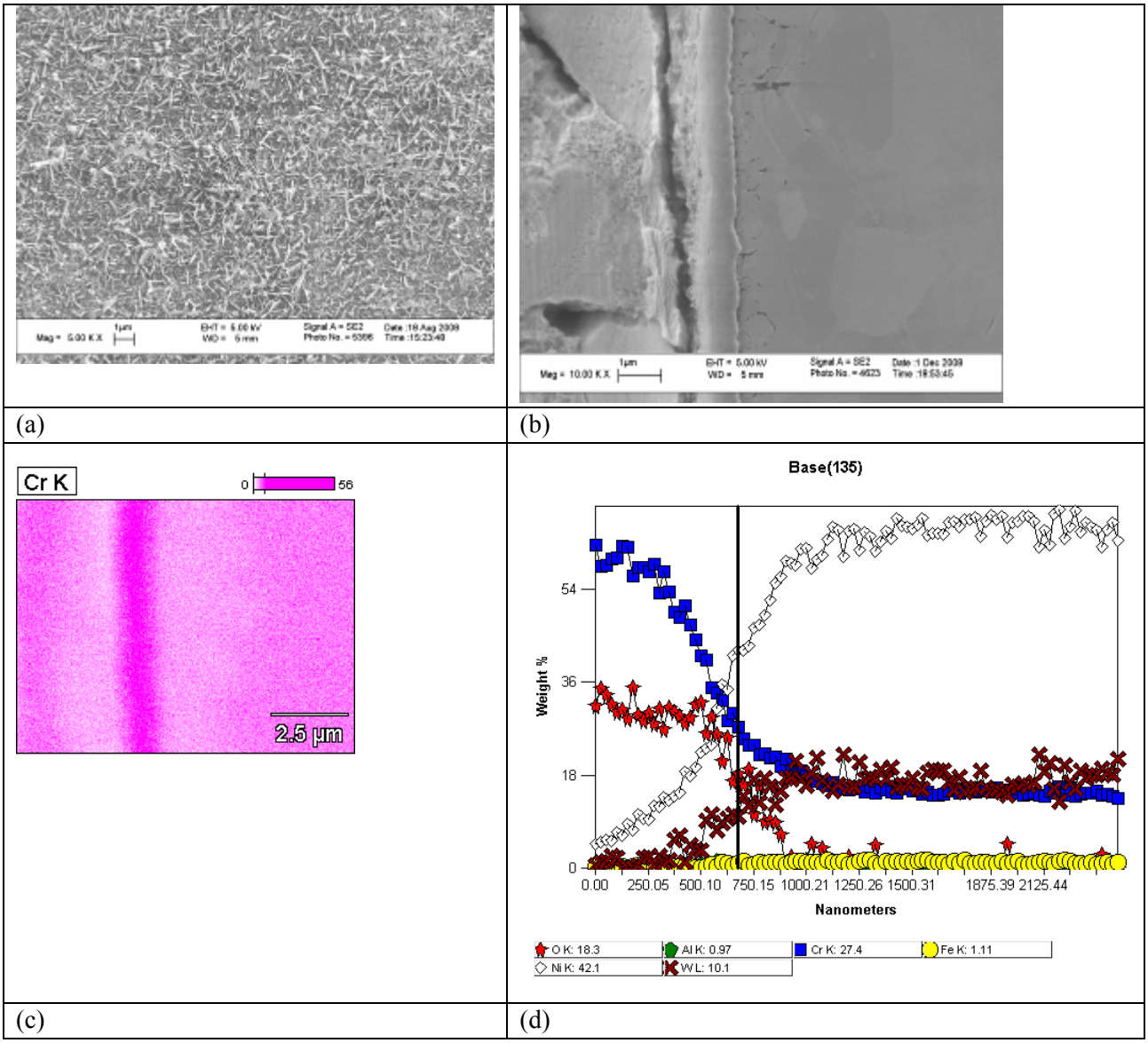

Figure 31: (a) SEM-EDS analysis of the oxide layer formed on Haynes 230 after exposure for 1500 hours, (a) plan view, (b) cross-sectional view, (c) x-ray mapping showing enrichment of Cr, and (d) EDS line scan showing a Cr-rich oxide layer.

Alloy PE16 performed similarly to Alloys 625 and Haynes 230 in terms of the general oxide layer structure and thickness and derived its corrosion resistance from a Cr-rich oxide layer on the surface. This alloy also exhibits a thin Al_2O_3 inner layer. Figure 32shows cross-sectional image of the oxide layer and the corresponding EDS compositional line scan for alloy PE 16 after exposure for 1500 hours.

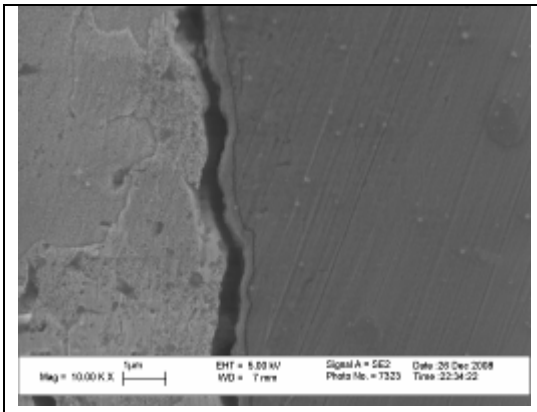

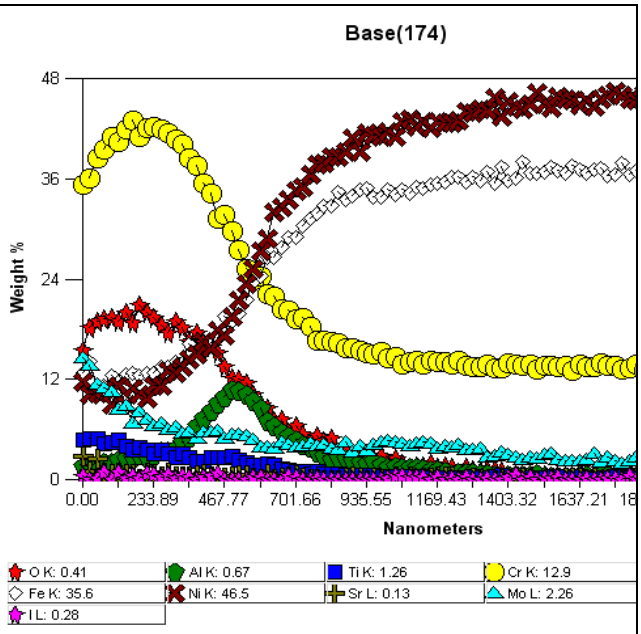

(a) (b)

Figure 32: (a) SEM cross-sectional image of the oxide layer formed on Alloy PE16 after 1500 hours exposure and (b) the corresponding EDS compositional line-scan.

The ferritic alloy PM2000 exhibited the best corrosion resistance. The surface of this alloy showed an Al_2O_3 layer on account of the high Al content of this alloy (5.5%). This is particularly interesting in light of the fact that the two other ferritic (T91 and HCM12A) exhibited very poor corrosion resistance, despite their high Cr-contents. This observation attests to the importance of Al in imparting corrosion resistance at 650^{o}C in SCO_2 environment. Figure 33shows the results of the SEM-EDS analysis of the alloy PM2000.

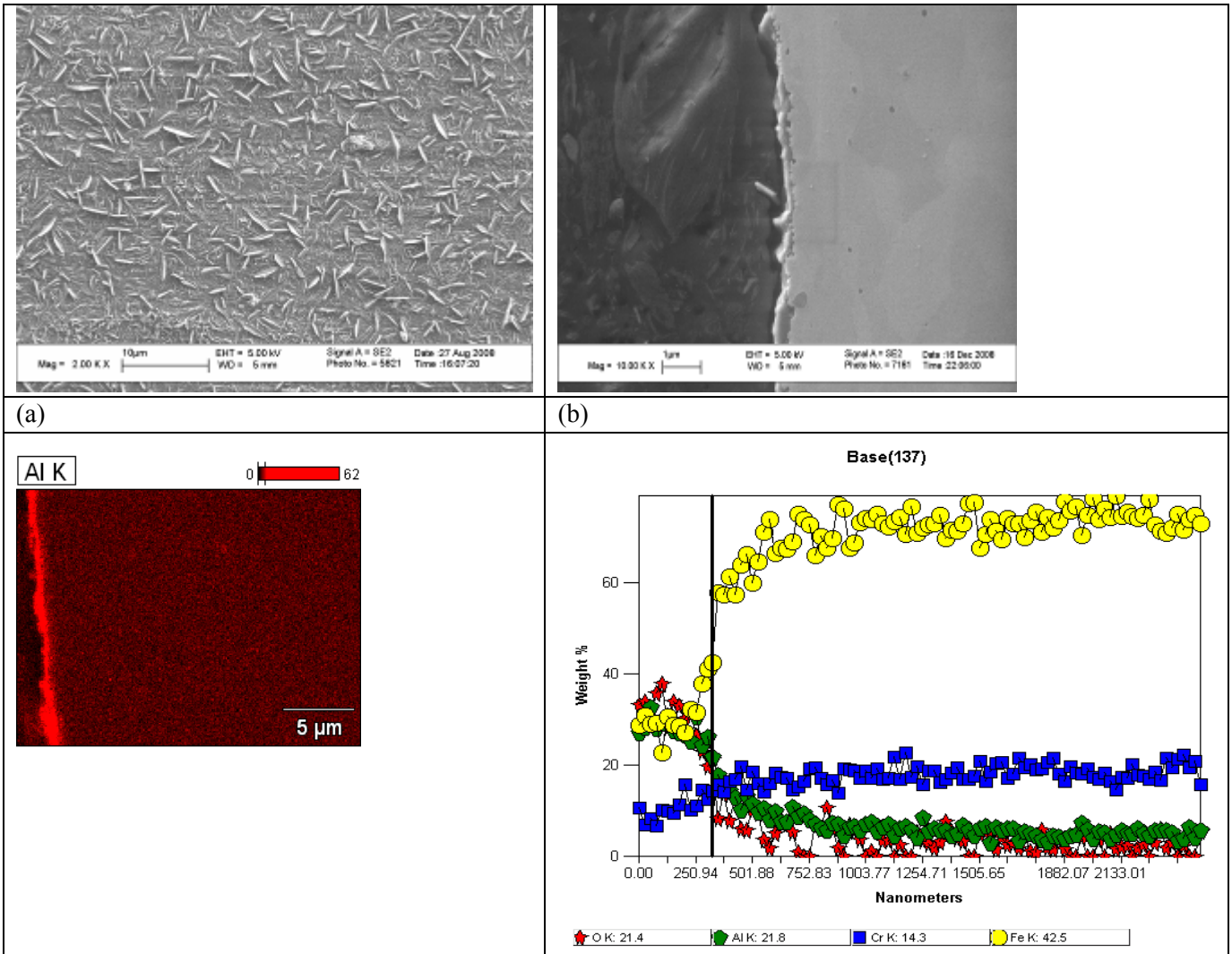

Figure 33: (a) SEM-EDS analysis of the oxide layer formed on PM2000 after exposure for 1500 hours, (a) plan view, (b) cross-sectional view, (c) x-ray mapping showing Al-rich oxide layer, and (d) EDS line scan confirming an Al-rich oxide layer.

316 stainless steel exhibited poor corrosion resistance. Figure 34shows SEM analysis of this steel after exposure to SCO_2 at 650°C. The oxide layer showed large grains and evidence of spallation. The outer layer of the oxide consisted of magnetite (Fe_3O_4) and the inner layer consisted of (Fe,Cr) spinel oxide layer.

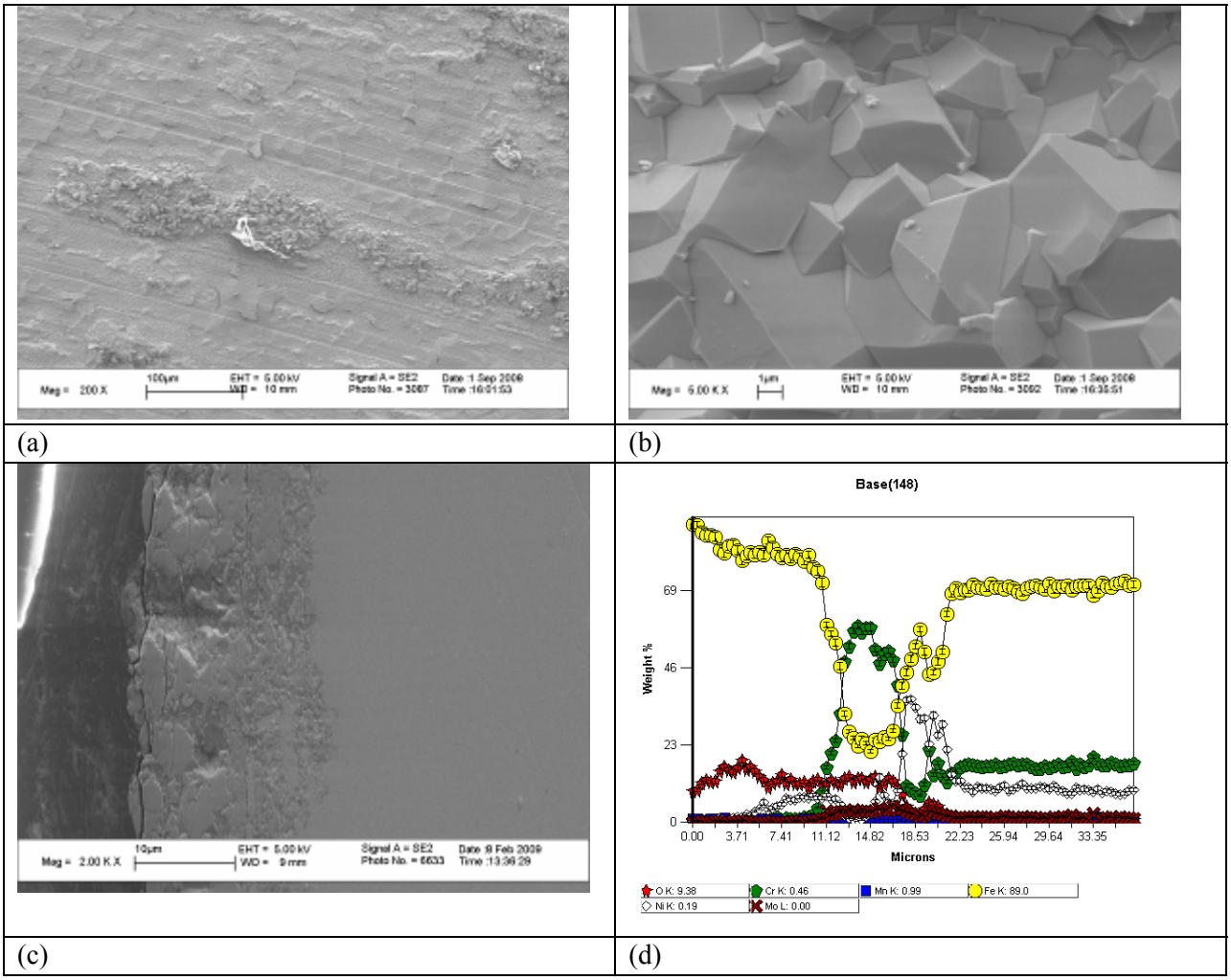

Figure 34: (a) SEM-EDS analysis of the oxide layer formed on 316 stainless steel after exposure to S-CO2 at 650C, (a) plan view (1000 hours exposure), (b)plan view(1000 hours exposure), (c) cross-sectional view (1500 hours exposure), and (d) EDS line scan across the oxide layer (1500 hours exposure)

310 stainless steel showed better corrosion resistance than 316 stainless steel. The structure of the oxide layer was similar in that it consisted of an outer Fe_3O_4 layer and an inner (Fe,Cr) spinel oxide layer. As in the case of 316 stainless steel oxide spallation was observed. Figure 35 shows the cross-sectional image of the oxide layer and the corresponding EDS line scan analysis of the oxide layer formed on 310stainless steel after exposure to SCO_2 at 650^{o}C for 1500 hours.

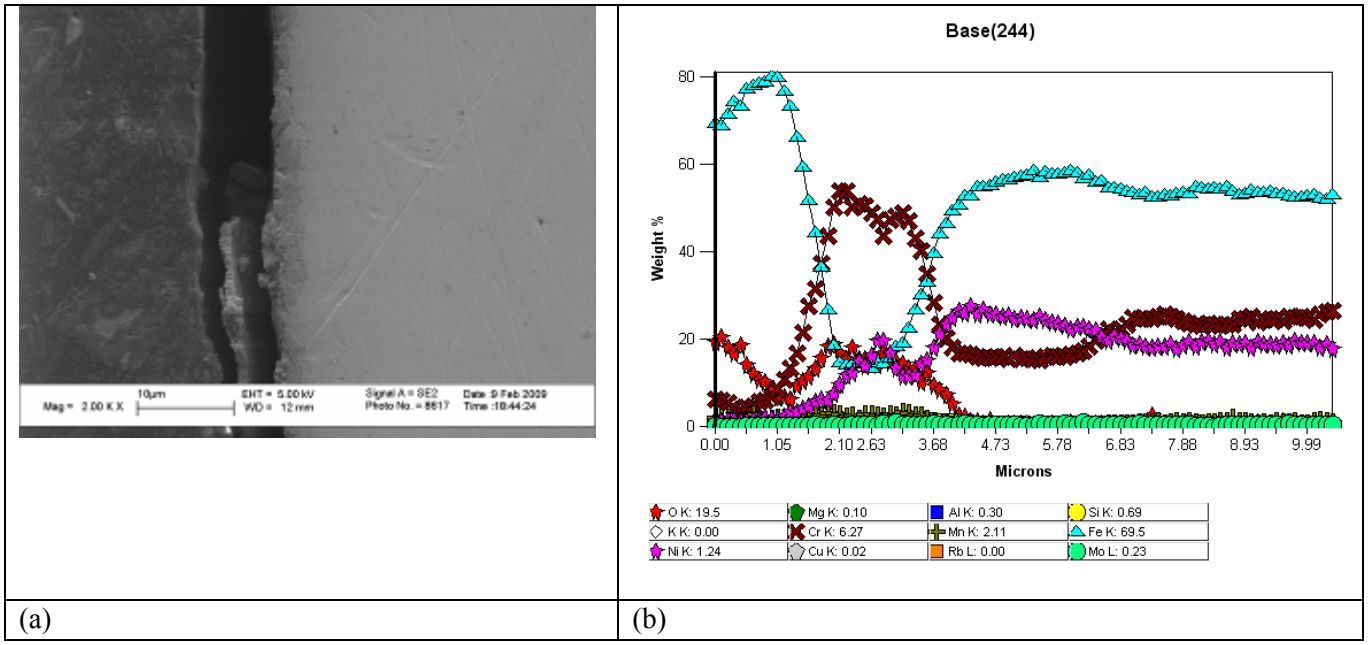

(a) (b)

Figure 35: (a) SEM cross-sectional image of the oxide layer formed on 310 stainless steel after 1500 hours exposure and (b) the corresponding EDS compositional line-scan.

2.5 Alloys 800H, AL-6XN, F91, and HCM12A (detailed studies)

Austenitic and ferritic-martensitic (9-12 wt% Cr) steels are two important categories of candidate materials for core components and reactor internals. Incoloy alloy 800H (UNS N08810) has high strength and corrosion resistance at high temperatures up to 760°C supported by a current American Society of Mechanical Engineers (ASME) code. It has been broadly utilized in furnace components and equipment, and sheathing for electrical heating elements since its introduction to the market in the 1950s. Alloy 800H (Fe-31Ni-20Cr) is an austenitic solid-solution steel, generally used in the annealed condition, with a microstructure consisting of the matrix austenite phase and small amounts of precipitates such as titanium nitrides, titanium carbides, and chromium carbides. The excellent oxidation resistance of alloy 800H is attributable to the high chromium and nickel contents. The chromium in this alloy promotes the formation of a protective surface oxide, and the nickel enhances the stability of the protective oxide, especially during cyclic exposure to high temperatures [[i]].

Alloy AL-6XN (UNS N08367), introduced into market in the 1980s, is a low carbon, high purity, nitrogen-bearing super-austenitic stainless steel. It was designed to be a seawater resistant material and has since been demonstrated to be resistant to a broad range of very corrosive environments. The combined features of increased strength, due in part to the interstitial strengthening effect of nitrogen, with improved corrosion resistance, because of the high nickel and molybdenum contents, have led to extensive usage of AL-6XN in chemical plants and power plants. Alloy AL-6XN (Fe-24Ni-20Cr-6Mo-.2N) is metallurgically stable to 510°C. Secondary (sigma) phase may precipitate at grain boundaries due to the high chromium and molybdenum contents when the alloy is subjected to long exposures to higher temperatures in the range of 650-980°C [[ii]]. Sigma phase precipitation will impair the corrosion resistance of AL-6XN alloy long before it influences the mechanical properties [[iii]].

Ferritic-martensitic steels have been widely studied and developed for applications in the energy industry. Their performance in various energy systems has been reviewed by Klueh and Harries [[iv]]. For example, F91 (9Cr-1Mo; 'F' is designated for forgings. It is also known as F91 or P91 for different forms such as tubing or

piping) has been increasingly used for super heater components with steam inlet temperatures up to 593°C and reactor components such as cladding applications. With the T/P91 as the basis, HCM12A (12Cr-MoVNbWCu, also known as T122 or P122 for tubing or piping) had been developed in Japan for improved performances at higher temperatures up to 620°C and pressures up to 34 MPa [v].

Literature reports on corrosion of steels exposed to pure S-CO_2 are very limited. Austenitic stainless steels 304L and 316 had shown insignificant corrosion (within ~1 μg/cm^2 weight loss) when they were exposed to pure S-CO_2 at 50°C and 24.1 MPa for 24 hours [vi]. Although alloys 800H, AL-6XN, F91, and HCM12A have been used in a variety of applications for a long period of time, their corrosion behavior in pure S-CO_2 has not been reported. Alloy AL-6XN has a Cr content similar to alloy 800H ($Cr_{800H} \approx Cr_{AL\text{-}6XN}$) but with a high concentration of Mo (~6 wt%) substituting part of the Ni content ($Ni_{800H} \approx Ni_{AL\text{-}6XN} + Mo_{AL\text{-}6XN}$). It is interesting to compare the corrosion behavior between the two austenitic alloys as well as the two ferritic-martensitic steels with different Cr content. This work presents the corrosion behavior of these four steels exposed to pure SC-CO_2 as part of the efforts in evaluating candidate materials for use in advanced nuclear systems.

Commercial steels of Incoloy 800H, AL-6XN, F91, and HCM12A were used in this study. Their typical measured chemical compositions are listed in Table 1. Sample disks in a diameter of ~15.9 mm and thickness of ~0.5 mm were cut from the steels. A ~3mm diameter hole close to the disks edge was drilled on each sample for fixing it during the testing. The samples with a surface finish of 32 root-mean-square (rms) roughness were ultrasonically cleaned prior to exposure to high-purity CO_2 (99.9998%) at 650°C and 20.7 MPa with a flow rate of ~0.3 g/min for a variety of times up to 3000 hours.

The weight of the samples prior to and after successive 500-hour exposures was measured by a precision Sartprois CPA26P weighing balance with a readability of 2 μg. The samples were analyzed by using scanning electron microscopy (SEM), energy dispersive X-ray spectroscopy (EDS), focused ion beam (FIB), X-ray diffraction (XRD), and X-ray photoelectron spectroscopy (XPS). A LEO 1530 field emission SEM integrated with a Thermo-Noran SIX EDS system was used for characterizing plan-view and cross-section samples. Cross-section samples were mounted and polished with SiC abrasive paper down to 1200 grit followed by sequential polishing with 1 μm diamond paste, alpha alumina, and colloidal silica solutions. A FIB integrated in a Zeiss 1500XB crossbeam workstation was used to prepare cross-section samples with thin oxide scales. A STOE diffractometer was used for phase identification. A Perkin-Elmer PHI 5400 ESCA (electron spectroscopy chemical analysis) system was employed for surface chemistry analysis.

2.5.1 Gravimetry

The weight measurement results of the austenitic steels 800H and AL-6XN samples are summarized in Figure 36. Weight gain was observed on these samples, which increased with exposure time and reached a relatively stable weight gain after being exposed for ~1000 hours. The AL-6XN samples showed a larger weight gain than the 800H samples except for the short time exposed samples (i.e. 500 hours). Slight oxide exfoliation may have occurred on the AL-6XN samples exposed for 500 hours. Both of the alloys 800H and AL-6XN showed remarkably large weight gain compared to the ~1 μg/cm^2 weight loss of stainless steels 304L and 316 exposed to S-CO_2 at 50°C and 24.1 MPa for 24 hours [vi], which suggests the critical effect of testing temperature and time.

Compared to the austenitic steels, significant weight gain was observed for the ferritic-martensitic steels T91 (8.18 ± 1.24 mg/cm^2) and HCM12A (13.80 ± 3.45 mg/cm^2) based on the data of 6 samples per steel exposed to the S-CO_2 for 500 hours. Distinct oxide scale exfoliation was observed on both steels to different degrees. Due to the large weight gain and excessive exfoliation these alloys were removed for the longer-term study.

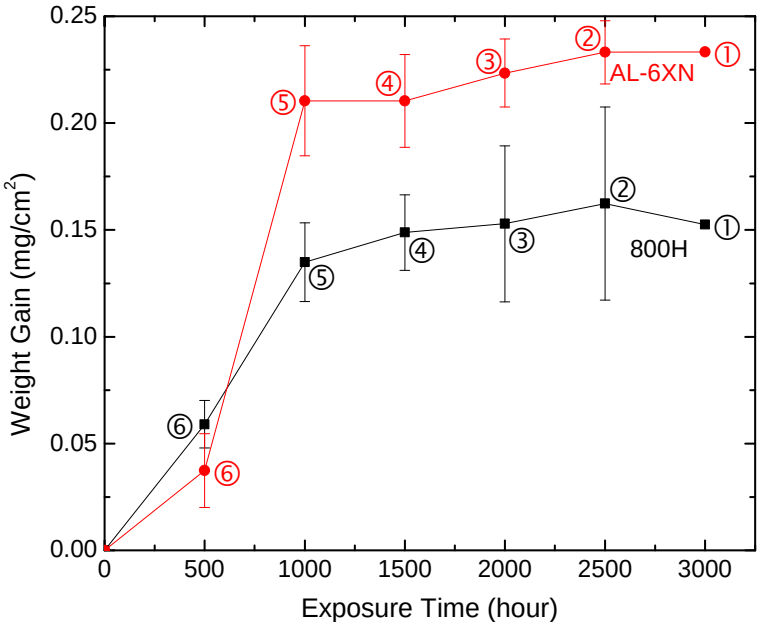

Figure 36: Weight gain (with standard deviation) of the austenitic steels 800H and Al-6XN exposed to the S-CO2 at 650C and 20.7 MPa. The circled numbers denot the corresponding number of samples for each data point

2.5.2 Austenitic steels

The surface morphologies of the alloy 800H samples exposed to the S-CO_2 at 650°C for 500 and 1500 hours are shown in Figure 37. The surface morphologies of the samples exposed for the other exposure times are similar to the samples exposed for 1500 hours. Grooves generated from sample preparation are still observable on these samples, especially for the short time exposed samples, which suggests the thin nature of the oxide scale. The short-time exposed samples are not completely covered by oxide scale. Although the long-time exposed samples are completely covered by oxide scale, the oxide scale is not homogeneous in the plan-view. The detailed morphologies of the features labeled a-d are also shown in Figure 37. Grooves and pits in a sub-micron size were evident on the surface uncovered from oxide scale (a). Nodular oxide scale (b) was formed on the short-time exposed samples, which was mostly decorated with flakes in a size from sub-micron to micron (c). These types of flakes were also observed on HCM12A samples exposed to supercritical water at 500°C and 25 MPa with 2 part-per-million (ppm) dissolved oxygen, and were identified as Cr_2O_3 [vii]. Many large angular oxide grains in a micron size (d) were formed on the long-time exposed samples. Such angular oxide partially covers the sample surface.

Cross-section microstructure of the alloy 800H samples at the locations of Figure 37*(c) and (d)*, prepared by FIB to maximize the possibility of presenting the features of the thin oxide scales, is shown in Figure 38. Although some FIB artifacts, e.g. vertical grooves resulting from the heterogeneity of the oxide scale and defects, are observable on the images, they do not affect the nature of the oxide scale. A two-layer oxide scale with a thickness of ~0.8 µm was formed on the short time exposed samples. The outer layer, incompletely covered the samples as shown in the plan-view images in Figure 37, is enriched with Cr together with some Mn and Fe. Some sub-micron pores and nano-pores exist in the outer layer with larger pores close to the outer side. A continuous thin layer (in nanometers) of oxide enriched with Al formed directly on the metallic substrate including the regions uncovered with the outer oxide. Some nano-pores and internal oxidation with Al-rich oxide were also observed at the oxide-metal interface. The oxide scale on the long-time exposed samples is also primarily composed of two layers. The thickness of the oxide scale ranges from ~2.3 – ~4.9 µm, which is not as

uniform as that on the short-time exposed samples. The outer layer, enriched with Fe, shows an angular interface between the oxide and the deposited Pt-layer for protecting the surface during FIB specimen preparation, which corresponds to the angular oxide shown in Figure 37*(d)*. Some sub-micron pores still exist in the outer layer. The inner layer, enriched with Cr, embraces some Ni-enriched metallic islands. The continuous Al-rich nano oxide layer formed on the short-time exposed samples becomes discontinuous in the long-time exposed samples at the oxide-metal interface, where some sub-micron pores also exist.

The surface morphologies of the AL-6XN samples exposed to the SC-CO_2 at 650°C for 500 and 1500 hours are shown in Figure 39. Similar to the short-time exposed alloy 800H samples, grooves are also shown on the short-time exposed alloy AL-6XN samples. But such grooves are not shown on the long-time exposed samples, which suggest the formation of thicker oxide scale compared to that on the alloy 800H samples. The detailed morphologies of the features labeled with a-d are also shown in Figure 39. Sub-micron pits are shown at the regions uncovered with oxide scale (a). The oxide scale with cracks (b) formed on the short-time exposed samples shows much denser flakes than those shown in Figure 37*(c)*. The oxide grains on the long-time exposed samples (c) are approximately in the same size, but not as sharply angular, as those formed on the alloy 800H samples as shown in Figure 37 *(d)*. Some platelets composed of dense oxide (d) in a diameter of tens of microns are discretely distributed on the long-time exposed samples.

Cross-section microstructure of the alloy AL-6XN samples at the locations of Figure 39*(b) and (d)*, prepared by FIB is shown in Figure 40. The oxide scale with a thickness of ~0.8 μm, enriched with Cr, was observed on the short-time exposed sample as shown in Figure 40. It usually debonds from the metallic substrate, resulting in a gap between the oxide and the substrate. Such debonding of the oxide scale is believed to be due to the formation of volatile molybdenum trioxide (MoO_3), which is one of the products of oxidation of alloy AL-6XN and is usually evaporated from the metal surface at high temperatures [ii]. The turned up edges of the oxide showing a high contrast in Figure 39 (500 hrs) result from the debonding of the oxide from the substrate. The thickness of the long-time exposed alloy AL-6XN samples (~3.3 – ~6.1 μm) is thicker than that on the alloy 800H samples, which is consistent with the greater weight gain of the alloy AL-6XN samples as shown in Figure 36. The oxide scale on the long-time exposed samples is composed of two layers with some discretely distributed platelets at surface. The platelets with a thickness of ~1.1 μm, identified as chromium oxide with EDS, exist on the oxide scale with a big gap between the platelet and the oxide scale. The platelets are believed to come from the debonded scale during the short-time exposure. Similar to the oxide scale on the long-time exposed alloy 800H samples, the outer and the inner oxide layers are enriched with Fe and Cr, respectively. Pores ranging from microns to nanometers exist in the oxide scale with larger pores close to the outer layer. Many sub-micron precipitates in bright contrast, as shown in *Figure 5.2.5*, were observed in metallic substrate of the long-time exposed alloy AL-6XN samples. Such precipitates are believed to be sigma phase due to their Mo-enrichment.

XRD was employed to identify the phases of the SC-CO_2 exposed samples. The typical XRD patterns of the short-time (500 hours) and long-time (1500 hours) exposed alloy 800H and AL-6XN samples are shown in Figure 41. The pattern of austenite (metallic substrate) showed the strongest intensity for both the alloys 800H and AL-6XN samples. Thus, the y-axis of Figure 41 is truncated to illustrate the phases of the oxide scales. The oxide scale of the short-time exposed alloy 800H sample is primarily composed of chromium oxide (e.g. $Cr_{1.3}Fe_{0.7}O_3$ or Cr_2O_3) with some Cr- and Mn-enriched spinel (e.g. $(Cr,Mn,Fe)_3O_4$) and trace amount of alumina (e.g. Al_2O_3). The long-time exposure of the alloy 800H sample did not change the constitution of the oxide phases but altered the fraction to be primary Fe-enriched spinel with some chromium oxide and small amount of alumina.

Compared to the alloy 800H samples, the oxide scale of the short-time exposed alloy AL-6XN sample is primarily composed of chromium oxide with a trace amount of spinel. In addition to the oxide phases, sigma

phase (e.g. $Fe_{18}Cr_6Mo_5$) was identified, which corresponds to the bright precipitates dispersed in the metallic substrate as shown in Figure 40. The effect of the sigma phase on the corrosion of AL-6XN in the S-CO_2 is still not clear although it is generally detrimental to corrosion resistance [ii]. The oxide scale still maintained primary a chromium oxide after a long-time exposure, but the fraction of spinel was significantly increased.

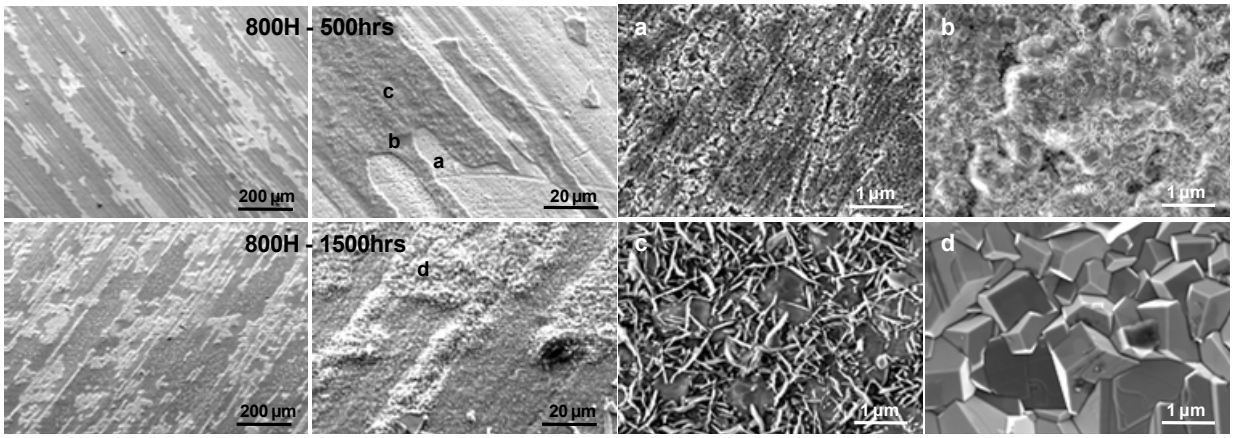

Figure 37: Surface morphologies of the ally 800 H samples exposed to the S-CO2 at 650C for 500 and 1500 hours. The detailed morphologies of the features labeled with a-d are shown in the secondary electon imges on the right.

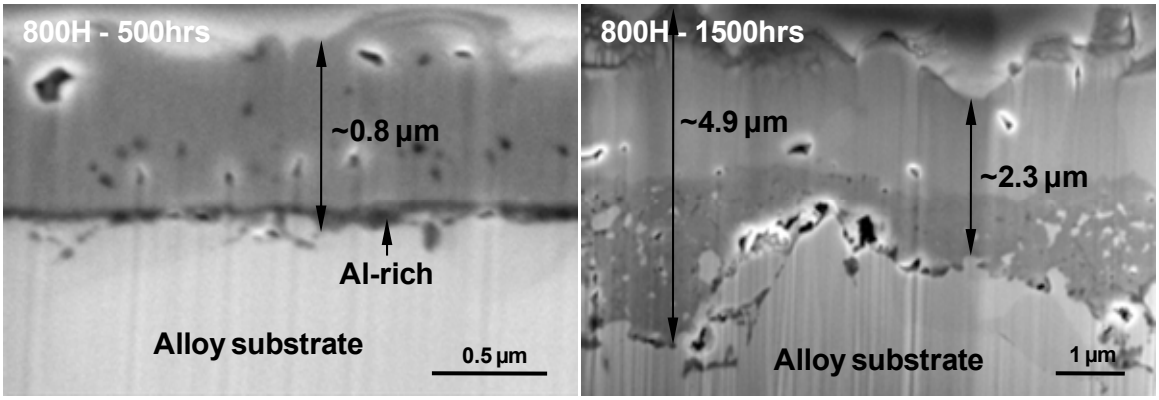

Figure 38: Seconday electon images of the cross-secional alloy 800H samples exposed to the s-Co2 at 650C for 500 and 1500 hours

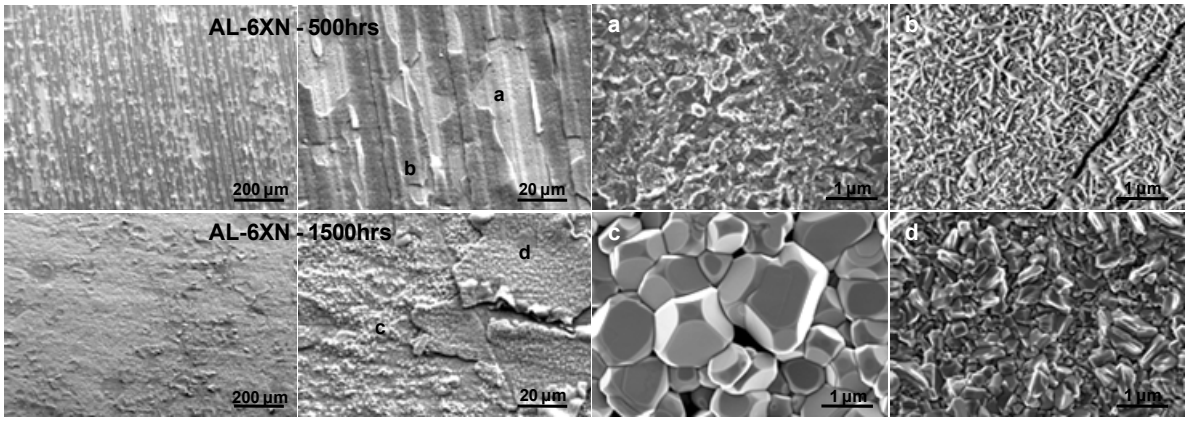

Figure 39:Surface morphologies of the alloy AL-6XN samples exposed to the S-CO2 at 650C for 500

and 1500 hours. The detailed morphologies of the features labeled with a-d are shown in the secondary electron images on the right.

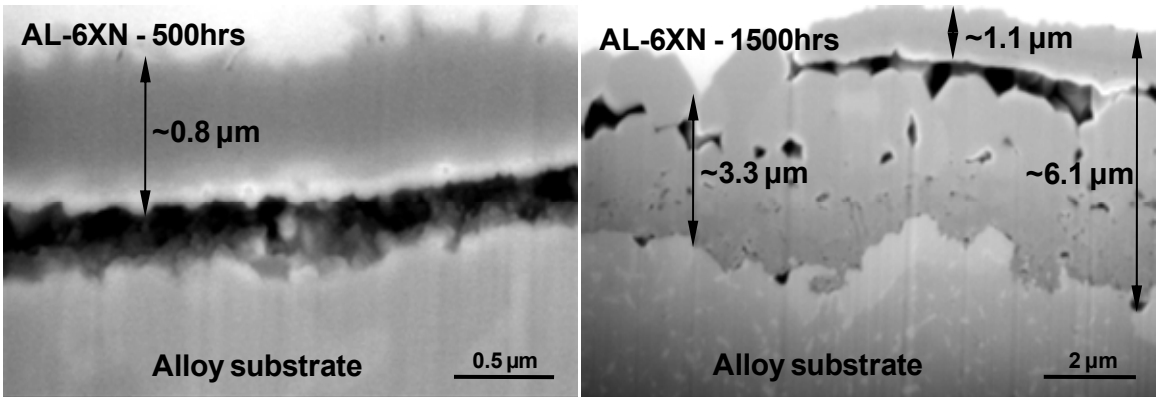

Figure 40: Secondary electron images of the cross-sectional alloy AL-6XN samples exposed to the S-CO2 at 650C for 500 and 1500 hours

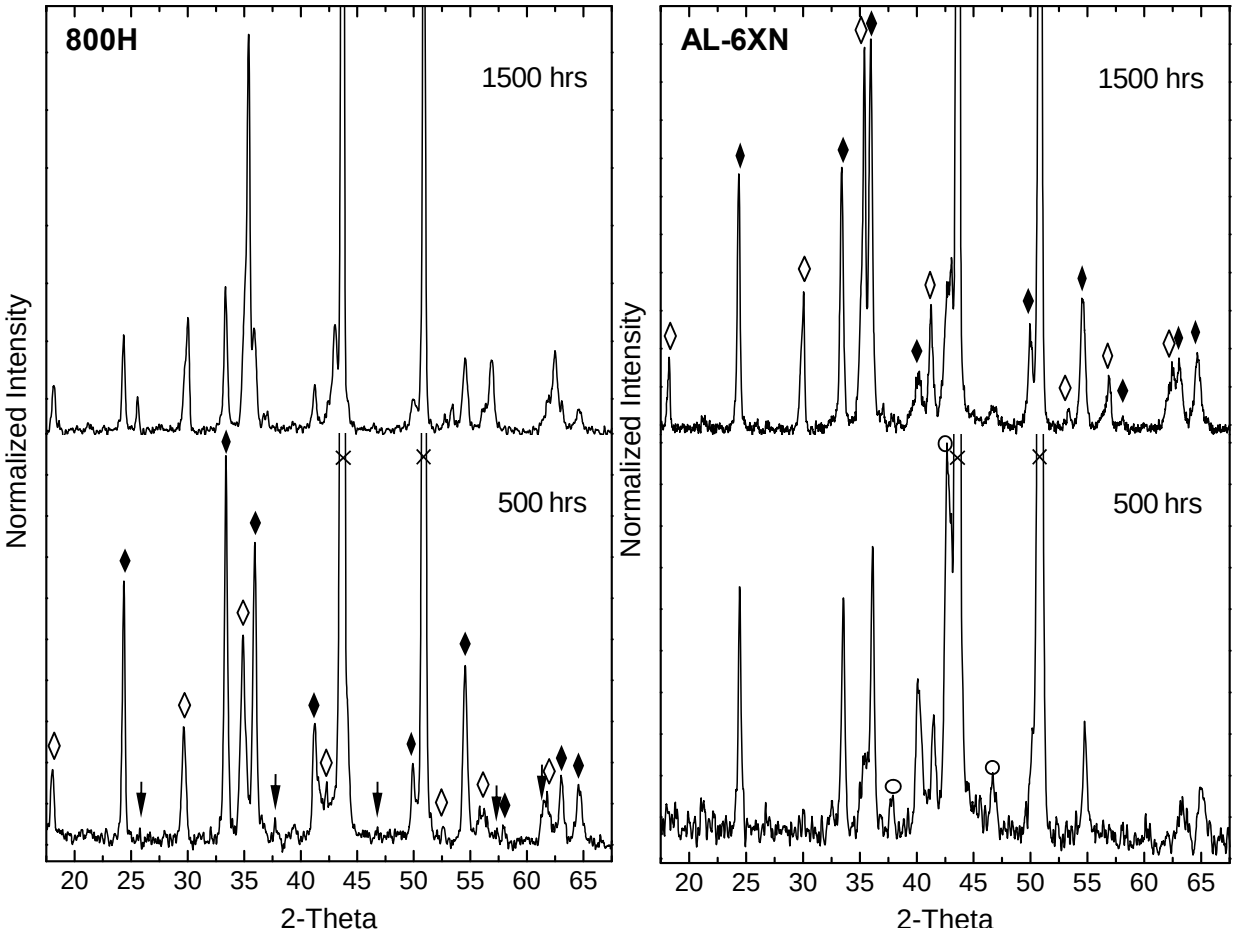

Figure 41: X-ray diffraction patterns of the alloys 800H and AL-6XN samples exposed to the SC-CO2 at 650°C for 500 and 1500 hours. The symbols ◊, ♦, ↓, ○, and × denote spinel (e.g. (Cr,Mn,Fe)3O4 [44-909]), chromium oxide (e.g. Cr1.3Fe0.7O3 [35-1112] or Cr2O3 [38-1479]), alumina (e.g. Al2O3 [10-173]), sigma phase (Fe,Ni)3(Cr,Mo)2 (e.g. Fe18Cr6Mo5 [8-200]), and austenite (i.e. substrate), respectively

.

2.5.3 Ferritic-martensitic steels

The surface morphologies and oxide scale structure of the ferritic-martensitic steels are distinct from the austenitic steels. The plan-view and cross-section images of the 500 hours exposed F91 and HCM12A samples are shown in Figure 42. The plan-view images show that the surface morphologies of the two steels are pretty similar to each other with angular oxide grains and some cracks. A typical oxide layer structure with a thickness of ~45.7 μm was observed on both sides of the sample disk. But a significantly thicker oxide scale (~127 μm) was observed at the peripheral of the sample disk. The oxide scale is primarily composed of outer magnetite (without Cr) in large columnar grains and inner spinel (with Cr) in fine equiaxial grains. A thin layer of internal oxidation (~5 μm) was also observed following the thick oxide scale at the peripheral of the sample disk. Many large pores in a micron size exist in the outer layer. Some of the mounting materials (white) were trapped in the pores during sample grinding and polishing. Compared to the cross-section sample of the F91, the thick oxide scale on the HCM12A sample was completely exfoliated during sample cutting for mounting cross-section samples. The mounted sample only shows a thick internal oxidation layer (~25.6 μm) enriched with Cr and some W. Some cleaved oxide scale with a thickness of ~73.5 μm, detaching from the substrate, was retained on the rest of the sample, which shows the same oxide layer structure as the F91. The retained oxide scale thickness at the peripheral of the HCM12A sample disk is similar to that at the other regions. The HCM12A samples showed a larger weight gain than the F91 samples, which is contradictory to the expected smaller weight gain of HCM12A samples because of its higher Cr content. The F91 samples may have suffered from a more extensive oxide exfoliation than the HCM12A samples during the testing due to the smaller weight gain but significant variation in the oxide scale thickness of the F91.

The XRD patterns of the F91 and HCM12A samples are shown in Figure 43. Only magnetite (Fe_3O_4) with a strong {100} texture was revealed by the XRD pattern of the F91 since the X-ray is attenuated within ~9 μm of the magnetite [viii]. Compared to the F91, the XRD pattern of the HCM12A is primarily composed of magnetite (without texture) with trace amounts of chromium oxide and tungsten oxide. The peaks of chromium oxide and tungsten oxide came from the internal oxide region, where exfoliation occurred due to sample cutting, because neither Cr nor W was observed in the surface oxide scale during EDS scan.

The XPS spectra as shown in Figure 44 compare the surface chemistry of the austenitic and ferritic-martensitic steels exposed to the S-CO_2 for 500 and 1500 hours. The presence of the elements and their corresponding states/oxide is consistent with the SEM and XRD analyses, (e.g. the presence of Cr and Mn oxide on the 500 hours exposed sample), but additional Fe oxide on the 1500 hours exposed alloy 800H samples. The presence of Al oxide on the short-time exposed alloy 800H sample cannot be well revealed because of the overlapping peaks between Al (2p) and Cr (3s). The presence of Ti (2p) on the long-time exposed alloy 800H sample, with a binding energy of Ti 2p3/2 at 458.6 eV associated with TiO_2 [ix], indicates that the alloying element in alloy 800H contributed to not only the formation of carbide and nitride in the alloy but also the formation of the oxide at surface, which is supposed to have a comparatively similar protective effect as alumina and chromium oxide. The presence of TiO_2 (Figure 44) and Al_2O_3 (Figure 38 and Figure 41) and their distribution in the oxide scale of the alloy 800H samples are consistent with the report on a Nimonic alloy PE16 exposed to CO_2 at 700-800°C and 0.1 MPa for up to 10250 hours [x], although the contents of the Ti and Al in the alloy 800H is less than half of those in the alloy PE16. Both the 500 hours exposed F91 and HCM12A samples show the presence of Fe oxide. But additional Cr oxide and W oxide with a binding energy of W 4d5/2 at 247.7 eV [ix] (the inset) exist on the HCM12A sample, which came from the internal oxidation region, where exfoliation occurred due to sample cutting. The binding energy of Mo 3d5/2 at 232.3 eV [ix] indicates the presence of MoO_3 (the inset), which exists on all the alloys samples and its intensity increases with exposure time. This observation confirms that volatile MoO_3 was formed from the AL-6XN samples because of its high

Mo content and deposited onto the other samples during the exposure. The comparison of the corrosion behavior of the alloys 800H, AL-6XN, F91, and HCM12A exposed to the S-CO_2 at 650°C and 20.7 MPa is summarized in Table 4.

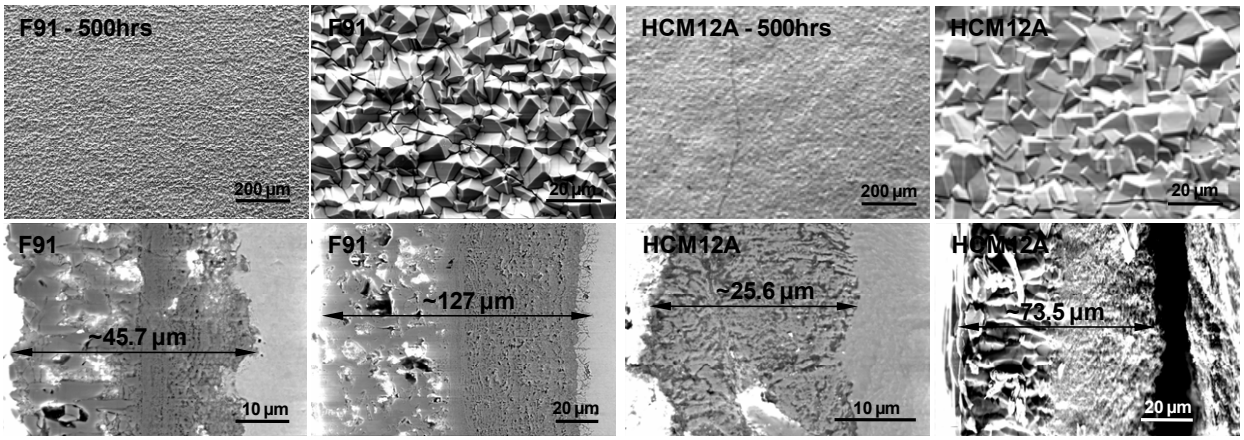

Figure 42: Surface morphologies and cross-section of the F91 and HCM12A samples exposed to the SC-CO2 at 650°C for 500 hours.

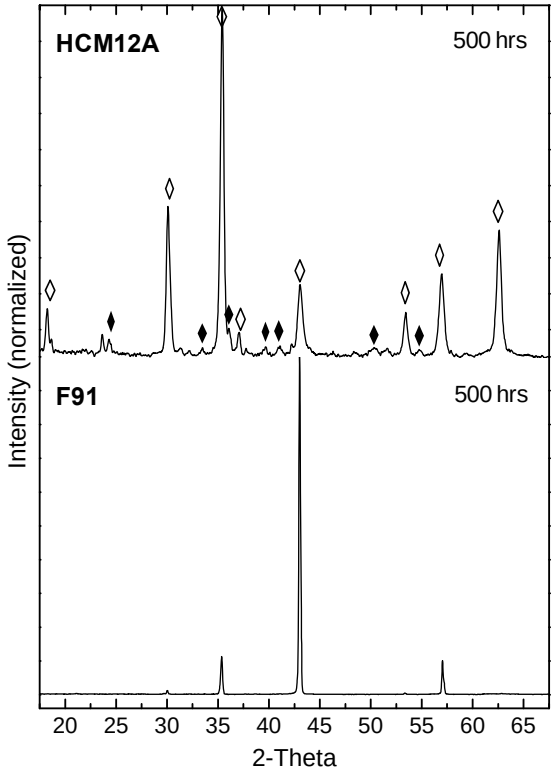

Figure 43: X-ray diffraction patterns of the F91 and HCM12A samples exposed to the SC-CO2 at 650°C for 500 hours. The symbols ◊ and ♦ denote magnetite (e.g. Fe3O4 [19-629]) and chromium oxide (e.g. Cr1.3Fe0.7O3 [35-1112]), respectively. The unlabeled peaks in the HCM12A pattern correspond to tungsten oxide (e.g. WO3 [01-089-8052]).

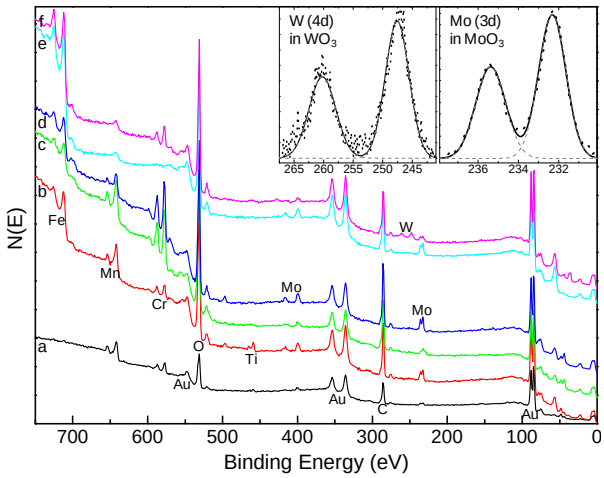

Figure 44: XPS spectra of the surfaces of the SC-CO2 exposed samples: a) 800H/500 hours, b) 800H/1500 hours, c) AL-6XN/500 hours, d) AL-6XN/1500 hours, e) F91/500 hours, and f) HCM12A/500 hours. The high-resolution spectra of Mo 3d (from d) and W 4d (from f) are shown as insets. Gold (Au) was used as a standard for the spectra.

Table 4: Comparison of the corrosion behavior of the austenitic (A) alloys 800H and AL-6XN and ferritic-martensitic (F-M) steels F91 and HCM12A exposed to SC-CO2 at 650°C and 20.7 MPa.

Alloy		Weight gain (mg/cm^2)	Oxide Scale		Remarks
			Thickness (μm)	Phase	
A [a]	800H	0.15±0.02	~2.3-4.9	Spinel domains (Fe-rich), Spinel (Cr-Mn rich), chromium oxide, alumina	The presence of alumina showed good adhesion between the substrate and the oxide scale
	AL-6XN	0.21±0.02	~3.3-6.1	Chromium oxide platelets, Spinel (Fe-Mn rich), chromium oxide	1. Volatile MoO_3 formed during exposure resulting in slight exfoliation on the short-time exposed samples, larger pores in the oxide scale (compared to 800H), and contamination on the other samples; 2. Sigma phase formed in the substrate during the exposure
F-M [b]	F91	8.18±1.24	~45.7-127 [c]	Magnetite (without Cr), spinel (with Cr), internal oxidation (Cr-rich)	Significantly thicker internal oxidation layer in the HCM12A with tungsten oxide in addition to chromium oxide compared to the F91
	HCM12A	13.80±3.45	~99.1		

Note: a. With 1500 hours exposure samples as an example;
b. With 500 hours exposure samples as an example;
c. With the oxide scale from the sample with weight gain as an example

2.6 Conclusion of the Micro Analysis

The corrosion behavior of commercial austenitic steels 800H and AL-6XN and ferritic-martensitic steels F91 and HCM12A exposed to SC-CO_2 at 650°C and 20.7 MPa for up to 3000 hours was studied by means of gravimetry, SEM, EDS, FIB, XRD, and XPS. The austenitic steels showed better corrosion resistance than the ferritic-martensitic steels as demonstrated with smaller weight gain with thinner oxide scale without noticeable exfoliation. The alloy 800H showed better corrosion resistance than the alloy AL-6XN as demonstrated by the thinner compact oxide scale. The high Mo content in alloy AL-6XN resulted in the formation of volatile MoO_3 during the exposure at 650°C, which promoted the debonding of the chromium oxide from the substrate during a short-time exposure, increased the porosity in the oxide scale, and contaminated the other alloys samples during the same exposure. The high contents of the trace alloying elements Ti and Al in alloy 800H compared to the other alloys contributed to the formation of oxides such as TiO_2 and Al_2O_3. The results indicate that alloy 800H is a good candidate material for use in S-CO_2. The corrosion resistance of alloy AL-6XN is not as good as alloy 800H at such high temperature (650°C). The ferritic-martensitic steels did not show good corrosion resistance due to their thick oxide scale and associated excessive exfoliation resulting in a large variation in weight changes.

Cited Sources:

[1] Incoloy Alloy 800H & 800HT, Technical Bulletin, Special Metals Publication SMC-047, March 2004. Available from: http://www.specialmetals.com.

[1] AL-6XN Alloy, Allegheny Ludlum Corporation, 2002. Available from: http://www.alleghenyludlum.com.

[1] J.F. Grubb, Elevated temperature stability of a 6% Mo superaustenitic stainless steel, NACE Corrosion 96 Conference, Denver, CO, NACE International, Paper No. 426, 1996.

[1] R.L. Klueh, D.R. Harries, Development of high (7-12%) chromium maretnsitic steels. In: High-Chromium Ferritic and Martensitic Steels for Nuclear Applications, ASTM International, 2001.

[1] R. Viswanathan, W.T. Bakker, Materials for boilers in ultra supercritical power plants. In: Proceedings of 2000 International Joint Power Generation Conference (IJPGC2000-15049), Miami Beach, Florida, July 23-26, 2000.

[1] E.M. Russick, G.A. Poulter, C.L.J. Adkins, N.R. Sorensen, Corrosive effects of supercritical carbon dioxide and cosolvents on metals, The Journal of Supercritical Fluids 9 (1996) 43-50.

[1] L. Tan, Y. Yang, T.R. Allen, Oxidation behavior of iron-based alloy HCM12A exposed in supercritical water, Corrosion Science 48 (2006) 3123-3138.

[1] B.L. Henke, E.M. Gullikson, J.C. Davis, X-ray interactions: photoabsorption, scattering, transmission, and reflection at E=50-30000 eV, Z=1-92, Atomic Data and Nuclear Data Tables 54 (1993) 181-342.

[1] NIST X-ray Photoelectron Spectroscopy Database, Version 3.5 (National Institute of Standards and Technology, Gaithersburg, 2003); http://srdata.nist.gov/xps/.

[1] M.J. Bennett, M.R. Houlton, J.W. McMillan, C.F. Knights, R.W.M. Hawes, F.C.W. Pummery, The oxidation behavior of the Nimonic alloy PE16 in carbon dioxide at 700-800°C, Oxidation of Metals 15 (1981) 231-249.

3 TASK 2 – Heat transfer measurements

3.1 Introduction

3.1.1 Motivation

The use of a supercritical carbon dioxide Brayton cycle has been gaining interest in recent years as a candidate power conversion cycle for lead-cooled fast reactors and sodium-cooled fast reactors ([1] and [2]), and has been suggested for very high temperature reactors [3] . . . want to understand heat transfer behavior of SCO2 in order to better model cycle performance and prevent pinch points in HXers at lower LMTD's.

3.1.2 Objectives and Contributions

- Review existing literature and sources w.r.t. the entire PCHE manufacturing process (including etching, bonding, and pressure containment) as thermal-hydraulics cannot be optimized in isolation
- Add cooling-mode data for a range of interest with SCO2 in various PCHE channels
- Develop and compare models for thermal-hydraulic performance of different PCHE channel geometries suitable for design purposes (FLUENT is nice but really slow)

3.2 Background

As summarized by Dostal [4], supercritical Brayton cycles have been studied since the 1940's with significant contributions in the late 1960's by Feher and Angelino, but were not deployed particularly due to a lack of compressor operating experience near the critical point, lack of compact heat exchangers at high pressures, and the relatively lower temperatures of nuclear heat sources in the past. In the past 10 years however there has been renewed interest as laid out in the Generation IV International Forum technology roadmap [1] in supercritical CO2 (SCO2) Brayton cycles for current high-temperature gas, liquid metal, and liquid sodium –cooled reactors to reduce plant capital costs and improve efficiency.

The benefits of the SCO2 cycle over another competing Brayton cycle such as the helium Brayton cycle proposed for the Very-High Temperature Reactor (VHTR) are compared more extensively by Dostal, but the primary benefit is that operating the compressor near the critical point of carbon dioxide significantly lowers the compressor work and improves the efficiency of the cycle. This can most easily be seen by comparing the properties of the two fluids, carbon dioxide and helium, over the temperature range of interest in [1]; from approximately 30 °C to 850 °C and 7 to 25 MPa for CO2 and 3 to 9 MPa for helium.

The fundamental property relation for a single-component fluid at thermodynamic equilibrium [5] can be stated for specific enthalpy, specific entropy, and specific volume as shown in Equation (2). By assuming that the turbomachinery involved in each Brayton cycle is reversible the change in specific entropy for the compression and expansion processes can be neglected and the work produced by the turbine and required by the compressor will simply be proportional to the integral of the specific volume (or density) and the pressure ratio.

$$dh = \underbrace{T\,ds}_{0} + v\,dP = \frac{1}{\rho}\,dP \qquad (1)$$

For equivalent pressure ratios (cycles with only one compression stage) and neglecting the power required for other support equipment, the largest power output is then achieved at the largest differential in specific volume. For these ranges helium behaves almost like an ideal gas, Equation (2), as shown in *Figure 45* where the temperature is linear with specific volume and isobars are nearly parallel, and so for the approximate temperature differential of interest between 900 K and 300 K the specific volume of helium (or any other fluid

that behaves like an ideal gas in this range) changes by at most a factor of 3.

$$v = \frac{RT}{p} \quad (2)$$

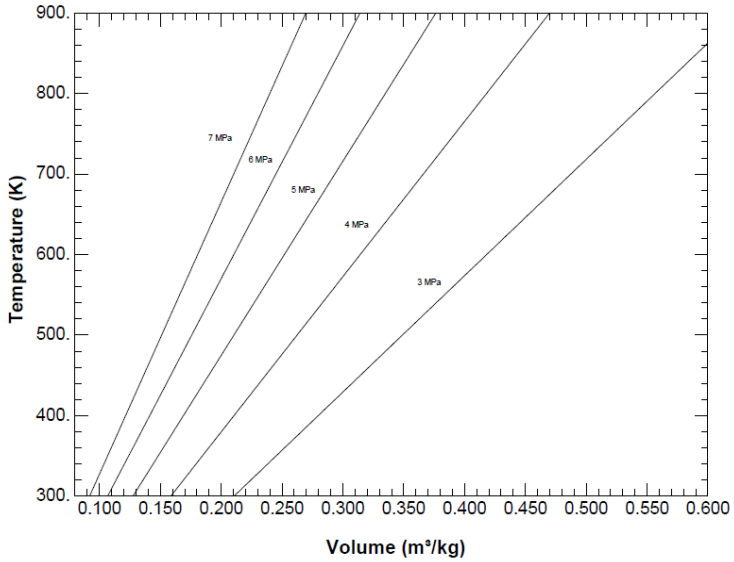

Figure 45: A temperature - volume diagram for helium between 300 and 900 [K] and 3 and 7 [MPa]

Carbon dioxide however behaves much differently near the critical point than an ideal gas, as shown in Figure 45 , and so the density can change by as much as a factor of 10 between the expansion and compression process. Rankine cycles operate across the two-phase dome and can achieve even larger differences in specific volume such that the pump work on the liquid phase is negligible, but the two-phase condition and the high difference in specific volume at lower pressures requires more complex arrangements of turbine stages and possibly re-heat in order to avoid damage to the turbine blades by small droplets of condensate.

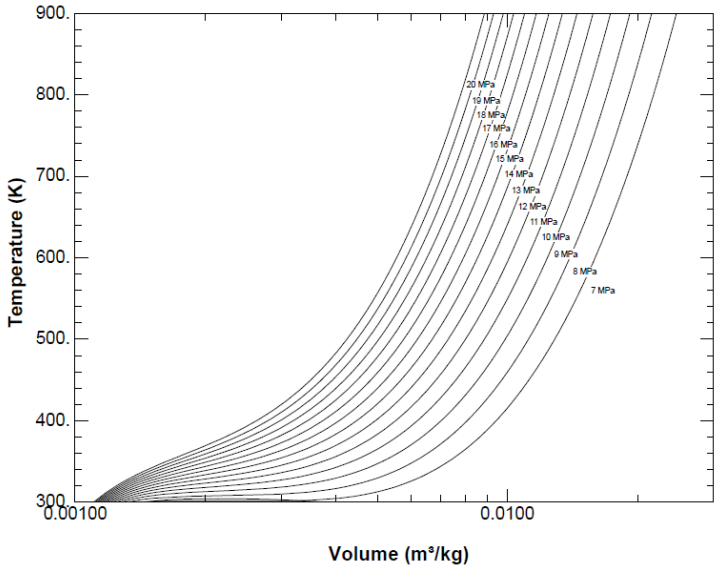

Figure 46: A diagram of the temperature-volume behavior of carbon dioxide between 300 and 900 [K] and 3 and 7 [MPa].

The specific layout of the SCO2 Brayton cycle recommended by Dostal [4] for temperatures above 500 °C after detailed optimization studies is the recompression cycle, consisting of a pre-cooler, two compressors, a low and

high temperature recuperator, a turbine, and the reactor core, as shown Figure 46. This cycle can achieve similar efficiencies at 550 °C to the helium Brayton cycle at 800 °C but with a simpler and more compact system due to the reduced size of the turbomachinery and the use of high-pressure compact heat exchangers known as Printed Circuit Heat Exchangers (PCHEs).

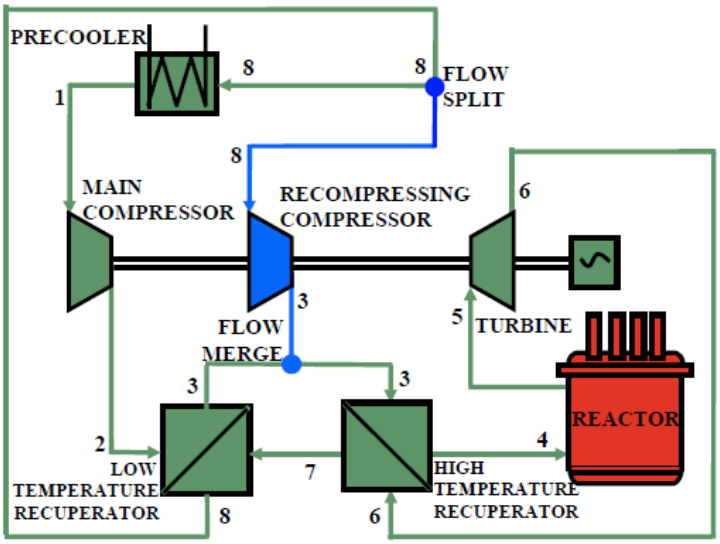

Figure 47: A diagram of the recompression supercritical carbon dioxide Brayton cycle, from Dostal [4].

3.2.1.1 Heat Exchanger Operating Conditions

The pre-cooler, low-temperature (LT) recuperator, and high-temperature (HT) recuperator of the recompression supercritical carbon dioxide Brayton cycle are all planned to be PCHE-type compact heat exchangers, and will operate close to the critical point of carbon dioxide. In order to take maximum advantage of the heat source and compression work, as well as avoid possible complications in the design of or damage to the main compressor caused by dropping into the two-phase dome, the thermal and hydraulic performance of the printed-circuit heat exchangers (PCHEs) must be known.

The various designs proposed by Dostal [4] optimized for different turbomachinery and reactor outlet temperature assumptions suggest total mass flow rates around 3200 kg/s and recompression fractions around 40%, leading to pre-cooler and LT, high-pressure side recuperator mass flow rates around 1300 kg/s. Using the straight-channel, single-banked PCHE designs from Dostal and an estimate of 0.4 from Hesselgreaves [6] for the porosity of a high-pressure PCHE, the mass fluxes through each side of the various heat exchangers can be determined as shown in *Table 5*.

Table 5: Design geometry of the recompression SCO2 cycle heat exchangers from Dostal [4], as well as estimated mass flow rates and mass fluxes through each CO2 side of the heat exchangers assuming porosities of 0.4.

Parameter	Pre-Cooler	LT Recup. (LP / HP)	HT Recup. (LP / HP)
Core Volume [m^3]	21	46.05	52.95
Active Length [m]	1.1	1.75	2.05
Approx. A_c [m^2]	3.8	5.26 / 5.26	5.17 / 5.17
Mass Flow Rate [kg/s]	1300	3200 / 1300	3200 / 3200
Mass Flux [kg/m^2-s]	340	608 / 250	620 / 620

Experiments in this work are carried out at two levels of mass flux similar to those estimated in the recompression SCO2 Brayton cycle heat exchangers of 326 and 762 [kg/m^2-s] in line with work done by Kruizenga [7] primarily on straight channels in different flow orientations, and corresponding experimentally to 15 and 35 kg/hr for straight and zig-zag channels based on the design geometry, or 19 and 44 kg/hr for channels

with airfoil fins based on the design geometry.

The state points for the basic, advanced, and high-performance recompression SCO2 cycle from Dostal are shown in *Figure 48* and listed in *Table 6*. Conditions for the CO2 flowing within the heat exchangers range from 32 to 580 °C with pressures between 7.7 and 20 MPa. However, it can be seen from *Figure 46* that most of the non-ideal property variations occur at temperatures less than about 100 °C (400 K on the plot), and are most extreme at pressures closer to the critical pressure. Conditions within this study are therefore limited to the range of cooling-side pressures (low-side pressures) and temperatures less than 100 °C such as those experienced in the low-pressure leg of the low-temperature recuperator and the pre-cooler.

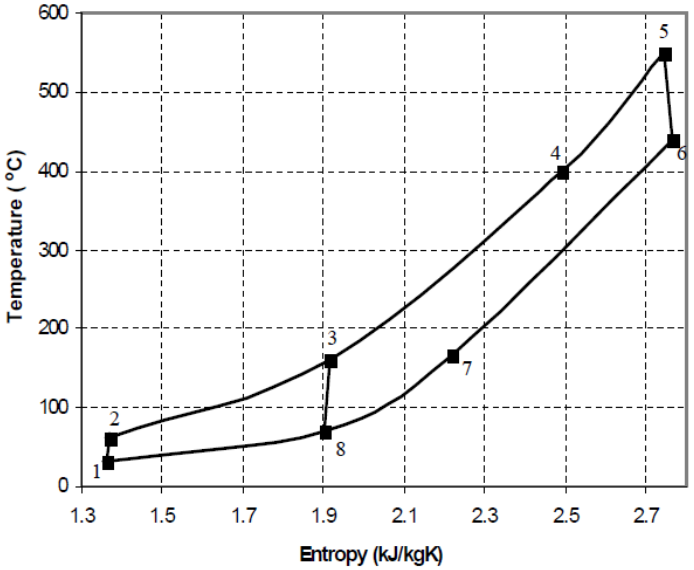

Figure 48: A T-s diagram for the recompression SCO2 cycle from Dostal [4].

Table 6: Design state points for the recompression SCO2 cycle from Dostal [4].

Design Type	Basic [C / MPa]		Advanced		High-Performance	
State 1	32	7.692	32	7.692	32	7.692
State 2	61.1	20	61.1	20	61.1	20
State 3	157.99	19.988	157.11	19.981	159.88	19.999
State 4	396.54	19.957	488.75	19.922	531.33	19.944
State 5	550	19.827	650	19.792	700	19.814
State 6	440.29	7.901	534.31	8.039	578.31	7.929
State 7	168.34	7.814	165.83	7.878	169.85	7.802
State 8	69.59	7.704	68.91	7.702	71.05	7.704

3.2.2 Supercritical Fluid Properties

A fluid becomes supercritical at pressures above the critical pressure or equivalently at temperatures above the critical temperature as shown schematically in *Figure 49*. For a pure fluid the critical point is rigorously defined (see Klein and Nellis [5]) as the point for which both the first and second partial derivatives of pressure with respect to volume are both equal to zero at a constant temperature, the critical temperature, as shown in (3) and by the point of inflection along the critical isotherm in *Figure 50*.

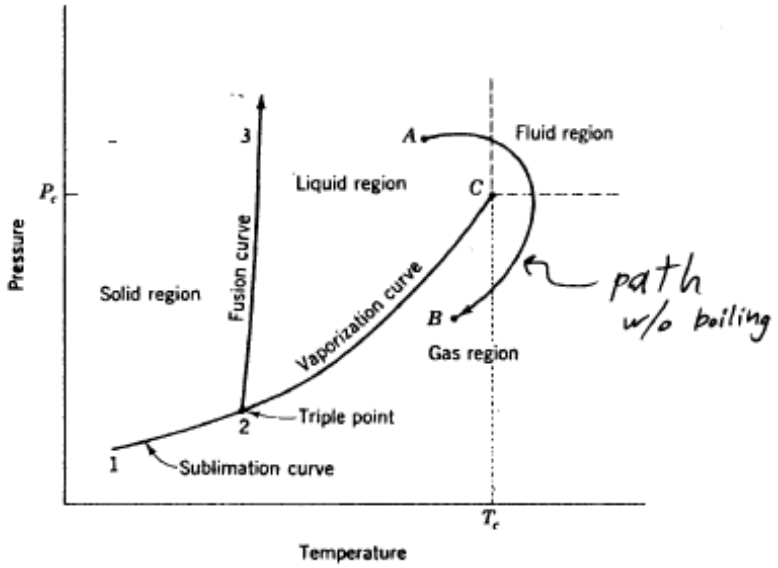

Figure 49: A diagram of states for a generic pure fluid as determined by its temperature and pressure

$$\left(\frac{\partial P}{\partial v}\right)_{T_c} = \left(\frac{\partial^2 P}{\partial v^2}\right)_{T_c} = 0 \qquad (3)$$

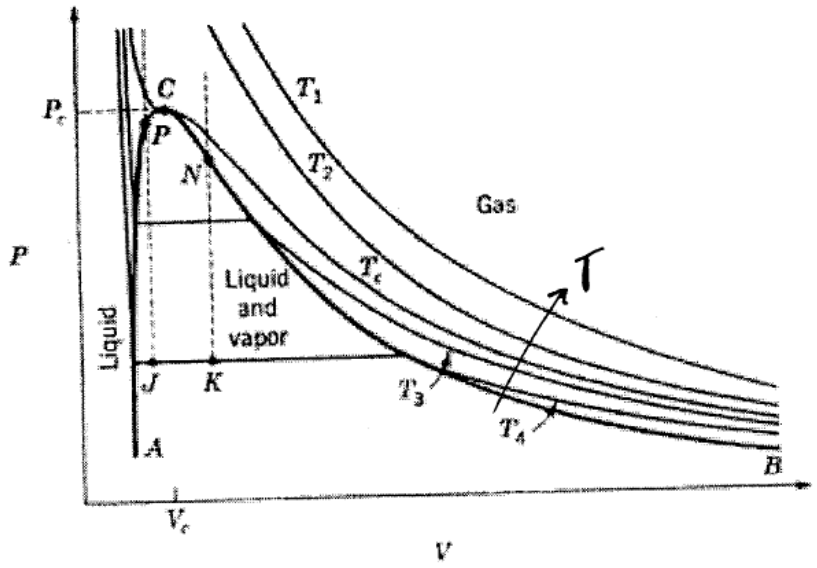

Figure 50: A diagram of pressure-volume behavior for a generic pure fluid with the saturation curve and critical isotherm shown.

Physically this definition of the critical point describes how a pure fluid undergoing an isothermal change in pressure (or isobaric change in temperature) will smoothly change specific volume (or enthalpy or other extensive property) without the development of a phase interface between fluid regions of distinctly different specific volumes above the critical temperature (or pressure, respectively). This is distinctly different from sub-critical fluid behavior where at a certain pressure (or temperature), the saturation pressure (or temperature), particles of the fluid with slightly different energies will agglomerate into regions of distinct specific volume described as distinct phases. Supercritical fluids will therefore remain as a single phase without encountering a saturation or two-phase region.

While supercritical fluids remain single-phase they can be behave "liquid-like" or "gas-like" depending on their pressure and temperature. This behavior can most easily seen by plotting the compressibility factor Z, defined in Equation **(4)**, versus the pressure as shown in *Figure 51* along with several lines of constant temperature. A compressibility factor near 1 indicates that the fluid can be modeled as an ideal gas, while departures from 1 indicate non-ideal behavior. A notable departure is the extension from the saturated liquid line where the specific volume is nearly constant and the compressibility factor is linear with pressure at constant temperature. For reference, the critical properties of carbon dioxide are listed in *Table 7* along with those for water and air.

Table 7: The critical properties of several fluids from Pioro[8].

Fluid	P_{crit} [MPa]	T_{crit} [C]	v_{crit} [m^3/kg]	Z_{crit} [-]
Carbon Dioxide	7.3773	30.978	2.139e-3	0.274
Water	22.064	373.95	3.1018e-3	0.243
Air	3.8	-140.5	3.000e-3	-

$$Z = \frac{Pv}{RT} \qquad (4)$$

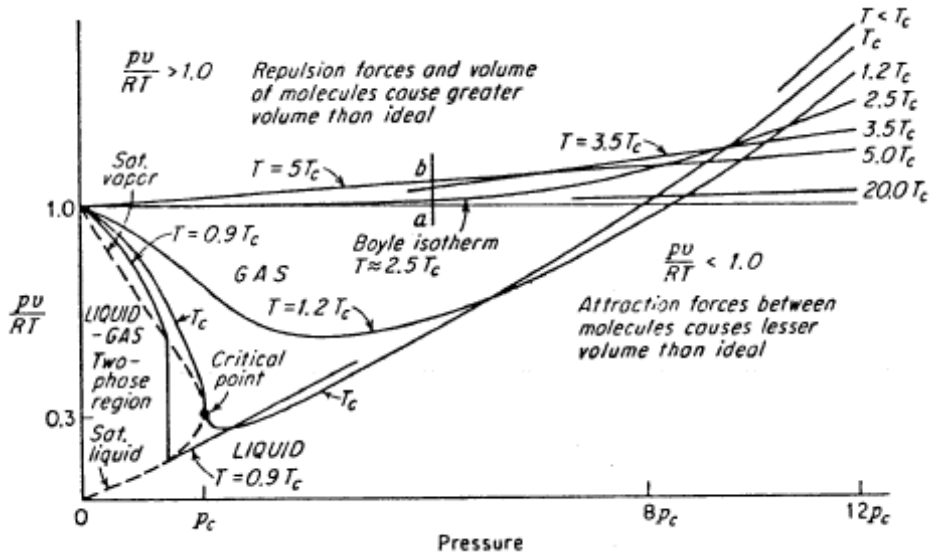

Figure 51: A diagram of compressibility versus pressure for a generic pure fluid with the saturation curve and several isotherms shown (REPLACE WITH CLEANER VERSION AND CITE?).

As expected it can be seen that at low pressures and all temperatures the fluid is approximately an ideal gas, while at temperatures about 2.5 times the critical temperature and higher the fluid is also approximately an ideal gas. Additionally at pressures above the saturation pressure and temperatures below the critical temperature the compressibility factor is nearly linear with pressure indicating that the fluid behaves like a liquid. The central area of *Figure 51* for a variety of pressures and temperatures up to about 2.5 times the critical temperature show where the compressibility factor is well below one and the fluid behaves as a real gas.

The properties of a supercritical fluid therefore vary between those of a gas and those of a liquid, with the largest variation in properties occurring around the critical or pseudo-critical temperature. The pseudo-critical temperature is defined as the point along a line of constant pressure where the specific heat capacity of the fluid reaches a maximum, as shown *Figure 52* for carbon dioxide for several different pressures. The peak in specific heat capacity gets lower as the pressure increases for temperatures around the critical temperature due to the fact that the fluid behaves more "liquid-like" as shown previously in *Figure 51*.

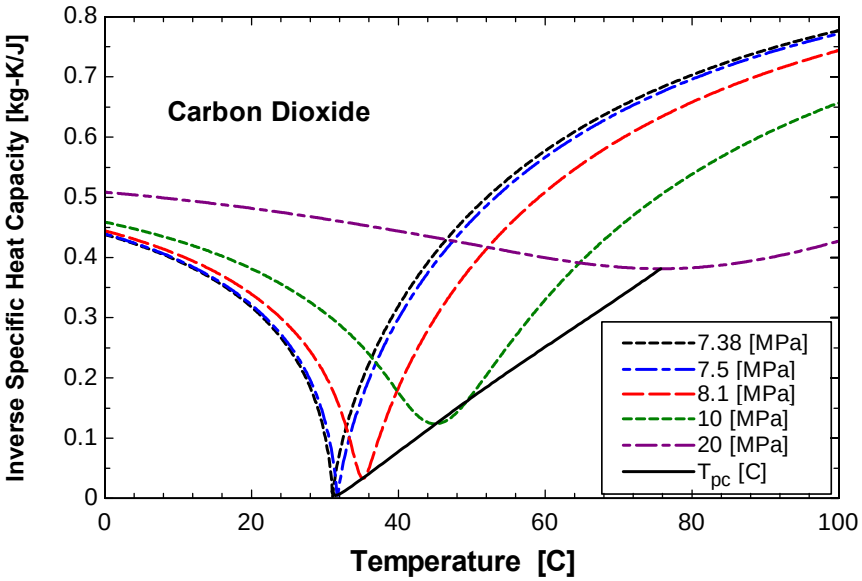

Figure 52: A plot of the inverse of specific heat versus temperature of carbon dioxide with several isobars and the pseudo-critical line shown.

Because the pseudo-critical temperature must be found using a maximization algorithm, it is useful to curve fit the variation of pseudo-critical temperature with pressure from a fluid property source. Liao and Zhao [9] have fit data from REFPROP v6.01 to Equation **(5)** where T_{pc} is in °C and P is the absolute pressure in bars which by their examples should apply to pressures above the critical pressure to 10 MPa. A different curve fit was performed by this author using the property routines in Engineering Equation Solver (EES) [10], and is shown in Equation **(6)** where T_{pc} is in °C and P is the absolute pressure in MPa for pressures between the critical pressure and 20 MPa. The difference between the two is only about 0.2% over the range for Liao and Zhao's curve fit from the critical pressure to 10 MPa, so Equation **(6)** will be used to calculate T_{pc} throughout this test.

$$T_{pc} = -122.6 + 6.124P - 0.1657P^2 + 0.01773P^{2.5} - 5.608\text{E-}4P^3 \quad \textbf{(5)}$$

$$T_{pc} = -28.4 + 10.3P - 0.3359P^2 + 4.063\text{E-}3P^3 \quad \textbf{(6)}$$

Figure 53 through *Figure 56* show several other thermodynamic and transport properties of carbon dioxide just above the critical point for several pressures demonstrating the large property variations near the pseudo-critical temperature. Some general trends from these plots can be seen including the single point of inflection found in the variation of the density, specific enthalpy, and dynamic viscosity, while the trend in specific heat and thermal conductivity all show at least one peak and multiple points of inflection, the first due to the specific heat capacity being based on partial derivative of the specific enthalpy with its peak reflecting the point of inflection in the specific enthalpy. The plots of specific heat and thermal conductivity are shown as the inverse of each value to avoid logarithmic scales. Pioro [8] goes through another discussion of supercritical properties, and cautions that some early correlations do not account for the considerable peak in thermal conductivity near the pseudo-critical point.

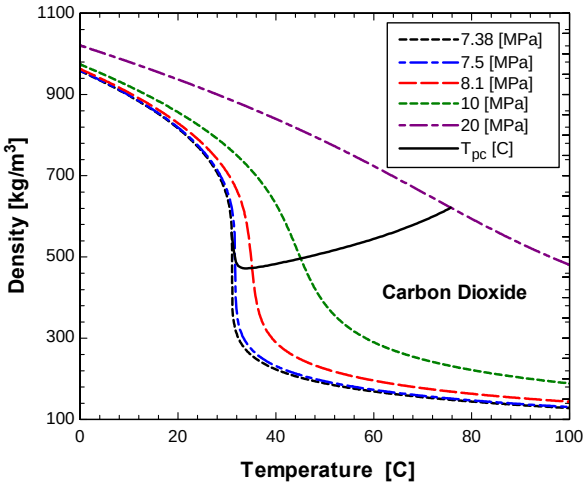

Figure 53: A plot of the temperature versus density of carbon dioxide with several isobars and the pseudo-critical line shown.

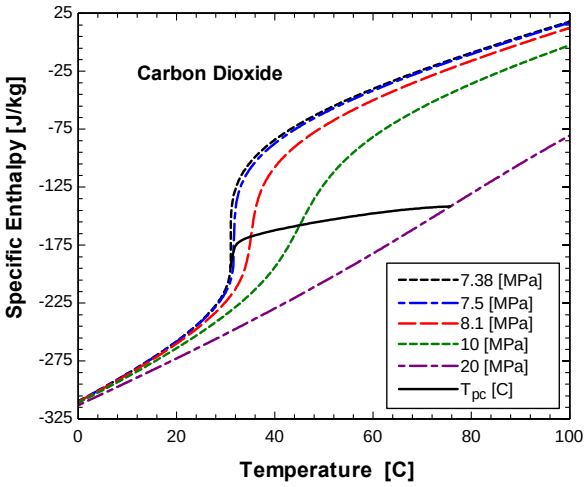

Figure 54: A plot of the temperature versus specific enthalpy of carbon dioxide with several isobars and the pseudo-critical line shown.

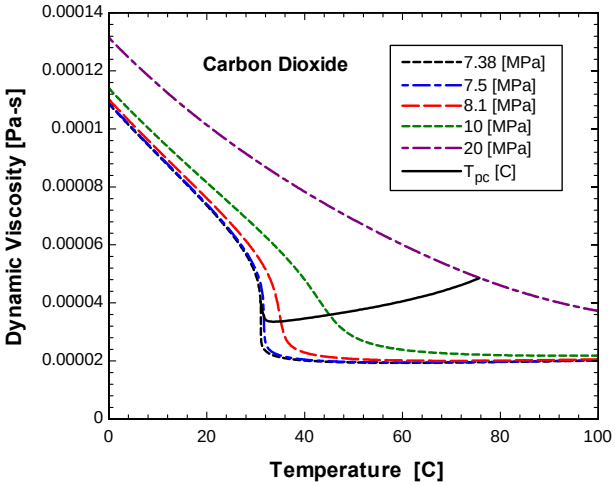

Figure 55: A plot of the dynamic viscosity versus temperature of carbon dioxide with several isobars and the pseudo-critical line shown.

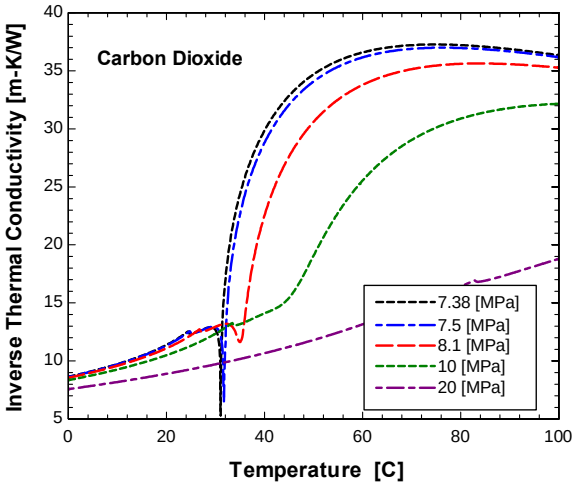

Figure 56: A plot of the inverse of thermal conductivity versus temperature of carbon dioxide with several isobars shown. The pseudo-critical line is left off for clarity.

3.2.2.1 Turbulent Single-Phase Pressure Drop in Straight Ducts

As a fluid flows in some arbitrary channel it can experience many different effects that lead to pressure variation along the channel as discussed by Nellis and Klein [11] and Miller [12], among others. The fluid flowing nearest a solid surface will be attracted to the surface due to intermolecular forces and match the speed of the surface. Fluid farther and farther from the surface is then slowed in turn due to intermolecular forces in the fluid and a velocity gradient develops throughout the flow. The effect of the solid surface on the fluid can be characterized by the shear force between the fluid and the solid surface, with this shear force increasing axially along the channel up to some steady-state value for internal flow in a straight constant cross-section channel containing a steady constant-property fluid flow as the impact of the slow moving fluid at the wall is felt deeper into the channel, with the section of portion of the flow impacted by the wall termed the boundary layer. This wall shear force results in an irreversible pressure drop along the channel as the pressure force driving the fluid flow is balanced by an incremental wall shear force on the fluid.

The irreversible pressure drop due to the wall shear force is described as frictional pressure loss, and is typically

correlated using the Darcy friction factor as shown in Equation (7), referred to simply as the friction factor throughout this text. Note that the actual path length L_s of the channel should be used rather than the heat transfer flow length L, although the two are the same for straight PCHE geometries.

$$\Delta P_{friction} = f \frac{L_s}{d_{hyd}} \frac{1}{2} \frac{G^2}{\rho} \tag{7}$$

The friction factor for a single-phase constant property flow can be calculated most generally according to the implicit Colebrook equation [13] given here as Equation (8), which includes the effects of both the Reynolds number of the flow and the relative roughness of the channel walls. A more complex but explicit method for calculation of the Colebrook equation is given by Clamond [14] where high accuracy is required but the computational expense of the implicit form of the Colebrook equation is prohibitive. Many other explicit single-phase friction factor correlations which are less complex to implement than Clamond's method have been proposed including the Blasius correlation [11] for smooth tubes shown as Equation (9), and the Haaland [15] equation shown as Equation (10).

$$\frac{1}{\sqrt{f}} = -2\log_{10}\left(\frac{RR}{3.7} + \frac{2.51}{Re\sqrt{f}}\right) \tag{8}$$

$$f = 0.316Re^{-0.25} \tag{9}$$

$$f = \frac{1}{\left(1.8\log_{10}\left[\left(\frac{RR}{3.7}\right)^{1.11} + \frac{6.9}{Re}\right]\right)^2} \tag{10}$$

Changes in flow geometry along the channel such as the introduction of a new wall surface, area variation, bending of the channel, and sharp wall discontinuities due to ribbing or fining all cause some amount of streamline curvature within the flow that results in pressure gradients perpendicular to the flow streamline as fluid particles with higher inertia migrate toward the concave side of the curvature and fluid particles of lower inertia migrate toward the convex side of the curvature. In the case of turning flow in bends this pressure gradient will introduce a secondary flow in the channel that can have implications for flow separation and heat transfer. As the radius of streamline curvature becomes smaller a reverse flow or recirculation region can develop between the concave side of the streamlines and the wall where low energy fluid collects. These recirculation regions can also develop in areas where the flow impinges a wall, and lead to large mixing and turbulence generation and cause higher pressure losses and heat transfer. Area variation within the channel and that caused by recirculation volumes requires from continuity that the main flow speed up, resulting in steeper velocity gradients and subsequently higher shear forces at the wall.

These geometric effects are lumped together as local losses, and are typically given as either a loss coefficient or an equivalent pipe length, as defined in Equation (11). The loss coefficient K is usually the preferred method for presenting local losses for detail design as it does not confound the data with an implicit assumption on how the friction factor should be calculated when used equivalent pipe diameters, while the equivalent pipe length is useful when the fluid and properties are known and an estimate of the additional pressure drop due to local loss is sufficient.

$$\frac{\Delta P_{local}}{G^2/2\rho} = K_{loss} = f\left(\frac{L_{equivalent}}{d_{hyd}}\right) \tag{11}$$

Loss coefficients are very specific to the actual flow channel geometry and will be discussed later according to each heat exchanger surface, but the most comprehensive volumes on local losses are those by Idel'chik [16] and Miller [12].

Bulk fluid density changes require recoverable changes in pressure according to Equation (12) from Pioro [8], and should not be confused with irreversible frictional and local pressure losses. As implied by the first form of this equation, this effect comes simply from an integral balance of momentum along the channel assuming only a change in fluid density and no other pressure effects such as wall friction.

$$\Delta P_{acceleration} = G^2\left(\frac{1}{\rho_{out}} - \frac{1}{\rho_{in}}\right) \tag{12}$$

Body forces such as gravity or an accelerating reference frame can cause pressure gradients within a flow that may assist or oppose the main flow depending on the orientation of the channel and gravity vectors, and may have non-uniform effects on the flow where fluid property gradients exist. This effect can be calculated by Equation (13) from Pioro [8] where the angle θ is the angle measured from the horizontal plane to the flow direction vector (0° for horizontal, 90° for vertical flow, and -90° for downward flow). All test conducted for this work were done in a horizontal configuration so that gravitational effects are negligible, and no other body forces act on the fluid.

$$\Delta P_{gravity} = g\left(\frac{t_{out}\rho_{out} + t_{in}\rho_{in}}{t_{out} + t_{in}}\right) L\sin(\theta) \tag{13}$$

The total pressure drop associated with these effects is reasonably estimated as the sum of the net effect of each different contributions to the change in pressure along the channel, including frictional effects, local effects causing streamline curvature and or channel cross-sectional area variation, acceleration effects due to axial fluid property gradients, and the effects of a body force on the fluid like gravity, as described by Pioro [8] and shown in Equation (14).

$$\Delta P = \sum \Delta P_{friction} + \sum \Delta P_{local} + \sum \Delta P_{acceleration} + \sum \Delta P_{body\ forces} \tag{14}$$

3.2.2.2 Turbulent Single-Phase Heat Transfer in Straight Ducts

As discussed by Nellis and Klein [11] among others, a thermal boundary layer is formed as a flowing fluid is heated or cooled similar to the boundary layer formed due to viscosity and the presence of a wall in isothermal flow. A dimensional analysis within the boundary layer suggests several important non-dimensional parameters that describe the character of the flow, including the Reynolds, Prandtl, and Eckert numbers shown as Equations (15) through (17). Correlations for heat transfer across a fully-developed boundary layer typically involve these variables to describe the effects of axial conduction, radial conduction and convection, and viscous dissipation in the flow.

$$Re = \frac{\rho \bar{v} d_{hyd}}{\mu} \sim \frac{Inertial\ Force}{Viscous\ Force} \tag{15}$$

$$Pr = \frac{\mu c_p}{\mu} = \frac{\nu}{\alpha} \sim \frac{Viscous\ Diffusion}{Thermal\ Diffusion} \tag{16}$$

$$Ec = \frac{\bar{v}^2}{c_p \Delta T} \sim \frac{Kinetic\ Energy}{Thermal\ Energy} \quad (17)$$

The product of the Reynolds and Prandtl number is also known as the Peclet number, the squared inverse of which is proportional to the ratio of axial conduction to radial conduction and convection as shown in Equation (19). The product of the Prandtl and Eckert numbers is also known as the Brinkman number, as shown in Equation (19), and is proportional to the ratio of viscous dissipation effects to radial conduction and convection effects. As discussed in Section 3.2.1.1, the operating conditions investigated in this study range between pressures of 7.5 and 8.1 MPa, temperatures between 32 and 100 °C, and mass fluxes of 326 and 762 kg/m^{2}s. *Figure 57* shows the variation of the Peclet term from Equation (19), while *Figure 58* shows the variation of the Brinkman number from Equation (19) for several heat fluxes using the Dittus-Boelter correlation shown later in Equation (20). Only one mass flux is shown as the factor of 2 difference has little effect on the order of magnitude of these parameters. Over the expected conditions both values are far less than 1 for all but the smallest heat fluxes, indicating that both axial conduction and viscous dissipation effects can reasonably be neglected when investigating heat transfer correlations and reducing experimental data.

$$\frac{1}{Pe^2} = \frac{1}{Re^2 Pr^2} \sim \frac{Axial\ Conduction}{Radial\ Conduction\ and\ Convection} \quad (18)$$

$$Br = PrEc \sim \frac{Viscous\ Dissipation}{Radial\ Conduction\ and\ Convection} \quad (19)$$

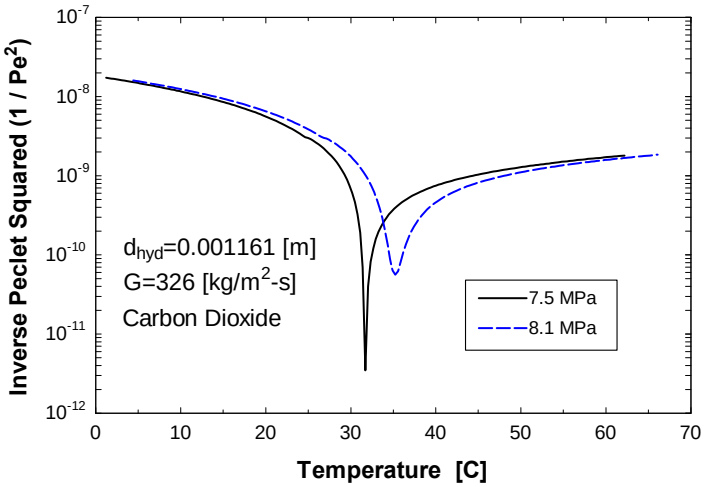

Figure 57: The variation in the squared inverse of the Peclet number vs. temperature at several pressures.

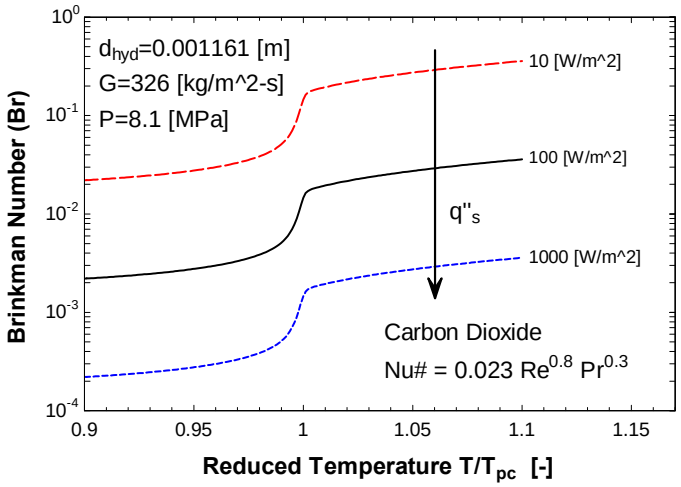

Figure 58: The variation in the Brinkman number vs. temperature at several heat fluxes.

Many different correlations have been developed on a non-dimensional basis using the Reynolds and Prandtl numbers, but only two main formulations exist as discussed by Friend and Metzner ([17], [18]) and more recently by Aravinth [19], among others: the Dittus-Boelter form as shown in Equation (20) and the Prandtl formulation derived from integrating the diffusion terms in the governing equations under some set of assumptions and involving some dependence on the wall shear stress.

$$Nu = C\,Re^{n}Pr^{m} \tag{20}$$

The Dittus-Boelter ([20], reprinted as [21]) form is usually used as shown in Equation (20) with a coefficient of 0.023 and exponents of 0.8 on the Reynolds number and 0.4 or 0.3 on the Prandtl number for when the fluid is being either heated or cooled, respectively. However Winterton [22] explains that the exact coefficient of 0.023 does not match the original paper by Dittus and Boelter typically cited and actually comes from the correlation as recommended by McAdams [23].

This correlation was developed incrementally using data to fit the coefficients as shown well by McAdams by first noting a linear trend between the Nusselt and Reynolds numbers for fluids of the same Prandtl number when plotted on a log-log scale, and a linear trend when plotting fluids with different Prandtl numbers at the same Reynolds number also on a log-log scale. This data suggests a power-law relationship between the Nusselt number and the Reynolds and Prandtl numbers, which each have independent effects. An important aspect of this development is that the fluid data considered involved fluids with almost constant properties such as various gases, water, and oils, and so the original form is only rigorously appropriate when fluid properties can be considered constant.

The Prandtl-type formulation seems to have first been discussed by Prandtl [24], with notable improvements proposed by many authors including one of the most widely-used incarnations among mechanical engineers by Gnielinski [25], shown in Equation (21).

$$Nu = \frac{\left(\frac{f}{8}\right)(Re - 1000)Pr}{1 + 12.7\sqrt{\frac{f}{8}}\left(Pr^{\frac{2}{3}} - 1\right)} \tag{21}$$

Prandtl-type correlations are developed, as discussed well by Aravinth [19], by integrating the diffusion terms of the governing boundary layer equations through the boundary layer assuming multiple layers where either the

effects of turbulent eddies or molecular diffusion can be neglected. Relating the results from the momentum and energy equations shows the dependence of the Nusselt number on the wall shear stress, which is calculated by assuming some correlation for the friction factor.

Aravinth assumes specifically a two-layer model, including a sub-layer that involves both effects from both molecular and turbulent viscosity, and a buffer layer that only involves turbulent effects, and arrives most generally at Equation (22) after substituting the Darcy friction factor for consistency. The dimensionless temperature and velocity at the interface are dependent on ones chosen assumption for the variation of eddy viscosity and eddy diffusivity, as well as height of the interface between the two layers above the wall.

$$Nu = \frac{\left(\frac{f}{8}\right) RePr}{1 + \sqrt{\frac{f}{8}}\left(T_{int}^{+} - u_{int}^{+}\right)} \tag{22}$$

This form of the correlation is interesting as it can be reduced down to an almost identical expression as that given by Gnielinski (apart from reducing the Reynolds number by 1000), and for Prandtl numbers larger than 100 becomes almost identical to the Dittus-Boelter correlation. The relative thicknesses of the diffusion-dominated and eddy-dominated regions of the thermal and momentum boundary layers are clearly important when estimating the heat transfer from a fluid flow.

3.2.2.3 Effects of Variable Properties

All the correlations presented so far for the friction factor and Nusselt number are intended for a constant property fluid. In order to capture the effects of variable fluid properties within the boundary layer on both thermal and hydraulic performance the form of a constant property correlation can be fit to variable property data, the constant property correlation can be multiplied by one or more correction factors, the properties used in the correlation can be evaluated at some reference temperature, or some combination of all three of these can be used.

Two correlations that Pioro [8] recommends for supercritical fluid flow friction factors are the Kondrat'ev correlation and the Filonenko correlation, given here as Equations (23) and (24). Comparing these correlations with similar constant-property correlations, the Blasius correlation from Equation (9) and the Haaland correlation from Equation (10), it is clear that the form of the correlations are similar but that their respective coefficients have been adjusted to better match their respective data sets for the flow of fluids at supercritical pressures in smooth tubes.

$$f = 0.188 Re^{-0.22} \tag{23}$$

$$f = \frac{1}{(1.82 \log_{10} Re_b - 1.64)^2} \tag{24}$$

Similarly Jackson's correlation [26] has been used to calculate variable-property supercritical Nusselt numbers, as shown in Equation (25), while Pioro [8] suggests the correlation proposed by Pitla et al. for supercritical carbon dioxide in horizontal tubes shown as Equation (26), where the two Nusselt numbers are calculated at the wall and bulk temperature using the Gnielinski correlation from Equation (21) and specifically using the Filonenko correlation, Equation (10), as the friction factor in the Gnielinski correlation. The central part of Jackson's correlation involves re-fitting the Dittus-Boelter correlation mentioned previously as Equation (20), with the addition of two property ratio correction factors what will be discussed next. Pitla's correlation explicitly uses the constant-property Gnielinski with the assumption that the wall and bulk properties should bound the heat transfer effects of variable fluid properties.

$$Nu = 0.0183 Re_h^{0.82} Pr_h^{0.5} \left(\frac{\rho_w}{\rho_b}\right)^{0.3} \left(\frac{\bar{c}_p}{c_{p,b}}\right)^n$$

$$n = \begin{cases} 0.4 & for\ T_b \leq T_w \leq T_{pc}\ or\ 1.2T_{pc} \leq T_b \leq T_w \\ 0.4 + 0.2\left(\frac{T_w}{T_{pc}} - 1\right) & for\ T_b \leq T_{pc} \leq T_w \\ 0.4 + 0.2\left(\frac{T_w}{T_{pc}} - 1\right)\left(1 - 5\left[\frac{T_b}{T_{pc}} - 1\right]\right) & for\ T_{pc} \leq T_b \leq 1.2T_{pc}\ and\ T_b \leq T_w \end{cases} \quad \textbf{(25)}$$

$$\bar{c}_p = \frac{i_w - i_b}{T_w - T_b}$$

$$Nu = \left(\frac{Nu_w|_{Gnielinski} + Nu_b|_{Gnielinski}}{2}\right)\frac{k_w}{k_b} \quad \textbf{(26)}$$

The property ratio method was first used with other properties in the correlation evaluated at the bulk temperature by Sieder and Tate [27] after Colburn [28] used the method along with the film temperature to calculate properties in his correlations. Sieder and Tate found that a best fit to available heating and cooling data for the turbulent flow of water and oil was obtained using Equations (28) and (28), where f_{iso} and Nu_{iso} are the respective correlations evaluated using constant properties, $\mu_{b,ave}$ is the viscosity evaluated using the average bulk temperature along the channel, and μ_w is the viscosity evaluated using the average wall temperature.

$$\frac{f}{f_{cp}} = 1.02\left(\frac{\mu_{b,ave}}{\mu_w}\right)^{-0.14} \quad \textbf{(27)}$$

$$\frac{Nu}{Nu_{cp}} = 1.00\left(\frac{\mu_{b,ave}}{\mu_w}\right)^{0.14} \quad \textbf{(28)}$$

The exact exponent and form of this property ratio correction factor has varied considerably as reviewed by Kakuç and Liu [29] depending on the data and experimental conditions various researchers have tried to correlate, and is often simplified for sub-critical gasses whose viscosity varies according to a power-law relationship with the absolute temperature as shown in Equation (29).

$$\left(\frac{\mu_b}{\mu_w}\right)^n \approx \left(\frac{T_{wk}}{T_b}\right)^m \quad \textbf{(29)}$$

Pioro [8] reviews several suggestions for correcting a constant-property friction factor to experimental data, including n equal to -0.22, as well as the use of the property ratio method with density for heating data with n equal to 0.74 when only the density ratio is used, and n equal to -0.15 when the correction factor is the product of the viscosity and density ratios as shown in Equation (30).

$$\frac{f}{f_{cp}} = \left(\frac{\mu_b}{\mu_w}\frac{\rho_b}{\rho_w}\right)^n \quad \textbf{(30)}$$

Because of the many different empirical fits of the Nusselt number at supercritical conditions using a combination of the Dittus-Boelter correlation form and some combination of fluid property correction factors, Pioro [8] notes that the generalized correlation accounting for variable fluid properties as well as boundary layer development effects can be stated generally as Equation (31), where the exponents are tabulated from many researchers but those on the Reynolds and Prandtl numbers are near those by Dittus and Boelter, and subscripts indicate the reference temperature required to evaluate properties in each term such as the bulk or wall temperature. While this type of complex equation can be useful in fitting experimental data for later use, having 8 direct coefficients and more variability due to the choice of reference temperature suggests that any specific correlation contains little predictive insight into the actual physics of fluid flows at supercritical pressures. Some of the general trends in these fitting variables are noteworthy, including that the exponents on the Reynolds and Prandtl numbers are typically close to their values in the DIttus and Boelter equation and that where all fluid property ratios are evaluated as the ratio of the property calculated used the bulk and wall temperatures, respectively, the exponents m3, m4, m5, and m6 have a magnitude typically less than 1 and are negative, positive, negative, and positive, respectively.

$$Nu = C_1 Re_{t,x}^{m_1} Pr_{t,x}^{m_2} \left(\frac{\rho_{t,x}}{\rho_{t,x}}\right)^{m_3} \left(\frac{\mu_{t,x}}{\mu_{t,x}}\right)^{m_4} \left(\frac{k_{t,x}}{k_{t,x}}\right)^{m_5} \left(\frac{c_{p,t,x}}{c_{p,t,x}}\right)^{m_6} \left(1 + C_2 \frac{d_{hyd}}{L}\right)^{m_7} \quad \textbf{(31)}$$

The reference temperature method has been used in conjunction with or instead of the property ratio method, and consists of evaluating the properties used in correlations like those discussed previously at a suitable reference temperature that most closely approximates the properties within a turbulent boundary layer such as the film temperature, the arithmetic average of the wall and bulk temperatures, or at a reference temperature determined from experimental data as a function of the weighted average of the wall and bulk temperatures as demonstrated by Deissler and Taylor [30]. The pressure is usually assumed effectively constant throughout the channel. Deissler's method applied to gases or liquids with fairly simple relationships between their properties and temperature works well on its own and results in a weighting factor that increases monotonically, but for supercritical water the weighting factor various considerably with heat flux in both trend and magnitude as shown in *Figure 59* for the friction factor and in *Figure 60* for the Nusselt number. Like the generalized correlation from Pioro this method seems again to work well at making experimental data more usable, but due to its complexity does not bode well for a fluid-agnostic method of correlating thermal and hydraulic performance.

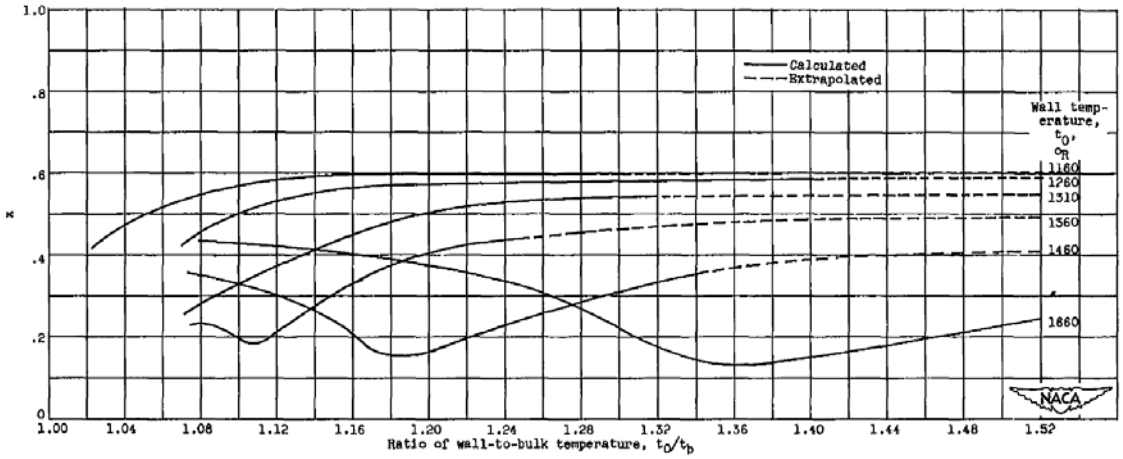

Figure 59: A plot of weighting factor x versus the ratio of wall and bulk temperature, where x is defined by $T(x) = x\,(T_w - T_b) + T_b$, for the friction factor of water at a pressure of 5000 psi from Deissler and Taylor [30].

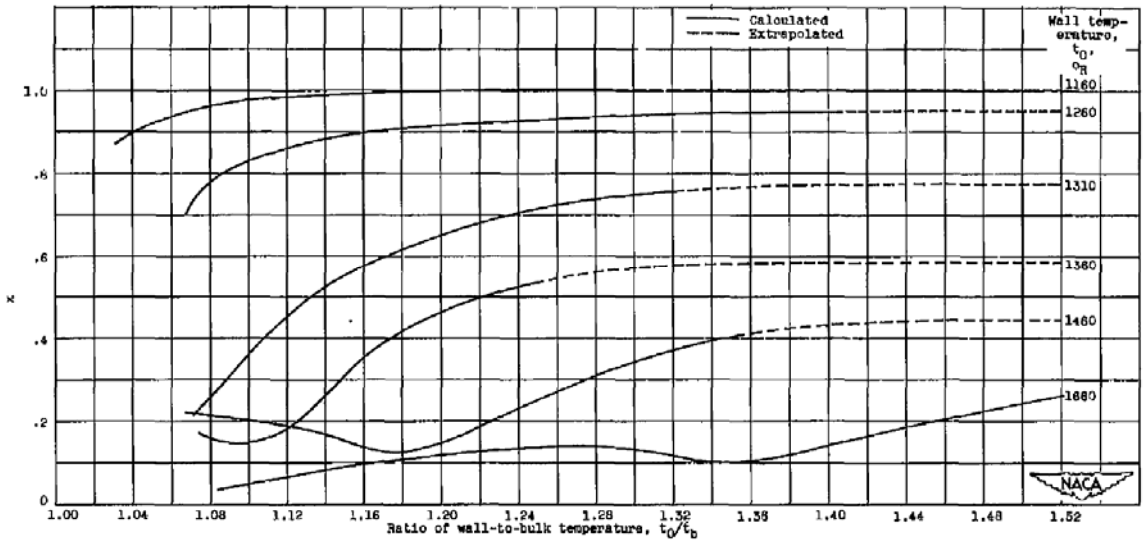

Figure 60: A plot of weighting factor x versus the ratio of wall and bulk temperature, where x is defined by $T(x) = x\,(T_w - T_b) + T_b$, for the Nusselt number of water at a pressure of 5000 psi from Deissler and Taylor [30].

3.2.3 Types of Compact Heat Exchangers

Compact heat exchangers (CHEs) are typically classified as heat exchangers with a surface area density higher than 300 m^2/m^3 according to the surface area and total unit volume as defined by Equation (32) or alternatively according to the porosity and hydraulic diameter as defined by Equations (32) through **(35)** from Hesselgreaves [6].

$$\beta = \frac{A_s}{V} \tag{32}$$

$$d_h = \frac{4V_{fluid}}{A_s} \tag{33}$$

$$\phi = \frac{V_{fluid}}{V} \tag{34}$$

$$\beta = 4\left(\frac{A_s}{4V_{fluid}}\right)\left(\frac{V_{fluid}}{V}\right) = \frac{4\phi}{d_h} \tag{35}$$

Many different types of compact heat exchangers have been developed to meet a variety of process, environmental, and cost constraints, and for each general type many more variations in surface geometry have been tested. Several CHEs have similar basic parallel plate to tube-like channel geometries and stacked-plate construction methods including plate or plate and frame heat exchangers (PHEs), plate-fin heat exchangers (PFHEs) or sometimes called formed-plate heat exchangers when they are diffusion bonded (FPHEs), Marbond™ or more generically chemically-blanked plate heat exchangers (CBHEs), and chemically-machined plate heat exchangers (CMHEs) that will be referred to throughout this document in line with other literature as printed circuit heat exchangers (PCHEs). It should be noted that term PCHE has been used by some authors with a trademark [31], though the company founded by the developers of the printed circuit heat exchanger do not use a trademark in their website and technical publications [32]. CHEs other than PCHEs will be introduced here briefly for comparison, but those looking for a more extensive review can refer to Hesselgreaves [6], or for more recent details focusing on applications to solar thermal receivers to Li et al. [33]. A summary of typical

characteristics of these CHEs from both Hesselgreaves and Li et al. are presented in *Table 8*, although Dostal [4] discusses that Heatric™ prefers to quote prices in terms of $/kg, typically 30 to 50 $/kg on average, of the delivered PCHE since the thermal duty can be changed so easily by varying the surface geometry of the plates.

Table 8: A comparison of several compact heat exchanger characteristics with data from [6] and [33].

CHX Type	P_{max} [MPa]	T [C]	β [m^2/m^3]	d_h [mm]	Cost [$-K/W]
PHE (Gasketed)	2.5 to 3.5	-35 to 250	120 to 660	2 to 10	0.03 to 0.06
PFHE (Brazed)	9 to 12	Cyro to 700	800 to 1,500	1 to 2	0.3
PFHE (Diffusion-Bond)	20 to 62	Up to 800	700 to 800	1 to 2	None Given
CBHE	40	-200 to 900	Up to 10,000	0.33 to 1	None Given
PCHE	50 to 100	-200 to 900	200 to 5,000	0.5 to 3	0.6 to 0.9

Plate and frame heat exchangers consist of a series of plates mechanically formed into some combination of chevron, longitudinal, and lateral corrugations. As shown in *Figure 61*, these plates are stacked together in a frame assembly using alignment slots and capped at either end with stiffer flat plates. Alternating plates can be sealed as desired using gasket material to achieve different parallel and counter-flow arrangements, as well as multi-pass arrangements. The primary benefits of this type of heat exchanger include its low cost, modularity, and capability to be mechanically cleaned by separating the plate stack.

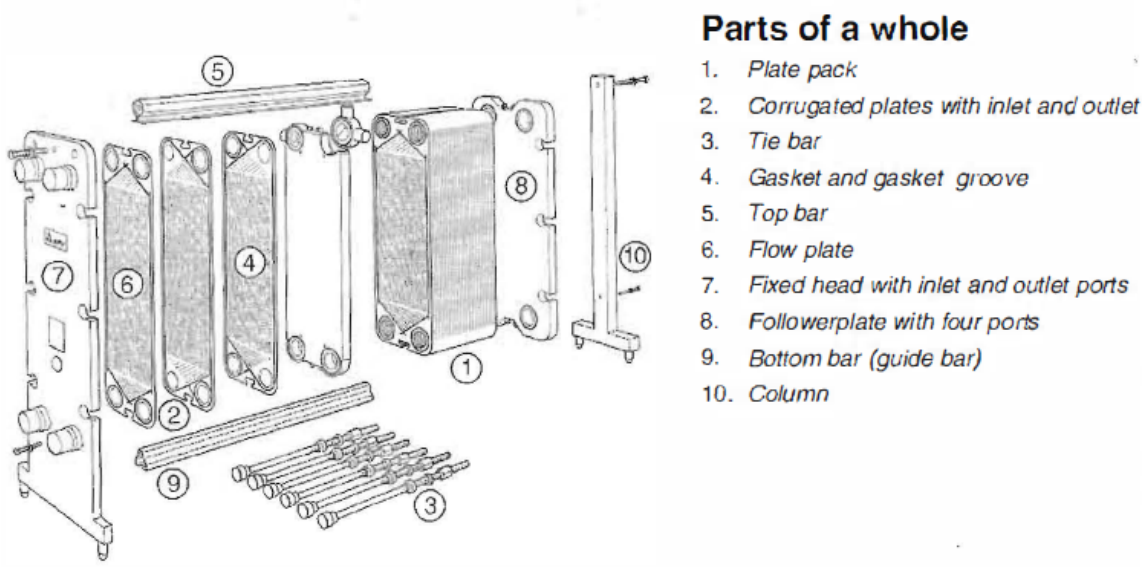

Figure 61: A diagram of a plate and frame heat exchanger from Hesselgreaves [6].

Both brazed and diffusion-bonded plate-fin heat exchangers (PFHEs) consist of a collection of corrugation and parting sheets, as well as edge bars as shown for a single layer in *Figure 62*, that are dip or vacuum-brazed or diffusion-bonded together to form a single heat exchanger core. One or more of these cores are then welded together and headers and nozzles attached to complete the unit as shown in *Figure 63* for a single core. Many different types of corrugation plates and arrangements of the stack into parallel, cross, or counter flow for one or more fluid passes can be used. These CHEs are used extensively due to their low cost, high degree of compactness, and flexibility in flow arrangements, but unlike PHEs are sealed and must be chemically cleaned when required. An interesting extension of the PFHE concept is a combination of alternating corrugated and printed circuit plate layers diffusion-bonded together to form a hybrid heat exchanger that can efficiently and compactly transfer heat between a high-pressure, high-density fluid and a low-density fluid rather than using multiple printed-circuit plate layers to achieve the same cross-sectional flow area for the low-density fluid pass.

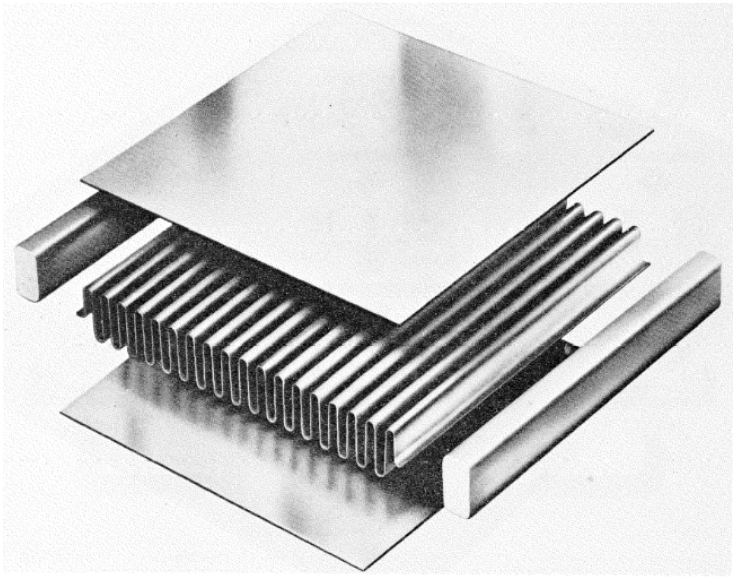

Figure 62: A diagram from Taylor [34] of a single PFHE layer including the corrugation sheet, parting sheets, and side bars.

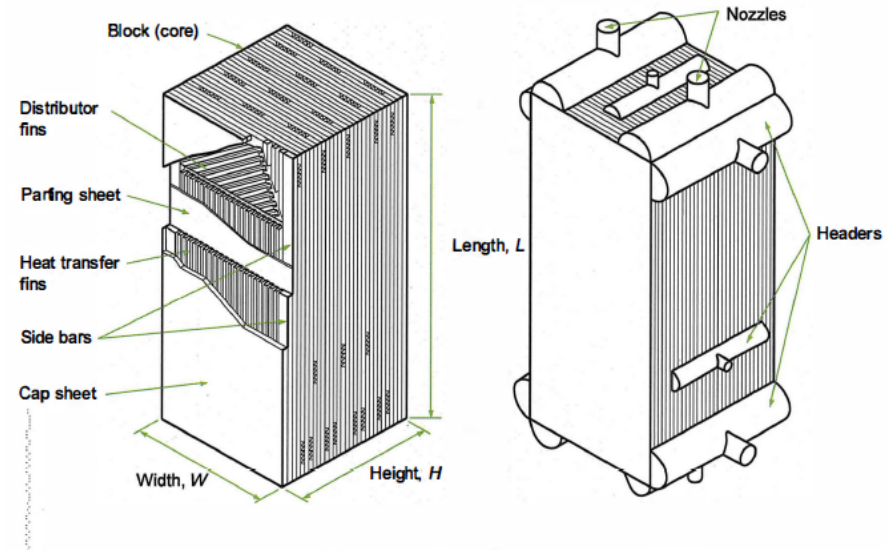

Figure 63: A diagram of a PFHE as well as typical header and nozzle attachments from the ALPEMA Standards [35].

A chemically-blanked heat exchanger (CBHE), or Marbond™ heat exchanger as produced by Chart Heat Exchangers and shown in *Figure 64*, is formed from a stack-up of diffusion-bonded thin plates that have been photo-chemically blanked to form many slots. When assembled these slots align to form an intricate network of flow passages capable of exchanging heat between multiple streams in combinations of parallel, cross, and counter-flow. As explained by Black et al. [36], one of the advantages of chemical blanking used for this type of heat exchanger over the chemical machining used for PCHEs is that by etching through the plate the resulting slot can have sides almost perpendicular to the plate face, while the chemical machining process will necessarily leave three-dimensional rounding and defects when etching a homogenous material as discussed in more detail in Section **Error! Reference source not found.** of this text. Like PFHEs this heat exchanger is sealed and must also be chemically cleaned.

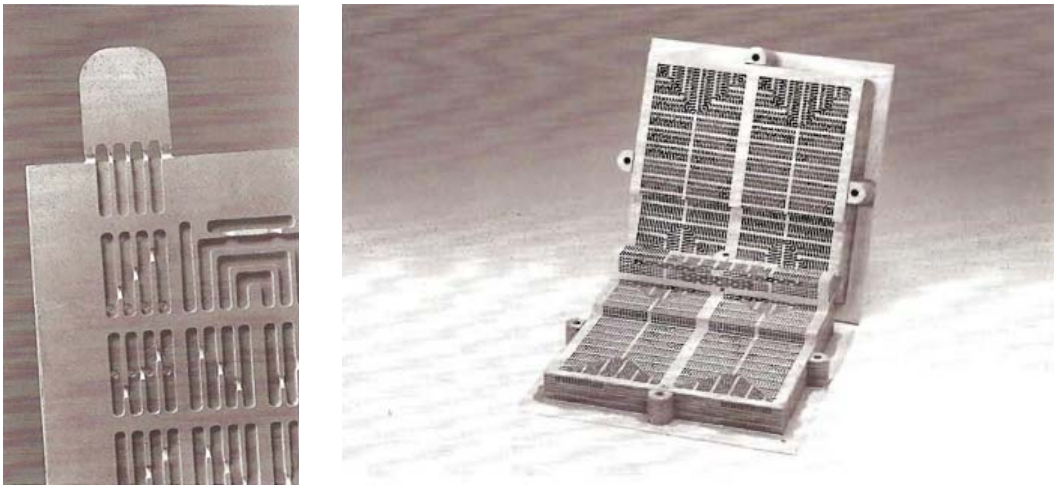

Figure 64: Detail and cut-away views of a CBHE from Hesselgreaves [6].

A printed circuit heat exchanger (PCHE) is fabricated from a series of chemically-machined flat plates stacked and diffusion-bonded into a heat exchanger core, resulting in a very similar form to the PFHE as shown in *Figure 63*. PCHE plates have an advantage over PFHE corrugations in that much more varied and complex flow geometries can be produced as shown in *Figure 65*. Just like PFHE cores PCHE cores can be welded into larger assemblies and fitted with headers and nozzles as shown in *Figure 66* and *Figure 67*, though integral header designs more similar to the header arrangement of PHEs are also available. PCHE and PFHE surfaces have also been combined in novel ways to form hybrid heat exchangers that benefit from the high pressure containment of PCHE plate surfaces and the high cross-sectional area and fin enhancement of PFHEs. The main disadvantages of PCHEs are their current high cost, that they must be cleaned chemically, and that the chemically-machined channels have a characteristic semi-circular shape due to etch factor or etching anisotropy effects as discussed by Black et al. [36] and in more detail in Section **Error! Reference source not found.** of this text.

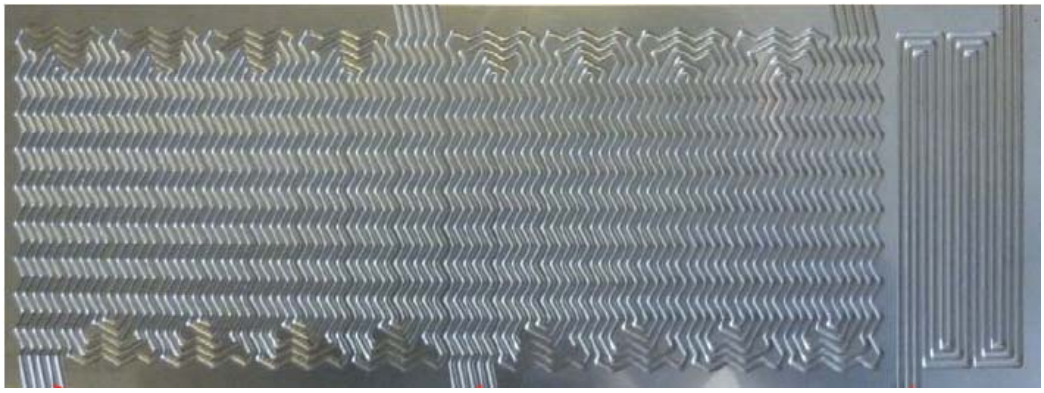

Figure 65: Image of a multi-stream PCHE plate from Le Pierres et al. [37].

Figure 66: Images of welding and assembly of PCHE cores from Southall et al. [38].

Figure 67: Image of a completed PCHE from Southall et al. [38].

3.2.3.1 Comparing Heat Exchanger Surface Performance

The most often used method for comparing heat exchangers uses the ratio of the Fanning (or Darcy) friction factor and the Colburn j factor (or the inverse of this ratio termed the "Flow Area Goodness Factor") where C_f and j are defined in Equations (36) and (37). Note that other texts use f for the Fanning friction factor, but C_f will be used throughout this work in order to differentiate the Fanning (C_f) and Darcy ($f = 4\ C_f$) friction factors. Lower ratios of C_f/j and higher ratios of j/C_f are preferred.

$$C_f = \frac{\tau_w}{\frac{1}{2}\rho \bar{v}^2} = \frac{1}{2}\Delta P_{frictionm}\frac{d_{hyd}}{L}\frac{\rho}{G^2} \tag{36}$$

$$j = \frac{Nu}{RePr^{\frac{1}{3}}} = StPr^{\frac{2}{3}} = \frac{h\rho\mu}{kPr^{1/3}G} \tag{37}$$

The reasoning behind the Colburn j factor as explained by Kays and London [39] comes from the fact that the Nusselt number of a surface is typically dependant on the Prandtl number to the 1/3 power and the Reynolds number to a power close to unity, like in the Dittus and Boelter correlation in Equation (20), or exactly equal to

unity for a flat plate, so that dividing the Nusselt number in this way creates a parameter primarily dependant on the Reynolds number of the flow. Since the friction factor and Colburn j factor are each weak functions of Reynolds number their ratio does not vary a great deal with Reynolds number. This method is used frequently in papers from Heatric such as *Figure 68* from Southall et al. [40] comparing several types of plate-fin and PCHE surface geometries, although the vertical axis is always left without a numerical scale.

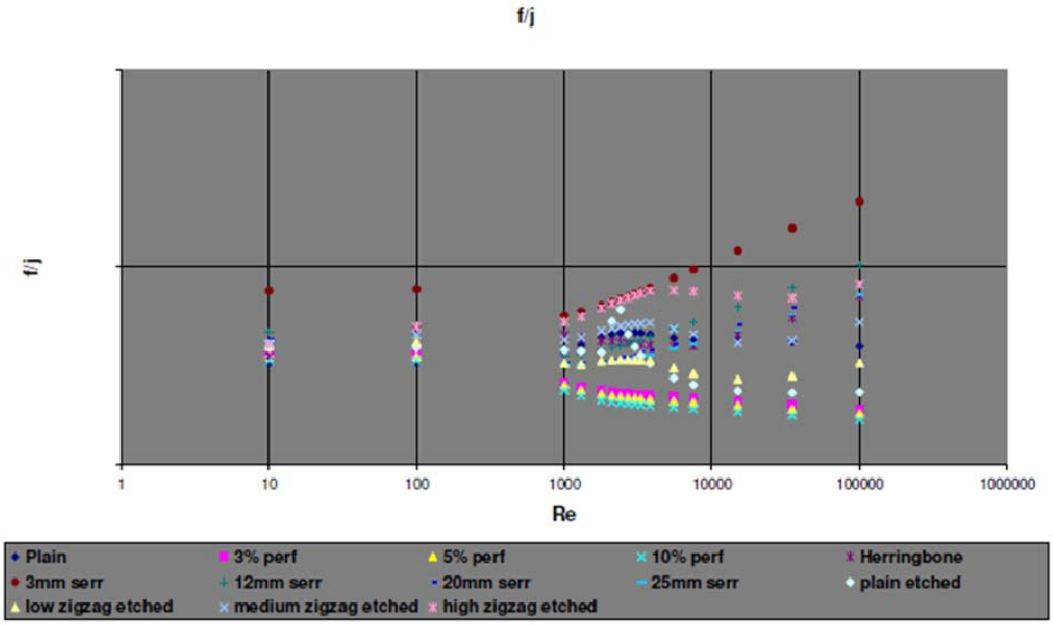

Figure 68: A plot of the ratio of the fanning friction factor (shown temporarily as f) and the Colburn j factor of several PFHE and PCHE surfaces, from Southall et al. [40].

Hesselgreaves [6] derives several relationships involving this term that are useful in sizing heat exchangers, including a dimensional operating parameter, a non-dimensional face area parameter, a dimensional volume parameter, aspect ratio parameter, and weight expression, as well as a relation for equivalent pumping power.

There are also a few notable values of the flow area goodness parameter f/j that are useful to keep in mind when using this parameter for comparisons. As derived for example in Nellis and Klein [11], the Reynolds analogy assumes that the thermal and momentum boundary layers along a flat plate grow at the same rate, and so the ratio of the Fanning friction factor to the Colburn j factor can be stated as shown in Equation (38), resulting in a flow area goodness parameter as shown in Equation (39). Nellis and Klein also show the derivation of the modified Reynolds analogy, or the Chilton-Colburn analogy, by assuming that the thermal and momentum boundary layers grow instead proportional to the Prandtl number to some power as shown in Equation (40) for an exponent of 1/3. This leads to a constant area goodness factor of 2, as shown explicitly in Equation (41). Finally, any two correlations for the Fanning friction factor (or Darcy friction factor divided by 4) and Nusselt number can be combined to form a reference flow area goodness factor, as shown in Equation (42) using the Blasius correlation from Equation (9) and the DIttus and Boelter correlation from Equation (20). These values compare well with those from Kays and London (1984) as reported by Hesselgreaves [6] of between 3 and 6 for different compact heat transfer surfaces.

$$\frac{C_f Re_x}{Nu_x} = 2 \qquad (38)$$

$$\left.\frac{C_f}{j}\right|_{\substack{Reynolds\\Analogy}} = \frac{C_f Re}{Nu} Pr^{\frac{1}{3}} = 2Pr^{\frac{1}{3}} \tag{39}$$

$$\frac{C_f Re_x Pr^{\frac{1}{3}}}{Nu_x} = 2 \tag{40}$$

$$\left.\frac{C_f}{j}\right|_{\substack{Chilton-Colburn\\Analogy}} = \frac{C_f Re Pr^{\frac{1}{3}}}{Nu} = 2 \tag{41}$$

$$\left.\frac{C_f}{j}\right|_{Blasius-DB} = \frac{1}{4}\frac{0.316}{Re^{0.25}}\frac{RePr^{\frac{1}{3}}}{0.023Re^{0.8}Pr^{\frac{1}{3}}} = \frac{3.435}{Re^{0.05}} \approx 3.435 \tag{42}$$

Another method proposed by Ruhlich and Quack ([41] and [42]) for regenerators and reviewed previously by Kruizenga [7] uses a porosity-based hydraulic diameter and average velocity as defined in Equations **(43)** and **(44)** based on the diagram in *Figure 69*. As shown in Equation **(45)**, this allows the definition of Reynolds number depending only on the regenerator matrix volume, porosity, and an estimate of the matrix surface area per unit volume. Finally, the ratio of the number of pressure heads (NPH) to the number of transfer units (NTU) is determined as expected being careful to use the porosity-based hydraulic diameter as the length scale when needed according to Equation **(46)**.

$$d_{hyd,\phi} = \frac{4V_{fluid}}{S} = \frac{4\phi(HWL)}{S} \tag{43}$$

$$\bar{v} = \frac{\dot{m}}{\rho(WH)}\frac{(WH)}{A_c} = \frac{\dot{m}}{\rho(WH)}\frac{1}{\phi} \tag{44}$$

$$Re_\phi = \frac{\rho \bar{v} d_{hyd,\phi}}{\mu} \tag{45}$$

$$\frac{NPH}{NTU} = f\frac{L}{d_{hyd,\phi}}\left(\frac{Nu_\phi}{Re_\phi Pr}\frac{4L}{d_{hyd,\phi}}\right)^{-1} = \frac{fRe_\phi Pr}{4Nu_\phi} \tag{46}$$

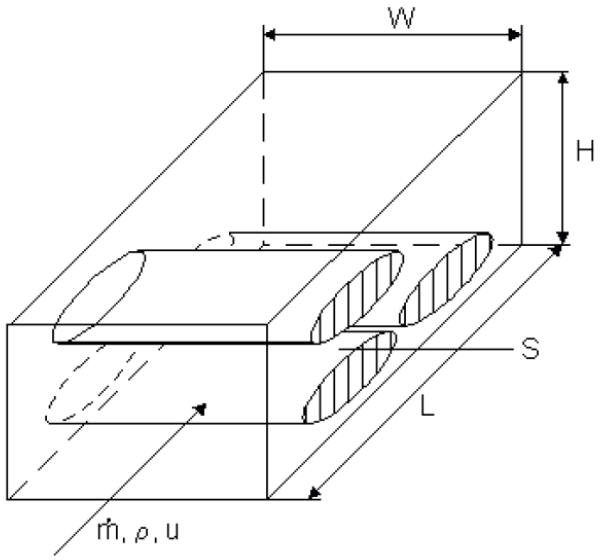

Figure 69: A diagram of a new regenerator comparison methodology proposed by Ruhlich and Quack [42].

This method however is more applicable to regenerators where the flat wall surface area outside of the matrix structure is negligible in terms of heat transfer, and non-cyclic heat exchangers must be corrected to include wall surface area or a misleading hydraulic diameter will be calculated. In the case of PCHEs where the fins between channels can be treated as primary surfaces, this reduces in more standard notation to Equation **(47)**, which is simply a re-arrangement of Equation **(35)**. Following through the rest of the derivation and substituting the definition of the Colburn j factor from Equation **(37)** yields Equation **(48)** which shows the NPH/NTU method for non-cyclic heat exchangers is equivalent to scaling the flow area goodness factor by the Prandtl number of the fluid and a factor of 4. Because the Colburn j factor already captures the majority of the Prandtl number dependence of the flow area goodness factor, this extra dependence is actually un-helpful as plots of NPH/NTU must then be stated for a specific Prandtl number as is done by Ruhlich and Quack as reproduced in *Figure 70*.

$$d_{hyd} = \frac{4V_{fluid}}{A_s} = \frac{4\phi}{\beta} \tag{47}$$

$$\frac{NPH}{NTU} = \frac{fRe_{d_h}Pr}{4Nu_{d_h}} = \frac{1}{4}\frac{f}{St} = \frac{1}{4}\frac{f}{j}Pr^{\frac{2}{3}} \tag{48}$$

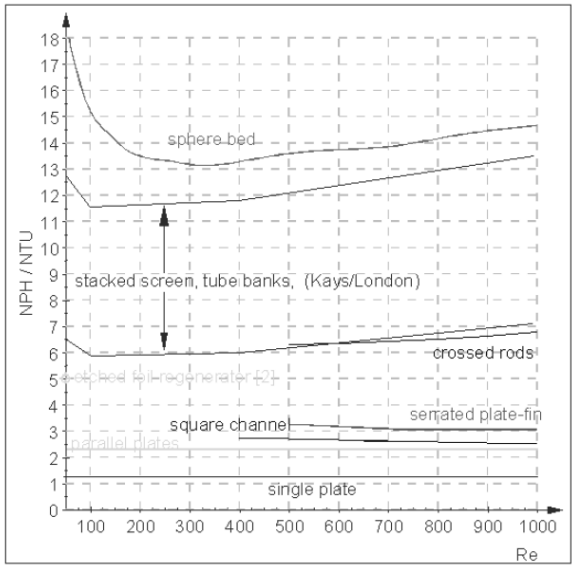

Figure 70: Laminar flow comparison of several regenerator types using porosity-based parameters for a Prandtl number of 0.7, from Ruhlich and Quack [41].

Finally one recent method proposed by Fan et al. [43] involves plotting the Nusselt number (or Colburn j factor) versus the (Darcy) friction factor both scaled to some standard performance measure, as shown in *Figure 71* from Li et al. [33] for various flow modifications to plate and frame heat exchanger surfaces, assuming that both parameters are only functions of Reynolds number.

The advantage of this method is that by assuming constant fluid properties, equal heat transfer areas, equal cross-sectional areas, and equal hydraulic diameters, several different levels of performance baselines can be referenced in the same plot. Fan et al. develops three baselines under these assumptions; relations for the ratio between the enhanced and reference surfaces of the heat rate under identical pumping power (line between zones 1 and 2), the heat rate under identical pressure drop (line between zones 2 and 3), and the heat rate under identical flow rate (line between zones 3 and 4), as noted in the figure with each level becoming increasingly more difficult to achieve. These baselines only show lines where the heat flow ratio is unity, but parallel lines can be extended up and to the left on the plot for higher ratios accordingly with each baseline, so that the best position on the plot would be in the top left (high thermal ratio and low hydraulic ratio) although any position in zones 2, 3, and 4 is beneficial from an energy standpoint. These implications are summarized in *Table 9* as they can be initially confusing.

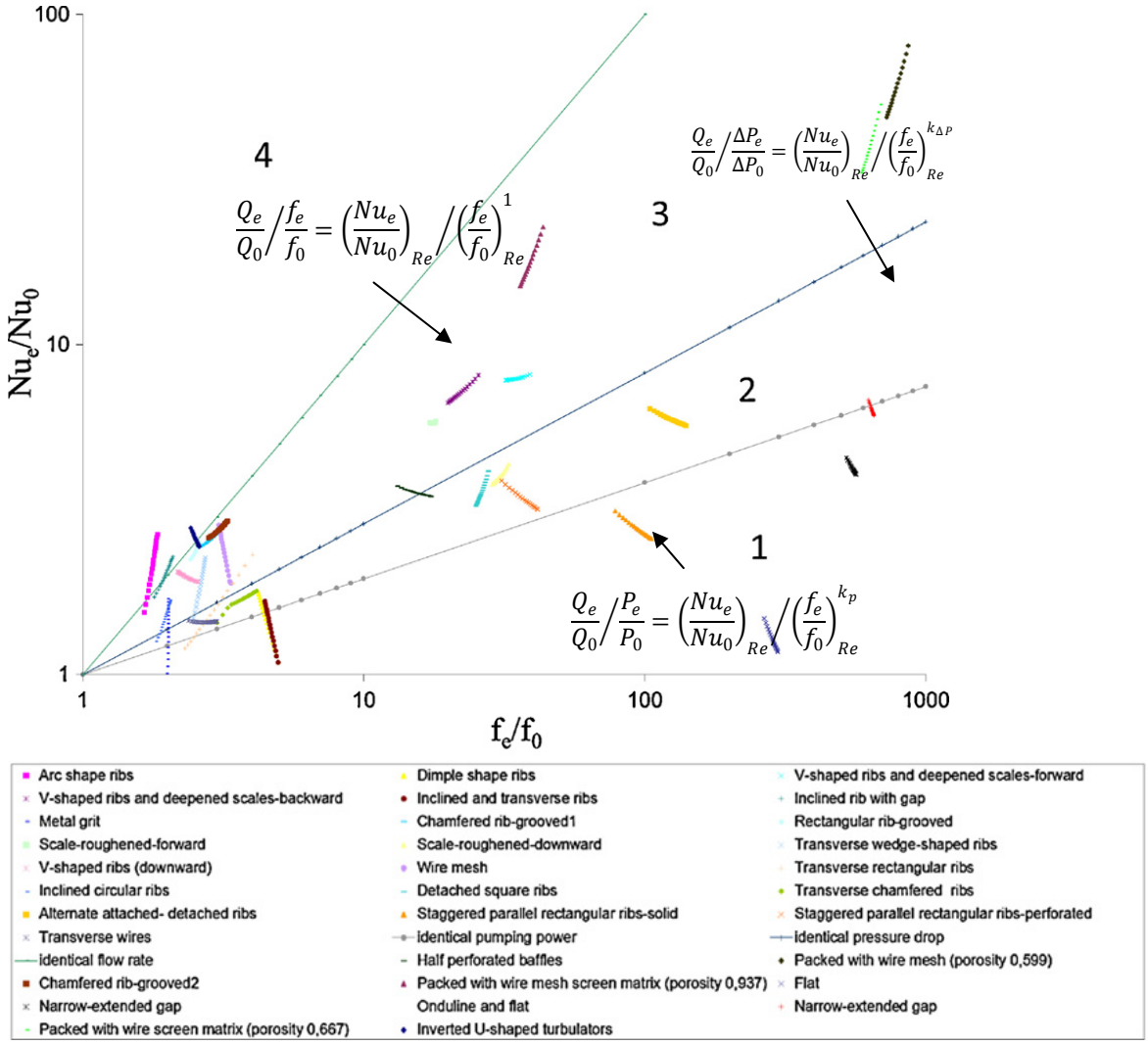

Figure 71: A comparison of the Nusselt number versus the Darcy friction factor scaled to the performance of flow between flat plates for a plate and frame heat exchanger, from Li et al. [33] (equations and arrows mine).

Table 9: A summary of the meaning behind the zones shown in Figure 71 from Li et al. [33] based on Fan et al. [43].

Point in:	Meaning
Zone 1	The increase in heat transfer rate ratio is too small to outweigh the increase in the pumping power ratio.
Between 1 and 2	The increase in heat transfer rate ratio just matches the increase in the pumping power ratio.
Zone 2	The increase in heat transfer rate ratio is larger than the increase in the pumping power ratio.
Between 2 and 3	The increase in heat transfer rate ratio just matches the increase in the pressure drop ratio ***and*** is larger than the increase in pumping power ratio.
Zone 3	The increase in heat transfer rate ratio is larger than the increase in the pressure drop ratio ***and*** is larger than the increase in pumping power ratio.
Between 3 and 4	The increase in heat transfer rate ratio just matches the increase in the flow rate ***and*** is larger than the pressure drop ratio ***and*** is larger than the increase in

	pumping power ratio.
Zone 4	The increase in heat transfer rate ratio is larger than the increase in the flow rate ***and*** is larger than the pressure drop ratio ***and*** is larger than the increase in pumping power ratio.

3.3 Printed Circuit Heat Exchangers

3.3.1 Manufacturing and Assembly

The surface geometry of a printed circuit heat exchanger (PCHE) is produced using a process of chemical machining on a flat plate. This manufacturing process is similar to that used to fabricate printed circuit boards for electronics, thus lending to their common description as PCHEs rather than the more generic term chemically-machined plate heat exchanger (CMHE). This manufacturing process distinguishes PCHEs from other types of flat-plate compact heat exchangers mentioned previously, although the general shape of the flow channels in all three of these heat exchanger types can be similar. Chemical machining will be introduced here briefly as aspects of the manufacturing process dictate geometrical characteristics of any potential PCHE channel, but a more general review with references to studies on process conditions is given by Allen [44].

3.3.1.1 Plate Fabrication

As outlined by Black et al. [36] and Mylavarapu [45], a basic photochemical machining process involves cleaning, masking the surface of a PCHE plate and exposing the mask to achieve the desired 2-dimensional pattern, then immersing the plate in an etchant bath for a period of time until the desired etched depth is reached, as depicted in *Figure 72*. *Table 10* compares several typical manufacturing parameters for both conventional end milling and chemical machining including feed rates, surface finish, and accuracy as well as the measured surface finish for the PCHE test plates used in this study. The two manufacturing methods can produce similar surface finishes with similar accuracy, but the penetration rate of chemical machining is clearly several orders of magnitude less than the feed rate of end milling. This drawback is compensated by the significantly lower cost or chemical machining tooling as well as the ability to achieve relatively low penetration rates across a large surface area on several parts at once.

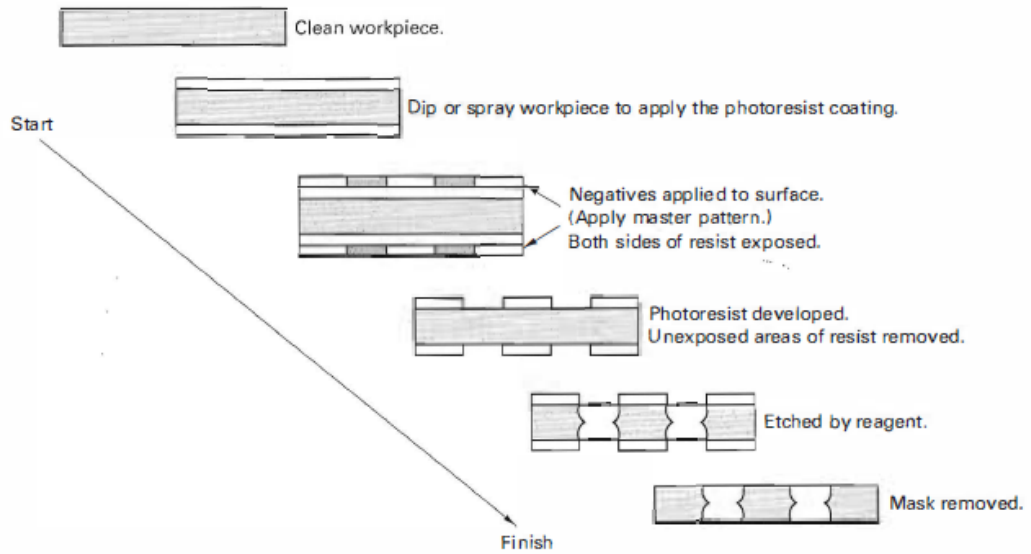

Figure 72: A diagram of the photochemical machining process from Black et al [36]. Note that PCHE plates are typically etched on only one side while chemically blanked plate heat exchangers (CBHE or Marbond™) are etched through from both sides (blanked) as shown.

Table 10: A comparison of several manufacturing parameters from Black et al [36]. Note that the feed rate for chemical machining is actually the etchant penetration rate.

Method / Example	Feed Rate [mm/min]	Finish [µm]	Accuracy [mm]
End Milling	25 to 5000	1.5 to 3.75 (AA)	0.025 to 0.05
Chemical Machining	0.013 to 0.076	0.2 to 6.35	0.025 to 0.05
UW PCHE Channels	-	2.2 (average)	-
Ishizuka et al. [46]	-	2 to 3 (average)	-
Mylavarapu et al. [45]	-	0.4 (average)	-

Chemical machining has several important defects that must be considered when designing a PCHE channel, including overhang, islanding, and dishing as shown as (a), (b), and (c), respectively in *Figure 73*. All three defects occur due to inhomogeneity in the etchant solution near the part either due to improper agitation of the etchant bath or improper cleaning of the part surface.

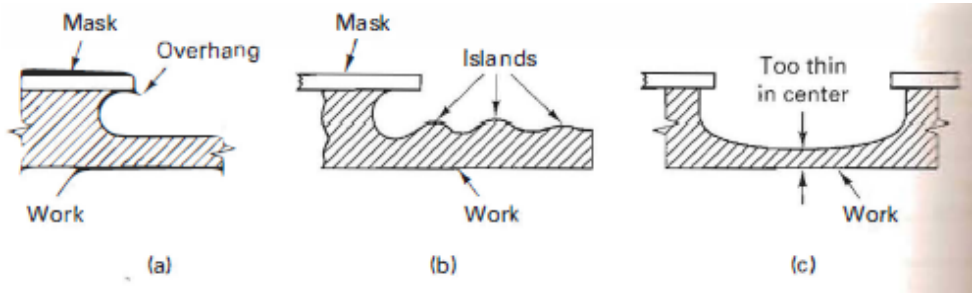

Figure 73: A diagram of photochemical machining defects including (a) overhang, (b) islanding, and (c) dishing, from Black et al [36].

As the etchant will attack any exposed surface area PCHE channels have a characteristic roundness that can vary between a section of an ellipse, a section of a circle, and that of a rectangular channel with rounded interior corners depending on the etch depth, width, and the manufacturing conditions. This rounding is known as the etch factor or etch radius E, defined according to Equation **(49)** where for now the channel height is given as the depth of cut d and the undercut as U, and shown in *Figure 74*, or inversely as the anisotropy A for photochemical machining. The mask dimensions must therefore be reduce symmetrically by twice the expected undercut based on the etch factor.

$$E = \frac{U}{d} = \frac{1}{A} \tag{49}$$

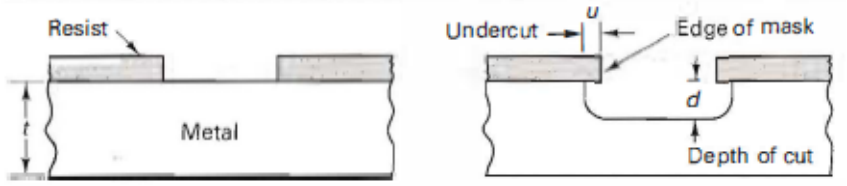

Figure 74: A diagram of the etch radius in photochemical machining from Black et al [36].

The effect of the etch factor is clearly visible on plate cross sections shown by *Figure 75* from Southall [47], *Figure 76* of the s-shaped fin channels from Tsuzuki et al. [48], as well as those manufactured for UW-Madison by Microphoto Inc. as shown by the measured point-cloud representation of the 80-degree zig-zag plate unit cell in *Figure 77*. The process used to produce this measurement is discussed in Section 3.4.4, but the measurements indicate continuous channels are circular segments rather than being semi-circular with a depth only about 70% of the profile radius. This discrepancy is likely not noticed as most researchers assume a semi-circular profile based on a top-down view of the etched channels, see *Figure 78*, and may change after diffusion bonding as suggested by the crushing at the top of the PCHE "fin" in *Figure 75*.

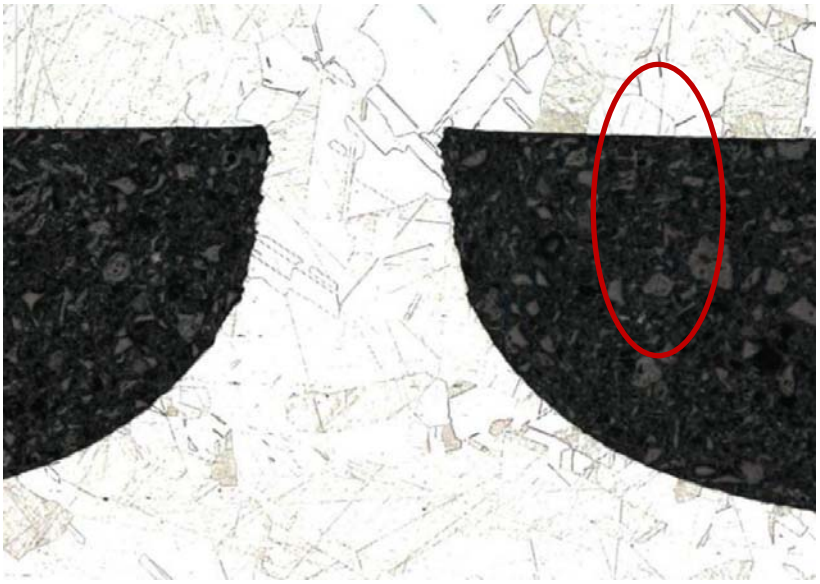

Figure 75: A micrograph of a Heatric PCHE plate section showing the smooth roundness of the bottom of the channel indicative of undercutting as well as a rougher area near the top of the fin likely due to compression during diffusion bonding, from Southall [47].

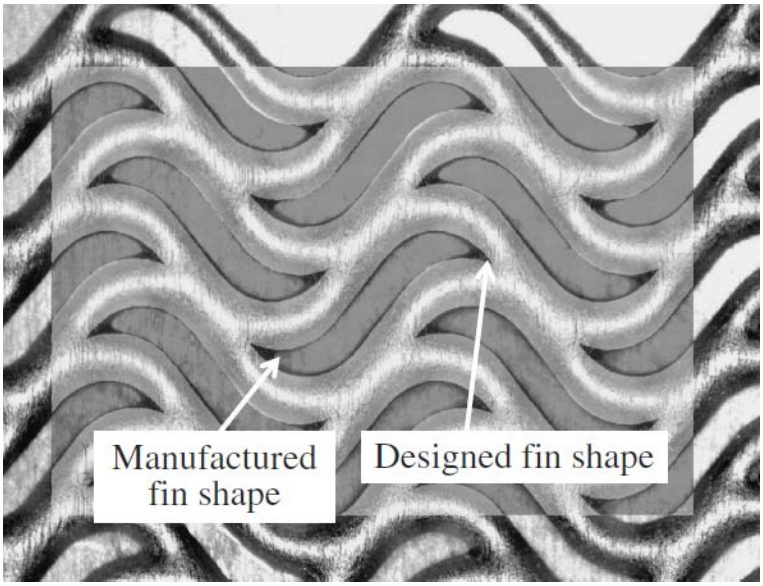

Figure 76: A plan view of the s-shaped fin PCHE surface investigated by Tsuzuki et al. [48] showing in particular the rounding effect of the etch factor on the sharp-designed leading and trailing edges of the fin.

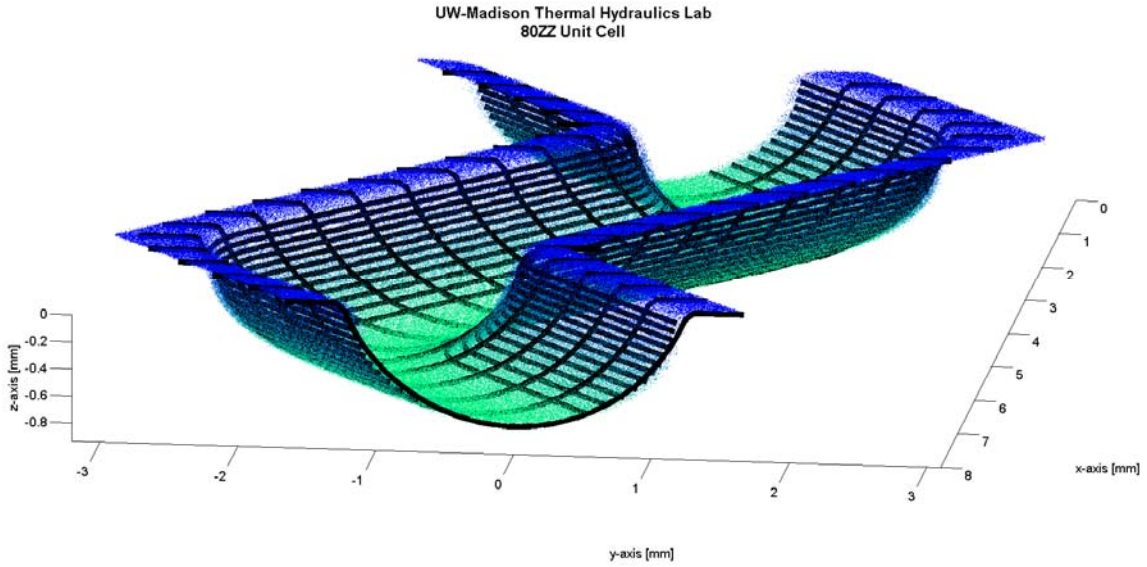

Figure 77: The measured average unit cell of the 80-degree zig-zag channel plate surface with interpolation lines overlaid in black and depth shown as a color gradient from dark blue to light green.

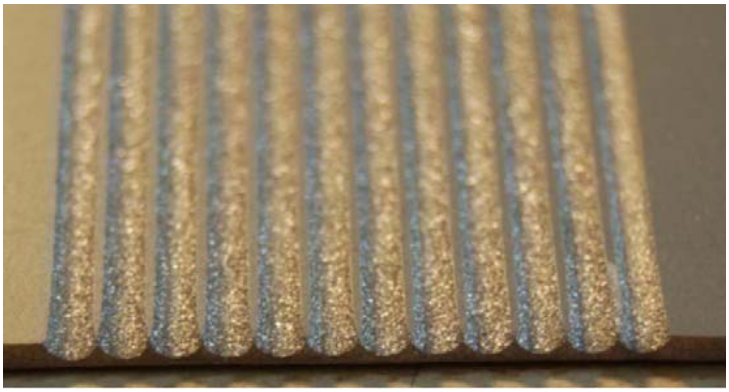

Figure 78: An image of the etched channel cross-section from Mylavarapu et al. [49].

3.3.1.2 Core Assembly

Once fabricated, individual PCHE plates, and optionally additional corrugated fins and parting sheets for hybrid PCHE-PFHE designs, are stacked and can be diffusion bonded together in a variety of different arrangements to form a heat exchanger core. This core is an intermediate step in the fabrication of a PCHE and is limited in size by the lesser of the chemical machining equipment limitations (photomask application, exposure, and etchant bath length and width) and the diffusion bonding furnace bed size (length and width) and pressure loading limits (total stack height). For instance, currently Heatric™ manufactures cores up to a limit of 1.5 m x 0.6 m x 0.6 m according to Le Pierres et al. [37], primarily driven by the widest roll-on photoresist film of 0.6 m according to Dostal et al. [4].

Current literature on diffusion bonding by Southall et al. [40], Southall ([47],[50]), and Southall and Dewson [38] go through general descriptions of the diffusion bonding process used for Heatric™ heat exchangers, and recent work by Mylavarapu et al. ([51], [52], [49], and [53]) specifically with Inconel Alloy 617 (UNS N06617) gives some temperature, pressure, time, and surface treatment details for diffusion bonding tests, but exact process descriptions seem to remain proprietary.

The diffusion bonding process is a solid-state joining technique in which the individual layers of the PCHE block are cleaned, coated as needed with a thin layer of material to encourage grain growth, stacked together in a vacuum chamber and taken to a temperature approximately 60 to 80% of the melting temperature of the material and compressed under some applied strain for a matter of minutes to hours to allow material at the plate

boundaries to inter-diffuse and form grains across the interface ([47], [51]). An example stack-up of a hybrid PCHE and PFHE core is shown in *Figure 79*, while *Figure 80* shows a micrograph of a PCHE cross-section after diffusion bonding demonstrating grain growth between the bonded plates.

Figure 79: A photo of a hybrid PCHE and PFHE core, from Southall [40]. The channel perspective can make it difficult to identify, but from the top layer one can see a plate fin layer with side and end bars laid in the plain of the fin corrugations, a parting sheet, a printed circuit layer, and a total of 5 repetitions of this pattern.

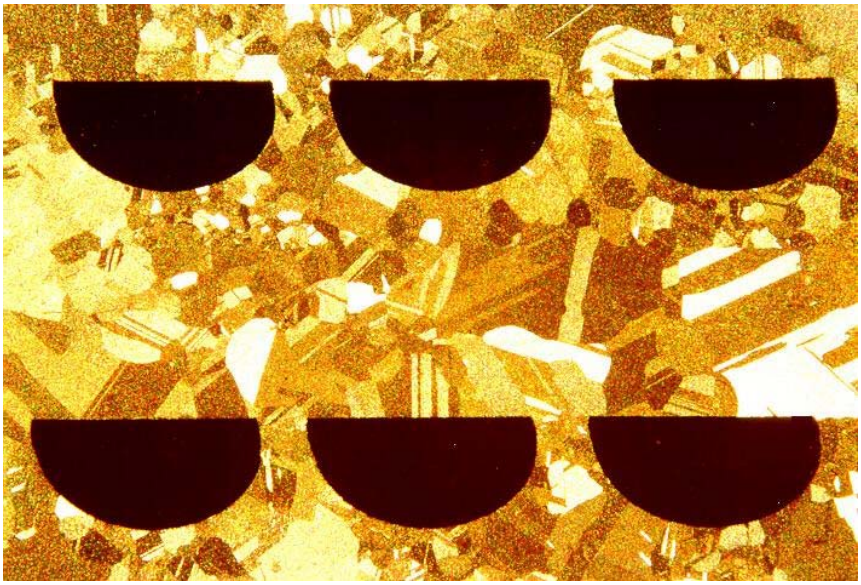

Figure 80: A micrograph from Southall [40] of grain growth after diffusion bonding between the PCHE plate layers.

A careful inspection of *Figure 80*, more easily seen in *Figure 75*, reveals slight deformation or crushing at the top of the PCHE "fin" due to the high temperatures and pressures applied during diffusion bonding. This effect demonstrates that there will be some lower limit in the fin thickness to avoid excessive crushing during diffusion bonding, as well as a lower limit in the thickness of the plate underneath each individual channel due to handling requirements to assemble and align the individual plates in the PCHE core. Both of these thickness limits suggest that for higher porosities (thinner fin and wall thicknesses) the use of plate-fin surfaces is required due to the non-ideal channel aspect ratios produced by chemical machining.

Southall ([50],[47],[38]) describes several tests conducted with 316/316L stainless steels to determine the room-temperature 0.2% proof stress, ultimate tensile strength, and 600 °C creep performance of samples after diffusion bonding. All samples experienced only a slight reduction in strength demonstrating a return to the annealed strength of the as-receive steel, and still met the ASME SA240 strength requirements as long as the as-received stock material slightly exceeding ASME SA240.

To meet thermal duties larger than what a single PCHE core can handle, multiple cores can be welded together and manifolded separately or with a single manifold per side to complete the PCHE as shown in Figure 66 and Figure 67. Southall [40] notes that care must be taken so that thermal stresses are not higher than the core-to-core welds can accommodate at the PCHE operating pressure or cores should be plumbed together in series connected by short piping sections to reduce pressure losses.

The pressure containment requirements for the heat exchanger core can also be reduced by placing the core (or multiple cores) inside a separate pressure vessel using one of the fluids to pressurize the vessel to its operating pressure so that the PCHE need only be designed according to the differential pressure between the channels rather than the maximum differential pressure between the fluid streams and the atmosphere. This would allow closer channel spacing and thinner fin corrugations for plate-fin layers with the associated benefits in heat transfer, but would likely increase the volume and cost of the final PCHE as a thick, high-strength pressure vessel would be required to contain the PCHE core volume.

3.3.2 Surface Geometries

3.3.2.1 Types of Surface Geometries

Several different printed circuit heat exchanger geometries have been discussed in literature and can be broadly categorized as either continuous or discontinuous-fin surface types. Continuous surfaces include straight, sinusoidal, and zig-zag channels, while discontinuous surfaces include louver, sinusoidal fin, and airfoil fin geometries, with a few of these surfaces shown as two-dimensional patterns in *Figure 81*.

Figure 81: Two-dimensional patterns of various PCHE geometries including (a) sinusoidal fin, (b) rounded sinusoidal fin, (c) sinusoidal, (d) sharp zig-zag, and (e) airfoil fin channels.

These ideal surface geometry patterns are often used in numerical analysis assuming that the pattern is uniform throughout the depth of the PCHE channel even though actual chemical etching processes prevent this possibility. Continuous channels such as the straight, sinusoidal, and zig-zag channels can be more easily modeled with varying depth by assuming a semi-circular or some other profile that is uniform along the path length of the channel, but especially for high-angle zig-zag channels the corner roundness can have a major impact on the hydraulic performance of the surface as shown by Van Abel [54].

Straight channels can be analyzed fairly easily analytically as summarized in *Table 11* assuming that the cross-section profile of the channel along the YZ axis is a circular segment. Note that for the case when h is equal to r these equations reduce to the typical assumption of a semi-circular profile.

Table 11: A summary of diagrams and useful equations for straight circular segment PCHE surfaces.

Straight	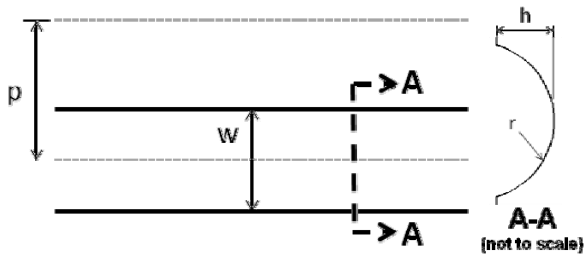	$\alpha = 2\text{acos}\left(\frac{r-h}{r}\right)$ $A_c = \frac{r^2}{2}(\alpha - \sin(\alpha))$ $per = \alpha r + 2r\sin\left(\frac{\alpha}{2}\right)$

Zig-zag channels are more difficult to analyze analytically while including both the effects of pattern and profile rounding. By approximating the channel as having a constant width, as would happen if the interior corner and exterior corner fillet radii were equal, the cross-sectional area and perimeter of the channel can be estimated as shown in *Table 12*. Note that in the diagram the cross-sectional radius is used as this more easily relates to the volume and surface area, but that for zig-zag channels the radius perpendicular to the flow path is more correct when calculating a hydraulic diameter for use with pipe flow correlations. An additional factor is useful for zig-zag channels to describe the increased path length of the channel per unit length in the mean flow direction for instance to approximate the zig-zag surface area as the product of Ls and the channel perimeter. Note this analysis assumes each zig-zag bend has a circular radius, but a similar analysis can be conducted for less-common sinusoidal zig-zag channels.

Table 12: A summary of diagrams and useful equations for circular segment rounded zig-zag PCHE surfaces.

Zig-Zag (ZZ)	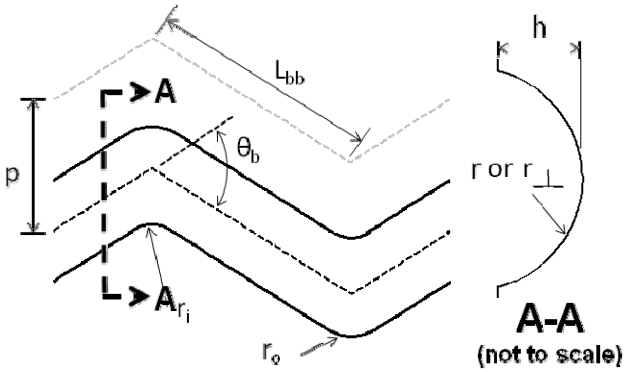	$r_\perp = r\cos\left(\frac{\theta_b}{2}\right)$ $\alpha = 2\text{acos}\left(\frac{r-h}{r}\right)$ $A_c \approx \frac{r^2}{2}(\alpha - \sin(\alpha))$ $per \approx r\alpha + 2r\sin\left(\frac{\alpha}{2}\right)$ $\frac{L_s}{L} \approx \frac{1+\frac{r_i}{L_{bb}}\left(\theta_b - 2\tan\left(\frac{\theta_b}{2}\right)\right)}{\cos\left(\frac{\theta_b}{2}\right)}$

Airfoil fin channels are more difficult still, and require some numerical calculations to understand the geometry of an airfoil-channel surface. For a symmetric NACA00xx airfoil, defined by Equation (50) where the xx is the thickness parameter t in percent, Kruizenga [7] provides an analysis of the axial pitch "s" that produces the most constant cross-sectional area along the channel for a NACA0020 airfoil profile, but does not analyze the full unit cell length of 2s and did not include the top-right airfoil section shown in top left of *Figure 82*. This figure shows a typical free cross-sectional length plot for an airfoil fin surface referenced to the plane view of the surface. The discontinuities present due to the presence and absence of an airfoil section are clearly visible near an axial position of 0.2, 0.8, and 1, with a span of lengths between 0.4 and 0.47. This span will only vary with different ratios of axial pitch to chord length, and the standard deviation of the cross-sectional length can be determined as shown to the right in *Figure 82*, where for a variety of thickness parameters the most-constant cross-sectional area will occur when the axial pitch is approximately 76% of the chord length. This differs slightly from the 86% of the chord length found but Kruizenga and used to design the plates in this study.

$$y(x) = \frac{tc}{0.2}\left(0.2969\sqrt{\frac{x}{c}} - 0.1260\left(\frac{x}{c}\right) - 0.3516\left(\frac{x}{c}\right)^2 + 0.2843\left(\frac{x}{c}\right)^3 - 0.1036\left(\frac{x}{c}\right)^4\right) \quad \textbf{(50)}$$

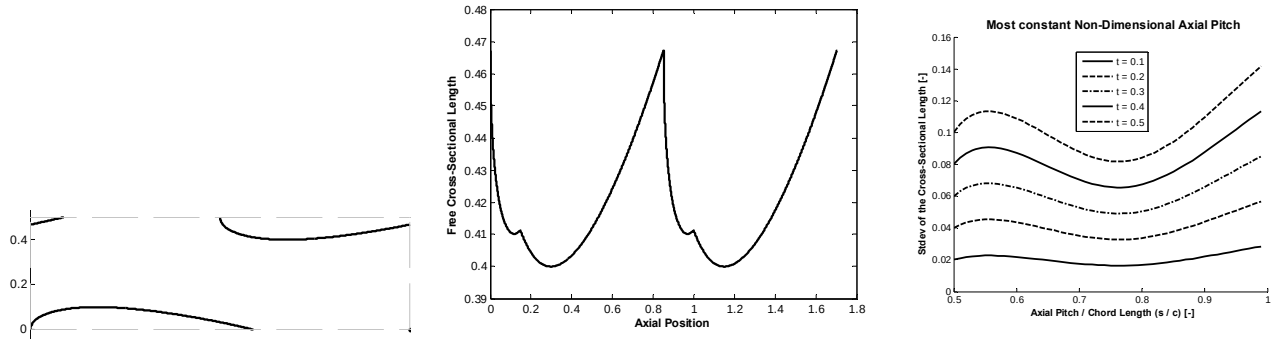

Figure 82: Left: A plane view of a sample airfoil fin channel and the resulting free cross-sectional length distribution along the flow axis. Right: A plot of the standard deviation of the free flow cross-sectional length distribution as a function of the ratios of airfoil thickness to chord length and axial pitch to chord length.

The airfoil profile given in Equation (50) can also be integrated to determine the cross-sectional area and the perimeter of a single airfoil both as functions of only the thickness and chord length as shown in the first two equations of *Table 13*. These parameters, along with the axial and lateral pitches, and the channel depth can be used to estimate the surface area of an airfoil fin channel. The minimum cross-sectional area can also be estimated from the channel depth and the minimum free-flow cross-sectional length of the surface which from *Figure 82* can be determined from the lateral pitch and the airfoil profile evaluated at an x/c value of 0.3 if the ratio of the axial pitch to the chord length is less than 0.7. The actual surface area and cross-sectional area will be slightly different due to etch factor effects with more details presented in Section 3.4.4.

Table 13: A summary of diagrams and useful equations for rounded airfoil fin PCHE surfaces.

Airfoil Fins (AF)

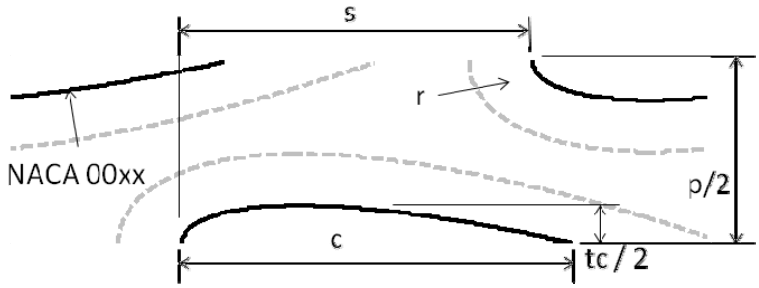

$$\frac{A_{c,AF}}{2tc^2} = 0.340437511$$

$$\frac{per_{AF}}{c} \approx 1.99028537 + 2.12185639t + 1.151409t^2 - 0.381656972t^3$$

$$\frac{r_s}{r} = \begin{cases} \frac{\pi}{2} - 2 + \frac{h}{r} & \text{for } \frac{r}{h} \leq 1 \\ \operatorname{acos}\left(1 - \frac{h}{r}\right) - \sin\left(\operatorname{acos}\left(1 - \frac{h}{r}\right)\right) & \text{for } \frac{r}{h} > 1 \end{cases}$$

$$A_{s,unitcell} \approx 2\left(ps - 2tc^2\frac{A_{c,AF}}{2tc^2}\right) + c\frac{per_{AF}}{c}r\frac{r_s}{r}$$

$$A_{c,min} \approx hl_{min} - h\left(\frac{p}{2} - y(0.3c)\right)$$

For reference another surface that has been investigated by other researchers is the sinusoidal fin or sinusoidal fin surface, as shown in *Table 14*. This fin pattern is constructed by shifting a sinusoidal curve defined by the fin length and fin angle at right angles to the fin angle by the half-width of the fin. This results in two intersecting sinusoidal curves that define the fin. This fin, like the airfoil fin, is actually defined geometrically by the fin angle and the ratio of the fine width and fin length, with the last parameter only determining the scaling of the fin

geometry. Note that this fin definition is actually only valid for fin angles above 46 degrees, after which the top and bottom sinusoids must be shifted in some way not perpendicular to the fin angle as was apparently done by Tsuzuki et al. in parametric studies below 45 degrees [48].

Table 14: A summary of diagrams and useful equations for sinusoidal fin PCHE surfaces.

Sinusoidal Fins (SF)	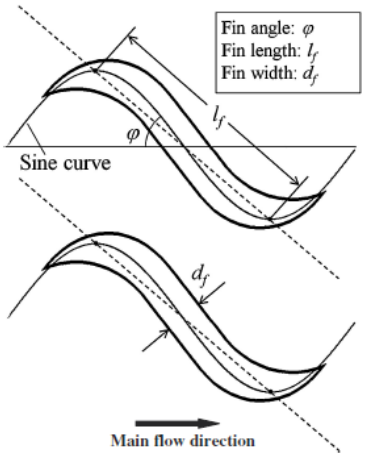	$\psi = \text{atan}\left(\frac{\tan(\varphi)}{\pi}\right)$ $l_x = \frac{l_f}{2}\cos(\psi)$ $l_y = \frac{l_f}{2}\sin(\psi)$ $y = l_y \sin\left(\frac{\pi}{l_x}\left(x \pm \frac{d_f}{2}\sin(\varphi)\right)\right) \pm \frac{d_f}{2}\cos(\varphi)$ $\frac{x_{tip}}{l_f} = \pm\frac{\cos(\psi)}{2\pi}\text{acos}\left(\frac{-\frac{d_f}{l_f}\frac{\cos(\varphi)}{\sin(\psi)}}{\sin\left(\frac{d_f}{l_f}\pi\frac{\sin(\varphi)}{\cos(\psi)}\right)}\right)$

3.3.2.2 Methods of Surface Geometry Measurement

Often in literature models and designs assume a fairly precise, sharp-edged geometry that is not achievable with current chemical machining techniques. Because of this it is useful to measure the actual surface geometry in some way to account for deviations from design dimensions.

This simplest and most common method of inspection involves simply measuring the two-dimensional pattern of the etched surface or the cross-sectional profile taken by cutting a diffusion-bonded sample. The accuracy of this method can be improved by taken a rubbing of the surface by lightly rubbing a pencil on paper affixed to the etched surface and measuring the image created rather than the surface directly. Samples of this method for three of the plates used in this work and that by Kruizenga [7] are shown in *Figure 83*.

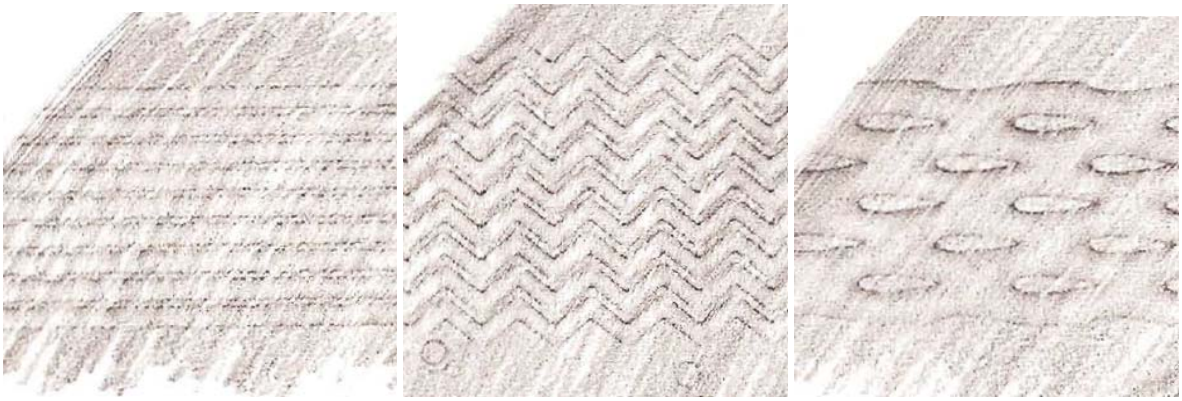

Figure 83: Example rubbings from 3 different PCHE plate surfaces (straight, zig-zag, and airfoil from left to right).

The average roughness of the PCHE surface should also be measured. *Table 9* summarizes several surface roughness reported in literature varying from 0.4 to 3 microns, where even at a level of 2 microns for the PCHE surfaces used in this work and by Kruizenga [7] showed much better frictional pressure drop agreement between calculations and experiment when surface roughness was accounted for.

Finally the most detailed surface measurement involves taking a white-light scan of the etched geometry. This

process produces a stereolithography (.stl) file with measurement accuracy on the order of 25 microns that can be processed as explained in Section 3.4.4 to evaluate the actual dimensions of the etched geometry.

3.3.3 Pressure Containment

The pressure containment potential of a compact heat exchanger involves the consideration of many factors as discussed by Taylor [34], including static and cyclic pressure and temperature effects on the heat exchanger core (matrix), headers, and supports. Although the design of standard headers consisting of a cylindrical section welded to the side of a heat exchanger core can have an impact on the core design by limiting either the height or width of the core further than the constraints imposed by manufacturing processes, recent developments by Heatric™ [37] show that manifolds and porting integral to the heat exchanger core for PCHEs may reduce the size and complexity of these headers. In either case, discussion here will be limited to the pressure containment in the main channel section of a basic heat exchanger core as this more directly impacts channel geometries and thermal performance.

A basic PCHE core, focusing on a unit-cell volume of a parallel or counter-flow configuration, consists of a multitude of parallel channels that may be vertically aligned or staggered depending on the design surface geometry as shown in *Figure 84*.

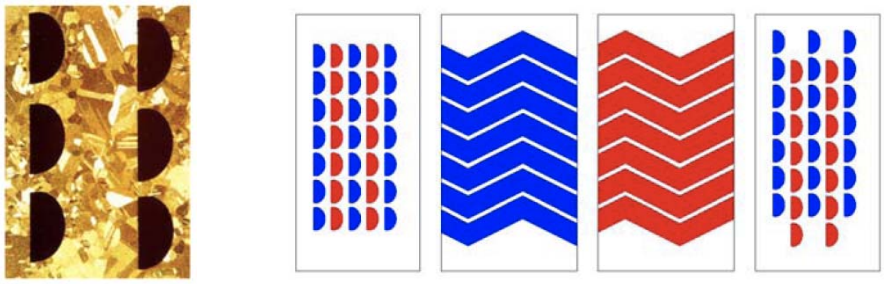

Figure 84: A micrograph of a PCHE cross-section perpendicular to the flow direction, along with a diagram showing cross-sections at two different locations of stacked zig-zag channels indicating that channels may not be equally aligned even in the same block.

Hesselgreaves [6] suggests a method to estimate the required channel spacing and fin or ridge thickness from the required pressure containment based on Taylor's [34] methods for plate-fin heat exchangers (PFHE), although Taylors original equation does not seem to agree with that used by Hesselgreaves, where the former is given by Equation (51) and the latter is given by Equation (52).

$$\frac{P_g}{S_{all}} = Nt \tag{51}$$

$$\frac{P_g}{S_{all}} = ((Nt)^{-1} - 1)^{-1} \tag{52}$$

Note that the full gauge pressure is used in each equation rather than a differential pressure between streams following the calculation procedures accepted for PFHEs. A more complete treatment of estimating the mechanical design of PCHE channels is given by Le Pierres [37] which allows the specification of both the fin or ridge thickness (p – w according to *Figure 85*), as well as the minimum thickness vertically between any two rows of channels (t – h).

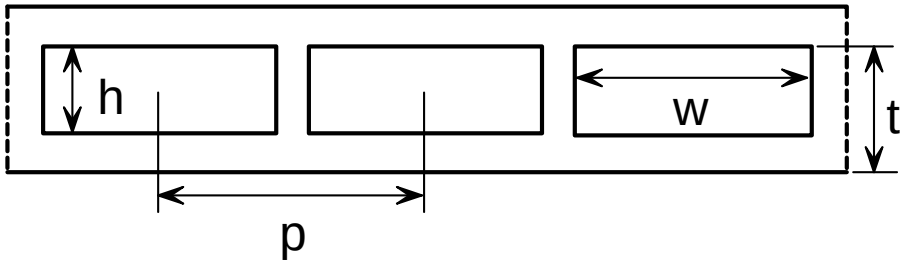

Figure 85: A diagram of a section of a PCHE stack-up where channel cross-sections are idealized by their circumscribing rectangles, where h is the channel height, w is the channel width, p is the lateral channel pitch, and t is the plate thickness.

According to this method, based on criteria from ASME 13-9 as K approaches 0, the membrane stress S_m for both the ridge or bottom thickness must less than the maximum allowable stress SE for the material, while the total stress S_t must be less than 1.5 times the same value in order to acceptably contain the pressure in the channels, as described by Equation (53), where S_b is the bending stress in the material.

$$S_m \leq SE \text{ and } S_t = S_m + S_b \leq 1.5SE \tag{53}$$

First, to determine the minimum thickness between channels horizontally, the bending stresses on this wall material are assumed to be 0, while the membrane stresses are given by Equation (54), with geometric parameters defined by *Figure 85*.

$$S_m = \frac{P_g w}{p - w} \tag{54}$$

Next, to determine the minimum thickness between channels vertically, the net bending stress and membrane stress are calculated as shown in Equations (55) and (56).

$$S_b = \frac{P_g w^2}{(t - h)^2} \tag{55}$$

$$S_m = \frac{P_g h}{2(t - h)} \tag{56}$$

These three equations can be substituted into the constraint equations yielding three different constraints relating the geometric parameters w, p, h, and t to the gauge pressure and allowable stress in the material.

This method can be extended by assuming that the material has a uniform allowable stress throughout, which would include any factors accounting for weaknesses from the parent material strength due to diffusion bonding, and by non-dimensionalizing the variables as shown in Equation (57). The minimum of the three non-dimensionalized constraint equations, Equations (58) through (60), can then be found to determine the maximum pressure containment ratio dP/SE for any combination of width fraction wf, depth fraction df, and aspect ratio AR.

$$wf = \frac{w}{p}, \quad df = \frac{h}{t}, \quad AR = \frac{h}{w} \tag{57}$$

From $S_m \leq SE$ and Eq. (54): $\frac{P_2}{SE} \leq wf^{-1} - 1$ **(58)**

From $S_m \leq SE$ and Eq. (56): $\frac{P_2}{SE} \leq 2(df^{-1} - 1)$ **(59)**

From $S_t = S_m + S_b \leq 1.5SE$ and Eq. (55) and (56):

$$\frac{P_2}{SE} \leq \frac{3}{2}\left(\frac{1}{2}(df^{-1} - 1)^{-1} + AR^{-2}(df^{-1} - 1)^{-2}\right)^{-1} \quad \textbf{(60)}$$

Note that Equation (58) is exactly equivalent to Equation (52) from Hesselgreaves after non-dimensionalization. Contours of this piecewise function are shown in *Figure 86* for an aspect ratio 0.5, which is typical of a semi-circular PCHE channel. Overlaid on these contours are lines of constant area ratio, as defined by Equation (61), which indicates the maximum possible flow area as a fraction of the total unit cell cross-sectional area. Significantly, all of these results are scale-invariant provided that the channels are not actually sharp-cornered rectangles and instead have enough filleting to reduce any possibility of stress concentrations.

$$AcR = \frac{wh}{pt} \quad \textbf{(61)}$$

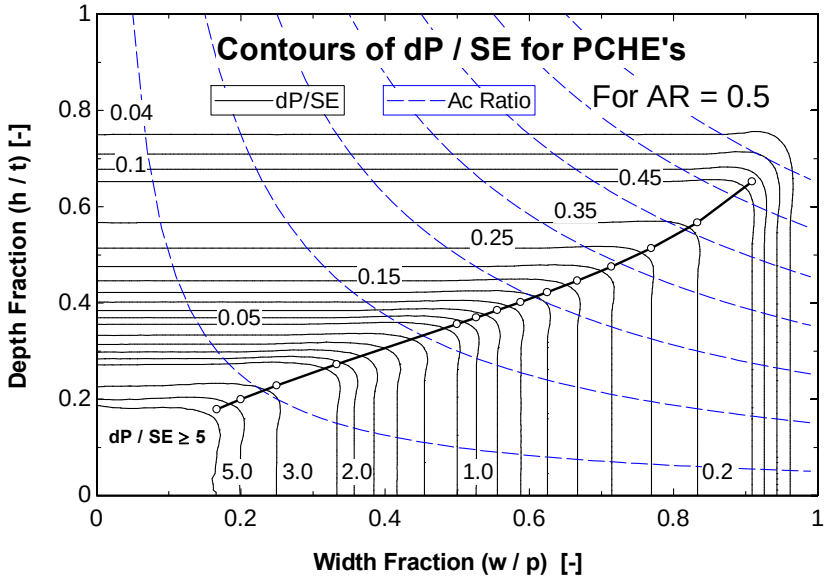

Figure 86: A plot of contours of the pressure containment ratio as a function of width fraction and depth fraction for an aspect ratio of 0.5, with lines of constant area ratio overlaid. The maximum pressure containment ratio as a function of cross-sectional area ratio is also shown by the connected open circles.

Figure 86 demonstrates that for each line of constant cross-sectional area ratio, there is a maximum pressure containment ratio for a channel of the given aspect ratio, shown by the line of connected open circles, assuming that both the width fraction and depth fraction can be varied independently through their full possible range. Then conversely, by specifying the pressure containment ratio along with the aspect ratio, the maximum possible cross-sectional area ratio can be determined as shown in *Figure 87* for several different channel aspect ratios.

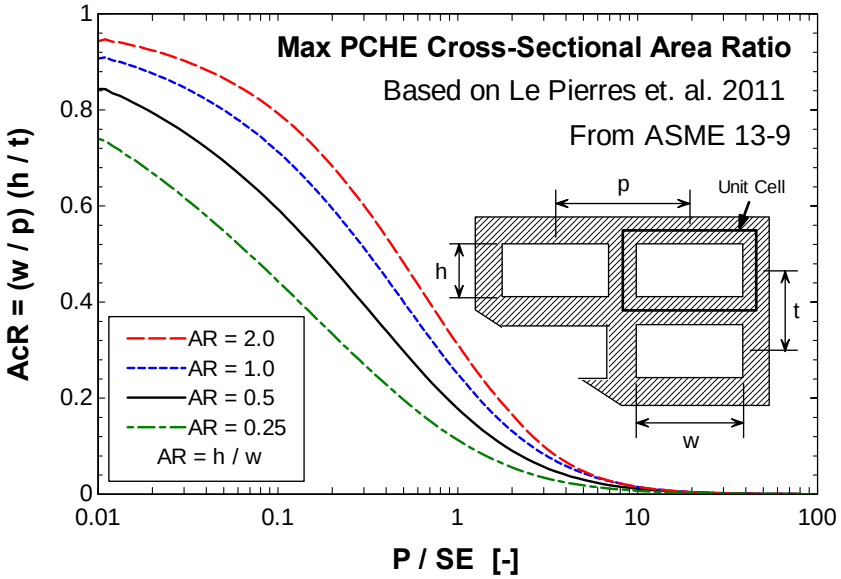

Figure 87: A plot of the maximum possible cross-sectional area ratio as a function of pressure containment ratio for several aspect ratio PCHE channels.

This maximum cross-sectional area ratio is exactly equal to the porosity of the heat exchanger core for straight channels of a constant cross-section and nearly equal to the porosity when the channels are not straight and/or the minimum cross-sectional area is used and the variation in cross-sectional area along the channel is not significant.

The difference between straight and non-straight channels like a zig-zag channel comes from the additional volume that must exist in-between the zigs and zags at the edge of the channel pattern when the channels are etched into a rectangular plate (without this additional volume the edges of a volumetric unit cell would be aligned with the channel path; so a zig-zag channel would have flat faces perpendicular to the flow and zig-zag shaped sides). This additional volume will necessarily reduce the porosity of the core, and can be calculated for a channel following a zig-zag path as shown in Equation (62), where L_{bb} is the bend-to-bend length, p is the lateral pitch, θ_b is the bend deflection angle, and N is the number of channels on a single plate. From this equation it is clear that for typical ratios of L_{bb} / p around 2 that the change in porosity due to this extra edge material quickly becomes negligible as the number of channels increases, and can largely be ignored for typical core geometries where the number of channels per plate is around 100.

$$\phi = (AcR)(EdgeFac_{zz}) = AcR\,\frac{1}{1+\frac{L_{bb}}{p}\sin\left(\frac{\theta_b}{2}\right)\frac{1}{N}} \qquad (62)$$

The discrepancy due to a variable cross-sectional area will be more complex and depend strongly on the channel surface geometry, but by using the minimum cross-sectional area the actual porosity will slightly under-estimated by the cross-sectional area ratio.

As this method is based on the maximum cross-sectional area ratio based on the circumscribing rectangle for the channel cross-section, the actual cross-sectional area ratio will be less for typical etched channels which take on a circular segment profile. The actual porosity can then be calculated as shown in Equation (63), where A_c / $A_{c,rect}$ is the ratio of the channel cross-sectional area to the cross-sectional area of the circumscribing rectangle. This ratio evaluates for the case of a semi-circular profile to π / 4 or approximately 79%, continues to reduce the porosity.

$$\phi = \phi_{rect} \frac{A_c}{A_{c,rect}} \tag{63}$$

Additionally, the surface area density can be determined from Equation **(35)** by setting the hydraulic diameter, which effectively scales the heat exchanger and determines its level of compactness. Note that the hydraulic diameter must be based as shown on the volume and surface area of the channels as the hydraulic diameter based on the area and perimeter of a cross-section perpendicular to the mean flow direction does not correctly account for the increased surface area per unit axial distance when the channel is not straight. For instance, Equation (64) shows the effective surface area density for zig-zag channels with the L_s / L term accounting for this enhanced surface area. *Figure 88* shows the range of this term rounded zig-zag channels with the two zig-zag style plates used in this work shown for reference.

$$\beta = 4\left(\frac{A_{c,fluid}}{A_{c,unitcell}}\frac{L}{L}\right)\left(\frac{per}{4A_{c,fluid}}\frac{L_s}{L}\right) = \frac{4\phi}{d_h} \tag{64}$$

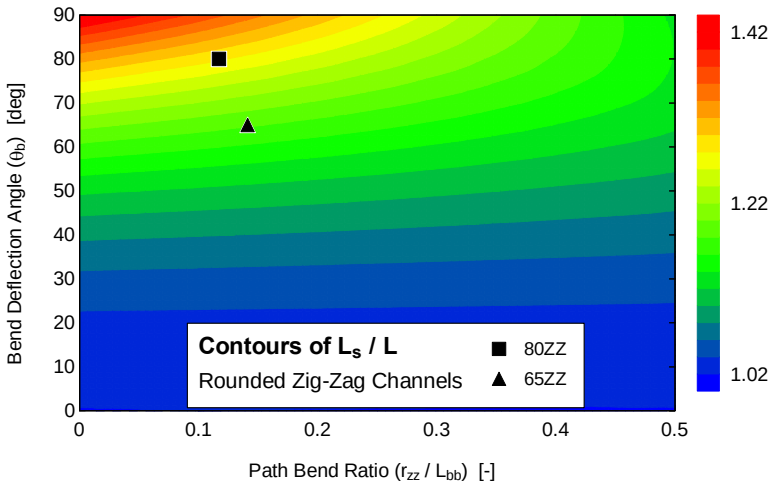

Figure 88: A plot of the contours of the length ratio for a rounded zig-zag channel path with the length ratios for the two zig-zag styles discussed in this work.

These results allow the maximum cross-sectional shape and porosity of the PCHE core to be determined entirely from the operating pressure in the channels, the strength of the PCHE core material, and the desired aspect ratio of the channels. The surface area density can also be determined based on the hydraulic diameter of the channels.

For example, Southall [47] has shown that Heatric diffusion bonding methods of 316/316L stainless steel can achieve 0.2% proof stress values of around 200 MPa, which Taylor [34] recommends dividing by 1.5 for use as the material strength in PFHE mechanical design calculations. Assuming a required pressure containment of 10 MPa and a channel design with a circumscribing rectangle aspect ratio of 0.5 the pressure containment ratio is 0.075. According to *Figure 87,* the maximum possible cross-sectional area ratio is roughly 0.6, with width and depth fractions from *Figure 86* of 0.55 and 0.35, respectively. Assuming the number of channels per plate is around 100 the edge factor correction for a zig-zag pattern channel is negligible and the cross-sectional area ratio is equal to the porosity for channels with a rectangular cross-section. Assuming the channel is approximately semicircular the true porosity is about 80% of the porosity for rectangular cross-section channels, or about 0.48. This value is in the range described by Hesselgreaves for typical PCHE porosities of 0.4 to 0.55. Finally, assuming channels with a hydraulic diameter around 1 mm, the surface area density can be estimated as being between about 1900 and 2900 m^2/m^3 depending on the zig-zag channel pattern parameters.

Note that this is the maximum PCHE porosity and surface area density, and that additional core volume required to account for integral or welded headers (sidebars, additional plate layers, or integral header and distributer length) is usually included in the core dimensions given in a typical PFHE as recommended by Taylor [34] and from most literature.

3.3.4 Fin Effectiveness

As discussed previously the pressure containment potential of PCHEs comes at a cost to the limited porosity due to channel rounding from chemical machining. The material between PCHE channels, typically referred to as fins or ridges, are therefore usually much thicker than in PFHEs due to the higher pressure containment design. As discussed by Nellis and Klein [11] among others, the fin-like nature of this material can be characterized by the Biot number relating approximately the conductive and convective thermal resistance lateral to the major fin length as defined in Equation **(65)**. A lower value of the Biot number suggests that the fin satisfies the extended surface approximation. As shown in Equation **(66)** this can be related to the variables defined previously in *Figure 85* for a generic PCHE cross-section and fluid and material properties.

$$Bi = \frac{R_{cond}}{R_{conv}} = \frac{th_f}{2Ak_{mat}}\frac{hA}{1} \tag{65}$$

$$Bi \approx \frac{1}{2}\frac{w}{d_{hyd}}(wf^{-1} - 1)Nu\frac{k}{k_{mat}} \tag{66}$$

For a rectangular cross-section PCHE channel the hydraulic diameter can be related to the width and aspect ratio as shown in Equation **(67)**. Thermal conductivities of stainless steels and titanium are less than 20 W/m-K, while thermal conductivities of CO2 for the temperature and pressure range of the precooler from *Figure 56* are greater than 0.02 [W/m-K] (50 K-m/W as shown). Using the Dittus-Boelter correlation (Equation **(20)**), Nusselt numbers for supercritical carbon dioxide in this temperature and pressure range are usually above 100, leading to a minimum Biot number relationship as shown in Equation **(68)**. The ideal width fraction for typical PCHE porosities around 0.5 from *Figure 86* lead to width fractions around 0.9, but actual width fractions are usually much more conservative for PCHEs and much closer to unity for lower-pressure PFHEs. Using the ideal width fraction leads to a minimum Biot number around 0.01. Clearly for rectangular channels the fins would satisfy the extended surface approximation as is typical for PFHE surfaces, but for PCHEs this is only the minimum Biot number for a surface. Due to the etch factor of the chemical machining process the fin quickly increases in width, leading to the very top of the fin roughly satisfying the extended surface assumption while the bottom does not. Because of this complexity the entire channel perimeter of a PCHE channel is usually treated as a primary rather than an extended (secondary) surface.

$$d_{hyd} = \frac{2w}{AR^{-1} + 1} \tag{67}$$

$$Bi \sim 0.1(wf^{-1} - 1) \tag{68}$$

3.3.4.1 Expectations for PCHE Surfaces

Before reviewing experimental and numerical evaluations of particular PCHE surface geometries, it is useful to review existing correlations for hydraulic performance of similar flow geometries that exist in other forms including pipe bends trashracks.

Pipe bends present a surprisingly complex flow situation given their seemingly simple geometry. Both Miller

[12] and Idel'chik [16] have excellent discussions of flow and pressure drop implications in pipe bends, and a great deal of intuitive understanding of the flow can be gained from both sources. A compact diagram of the flow situation is shown as *Figure 89* from Idel'chik. For both circular and rectangular cross-sections, as an initially uniform flow approaches the curved section, a secondary swirling flow develops due to the creation of Goertler vortices as shown in cross-sections B and C, while at the same time separation zones at the outer corner and on the inner wall of the downstream channel appear. The size of the separation zones and the strength of the secondary flow depend greatly on the geometry of the curved section, where a strong swirling flow can help re-energize the fluid downstream of the convex wall and reduce the size of the separation zone as discussed by Miller, and where very gradual curvature of the section can almost eliminate the separation zone downstream of the convex wall. A particularly interesting effect of the vortex pairs caused by the secondary flow pattern is that the flow situation in one half of the bent curved pipe will likely be similar to the flow pattern in a semi-circular channel due as the symmetry plane and the bend plane are the same. Differences will remain as the symmetry plane does not enforce a no-slip condition on the flow which will impact friction losses, but the effects of the separation zones and secondary swirling flow on the loss coefficient of the bend may be similar.

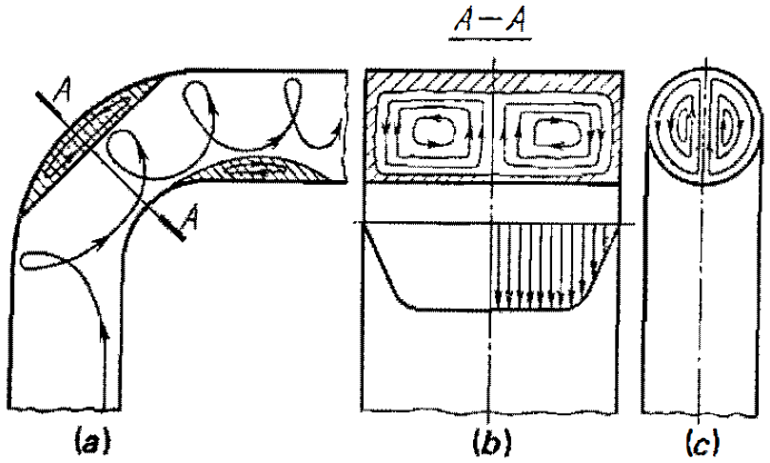

Figure 89: A diagram of the separation regions, swirling flow, and vortex pairing in a curved channel; from Idel'chik[16].

The scaling of the geometric parameters of a curved section can be seen in loss coefficient diagram of Miller based on extensive isothermal, single-phase air and water tests, shown as *Figure 90*. The diagram, showing the loss coefficient in a rectangular cross-section bend with an aspect ratio of 0.5 as a function of the bend angle and the bend radius ratio of the bend at a Reynolds number of 10^6, indicates that for a given bend angle there is a minimum loss coefficient found at a specific bend radius ratio between 0.8 and 2 for the entire range of bend angles. Similar plots are shown for circular cross-section pipes and different aspect ratio rectangular channels with similar behavior. The loss coefficients are shown specifically for a Reynolds number of 10^6 as Miller found they tend to asymptotically approach a constant value at high Reynolds numbers. Miller also provides a chart to adjust the loss coefficient for lower values, shown in *Figure 91*.

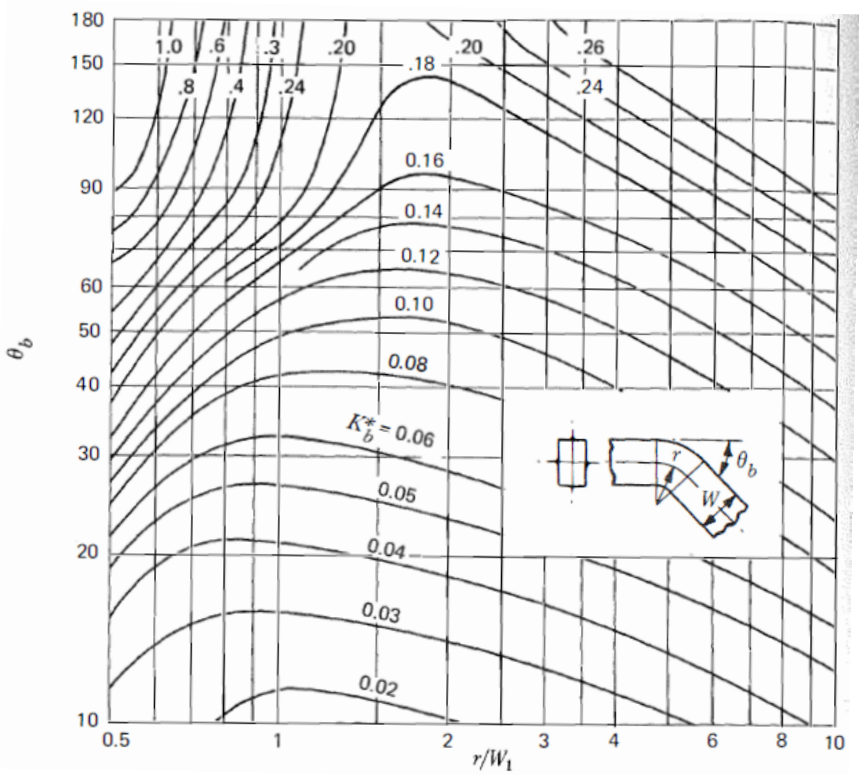

Figure 90: A diagram of the loss coefficient K_b^* for a bend in a rectangular pipe with an aspect ratio of 0.5 as a function of the bend angle θ_b and the bend radius ratio r/w at a Reynolds number of 10^6; from Miller [12].

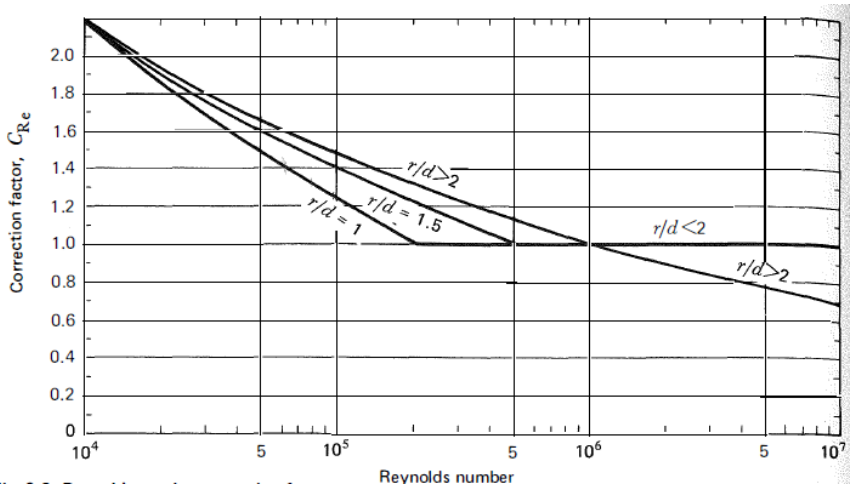

Figure 91: A diagram of the Reynolds number correction factor as a function of Reynolds number and the bend radius to diameter or bend radius to channel width ratio.

Significant time is spent by Idel'chik, although not by Miller, on the importance of the interior corner of the bend on the loss coefficient of the bend. *Figure 92* shows two plots from Idel'chik demonstrating first (left), that the roundness of the interior corner has an almost order of magnitude higher impact on the loss coefficient relative to the impact of the roundness of the exterior corner, while the second (right) shows the impact of wall roughness at various locations in the bend, where lines 1 and 2 have a rough interior corner and lines 3 and 4 have a smooth interior corner; line 1 having all rough walls and line 4 having all smooth walls. This suggests that a sufficiently rounded, smooth interior wall is critical to achieving low form loss around a bend.

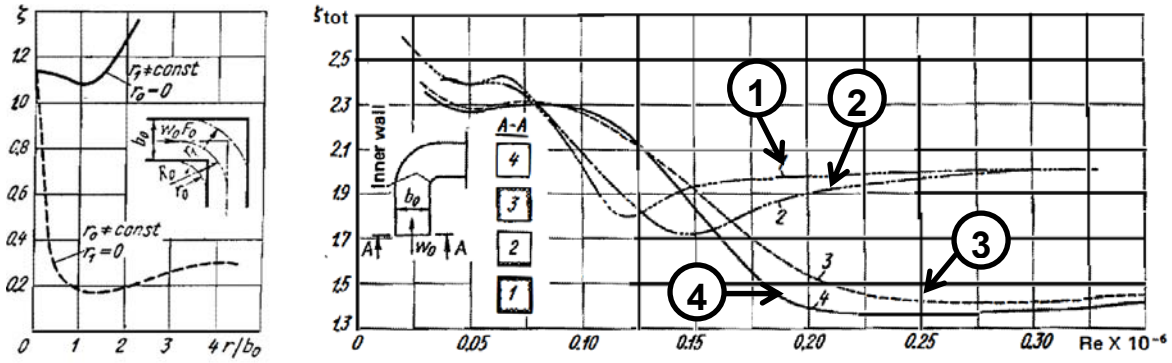

Figure 92: (left) A plot indicating the asymmetric importance of interior corner roundness relative to exterior corner roundness, where the solid line shows the loss coefficient for a 90-degree bend with a sharp interior corner as the roundness of the exterior corner is increased as scaled by the channel width, and the dashed line shows the opposite where the interior corner is rounded and the exterior corner is kept sharp; (right) A plot indicating the importance of interior corner roughness relative to roughness throughout the curved section, where the total loss across a bend is shown as a function of the Reynolds number of the flow. Line 1 shows a bend with roughness on the entire interior, while line 2 shows a bend with the same roughness applied only to the interior corner, line 3 shows a bend with a smooth interior wall and a rough wall elsewhere, and line 4 shows a bend with all smooth walls. Both from Idel'chik [16].

Finally, both sources discuss the effects of bend-bend interactions. *Figure 93* shows approximate flow distributions and measured total loss coefficients from Idel'chik for two combined bends demonstrating that, due to several reasons discussed by Miller including disruption of the flow re-development region, changes to the inlet velocity profile of the next bend, and direct static pressure interactions between two closely-joined bends, the loss coefficient for the combined bends can be anywhere from half that for a single bend up to twice that for a single bend at a far enough separation length. There is also a local minimum at a moderate separation distance, which is the only minimum present in the chart by Miller, *Figure 94*, where in Miller the combined loss coefficient continues to reduce with smaller separation length rather than falling towards half the value of an isolated bend as shown by Idel'chik.

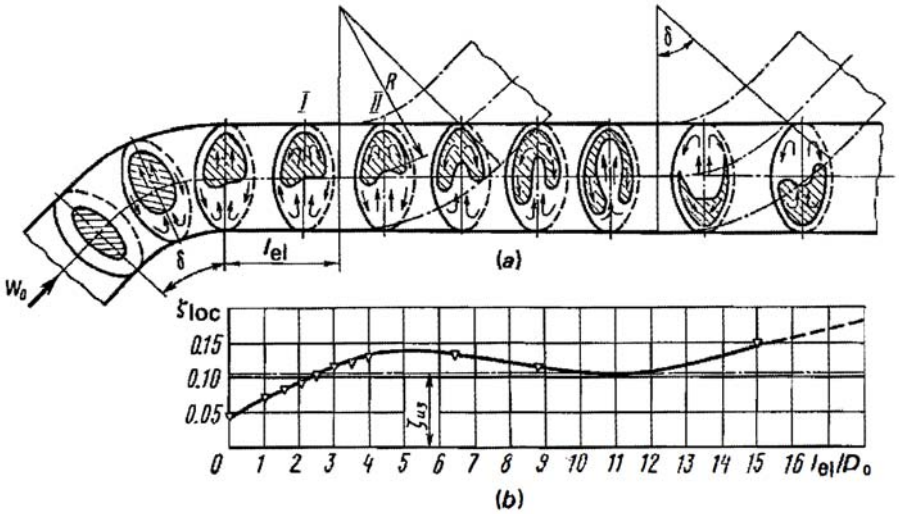

Figure 93: A diagram of a "gooseneck" configuration involving two identical bends with a variable separation length lel. Approximate flow distributions within the channel are shown at various cross-sections (a), while the plot (b) shows measured loss coefficients for the combination of bends as a function of separation length scaled by the pipe diameter. The loss coefficient for an isolated bend is shown (approximately 0.10). From Idel'chik[16].

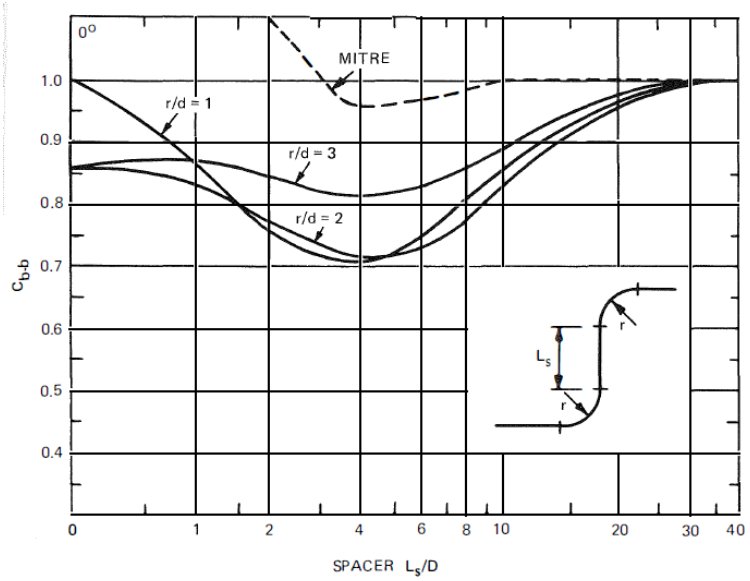

Figure 94: A plot by Miller of the bend-bend interaction coefficient for two in-plane 90-degree bends of various radius ratios and separation lengths; from Miller [12].

The channel rounding produced by the chemical machining process should therefore cause an un-intentional reduction in the form loss from the bends, and these trends suggest that curvature should be designed into zig-zag PCHE channels rather than relying only on the etch factor from fabrication. From these various concepts a few guidelines can be developed for achieving the lowest loss coefficient for a channel of identical bends like that found in PCHE zig-zag channels as shown in *Table 15*. These recommendations are all based on non-dimensional variables other than the bend angle, and therefore should be considered for an arbitrary channel cross-section as determined by other design criteria.

Table 15: Guidelines for optimal zig-zag PCHE channel hydraulic performance based on Miller [12] and Idel'chik [16].

General Zig-Zag PCHE Channel Hydraulic Guidelines
1. The radius of the bend should be between a value of about 1 and 2 times the channel width.
2. The bend angle should be minimized above bend angles of about 40 degrees.
3. The interior corner should be rounded and polished preferentially when possible.
4. Small spacing lengths should be used between bends; approximately 1 to 10 pipe diameters.

Miller also recommends a quantitative prediction method that can be applied to a series of zig-zag bends which amounts to a procedure for calculating a loss coefficient with some power-law relationship to the Reynolds number and a more complex relationship to other geometric parameters. The procedure is summarized for low aspect ratio rectangular channels in Equations **(69)** through **(74)** in *Table 16*. This value would be used in Equation **(14)** along with the other contributions to the pressure drop to find the total pressure difference along the channel.

Table 16: A summary of Miller's procedure for calculating the form loss for a series of identical bends for a low aspect ratio rectangular channel [12].

Miller's Correlation for a Series of Identical Bends in a Rectangular Channel
$\frac{\Delta P_{form}}{G^2/2\rho} = K_{bb} = C_{bb}^{*} N_b K_b^{*} C_{Re} C_f^{*}$ **(69)**

where $C_{bb} = g\left(\frac{L_{bb}}{w}, \frac{r}{w}, AR\right) = \begin{cases} 1 - C_{bb}\big|_{\text{Error! Reference source not found.}} & \text{for AR} < \\ \frac{2}{\text{else see Miller [12]}} \end{cases}$ **(70)**

N_b is the number of bends **(71)**

$K_b^s = g\left(\theta_b, \frac{r}{w}, AR\right) = \begin{cases} K_b^s\big|_{\text{Error! Reference source}} \\ \text{else see MI} \end{cases}$ **(72)**

$$C_{Re} = \frac{K_b^s}{K_b^s - 0.2\, g\left(Re_r, \frac{r}{w}\right)\Big|_{\text{Error! Reference}}} \quad \text{AR}$$ **(73)**

$$C_f^s = \frac{f_{rough}}{f_{smooth}}$$ **(74)**

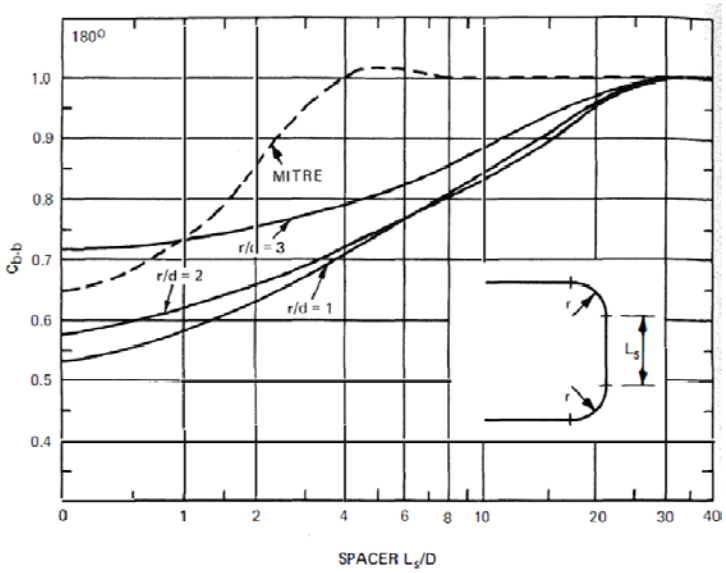

Figure 95: A chart of the bend-bend correction factor for use with low aspect ratio rectangular channels, from Miller [12]. For zig-zag PCHE channels the spacer length ratio L_s / D is the ratio of the zig-zag bend length to the channel width L_{bb} / w, while the bend radius ratio r / d is the ratio of the bend radius to the channel width r / w.

Miller also gives recommendations for trashracks consisting of bars of various cross-sectional profiles as shown in *Figure 96*. The general trend for all geometries is that the form loss coefficient for some body in the flow with small frontal dimension relative to its length will be some power-law function of the ratio of minimum free to total cross-sectional area in the channel. However, the streamlined profiles have a much less steep trend with this cross-sectional area than other geometries, with the loss coefficient more than a factor of two less than that for a non-streamlined geometry.

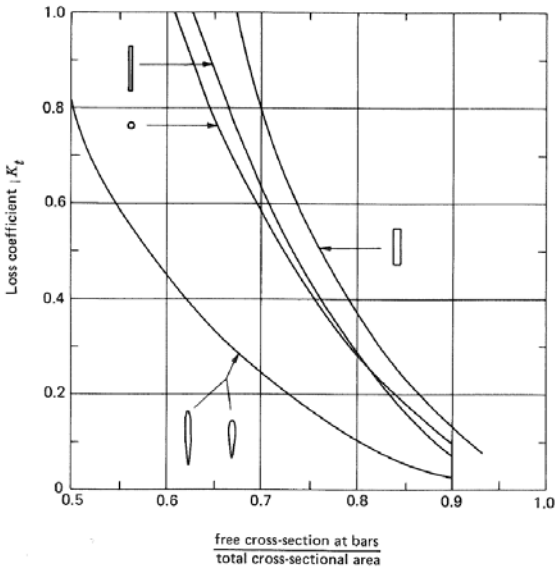

Figure 96: Loss coefficients for a single trashrack plane consisting of bars of various cross section from Miller [12], assumed at sum large Reynolds number consistant with findings of the Reynolds number dependence of pipe bend loss coefficients described by Miller.

3.3.4.2 PCHE Experimental Results

Many studies have been conducted in order to understand the performance of different PCHE surface geometries in consideration of various operating conditions. Most studies consider experimental and numerical investigations into various zig-zag channel geometries as these are currently available from Heatric™, although a few investigations have considered straight channels, sinusoidal fin surfaces and airfoil fin surfaces. All studies reviewed and their respective empirical or recommended correlation, whichever is most accurate, are listed in *Table 17*. These studies only use supercritical carbon dioxide flowing in a range of turbulent Reynolds numbers, while studies using other fluids including air, water, and helium have typically focused on laminar flow conditions (see [55], [56], [57], [58], [59], and particularly the parametric study of zig-zag channels [60]).

Table 17: A summary of experimental tests using SCO2 and empirical correlations for PCHEs.

Study	Type	Test Range	Empirical Correlations
Ishiduka et al. [46], [61]	65ZZ (Hot)	2.2 < P [MPa] < 3.5 150 < T [C] < 280 2.4e3 < Re [-] < 6e3	$f = 0.1868 + -8e\text{-}6Re$
	80ZZ (Cold)	6.5 < P [MPa] < 10.7 60 < T [C] < 120 5e3 < Re [-] < 13e3	$f = 0.4092 + -8e\text{-}6Re$
		Assumes linear T, P	$U_{loc} = 44.16 \mid 0.2104Re$
		From Measurements	$U = 15.943 + 0.1106Re$
Nikitin et al. [62]	65ZZ (Hot)	2.2 < P [MPa] < 3.2 280 < T [C] < 300 2.4e3 < Re [-] < 6e3	$f = 0.1798 - 5.608e\text{-}6Re$ $h = 2.52Re^{0.681}$
	80ZZ (Cold)	6.5 < P [MPa] < 10.5 90 < T [C] < 108 5e3 < Re [-] < 13e3	$f = 0.3727 - 6.180e\text{-}6Re$ $h = 5.49Re^{0.625}$

Study	Type	Test Range	Empirical Correlations
Ngo et al. [63]	52SF (Both)	2.2 < P [MPa] < 12 35 < T [C] < 280 3e3 < Re [-] < 20e3 0.75 < Pr [-] < 2.2	$f = 1.818Re^{-0.340}$ $Nu = 0.1740Re^{0.658}Pr^{0.430}$
	104ZZ (Both)	2.2 < P [MPa] < 12 35 < T [C] < 280 3e3 < Re [-] < 20e3 0.75 < Pr [-] < 2.2	$f = 0.7696Re^{-0.091}$ $Nu = 0.1696Re^{0.629}Pr^{0.317}$
Moisseytev et al. [31]	76ZZ ? (Hot)	7.9 < P [MPa] < 8.5 50 < T [C] < 160	$f_0 = \begin{cases} 64Re^{-1} & Re < 1300 \\ 0.3164Re^{-0.25} & Re \geq 2300 \end{cases}$ $a_f = 4.5e\text{-}3\tan\left(\frac{\theta_b}{2}\right)$ $c = \frac{\ln\left(\frac{1 + 223283a_f^2}{1 + a_f(1300 + 50)}\right)}{\ln\left(\frac{100000}{1300}\right)}$ $k = \frac{1 + a_f(1300 + 50)}{1300^c}$
	90ZZ ? (Cold)	13 < P [MPa] < 20 40 < T [C] < 160	$\frac{f}{f_0} = \begin{cases} 1 + a_f(Re + 50) & Re < 1300 \\ kRe^c & Re \geq 1300 \end{cases}$ $a_f = 0.6 + 0.5\tan\left(\frac{\theta_a}{2}\right)$ $f_{turb} = a_f(0.1341)Re^{-0.2319}$ $f_{0lam} = 4.1Re^{-1}$ $f_{0trans} = 352Re^{-1.4562}$
	Estimates of Heatric™ data	1e1 < Re [-] < 1e5	$a_{flam} = \frac{a_f 0.1341(1300)^{-0.2319}\frac{1300}{4.1} - 1}{1300 + 50}$ $\left.\frac{f}{f_0}\right\|_{lam} = 1 + a_{flam}(Re + 50)$ for Re<2300
Kruizenga et al. [64], [65], [66]	Straight	7.5 and 8.1 [MPa] 20 < T [C] < 75 5e3 < Re [-] < 20e3 0.7 < Pr [-] < 60*	Colebrook Correlation (Equation (8)) $Nu = Nu_{\text{Eq Error! Reference source:}}$ $Nu = Nu_{\text{Eq Error! Referenc}}$

Study	Type	Test Range	Empirical Correlations
			$Nu = Nu_{EqError\|Reference}$
Kruizenga [7]	65ZZ	7.5 and 8.1 [MPa] 20 < T [C] < 66 4e3 < Re [-] < 45e3 1 < Pr [-] < 60*	$f = 4.3 f_{EqErr}$
			$Nu = 2.8 Nu_{EqErr}$
	80ZZ	7.5 and 8.1 [MPa] 20 < T [C] < 66 4e3 < Re [-] < 45e3 1 < Pr [-] < 60*	$f = 5.4 f_{EqErr}$
			$Nu = 3.8 Nu_{EqErr}$

*Large Prandtl number spikes are possible from these tests through the psuedocritical point.

Some of the earliest work reported completely in literature is that by Ishiduka et al. ([46] and [61]) who tested a double-banked 316L Stainless Steel 3 kW heat exchanger produced by Heatric™ at the Tokyo Institute of Technology (TIT). This geometry has been reported in different ways in literature with several typographical errors so *Table 18* summarizes this author's best interpretation according to the zig-zag channel definitions of Section 3.3.2.1 and the nomenclature of this work. Empirical correlations found to predict their data are summarized in *Table 17*, where here the friction factor is an effective friction factor combining the effects of both friction and form pressure loss. The local total heat transfer coefficient relation is determined by assuming linear temperature and pressure profiles along the PCHE channels and completing the energy balance, while the overall heat transfer coefficient is determined from measured results. These empirical correlations do not consider the effects of the Prandtl number because this varies only between about 0.7 and 1.0 for their testing range due to the CO2 in both sides of the PCHE being at temperatures well above the pseudo-critical or saturation temperature at any given pressure. In order to use more robust correlation forms in their in-house simulation codes Ishiduka recommended multiplying the Gneilinski correlation (Equation **(21)**) for the local Nusselt number by a factor of 2.3 based on fitting the experimental overall heat transfer coefficients, and the sum of a smooth-tube friction correlation similar to the Blasius correlation (Equation **(9)**) and the pipe elbow form loss correlation from Weisbach [67] shown as Equations **(75)** and **(76)**, respectively, with the form loss terms multiplied by 1.38 for the 65-degree zig-zag channels and 1.51 for the 80-degree zig-zag channels.

$$f = 0.0112 + Re^{-0.32} \tag{75}$$

$$K_{elbow} = 0.9457 \sin\left(\frac{\theta_b}{2}\right)^2 + 2.047 \sin\left(\frac{\theta_b}{2}\right)^4 \tag{76}$$

Using the same PCHE described in *Table 18*, Nikitin et al. [62] uses a slightly different test range and describes in more detail how heat losses from the PCHE core and headers were accounted for in their data reduction. Numerical simulations in FLUENT™ are used to estimate the local heat transfer coefficient along the PCHE channels, and a more complex fitting procedure is used to produce updated empirical correlations for the local heat transfer coefficient and the effective friction factor also shown in *Table 17*. The updated correlations are still only functions of the Reynolds number, however, due to the limited range of Prandtl numbers tested.

Table 18: Geometry of the double-banked (HCH) 3 kW 316L stainless steel Heatric™ PCHE tested by the Tokyo Institute of Technology (based on [46], [61], [62]).

Description	Symbol	Unit	"Hot" Side	"Cold" Side
Core Dry Mass	-	kg	40	

Core Dimensions	-	mm	71 x 76 x 896 (843 counterflow)	
Channel Pattern	-	-	Zig-Zag	Zig-Zag
Number of Plates	-	-	12	6
Channels per Plate	-	-	12	11
Plate Thickness	t	mm	1.63	1.63
Channel Pitch	p	mm	2.97	3.25
Bend-to-bend Length	L_{bb}	mm	5.33	4.73
Bend Angle	θ_b	deg	65	80
Inner Radius	r_i	mm	Not Reported	
Outer Radius	r_o	mm	Not Reported	
Path Radius	r_s	mm	Not Reported	
Profile Radius	r	mm	0.801	0.689
Channel Depth	h	mm	0.9	0.9
Number of Bends	Nb	-	~187	~233
Hydraulic Diameter ($4A_c$/per)	$d_{hyd,\perp}$	mm	1.15	1.15
Hydraulic Diameter ($4V_f/A_s$)	d_{hyd}	mm	0.914	0.810
Channel Cross-Sectional Area*	-	mm^2	1.166	1.032
Surface Area	-	m^2	0.697	0.356
Average Roughness	e	m	3e-6	3e-6
Porosity	Φ	-	< 0.24	< 0.20
Surface Area Density*	β	m^{-1}	< 1054	< 962

*Reported value is 1050 based on the total active core volume and surface area

Ngo et al. [63] describes tests using the same facility as Nikitin and Ishiduka on two double-banked 316L stainless steel PCHEs consisting of zig-zag channels and sinusoidal fins with very similar geometry as summarized in *Table 19* for the zig-zag channel and *Table 20* for the sinusoidal fins. A larger range of inlet Prandtl numbers were investigated than previously had been done at the TIT, and an integral formulation of the logarithmic mean heat transfer equation was used to fit effective friction factor and effective Nusselt number correlations to the data as summarized in *Table 17*. Although the data can be more accurately fit to the hot and cold sides of each heat exchanger separately, as the geometries are the same the more general correlations given are shown.

Table 19: Geometry of the double-banked (HCH) Zig-Zag 316L stainless steel PCHE tested by the Tokyo Institute of Technology (based on [63]).

Description	Symbol	Unit	"Hot" Side	"Cold" Side
Core Dimensions	-	mm	29 x 76 x 745.2	
Channel Pattern	-	-	Zig-Zag	Zig-Zag
Number of Plates	-	-	8	4
Channels per Plate	-	-	12	11
Plate Thickness	t	mm	1.5	1.5
Channel Pitch	p	mm	3.426	3.426
Bend-to-bend Length	L_{bb}	mm	6.14	6.14
Bend Angle	θ_b	deg	104	104
Inner Radius	r_i	mm	Not Reported	
Outer Radius	r_o	mm	Not Reported	
Path Radius	r_s	mm	Not Reported	
Profile Radius	r	mm	0.831	0.831
Channel Depth	h	mm	0.94	0.94
Number of Bends	Nb	-	~200	~200
Hydraulic Diameter ($4A_c$/per)	$d_{hyd,\perp}$	mm	1.09	1.09
Hydraulic Diameter ($4V_f/A_s$)	d_{hyd}	mm	0.70	0.70
Channel Cross-Sectional Area	-	mm^2	1.23	1.23
Surface Area	-	mm^2	0.4653	0.2353

Relative Roughness	-	-	Not Reported	
Porosity	Φ	-	< 0.246	< 0.246
Surface Area Density	β	m^{-1}	< 1415	< 1415

Table 20: Geometry of the double-banked (HCH) sinusoidal fin 316L stainless steel PCHE tested by the Tokyo Institute of Technology (based on [63]).

Description	Symbol	Unit	"Hot" Side	"Cold" Side
Core Dimensions	-	mm	29 x 76 x 745.2	
Channel Pattern	-	-	Sinusoidal fin	Sinusoidal fin
Number of Plates	-	-	8	4
Channels per Plate	-	-	12	11
Plate Thickness	t	mm	1.5	1.5
Channel Pitch	p	mm	3.426	3.426
Bend-to-bend Length	L_f	mm	6.14	6.14
Fin Angle (~ θ_b / 2 of zig-zags)	θ	deg	52	52
Fin Radius	R	mm	Not Reported	
Fin Thickness	d_f	mm	0.8	0.8
Channel Depth	H	mm	0.94	0.94
Hydraulic Diameter ($4V_f/A_s$)	d_{hyd}	mm	1.09	1.09
Total Cross-Sectional Area	-	mm^2	118.2	54.2
Surface Area	-	mm^2	0.5099	0.2559
Relative Roughness	-	-	Not Reported	

Moisseytev et al. [31] tested a 316 stainless steel PCHE produced by Heatric™ at Argonne Natinoal Laboratories (ANL) designed to be representative of a section of the low-temperature recuperator in a SCO2 Brayton cycle, with reported dimensions given in *Table 21*. ANL was limited in the details that could be measured and published for their specific PCHE so several estimated values are given, however there is not enough stated or assumed geometry available to fully define the surfaces inside the PCHE core. Nine CO2-CO2 tests were presented and several models were evaluated for their ability to predict the test data, as well as data presented previously by Heatric™ [40] without scales shown from Moisseytev et al. in *Figure 97* with scales estimated by using straight pipe correlations and assuming that low, medium, and high zig-zag angles correspond to about 25, 60, and 105 degrees, respectively. This very comprehensive correlation for the friction factor and Colburn j factor involves fitting modification parameters to straight channel correlations, and depends only on the bend angle and the Reynolds number as shown in *Table 17*. This correlation was found by the authors to predict thermal performance well but consistently overpredicted the hot-side (low bend angle, low pressure) friction factor.

Table 21: Geometry of the 316 stainless steel PCHE produced by Heatric™ and tested at Argonne National Laboratories (based on [31]).

Description	Symbol	Unit	"Hot" Side (B)	"Cold" Side (A)
Core Dry Mass	-	kg	200	
Core Dimensions	-	mm	120 x 200 x 1200	
Channel Pattern	-	-	Zig-Zag	Zig-Zag
Pressure Rating	-	MPa	8.2	21.6
Bend Angle*	θ_b	deg	76	90
Profile Radius*	r	mm	0.75	0.75
Channel Depth*	h	mm	0.75	0.75
Other values not reported or guessed.				

*Guessed by the authors in [31].

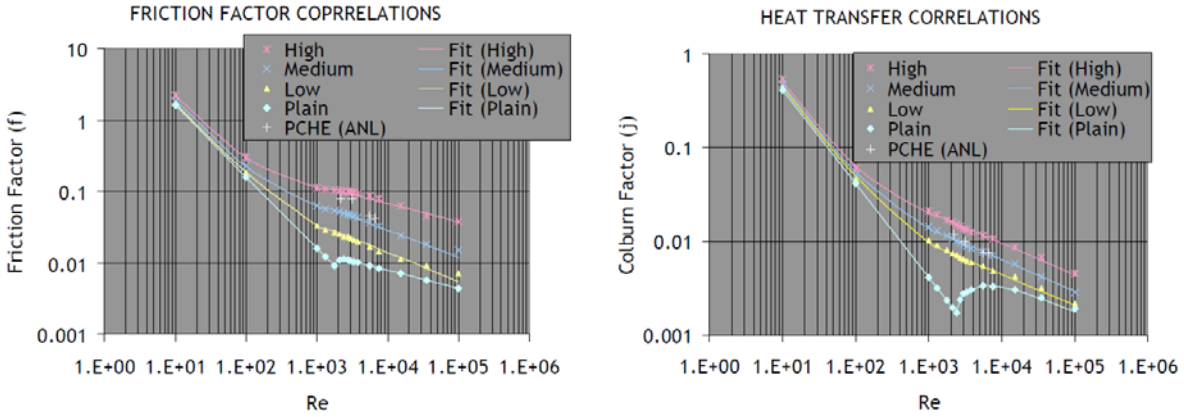

Figure 97: Charts of the data estimated from previously published, unscaled Heatric [40] tests as well as that from ANL, along with fit curves according to the general zig-zag PCHE channel correlations given by Moisseytev et al. [31]. Note that the friction factor shown here is the fanning friction factor which is ¼ of the friction factor calculated as shown in *Table 17*.

Kruizenga et al. ([64], [65], [66], and [7]) provides details on straight channel, described in *Table 22*, PCHE geometries for several inlet pressures and temperatures dropping through the pseudo-critical temperature and developed the experimental facility and techniques used in this study. As described in more detail in Section 3.4, unlike other experimental facilities the facility at UW Madison allows the measurement of the wall temperature profile along the channels of a single PCHE plate, and therefore a more accurate measurement of the pseudo-local Nusselt number than can be achieved by deducing heat transfer coefficients from simulations of a full PCHE core knowing only the inlet and outlet conditions. Kruizenga tested combinations of heat flux and orientation including both horizontal heating and cooling, up-flow cooling, and down-flow cooling, but only conclusions from horizontal cooling will be discussed in this work.

Table 22: Geometry of the single 316 stainless steel PCHE plate tested by Kruizenga at UW-Madison (based on [7]).

Description	Symbol	Unit	"Hot" Side
Channel Pattern	-	-	Straight
Channels per Plate	-	-	9
Channels Length	L	mm	500
Plate Thickness	t	mm	6.3
Channel Pitch	p	mm	2.515
Profile Radius	r	mm	0.95
Channel Depth	h	mm	0.95
Hydraulic Diameter ($4A_c/per$)	$d_{hyd\perp}$	mm	1.16
Hydraulic Diameter ($4V_f/A_s$)	d_{hyd}	mm	1.16
Channel Cross-Sectional Area	-	mm^2	1.42
Channel Perimeter	-	mm^2	4.88
Average Roughness	-	mm	2.2e-3
Porosity	Φ	-	< 0.358
Surface Area Density	β	m^{-1}	< 308

Kruizenga found that Jackson's correlation (Equation **(25)**) worked well for cooling-mode heat transfer at temperature higher than 1.2 times the pseudo-critical temperature, but that below this Jackson's correlation overpredicts the heat transfer. This prediction could greatly improved by multiplying Jackson's correlation by another ratio of the specific heat evaluated at the bulk temperature and at the psuedocritical temperature assuming the CO2 behaves as an ideal gas (for some very low pressure) raised to a power of -0.19. Kruizenga had more success using the Dittus-Boelter correlation for cooling (Equation **(20)**) evaluated at the film temperature, and found an improved estimate but using a Reynolds and Prandtl number in the Dittus-Boelter

correlation evaluated at integral average fluid properties between the wall and bulk temperatures. The frictional pressure drop was found to be well predicted by the Colebrook equation (Equation (8)), as summarized in *Table 17*.

Kruizenga also presents a more sparse dataset on 65-degree and 80-degree bend zig-zag channels [7], the geometry of which is described in more detail later in Section 3.4, finding that as an initial estimate for pressure drop the Colebrook correlation could be multiplied by the effective over the axial length of the zig-zag channel and a constant factor fit to data (4.3 for the 65ZZ channel and 5.4 for the 80ZZ channel), and that Jackson's correlation could be multiplied by a constant factor to estimate the Nusselt number (2.8 for the 65ZZ channel and 3.8 for the 80ZZ channel). The use of a combination of a friction loss correlation and a form loss correlation such as that for miter bends is also suggested, but requires an additional fitting factor of about 0.5 for both geometries to match the experimental data making it redundant as an empirical correlation, but suggests that form loss correlations may provide some predictive power since the fitting factor is the same for both geometries.

3.4 Experimental Facility

3.4.1 Overview of the Experimental Facility

The experimental facility used for this work is identical to the facility used by Kruizenga for straight and zig-zag channel tests, but details will be summarized here for reference. The experimental facility consists of two main loops as shown in the schematic diagram in *Figure 98*, consisting of the recirculation loop on the left and the test section loop on the right.

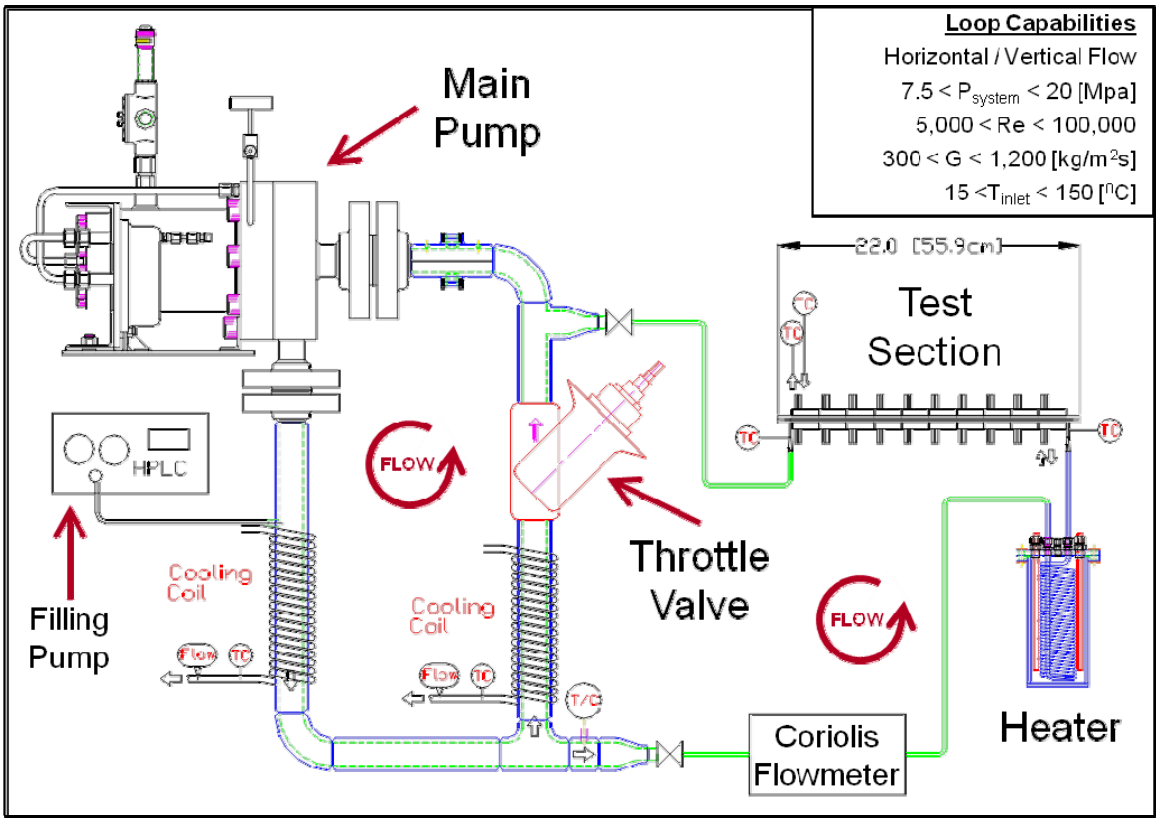

Figure 98: A schematic drawing of the SCO2 PCHE test facility with test capabilities shown.

The recirculation loop consists of a ChemPump (Model GCT-1.5K-20S) powered by a Danfoss adjustable frequency inverter (VLT type 30004) controlled through a PID scheme implemented in National Instruments

Labview™ 8.5 and a Kerotest diverter valve, along with a tube-in-tube heat exchanger and several copper coil wrappings to cool the recirculation loop when needed. The pump is capable of delivering flow rates up 14 m^3/hr, hydraulic heads up to 15 m, and pressures up to 20 MPa. The recirculation loop is instrumented with one K-type thermocouple and a Siemens gauge pressure transducer (Model 7MF4432-1GA10-1NC1-Z) capable of pressures from 0 to 40 MPa gauge with better than 0.1% accuracy over the full range. A portable chiller (Neslab HX-150DD) provides cooling water to the wrapped copper coils and heat exchanger in order to keep the CO2 at a high enough density for a given pressure to reach test conditions. The CO2 inventory is controlled using a Chrom Tech SFC24 pump for both primary loop filling and making adjustments to the loop pressure.

The test section loop consists of a coriolis flowmeter (Siemens Model 7ME4100-1DM11-1DA1), a custom can heater, the test section, and an additional tube-in-tube heat exchanger plumbed to a portable chiller (NESLAB RTE 111 Digital) to provide additional cooling or heating of the test section outlet flow as needed. As described by Kruizenga, the can heater contains 3 meters of coiled 316 stainless steel tubing in a stainless steel can, along with five 1 kW cartridge heaters placed near the coiled tubing. The tubing and heaters are then potted in fine copper powder to distribute the heat and prevent hot spots on the tubing. The cartridge heaters are regulated by a silicone controlled rectifier (SCR) controlled through a PID scheme implemented in LabView.

3.4.2 Test Section

The test section consists of two 316 stainless steel plates with dimensions representative of printed-circuit heat exchangers, with one smooth plate having only a 1/16 in O-ring groove milled to accept Viton gasket cord stock mated to another which has been chemically etched by Microphoto Inc. with one of a variety of channel geometries as shown in *Figure 99*. Each etched plate has an axial flow channel length of 0.5 [m], with plenums milled at both the inlet and outlet to distribute SCO2 to the flow channels. Design drawings for the smooth plate, the two zig-zag plates, and the two airfoil fin plates used in the study are shown in **Error! Reference source not found.**.

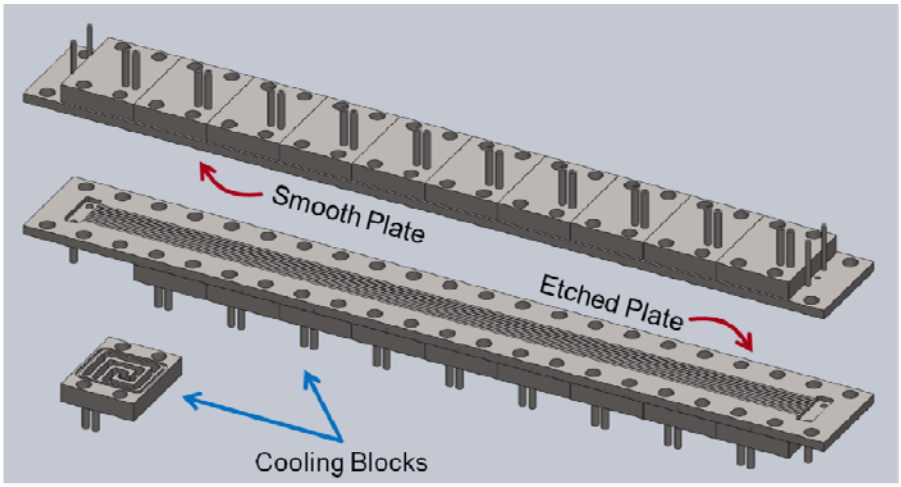

Figure 99: A solid model of the test section plate and cooling block assembly.

As shown in *Figure 100*, two type-E special limit of error thermocouples calibrated against a NIST-traceable RTD are located in each plenum to measure inlet and outlet temperatures of the SCO2 flow, as well as pressure ports for inlet pressure measurement using a Siemens gauge pressure transmitter (Model 7MF4432-1GA10-1NC1-Z) and to measure the differential pressure across the test section using a Rosemount pressure transmitter (Model 3051CD-3A22A1AS2B4M5E5). The heat transfer length is subdivided into 10 sections with aluminum cooling blocks bolted to the outside of each plate. Type E thermocouples are implanted in the center of each sub-section on each plate just above the flow channels in 1 [mm] holes fabricated using electrical discharge machining by Wire Tech EDM in Los Alamitos, CA and filled with 63/37 tin/lead solder to prevent disruption of plate wall temperature gradients as discussed by Kruizenga [7]. Each cooling block is provided with a flow of cooling water by a portable cooling bath (Neslab HX-150DD), with the volumetric flow rate into each cooling block measured by a McMillan Company liquid flow meters (Model 101-M003) and the inlet and outlet

temperatures of each cooling block measured with type E thermocouples.

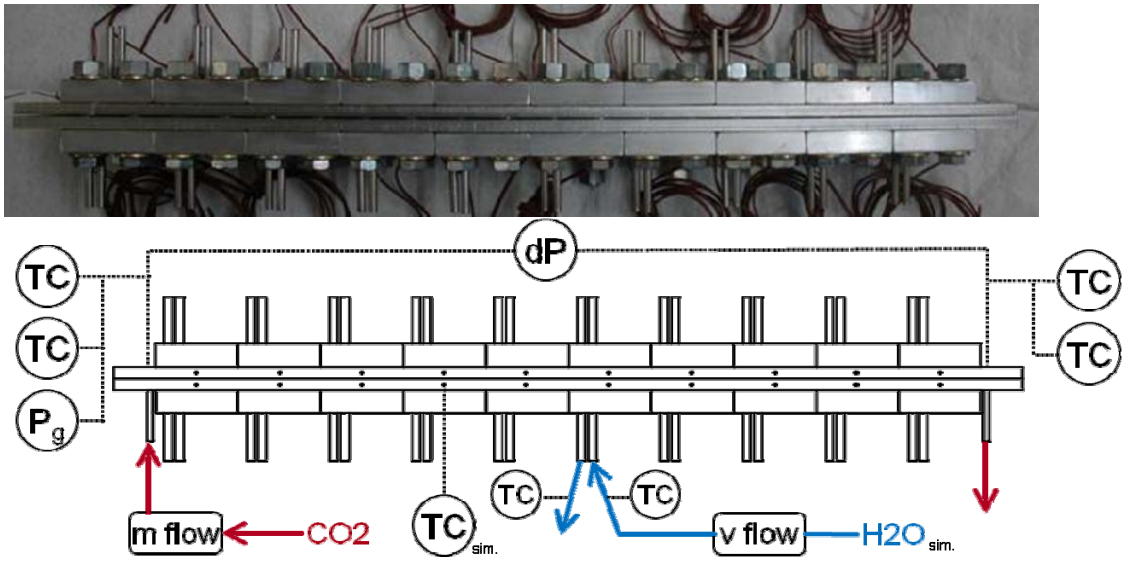

Figure 100: A photograph and diagram of the test section with various measurement locations marked.

As pointed out by Van Abel [54] axial conduction can be an issue with data from the very first and very last test section. Additional insulation was added to the ends of the test section as shown in *Figure 101* to minimize this effect and achieve more efficient data collection.

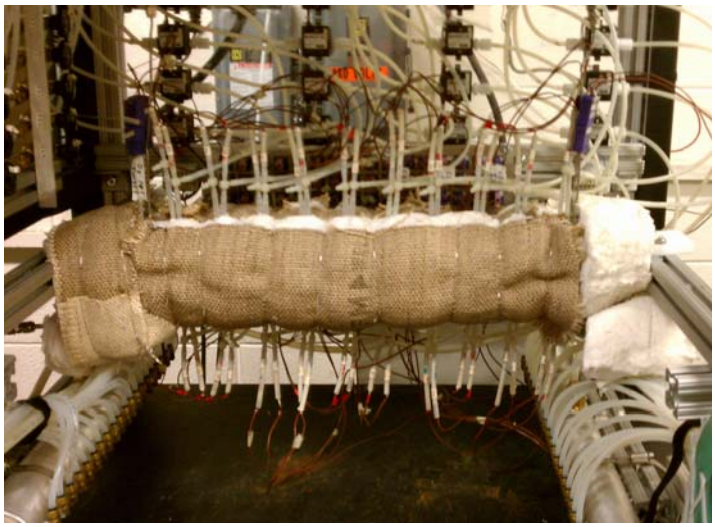

Figure 101: A picture of the fully-insulated test section.

3.4.3 Data Acquisition

Data acquisition is accomplished using a desktop PC running Windows XP and National Instruments (NI) LabView version 8.5. A NI PCI-6052E card is installed to interface with a NI SCXI-1000 Chasis. The chasis is mounted with three NI SCXI-1303 modules to record data from 66 thermocouples, 20 flowmeters, 3 pressure transmitters, and the coriolis flowmeter. Analog communications with the SCR and the VFD for the pump are performed using a feed-through NI SCXI-1302. For a single run data is collected at a rate of 1 Hz for 500 data points after the test section conditions, and especially test section wall temperatures, have not changed for approximately 5 minutes.

The most significant change to the test facility from that described by Kruizenga [7] involves updates to the LabView virtual instrument (VI), screenshots of which are shown in *Figure 102* and *Figure 103*. The VI was re-

designed into a master-slave scheme to allow more online changes to the system including variation of sampling rates, online loading of calibration files, and online activation and deactivation of all control output tasks and the data acquisition task. *Figure 102* shows the main output pane of all the available data signals as well as calculations applied to each sub-section of the PCHE channel. Capability was also added to read in property data tables generated by REFPROP ([68], [69]) using Matlab™ that allows online estimation of the bulk and wall temperature profiles along the test section even through the pseudo-critical point as shown in *Figure 103*. This capability enables the calculated difference between the wall and bulk temperature to be determined and the heat flux adjusted as needed to increase this difference while still maintaining a sufficient temperature difference in each water side cooling block for each heat flow to be accurately determined.

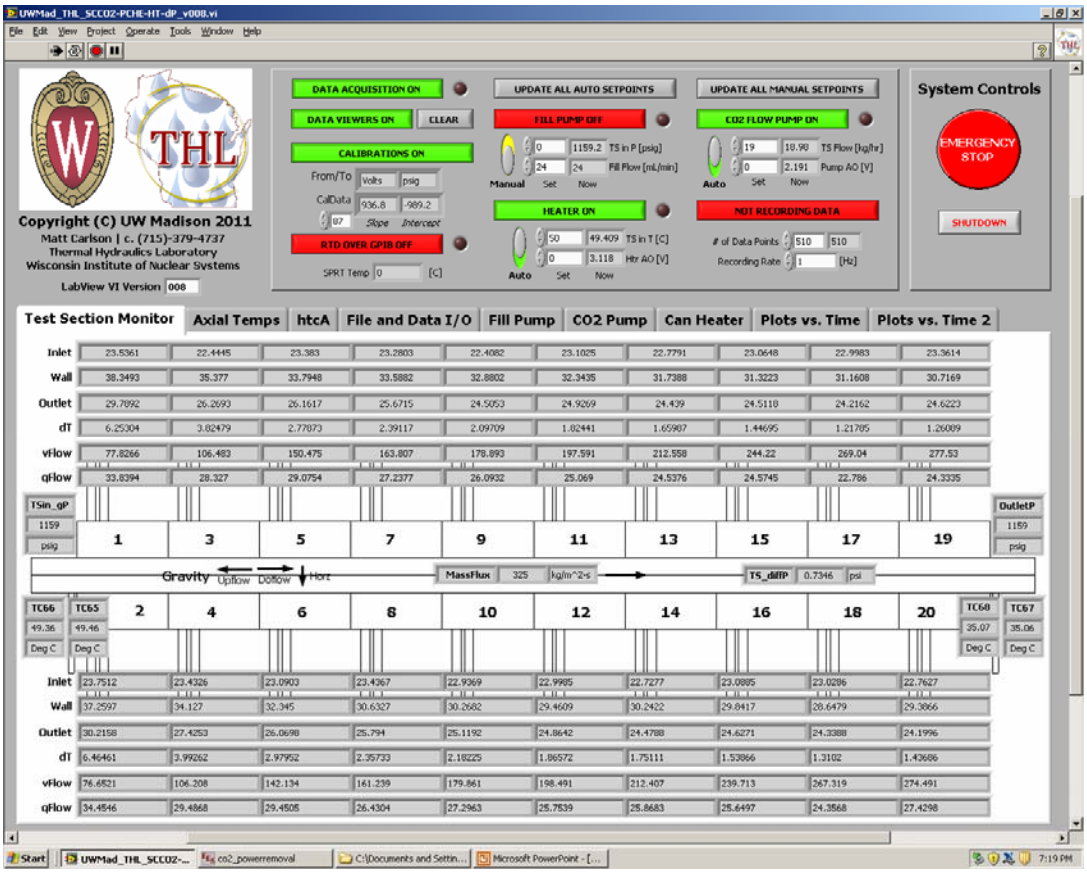

Figure 102: A screenshot of the main data view pane in the LabView VI.

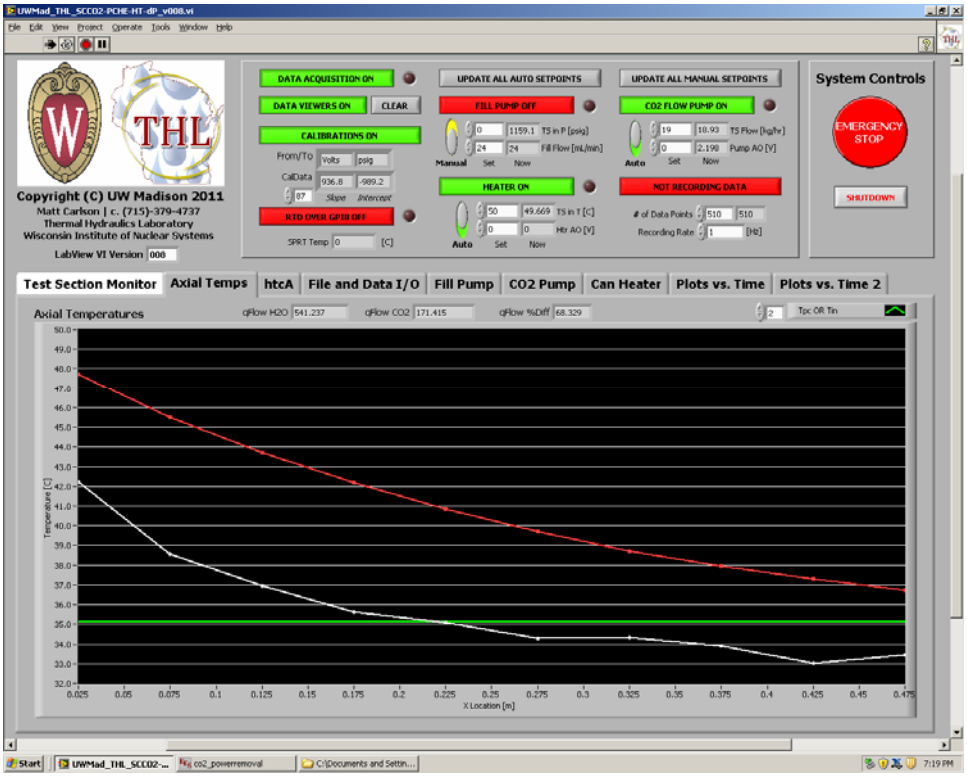

Figure 103: A screenshot of the axial temperature distribution estimated in the test section during operation. The top red line shows the bulk temperature, the next lower white line shows the wall temperature, and the horizontal green line shows the estimated pseudo-critical temperature at this pressure.

3.4.4 PCHE Plate Surface Geometry Measurements

3.4.4.1 Generic PCHE Plate Analysis

In order to measure the surface geometry of the printed circuit heat exchanger (PCHE) test plates that were fabricated for this experiment, small sections of the two zig-zag, two airfoil, and converging channel plates measuring approximately 75 mm square were scanned with a Capture 3D Model Atos II SO white light scanner by Advanced Design Concepts Inc. with small object lenses and a scan resolution of approximately 0.025 mm. This process produced binary stereo-lithography (.stl) files of the surface of each plate. The plate surface is represented by a collection of triangular facets, where the 3 vertexes and the normal vector are specified for each triangle in the file [70].

A script was created called "CheckChannelProfile," reproduced in **Error! Reference source not found.**, which performs the following steps to measure the channel surface with additional user options and dialogue explained to simplify the process.

The binary STL file is first read into Matlab™ R2011a and converted into a point cloud representing only the unique vertex points of the .stl file by the function "binstl2ptcloud" reproduced in **Error! Reference source not found.**.

This raw point cloud data is sometimes not well-aligned to the principle axis of the plate, as shown in *Figure 104* through *Figure 106*, where most noticeably the point cloud is significantly rotated around the x-axis. The point cloud can also contain bending artifacts from the way the plate was supported in the scanner bed, simply-supported on the narrow edges due to gravity and free on the long edges (SFSF), as shown in *Figure 105*.

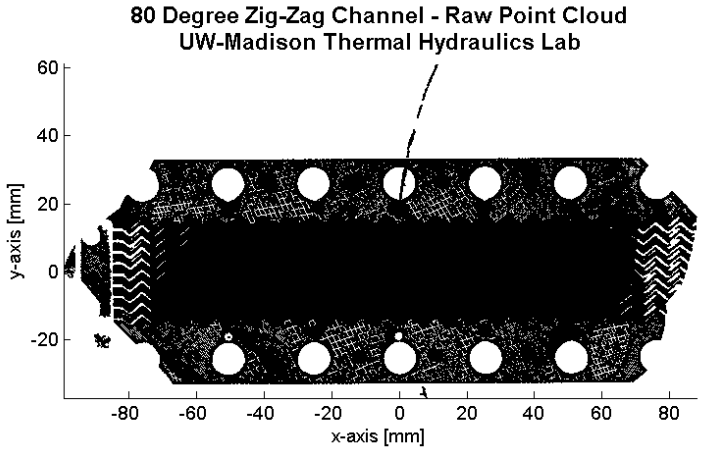

Figure 104: A XY view of the raw point cloud data from the 80 degree zig-zag channel surface scan.

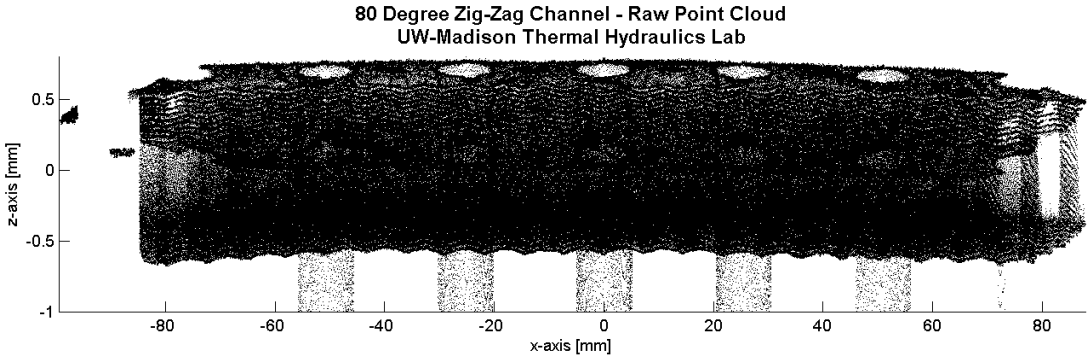

Figure 105: A XZ view of the raw point cloud data from the 80 degree zig-zag channel surface scan.

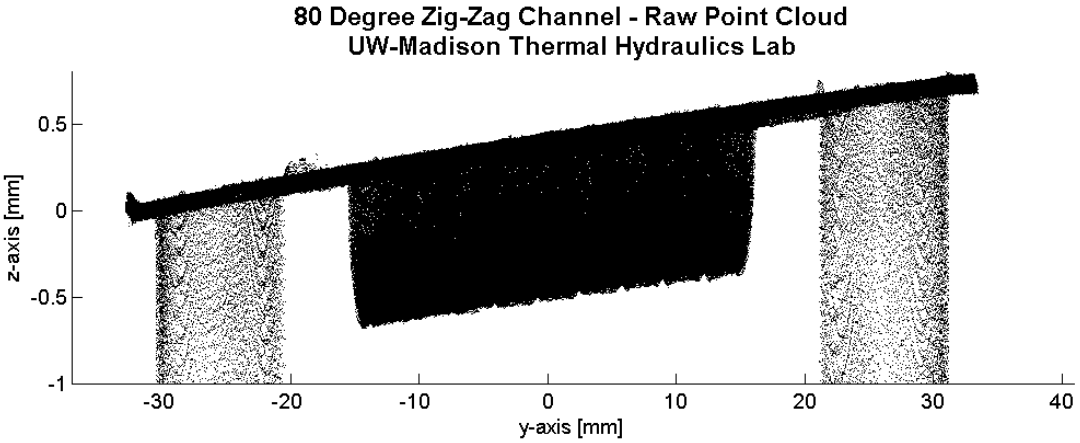

Figure 106: A YZ view of the raw point cloud data from the 80 degree zig-zag channel surface scan.

The function "allignplate2xyz," reproduced in **Error! Reference source not found.**, allows the user to select multiple points along the top surface of the plate, as well as three points each in two of the bolt holes along one side of the plate, and then automatically performs the solid body rotations necessary to orient the point cloud in the principal axis of the plate and corrects for any plate bending according to the approximately sinusoidal shape function of a SFSF-supported rectangular plate. The alignment markings from this process are shown overlaid on the raw point cloud in *Figure 107*, where the points on the top of the plate are fit to a top that provides the principle XY plane of the point cloud as shown by the grid and the center point shown in blue, and the centers of

the two holes selected, shown as red circles, are used to align the fit XY plane to the plate x-axis. Finally, the top plane points are used again by fitting them to a sinusoidal curve along the principal x-axis to correct for any SFSF bending present in the plate.

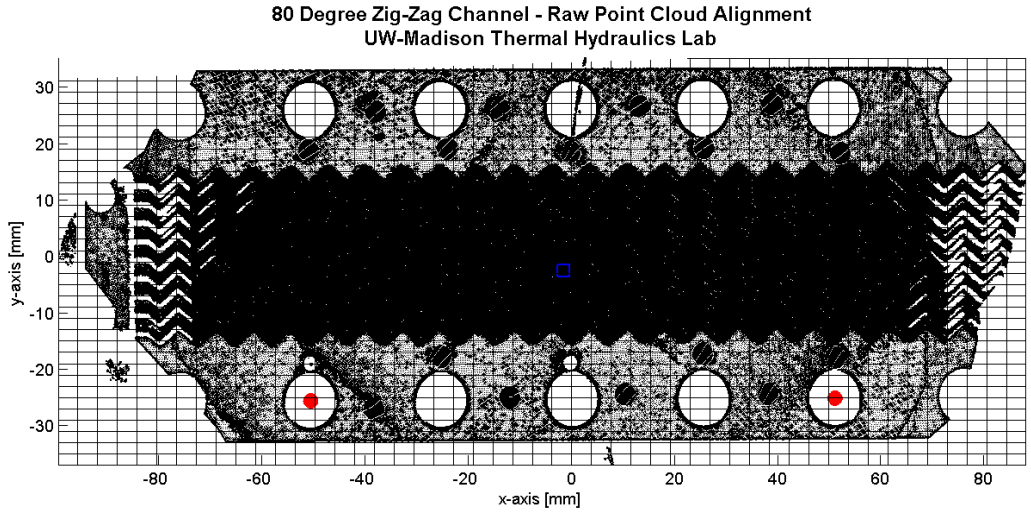

Figure 107: A XY view of the raw point cloud data from the 80 degree zig-zag channel surface scan with the calculated fitting top plane, center point as a blue square, and the centers of the two holes selected shown as red circles.

The aligned point cloud is then trimmed according to user specifications to extract the most usable points of the surface scan using the function "trimptcloud" reproduced in **Error! Reference source not found.**, with the result shown for the 80 degree zig-zag channel in *Figure 108*.

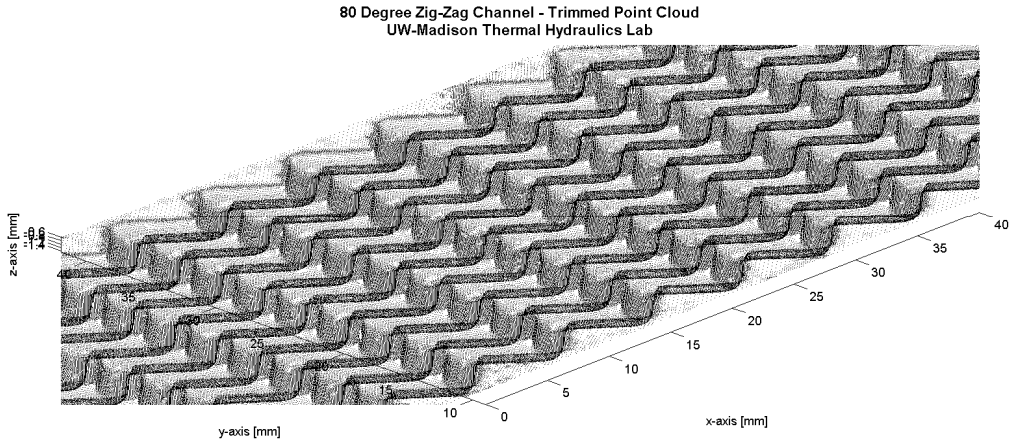

Figure 108: An isometric view of the trimmed point cloud data from the 80 degree zig-zag channel surface scan.

The design geometry is needed to further collapse the point cloud data into an averaged unit cell that can be easily measured.

3.4.4.2 Rounded Zig-Zag Channels

The function "zigzag2unitcell" is next called, reproduced in **Error! Reference source not found.**, which has the user select the 4 lines outlining a single bend in the channel at a cutting plane mid-way down the channel depth to provide approximate alignment of the zig-zag channels and identify the phase of the effective triangle-wave path of the channel in the current coordinate system. The channels are then collapsed together based on this

alignment and the design geometry by shifting the points between each set of red lines in *Figure 109* to align each channel on top of each-other in the y-direction, and by shifting all the points in the x-direction by the design unit cell length to fall on top of each-other in the x-direction.

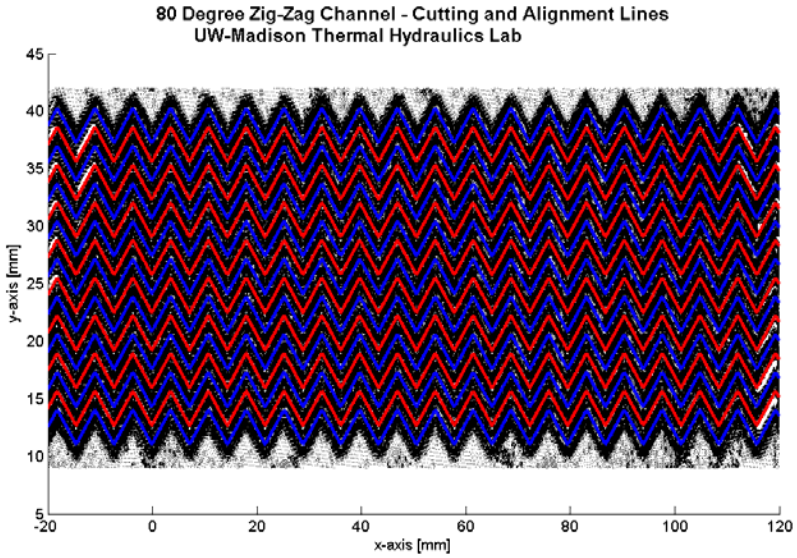

Figure 109: A XY view of the trimmed point cloud data from the 80 degree zig-zag channel surface scan with cutting (red) and alignment (blue) lines used to collapse the point cloud into a unit cell overlaid.

The resulting unit cell point cloud can then be measured by the function "measure_zzunitcell," reproduced in **Error! Reference source not found.**, which uses a custom rounded triangle-wave defined by the function "RndTriWave," reproduced in **Error! Reference source not found.**, to fit depth-wise slices of the unit cell, and "SemiCircChan," reproduced in **Error! Reference source not found.**, to fit slices along the x-axis to the profile of a circular segment. The unit cell, along with fit curves showing representative depth-wise and x-axis slices in black, is shown in *Figure 110*.

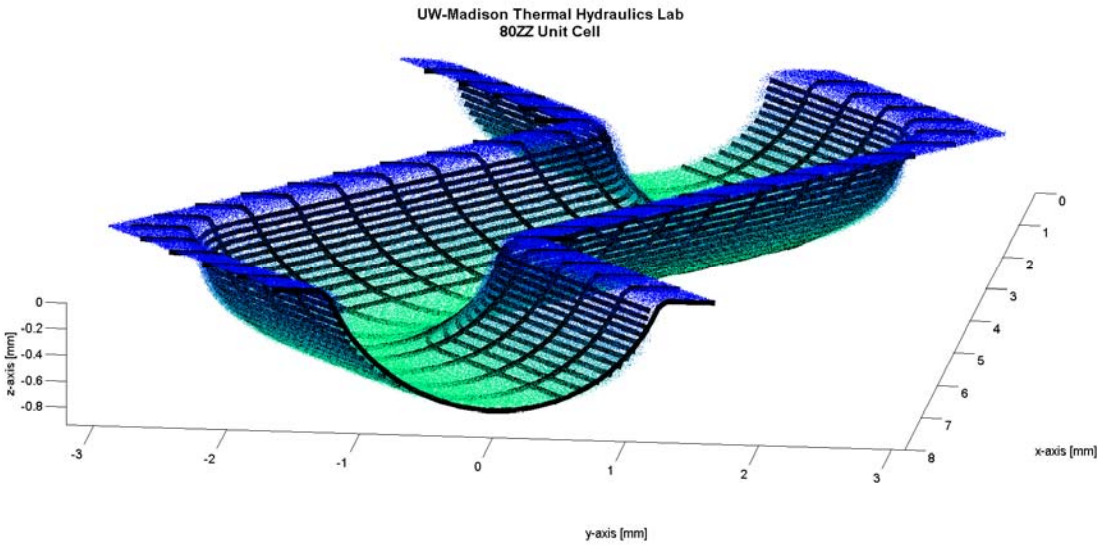

Figure 110: 80-degree zig-zag channel unit cell point cloud shaded from blue near the plate surface to green at the bottom of the channel, and with several depth-wise and axial cutting plane fit curves shown in black.

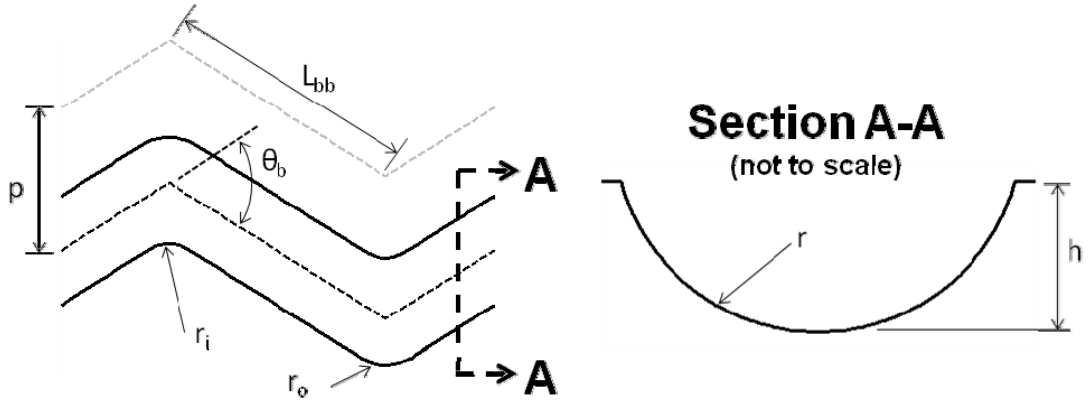

Figure 111: A diagram for an arbitrary rounded zig-zag PCHE channel unit cell.

The resulting measurements of this averaged unit cell represent the approximate profile of the zig-zag channel surface, shown as a schematic diagram in *Figure 111*, with the measured corner radii and the profile radii (central path line where both corners have equal radii) shown in *Figure 112* versus depth, the bend-to-bend length also versus depth in *Figure 113*, the bend deflection angle versus depth in *Figure 114*, and the channel depth and radius shown in *Figure 115* assuming the channel approximates a circular segment. The averages and uncertainties of each of these measurements, along with the design geometry and the resulting calculated channel parameters, are summarized in
Table 23. All uncertainty values are based on the standard deviation of the measurements or the approximate scanner resolution; whichever is the largest.

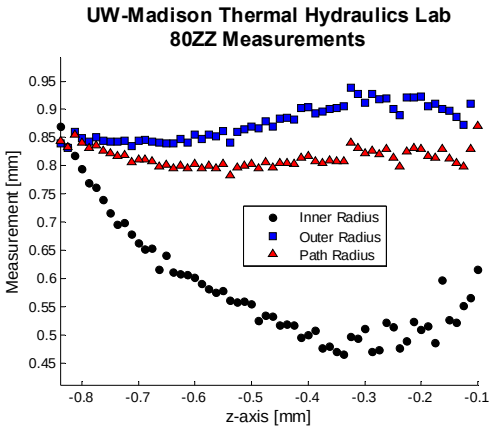

Figure 112: Measured inner and outer corner radii, as well as the central path line radii versus depth for the 80-degree zig-zag surface.

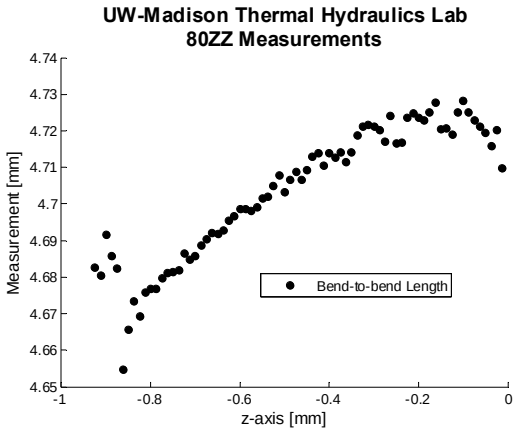

Figure 113: Bend-to-bend length versus depth for the 80-degree zig-zag surface.

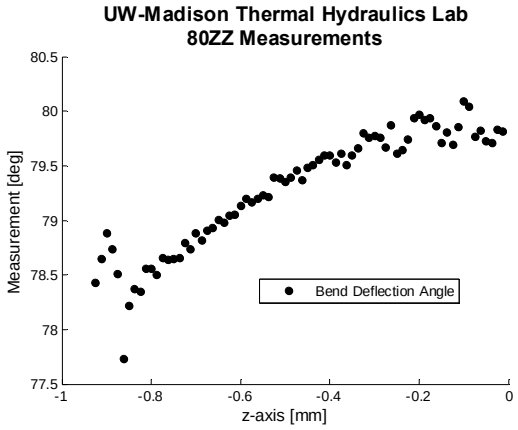

Figure 114: Bend deflection angle versus depth for the 80-degree zig-zag surface.

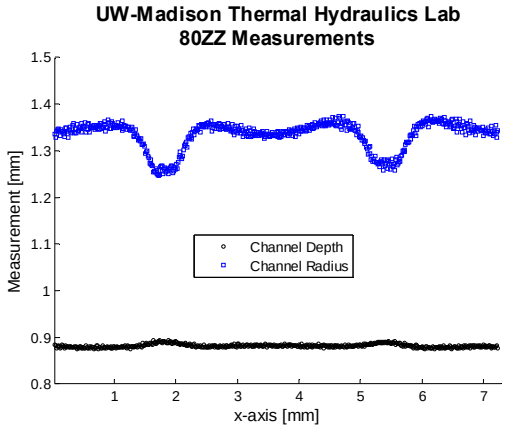

Figure 115: Channel depth and circular segment radius versus x-axis position for the 80-degree zig-zag surface.

Table 23: Design and measured geometry of the 80-degree zig-zag channel surface.

Description	Symbol	Unit	Design	Measured	Uncertainty
Bend-to-bend Length	L_{bb}	mm	4.724	4.704	0.037
Bend Angle	θ_b	deg	80	79.29	0.53
Inner Radius	r_i	mm	0	0.583	0.1
Outer Radius	r_o	mm	0	0.876	0.031
Path Radius	r_s	mm	0	0.815	0.025
Channel Pitch	p	mm	3.277	3.277	0.025
Profile Radius	r	mm	0.95	1.334	0.06
Channel Depth	h	mm	0.95	0.882	0.025
Number of Bends	Nb	-	138	138	-
Hydraulic Diameter ($4A_c$/per)	$d_{hyd\perp}$	mm	1.116	1.096	0.0286
Hydraulic Diameter ($4V_f/A_s$)	d_{hyd}	mm	1.16	1.117	0.0299
Channel Cross-Sectional Area	-	mm^2	1.418	1.62	0.0777
Unit Cell Surface Area	-	mm^2	46.2	54.35	1.55
Relative Roughness	-	-	6.418e-3	7.227e-3	0.381e-3

This same procedure is repeated for the 65-degree zig-zag channel surface geometry as shown in *Figure 116* through *Figure 119* and
Table 24.

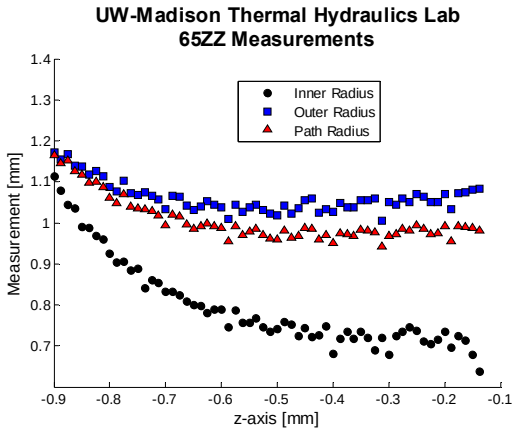

Figure 116: Measured inner and outer corner radii, as well as the central path

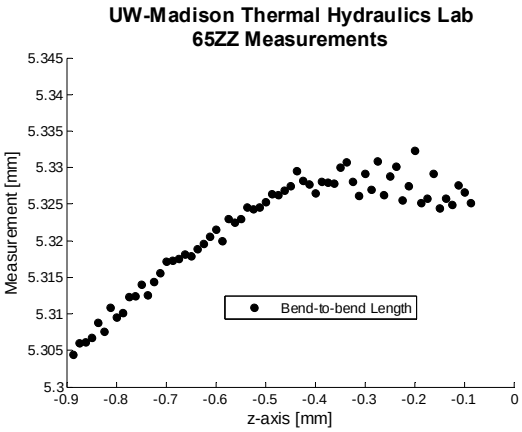

Figure 117: Bend-to-bend length versus depth for the 65-degree zig-zag surface.

line radii versus depth for the 65-degree zig-zag surface.

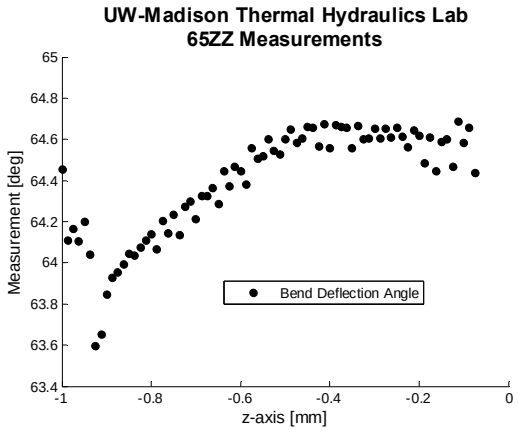

Figure 118: Bend deflection angle versus depth for the 65-degree zig-zag surface.

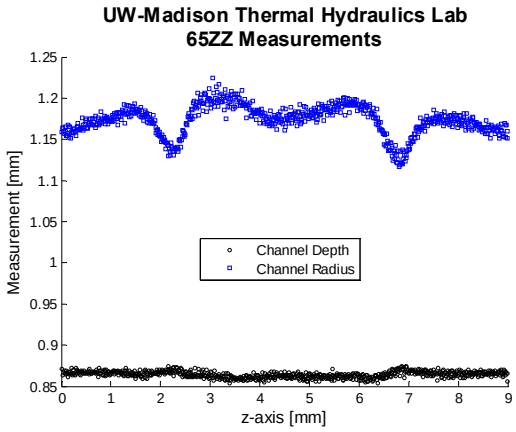

Figure 119: Channel depth and circular segment radius versus x-axis position for the 65-degree zig-zag surface.

Table 24: Design and measured geometry of the 65-degree zig-zag channel surface.

Description	Symbol	Unit	Design	Measured	Uncertainty
Bend-to-bend Length	L_{bb}	mm	5.334	5.322	0.025
Bend Angle	θ_b	deg	65	64.4	0.026
Inner Radius	r_i	mm	0	0.796	0.11
Outer Radius	r_o	mm	0	1.062	0.037
Path Radius	r_s	mm	0	1.007	0.053
Channel Pitch	p	mm	2.972	2.972	0.025
Profile Radius	r	mm	0.95	1.174	0.025
Channel Depth	h	mm	0.95	0.864	0.025
Number of Bends	Nb	-	111	111	-
Hydraulic Diameter ($4A_c$/per)	$d_{hyd\perp}$	mm	1.135	1.071	0.028
Hydraulic Diameter ($4V_f/A_s$)	d_{hyd}	mm	1.161	1.086	0.029
Cross-Sectional Area	-	mm^2	1.418	1.446	0.06
Unit-Cell Surface Area	-	mm^2	52.18	55.24	0.97
Relative Roughness	-	-	6.418e-3	7.313e-3	0.388e-3

3.4.4.3 Rounded Airfoil fin Array Channels

The function "airfoil2unitcell" is next called, reproduced in **Error! Reference source not found.**, which has the user select the points defining a bounding polygon to contain each row of airfoils in the channel at a cutting plane mid-way down the channel depth to provide approximate alignment of the airfoil channels and identify the axial and lateral pitch of the airfoil array in the current coordinate system. This process also identifies and corrects for noticeable tilt in the airfoil pattern relative to the principle axis of the plate due to manufacturing errors. The channels are then collapsed together based on this alignment and the design geometry by shifting the points between each set of red and blue lines, shown for the center row of airfoils in *Figure 120*, to align each airfoil side on top of each-other in the y-direction accounting for the axial pitch spacing, and by shifting all the points in the x-direction by the axial pitch spacing to fall on top of each-other in the x-direction.

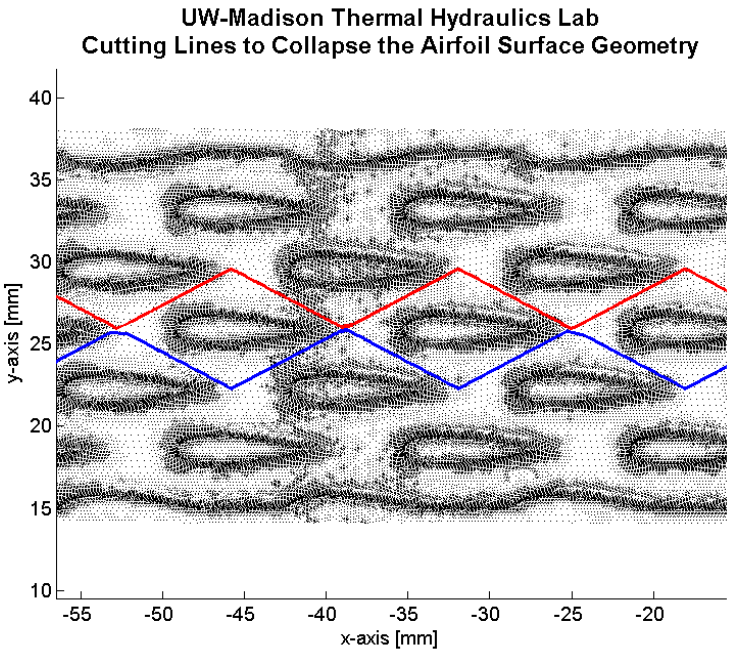

Figure 120: A XY view of the trimmed point cloud data from the 8.1 mm NACA0020 surface scan with cutting lines for the center row of airfoils (red and blue) used to collapse the point cloud into a unit cell overlaid.

The resulting unit cell point cloud can then be measured by the function "measure_afunitcell," reproduced in **Error! Reference source not found.**, which uses a custom symmetric NACA airfoil-wave defined by the function "SymNACAWave," reproduced in **Error! Reference source not found.**, to fit depth-wise slices of the unit cell, and a custom filleted step function "StepFillet," reproduced in **Error! Reference source not found.**, to fit the front and side fillet radius profiles to a filleted step function. The unit cell, along with fit curves showing representative depth-wise and step fillet slices in black, is shown in *Figure 121*.

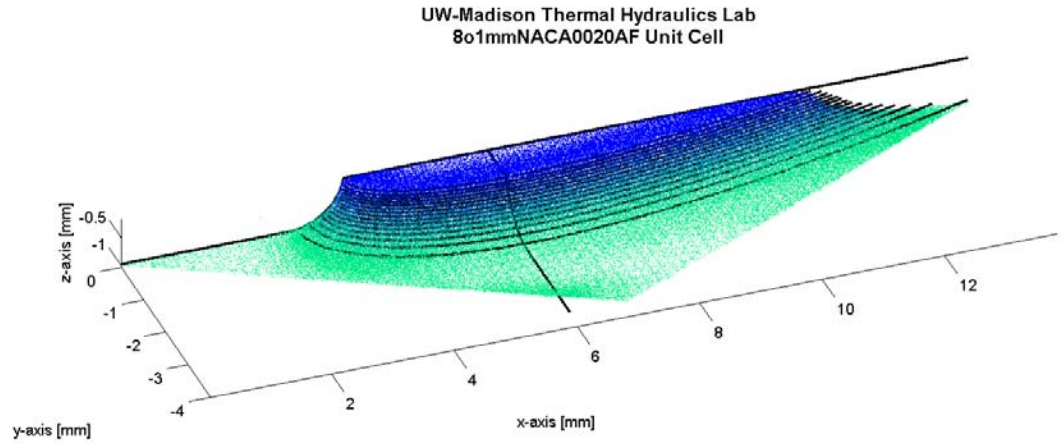

Figure 121: The 8.1mm NACA0020 unit cell point cloud shaded from blue near the plate surface to green at the bottom of the channel, and with several depth-wise and step fillet cutting plane fit curves shown in black.

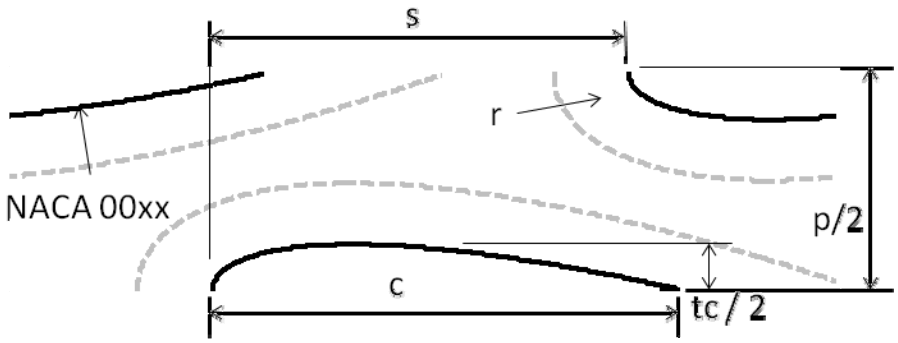

Figure 122: A diagram for an arbitrary rounded symmetrical NACA pillar array PCHE channel unit cell. The dashed grey line represents the outer bottom edge of a depth-wise fillet of radius r which is constructed on the inside bottom edge of the main airfoil profile shown in black.

The resulting measurements of this averaged unit cell represent the approximate profile of the airfoil surface, shown as a schematic diagram in *Figure 122*, with the measured chord length shown in *Figure 123* versus depth, the ratio of thickness to chord length also versus depth in *Figure 124*, and the fit of a YZ slice of the airfoil profile at the widest section to the "StepFillet" function shown in *Figure 125* with the profile measurements overlaid. The averages and uncertainties of each of these measurements, along with the design geometry and the resulting calculated channel parameters, are summarized in *Table 25*. All uncertainty values are based on the standard deviation of the measurements or the approximate scanner resolution; whichever is the largest.

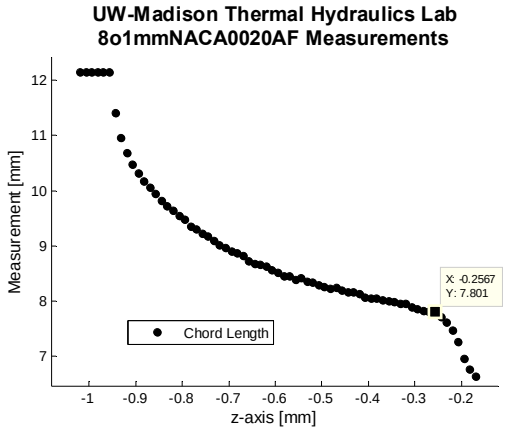

Figure 123: Measured chord length versus depth for the 8.1 mm NACA0020 surface.

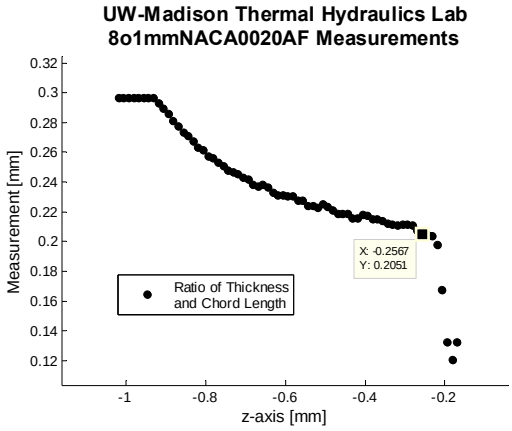

Figure 124: Ratio of thickness and chord length versus depth for the 8.1 mm NACA0020 surface.

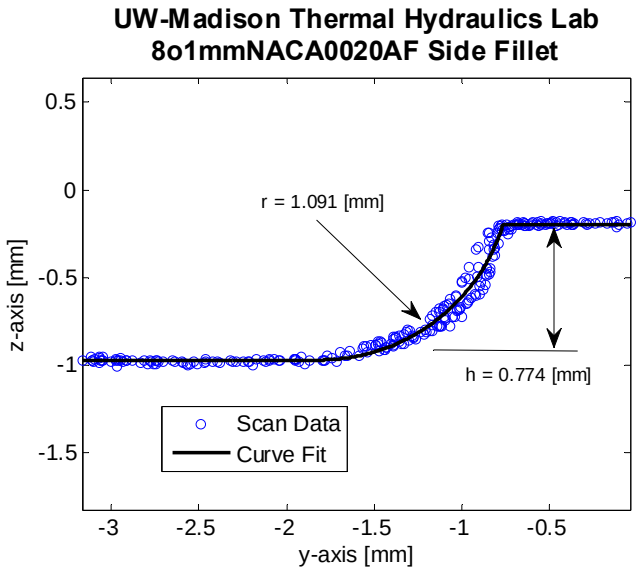

Figure 125: A plot of the averaged unit cell YZ slice at the widest section of the airfoil fit to the "StepFillet" function with the measured height and radius overlaid for the 8.1 mm NACA0020 surface.

Table 25: Design and measured geometry of the 8.1 mm NACA0020 channel surface.

Description	Symbol	Unit	Design	Measured	Uncertainty
Chord Length	c	mm	8.1	7.801	0.05
Thickness / Chord Length	t	-	0.2	0.205	0.05
Fillet Radius	r	mm	0	1.091	0.05
Channel Depth	h	mm	0.95	0.774	0.05
Axial Pitch	s	mm	6.9	6.933	0.025
Lateral Pitch	p	mm	7.3	7.296	0.025
Number of Rows	Nr	-	72	72	-
Airfoils per Row	Naf	-	3	3	-
Hydraulic Diameter ($4V_f/A_s$)	d_{hyd}	mm	1.447	1.337	0.0834
Cross-Sectional Area	-	mm^2	16.19	13.23	1.247
Unit-Cell Surface Area	-	mm^2	101.8	90.89	3.906
Relative Roughness	-	-	5.253e-3	6.285e-3	4.975e-4

This same procedure is repeated for the 4.0 mm NACA0020 channel surface geometry as shown in *Figure 126* through *Figure 128* and *Table 26*.

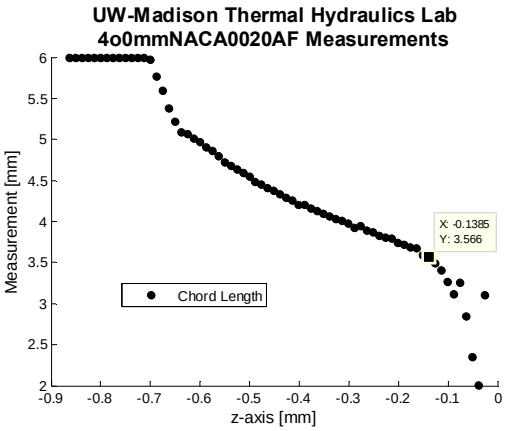

Figure 126: Measured chord length versus depth for the 4.0 mm NACA0020 surface.

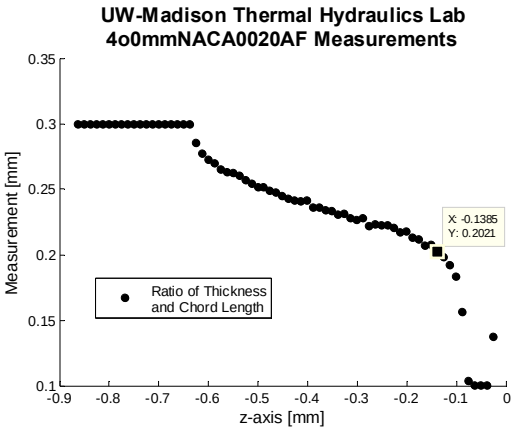

Figure 127: Ratio of thickness and chord length versus depth for the 4.0 mm

NACA0020 surface.

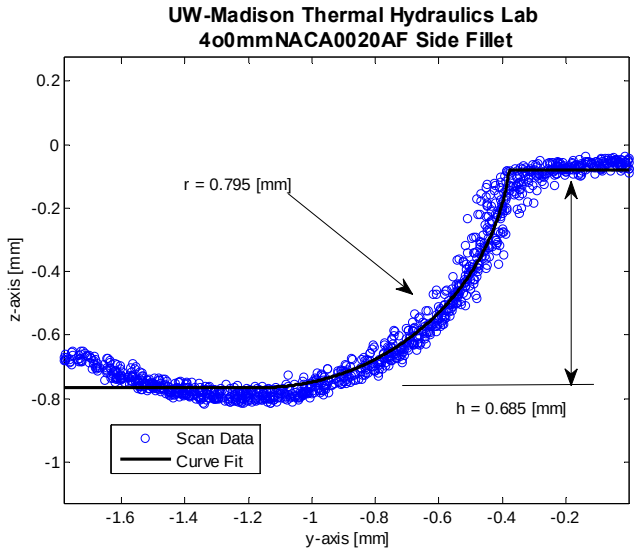

Figure 128: A plot of the averaged unit cell YZ slice at the widest section of the airfoil fit to the "StepFillet" function with the measured height and radius overlaid for the 4.0 mm NACA0020 surface.

Table 26: Design and measured geometry of the 4.0 mm NACA0020 channel surface.

Description	Symbol	Unit	Design	Measured	Uncertainty
Chord Length	c	mm	4.0	3.566	0.05
Thickness / Chord Length	t	-	0.2	0.202	0.05
Fillet Radius	r	mm	0	0.795	0.05
Channel Depth	h	mm	0.95	0.685	0.05
Axial Pitch	s	mm	3.5	3. 466	0.025
Lateral Pitch	p	mm	3.6	3. 657	0.025
Number of Rows	Nr	-	144	144	-
Airfoils per Row	Naf	-	6	6	-
Hydraulic Diameter ($4V_f/A_s$)	d_{hyd}	mm	1.205	1.112	0.0736
Cross-Sectional Area	-	mm^2	15.96	12.07	1.151
Unit-Cell Surface Area	-	mm^2	30.18	24.94	0.8546
Relative Roughness	-	-	5.634e-3	7.259e-3	6.171e-4

3.5 Data Reduction and Uncertainty

3.5.1 Primary Variables

Several basic variables are determined from measurements in order to be used in comparisons with other data and correlations, including the heat removal profile, bulk state profile (enthalpy and pressure for this experiment), wall temperature profile, and the representative average channel state (temperature and pressure for this experiment). From these variables and the dimensions of the channel the mass flux, heat flux profile, bulk temperature profile, heat transfer coefficient and Nusselt number, and bulk and average Reynolds and Prandtl numbers can be determined as explained in the following sections. These methods are essentially the same as those used by Kruizenga [7] but have been implemented entirely in Matlab™ using REFPROP v9.0 for fluid properties ([68], [69]) for increased speed when handling large datasets. Data reduction codes are attached as **Error! Reference source not found.**.

3.5.1.1 Heat Removal Rate

The heat removal rate for the water side is first calculated from an energy balance across each cooling block

using the known difference between the inlet and outlet temperatures and the assumed atmosphereic pressure as shown in Equation (77). It is assumed that a negligible amount of energy is lost through the cooling block walls due to use of approximately 2 in of insulation around the entire test section and the relatively low temperatures of the cooling water which is typically less than 25 °C for even the hottest runs. Water properties are calculated based on the arithmetic average of the inlet and outlet temperatures as the water fluid properties do not vary considerably over the typically 1 to 10 °C temperature difference.

$$\dot{Q}_{H2O} = \dot{V}\rho|_{T,P_{atm}} c_p|_{T,P_{atm}} [T_{OUT} - T_{IN}] \quad (77)$$

3.5.1.2 Mass and Heat Fluxes

The mass and heat fluxes, shown in Equation (78) and (79), are simply the measured mass flow rate and the total cooling block heat flow per sub-section divided by the appropriate geometric factors of each surface type.

$$G = \frac{\dot{m}}{A_c} \quad (78)$$

$$q'' = \frac{\dot{q}_{top} + \dot{q}_{bot}}{A_s} \quad (79)$$

3.5.1.3 Bulk Fluid State

The bulk fluid enthalpy is calculated iteratively starting from the inlet enthalpy based on the inlet temperature and pressure, with the enthalpy after each subsequent cooling block determined usng the measured mass flow rate and calculated heat flows out of each cooling block as shown in Equation **(80)** and *Figure 129*. The average enthalpy in the cooling block is then calculated assuming a constant heat flux along the length of each cooling block as shown in Equation **(81)**. The pressure drop along the PCHE surface is assumed to be linear based on numerical simulations by Kim et al. [71], although Van Abel [54] recently showed using analysis in Fluent of several experiments that the profile likely bends away from a linear profile. The pressure at each of the 10 subsection is therefore determined according to Equation (82). Finally the bulk temperature and any other state-dependent property such as the Prandtl number can be calculated for CO2 based on the calculated enthalpy and pressure at each sub-section.

$$i_{j+1} = i_j - \frac{\dot{q}_{top} + \dot{q}_{bot}}{\dot{m}} \quad (80)$$

$$i = \frac{i_{j+1} + i_j}{2} \quad (81)$$

$$P = P_{in} + \frac{(P_{in} - dP)}{L}\left(x_j + \frac{L}{10}\right) \quad (82)$$

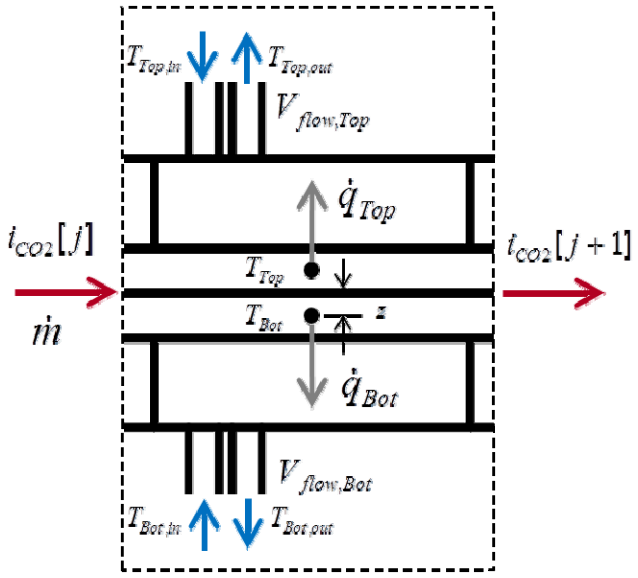

Figure 129: Diagram of the heat transfer coefficient calculation for each cooling block section.

App A.1.1 Wall Surface Temperature

The wall surface temperature on each plate side is calculated according to a plane-wall conductance equation as shown in Equation (83), where the thermal conductivity of the stainless steel is treated as temperature dependant. The internal wall temperature measurement thermocouples were place based on three-dimensional numerical analysis by Kruizenga to allow the use of a simple plane-wall conduction equation (about 3.175 mm away from the channel surfaces), where the effective cross-sectional area for conduction is determined to be based on the full axial length of the cooling block (50.75 mm) but only the width of the cooling water flow area (35.28 mm).

$$T_{w,side} = T_{w,meas} + \frac{\dot{q}_{side} z}{k_{mat} A_{c,eff}} \quad \textbf{(83)}$$

3.5.1.4 Heat Transfer Coefficient

The heat transfer coefficient is now calculated from the calculated wall heat removal rates, bulk temperature, and the arithmetic average of the top and bottom (smooth and etched) wall surface temperatures, along with the channel surface area for each sub-section as shown in Equation (84). The Nusselt number using the thermal conductivity based on the bulk temperature can also be calculated in the typical way as shown in Equation (85).

$$h = \frac{\dot{q}_{top} + \dot{q}_{bot}}{A_s \left(T_b - 0.5 \left(T_{w,top} + T_{w,bot} \right) \right)} \quad \textbf{(84)}$$

$$Nu = \frac{h d_{hyd}}{k|_{T_b}} \quad \textbf{(85)}$$

3.5.1.5 Average Channel State

The average channel temperature and pressure are calculated based on an arithmatic average of the inlet and outlet temperatures and pressures. From this the average channel state is known and an average Reynolds number can be determined according to Equation (86).

$$\overline{Re} = \frac{G d_{hyd}}{\mu|_{\bar{T},\bar{P}}} \quad \textbf{(86)}$$

3.5.1.6 Contraction, Expansion, and Acceleration Pressure Drops

In order to separate out the combined form and friction pressure drops in the PCHE surfaces from the total differential pressure measured between the inlet and outlet plenums of the channels, the inlet contraction, outlet expansion, and accerlation form losses are determined as shown in Equations (87) and (88) for the inlet and outlet form losses from Idel'chik and Equation (12) mentioned previously for the acceration pressure change. The area ratio A1 / A2 is the ratio of the smaller to the larger cross-sectional area for both correlations.

$$dP_{cont} = 0.5\left(1 - \frac{A_1}{A_2}\right)^{0.75} \frac{1}{2}\rho_{IN} v_{IN}^2 \quad \textbf{(87)}$$

$$dP_{exp} = \left(1 - \frac{A_1}{A_2}\right)^2 \frac{1}{2}\rho_{OUT} v_{OUT}^2 \quad \textbf{(88)}$$

3.5.2 Measured Uncertainties

Quantification of experimental uncertainties is critical to determining the validity of measured data, and therefore its reliability for use in developing correlations, comparison to other experimental results, and verification of computer simulations. The sensitivity of various SCO2 fluid properties near the critical point and the higher heat transfer coefficients of zig-zag and airfoil fin channels further constain the acceptable measurement uncertainty. This challenge was met by designing the the experimental facility in order to achieve high stability and to allow for frequent calibration of critical instruments as discussed by Kruizenga [7]. The various un-calibrated and calibrated uncertainties, measurement stability, and calibration frequency are summarized in *Table 27*, with a more detailed discussion of the uncertainty calculation and calibration methods in subsequent sections. Note that the thermocouples are listed as calibrated about every 3 weeks but are zeroed every day of testing to account for minor drift in the reading.

Table 27: Typical uncertainty and precision of the measurement instrumentation involved in these tests. Although un-calibrated uncertainties can vary somewhat with the reading, calibrated uncertainties do not vary considerably.

Measurement	Critical Value	Un-Calibrated Uncertainty	Calibrated Uncertainty	Typical Reading StDev	Frequency [wks]
CO_2 Mass Flow Rate [kg/hr]	15	< 2.01	0.0527	0.1	52
TS Inlet Pressure [MPa]	7.5	< 0.221	0.0039	0.0025	52
TSPressure Drop [kPa]	7	< 1.086	0.393	0.1	52
CO_2 In / Outlet T [°C]	T_{pc}	< 1	0.15	0.0075	3
Test Section Wall T [°C]	T_{pc}	< 1.7	0.2 (0.5)*	0.025	3 + zeroed
H2O Volume Flow [mL/min]	80	< 30	3	0.5	26
H2O In / Outlet Temps [°C]	dT = 1	< 1	dT = 0.1	0.025	3 + zeroed
H2O Pressure [psi]	-	0.145	-	-	-

*Uncertainty of 0.2 for temperatures less than 50 °C and 0.5 above 50 °C.

3.5.2.1 Test Section Mass Flow Rate

The mass flow rate through the test section is measured using a Siemens Sitrans F C MASSFLO sensor type 2100 DI 6 and transmitter type 6000 Compact IP 67 before the inlet to the test section heater as shown in *Figure 98*. The transmitter provides a 4 to 20 mA signal linearly-proportional to the measured mass flow rate between 0 and 1000 kg/hr [72]. This signal is read into the data acquisition by measuring the corresponding voltage difference across a 220 ohm resistor using a NI SCXI-1303 terminal block in a NI SCXI-1102 module.

The manufacturers' literature states that the typical uncertainty of a reading at the display is 0.1% of the actual mass flow rate, or a maximum expected uncertainty of ±0.035 kg/hr at a flow rate of 35 kg/hr. However, this estimate does not factor in the low flow rate measured by the meter which is less than 5% of the maximum measurable flow rate, as well as other uncertainties involved with the data acquisition (DAQ) system. Using the uncertainty information provided for each component in the DAQ system, an estimate of the un-calibrated, un-zeroed uncertainty can be obtained assuming a perfectly precise mean mass flow rate signal as shown in *Table 28*.

Table 28: An estimate of the largest expected un-calibrated and un-zeroed test section mass flow rate uncertainty.

Contribution	Relative Effect	Value	Uncertainty	Unit
Actual Mass Flow Rate		**15**	**±0**	**kg/hr**
Sitrans F C MASSFLO (MASS 2100 DI 6 MASS 6000 IP 67)				
Reference Condition	Upper Mass Flow Rate Setting	50	±0	kg/hr
Reference Condition	Maximum Mass Flow Rate	1000	±0	kg/hr
Reference Condition	Deviation from Ref. Temperature	0	±0	K
Reference Condition	Deviation from Supply Voltage	0	±0	%
Linearity Error	±0.1% of flow rate		±0.015	kg/hr
Repeatability Error	±0.05% of flow rate		±0.0075	kg/hr
Max Zero Point Error	±0.05 [kg/hr]		±0.05	kg/hr
Use of Current Output	±(0.1% of flow + 0.05% of FSO)		±0.515	kg/hr
Ambient Temperature	Display: < ±0.003% of flow rate / K		±0	kg/hr
	AO: < ±0.005% of flow rate / K		±0	kg/hr
Power Supply	< ±0.005% of flow rate / 1% change		±0	kg/hr
Display Sub-Total			±0.518	kg/hr
Analog Output Sub-Total			±0. 518	kg/hr
Output Current		**8.8**	**±0.166**	**mA**
Load Resistance				
Load Resistor	±5% of value	220	±11	Ω
	Output Voltage	**1.936**	**±0.1034**	**V**
NI SCXI-1303 terminal block; NI SCXI-1102 module				
Reference Condition	Full Scale Reading	10	±0	V
Nonlinearity	0.005% FSR		0.0005	V
Offset Error	600 μV		±0.0006	V
Gain Error	0.04% of reading		±0.00077	V
Offset Temp Coefficient	20 μV/°C		±0	V
NI DAQ Sub-Total			±0.0011	V
Voltage Sub-Total			±0.1034	V
Measured Mass Flow Rate		**15**	**±2.0123**	**kg/hr**

This level of uncertainty is unacceptable for this test, so once installed the system is run through a range of flow rates, and the flow rate displayed on the meter and that calculated in the DAQ system are recorded. This information is used to generate a linear calibration curve. This curve is input into the data acquisition program from a calibration record file combining calibration information for all acquired signals. This process removes bias errors associated with the DAQ system and the load resistor, as well as the bias produced from using the current output signal of the meter rather than the pulse output. Finally, the flow meter is zeroed every 3 weeks, resulting in a final calculated uncertainty as shown in *Table 29*.

Table 29: An estimate of the largest expected calibrated and zeroed test section mass flow rate uncertainty.

Contribution	Relative Effect	Value	Uncertainty	Unit
Actual Mass Flow Rate		**15**	**±0**	**kg/hr**
Sitrans F C MASSFLO (MASS 2100 DI 6 MASS 6000 IP 67)				
Reference Condition	Upper Mass Flow Rate Setting	50	±0	kg/hr
Reference Condition	Maximum Mass Flow Rate	1000	±0	kg/hr
Reference Condition	Deviation from Ref. Temperature	0	±0	K
Reference Condition	Deviation from Supply Voltage	0	±0	%
Linearity Error	±0.1% of flow rate		±0.015	kg/hr
Repeatability Error	±0.05% of flow rate		±0.0075	kg/hr
Max Zero Point Error	±0.05 [kg/hr]		±0.05	kg/hr
Use of Current Output	±(0.1% of flow + 0.05% of FSO)		±0	kg/hr
Ambient Temperature	Display: < ±0.003% of flow rate / K		±0	kg/hr
	AO: < ±0.005% of flow rate / K		±0	kg/hr
Power Supply	< ±0.005% of flow rate / 1% change		±0	kg/hr
Display Sub-Total			±0.0574	kg/hr
Measured Mass Flow Rate		**15**	**±0.0574**	**kg/hr**

3.5.2.2 Test Section Inlet Pressure

The inlet pressure to the test section is measured using a Siemens Sitrans P 7MF4032 gauge pressure transmitter from the inlet pressure tap shown in *Figure 98*. The transmitter provides a 4 to 20 mA signal linearly-proportional to the measured gauge pressure between 4 and 400 bar (0.4 to 40 MPa) [73]. Note that the transmitter can be re-ranged for optimal signal resolution as-needed without affecting the calibration of the sensor and transmitter. This signal is read into the data acquisition system by measuring the corresponding voltage difference across a 237 ohm resistor using a NI SCXI-1303 terminal block in a NI SCXI-1102 module.

Based off the manufacturers' literature, an estimate of the un-calibrated, un-zeroed uncertainty can be obtained assuming a perfectly precise mean pressure signal as shown in *Table 30*. Note that the affect of external atmospheric pressure variation and variable room pressure due to HVAC operation and fume hood venting nearby is accounted for as uncertainty in the actual test section pressure, and is very small relative to the pressure of interest.

Table 30: An estimate of the largest expected un-calibrated and un-zeroed test section pressure uncertainty.

Contribution	Relative Effect	Value	Unc	Unit
Actual Test Section Inlet Pressure		**1087**	**±0.145**	**psia**
Sitrans P 7MF4032 Gauge Pressure Transmitter				
Reference Condition	Span Maximum Pressure	2000	±0	psig
Reference Condition	First Commissioning Date	5/1/2000	±0	-
Reference Condition	Deviation from Supply Voltage	6	±0	V
Reference Error	< ±0.1% of reading		±1.088	psi
Long-term Drift	< ±0.1% every 6 months at max span		±22.84	psi
Ambient Temp - Zero Effect	< ±0.05% / 10 K at max span		±0	psi
Ambient Temp - Span Effect	< ±0.1% / 10 K at max span		±0	psi
Power Supply	< ±0.005% / 1 V change		±0.326	psi
Mounting Orientation	< ±0.05 mbar / 10 deg off vertical		±0	psi
Dead Weight Pressure Source	< ±0.05 % of test pressure		±0.544	psi

Sub-Total			±22.87	psi
Output Current		**12.70**	**±0.183**	**mA**
Load Resistance				
Load Resistor	±1% of value	237	±2.37	Ω
Output Voltage		**3.0104**	**±0.0528**	**V**
NI SCXI-1303 terminal block; NI SCXI-1102 module				
Reference Condition	Full Scale Reading	10	±0	V
Nonlinearity	0.005% FSR		0.0005	V
Offset Error	600 μV		±0.0006	V
Gain Error	0.04% of reading		±0.0012	V
Offset Temperature Coefficient	20 μV/°C		±0	V
NI DAQ Sub-Total			±0.00144	V
Voltage Sub-Total			±0.05282	V
Measured Test Section Inlet Pressure		**1087**	**±32.06**	**psia**

To obtain more confidence in the measured results, a linear calibration curve is used in the LabView™ data acquisition program based off of calibration against an EG+G Chandler Engineering dead weight pressure tester. This unit provides a pressure source between 0 and 2000 psig ±0.05% (0 to 13.8 MPa gauge) to the sensor. The applied pressure and the pressure displayed on the transmitter are recorded through several points over the desired span and used to generate a linear fitting curve to correct the original value read into the DAQ system. Using this process eliminates the uncertainty associated with the transmitter reference accuracy, long-term stability previous to calibration, and the power supply. This calibration is repeated about every 52 weeks.

The load resistor and DAQ system bias uncertainties are next removed by installing the pressure transmitter and filling the experimental setup through a range of pressures to obtain data on the displayed reading at the transmitter and the calculated value obtained through the DAQ system using nominal values to convert the measured analog signal to a pressure value. This data can be used to generate a second linear fit curve to correct the analog output to match the displayed value on the sensor.

Finally, the two calibration curves can be combined to yield a single linear fit involving a slope and offset for the pressure transmitter. This curve is input into the data acquisition program from a calibration record file combining calibration information for all acquired signals. Finally, the calculated calibrated uncertainty reduces to that shown in *Table 31*.

Table 31: An estimate of the largest expected calibrated and zeroed test section pressure uncertainty.

Contribution	Relative Effect	Value	Unc	Unit
Actual Test Section Inlet Pressure		**1087**	**±0.145**	**psia**
Sitrans P 7MF4032 Gauge Pressure Transmitter				
Reference Condition	Span Maximum Pressure	2000	±0	psig
Reference Condition	First Commissioning Date	5/1/2000	±0	-
Reference Condition	Deviation from Supply Voltage	6	±0	V
Reference Error	< ±0.1% of reading		±0	psi
Long-term Drift	< ±0.1% every 6 months at max span		±0	psi
Ambient Temp - Zero Effect	< ±0.05% / 10 K at max span		±0	psi
Ambient Temp - Span Effect	< ±0.1% / 10 K at max span		±0	psi
Power Supply	< ±0.005% / 1 V change		±0	psi
Mounting Orientation	< ±0.05 mbar / 10 deg off vertical		±0	psi
Dead Weight Pressure Source	< ±0.05 % of test pressure		±0.544	psi

Measured Test Section Inlet Pressure	**1087**	±0.544	psia

3.5.2.3 Test Section Pressure Drop

The pressure drop across the test section is measured using a Rosemount 3051CD differential pressure transmitter from the two pressure taps shown in *Figure 98*. The transmitter provides a 4 to 20 mA signal linearly-proportional to the measured differential pressure within a maximum range of 36.127 psi (249 kPa) [74]. Note that the transmitter can be re-ranged for optimal signal resolution as-needed without affecting the calibration of the sensor and transmitter. This signal is read into the data acquisition by measuring the corresponding 1 to 5 volt difference across a 249 ohm resistor using a NI SCXI-1303 terminal block in a NI SCXI-1102 module.

Based off the manufacturers' literature, an estimate of the un-calibrated, un-zeroed uncertainty can be obtained assuming a perfectly precise differential pressure signal as shown in *Table 32*.

Table 32: An estimate of the largest expected un-calibrated and un-zeroed test section differential pressure uncertainty.

Contribution	Relative Effect	Value	Unc	Unit
Actual Test Section Differential Pressure		**1.015**	**±0**	**psi**
Rosemount 3051CD Differential Pressure Transmitter				
Reference Condition	Upper Range Limit (URL)	36.127	±0	psi
Reference Condition	Max Span Differential Pressure	30	±0	psi
Reference Condition	Max Line Pressure	1410	±0	psi
Reference Condition	First Commissioning Date	12/21/2003	±0	-
Reference Condition	Deviation from Supply Voltage	6	±0	V
Reference Accuracy	< ±0.065% of span		±0.0195	psi
Long Term Stability	< ±0.125% of URL over 5 years		±0.07	psi
Line Pressure - Zero Effect	< ±0.05% of URL / 1000 psi		±0.02547	psi
Line Pressure - Span Effect	< ±0.1% of URL / 1000 psi		±0.05094	psi
Ambient Temperature	±(0.0125% of + 0.0625% of span)		±0	psi
Power Supply	< ±0.005% of span / 1 V change		±0.009	psi
Mounting Orientation	zero shift up to ±1.125 inH2O		±0.04064	psi
Dead Weight Pressure Source	< ±0.05 % of test pressure		0	psi
Sub-Total			±0.1013	psi
Output Current		**4.54**	**±0.054**	**mA**
Load Resistance				
Load Resistor	±1% of value	249	±2.49	Ω
Output Voltage		**1.131**	**±0.01757**	**V**
NI SCXI-1303 terminal block; NI SCXI-1102 module				
Reference Condition	Full Scale Reading	10	±0	V
Nonlinearity	0.005% FSR		0.0005	V
Offset Error	600 μV		±0.0006	V
Gain Error	0.04% of reading		±0.00045	V
Offset Temperature Coefficient	20 μV/°C		±0	V
NI DAQ Sub-Total			±0.0009	V
Voltage Sub-Total			±0.0176	V
Measured Test Section Differential Pressure		**1.015**	**±0.1575**	**psi**

To obtain more confidence in the measured results, a linear calibration curve is used in the LabView™ data acquisition program based off of calibration against an EG+G Chandler Engineering dead weight pressure tester. This unit provides a pressure source between 0 and 2000 psig ±0.05% to one leg of the sensor, while the other leg is open to atmosphere to apply a differential pressure between zero and the full-scale of the sensor. The applied differential pressure and the differential pressure displayed on the transmitter are recorded through several points over the desired span and used to generate a linear fitting curve to correct the original value read into the DAQ system. Using this process eliminates the uncertainty associated with the transmitter reference accuracy, long-term stability previous to calibration, and the power supply.

The load resistor and DAQ system bias uncertainties can next be reduced by installing the differential pressure transmitter and running the experimental setup through a range of differential pressures to obtain data on the displayed reading at the transmitter and the calculated value obtained through the DAQ system using nominal values to convert the measured analog signal to a pressure value. This data can be used to generate a second linear fit curve to correct the analog output to match the displayed value on the sensor.

Finally, the two calibration curves can be combined to yield a slope and offset for the pressure transmitter. This curve is input into the data acquisition program from a calibration record file combining calibration information for all acquired signals. After zeroing the transmitter to eliminate effects of mounting position and zero error due to line pressure, the calculated calibrated uncertainty reduces to that shown in *Table 33*. Note that the span error due to line pressure and temperature effects on the transmitter are still considered as they vary between the calibration location and the test setup and cannot be zeroed out.

Table 33: An estimate of the largest expected calibrated and zeroed test section differential pressure uncertainty.

Contribution	Relative Effect	Value	Unc	Unit
Actual Test Section Differential Pressure		**1.015**	**±0**	**psi**
Rosemount 3051CD Differential Pressure Transmitter				
Reference Condition	Upper Range Limit (URL)	36.127	±0	psi
Reference Condition	Max Span Differential Pressure	30	±0	psi
Reference Condition	Max Line Pressure	1410	±0	psi
Reference Condition	First Commissioning Date	12/21/2003	±0	-
Reference Condition	Deviation from Supply Voltage	6	±0	V
Reference Accuracy	< ±0.065% of span		±0	psi
Long Term Stability	< ±0.125% of URL over 5 years		±0	psi
Line Pressure - Zero Effect	< ±0.05% of URL / 1000 psi		±02547	psi
Line Pressure - Span Effect	< ±0.1% of URL / 1000 psi		±0.05094	psi
Ambient Temperature	±(0.0125% of + 0.0625% of span)		±0	psi
Power Supply	< ±0.005% of span / 1 V change		±0	psi
Mounting Orientation	zero shift up to ±1.125 inH2O		±0	psi
Dead Weight Pressure Source	< ±0.05 % of test pressure		±0.00051	psi
Measured Test Section Differential Pressure		**1.015**	±0.05695	psi

3.5.2.4 Test Section Inlet and Outlet CO2 Temperatures

The primary thermocouples measuring the inlet and outlet temperatures of the CO2 through the test section are Omega type E thermocouples, model EQSS-116E-6 SLE with a nominal uncertainty of 1 °C, calibrated against a National Institute of Standards and Technology (NIST) traceable Standard Platinum Resistance Thermometer (SPRT), Hart Scientific model 5624 in a stagnant Paratherm NF™ oil bath for a variety of test points in the range of interest (typically 20 to 100 °C) with closer grouping near the pseudo-critical temperatures of CO2 for the range of CO2 pressures investigated. The SPRT and thermocouples are held partially-immersed in the bath and data is taken using the existing DAQ system and the same connections used during tests (the bath is place just

behind the test stand).

The temperature read by the SPRT between 0 °C and 961.78 °C is given by the equations for the International Scale of 1990 (ITS-90) [75]. The coefficients a_6, b_6, c_6, and d are provided by Hart Scientific based on their calibration of the SPRT. This yields a total uncertainty in the temperature measured by the SPRT of less than 0.05 °C over the full range, and a long-term strain-free stability far less than 0.05 °C. As recommended by Hart Scientific, this SPRT is intermittently tested at the ice point of high-purity water to check for error in the SPRT reading due to strain of the sensing element.

The resistance of the SPRT is measured by a Fluke 8842A workbench multimeter. The resistance reading is sent to a LabView Virtual Instrument (VI) through a National Instruments high-speed GPIB to USB digital connection. In the LabView VI, the temperature of the RTD tip is calculated and logged along with the un-calibrated thermocouple measured temperatures during calibration tests.

From these tests a linear calibration curve is determined between the un-calibrated thermocouple reading and the SPRT reading using the calibration program in **Error! Reference source not found.**. As discussed by Kruizenga [7] thermocouples are not stable enough to achieve an accuracy of 0.05 °C but from the calibration tests an uncertainty of 0.15 °C seems appropriate.

3.5.2.5 Test Section Wall Temperatures

The internal wall temperatures are measured using Omegaclad Type E 304 stainless steel-sheathed thermocouples with MGO insulation fabricated in-house, welded under an inert gas environment, and taken from a single wire spool (Lot # E930413-04) to reduce in-homogeneities between batches. These thermocouplse have a nominal uncertainty of the greater of 1.7 °C or 0.5% of the reading above 0 °C before calibration. The thermocouples are read by a National Instruments SCXI™ - 1303 32-Channel Isothermal Terminal Block in a SCXI-1100 Data Acquisition Module.

The wall thermocouples are calibrated by flowing CO2 at various temperatures between 20 and 50 °C with the cooing block water flow stopped and allowing the test section to reach a steady state condition without heat flux. The wall temperature profile is then assumed to be linear along the test section to account for temperature changes of less than 0.4 due to Joule-Thomson effects for zig-zag channels and minor heat losses on the order of a few watts. The calibration program used is included in **Error! Reference source not found.**. The same calibration procedure is conducted for at least one temperature, usually around 25 °C, each day before tests are conducted to zero the wall thermocouples to account for minor calibration drift.

The calibration and wall thermocouple zeroing tests can also be planned to achieve some isothermal flow test points in order to expand the pressure drop measurement dataset.

3.5.2.6 Coolant Volumetric Flow Rate

The volumetric flow rate of the cooling water is measured for each of the 20 cooling blocks by McMillan Company Model 101-M006 turbine-type liquid flow meters with a nominal accuracy before calibration of 1.5% of the full scale of 1000 mL/min, or about 12 mL/min for a maximum uncertainty.

The volumetric flowmeters are calibrated by connecting them in series and flowing room temperature water through them into a container on a Sartorious CP (Model CPA34001S) scale with the flow rate and timing monitored through the DAQ. From these measurements a linear calibration curve is created between the measured volumetric flow rate signals from each flowmeter and the measured flow rate of water using the sale and DAQ system. Using the calibration curve the typical flowmeter uncertainty is less than 3 mL/min.

3.5.2.7 Cooling Block Inlet and Outlet Temperatures

The cooling water inlet and outlet temperatures at each cooling block are measured using Omega Type E-SLE wire with a nominal uncertainty of 1 °C fabricated in-house, welded under an inert gas environment, and taken

from a single wire spool (Lot # HCH10813P) to reduce in-homogeneities between batches.

The cooling block outlet termperature thermocouples are calibrated relative to the inlet thermocouples over a range of temperatures between 15 and 30 °C in order to achieve a very low calibrated uncertainty in their difference of 0.1 °C. The linear calibration curve is generated according to the script in **Error! Reference source not found.**. The full 1 °C uncertainty value is still used for any calculations based on a single thermocouple such as the coolent fluid properties. This relative calibration is repeated for a single temperature at the start of the day before taking data in order to zero the thermocouples and account for minor calibration drift.

3.5.2.8 Coolant Pressure

The coolant pressure is not explicitly measured, but is assumed to be equal to standard atmospheric pressure of 101 ±1%, with the variation including any effects due to weather and indoor air pressure variations. Due to the nearly constant fluid properties this additionaly uncertainty is negligible but is included in the data reduction calculations for future tests where the coolent may be different.

3.5.3 Uncertainty Propagation

Uncertainty propagation is accomplished automatically using a standard root-sum-of-squares method assuming the measured variables have a gaussian probability distribution as shown generically in Equation **(89)**. The utility used for uncertainty propagation in the data reduction code is attached as **Error! Reference source not found.**. Each measured variable is read into the data analysis code and matched with its measurement uncertainty, with every subsequent variable calculated with its appropriate propagated uncertainty.

$$\sigma_{f(x_1,x_2,\ldots,x_n)} = \sqrt{\sum_{i}^{n}\left(\frac{\partial f}{\partial x_i}\sigma_{x_i}\right)^2} \qquad \textbf{(89)}$$

3.6 Horizontal Cooling-Mode Results

Using the test facility, procedures, and data reduction discussed, 244 data runs were completed using two different styles each of zig-zag and airfoil fin test plates in a horizontal orientation in addition to the 32 data runs completed by Kruizenga using the 65-degree zig-zag and 80-degree zig-zag plates covering a range of temperatures from approximately 25 to 100 °C, pressures of 7.5 and 8.1 MPa, and mass fluxes of 326 and 762 kg/m^{2}s as summarized in *Table 34*. Data from 102 runs with the straight channel geometry from Kruizenga [7] are also compared to the new data taken.

Due to the additional uncertainties in the measured Reynolds number during cooling tests, wall thermocouple calibration runs were planned to match certain Reynolds number criteria and additional isothermal pressure drops were taken. Data for both zig-zag channels and both airfoil fin channels will be presented and discussed in the following sections, and finally compared with data from past researcher and candidate correlations. Note that while each cooling run provides up to 10 heat transfer coefficient data points not all of these data points could be used due to the high sensitivity of CO2 fluid properties near the critical point leading to some unrealistic calculations at the heat fluxes achievable in this facility or unreliably high values of propagated uncertainty.

Table 34: A summary of the tests considered in the study.

Test Plate	Type	P [MPa]	G [kg/m^{2}s]	Runs
Straight	Cooling	7.5	326	102 total
		8.1	326	
		8.1	762	
80-degre Zig-Zag	Isothermal	-	-	35

	Cooling	7.5	326	43 total
		8.1	326	
		8.1	762	
65-degre Zig-Zag	Isothermal	-	-	28
	Cooling	7.5	326	41 total
		8.1	326	
		8.1	762	
8.1mm NACA0020	Isothermal			34
	Cooling	7.5	326	43 total
		8.1	326	
		7.5	762	
4.0mm NACA0020	Isothermal	-	-	17
	Cooling	7.5	326	27 total
		8.1	326	
		8.1	762	

3.6.1 Zig-Zag Channels

Two different zig-zag channels were considered for this study as described in Section 3.4.4.2, both with equal design hydraulic diameters perpendicular to the flow path but with different bend angles of 65 and 80 degrees taken from the work by Ishiduka et al. [61]. *Figure 130* and *Figure 131* show the hydraulic results of the two zig-zag channels. The results are broken up into isothermal and cooling-mode data as the cooling-mode data typically is more scattered than the isothermal data. All contributions shown are calculated as pressure coefficients according to Equation (90).

$$K = \frac{\Delta P}{\frac{1}{2}\frac{G^2}{\rho}} \tag{90}$$

The etch facter during fabrication can noticeably change the cross-sectional area of the channels and therefore the mass flux within the channels, so results using both the design and measured geometry are shown. The 80-degree zig-zag channel cross-sectional area increases by about 14%, with a corresponding increase in the pressure loss coefficient, while the 65-degree zig-zag channel cross-sectional area only increases by about 2% and does not noticeably change the results. This same effect is expected in the friction factor determined from pressure drop results, so that without careful measurement even a 10% difference between the expected and actual cross-sectional area will cause a 20% difference in the resulting calculated friction factor. The measured geometry will be used for all subsequent plots.

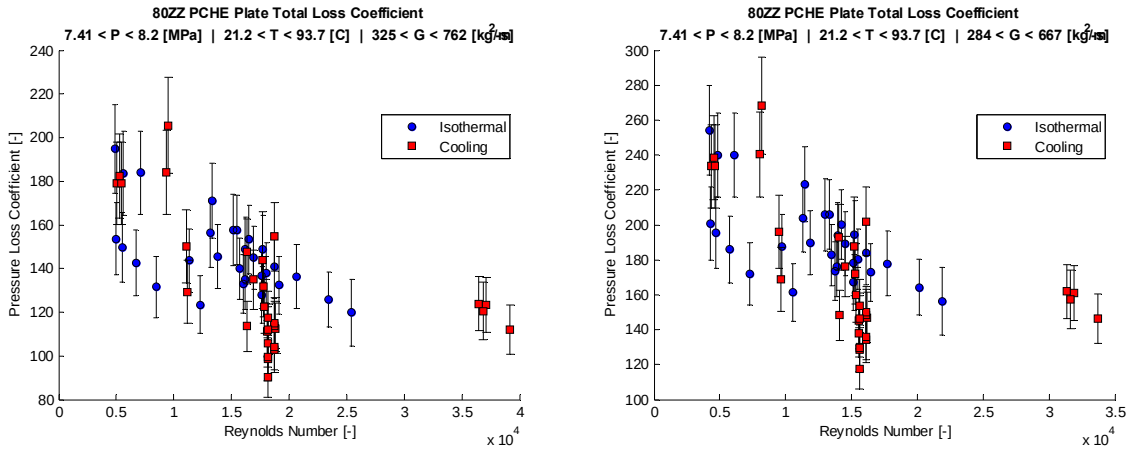

Figure 130: A plot of the 80-degree zig-zag channel isothermal and cooling-mode pressure loss coefficient using the design and measured geometry respectively with error bars indicating propagated uncertainty.

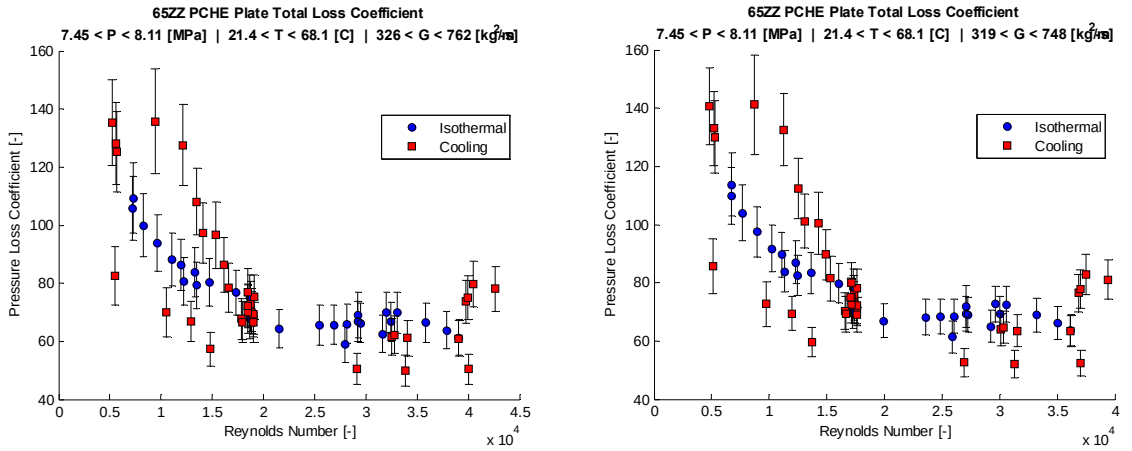

Figure 131: A plot of the 65-degree zig-zag channel isothermal and cooling-mode pressure loss coefficient using the design and measured geometry respectively with error bars indicating propagated uncertainty.

Figure 132 and *Figure 133* show a breakdown of the calculated acceleration, inlet contraction, outlet expansion, and friction loss coefficients calculated using Equation **(8)** for both the 65 and 80 degree zig-zag channels, as well as the loss coefficient of the remaining pressure drop which is attributed to form loss. For these zig-zag channels the form loss clearly dominates the other contributions to pressure loss.

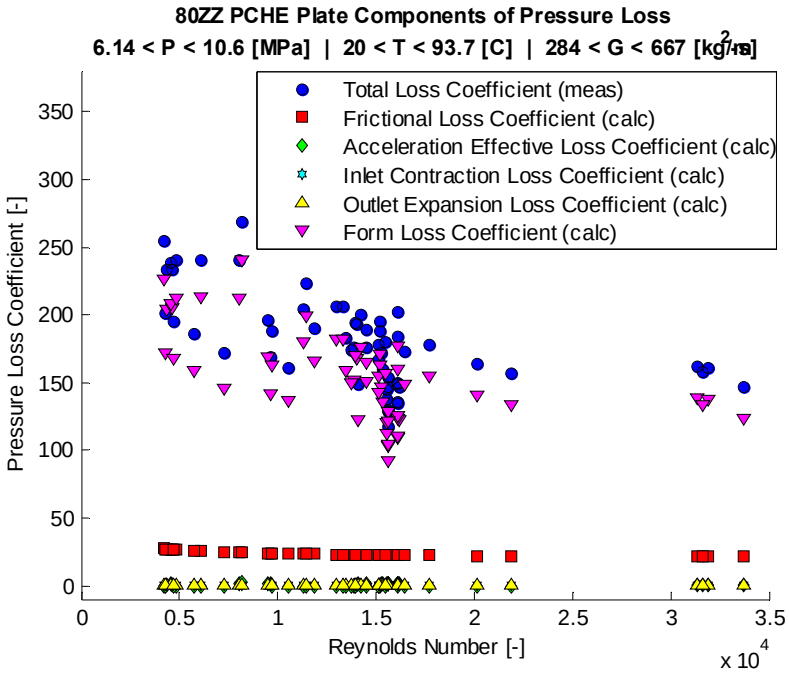

Figure 132: 80-degree zig-zag channel calculated pressure loss components using the measured geometry. Note that calculated acceleration, inlet contraction, and outlet expansion points are approximately the same and overlap.

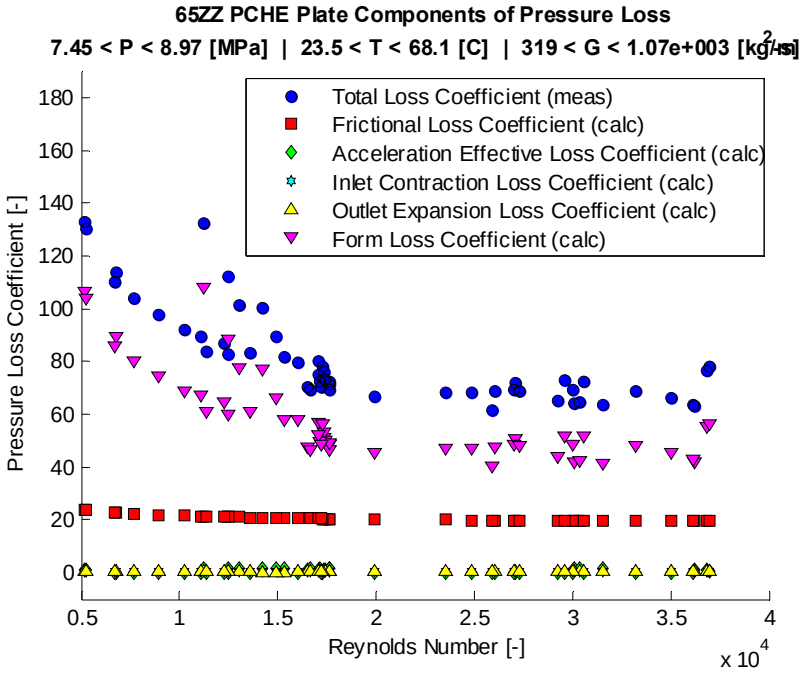

Figure 133: 65-degree zig-zag channel calculated pressure loss components using the measured geometry. Note that calculated acceleration, inlet contraction, and outlet expansion points are approximately the same and overlap.

While this effective friction factor would seem to scale properly for the same perpendicular hydraulic diameters, bend angle, and ratios of channel bend radius to channel width and channel width to bend-to-bend length, it would be more useful to separate the influence of these various parameters as Moisseytev et al. [31] did in their general correlation including the bend angle so that designs can be more easily optimaized.

As described previously Miller's correlation for a low aspect ratio rectangular zig-zag channel (see Section 3.3.4.1) includes all of these effects in at the cost of being more complex than that by Moisseytev et al. The results of this correlation are shown plotted relative to the calculated form loss coefficient per bend for both the 65-degree and 80-degree zig-zag channels in *Figure 134*. The most uncertain variable in this correlation is the K_b^* value, so several values are shown for both surfaces. Without modification the correlation is fairly close for the 80-degree zig-zag channel but less so for the 65-degree zig-zag channel. As these correlations are based off of rectangular channel geometries, it seems likely that for the circular-segment profile of PCHE channels a different K_b^* value plot should be generated. However as these correlations were developed from isothermal air and water flows in pipes, the data required would be much more easily obtained and could likely be found through numerical studies.

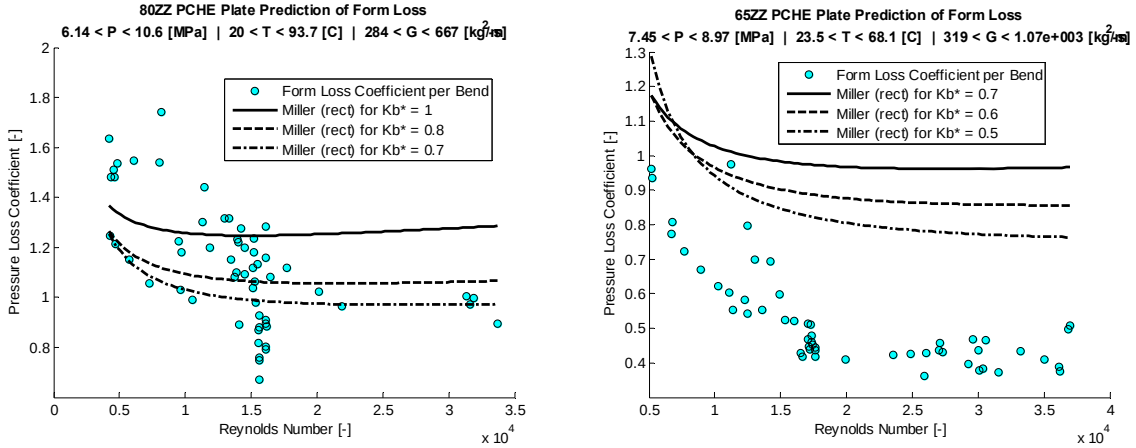

Figure 134: A comparison of Miller's correlations for zig-zag pipe channels vs. the calculated form loss coefficient per bend for the 80-degree zig-zag channel and the 65-degree zig-zag channel using measured geometry.

Thermal results from the two zig-zag channels at low mass flux and pressure, low mass flux and high pressure, and high mass flux and high pressure are shown in *Figure 135* through *Figure 140*. The same general trend as has been seen by previous researchers of gas-like high Nusselt numbers above the pseudo-critical point, a peak in Nussselt number just above the critical point for these cooling tests, and then lower liquid-like Nusselt numbers below the critical point is present. Data have been selected based on two different criteria levels of relative uncertainty depending on the reduced temperature due to the fact that propagated uncertainty outside the influence of the critical point is mainly due to the uncertainty of the test instrumentation and the mean calculated values are typically close to the true values, while near the critical point the much higher sensitivity of fluid properties causes mean calculated values to be much more scattered for the same test instrumentation uncertainty.

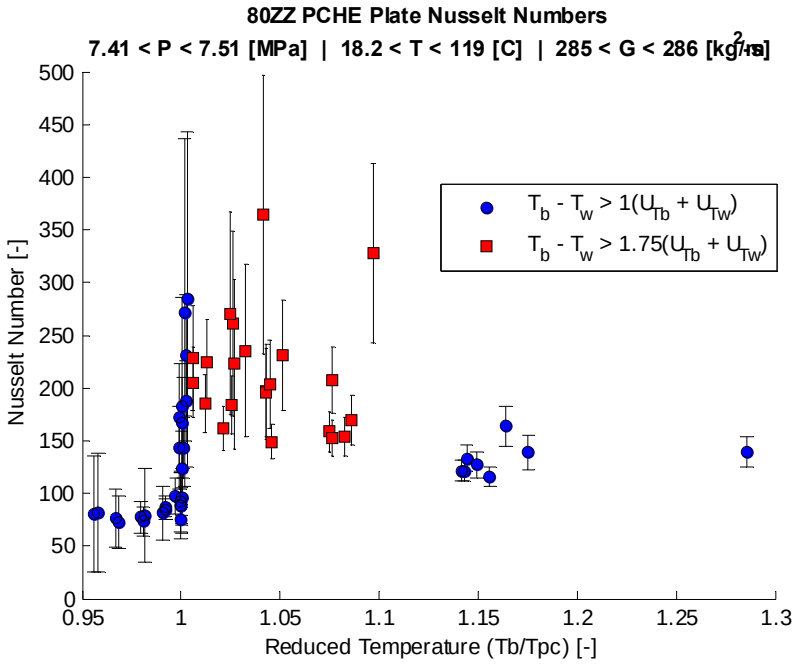

Figure 135: 80-degree zig-zag channel Nusselt number vs. reduced temperature at 7.5 MPa and low mass flux for cooling-mode flow using the measured geometry with error bars indicating propagated uncertainty.

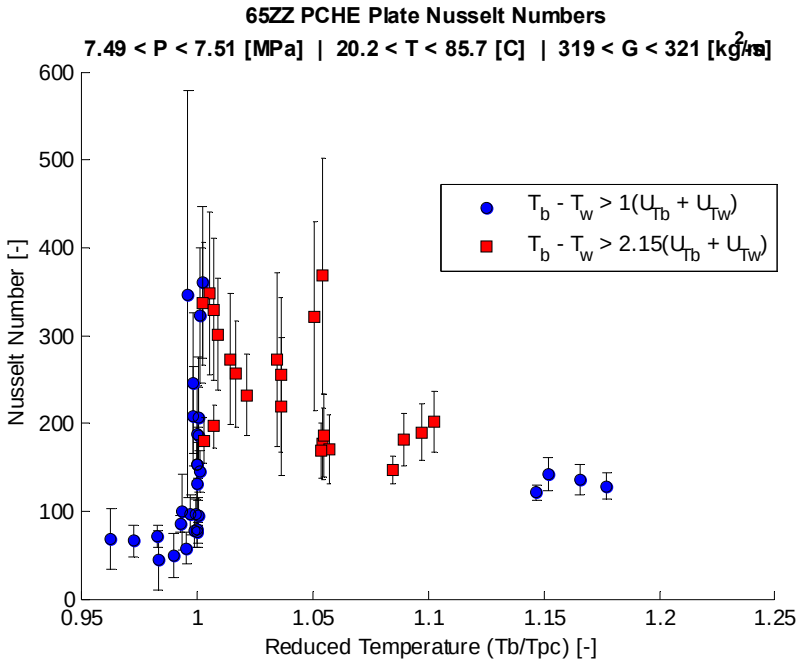

Figure 136: 65-degree zig-zag channel Nusselt number vs. reduced temperature at 7.5 MPa and low mass flux for cooling-mode flow using the measured geometry with error bars indicating propagated uncertainty.

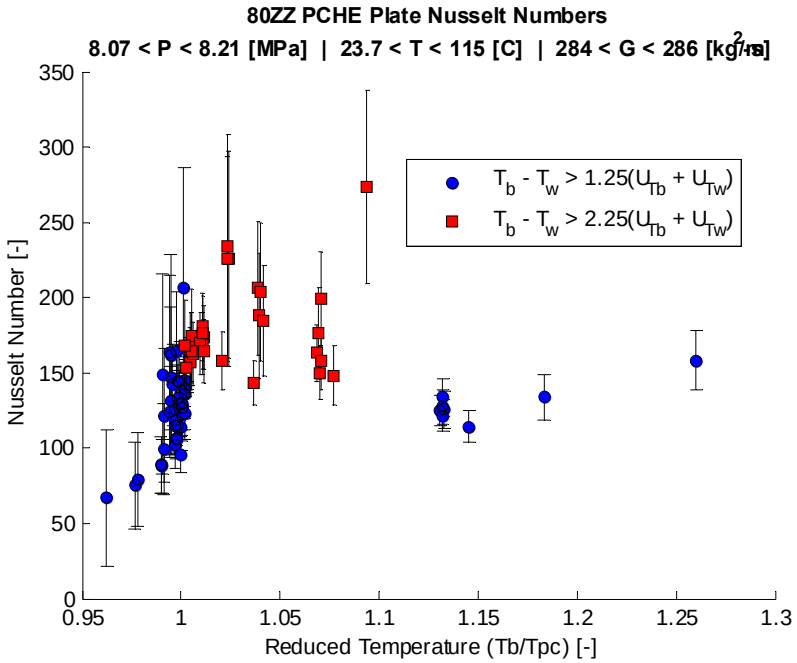

Figure 137: 80-degree zig-zag channel Nusselt number vs. reduced temperature at 8.1 MPa and low mass flux for cooling-mode flow using the measured geometry with error bars indicating propagated uncertainty.

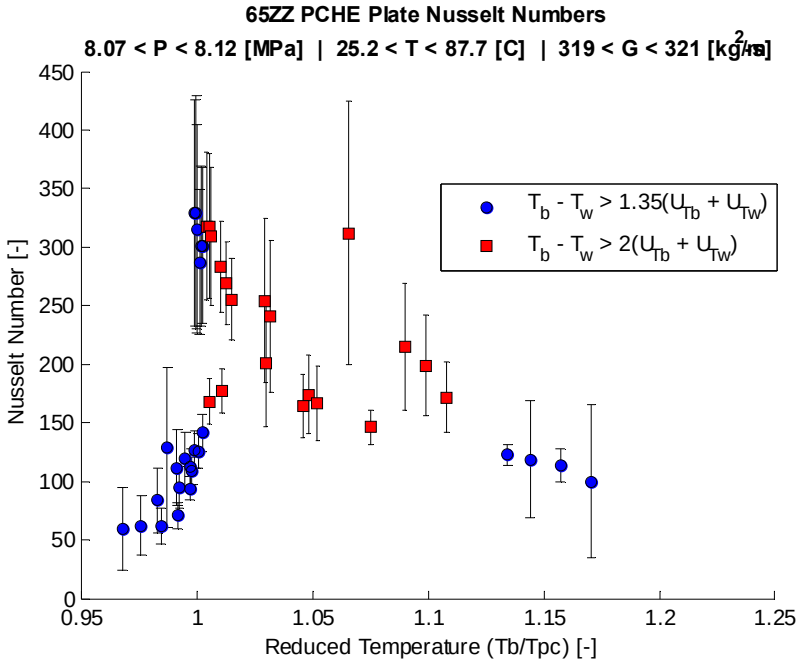

Figure 138: 65-degree zig-zag channel Nusselt number vs. reduced temperature at 8.1 MPa and low mass flux for cooling-mode flow using the measured geometry with error bars indicating propagated uncertainty.

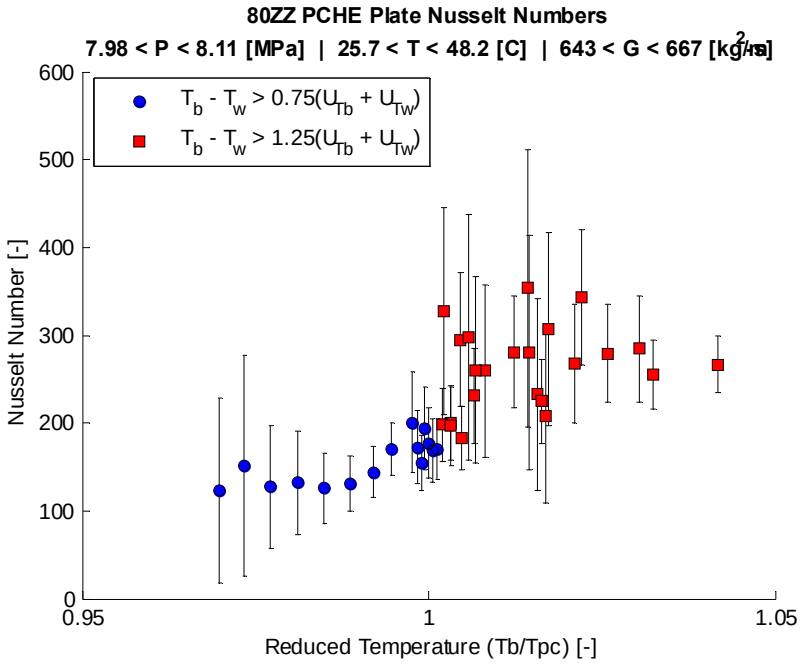

Figure 139: 80-degree zig-zag channel Nusselt number vs. reduced temperature at 8.1 MPa and high mass flux for cooling-mode flow using the measured geometry with error bars indicating propagated uncertainty.

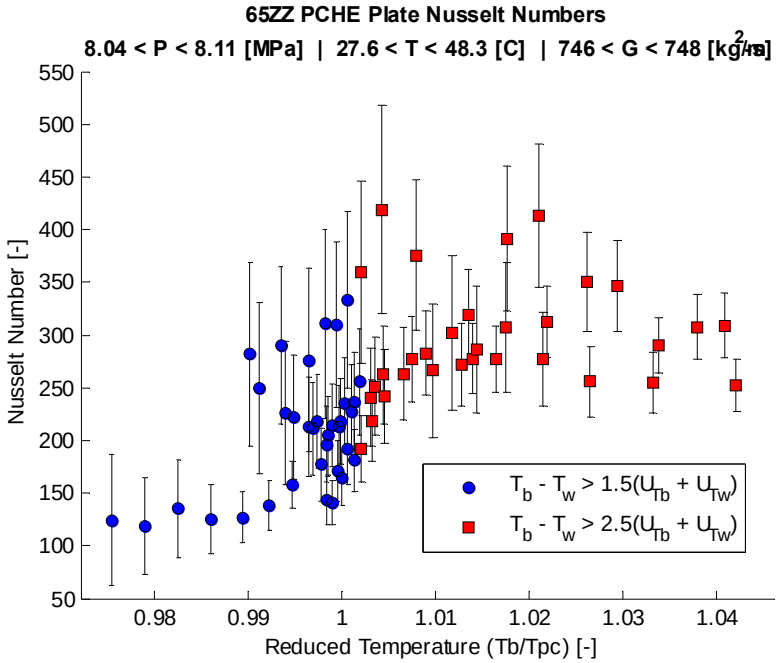

Figure 140: 65-degree zig-zag channel Nusselt number vs. reduced temperature at 8.1 MPa and high mass flux for cooling-mode flow using the measured geometry with error bars indicating propagated uncertainty.

3.6.1.1 Airfoil fin Channels

Two different airfoil channels were considered for this study as described in Section 3.4.4.3, both with equal design cross-sectional flow areas that were slightly larger than those of the zig-zag channels but with different airfoil chord lengths of 8.1 and 4.0 mm. *Figure 141* and *Figure 142* show the hydraulic results of the two zig-zag channels. The results are broken up into isothermal and cooling-mode data as the cooling-mode data typically is more scattered than the isothermal data. All contributions shown are calculated as pressure coefficients according to Equation (90). Like the zig-zag channels the etch factor greatly influences the surface geometry, but in this case the cross-sectional area decreases by about 22% for the 8.1 mm airfoil fin channels and 32% for the 4.0 mm airfoil fin channels. These are significant differences and therefore the pressure loss coefficient calculated reduces to almost half of what would be calculated with design values. The

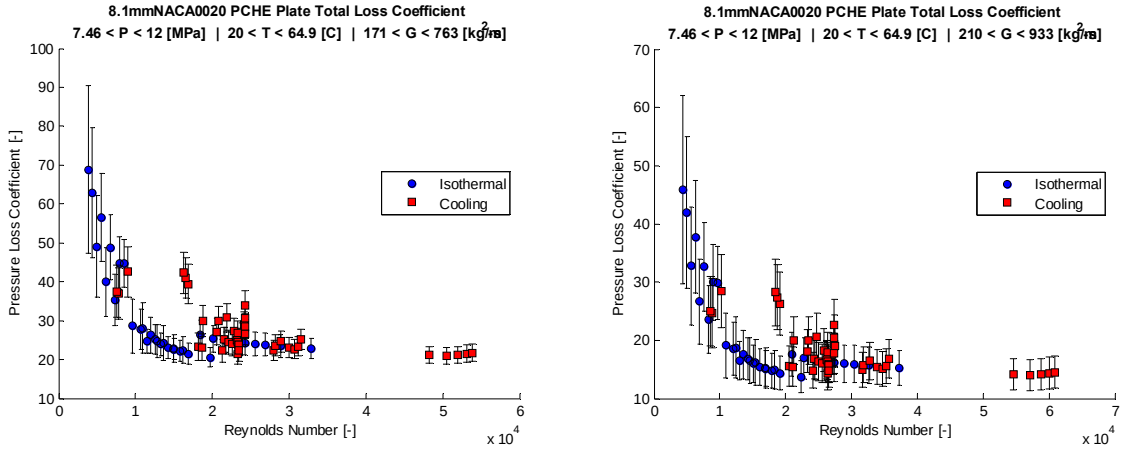

Figure 141: 8.1 mm NACA0020 total loss coefficient vs. Reynolds number for cooling-mode flow using the design and measured geometry respectively with error bars indicating propagated uncertainty.

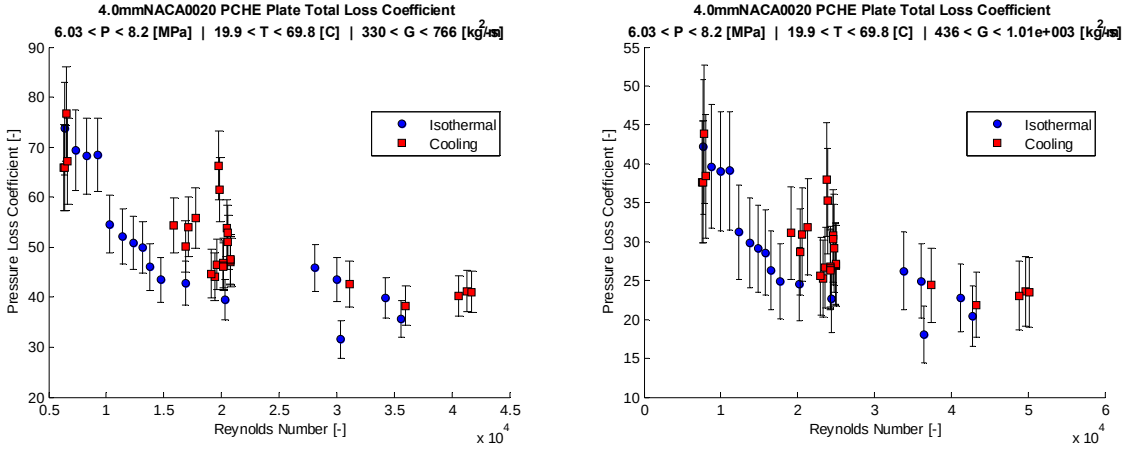

Figure 142: 4.0 mm NACA0020 total loss coefficient vs. Reynolds number for cooling-mode flow using the design and measured geometry respectively with error bars indicating propagated uncertainty.

Figure 143 and *Figure 144* show a breakdown of the calculated acceleration, inlet contraction, outlet expansion, and friction loss coefficients calculated using Equation **(8)** for both the 8.1 mm and 4.0 mm chord length airfoil fin channels, as well as the loss coefficients of the remaining pressure drop which is attributed to form loss. Using the measured geometry the expected frictional loss is nearly the entire loss coefficient.

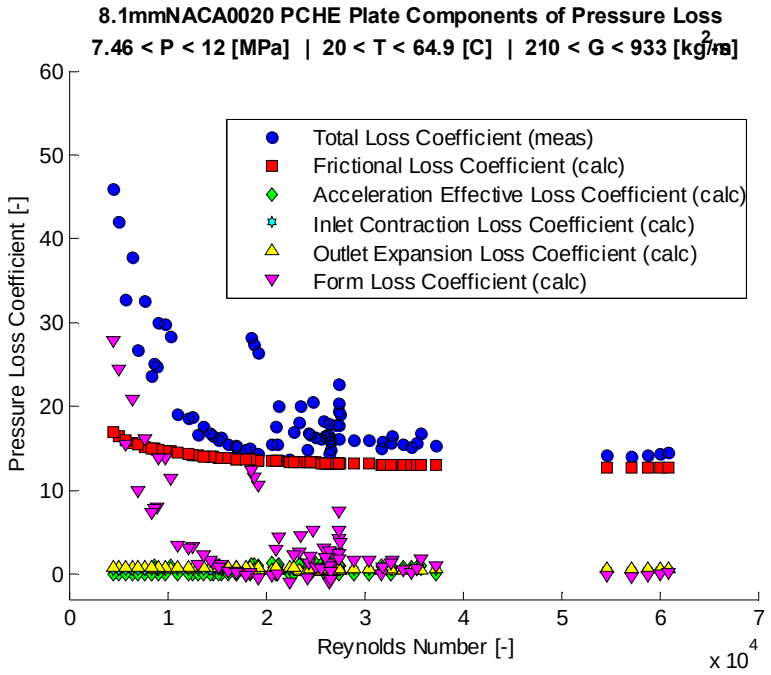

Figure 143: 8.1 mm NACA0020 airfoil fin channel calculated pressure loss components using the measured geometry. Note that calculated acceleration, inlet contraction, and outlet expansion points are approximately the same and overlap.

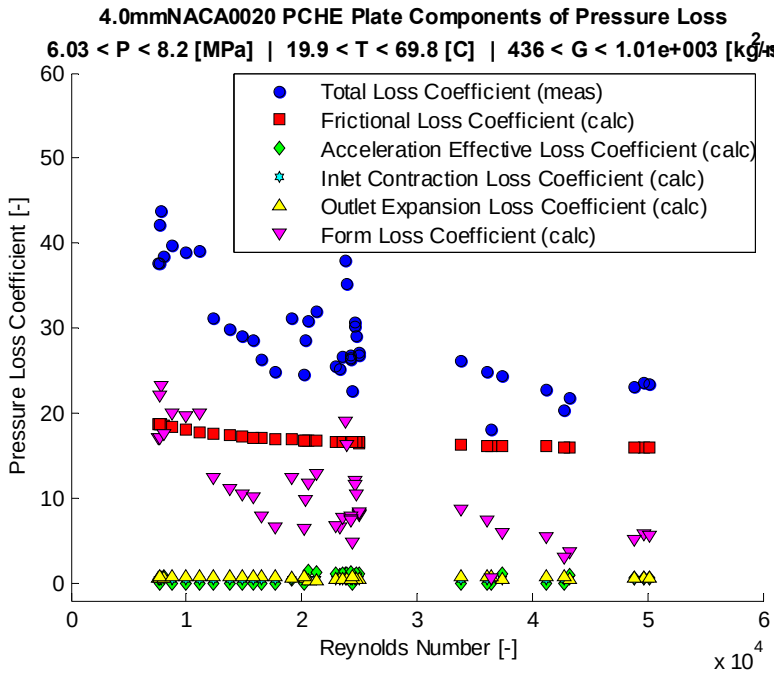

Figure 144: 4.0 mm NACA0020 airfoil fin channel calculated pressure loss components using the measured geometry. Note that calculated acceleration, inlet contraction, and outlet expansion points are approximately the same and overlap.

Thermal results from the two airfoil channels at low mass flux and pressure, low mass flux and high pressure, and high mass flux and low or high pressure are shown in *Figure 145* through *Figure 150*. The same general trend as has been seen by previous researchers of gas-like high Nusselt numbers above the pseudo-critical point, a peak in Nussselt number just above the critical point for these cooling tests, and then lower liquid-like Nusselt numbers below the critical point is present. Again, data have been selected based on two different criteria levels

of relative uncertainty depending on the reduced temperature due to the fact that propagated uncertainty outside the influence of the critical point is mainly due to the uncertainty of the test instrumentation and the mean calculated values are typically close to the true values, while near the critical point the much higher sensitivity of fluid properties causes mean calculated values to be much more scattered for the same test instrumentation uncertainty.

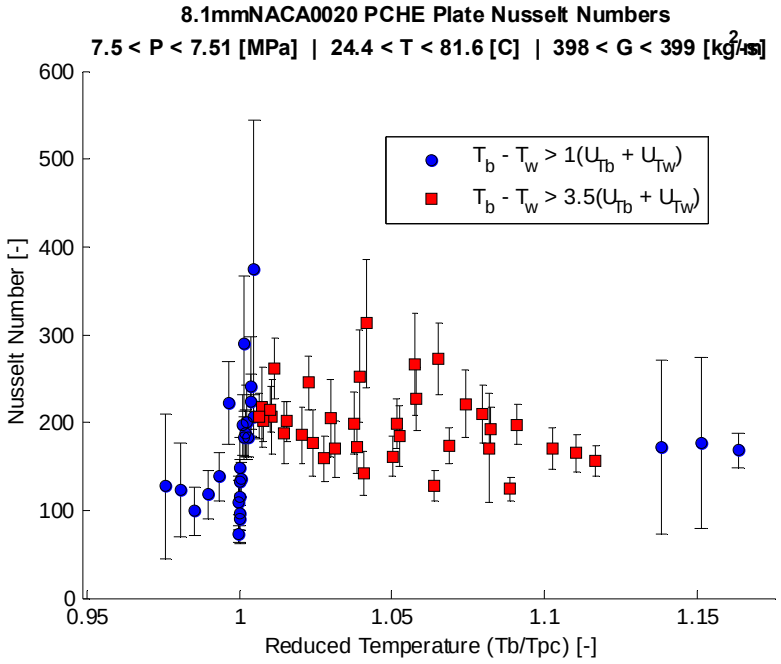

Figure 145: 8.1 mm NACA0020 airfoil fin channel Nusselt number vs. reduced temperature at 7.5 MPa and low mass flux for cooling-mode flow using the measured geometry with error bars indicating propagated uncertainty.

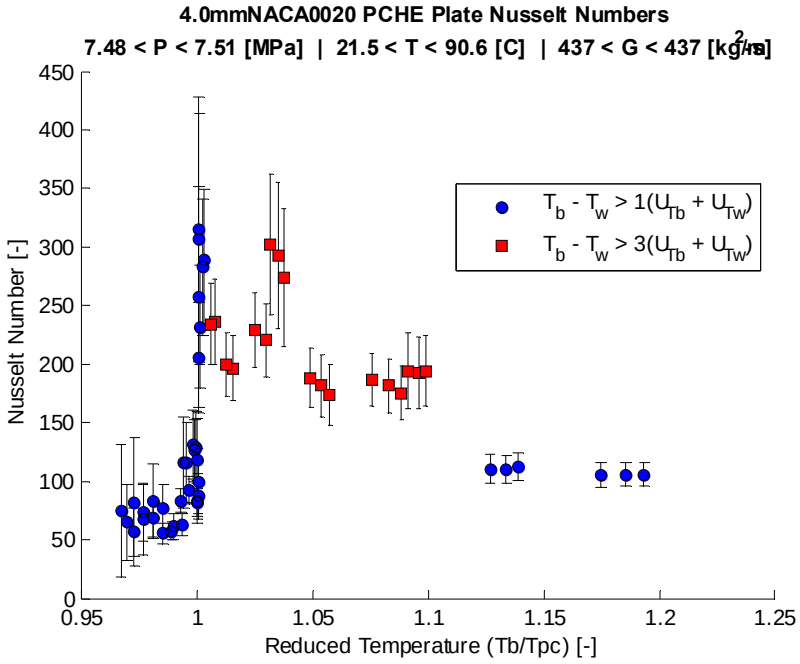

Figure 146: 4.0 mm NACA0020 airfoil fin channel Nusselt number vs. reduced temperature at 7.5 MPa and low mass flux for cooling-mode flow using the measured geometry with error bars indicating propagated uncertainty.

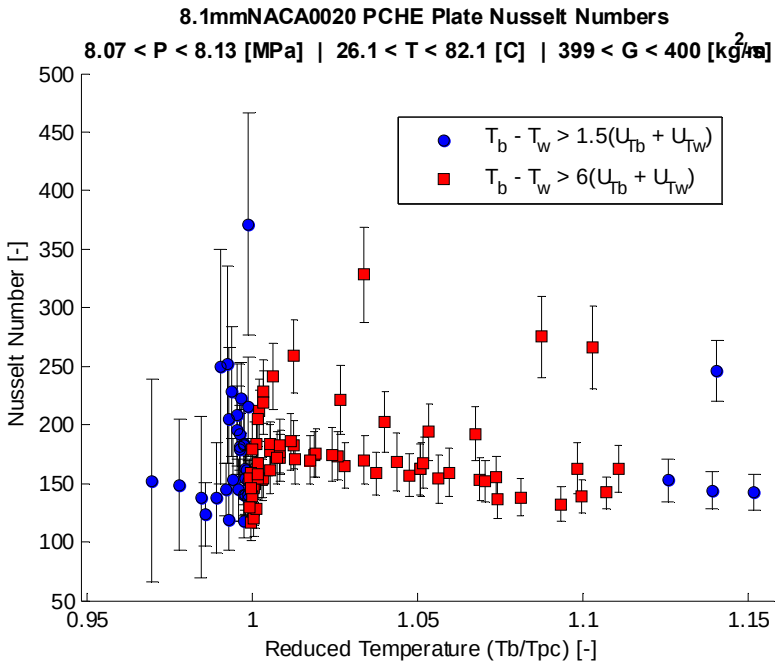

Figure 147: 8.1 mm NACA0020 airfoil fin channel Nusselt number vs. reduced temperature at 8.1 MPa and low mass flux for cooling-mode flow using the measured geometry with error bars indicating propagated uncertainty.

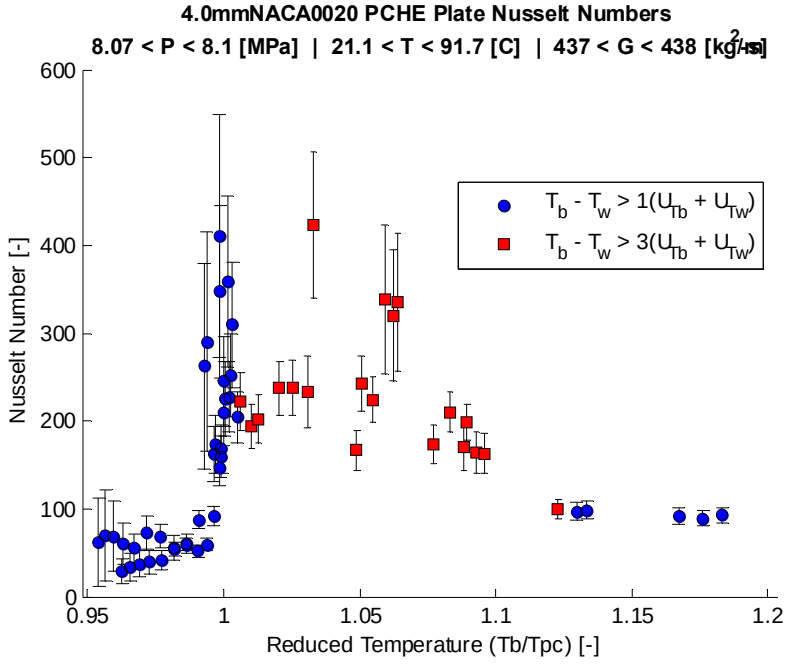

Figure 148: 4.0 mm NACA0020 airfoil fin channel Nusselt number vs. reduced temperature at 8.1 MPa and low mass flux for cooling-mode flow using the measured geometry with error bars indicating propagated uncertainty.

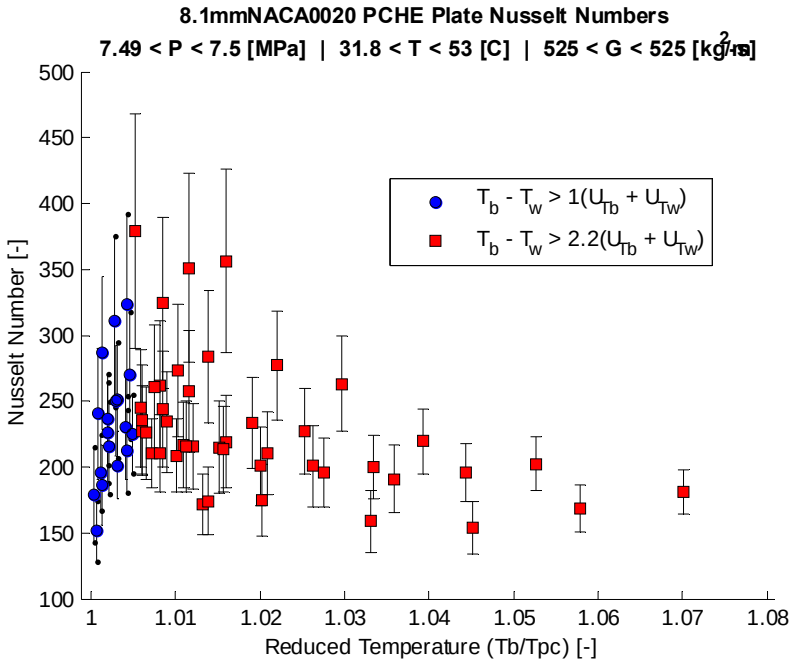

Figure 149: 8.1 mm NACA0020 airfoil fin channel Nusselt number vs. reduced temperature at 7.5 MPa and high mass flux for cooling-mode flow using the measured geometry with error bars indicating propagated uncertainty.

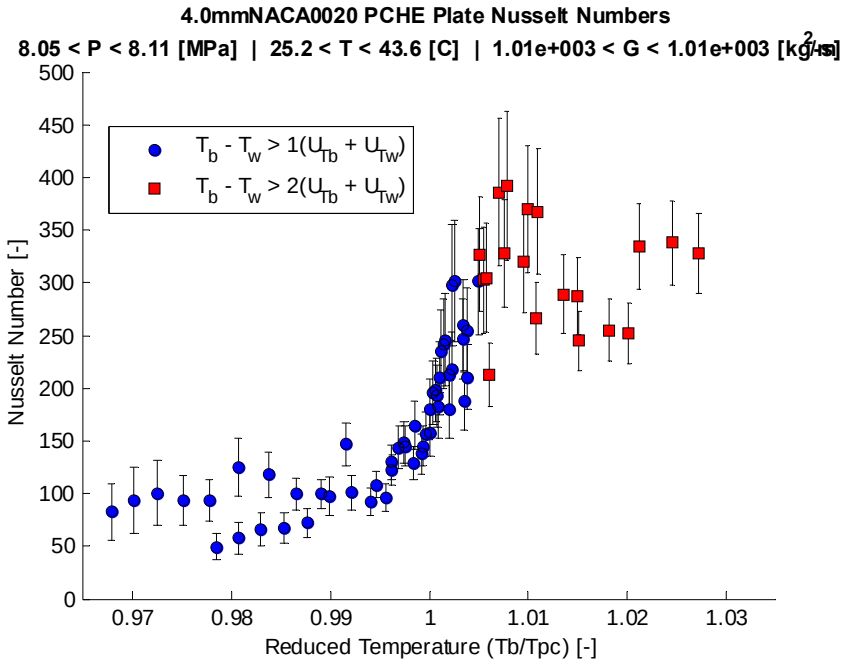

Figure 150: 4.0 mm NACA0020 airfoil fin channel Nusselt number vs. reduced temperature at 8.1 MPa and high mass flux for cooling-mode flow using the measured geometry with error bars indicating propagated uncertainty.

3.6.1.2 Comparison of Different Geometries

A comparison of the hydraulic and thermal performance for one combination of pressure and mass flux for the different PCHE surface geometries, including the original straight-channel data of Kruizenga [7], are shown in *Figure 151* through *Figure 153*. The variation in the effective Fanning friction factor is clearly much larger than the variation in Nusselt number; however all of the enhanced surfaces tend to have the same enhanced Nusselt

number as compared to the straight-channel data for both pressures. Several channel parameters and power-law fits to the effective Fanning friction factor are listed in *Table 35* for reference, including the circumscribing rectangular cross-sectional area used for pressure containment calculations. This value is artificially low due to the 6.35 mm thickness of the plate relative to the 1 mm channel depth being much larger than is typical for PCHE plates. This ratio suggests that for pressure containment capability, small airfoil channels should provide an equivalent increase in heat transfer over straight channels with a minimal increase in pressure drop.

Table 35: A summary of relavent geometric parameters fitting coefficient for the effective Fanning friction factor of the form aRe^b for each surface.

Surface	A_c [mm2]	A_s [mm2]	d_{hyd}	AcR	a	b
80ZZ	14.58	33754	1.096	0.107	0.76142	-0.24405
65ZZ	13.01	27594	1.085	0.104	1.0745	-0.34533
8.1mmAF	13.23	19784	1.337	0.115	1.3019	-0.46948
4.0mmAF	12.07	21715	1.112	0.106	0.40081	-0.32381

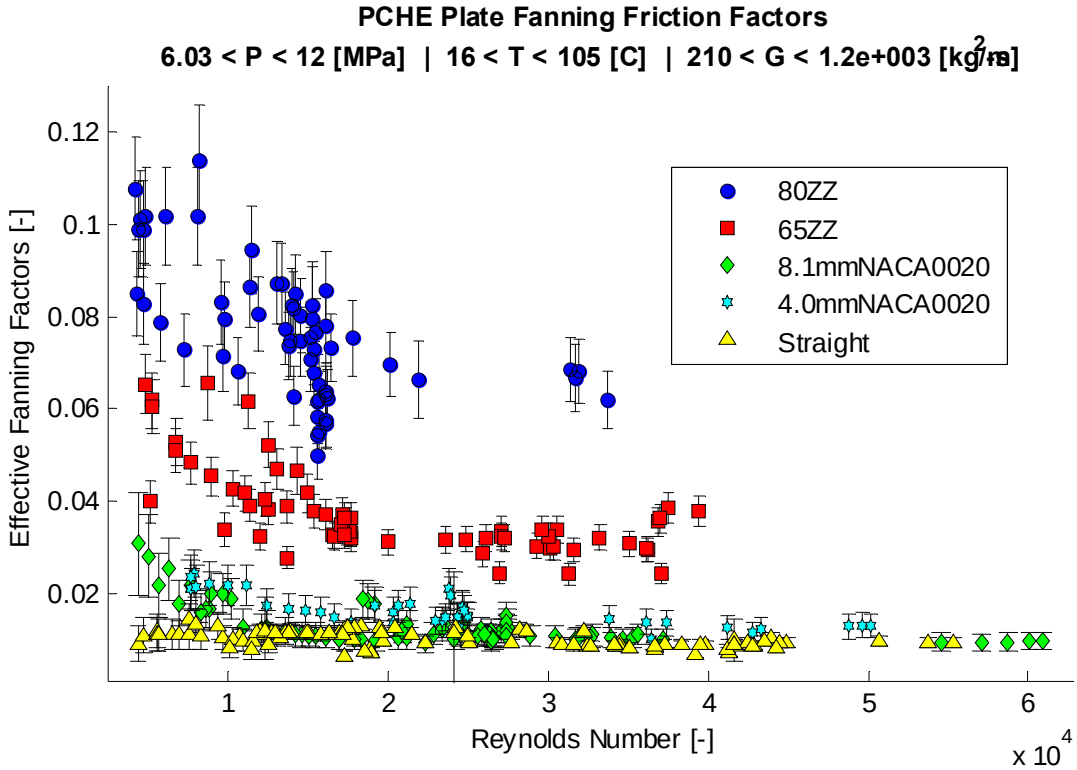

Figure 151: A combined comparison of the hydraulic performance of different PCHE channel geometries using the effective Fanning friction factor based on the total pressure drop and the channel path length.

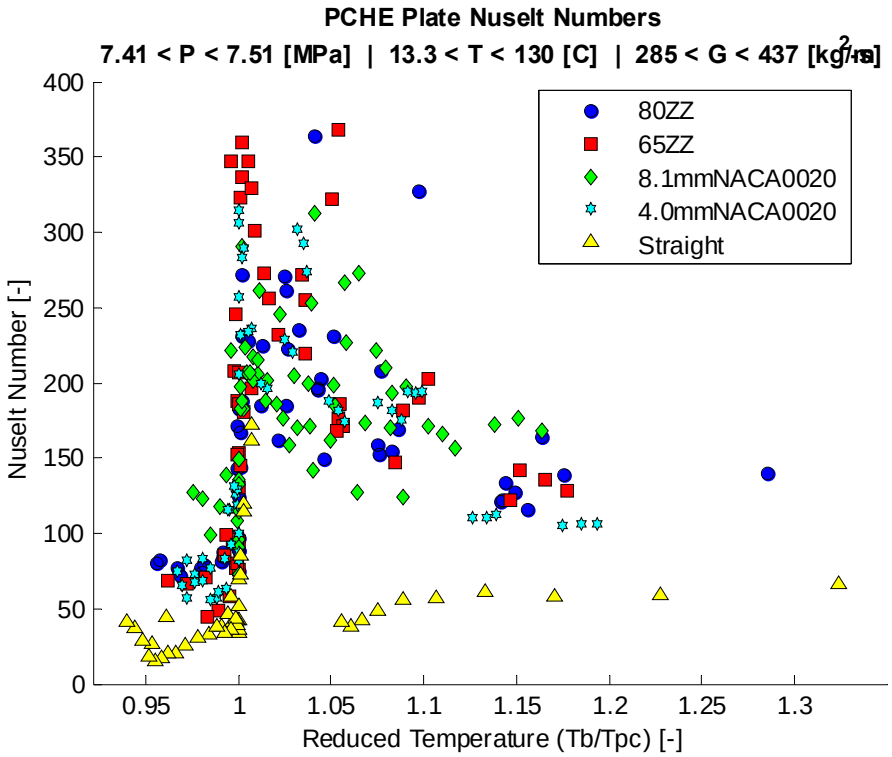

Figure 152: A combined comparison of the thermal performance of different PCHE channel geometries at a pressure of 7.5 MPa and a low mass flux.

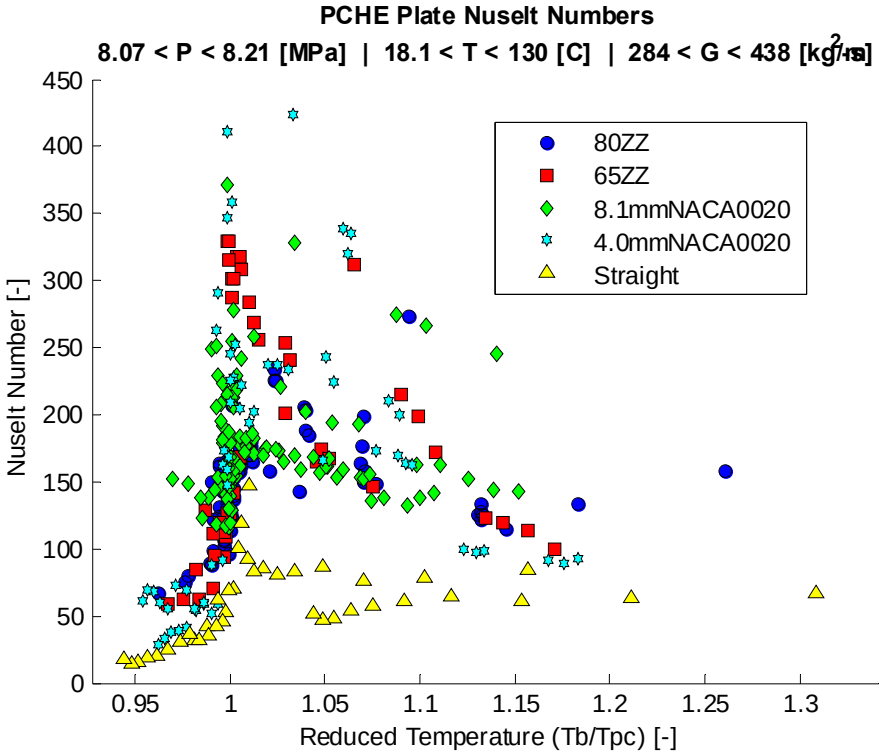

Figure 153: A combined comparison of the thermal performance of different PCHE channel geometries at a pressure of 8.1 MPa and a low mass flux.

3.7 Conclusions

In this work the background of supercritical fluid flows has been discussed noting that they are correlated differently from single-phase sub-critical through the use of additional variable property corrections or by re-fitting correlation forms to supercritical data. Various types of compact heat exchangers have also been discussed along with methods of comparing different plate-type surfaces. The fabrication process, surface geometries, pressure containment, and fin effectiveness of PCHEs have also been examined, along with a review of existing literature on PCHE experimental tests. Finally, test facility used for this work and detailed analyses of surface geometries are presented, along with horizontal cooling-mode results for each of the two zig-zag channel and airfoil fin surfaces.

Based on the comparisons between different surfaces at nearly equivalent cross-sectional area ratios the two airfoil geometries appear to perform much better than the zig-zag geometries, provided almost the same thermal performance with hydraulic losses reduced to almost the level of equivalent hydraulic diameter roughened tubes. However the pressure containment analysis presented in this work was intended for discrete channels, and it has not been shown for PCHEs that discontinuous surfaces such as the airfoil fin channels tested can be analyzed in the same method on an equivalent cross-sectional area basis.

References

[1] U.S. DOE Nuclear Energy Research Advisory Committee and the Generation IV International Forum, "A Technology Roadmap for Generation IV Nuclear Energy Systems," 2002.

[2] J. J. Sienicki, A. Moisseytev, D. H. Cho, M. Thomas, S. A. Wright, P. S. Pickard, G. Rochau and a. others, "International Collaboration on Development of the Supercritical Carbon Dioxide Brayton Cycle for Sodium-Cooled Fast Reactors under the Gneration IV International Forum Component Design and Balance of Plant Project," in *Proceedings of ICAPP '10*, San Diego, CA, USA, 2010.

[3] A. Moisseytev and J. J. Sienicki, "Extension of the Supercritical Carbon Dioxide Brayton Cycle for Application to the Very High Temperature Reactor," in *Proceedings of ICAPP '10*, San Diego, CA, USA, 2010.

[4] V. Dostal, M. J. Driscoll and P. Hejzlar, "A Supercritical Carbon Dioxide Cycle for Next Generation Nuclear Reactors," Massachusetts Institute of Technology - Advanced Nuclear Power Technology Program, Cambridge, MA, 2004.

[5] S. A. Klein and G. Nellis, Thermodynamics, New York: Cambridge University Press, 2012.

[6] J. E. Hesselgreaves, Compact Heat Exchangers, Kidlington, Oxford: Elsevier Science, 2001, p. 398.

[7] A. M. Kruizenga, "Heat Transfer and Pressure Drop Measurements in Prototypic Heat Exchangers for the Supercritical Carbon Dioxide Brayton Power Cycles," Madison, 2010.

[8] I. L. Pioro and R. B. Duffey, Heat transfer and hydraulic resistance at supercritical pressures in power engineering applications, New York: ASME Press, 2007, p. 360.

[9] S. M. Liao and T. S. Zhao, "Measurements of Heat Transfer Coefficients From Supercritical Carbon Dioxide Flowing in Horizontal Mini/Micro Channels," *Journal of Heat Transfer,* vol. 124, no. 3, pp. 413-420, 2002.

[10] S. A. Klein, *Engineering Equation Solver,* Madison, WI: F-Chart Software, 2012.

[11] G. Nellis and S. A. Klein, Heat transfer, Cambridge; New York: Cambridge University Press, 2009.

[12] D. S. Miller, Internal Flow Systems, BHRA Fluid Engineering, 1978.

[13] C. F. Colebrook, "Turbulent Flow in Pipes, with Particular Reference to Transition Region between Smooth and Rough Pipe Laws," *Institution of Civil Engineers of London -- Journal,* vol. 12, no. 4, pp. 393-422, 1939.

[14] D. Clamond, "Efficient Resolution of the Colebrook Equation," *Industrial & Engineering Chemistry Research,* vol. 48, no. 7, pp. 3665-3671, 2009.

[15] S. E. Haaland, "Simple and Explicit Formulas for the Friction Factor in Turbulent Pipe Flow," *Journal of Fluids Engineering,* vol. 105, no. 1, p. 89, 1983.

[16] I. E. Idel'chik and E. Friied, Handbook of hydraulic resistance, 2nd ed., Washington: Hemisphere Pub. Corp., 1986.

[17] W. L. Friend and A. B. Metzner, "Turbulent heat transfer inside tubes and the analogy among heat, mass, and momentum transfer," *AIChE Journal,* vol. 4, no. 4, pp. 393-402, 1958.

[18] A. B. Metzner and W. L. Friend, "Theoretical analogies between heat, mass and momentum transfer and modifications for fluids of high prandtl or schmidt numbers," *The Canadian Journal of Chemical Engineering,* vol. 36, no. 6, pp. 235-240, 1958.

[19] S. Aravinth, "Prediction of heat and mass transfer for fully developed turbulent fuid fow through tubes," *International Journal of Heat and Mass Transfer,* vol. 43, pp. 1399-1408, 2000.

[20] F. W. Dittus and L. Boelter, "Heat Transfer in Automobile Radiators of the Tubular Type," *University of California -- Publications in Engineering,* vol. 2, no. 13, pp. 443-461, 1930.

[21] F. W. Dittus and L. Boelter, "Heat Transfer in Automobile Radiators of the Tubular Type," *International communications in heat and mass transfer,* vol. 12, no. 1, pp. 3-22, 1985.

[22] R. Winterton, "Where did the Dittus and Boelter equation come from?," *International Journal of Heat and*

Mass Transfer, vol. 41, no. 4-5, pp. 809-810, 1998.

[23] W. McAdams, Heat Transmission, 2nd ed., York, PA: The Maple Press Company, 1942.

[24] L. Prandtl, Führer durch die strömungslehre, Braunschweig: F. Vieweg & Sohn, 1942.

[25] V. Gnielinski, "New equations for heat and mass transfer in turbulent pipe and channel flow," *International Chemical Engineering,* vol. 16, no. 2, pp. 359-368, 1976.

[26] J. D. Jackson and W. B. Hall, "Forced Convection Heat Transfer to Fluids at Supercritical Pressure," in *Insititution of Mechanical Engineers - Conference Publications*, 1979.

[27] E. N. Sieder and G. E. Tate, "Heat Transfer and Pressure Drop of Liquids in Tubes," *Industrial & Engineering Chemistry,* vol. 28, no. 12, pp. 1429-1435, 1936.

[28] A. P. Colburn, "A method of correlating forced convection heat-transfer data and a comparison with fluid friction," *International Journal of Heat and Mass Transfer,* vol. 7, no. 12, pp. 1359-1384, 1964.

[29] S. Kakac and H. Liu, Heat exchangers : selection, rating, and thermal design, Boca Raton, Fla.: CRC Press, 1998.

[30] R. Deissler and M. Taylor, "Analysis of Heat Transfer and Fluid Friction for Fully Developed Turbulent Flow of Supercritical Water with Variable Fluid Properties in a Smooth Tube," Lewis Flight Propulsion Laboratory, Cleveland, Ohio, 1953.

[31] A. Moisseytev, J. J. Sienicki, D. H. Cho and M. R. Thomas, "Comparison of Heat Exchanger Modeling with Data from CO2-to-CO2 Printed Circuit Heat Exchanger Performance Tests," in *Proceedings of ICAPP '10*, San Diego, CA, USA, 2010.

[32] Meggit Corporation, "Heatric Website," 2012. [Online]. Available: http://www.heatric.com/.

[33] Q. Li, G. Flamant, X. Yuan, P. Neveu and L. Luo, "Compact heat exchangers: A review and future applications for a new generation of high temperature solar receivers," *Renewable and Sustainable Energy Reviews,* vol. 15, no. 9, pp. 4855-4875, 2011.

[34] M. A. Taylor, "Pate-Fin Heat Exchangers: Guide to their Specification and Use," HTFS, Harwell, UK, 1990.

[35] ALPEMA, "The Standards of the Brazed Aluminum Plate-Fin Heat Exchanger Manufacturers' Association," Brazed Aluminium Plate-Fin Heat Exchanger Manufacturers' Association, 2010.

[36] J. T. Black, R. A. Kohser and E. P. DeGarmo, "Electronic Electrochemical Chemical and Thermal Machining Processes," in *DeGarmo's Materials & Processes in Manufacturing*, 10th ed., Hoboken, NJ: John Wiley & Sons, 2008, pp. 485-504.

[37] R. Le Pierres, D. Southall and S. Osborne, "Impact of Mechanical Design Issues on Printed Circuit Heat Exchangers," in *Proceedings of SCO2 Power Cycle Symposium 2011*, Boulder, CO, 2011.

[38] D. Southall and S. J. Dewson, "Innovative Compact Heat Exchangers," in *Proceedings of ICAPP '10*, San Diego, CA, USA, 2010.

[39] W. M. Kays and A. L. London, Compact Heat Exchangers, 2nd ed., New York: McGraw-Hil, 1964.

[40] D. Southall, R. Le Pierres and S. J. Dewson, "Design Considerations for Compact Heat Exchangers," in *Proceedings of ICAPP '08*, Anaheim, CA, USA, 2008.

[41] I. Ruhlich and H. Quack, "New Regenerator Design for Cryocoolers," in *Proceedings of the Seventeenth International Cryogenic Engineering Conference*, Bournemouth, UK, 1998.

[42] I. Ruhlich and H. Quack, "Investigations on Regenerative Heat Exchangers," *Cryocoolers,* vol. 10, pp. 265-274, 1999.

[43] J. F. Fan, W. K. Ding, J. F. Zhang, Y. L. He and W. Q. Tao, "A performance evaluation plot of enhanced heat transfer techniques oriented for energy-saving," *International Journal of Heat and Mass Transfer,* vol. 52, no. 1-2, pp. 33-44, 2009.

[44] D. M. Allen, "Photochemical Machining: from 'manufacturing's best kept secret' to a $6 billion per annum, rapid manufacturing process," *CIRP Annals - Manufacturing Technology,* vol. 53, no. 2, pp. 559-572, 2004.

[45] S. K. Mylavarapu, X. Sun and R. N. Christensen, "Photofabrication and Surface Roughness of Flow Channels for a Compact High-Temperature Heat Exchanger," in *Transactions of the American Nuclear*

Society Winter Meeting, Reno, Nevada, 2008.

[46] T. Ishizuka, Y. Kato, Y. Muto, K. Nikitin, T. L. Ngo and H. Hashimoto, "Thermal-Hydraulic Characteristics of a Printed Circuit Heat Exchanger in a Supercritical CO2 Loop," in *11th International Topical Meeting on Nuclear Reactor Thermal-Hydraulics*, Avignon, France, 2005.

[47] D. Southall, "Diffusion Bonding in Compact Heat Exchangers," in *Proceedings of the SCCO2 Power Cycle Symposium*, Troy, NY, 2009.

[48] N. Tsuzuki, Y. Kato, K. Nikitin and T. Ishizuka, "Advanced Microchannel Heat Exchanger with S-shaped Fins," *Journal of Nuclear Science and Technology,* vol. 46, no. 5, pp. 403-412, 2009.

[49] S. K. Mylavarapu, X. Sun, R. N. Christensen, R. R. Unocic, R. E. Glosup and M. W. Patterson, "Fabrication and design aspects of high-temperature compact diffusion bonded heat exchangers," *Nuclear Engineering and Design,* 2011.

[50] D. Southall, "Diffusion bonding in compact heat exchangers," in *Transactions of the American Nuclear Society*, 2009.

[51] S. K. Mylavarapu, X. Sun, R. N. Christensen and J. Vaughn, "On the Diffusion Bonding of Alloy 617 for High-Temperature Compact Heat Exchangers," in *Transactions of the American Nuclear Society Winter Meeting*, Washington, DC, USA, 2009.

[52] S. K. Mylavarapu, R. R. Unocic, X. Sun and R. N. Christensen, "On the Microstructural and Mechanical Characterization of Diffusion Bonded Alloy 617 Plate Specimens for High-Temperature Compact Heat Exchangers," in *Transactions of the American Nuclear Society Winter Meeting*, Washington, DC, USA, 2009.

[53] S. K. Mylavarapu, "Design, Fabrication, Performance Testing, and Modeling of Diffusion Bonded Compact Heat Exchangers in a High-Temperature Helium Test Facility," The Ohio State University, 2011.

[54] E. N. Van Abel, "Computational Studies On The Fluid Flow and Heat Transfer of Supercritical Carbon Dioxide In Printed Circuit Heat Exchangers," Madison, 2011.

[55] S. C. Song, H. C. No and C. S. Lee, "Performance of a Printed Circuit Heat Exchanger in an Air Open Test Loop," in *Transactions of the American Nuclear Society*, 2006.

[56] I. H. Kim, C. S. Lee and H. C. No, "Air and Helium Thermal Hydraulic Experiments for a Printed Circuit Heat Exchanger," in *Transactions of the American Nuclear Society*, 2007.

[57] I. H. Kim, H. C. No, J. I. Lee and B. G. Jeon, "Thermal hydraulic performance analysis of the printed circuit heat exchanger using a helium test facility and CFD simulations," *Nuclear Engineering and Design,* vol. 239, no. 11, pp. 2399-2408, 2009.

[58] I. H. Kim and H. C. No, "Thermal-hydraulic characteristics evaluations of the Printed Circuit Heat Exchanger in a Helium- Water Test Loop," in *Proceedings of ICAPP '10*, San Diego, CA, USA, 2010.

[59] I. H. Kim and H. C. No, "Thermal hydraulic performance analysis of a printed circuit heat exchanger using a helium-water test loop and numerical simulations," *Applied Thermal Engineering,* vol. 31, pp. 4064-4073, 2011.

[60] I. H. Kim and H. C. No, "Physical model development and optimal design of PCHE for intermediate heat exchangers in HTGRs," *Nuclear Engineering and Design,* vol. 243, pp. 243-250, 2012.

[61] T. Ishizuka, Y. Kato, Y. Muto, K. Nikitin and T. L. Ngo, "Thermal-Hydraulic Characteristics of a Printed Circuit Heat Exchanger in a Supercritical CO2 Loop," *Bulletin of the Research Laboratory for Nuclear Reactors,* vol. 30, pp. 109-116, 2006.

[62] K. Nikitin, Y. Kato and L. Ngo, "Printed circuit heat exchanger thermal–hydraulic performance in supercritical CO2 experimental loop," *International Journal of Refrigeration,* vol. 29, no. 5, pp. 807-814, 2006.

[63] T. L. Ngo, Y. Kato, K. Nikitin and T. Ishizuka, "Heat transfer and pressure drop correlations of microchannel heat exchangers with S-shaped and zigzag fins for carbon dioxide cycles," *Experimental Thermal and Fluid Science,* vol. 32, no. 2, pp. 560-570, 2007.

[64] A. Kruizenga, H. Li and M. Anderson, "Heating and Cooling mode Supercritical CO2 Heat Transfer," in

The 8th International Topical Meeting on Nuclear Thermal-Hydraulics, Operation and Safety, Shanghai, China, 2010.

[65] A. Kruizenga, M. Corradini, M. Anderson, A. Towne, R. Fatima and D. Ranjan, "Heat Transfer of Supercritical Carbon Dioxide in Printed Circuit Heat Exchanger Geometries," in *Proceedings of the 14th International Heat Transfer Conference*, Washington, DC, USA, 2010.

[66] A. Kruizenga, M. Anderson, R. Fatima, M. Corradini, A. Towne and D. Ranjan, "Heat Transfer of Supercritical Carbon Dioxide in Printed Circuit Heat Exchanger Geometries," *Journal of Thermal Science and Engineering Applications,* vol. 3, p. 031002, 2011.

[67] J. Weisbach, Die Experimental Hydraulik, J.G. Engelhardt, 1855, p. pg 149.

[68] E. W. Lemmon, M. L. Huber and M. O. McLinden, *NIST Standard Reference Database 23: Reference Fluid Thermodynamic and Transport Properties-REFPROP,* 9th ed., Gaithersburg: National Institute of Standards and Technology, Standard Reference Data Program, 2010.

[69] R. Span and W. J. Wagner, *J. Phys. Chem. Ref. Data,* vol. 25, no. 6, pp. 1509-1596, 1996.

[70] 3D Systems, Inc., "StereoLithography Interface Specification," October 1989.

[71] D. E. Kim, M.-H. Kim, J. E. Cha and S. O. Kim, "Numerical investigation on thermal-hydraulic performance of new printed circuit heat exchanger model," *Nuclear Engineering and Design,* vol. 238, pp. 3269-3276, 2008.

[72] Siemens, *SITRANS F C MASS 2100 Di 3-40 Operating Instructions,* 07/2010.

[73] Siemens, *SITRANS P pressure transmitter DS series (Smart) Manual - 7MF4032.*

[74] Emerson Process Management, *Rosemount 3051 Pressure Transmitter with HART Protocol, Reference Manual,* 2009.

[75] L. Crovini, H. J. Jung, R. C. Kemp, S. K. Ling, B. W. Mangum and H. Sakurai, "The Platinum Resistance Thermometer Range of the International Temperature Scale of 1990," *Metrologia,* vol. 28, pp. 317-325, 1991.

[76] T. L. Ngo, Y. Kato, K. Nikitin and N. Tsuzuki, "New printed circuit heat exchanger with S-shaped fins for hot water supplier," *Experimental Thermal and Fluid Science,* vol. 30, no. 8, pp. 811-819, 2006.

[77] N. Tsuzuki, Y. Kato and T. Ishiduka, "High performance printed circuit heat exchanger," *Applied Thermal Engineering,* vol. 27, no. 10, pp. 1702-1707, 2007.

[78] M. Carlson, A. Kruizenga, M. Anderson and M. Corradini, "Measurements of Heat Transfer and Pressure Drop Characteristics of Supercritical Carbon Dioxide Flowing in Zig-Zag Printed Circuit Heat Exchanger Channels," in *Supercritical CO2 Power Cycle Symposium*, Boulder, Colorado, 2011.

[79] H. Li, A. Kruizenga, M. Anderson, M. Corradini, Y. Luo, H. Wang and H. Li, "Development of a new forced convection heat transfer correlation for CO2 in both heating and cooling modes at supercritical pressures," *International Journal of Thermal Sciences,* vol. 50, no. 12, pp. 2430-2442, 2011.

4 TASK 3 - Turbomachinery Issues

4.1 Introduction

Power production continues to be a major concern to the longevity of our global prosperity. The current rate of consumption of traditional fossil fuels has placed increased stress on an already overdrawn finite fuel source and economic vitality dictates that both overall plant efficiency as well as net power output must continue to increase while simultaneously minimizing capital expenditures. The concept of maximizing plant output is nothing new. Nonetheless, the supercritical carbon dioxide Brayton (S-CO_2) cycle does exhibit novel characteristics which make it a potential candidate for the next generation power production cycle of choice.

This chapter is divided into four sections. The first section provides a conceptual explanation of how a supercritical fluid differs from a traditional gas- or liquid- phase substance. The second section extends the concepts to a cycle description of the S-CO_2 Brayton cycle and discusses how such a cycle differs from alternative cycle technology. The third section examines some of the more subtle secondary losses related to windage and pumping that are associated with the S-CO_2 cycle that motivate this research. The final section provides a short synopsis of the approach taken in this research.

4.1.1 Supercritical Fluid Property Variation and Traditional Power Cycles

According to Klein and Nellis (2011) the term "critical point" is defined by the mathematical relationship shown in equation (0.1)

$$\left(\frac{\partial P}{\partial \nu}\right)_T = 0 \quad Critical\ Point \tag{0.1}$$

where P is pressure, v is specific volume, and T is temperature. The critical point is located on the boundary of the two-phase region at the top of the vapor-dome, as shown in **Figure 154** for carbon dioxide. At this point, the phase boundary separating liquids and gases vanishes.

A supercritical fluid is a substance whose temperature and pressure lie above the critical point –i.e above the vapor dome in **Figure 154**. The properties in this region are neither that of a liquid nor a gas and exhibit unusual behavior, particularly close to the critical point. Physical properties such as density, specific heat, and viscosity show large gradients in this region. Note the drastic changes in specific volume for modest temperature changes along each isobar in Figure 1.1. Also plotted is a grouping of points that when drawn together is commonly referred to as the pseudocritical line, defined by equation (0.2).

$$\left(\frac{\partial^2 P}{\partial \nu^2}\right)_T = 0 \quad at\ the\ Pseudocritical\ Line \tag{0.2}$$

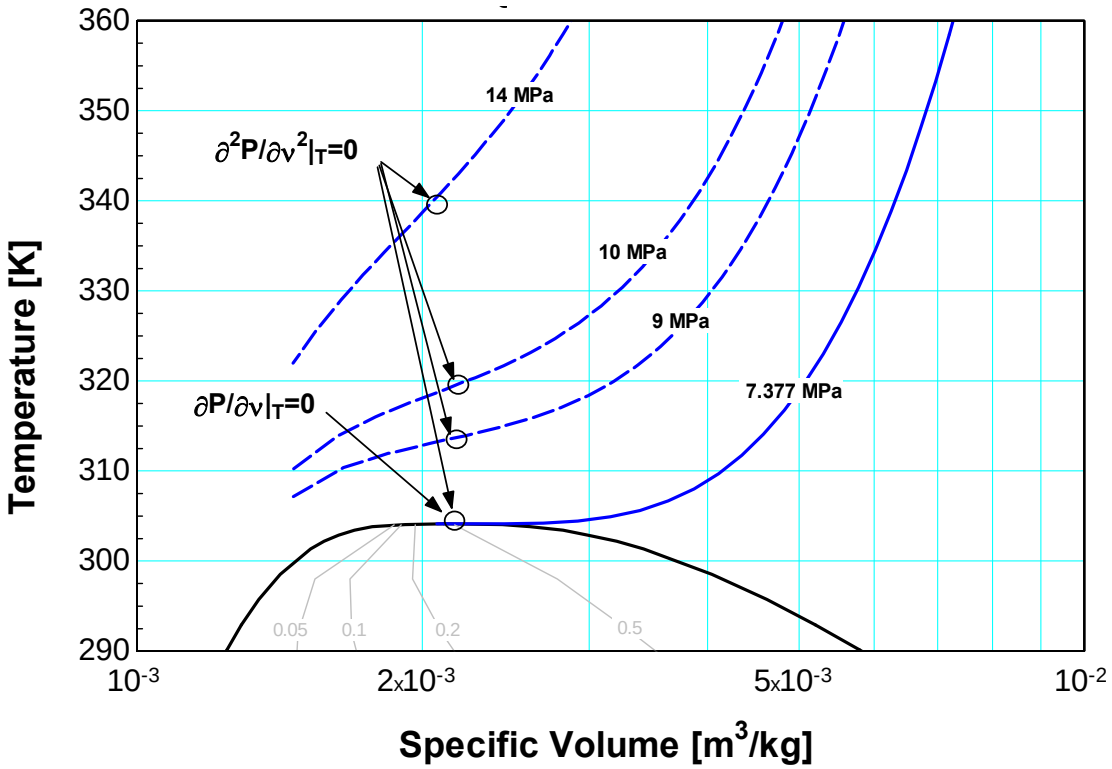

Figure 154 Temperature as a function of specific volume for carbon dioxide, the critical point and approximate location of points on the pseudocritical line are shown.

Researchers dating back to Sulzer (1949) have investigated possible uses the observed supercritical property variations for power production. The advantage of using a supercritical fluid in a power cycle is that power output and efficiency may be increased due to the reduced shaft work required in the compression region. An efficient cycle is one in which the compressor input work is low relative to the turbine output work – equation (0.3) defines the back work ratio:

$$BWR = \frac{\dot{W}_{compressor}}{\dot{W}_{turbine}} \qquad (0.3)$$

Compressing a low density fluid is disadvantageous as the required compressor work will consume a large portion of the turbine output, thereby decreasing both power output as well as cycle efficiency. In a supercritical Brayton cycle, the compression can occur in the region very close to the critical point which leads to high density fluid and low compressor work.

The Rankine cycle inherently takes advantage of density variations by compressing fluid in the liquid phase to decrease shaft work. The disadvantage of the Rankine cycle, however, is that it requires phase transition through evaporative and condenser stages. This transition requires more support equipment to minimize problems related to cavitation in the compressor region and high inertia droplet impingement during turbine expansion as was noted by Kruizenga (2010).

4.1.2 The Supercritical Carbon Dioxide Brayton Cycle and Competitors

Three cycles have been identified for near-future power production. The benefits and disadvantages of each cycle are related to the operating conditions where each technology presents distinct engineering challenges. Critical properties for the three cycles are shown in Table 1.1. Note that Helium has a much lower critical point than either of the other working fluids considered but attains high cycle efficiency as a byproduct of the high

capacitance rate and multi-staging approximating the ideal cycle.

Table 4-1: Critical Fluid Properties

Fluid	Critical Temperature [C]	Critical Pressure [MPa]
CO_2	30.95	7.377
He	-267.95	0.227
H_20	373.95	22.06

Dostal (2004) notes that the concept of a "supercritical cycle" is rather ambiguous as it encompasses all cycles where the working fluid passes through the supercritical region at one point or another. In this respect, there is a huge difference between the cycles such as the supercritical water cycle (commonly referred to as SCWR) and the S-CO_2 Brayton cycle.

The SCWR cycle is a Rankine cycle where the high pressure side operates above the critical point. The cycle removes the complications related to phase transition on the high pressure side, as noted by Licht (2007). The overall result is an increase in efficiency from roughly 33% in the current nuclear power cycle to 44% according to Licht (2004). In order to achieve this increase in efficiency, the proposed turbine temperature and pressure for this cycle are 500°C and 25 MPa.

The S-CO_2 cycle, in contrast, operates entirely above the critical point of carbon dioxide and therefore avoids phase transition altogether. The major benefit is that the cycle operates entirely above the critical point and the working fluid does not undergo a phase change. Note that the critical temperature is approximately ambient conditions and the critical pressure is significantly lower than that of water. The S-CO_2 cycle was predicted to achieve efficiencies as high as 42%, as was noted by Dostal (2009).

The Helium Brayton cycle, by comparison, achieves efficiencies higher than those of the SCWR and S-CO_2 cycles but requires a much higher turbine inlet temperature (800-900°C), as was noted by Wright (2006). This cycle is a long-term area of research.

The S-CO_2 Brayton cycle is the subject of the current investigation and is illustrated conceptually in **Figure 155** and **Figure 156**. The states referenced in **Figure 156** are shown in **Figure 155**.

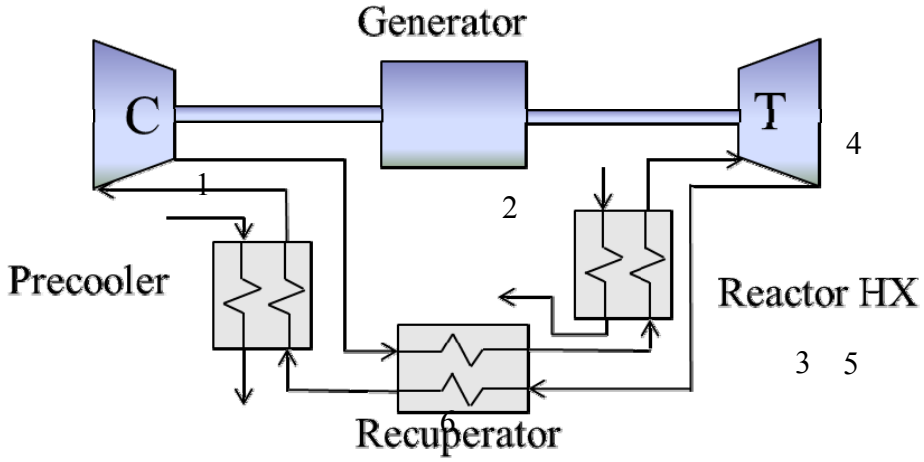

Figure 155 Schematic of S-CO_2 Brayton cycle

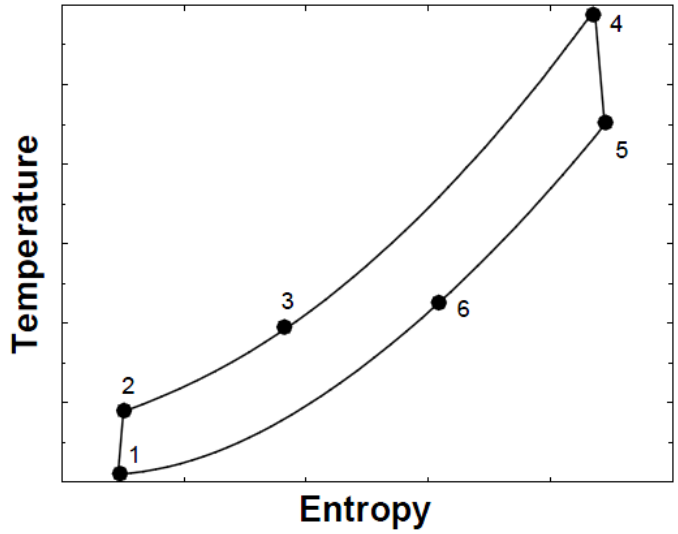

Figure 156 Simple diagram of Brayton cycle

4.1.3 Windage Losses

Proper turbomachinery design is crucial to meeting the performance targets associated with the S-CO_2 Brayton cycle. The objective of the current investigation is to examine the problem of leakage through the shaft seals implemented in the S-CO_2 Brayton cycle. The primary problem is that shaft seals cannot create a hermetic seal about a rotating mechanism across a large pressure gradient. As a result, the working fluid will leak out of the compressor and into the cavity region. **Figure 157** provides a very simplified diagram of this situation.

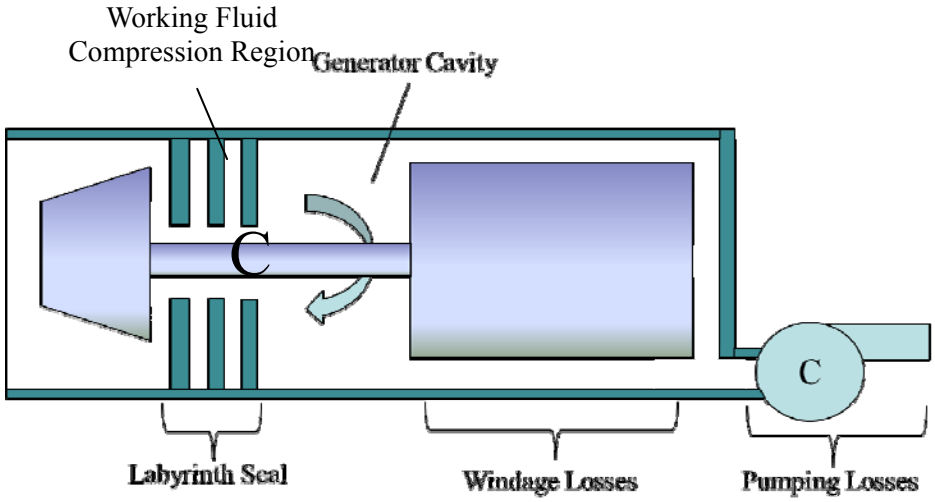

Figure 157 S-CO_2 compressor-generator assembly

The primary problem exists in the generator section, where frictional windage losses on the magnetic rotor are highly dependent on density as is shown in equation (0.13). **Figure 157** shows the primary compressor isolated from the generator cavity by labyrinth seals. Again, labyrinth seals do not provide a perfect seal so, by virtue of the natural pressure gradient from the working fluid compression region to the generator cavity region, a certain amount of leakage is expected. If the leakage issue is not addressed then the pressure will quickly increase in the generator cavity region to match the pressure in the working fluid compression region. In this situation, the

density increases to such levels as to make the windage losses unmanageable.

In an effort to circumvent the windage losses, one idea for decreasing the density in the generator cavity has been to incorporate a secondary system to draw out the residual working fluid from the cavity region. An offsetting performance penalty is related to the pumping losses that have been introduced into the overall system energy balance.

A natural tradeoff exists in this situation, where windage losses are inversely correlated to pumping losses as a function of cavity pressure. **Figure 158** provides a conceptual interpretation of this idea.

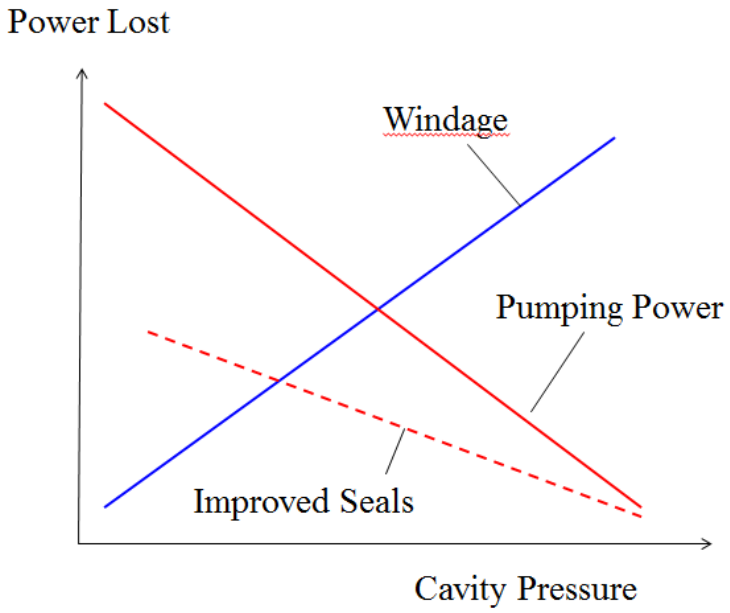

Figure 158 Conceptual interpretation of natural tradeoff in system demonstrating the effect of cavity pressure on overall power reduction

Figure 159 illustrates the power lost due to windage predicted using the dimensions of the turbine-compressor assembly at Sandia National Laboratories together with the design criteria shown in **Table 4-2**. Note that windage losses are particularly important to consider in smaller facilities with power input less than 1 MW because the surface area to volume ratio of such machines tends to be high.

Table 4-2 Design values of the turbine-compressor assembly at Sandia National Laboratories used in initial windage loss estimation

Desired Facility Parameters	Variable:	Value:
Thermal power input	W_{in}	390 KW
Electrical power output	W_{out}	150 kW_e
Comp upstream pressure	$P_{upstream}$	13.8 MPa
Rotor Cavity Property	Variable:	Value:
Rotor radius	R_{rotor}	25.4 mm
Rotor length	L_{rotor}	168 mm
Gap thickness	t_{gap}	3.175mm
Rotor speed	ω	75000

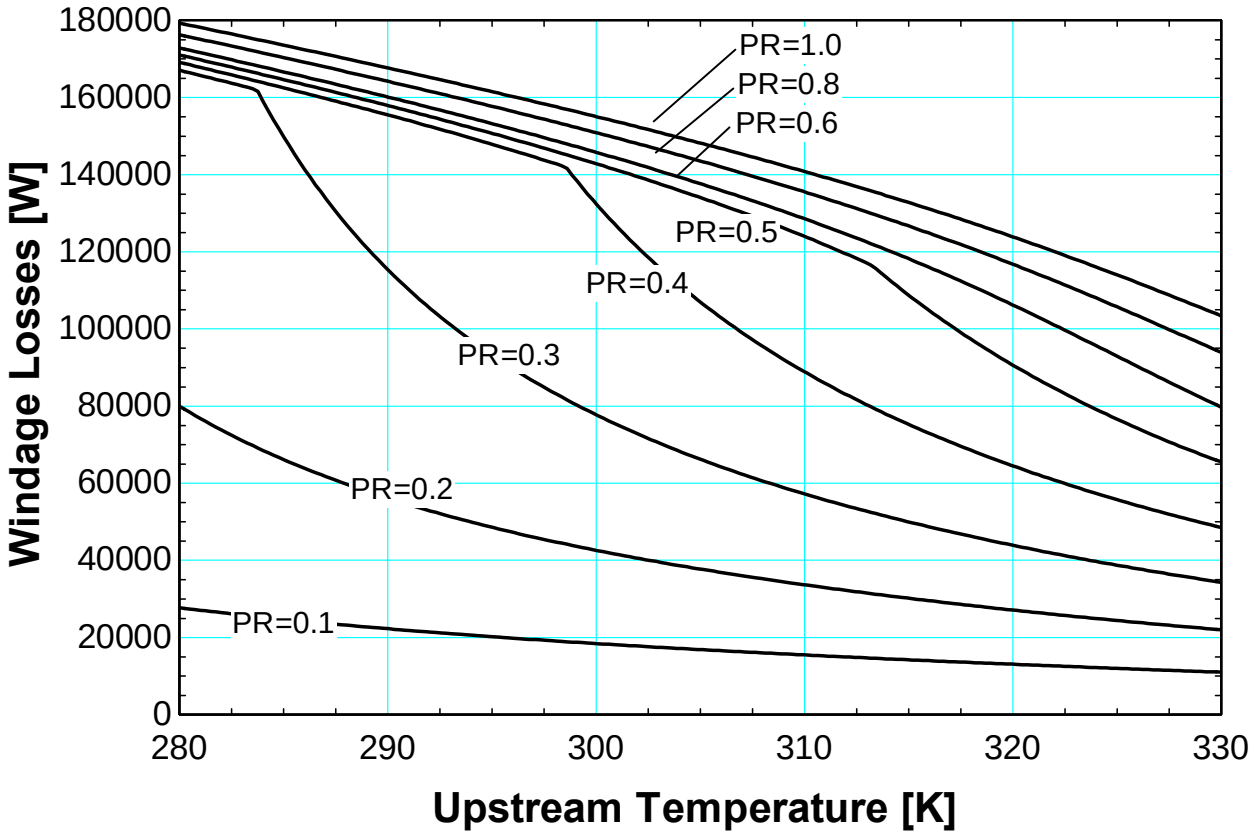

Figure 159 Calculated windage losses as a function of inlet temperature at different pressure ratios for the geometry shown in Table 4-2. The pressure ratio relates the cavity pressure to the compressor upstream pressure.

Figure 159 shows that the windage losses as a function of upstream temperature based on the design parameters identified in **Table 4-2** for the SNL brayton cycle shown in **Figure 160**. The analysis used to construct this graph is discussed below and takes advantage of the Engineering Equation Solver (EES) software package.

The model developed for this analysis allows the user to define the thermodynamic condition directly upstream of the shaft seals as demonstrated by equation (0.4). The specific enthalpy is then calculated from the property database integrated in EES, as shown in equation (0.5).

$$Model\ Upstream\ Inputs:\ P_{upstream}, T_{upstream} \quad (0.4)$$

$$h_{upstream} = Enthalpy\left(Carbon\ Dioxide, P = P_{upstream}, T = T_{upstream}\right) \quad (0.5)$$

A pressure ratio of interest is then selected which can be used to solve for the cavity pressure P_{cavity} as shown in equation (0.6).

$$PR = \frac{P_{cavity}}{P_{upstream}} \quad (0.6)$$

The flow is then assumed to throttle isenthalpically through the shaft seal to a cavity pressure of interest as shown in equation (0.7).

$$h_{cavity} = h_{upstream} \quad (0.7)$$

The density in this "cavity region" is then calculated according to equation (0.8) again using EES integrated property data.

$$\rho_{cavity} = Density\left(Carbon\ Dioxide, P = P_{cavity}, h = h_{cavity}\right) \quad (0.8)$$

The viscosity in the cavity region is calculated in one of two ways. As long as the thermodynamic state is outside the vapor dome, the viscosity is calculated based on equation (0.9).

$$\mu_{cavity} = Viscosity\left(Carbon\ Dioxide, P = P_{cavity}, h = h_{cavity}\right) \quad (0.9)$$

However, if the thermodynamic state lies inside the vapor dome, the following model proposed by Isbin et al. (1958) is used.

$$\mu_{2\phi,cavity} = \left[\frac{x}{\mu_g} + \frac{1-x}{\mu_l}\right]^{-1} \quad (0.10)$$

where x is the quality. The Vrancik (1986) model is traditionally used to estimate windage losses and is shown below as equation (0.13). Also shown is the definition for the skin friction coefficient $C_{d,fric}$ in equation (0.12) for turbulent flow between two parallel plates.

$$\mathrm{Re} = \frac{r_{rotor}\, t_{gap}\, \varpi\, \rho}{\mu} \quad (0.11)$$

$$\frac{1}{\sqrt{C_{d,fric}}} = 2.04 + 1.768 \ln\left(\mathrm{Re}\sqrt{C_{d,fric}}\right) \quad (0.12)$$

$$\dot{W}_{windage} = \pi C_{d,fric} \rho_{cavity} r_{rotor}^4 \varpi^3 L_{rotor} \quad (0.13)$$

In summary, it is clear that the cavity pressure (shown in **Figure 159** as a function of PR) must be reduced in order to minimize excessive windage losses. With no pressure reduction (i.e., PR =1), the windage loss is on the same order as the output of the cycle.

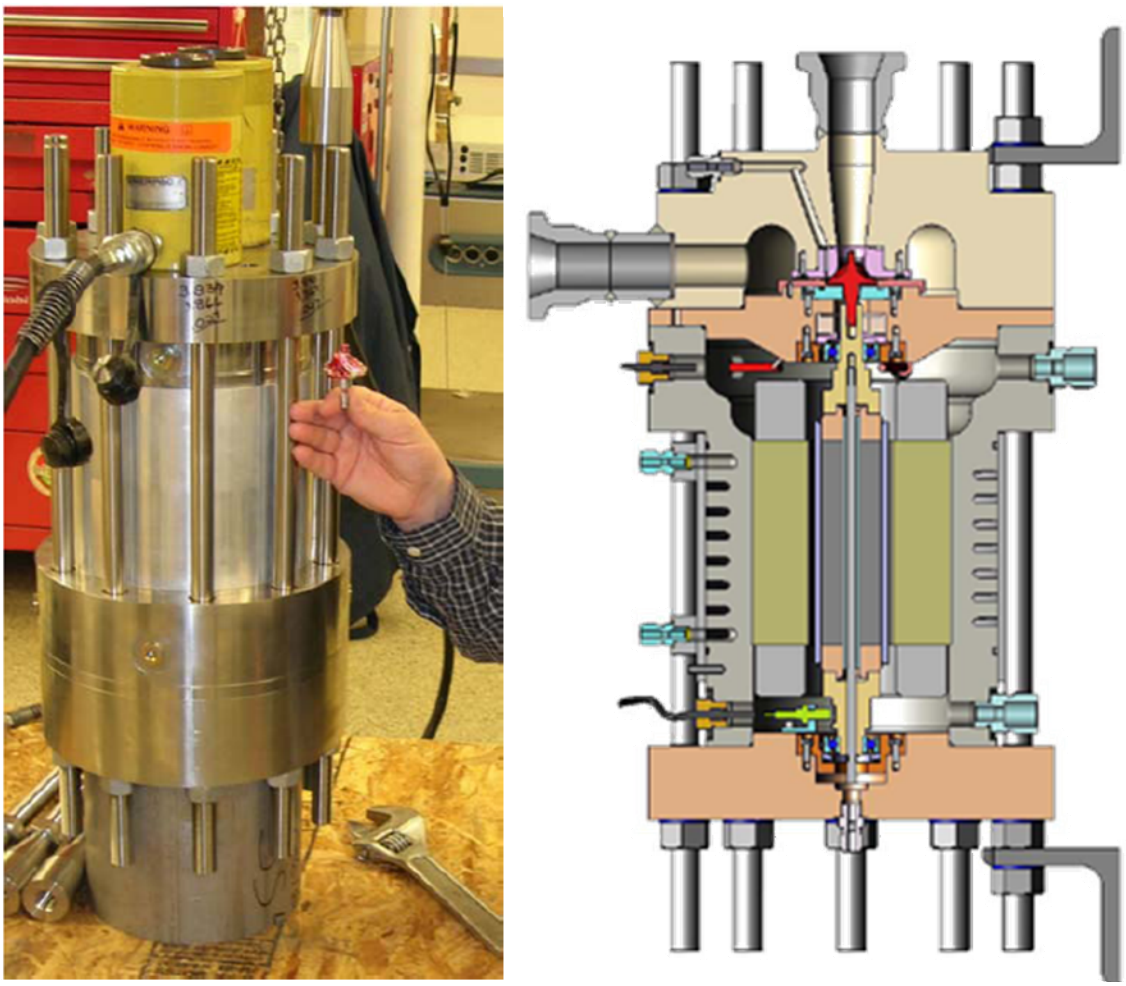

(a) (b)

Figure 160 Supercritical carbon dioxide brayton cycle developed by Sandia National Laboratory and Barber-Nichols. (a) Assembled version of S-CO2 cycle (b)

As a point of reference, **Figure 160** shows the supercritical carbon dioxide brayton cycle at Sandia National Laboratories which corresponds to the physical system discussed in this section. Note the diminutive physical size of the compressor wheel shown in **Figure 160** for this 150 kW_e output facility.

4.1.4 Experimental Approach to measuring Seal Leakage

The price for reducing windage loss is pump power. In order to design a system correctly it is necessary to know the pump power and therefore the effectiveness of the seals used to isolate the working fluid from the cavity region. The seals dictate the leakage rate into the cavity region and therefore dictate the pumping power.

The approach taken in the current investigation is to measure the leakage rate through shaft seals driven by large pressure gradients.

Supercritical fluids present an interesting challenge in terms of construction methodology as the sizing of turbomachinery is largely dictated by the operating conditions that are desired. Stability and reliability then becomes a problem as minor deviations in temperature and pressure result in large density and other property variations. The test facility conceived for this investigation is conceptually simple. The thermodynamic state is set directly preceding the test section near the supercritical point. The fluid is then throttled through a reconfigurable shaft seal test section to a desired pressure. The flow rate is measured through the test section.

Operating and control of a flow loop near the critical point is difficult as small changes in temperature result in large changes in density along an isobar. For this reason, the facility employs an active control system of the working fluid in order to regulate the pressure into the test section.

References

Dostal, V., Driscoll, M.J., and Hejzlar, P., 2004, “A Supercritical Carbon Dioxide Cycle for Next Generation Nuclear Reactors”. MIT-ANP-Series, MIT-ANP-TR-100.

Isbin, H.S., Moy, J.E., and DaCruz, J.R., 1958, “Two-phase steam water critical flow”, AICHE Journal, 3, pp. 361-365.

Klein, S.A., Engineering Equation Solver (EES), 1992-2011. ver. 8.957.

Klein, S.A., and Nellis, G.F, 2011, *Thermodynamics,* UW-Madison DoIT bookstore..

Kruizenga, A., 2010, Ph.D. dissertation. “Heat Transfer and Pressure Drop Measurements in Prototypic Heat Exchangers for the Supercritical Carbon Dioxide Brayton Power Cycles”.

Licht, J., Anderson, M., Corradini, M., and Bonazza, R., 2007, “Heat Transfer Phenomena in Supercritical Water Nuclear Reactors”.

Mignot, G., 2007, Ph.D. dissertation. “Critical Flow Experiment and Analysis for Supercritical Fluid”

Vrancik, J.E., “Prediction of windage power loss in alternators”, 1986.

Wright, S.A. Vernon, M.E., Pickard, P.S., 2006, “Concept Design for a High Temperature Helium Brayton Cycle with Interstage Heating and Cooling”, SAND2006-4147.

4.2 Literature Review: Pressure Drop

The objective of this chapter is to provide an understanding of the pressure drop associated with flows through passages similar to those for labyrinth seals. The pressure drop is an engineering quantity of interest that is readily measured based on the pressure loss between two axial locations. The observed pressure drop is a compilation of the contributing pressure losses that occur along a streamline of a fluid element. In general, the overall pressure drop can be dissected and recast in terms of major pipe flow losses and minor form loss pressure drops, as is denoted in equation (2.1).

$$\Delta P_{total} = \underbrace{\Delta P_{pipe-flow}}_{major\ losses} + \underbrace{\sum_{i}^{n}\left(\Delta P_{flow-disturbances}\right)_{i}}_{form\ losses} \tag{2.1}$$

This chapter is divided into two sections. The first section describes the form losses that occur in pipe flow due to a sudden contraction or expansion of the working fluid. The second section gives a detailed explanation of the major pressure losses that are typical in pipe flow and documents the different models that are available to account for each term.

4.2.1 Form Losses

Form losses are encountered in any pipe network where anything from pipe-elbows to orifice-plate metering devices will result in a sudden drop in pressure that is driven by a local disturbance of the flow. These form losses are typically referred to as "minor losses", but in reference to an orifice, nozzle, or flow metering device these losses can be particularly large.

4.2.1.1 Single Phase One-Dimensional Isentropic Expansion

In the context of shaft seals, the maximum pressure drop associated with a given flow rate is desired. The following analysis is based on the isentropic expansion of a single-phase fluid through an orifice. The model used for this purpose is based on previous work done by Gamal et al. (2006, 2008). This model is based on the St. Venant equations that are used to calculate the isentropic mass flow rate through an orifice based on the pressure difference between the upstream and downstream conditions. The derivation considers one-dimensional effects and applies to inviscid flow of an ideal gas.

Mass and energy balances for the orifice as a control volume are written in equations (2.2) and (2.3).

$$\cancel{\frac{dm}{dt}} = \dot{m}_{in} - \dot{m}_{out} \tag{2.2}$$

$$\dot{m}_{in}\left(h_{in} + \frac{\tilde{V}_{in}^2}{2} + \cancel{gZ_{in}}\right) - \dot{m}_{out}\left(h_{out} + \frac{\tilde{V}_{out}^2}{2} + \cancel{gZ_{out}}\right) + \cancel{\dot{Q}_{cv}} - \cancel{\dot{W}_{cv}} = \cancel{\frac{dU_{cv}}{dt}} \tag{2.3}$$

The system is assumed to be at steady state with negligible change in potential energy. The system also is assumed to be well insulated with no shaft work being done. Equations (2.2) and (2.3) can be combined to result in equation (2.4).

$$h_{in} - h_{out} = \frac{\tilde{V}_{out}^2 - \tilde{V}_{in}^2}{2} \qquad (2.4)$$

The process is regarded as internally reversible. Application of the fundamental property relation provides a relationship between the enthalpy difference and the pressure difference, as indicated in equation (2.5).

$$\cancel{T\,ds} = dh - v\,dp \rightarrow dh = v\,dp \rightarrow h_{out} - h_{in} = \int_{P_{in}}^{P_{out}} v\,dp \qquad (2.5)$$

By direct substitution of equation (2.5) into (2.4), the following relationship is derived as shown here in equation (2.6).

$$\frac{\tilde{V}_{out}^2 - \tilde{V}_{in}^2}{2} = \int_{P_{out}}^{P_{in}} v\,dp \qquad (2.6)$$

The integrand is evaluated by considering the isentropic state equation. The isentropic state equation considers the differential of $p = p(\rho, s)$, shown here as equation (2.7). In an isentropic process, however, the second term drops out of the pressure so that the pressure can be considered to become a function of density alone. Klein and Nellis (2011) present the following argument.

$$dp = \left(\frac{\partial p}{\partial \rho}\right)_s d\rho + \cancel{\left(\frac{\partial p}{\partial s}\right)_\rho ds} \rightarrow \frac{dp}{d\rho} = \left(\frac{\partial p}{\partial \rho}\right)_s \qquad (2.7)$$

The differential specific entropy of a pure fluid is defined by equation (2.8).

$$ds = \frac{du}{T} + \frac{P}{T} dv \qquad (2.8)$$

Modifying this equation in terms of the ideal gas law in combination with the specific enthalpy of an ideal gas leads to equation (2.9)

.

$$ds = \frac{C_v\,dT}{T} - \frac{R}{v} dv \qquad (2.9)$$

Equation (2.9) can be integrated to obtain equation (2.11).

$$\int_{s_1}^{s_2} ds = \int_{T_1}^{T_2} \frac{C_v(T)}{T} dT + R \int_{v_1}^{v_2} \frac{dv}{v} \qquad (2.10)$$

$$s_2 - s_1 = \int_{T_1}^{T_2} \frac{C_v(T)}{T} dT + R \ln\left(\frac{v_2}{v_1}\right) \quad \textit{for an ideal gas} \qquad (2.11)$$

For an ideal gas, the appropriate assumption is that $C_v(T)$ is a weak function of temperature and can be taken

as a constant $C_v(T) \rightarrow C_v = const$. This recasts equation (2.11) as equation (2.12).

$$s_2 - s_1 = C_v \ln\left(\frac{T_2}{T_1}\right) + R \ln\left(\frac{v_2}{v_1}\right) \quad \textit{for an ideal gas with constant } C_v \tag{2.12}$$

For an ideal gas:

$$C_p - C_v = R \tag{2.13}$$

Substituting the ideal gas law and invoking the specific enthalpy for an ideal gas into equation (2.12) yields (2.14).

$$s_2 - s_1 = C_v \ln\left(\frac{P_2}{P_1}\right) + C_P\left(\frac{v_2}{v_1}\right) \quad \textit{for an ideal gas with constant } C_p \textit{ and } C_v \tag{2.14}$$

For an isentropic process, this leads to the following:

$$C_v \ln\left(\frac{P_2}{P_1}\right) = -C_P \ln\left(\frac{v_2}{v_1}\right) \tag{2.15}$$

The specific heat ratio defined by equation (2.16) is commonly used to model the isentropic expansion of an ideal gas.

$$k = \frac{C_p}{C_v} \tag{2.16}$$

The final form of the expansion of an ideal gas undergoing an isentropic process is presented in equation (2.17).

$$p_{in} v_{in}^k = p\, v^k = const \rightarrow v = \left(\frac{p_{in} v_{in}^k}{p}\right)^{\frac{1}{k}} \tag{2.17}$$

The relationship shown in equation (2.17) is then substituted into equation (2.6) and integrated, as shown in equation (2.18), which results in equation (2.19).

$$\frac{\tilde{V}_{out}^2 - \tilde{V}_{in}^2}{2} = \int_{P_{out}}^{P_{in}} \left(\frac{P_{in} v^k}{p}\right)^{\frac{1}{k}} dp$$

$$\frac{\tilde{V}_{out}^2 - \tilde{V}_{in}^2}{2} = \left(\frac{k}{k-1}\right) P_{in}^{\frac{1}{k}} v_{in} \left[p^{\frac{k-1}{k}} \right]_{p_{out}}^{p_{in}} \tag{2.18}$$

$$\frac{\tilde{V}_{out}^2 - \tilde{V}_{in}^2}{2} = \left(\frac{k}{k-1}\right) P_{in} v_{in} \left[1 - \left(\frac{P_{out}}{P_{in}}\right)^{\frac{k-1}{k}} \right] \tag{2.19}$$

The continuity equation is invoked once again according to equation (2.20) in order to solve for the velocity at the inlet relative to the outlet velocity.

$$\dot{m}_{in} = \dot{m}_{out} \rightarrow \frac{\tilde{V}_{in} A_{c,in}}{v_{in}} = \frac{\tilde{V}_{out} A_{c,out}}{v_{out}}$$
$$\tilde{V}_{in} = \tilde{V}_{out} \left[\frac{A_{c,out}}{A_{c,in}} \right] \left[\frac{v_{in}}{v_{out}} \right] \tag{2.20}$$

The relationship presented in equation (2.17) is then substituted into equation (2.20) to arrive at equation (2.21).

$$\tilde{V}_{in} = \tilde{V}_{out} \left[\frac{A_{c,out}}{A_{c,in}} \right] \left[\frac{v_{in}}{\left(\frac{P_{in} v_{in}^{k}}{P_{out}} \right)^{\frac{1}{k}}} \right] \rightarrow \tilde{V}_{in} = \tilde{V}_{out} \left[\frac{A_{c,out}}{A_{c,in}} \right] \left[\frac{P_{out}}{P_{in}} \right]^{\frac{1}{k}} \tag{2.21}$$

Equation (2.21) is substituted back into equation (2.19) to arrive at (2.22). The result is simplified in terms of $\tilde{V}_{out}$ as shown in equation (2.23). Finally, continuity as presented in equation (2.20) and the isentropic relationship in equation (2.17) are used once again to arrive at equation (2.24).

$$\tilde{V}_{out}^{2} - \left\{ \underbrace{\tilde{V}_{out} \left[\frac{A_{c,out}}{A_{c,in}} \right] \left[\frac{P_{out}}{P_{in}} \right]^{\frac{1}{k}}}_{\tilde{V}_{in}} \right\}^{2} = \left(\frac{2k}{k-1} \right) P_{in} v_{in} \left[1 - \left(\frac{P_{out}}{P_{in}} \right)^{\frac{k-1}{k}} \right] \tag{2.22}$$

$$\tilde{V}_{out}^{2} = \frac{\left(\frac{2k}{k-1} \right) P_{in} v_{in} \left[1 - \left(\frac{P_{out}}{P_{in}} \right)^{\frac{k-1}{k}} \right]}{1 - \left\{ \left[\frac{A_{c,out}}{A_{c,in}} \right] \left[\frac{P_{out}}{P_{in}} \right]^{\frac{1}{k}} \right\}^{2}} \tag{2.23}$$

$$\tilde{V}_{out}^2 = \left\{ \underbrace{\frac{\dot{m} v_{out}}{A_{c,out}}}_{\tilde{V}_{out}} \right\}^2 \rightarrow \left\{ \underbrace{\frac{\dot{m} \overbrace{\left(\frac{P_{in} v_{in}^k}{P_{out}} \right)^{\frac{1}{k}}}^{v_{out}}}{A_{c,out}}}_{\tilde{V}_{out}} \right\}^2 = \frac{\left(\frac{2k}{k-1} \right) P_{in} v_{in} \left[1 - \left(\frac{P_{out}}{P_{in}} \right)^{\frac{k-1}{k}} \right]}{1 - \left\{ \left[\frac{A_{c,out}}{A_{c,in}} \right] \left[\frac{P_{out}}{P_{in}} \right]^{\frac{1}{k}} \right\}^2}$$

$$\dot{m} = \sqrt{\frac{A_{c,out}^2 \left(\frac{2k}{k-1} \right) P_{in} \left[\frac{P_{out}}{p_{in}} \right]^{\frac{2}{k}} \left[1 - \left(\frac{P_{out}}{P_{in}} \right)^{\frac{k-1}{k}} \right]}{v_{in} \left\{ 1 - \left\{ \left[\frac{A_{c,out}}{A_{c,in}} \right] \left[\frac{P_{out}}{P_{in}} \right]^{\frac{1}{k}} \right\}^2 \right\}}} \qquad (2.24)$$

The result is simplified as shown in equation (2.26) where equation (2.25) denotes the mass flux through the constricted cross-sectional area.

$$G = \frac{\dot{m}}{A_{c,out}} \qquad (2.25)$$

$$G_{1-D,isentropic,unchoked} = \sqrt{\frac{P_{in} \rho_{in} \left(\frac{2k}{k-1} \right) \left[\left(\frac{P_{out}}{P_{in}} \right)^{\frac{2}{k}} - \left(\frac{P_{out}}{P_{in}} \right)^{\frac{k+1}{k}} \right]}{1 - \left\{ \left(\frac{A_{c,out}}{A_{c,in}} \right)^2 \left(\frac{P_{out}}{P_{in}} \right)^{\frac{2}{k}} \right\}}} \qquad (2.26)$$

Equation (2.26) is the St. Venant's equation, modified in order to include an area ratio between the inlet channel and the constricted channel cross-sections.

Choking can occur if the velocity reaches the speed of sound. The mass flow rate then becomes independent of the downstream pressure and remains at a fixed value. The definition of the speed of sound is provided in equation (2.27), Moran and Shapiro (2004). Observe that the partial derivative has once again become the total derivative, as shown in equation (2.7).

$$c = \sqrt{-v^2 \left(\frac{\partial p}{\partial v} \right)_s} \rightarrow \sqrt{-v^2 \left(\frac{dp}{dv} \right)} \qquad (2.27)$$

The choked flow condition is obtained by referring back to equation (2.23) and setting the outlet velocity $\tilde{V}_{out}^2 = c^2 = -v^2 \left(\frac{dp}{dv} \right)$. The solution is provided by equation (2.28).

$$\tilde{V}_{out}^2 = c^2 \rightarrow \frac{\left(\frac{2k}{k-1}\right) P_{in} v_{in} \left[1 - \left(\frac{P_{out}}{P_{in}}\right)^{\frac{k-1}{k}}\right]}{1 - \left\{\left[\frac{A_{c,out}}{A_{c,in}}\right]\left[\frac{P_{out}}{P_{in}}\right]^{\frac{1}{k}}\right\}^2} = -v_{out,cr}{}^2 \left(\frac{dp}{dv}\right) \tag{2.28}$$

Equation (2.17) is differentiated to solve for $\frac{dp}{dv}$ as presented in equation (2.29).

$$p\,v^k = P_{in}\,v_{in}^k \rightarrow p = \frac{P_{in} v_{in}^k}{v^k} \rightarrow \frac{dp}{dv} = -k P_{in} v_{in}{}^k v^{-k-1} \tag{2.29}$$

The end result of equation (2.29) is then substituted into equation (2.28) to solve for the critical downstream pressure. The derivation is presented in equation (2.30) through equation (2.33). Note that the pressure that is determined is the downstream pressure, which corresponds to the downstream specific volume.

$$\underbrace{\frac{\left(\frac{2\cancel{k}}{k-1}\right)\cancel{P_{in}}\, v_{in}\left[1 - \left(\frac{P_{out,cr}}{P_{in}}\right)^{\frac{k-1}{k}}\right]}{1 - \left\{\left[\frac{A_{c,out}}{A_{c,in}}\right]\left[\frac{P_{out,cr}}{P_{in}}\right]^{\frac{1}{k}}\right\}^2}}_{\tilde{V}_{out}^2} = \underbrace{-v_{out,cr}{}^2 \underbrace{\left\{-\cancel{k}\,\cancel{P_{in}}\, v_{in}{}^k v_{out,cr}{}^{-k-1}\right\}}_{\frac{dp}{dv}}}_{c^2}$$

$$\left(\frac{2}{k-1}\right)\left[1 - \left(\frac{P_{out,cr}}{P_{in}}\right)^{\frac{k-1}{k}}\right] = \frac{v_{in}{}^{k-1}}{v_{out,cr}{}^{k-1}}\left[1 - \left\{\left[\frac{A_{c,out}}{A_{c,in}}\right]\left[\frac{P_{out,cr}}{P_{in}}\right]^{\frac{1}{k}}\right\}^2\right] \tag{2.30}$$

Invoking equation (2.17) again, the following relationship is derived – shown in equation (2.31).

$$v_{out,cr} = \left(\frac{P_{in} v_{in}^k}{P_{out,cr}}\right)^{\frac{1}{k}} : \left(\frac{v_{out,cr}}{v_{in}}\right)^k = \left(\frac{P_{in}}{P_{out,cr}}\right) ; \frac{v_{out,cr}}{v_{in}} = \left(\frac{P_{in}}{P_{out,cr}}\right)^{\frac{1}{k}}$$

$$\left(\frac{v_{out,cr}}{v_{in}}\right)^{k-1} = \frac{\left(\frac{P_{in}}{P_{out,cr}}\right)}{\left(\frac{P_{in}}{P_{out,cr}}\right)^{\frac{1}{k}}} = \left(\frac{P_{in}}{P_{out,cr}}\right)^{\frac{k-1}{k}} \tag{2.31}$$

$$\left(\frac{2}{k-1}\right)\left[1-\left(\frac{P_{out,cr}}{P_{in}}\right)^{\frac{k-1}{k}}\right]=\underbrace{\left\{\left(\frac{P_{out,cr}}{P_{in}}\right)^{\frac{k-1}{k}}\right\}}_{\left(\frac{v_{in}}{v_{out,cr}}\right)^{k-1}}\left[1-\left\{\left(\frac{A_{c,out}}{A_{c,in}}\right)\left(\frac{P_{out,cr}}{P_{in}}\right)^{\frac{1}{k}}\right\}^{2}\right] \tag{2.32}$$

$$\left(\frac{P_{out,cr}}{P_{in}}\right)^{\frac{1-k}{k}}+\left(\frac{k-1}{2}\right)\left(\frac{A_{c,out}}{A_{c,in}}\right)\left(\frac{P_{out,cr}}{P_{in}}\right)^{\frac{2}{k}}=\frac{k+1}{2} \tag{2.33}$$

The condition presented here as equation (2.33) is known as the critical pressure ratio at which choked flow occurs for a fixed upstream pressure. It is appropriate to think of this condition as a lower bound domain restriction of the pressure ratio $\frac{P_{out}}{P_{in}}$ for the unchoked flow equation shown here as equation (2.26). For $P_{out,cr} > P_{out}$, the mass flow rate will not increase and it is fixed at the value calculated by equation (2.34).

$$G_{1-D,choked}=\sqrt{\frac{P_{in}\,\rho_{in}\left(\frac{2k}{k-1}\right)\left[\left(\frac{P_{out,critical}}{P_{in}}\right)^{\frac{2}{k}}-\left(\frac{P_{out,critical}}{P_{in}}\right)^{\frac{k+1}{k}}\right]}{1-\left\{\left(\frac{A_{c,out}}{A_{c,in}}\right)^{2}\left(\frac{P_{out,critical}}{P_{in}}\right)^{\frac{2}{k}}\right\}}} \tag{2.34}$$

Figure 161 demonstrates the effect of pressure ratio *PR*, aspect ratio *AR*, and specific heat ratio *k* on the expansion factor *Y* defined by equation (2.38). The expansion factor shown here is effectively a dimensionless mass flux that relates the mass flux to the inlet thermodynamic state as shown in equation (2.35). The definition of the terms used in equation (2.38) are provided in equations (2.36), (2.37), and (2.16). The mass flux is shown in equation (2.39).

$$Y=\frac{G\left(PR,AR,k\right)}{\sqrt{P_{in}\rho_{in}}} \tag{2.35}$$

$$PR=\frac{\max\left(P_{out},P_{crit}\right)}{P_{in}} \tag{2.36}$$

$$AR=\frac{A_{c,out}}{A_{c,in}} \tag{2.37}$$

$$Y=\sqrt{\frac{\left(\frac{2k}{k-1}\right)\left[\left(PR\right)^{\frac{2}{k}}-\left(PR\right)^{\frac{k+1}{k}}\right]}{1-\left\{\left(AR\right)^{2}\left(PR\right)^{\frac{2}{k}}\right\}}} \tag{2.38}$$

$$G = Y\sqrt{P_{in}\,\rho_{in}} \quad (2.39)$$

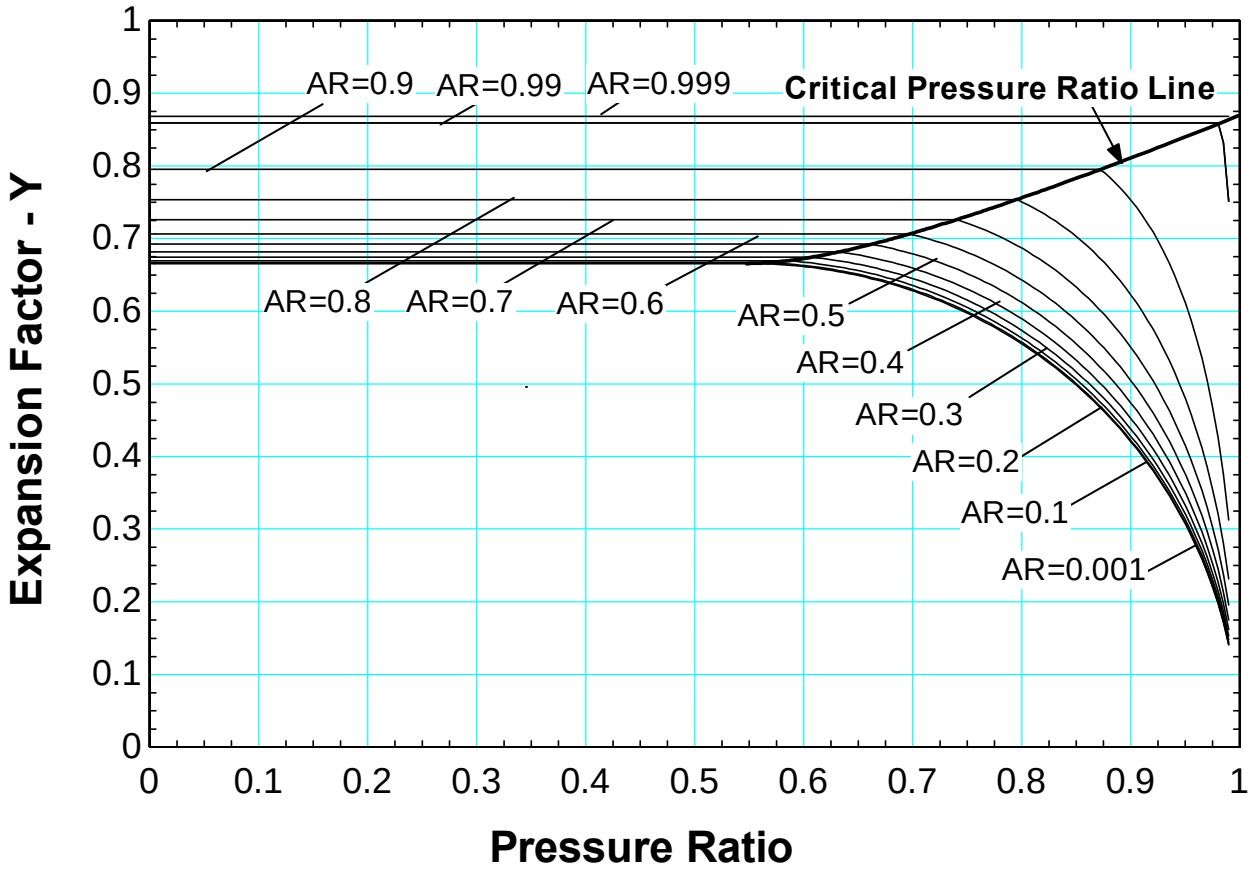

Figure 161 Expansion factor Y as a function of pressure ratio for various aspect ratios; also shown is the calculated critical pressure ratio line as defined by equation (2.33); The specific heat ratio was taken to be k=1.292, corresponding to carbon dioxide at 300 K and ideal gas conditions.

Figure 161 also shows that a theoretical minimum of the expansion factor exists as $AR \to 0$. The mass flux for *AR* approaching zero is expressed in equation (2.40)

$$G_{1-D,AR\to 0} = \sqrt{P_{in}\,\rho_{in}\left(\frac{2k}{k-1}\right)\left[\left(\frac{P_{out,critical}}{P_{in}}\right)^{\frac{2}{k}} - \left(\frac{P_{out,critical}}{P_{in}}\right)^{\frac{k+1}{k}}\right]} \quad (2.40)$$

The result is the well-known St. Venant's equation for constricted flow where the cross-sectional area of the constriction is much smaller than the inlet channel. Notice that the same result would have been developed if equation (2.41) was considered instead of (2.4). In the case defined below, the kinetic energy at the inlet is neglected which leads to the result reported in equation (2.40).

$$h_{in} - h_{out} = \frac{\tilde{V}_{out}^2 - \cancel{\tilde{V}_{in}^2}}{2} = \frac{\tilde{V}_{out}^2}{2} \quad (2.41)$$

Also of note, is that with the dependence of the aspect ratio eliminated, the critical pressure ratio becomes a constant as demonstrated in equations (2.42) and (2.43).

$$\left(\frac{P_{out,cr}}{P_{in}}\right)^{\frac{1-k}{k}} + \left(\frac{k-1}{2}\right)\cancel{\left(\frac{A_{c,out}}{A_{c,in}}\right)}\left(\frac{P_{out,cr}}{P_{in}}\right)^{\frac{2}{k}} = \frac{k+1}{2}$$

$$\left(\frac{P_{out,cr}}{P_{in}}\right)^{\frac{1-k}{k}} = \frac{k+1}{2} \tag{2.42}$$

$$\frac{P_{out,cr}}{P_{in}} = \left(\frac{k+1}{2}\right)^{\frac{k}{1-k}} \tag{2.43}$$

Equation (2.43) is the critical pressure ratio for flow through a constriction where $A_{c,in} >> A_{c,out}$. This well-documented relationship is often substituted for the pressure ratio shown in equation (2.40), resulting in the following relationship for the mass flux as a function of upstream conditions for choked flow conditions.

$$G_{1-D,choked,AR\to 0} = \sqrt{P_{in}\,\rho_{in}\left(\frac{2k}{k-1}\right)\left[\underbrace{\left(\left(\frac{k+1}{2}\right)^{\frac{k}{1-k}}\right)^{\frac{2}{k}}}_{\frac{P_{out,critical}}{P_{in}}} - \underbrace{\left(\left(\frac{k+1}{2}\right)^{\frac{k}{1-k}}\right)^{\frac{k+1}{k}}}_{\frac{P_{out,critical}}{P_{in}}}\right]}$$

$$G_{1-D,choked,AR\to 0} = \sqrt{P_{in}\,\rho_{in}\left(\frac{2k}{k-1}\right)\left(\frac{k+1}{2}\right)^{\frac{2}{1-k}}\left[1 - \frac{\left(\frac{k+1}{2}\right)^{\frac{k+1}{1-k}}}{\left(\frac{k+1}{2}\right)^{\frac{2}{1-k}}}\right]}$$

$$G_{1-D,choked,AR\to 0} = \sqrt{P_{in}\,\rho_{in}\left(\frac{2k}{k-1}\right)\left(\frac{k+1}{2}\right)^{\frac{2}{1-k}}\left[1 - \frac{1}{\left(\frac{k+1}{2}\right)^{\frac{1-k}{1-k}}}\right]}$$

$$G_{1-D,choked,AR\to 0} = \left(\frac{k+1}{2}\right)^{\frac{1}{1-k}}\sqrt{P_{in}\,\rho_{in}\left(\frac{2k}{\cancel{k-1}}\right)\left[\frac{\cancel{k-1}}{k+1}\right]} \tag{2.44}$$

$$G_{1-D,choked,AR\to 0} = \left(\frac{2}{k+1}\right)^{\frac{1}{k-1}}\sqrt{P_{in}\,\rho_{in}\left(\frac{2k}{k+1}\right)} \tag{2.45}$$

Equation (2.45) shows the critical mass flux as a parameter independent of pressure ratio for $P_{critical,AR\to 0} > P_{out}$.

4.2.1.2 Conceptual Basis for the Discharge Coefficient

The isentropic relationship derived in section 4.2.1.1 defines the ideal flow rate through a constricted channel. A reduction in the actual flow rate from this isentropic value will always occur as irreversible flow components are inherent to any process that occurs in finite time. Furthermore, the flow pattern previously described is strictly for one-dimensional flows. The discharge coefficient, defined by equation (2.46), is often employed as a matter of convenience to relate complicated three-dimensional flow effects to the one-dimensional isentropic relationship shown in section 4.2.1.1.

$$C_{discharge} = \frac{G_{actual}}{G_{1-D,isentropic}} \quad (2.46)$$

The cumulative effects of geometry and fluid property variations results in a complicated flow pattern through any constricted device. The literature provided in Linfield (2000) shows that the discharge coefficient is a function of the following parameters: wall angle α, inlet-to-constriction ratio AR, orifice shape χ, edge-radius-of-curvature to diameter ratio $\frac{R_{lip}}{d_h}$, gas specific heat ratio k, and pressure ratio PR. Linfield cites Shapiro (1953) to show that the effects of gravity and jet expansion into an infinite medium may be neglected. Finally, Ward-Smith (1979) also documents that the orifice thickness to diameter ratio $\frac{L}{d_h}$ plays a crucial role in causing additional pressure losses beyond the orifice entrance due to Fanno flow. The resulting functional relationship is shown in equation (2.47) where the parameters are demonstrated graphically in **Figure 162** and **Figure 163**. It is clear based on these parameters that the problem is very difficult to describe analytically and only lends itself to a description in two-dimensions at best. The following analysis considers some of these two dimensional effects.

$$C_d = C_d\left(\alpha, AR, \chi, \frac{R_{lip}}{d_h}, k, PR, \frac{L}{d_h}\right) \quad (2.47)$$

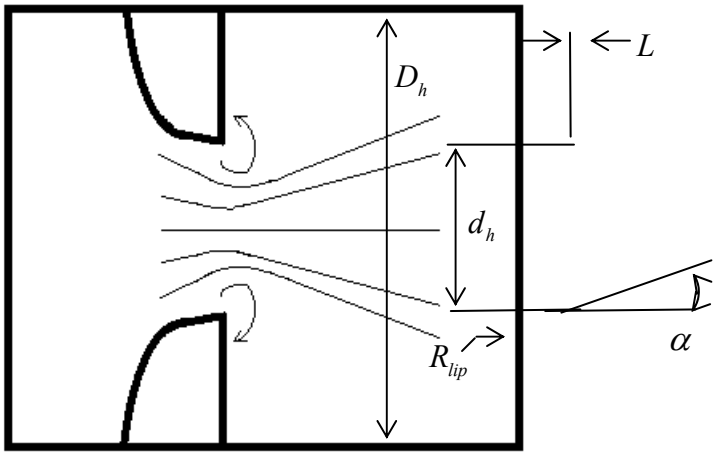

Figure 162 Geometrical properties related to critical discharge coefficient

The contraction coefficient is another means of relating the actual flow rate to the ideal flow rate. The definition is provided in equation (2.48) and graphically demonstrated in **Figure 163**.

$$C_c = \frac{A_{vena-contracta}}{A_{constriction}} = \frac{A_{vc}}{A_{c,out}} \qquad (2.48)$$

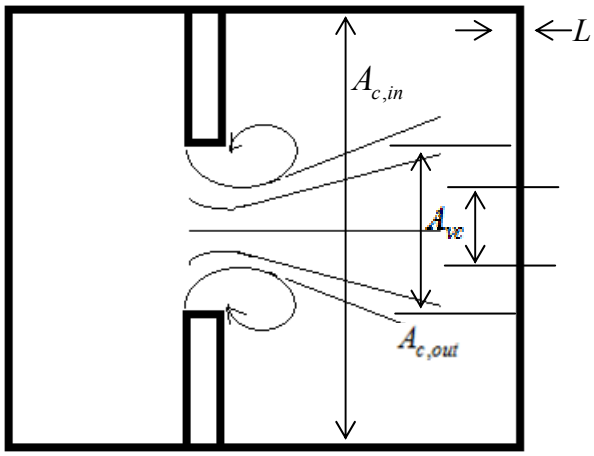

Figure 163 Ratio between the cross-sectional areas of the orifice to that of the vena contracta.

Equation (2.48) demonstrates that the flow rate is limited by the cross-sectional area of the vena contracta and not the area of the constriction. This is an important association which establishes that the flow will neck down further than the cross-sectional area of the flow restriction due to two-dimensional lip effects. The problem with this approach is that it is very difficult to measure the hydraulic diameter of the vena contracta. Furthermore, it would be not be in the best interest of the practicing engineer to develop an industry standard based on such a measurement intensive parameter. Nonetheless, the idea does provide a conceptual basis for one-dimensional model developed in Section 4.2.1.1.

An analytical solution exists for the discharge coefficient associated with a planar, incompressible, inviscid flow through a slot from an infinite reservoir, as defined by equation (2.49) – and shown in Dias (1987). The derivation is based on complex potential flow theory where the flow field is mapped onto the hodographic plane with the variable definitions provided by equation (2.50).

$$C_d\big|_{PR=1} = \frac{1}{1 + \int_0^1 \cot\left(\frac{\pi}{2}x\right)\sin(\alpha x)\,dx} \qquad \textit{for a planar slit} \qquad (2.49)$$

$$V^2 = u^2 + v^2 \quad ; \quad \theta = \tan^{-1}\left(\frac{v}{u}\right) \qquad \textit{hodographic plane transformation variables} \qquad (2.50)$$

Equation (2.49) can be integrated for various wall angles α to determine discharge coefficients for common two-dimensional flow configurations. Note that $\alpha = \frac{\pi}{2}$ corresponds to the classic result $C_d\big|_{PR=1} = \frac{\pi}{\pi+2} \cong 0.611$ or for a Borda-mouthpiece where $\alpha = \pi$ the discharge coefficient is $C_d\big|_{PR=1} = \frac{1}{2}$.

4.2.1.3 Critical versus Choked Flow

The discharge coefficient is highly dependent on the expansion rate of the medium. Three separate published regimes exist where results have been obtained experimentally and computationally for two-dimensional flows: incompressible, critical, and choked.

The literature confuses the two terms critical flow and choked flow quite often by using them interchangeably. Where it is true that all choked flows can be regarded as critical flows, it is not true that all critical flows are choked flows.

A critical flow results when the velocity of any particle in the flow reaches the sonic condition (i.e. the particle susceptible to the least amount of shear stress) defined by equation (2.27). In contrast, a choked flow results when the bulk of particles in the flow have reached the sonic condition.

$$\begin{aligned} \tilde{V}_{\max} &= c \qquad \textit{critical flow} \\ \tilde{V}_{bulk} &= c \qquad \textit{choked flow} \end{aligned} \tag{2.51}$$

This is a distinct difference that was not considered in the one-dimensional derivation. The solution methodology for the two-dimensional model is quite complicated and only the highlights of a derivation by Linfield (2000) are presented here.

An analytical solution exists to evaluate the onset of choking in two-dimensional planar flow. The result is illustrated in equation (2.52) which shows that one may obtain the choked pressure ratio by only knowing the wall angle α and specific heat ratio k.

$$\begin{aligned} V &= \frac{\alpha}{2} \\ V &= \sqrt{\frac{k+1}{k-1}}\tan^{-1}\left(\sqrt{\left(\frac{k-1}{k+1}\right)\left(M^2_{choked}-1\right)}\right)-\tan^{-1}\left(\sqrt{M^2_{choked}-1}\right) \\ PR^{planar}_{choked} &= \frac{1}{\left(1+\left(\frac{k-1}{2}\right)M^2_{choked}\right)^{\frac{k}{k-1}}} \end{aligned} \tag{2.52}$$

The solution for axisymmetric flow is substantially more involved. However it was noted in Linfield (2000) that Alder (1976) showed that the axisymmetric choked pressure ratio $PR^{axisymmetric}_{choked}$ was only slightly lower than that for planar flow. Linfield quotes $\alpha = 90^\circ, PR^{planar}_{choked} = 0.039$ is only slightly decreased to $\alpha = 90^\circ, PR^{axisymmetric}_{choked} = 0.035$.

4.2.1.4 Standard Graph Solution Methodology of Linfield (2000)

Linfield (2000) extended the work of Norwood (1962) and Alder (1976) by numerically evaluating the discharge coefficient for both planar and axisymmetric flows in subsonic and supersonic flow configurations. The subsonic approach is attributed to mathematical relationships developed in Shapiro (1953). Flow in the

supersonic regime is solved based on the solutions obtained for the subsonic approach by using them as initial conditions.

Linfield (2000) constructed a semi-empirical model called the *Standard Graph* to evaluate the discharge coefficient based on planar flow. The model uses a combination of analytical, computational, and experimental results to construct a flow map of the discharge coefficient as a function of the specific heat ratio, pressure ratio, and wall angle for flow through a planar duct.

The *Standard Graph* approach relies heavily on the analytical solution for a planar slit provided by equation (2.49). The assumptions employed in the construction of the *Standard Graph* are detailed in equation (2.53).

$$C_d = C_d\left(\alpha, AR = 0, \chi = planar, \frac{R_{lip}}{d_h} = 0, k, PR, \frac{L}{d_h} \to 0\right) \tag{2.53}$$

The model discerns that, if the discharge coefficient can be obtained at the incompressible limit where $PR \to 1$, a flow map can be constructed for all subsequent pressure ratios based on empirically fit equations for the information shown in equation (2.54).

$$\begin{aligned}
&C_d\big|_{PR=1} = f(\alpha,k); \qquad \left.\frac{\partial C_d}{\partial PR}\right|_{PR=1} = f(\alpha,k) \\
&C_d\big|_{PR=PR_{critical}} = f(\alpha,k) \quad \left.\frac{\partial C_d}{\partial PR}\right|_{PR=PR_{critical}} = f(\alpha,k) \\
&C_d\big|_{PR=PR_{choked}} = f(\alpha,k) \quad \left.\frac{\partial C_d}{\partial PR}\right|_{PR=PR_{choked}} = f(\alpha,k)
\end{aligned} \tag{2.54}$$

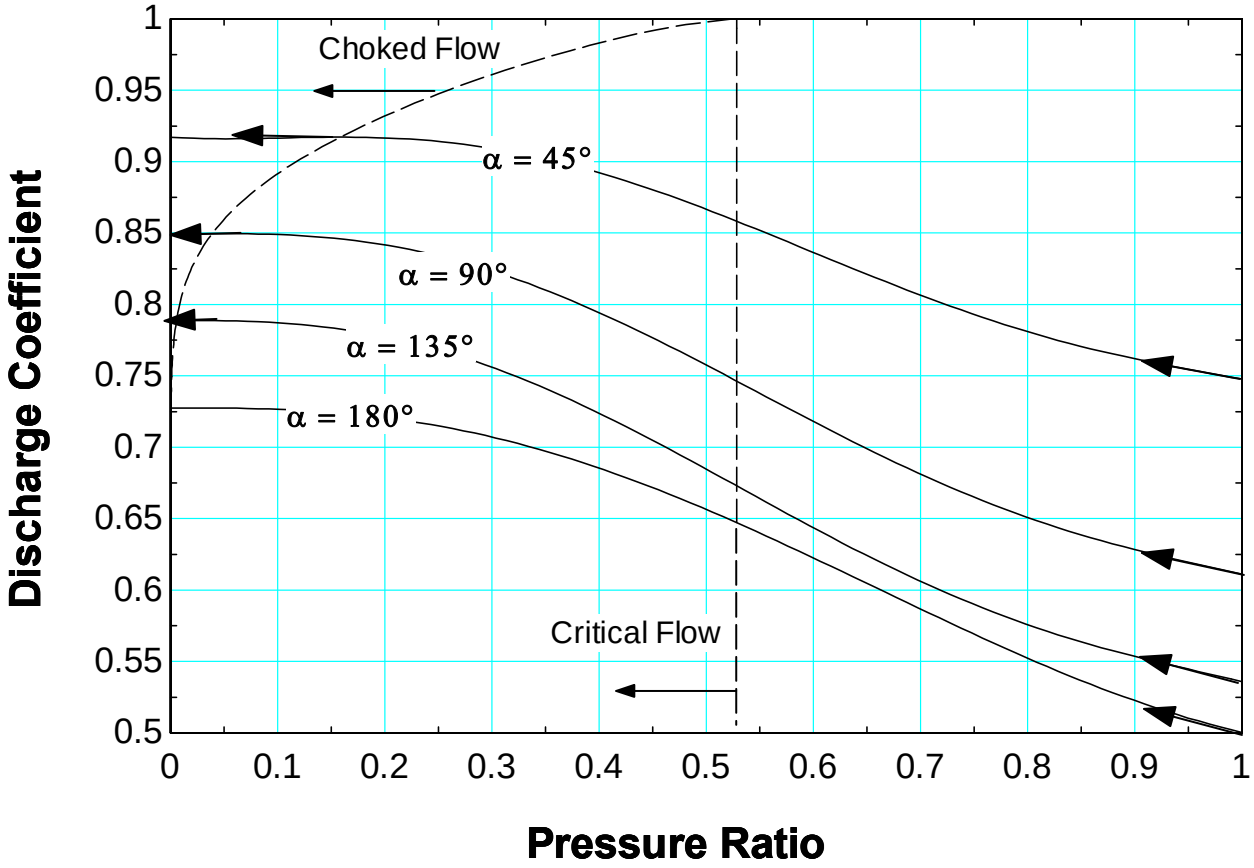

Figure 164 Standard Graph flow map methodology attributed to Linfield (2000). Graph depicts the discharge coefficient for an ideal gas with aspect ratio AR=0, specific heat ratio k=1.4, and wall angle α

Figure 164 is an illustration of the *Standard Graph* approach where the discharge coefficient is illustrated as a function of pressure ratio *PR* and wall angle α. The arrows shown in **Figure 164** locate the point and the derivative of the information required. Linfield has documented functions for all equations shown in (2.54) so that implementation of the *Standard Graph* approach is rather simple.

4.2.1.5 Curve-fits used to construct Standard Graph

Discharge Coefficient for Incompressible Flow at PR=1

The relationship presented in equation (2.55) shows that the discharge coefficient for an incompressible substance through a planar geometry at pressure ratios approximately equal to unity can adequately be defined strictly on the wall angle α. The slope of the line then deviates from that point according to equation (2.57) based on the argument presented in Buseman (1937) as summarized by Linfield (2000) – shown here as equation (2.56).

$$C_d\big|_{PR=1} \approx \frac{1}{1+\sqrt{1-\left(\frac{\sin\alpha}{\alpha}\right)^{1.15}}} \qquad (2.55)$$

$$C_d\Big|_{PR\approx 1}^{90^\circ} = \frac{1}{1+\frac{2}{\pi}\frac{\rho_{jet}}{\rho_o}} \cong \frac{1}{1+\frac{\rho_{jet}}{\rho_o}\sqrt{1-\left(\frac{\sin\alpha}{\alpha}\right)^{1.15}}} \tag{2.56}$$

$$\left.\frac{\partial C_d}{\partial PR}\right|_{PR=1} = \frac{-\sqrt{1-\left(\frac{\sin\alpha}{\alpha}\right)^{1.15}}}{k\left(1+\sqrt{1-\left(\frac{\sin\alpha}{\alpha}\right)^{1.15}}\right)^2} = -\frac{C_d\big|_{PR=1}\left(1-C_d\big|_{PR=1}\right)}{k} \tag{2.57}$$

Figure 165 shows the discharge coefficient as a function of wall angle α through a planar slit. The exact solution provided by equation (2.49) is shown to confirm the approximate solution provided by equation (2.55).

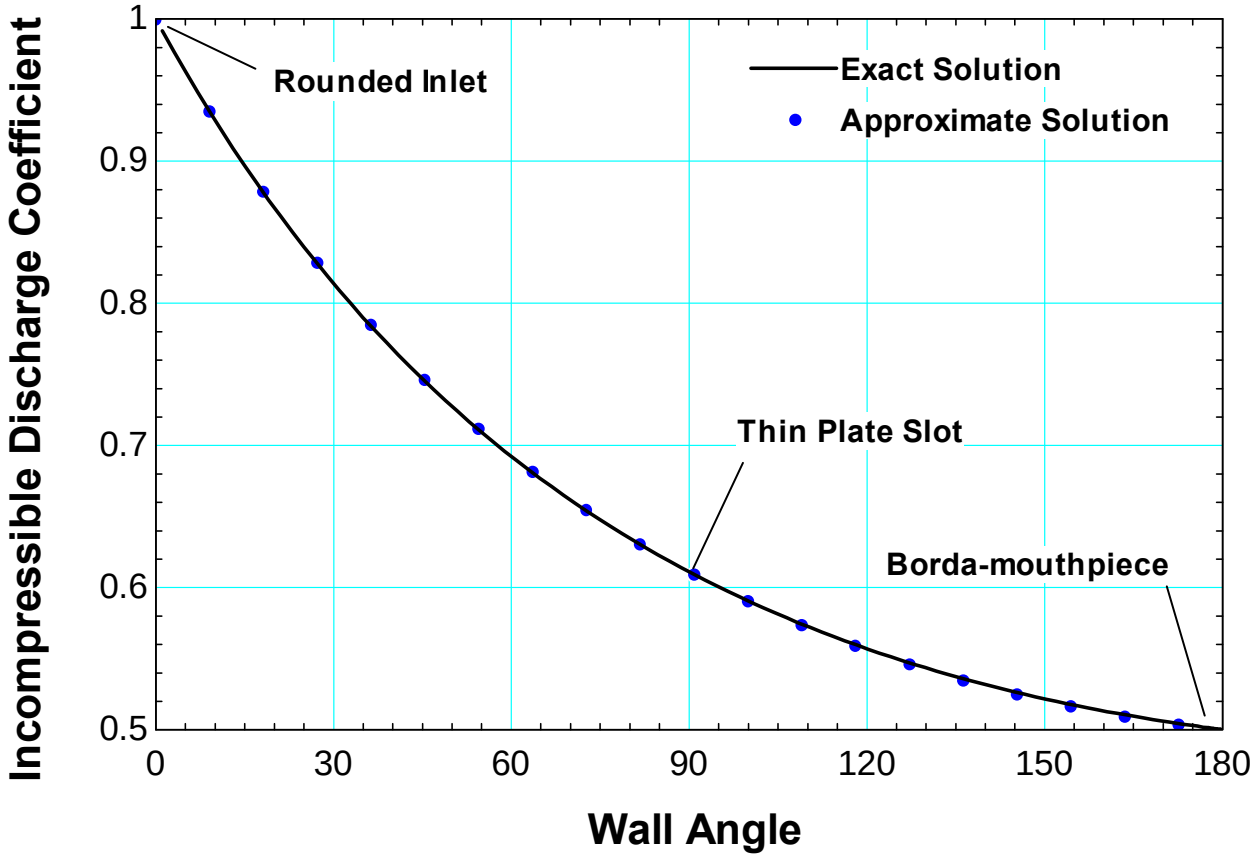

Figure 165 Discharge coefficient for *PR=1* as a function of wall angle α for planar flow; basis for Standard Graph approach, k=1.4

The discharge coefficient for an incompressible substance is the same at pressure ratios close to unity and is strictly a function of wall angle. The deviation in discharge coefficient from that point then changes according to the specific heat ratio k.

Discharge Coefficient at Critical Pressure Ratio

The critical pressure ratio was defined in equation (2.33). Linfield (2000) documents the following curve-fit relationships at this limit.

$$C_d\big|_{PR=PR_{critical}} = A(\bar{\alpha}) + k\,B(\bar{\alpha})$$
$$A = 1 - 0.5103\bar{\alpha} + 0.05644\bar{\alpha}^2 + 0.1360\bar{\alpha}^3$$
$$B = -0.07373\bar{\alpha} + 0.07731\bar{\alpha}^2 - 0.02848\bar{\alpha}^3 \quad (2.58)$$

$$\left.\frac{\partial C_d}{\partial PR}\right|_{PR=PR_{critical}} = \frac{\bar{\alpha}}{C(k) + \bar{\alpha}D(k)}$$
$$C = 0.1549 - 0.01177\,k$$
$$D = 0.934 + 0.6433k \quad (2.59)$$

Note that $\bar{\alpha}$ is a non-dimensional wall angle defined by equation (2.60) and the specific heat ratio k was defined in equation (2.16).

$$\bar{\alpha} = \frac{\alpha}{\pi} \quad (2.60)$$

Discharge Coefficient for Choked Flow

The following curve-fit relationships from Linfield (2000) apply to the development of the standard discharge coefficient graph in the choked flow regime. The coefficients shown in equation (2.61) are slightly different from those published in Linfield (2000). Furthermore, the sign of the second term has been modified such that $C_d = f(E, -kF)$ instead of $C_d = f(E, kF)$ in order to be consistent with the graphs actually presented in Linfield (2000).

$$C_d\big|_{PR=PR_{choked}} = E(\bar{\alpha}) - k\,F(\bar{\alpha})$$
$$E = 1 - 0.3052\bar{\alpha} + 0.1322\bar{\alpha}^2$$
$$F = 0.0483\bar{\alpha} - 0.04124\bar{\alpha}^2 + 0.06505\bar{\alpha}^3 \quad (2.61)$$

$$\left.\frac{\partial C_d}{\partial PR}\right|_{PR=PR_{choked}} = 0 \rightarrow C_d\big|_{PR<PR_{choked}} = C_d\big|_{PR\rightarrow 0} \quad (2.62)$$

$\bar{\alpha}$ is defined in equation (2.60).

4.2.1.6 Standard Graph Equivalent Discharge Coefficient Procedure

Linfield (2000) stipulates that the *Standard Graph* discharge coefficient approach developed in the previous section should apply to other constrictive devices with different wall angles α, inlet-to-constriction ratios AR, orifice shapes χ, and edge-radius-of-curvature to diameter ratios $\frac{R_{lip}}{d_h}$ provided that the discharge coefficient for the prototype device when evaluated in the incompressible limit shares a comparable discharge coefficient with those supported by the *Standard Graph*. The idea is expressed in equation (2.63) and illustrated in

$$C_d\Big|_{PR=1}^{prototype}\left(\alpha, AR \geq 0, \chi = \begin{matrix} planar \\ axisymmetric \\ other \end{matrix}, \frac{R_{tip}}{d_h} > 0, k\right) := C_d(\alpha)\Big|_{PR=1}^{standard\ graph} \quad desired \tag{2.63}$$

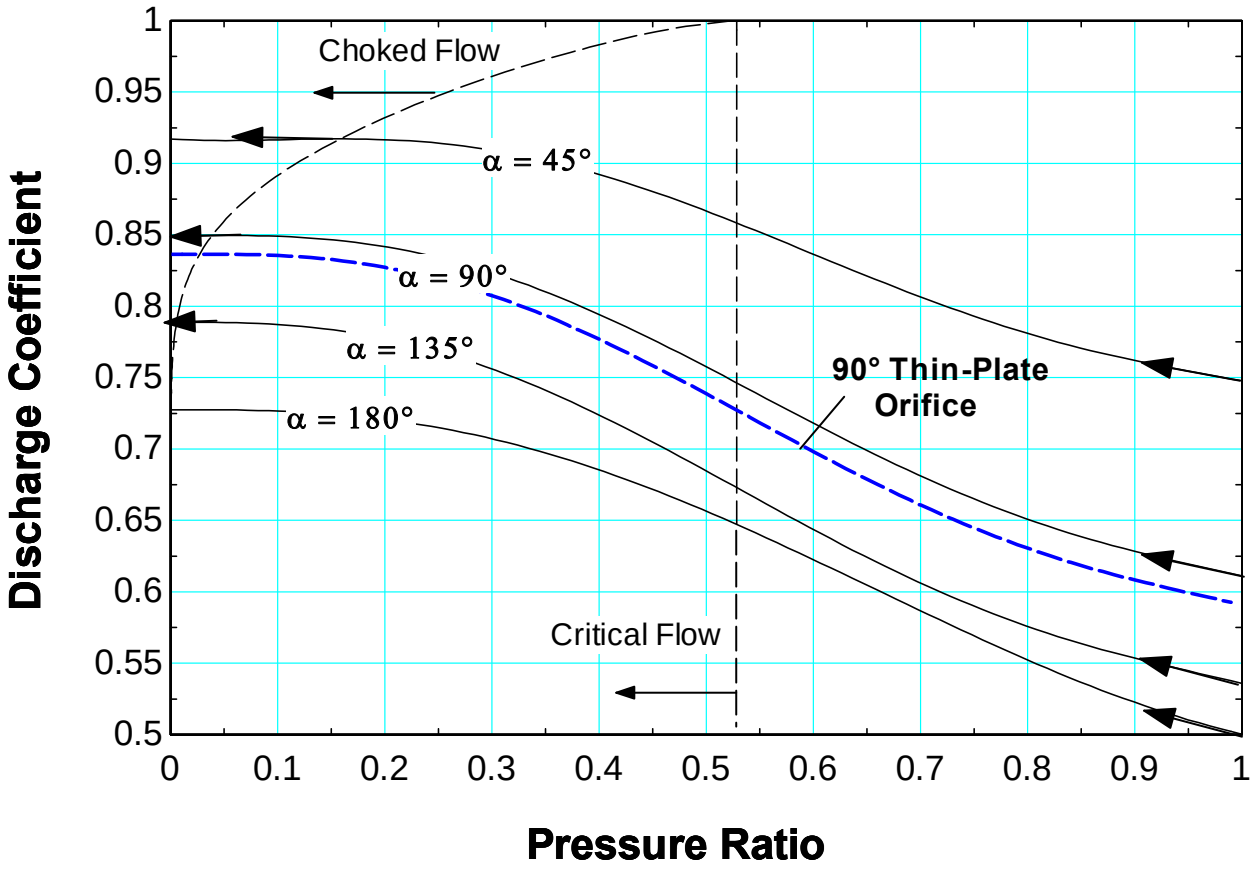

Figure 166 Conceptual basis for Standard Graph approach. The trend of the discharge coefficient of the prototype is estimated to be approximately equal to that of a planar element evaluated at a particular wall angle α, k=1.4

The concept of the *Standard Graph* approach dictates that the incompressible flow limit $C_d|_{PR=1}$ of the prototype must be known. Once this reference is known, the value of $C_d|_{PR=1}$ is input into equation (2.64) – which is a restatement of equation (2.55) – to solve for the wall angle $\alpha'_{standard\ graph}$. This procedure will effectively translate the prototypical orifice into a standard planar constriction evaluated at some arbitrary wall angle. The distribution of the planar constriction based on this effective wall angle is now the distribution of the adjusted prototype as demonstrated in the final iteration of the procedure outlined in equation (2.65).

$$\frac{\sin\alpha'_{standard\ graph}}{\alpha'_{standard\ graph}} \approx \left[1 - \left(\frac{1}{C_d|_{PR=1}} - 1\right)^2\right]^{\frac{1}{1.15}} \tag{2.64}$$

$$C_d\big|_{PR=1}^{prototype}\left(\alpha_{prototype}, AR \geq 0, \chi = \begin{matrix} planar \\ axisymmetric \\ other \end{matrix}, \frac{R_{tip}}{d_h} \geq 0, k\right) \qquad known$$

$$C_d'\big|_{PR=1}^{prototype}\left(\alpha_{prototype}, AR = 0, \chi = planar, \frac{R_{tip}}{d_h} = 0, k\right) = f\left(C_d\big|_{PR=1}^{prototype}\right) \qquad determined$$

$$C_d'\big|_{PR=1}^{prototype} \rightarrow \frac{\sin\alpha'_{standard\ graph}}{\alpha'_{standard\ graph}} \approx \left[1-\left(\frac{1}{C_d'\big|_{PR=1}^{prototype}}-1\right)^2\right]^{\frac{1}{1.15}} \rightarrow \alpha'_{standard\ graph} \quad solve\ \alpha'_{standard\ graph}$$

$$C_d'\big|_{PR=1}^{prototype} = C_d\big|_{PR=1}^{standard\ graph}\left(\alpha'_{standard\ graph}\right) \qquad translation\ achieved$$

$$C_d'\big|^{prototype} = C_d\big|^{standard\ graph}\left(\alpha'_{standard\ graph}\right) \qquad (2.65)$$

Two major issues exist with this approach. The first issue is the prototype mapping dependence on $C_d\big|_{PR=1}^{prototype}$ which must be measured or approximated by some method. The second major issue is determining the value of the variable $C_d'\big|_{PR=1}^{prototype}$ once $C_d\big|_{PR=1}^{prototype}$ is known. Fortunately a few ideas have been developed and will be explained in the following sections. Also shown are published results for $C_d\big|_{PR=1}^{axisymmetric}$ shown in Linfield (2000) and restated here as **Table 4-3** through **Table 4-5**.

Table 4-3 Published values of $C_d\big|_{PR=1}$ for a 90° slot and conical orifice with an aspect ratio $AR = 0$.

Author	Year	$C_d\big\|_{PR=1}^{planar}$	$C_d\big\|_{PR=1}^{axisymmetric}$
Analytical Solution		0.6110154…	
Rouse & Abul-Fetouh	1950		0.612
Garabedian	1956		0.579
Hunt	1967		0.578
Bloch	1969		$0.59131 \leq C_d \leq 0.59139$
Alder	1976	0.611	0.591
Pickett	1989	0.61101564	
Linfield	2000	0.61102	0.59137

Table 4-4 Published values of $C_d\big|_{PR=PR_{crit}}$ for a 90° slot and conical orifice with an aspect ratio $AR = 0$ and $k = 7/5$.

Author	Year	$C_d\big\|_{PR=PR_{crit}}^{planar}$	$C_d\big\|_{PR=PR_{crit}}^{axisymmetric}$
Chaplygin	1902	0.74	
Norwood	1962	0.745	
Alder	1976	0.745	0.726
Kosolapov & Sivoborod	1984	0.76	
Pickett	1989	0.744559129	
Linfield	2000	0.74456	0.72606

Table 4-5 Published values of $C_d|_{PR=PR_{choked}}$ for a 90° slot and conical orifice with an aspect ratio $AR=0$ and $k=7/5$. Note: ( )[1] notes values were obtained from reading a graph by Linfield.

Author	Year	$C_d\|_{PR=PR_{choked}}^{planar}$	$C_d\|_{PR=PR_{choked}}^{axisymmetric}$
Frankl	1947	0.85	
Norwood	1962	0.850	
Benson & Pool	1965	0.853	
Fenain et al	1974		0.837[1]
Alder	1976	0.849	0.830
Filippov et al	1982	0.842	0.819[1]
Kosolapov & Sivoborod	1984	0.85	0.832
Linfield	2000	0.84925	0.83083

4.2.1.7 Discharge Coefficient for Axisymmetric Flow

The discharge coefficient for incompressible axisymmetric flow through a circular orifice is explicitly stated as a function of the wall angle α in equation (2.66). Stated differently, the aspect ratio AR = 0 and the pressure ratio PR = 1.

$$C_d\Big|_{PR=1}^{axisymmetric}=\frac{1}{1+\sqrt{1-\left[\frac{\sin^2\alpha}{2(1-\cos\alpha)}\right]^{\beta}}} \qquad (2.66)$$

Linfield (2000) modified the β term from the exact solution of β=2 to β=0.94 to match the numerical value he obtained for a thin plate orifice $C_d|_{PR=1}^{\alpha=90^\circ}\approx 0.591$. The output from equation (2.66) is compared to the discharge coefficient obtained for incompressible flow through a planar flow restriction in **Figure 167**. The trends are very similar and the solutions reproduce the classic solutions of $C_d\left(\alpha=0^\circ\right)=1$ and $C_d\left(\alpha=180^\circ\right)=\frac{1}{2}$ respectively. Notice that the incompressible discharge coefficient through a circular orifice is shown to be only slightly lower than the planar flow counterpart.

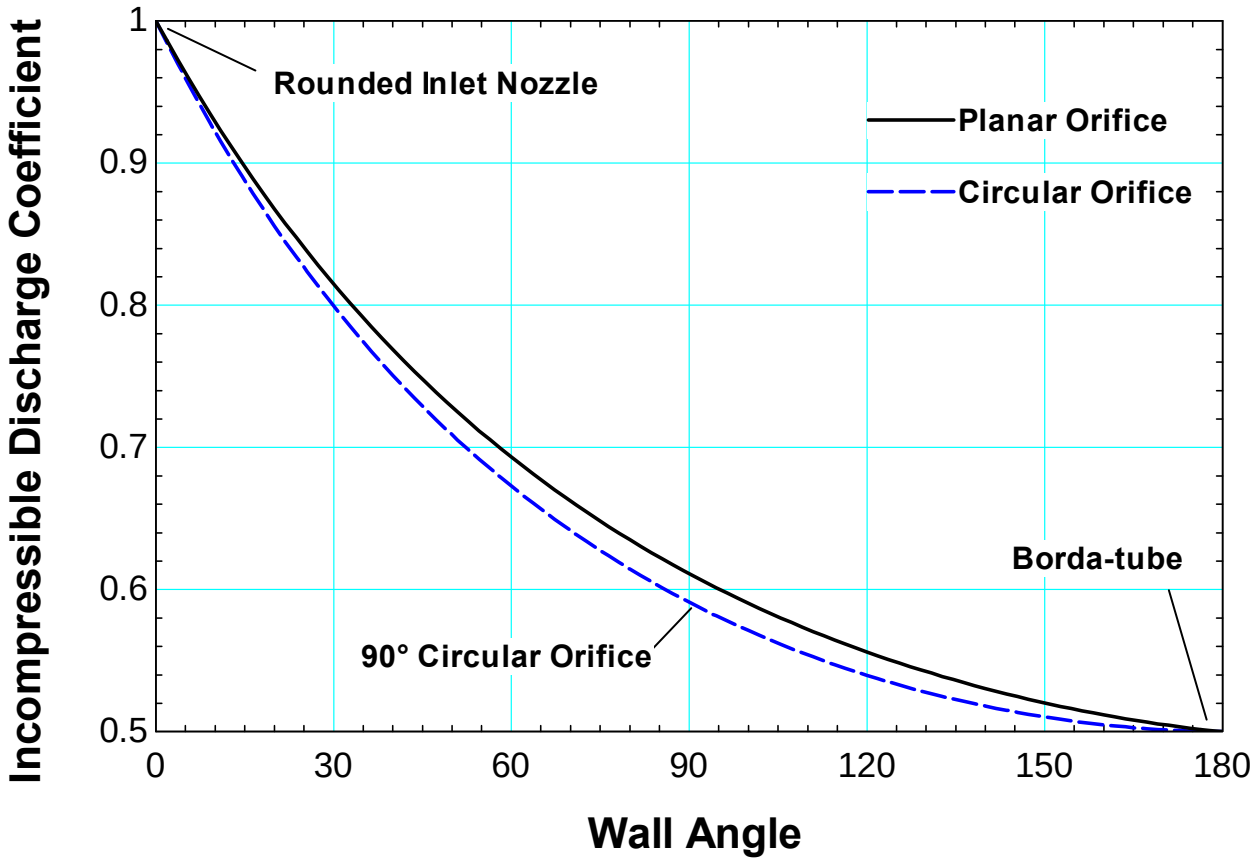

Figure 167 Discharge coefficient for *PR=1* as a function of wall angle α for planar flow and axisymmetric flow, k=1.4

4.2.1.8 Conical Orifices with Edge Rounding

Smoothing of the inlet flow pattern can also take place if the lip geometry is sufficiently rounded so that the flow remains attached to the wall of the orifice during the expansion process. The idea is to virtually eliminate any deviation between the area of the orifice and that of the vena contracta by retarding separation of the boundary layer. This is effectively why a long-radius nozzle such as the ISA 1932 referenced in White (2008) maintains a discharge coefficient near unity.

Edge rounding of the inlet lip is accommodated in the *Standard Graph* approach by solving equations (2.67) through (2.69) for the effective wall angle $\hat{\alpha}$. Once this value is obtained, the effective wall angle is used in equation (2.66) to locate the approximate incompressible discharge coefficient to be used in the *Standard Graph* approach.

$$\hat{\alpha} = \max\left(\alpha - \Delta\alpha, 0\right) \quad (2.67)$$

$$\Delta\alpha = A(\alpha)\ln\left[\left(\frac{R_{lip}}{d_h}\, x1000\right)^2 + 1\right] \quad (2.68)$$

$$A = 0.04626\alpha + 0.01163\alpha^2 \quad (2.69)$$

A combination of curve-fits and limiting restraints were used to construct the empirical relationships provided above. The two limits imposed on the empirical relationship are shown here in equation (2.70).

$$C_d(\alpha)\Big|_{\frac{R_{lip}}{d_h}\to 0} = C_d(\alpha)$$
$$C_d\Big|_{\frac{R_{lip}}{d_h}\geq 0.82} \approx 0.99 \qquad (2.70)$$

Note that an "ideal" sharp lip orifice is a non-physical object; there will always be blunting of the inlet lip as a result of any manufacturing process. For this reason, flow separation will always occurs slightly aft of the leading edge of the orifice. To a working approximation, the International Standards Organization (ISO, 1980) had defined a sharp lip for an orifice flow meter based on equation (2.71).

$$\frac{R_{lip}}{d_h} \leq 0.0004 \qquad (2.71)$$

The other limit discerned from equation (2.70) can be justified based on the listed ASME standard (1961) referenced by Linfield (2000) which stipulates that for all practical working approximations the discharge coefficient is approximately unity for rounded inlets where $\frac{R_{lip}}{d_h} \geq 0.82$. The model seems to under predict the discharge coefficient in this limit as is illustrated in **Figure 168** where $\frac{R_{lip}}{d_h} \geq 10$ seems to predict discharge coefficients closer to unity.

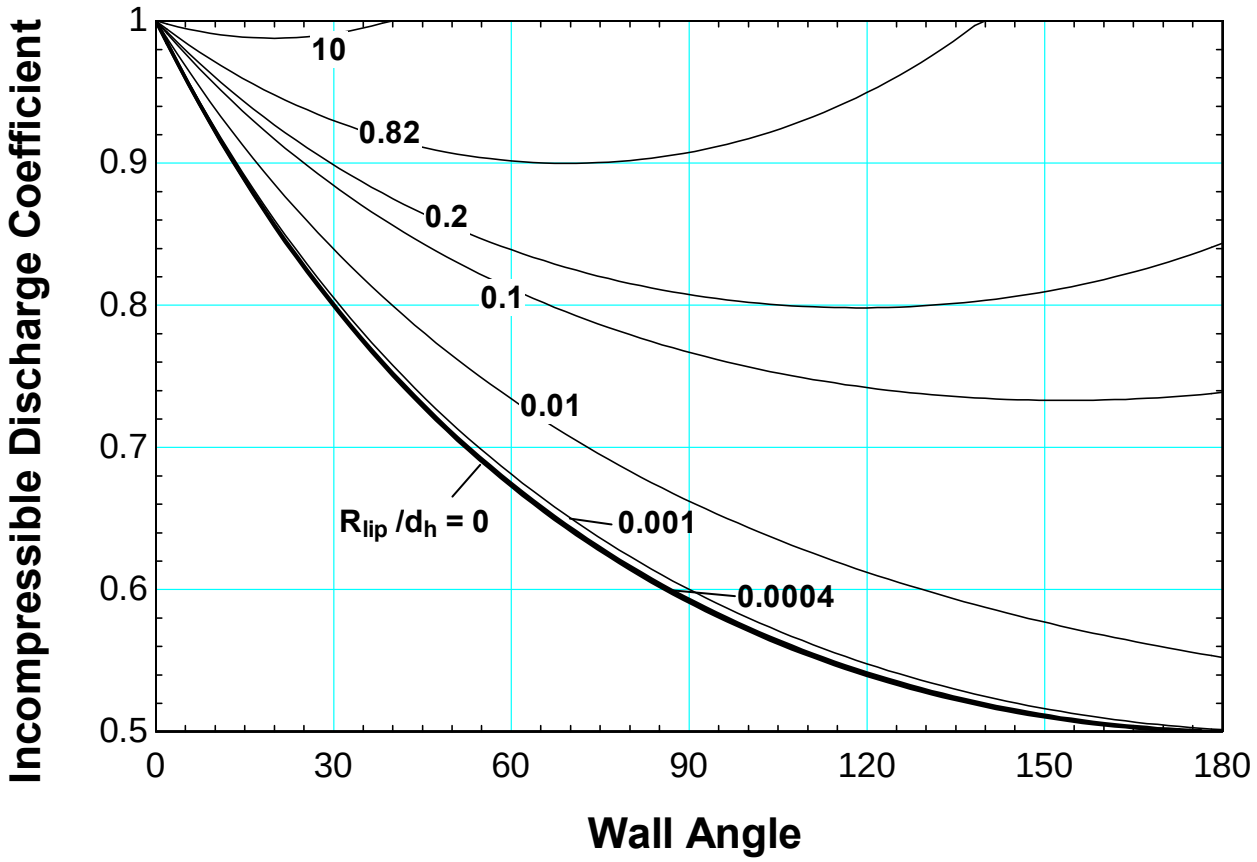

Figure 168 Discharge coefficient for *PR=1* as a function of wall angle α for flow through a restriction with different ratios of the lip radius to the diameter of the orifice, k=1.4

4.2.2 Major Pipe Losses which occur during Reattachment

Just as one could visualize the total pressure drop in a system as a compilation of major and minor losses, one could also break the problem down further by recasting the 'major losses' term in proportion to its constituents. This situation leads to equation (2.72) which states that an axial flow subject to major losses alone (i.e. no form losses) will still incur a pressure loss due to frictional, accelerant, and gravitational effects.

$$\underbrace{\Delta P_{pipe-flow}}_{major\ losses} = \Delta P_{frict} + \Delta P_{accel} + \Delta P_{grav} \qquad (2.72)$$

This section is primarily concerned with losses related to friction and flow development which occurs after the sudden expansion form loss detailed in Section 4.2.1.

Ward-Smith (1984) details that a relationship exists between the critical discharge coefficient C_d and orifice length to orifice diameter $\frac{L}{D_h}$. In particular, he illustrates that the functional relationship illustrated in **Figure 169** applies to circular orifices with $\frac{L}{D_h}$ ratios in the range shown.

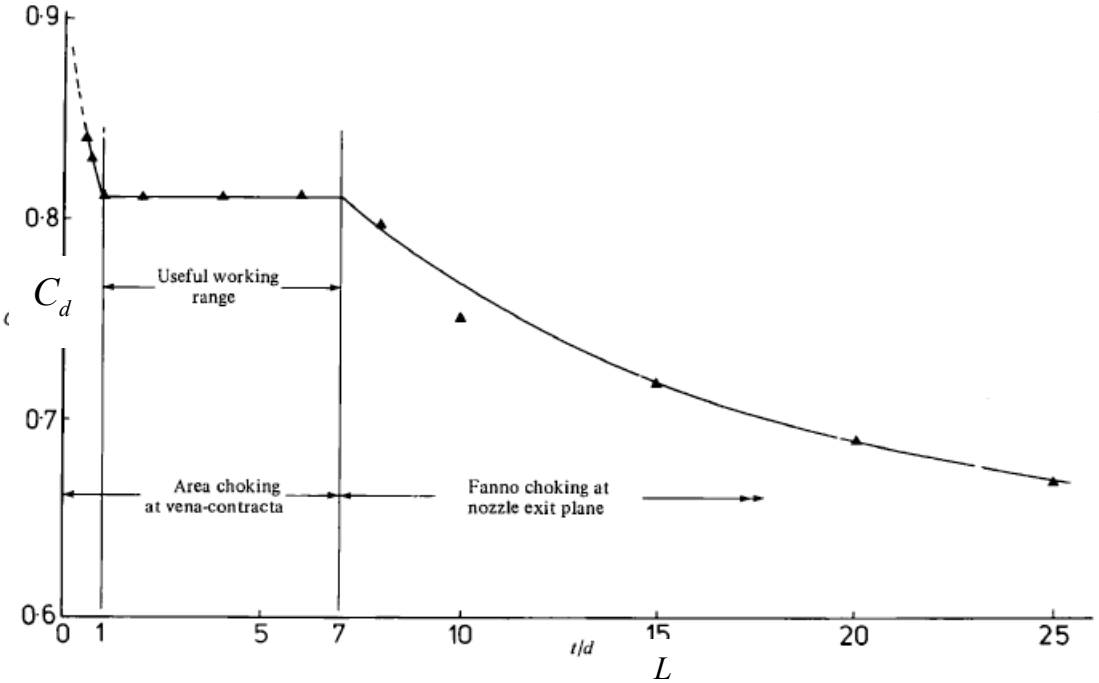

Figure 169 Functional relationship between discharge coefficient and the ratio of the orifice length to the orifice diameter. Reproduced from Ward-Smith (1979).

The following sections detail specific methods for estimating the frictional and accelerant pressure drops which occur aft of the orifice inlet.

4.2.2.1 Frictional Pressure Drop

Laminar Flow

The following discussion is a compilation of the information provided in Nellis and Klein (2009) and White (2008). The primary focus is to address the frictional pressure drop in the wake of the form loss step change in pressure addressed in Section 4.2.1.

Analytical solutions for laminar flow in a duct subject to friction have been obtained for various geometrical conditions. Laminar flow is especially susceptible to deviations in geometrical conditions so it stands to reason that exact solutions in this regime need to take into consideration all geometrical boundaries present in the duct of interest.

Nellis and Klein (2009) have published the exact solutions for hydrodynamically fully developed flow through a circular duct as shown in equation (2.73), flow through a concentric annulus in equation (2.74), and finally flow through two parallel plates in equation (2.75). Note that as the aspect ratio *RR* in equation (2.74) approaches 0 or 1, the equation naturally simplifies to flow through a cylinder and flow through two parallel plates respectively.

$$f_{fd,h} = \frac{64}{\mathrm{Re}_{D_h}} \quad (2.73)$$

$$f_{fd,h} = \frac{64}{\mathrm{Re}_{D_h}} \sqrt{\frac{\left(1-RR\right)^2}{1+RR^2-\left(\frac{1-RR^2}{\ln\left(RR^{-1}\right)}\right)}}$$

$$RR = \frac{R_{inner}}{R_{outer}} \qquad (2.74)$$

$$f_{fd,h} = \frac{96}{\mathrm{Re}_{D_h}} \qquad (2.75)$$

The average friction factor for laminar flow which includes entrance effects is given by Shah and London (1978) as was published in Nellis and Klein (2009). The formula is exact for a circular tube where $f_{fd,h}\,\mathrm{Re}_{D_h} = 64$ but was shown in Nellis and Klein (2009) to perform well under other geometrical conditions. The dimensionless length L^+ for hydrodynamically developing internal flow is reproduced here in equation (2.77).

$$\overline{f} \approx \frac{4}{\mathrm{Re}_{D_h}}\left[\frac{3.44}{\sqrt{L^+}} + \frac{\frac{1.25}{4L^+} + \frac{\overbrace{\left(f_{fd,h}\,\mathrm{Re}_{D_h}\right)}^{duct\ shape\ dependence}}{4} - \frac{3.44}{\sqrt{L^+}}}{1+\frac{0.00021}{\left(L^+\right)^2}}\right] \qquad (2.76)$$

$$L^+ = \frac{L}{D_h\,\mathrm{Re}_{D_h}} \qquad (2.77)$$

Turbulent Flow

Turbulent flow is effectively insensitive to duct shape but highly dependent on surface roughness. In this regime, kinetic energy is dissipated along the duct's wall via the viscous sublayer which can be on the order of the wall roughness if the material is course enough. The standard approach is to use either the Blasius (1911) solution shown in equation (2.78) if the walls are "smooth" or use the Colebrook (1939) solution presented in equation (2.79). Other explicit turbulent friction factor equations have been proposed throughout the years such as the one for multi-phase flow proposed by Churchill (1977) shown in equation (2.80). All of these equations are based on the Darcy friction factor definition.

$$Blasius\left(1911\right) \qquad f_{fd,h,e=0} = \frac{0.316}{\mathrm{Re}_{D_h}^{0.25}} \qquad 4000 < \mathrm{Re}_{D_h} < 10^5 \qquad (2.78)$$

$$Colebrook\left(1939\right) \qquad \frac{1}{\sqrt{f_{fd,h}}} = 3.48 - 1.7373\ln\left(\frac{2e}{D_h} + \frac{9.35}{\mathrm{Re}_{D_h}\sqrt{f_{fd,h}}}\right) \qquad (2.79)$$

$$Churchill\,(1977)\;\; f_{2\phi,fd,h} = 8\left\{\left(\frac{8}{\mathrm{Re}}\right)^{12} + \left(\left[2.457\ln\left(\frac{1}{\left(\frac{7}{\mathrm{Re}}\right)^{0.9} + 0.27\left(\frac{e}{D_h}\right)}\right)\right]^{16} + \left(\frac{37530}{\mathrm{Re}}\right)^{16}\right)^{-1.5}\right\}^{\frac{1}{12}} \tag{2.80}$$

The friction factor is used to compute the pressure drop according to equation (2.81) for a single phase fluid.

$$f = \tau_s \frac{8}{\rho U_m^2} = -\frac{dP}{dx}\frac{2D_h}{\rho U_m^2} \tag{2.81}$$

A number of models exist to compute the pressure drop for a two-phase fluid. The empirical model proposed by Müller-Steinhagen and Heck (1986) shown here as equations (2.82) through (2.87) was shown in Ould Didi et al. (2002) to provides excellent agreement with experimental data across a number of different two-phase flow regimes.

$$\left.\frac{dP}{dz}\right|_{fric,2\phi} = \Lambda\left(1-x\right)^{\frac{1}{3}} + \left.\frac{dP}{dz}\right|_{go} x^3 \tag{2.82}$$

$$\Lambda = \left.\frac{dP}{dz}\right|_{lo} + 2\left(\left.\frac{dP}{dz}\right|_{go} - \left.\frac{dP}{dz}\right|_{lo}\right)x \tag{2.83}$$

$$\left.\frac{dP}{dz}\right|_{lo} = f_l \frac{2G^2}{D_h \rho_l} \tag{2.84}$$

$$\left.\frac{dP}{dz}\right|_{go} = f_g \frac{2G^2}{D_h \rho_g} \tag{2.85}$$

$$f_{MSH,\phi} = f_\phi\left(e, \mathrm{Re}_{D_h}\right) \tag{2.86}$$

$$f_{MSH,\phi:fd,h,e=0} = \underbrace{\frac{0.079}{\mathrm{Re}_\phi^{0.25}}}_{\substack{\text{Correlation based on} \\ \text{Fanning friction factor}}} \tag{2.87}$$

The subscripts *l* and *g* denoted in the model stand for liquid and gas phase constituents respectively. *G* refers to the mass flux through the test section defined by equation (2.88) and the Reynolds' number Re_ϕ can be calculated for each phase based on equation (2.89).

$$G = \frac{\dot{m}}{A_c} \tag{2.88}$$

$$\mathrm{Re}_{D_h,\phi} = \frac{GD_h}{\mu_\phi} \tag{2.89}$$

Note that the friction factors used in equations (2.84) and (2.85) refer to the Fanning friction factor and not the Darcy friction factor obtained from equations (2.73) through (2.80). This concept is readily identified by

comparing equations (2.87) and (2.78). As such, any friction factor calculated by the Colebrook equation or Churchill equation should be divided by a factor of 4 in order to use in equations (2.84) and (2.85). The conversion is appropriately shown in equation (2.90).

$$\underbrace{f_{MSH,\phi}}_{\substack{Correlation\ based\ on \\ Fanning\ friction\ factor}} = \underbrace{\frac{f_{Colebrook}; f_{Churchill}}{4}}_{\substack{Correlation\ based\ on \\ Darcy\ friction\ factor}} \tag{2.90}$$

The average turbulent flow friction factor which includes entrance effects as shown in Nellis and Klein (2009) is reproduced here as equation (2.91).

$$\overline{f} = f_{fd,h}\left(1+\left(\frac{D_h}{L}\right)^{0.7}\right) \tag{2.91}$$

4.2.2.2 Acceleration Pressure Drop

The following discussion pertains to density driven pressure drops due to acceleration of the flow. The general equation for this type of pressure loss is provided in (2.92).

$$\Delta P_{accel} = G^2\left[\frac{1}{\rho_{out}} - \frac{1}{\rho_{in}}\right] \tag{2.92}$$

Single phase flows are not generally sensitive to this type of pressure loss. Two-phase flows are more vulnerable to this type of pressure loss and may be modeled using the density information provided in EES as well as the aforementioned equation attributed to Isbin et al. (1958) originally defined in equation (0.10) but reproduced here as equation (2.93).

$$\mu_{2\phi,cavity} = \left[\frac{x}{\mu_g} + \frac{1-x}{\mu_l}\right]^{-1} \tag{2.93}$$

4.2.3 Empirical Model for Labyrinth Seals

Suryanarayanan (2009) extended the work of Gamal et al. (2006, 2008). Suryanarayanan (2009) developed a model for the incompressible discharge coefficient (2.94) and expansion factor (2.95) of a gas through a labyrinth seal. The parameters used in equations (2.94) through (2.99) are identified in **Figure 170**.

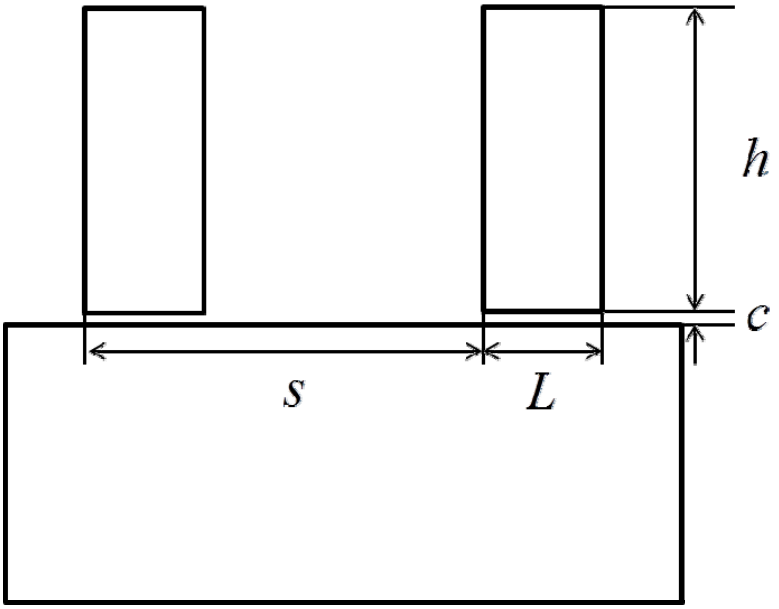

Figure 170 Parameters used in empirical model by Suryanarayanan (2009)

Equation (2.94) represents the incompressible discharge coefficient of the first seal in a labyrinth seal.

$$C_d\Big|_{PR=1}^{1^{st}\,seal} = \frac{0.7757 - 0.002051\,L/c}{\left(1 + 44.86\dfrac{L/c}{\mathrm{Re}_{D_h}}\right)^{0.2157}} \tag{2.94}$$

Equation (2.95) represents a compressibility factor that was determined to vary linearly with pressure ratio.

$$\psi = 0.558\,PR + 0.442 \tag{2.95}$$

The empirical discharge coefficient and compressibility factor are then input into equation (2.96) to determine the mass flux through the labyrinth seal.

$$G_{empirical} = C_d\big|_{labyrinth}\,\psi\sqrt{2\,\rho_{in}\left(P_{in} - P_{out}\right)} \tag{2.96}$$

The model was extended for subsequent throttling by employing the empirical relationships presented in (2.97) through (2.99). Note that equation (2.98) represents an empirical kinetic energy carry-over coefficient which accounts for the exiting flow between adjacent coaxial seals.

$$C_d\Big|_{labyrinth}^{2^{nd}-n^{th}\,seal} = C_d\Big|_{labyrinth}^{1^{st}\,seal}\left(0.925\,\gamma^{0.861}\right) \tag{2.97}$$

$$\gamma = \left(1 - 6.5\left(\frac{c}{s}\right) - 8.638\left(\frac{c}{s}\right)\left(\frac{L}{s}\right)\right)\left(\mathrm{Re} + R_0\right)^{\left(2.454\left(\frac{c}{s}\right) + 2.268\left(\frac{c}{s}\right)\left(\frac{L}{s}\right)^{1.678}\right)} \tag{2.98}$$

$$R_0 = \left(1 - 6.5\left(\frac{c}{s}\right) - 8.638\left(\frac{c}{s}\right)\left(\frac{L}{s}\right)\right)^{\left(\frac{-1}{2.454\left(\frac{c}{s}\right) + 2.268\left(\frac{c}{s}\right)\left(\frac{L}{s}\right)^{1.678}}\right)} \tag{2.99}$$

The applicability of the model is summarized in equation (3.1).

$$
\begin{aligned}
& PR \to 1 \\
& 0.0075 < \frac{c}{s} < 0.0375 \\
& 0.0075 < \frac{L}{s} < 0.5 \\
& 2.67 < \frac{L}{c} < 66.67 \\
& 0.75 < \frac{h}{s} < 4 \\
& 134 < \mathrm{Re}_{D_h} < 15000
\end{aligned} \tag{3.1}
$$

References

Alder, G.M., 1976, Ph.D. thesis. “Transonic Flow through Sharp-Lipped Convergent Nozzles”, University of Edinburgh.

Benson, R.S. and Pool, D.E., 1965, “The Compressible Flow Discharge Coefficients for a Two-Dimensional Slit”, Int. J. Mech. Sci., Vol. 7, pp. 337-353.

Buseman, A., 1937, “Note on Contraction Coefficients of Jets of Gas”, J. Research, US National Bureau of Standards, pp. 765-775.

Chaplygin, S.A., 1902, “Gas Jets”, Scientific Memoirs, Moscow University, English Translation: NACA TM1063, 1944.

Churchill, S.W., 1977, “Friction-factor equation spans all fluid-flow regimes”, Chemical Engineering, Vol. 84 pp. 91-92.

Colebrook, C.F., 1939, “Turbulent Flow in Pipes with Particular Reference to the Transitional Region between the Smooth and the Rough Pipe Laws”, J. Inst. Civil Eng. Vol 11, pp. 133-156.

Dias, F., Elcrat, A.R., and Trefethen, L.N., 1987, “Ideal jet flow in two dimensions”, J. Fluid Mech., vol. 185, pp 275-288.

Fenain, M., Dutouquet, L., and Solignac, J.L., 1974, “Calcul des Performances d’une Tuyere Propulsive Convergente. Comparaison avec L’Experience”, La Recherche Aerospatiale, No. 5, pp. 261-276.

Filippov, G.A., Saltanov, G.A., Sivoborod, V.A., Kosolapov, Y.S., 1982, “Discharge of Gases with Differing Adiabatic Exponents”, Izvestia Akademii Nauk SSSR, Energetika I Transport, Vol. 20, No. 1, pp 121-126, English Translation: Allerton Press Inc.

Frankl, F.I., 1947, “The Flow of a Supersonic Jet from a Vessel with Plane Walls”, Dokl. Akad. Nauk. SSSR Vol. 58, No. 3, pp. 381-384.

Garabedian, P.R., 1956, “The Mathematical Theory of Three-Dimensional Cavities and Jets”, Bulletin of the American Mathematical Society, Vol. 62, pp. 219-235.

Gamal, A.M., Ertas, B.H., and Vance, J.M., High-pressure pocket damper seals: leakage rates and cavity pressures. Proceedings of GT2006 ASME Turbo Expo 2006: Power for Land, Sea, and Air, May 8-11, 2006, Barcelona, Spain.

Gamal, A.M., 2007, Ph.D. thesis. “Leakage and Rotordynamic Effects of Pocket Damper Seals and See-Through Labyrinth Seals”, Texas A&M University, College Station.

Gamal, A.J., and Vance, J.M., 2008, “Labyrinth Seal Leakage Tests: Tooth Profile, Tooth Thickness, and Eccentricity Effects”, ASME, Vol. 130.

Gurevich, M.I., 1965, “The Theory of Jets in Ideal Fluids”, Academic Press, New York.

Hunt, B.W., 1968, “Numerical Solution of an Integral Equation for Flow from a Circular Orifice”. J. Fluid Mech., Vol. 31, pp. 361-377.
Isbin et al. (1958)

Klein, S.A. and Nellis, G.F., 2011, *Thermodynamics*, UW-Madison DoIT bookstore.

Kosolapov, Y.S. and Sivoborod, V.A., 1984, “Theoretical and Numerical Investigation of the Flow of Gas from Flat Slits and Axisymmetric Openings”, Izvestiya Akademii Nauk SSSR, Mekhanika Zhidkosti I Gaza No. 2, pp. 109-115, English Translation.

Linfield, K.W., 2000, Ph.D. thesis, “A Study of the Discharge Coefficient of Jets from Angled Slots and Conical Orifices”

Moran, M.J., and Shapiro, H.N., 2004, *Fundamentals of Engineering Thermodynamics*, 5th edition, Wiley,

Müller-Steinhagen, H., and Heck, K.A., 1986, “A simple friction pressure drop correlation for two-phase flow in pipes”, Chemical Engineering Processing, Vol. 20, pp. 297-308.

Nellis, G.F., and Klein, S.A., 2009, *Heat Transfer*, Cambridge: New York.

Norwood, R.E., 1962, “Two Dimensional Transonic Gas Jets”, Proc 4th US National Congress of Applied Mechanics, Vol. 2, pp. 1359-1367.

Ould Didi, M.B., Kattan, N., and Thome, J.R., 2002, “Prediction of two-phase pressure gradients of refrigerants inside horizontal tubes”, International Journal of Refrigeration, Vol. 25, pp. 935-947.

Pickett, J.S., 1989, “The Generalization and Evaluation of Solutions Occuring in Chaplygin’s Ideal Gas Jet Theory”, University of Toronto M.A.Sc. thesis.

Rouse, H., and Abul-Fetouh, A., 1950, “Characteristics of Irrotational Flow Through Axisymmetric Orifices”, J. App. Mech., pp. 421-426.

Shah, R.K. and London, A.K., 1978, *Laminar Flow Forced Convection in Ducts*, Academic Press, New York.

Shapiro, A.H., 1953, “The Dynamics and Thermodynamics of Compressible Fluid Flow”, Vol. 1 and 2, Ronald Press, New York.

Suryanarayanan, S., 2009, M.S. thesis, “Labyrinth Seal Leakage Equation”, Texas A&M University, College Station.

Ward-Smith, A.J., 1979, “Critical Flowmetering: The Characteristics of Cylindrical Nozzles with Sharp Upstream Edges”, Int. J. Heat & Fluid Flow, Vol. 1 No. 3 pp. 123-132.

White, F.M., 2008, *Viscous Fluid Flow*, McGraw-Hill.

4.3 Experimental Test Facility

The experimental apparatus designed and fabricated to aid in this research was developed to measure the flow rate of carbon dioxide driven by large pressure drops through typical shaft seal geometries. The design challenge was to construct a test facility that would operate continuously in the vicinity of the critical point of carbon dioxide (304.1K, 7.4MPa). Stability, low relative error and flexibility were identified as major design goals in the development of this test facility.

An analysis of the major components in the system as well as the methodology employed to design this test facility is provided in the sections that follow. Capturing phenomena near the critical point presents an interesting challenge as thermodynamic conditions vary substantially in this region making testing with any degree of accuracy particularly troublesome. A great deal of effort has been placed in the refinement of this test facility to meet the design challenges encountered in this project.

4.3.1 Experimental objectives, motivation, and approach

The objective of this research is to measure the flow of carbon dioxide through a shaft-seal interface driven by a large pressure gradient. The fluid parameters studied in this analysis include the upstream pressure, upstream density, and the downstream pressure. The seal geometry is manipulated to change the available flow area as well as other parameters that have been shown to vary the discharge coefficient. A conceptual illustration of the critical parameters is provided in **Figure 171**.

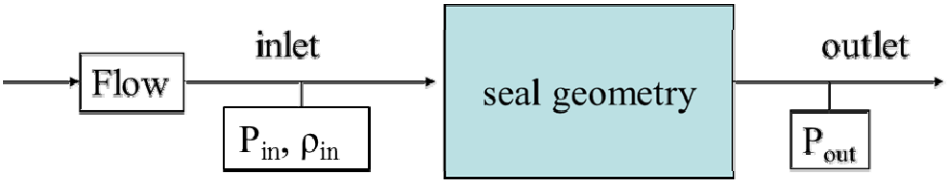

Figure 171 Critical parameters outlined for test facility

The motivation for this project is the necessity to quantify the leakage of supercritical carbon dioxide driven through large pressure gradients. The results of this project are crucial to the development of the overall S-CO_2 Brayton cycle. The current objective is to develop good engineering models to understand the fundamental process of a fluid at non-ideal gas conditions undergoing a rapid expansion. The derivation of the original compressibility model shown in Chapter 2 considers the ideal gas relationship outlined here as equation (3.2). One aspect of this research aims to see how significantly the flow deviates from the model based on the compressibility of an ideal gas.

$$pv^k = const \quad (3.2)$$

The desired ranges of the three fluid parameters illustrated in **Figure 171** are listed in **Table 4-6**. Primary importance was placed on designing a test facility to support a controllable and steady inlet thermodynamic state. Property variations in the vicinity of a fluid's critical point are large and facilitate the need for precise measurements and regulation. **Table 4-6** illustrates the requirements set forth in the design methodology behind this test facility; notice that the inlet densities vary over a 600 kg/m^3 span. The explanation for this large density span is illustrated in **Figure 172** where small temperature changes result in exaggerated changes in density along an isobar.

Table 4-6 Test Facility Operating Conditions

PARAMETER	VARIABLE	RANGE

Inlet Density	ρ_{inlet}	200 – 800 kg/m^3
Inlet Pressure	P_{inlet}	7.33 – 14 MPa
Outlet Pressure	P_{outlet}	1.4 – 14 MPa

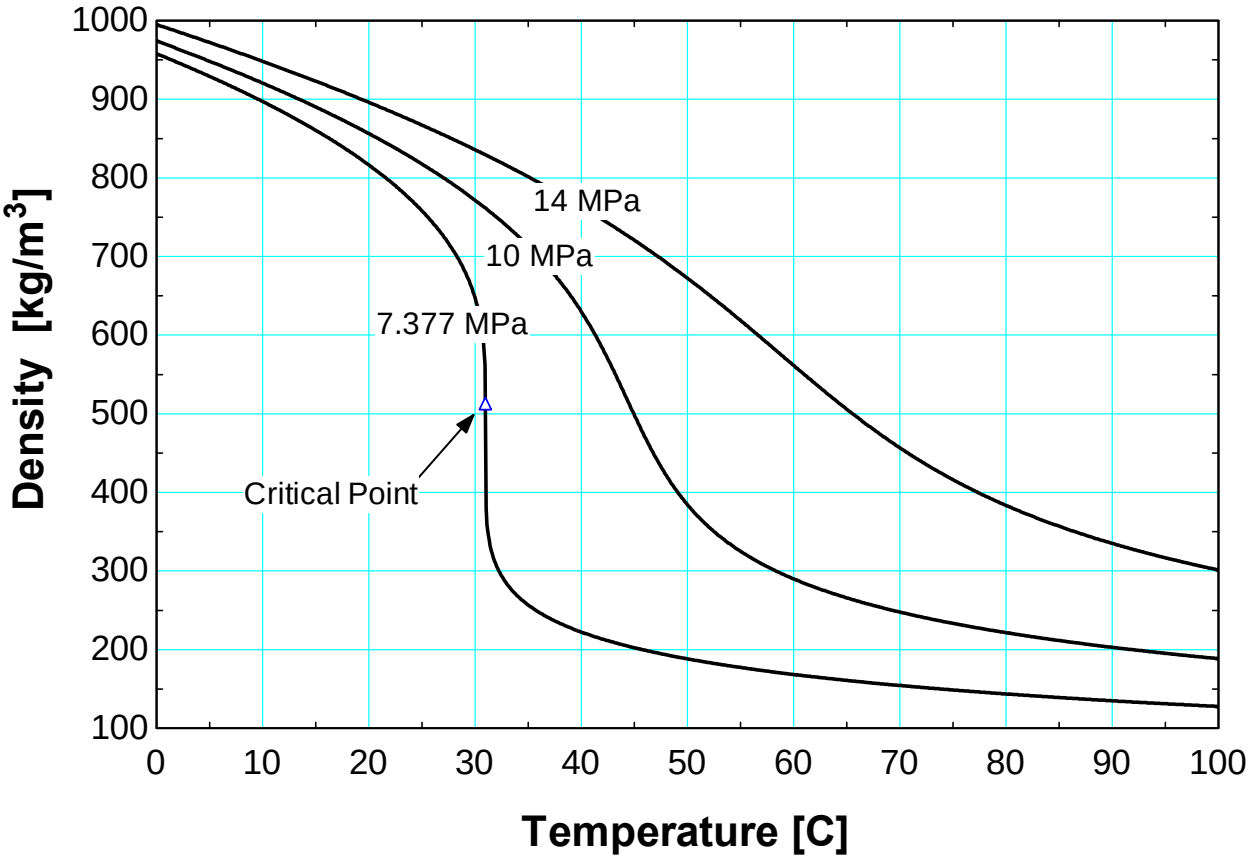

Figure 172 Thermodynamic property variation of carbon dioxide near the critical point

The approach taken in this project was to construct a test facility that would continuously cycle carbon dioxide through a constricted interface. An overview of the test facility conceived for this project is shown in **Figure 173**. The facility supports high pressures on the order of 14 MPa and two-phase downstream conditions.

Figure 173 shows a schematic of the measurement instrumentation integrated with the compression loop test facility. The crucial instrumentation used in this facility include a coriolis flow meter that measures the mass flow rate and density at the inlet to the test section as well as two pressure transducers that measure the pressures at the inlet and outlet of the test section. Type-E thermocouples are also placed throughout the facility.

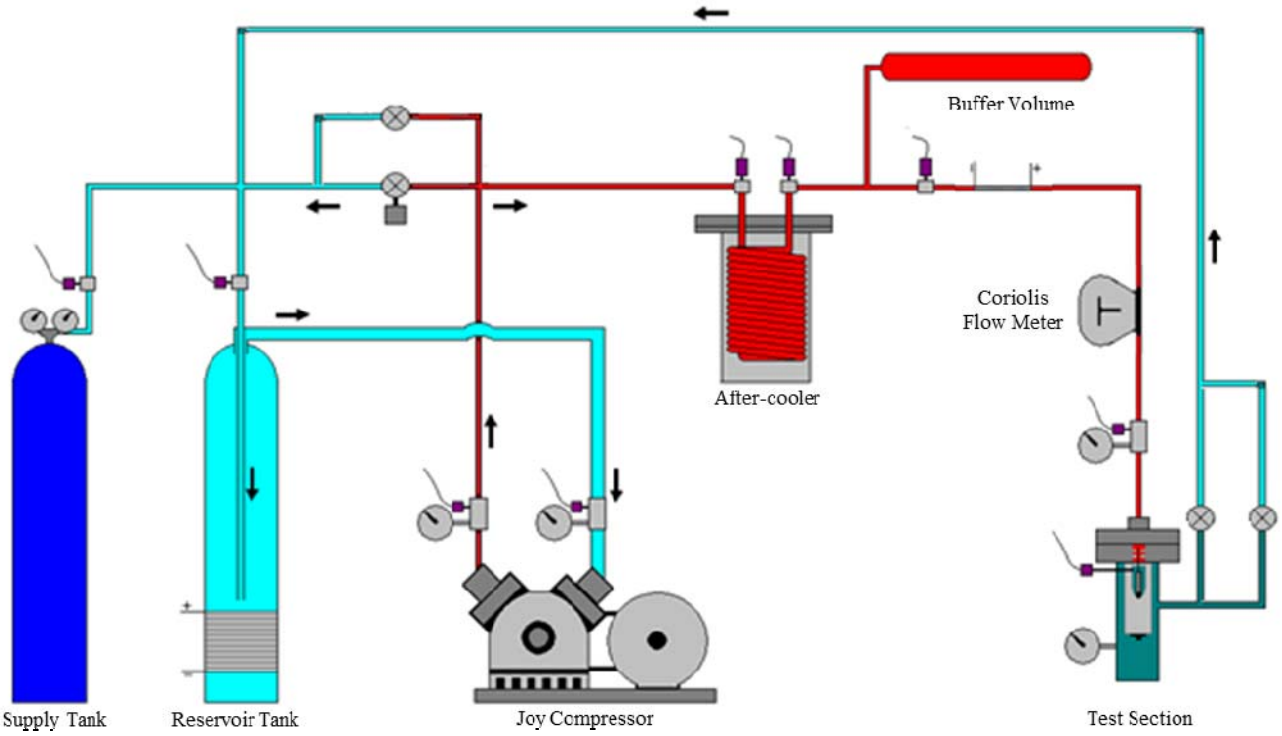

Figure 173 Test facility schematic; red=high pressure, cyan=low pressure

Figure 173 has been color-coded to provide an overview of the pressures in the system. The lines highlighted in red note the highest pressures found in the system and range from 7.4 -14 MPa. The dark cyan color notes the test section downstream pressure which is regulated by two valves anywhere from 1.4 – 14 MPa. The light cyan color represents the compressor inlet pressure which is maintained by the regulator attached to the supply tank from 1.38 – 3.45MPa. The supply tank is shown in blue and is shipped at room temperature as a two phase mixture often at about 5.5 MPa. Arrows are also drawn in the figure noting the direction of flow in that part of the system.

Many design obstacles were encountered in this project as a result of the wide range of thermodynamic conditions experienced by the working fluid. Of note, the fluid exhibits supercritical, two-phase, and gaseous behavior as it is continuously cycled in the loop. First, it is crucial to fix the inlet state as the proximity to the critical point dictates that small temperature deviations will result in large density variations leading to inadequate results. The flow exits the seal geometry as a two-phase mixture and must subsequently undergo a phase-change to cycle through the compressor. This parameter was particularly troublesome as the mass flow rate through the evaporator is highly dependent on the high pressure inlet density and could result in large pressure drops through the duct work if not adequately accounted for in the system. Finally, large pressure drops compounded with large flow rates facilitated the need for large equipment to promote continuous cycling of the working fluid.

4.3.2 Compression Loop Cycle

This section documents the modeling assumptions employed in the development of this test facility. A schematic of the facility is presented in **Figure 174** along with a cycle diagram provided in **Figure 175**. The thermodynamic states shown as 1 through 11 in **Figure 174** correspond to the points detailed in **Figure 175**.

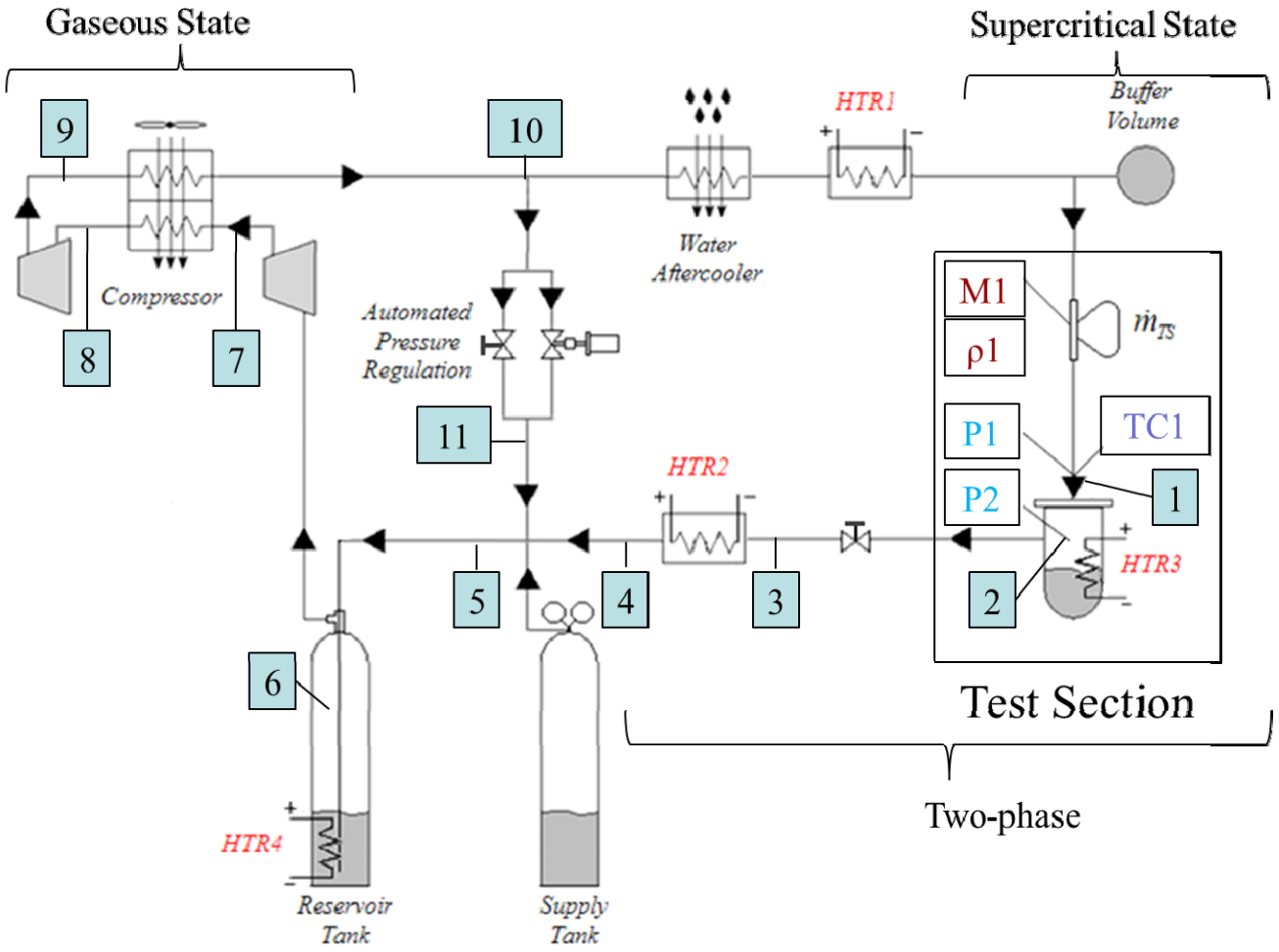

Figure 174 Schematic of UW compression loop facility

Figure 174 highlights the actual test section integrated with the compression loop facility. The primary instrumentation outlined in **Figure 171** is detailed here shown as reference points M1, ρ1, P1, P2, and TC1. These points respectively reference the location of measurement of mass flow rate and density with the coriolis mass flow meter, the upstream and downstream pressures, and the temperature at the inlet to the test facility. The test section is the primary focus of this research where the other components used in this facility are crucial to facility operation to support high capacity flow rates and stable operation. Secondary instrumentation has been omitted for clarity in this schematic.

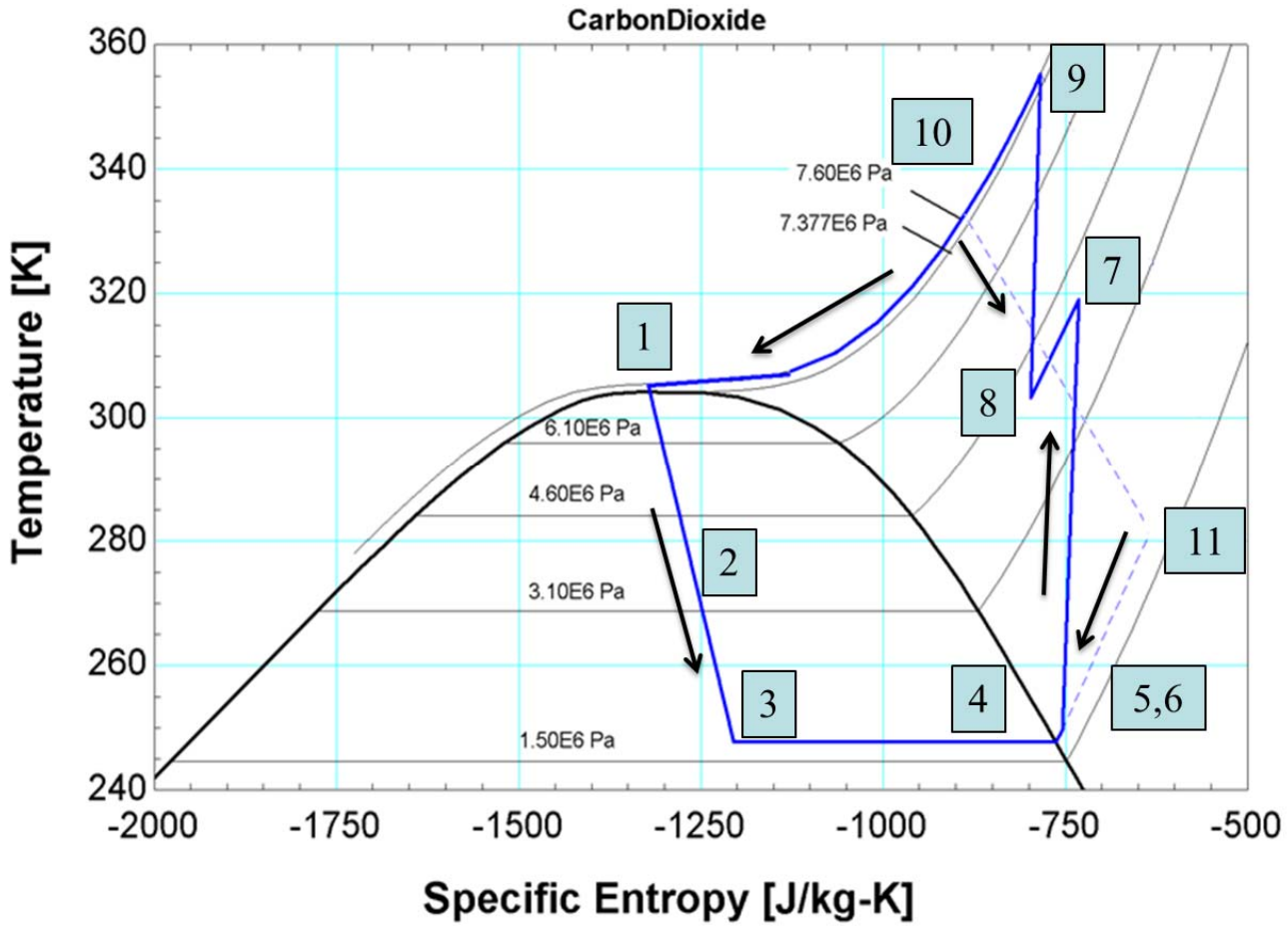

Figure 175 Temperature-entropy diagram of UW-Madison S-CO_2 Compression Loop facility

The cycle diagram in **Figure 175** details the thermodynamic states in the cycle. The primary loop complete with the test section loop is detailed here in blue with the excess loop presented as a dashed line in the background of the figure. The specific entropy of states 1 through 3 vary depending on the desired inlet density. State 1 here is shown in **Figure 175** starting from a nominal value of 7.6 MPa and 305 K which corresponds to an inlet density of about 500 kg/m^3 as seen in **Figure 172**.

The methodology employed in the design of this test facility begins by specifying the desired values for the inlet state as shown in equation (3.3). The thermodynamic state specified is taken above the critical pressure of carbon dioxide at 7.377 MPa with an inlet density near the critical point.

Supercritical Inlet State

$$P_1 = P_{inlet}$$
$$\rho_1 = \rho_{inlet} \qquad (3.3)$$

The specific enthalpy at the inlet state is specified according to equation (3.4) and evaluated in Engineering Equation Solver (EES).

$$h_1 = enthalpy\left(Carbon\ Dioxide, P_1, \rho_1\right) \qquad (3.4)$$

The flow is throttled through the test section to an outlet pressure specified by equation (3.5). The expansion process is presumed to be isenthalpic as expressed in equation (3.6). Note that if the outlet pressure is

sufficiently low, the flow will exit as a two-phase mixture as demonstrated in **Figure 176**.

$$P_2 = P_{outlet} \quad (3.5)$$

$$h_2 = h_1 \quad (3.6)$$

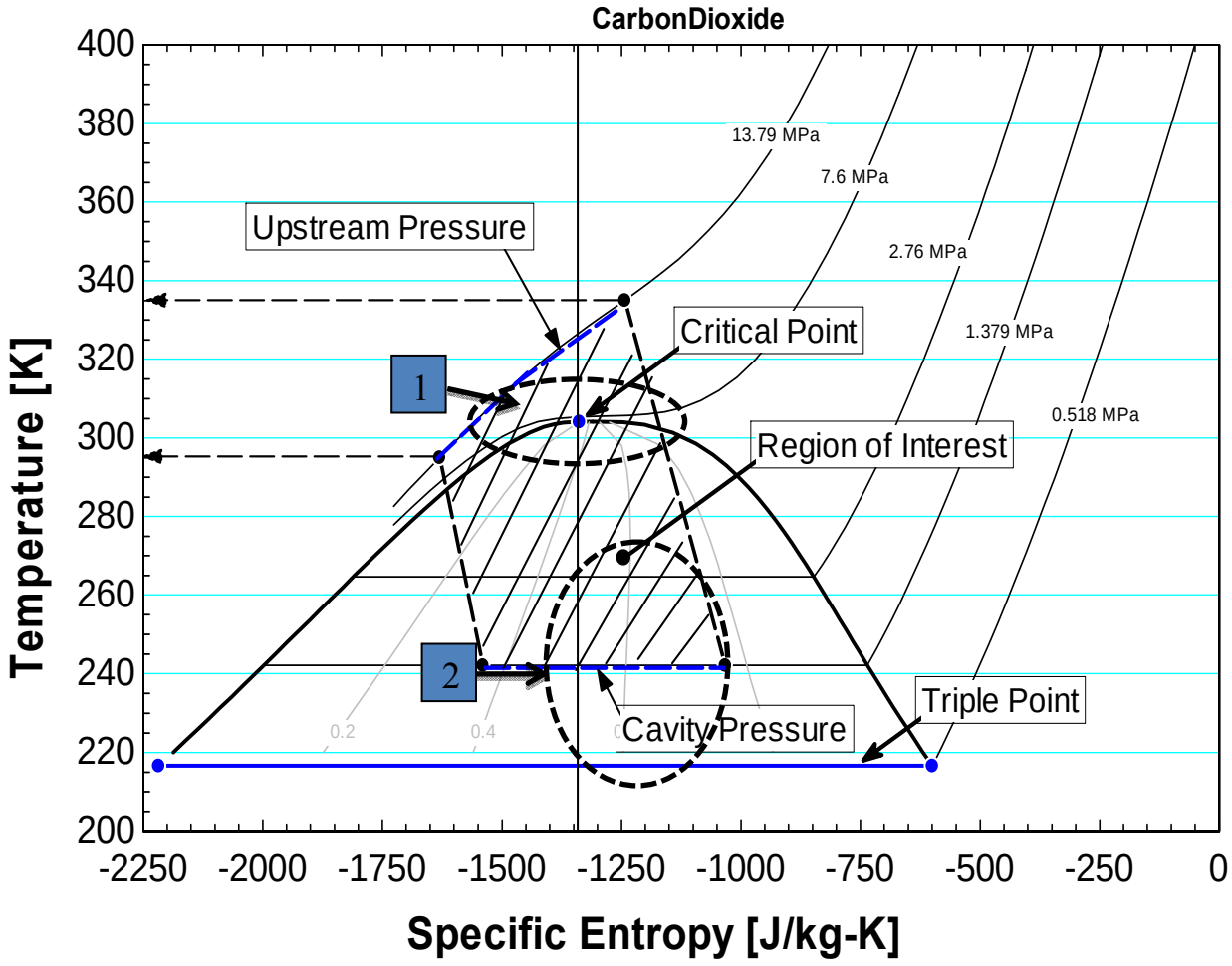

Figure 176 Test facility desired operating range

Figure 176 demonstrates the desired test facility operating range on a property diagram plot. The possible ranges of upstream and downstream states are circled and labeled 1 and 2 respectively. The broad range of test conditions detailed in **Figure 176** demonstrates the importance of designing the facility as flexible as possible in order to meet the range of inlet densities specified in **Table 4-6**.

The flow through the test section then undergoes a secondary throttling process through a valve to reach the lowest pressure of the facility dictated by the compressor inlet pressure as demonstrated in equation (3.7).

$$P_3 = P_{comp-inlet}$$

$$h_3 = h_2 \quad (3.7)$$

The flow is sent through an evaporator as demonstrated in equation (3.8).

$$P_4 = P_3$$
$$\dot{Q}_{evaporator} = \dot{m}_{test-section}\left(h_4 - h_3\right) \quad (3.8)$$

The working fluid cycled through the test section loop is then combined with the fluid from the excess flow loop as demonstrated in **Figure 177**. The mass and energy balances are shown in equation (3.9). Note that the excess flow loop referred to in equation (3.9) is solved in iterative fashion later in the program.

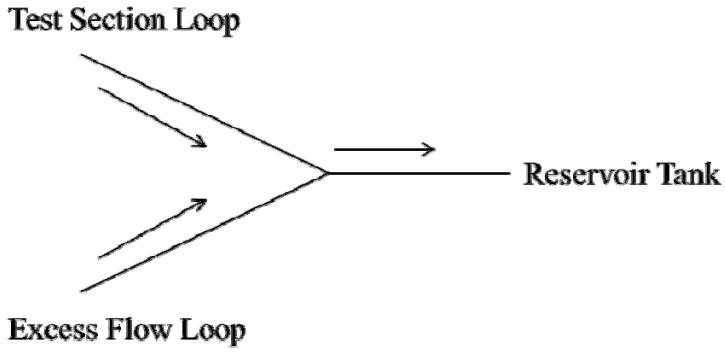

Figure 177 Convergent flow paths entering reservoir tank

$$\dot{m}_{test-section} + \dot{m}_{excess} = \dot{m}_{reservoir}$$
$$\dot{m}_{test-section}h_4 + \dot{m}_{excess}h_{11} = \dot{m}_{reservoir}h_5 \quad (3.9)$$

$$P_5 = P_4 \quad (3.10)$$

The flow is then collected in the reservoir tank as shown in equation (3.9). The tank is used to stratify the liquid and gaseous components of the flow in order to separate any residual liquid out of the flow. The bottle is heated in order to vaporize this residual liquid – the extracted carbon dioxide is then sent to the inlet of the compressor as indicated in equations (3.12) and (3.13).

$$P_6 = P_5 \quad (3.11)$$

$$h_5 = h_l\left(P_5\right) + h_g\left(P_5\right) \quad (3.12)$$

$$h_6 = h_g\left(P_6\right) \quad (3.13)$$

The total pressure differential across the two stages of the compressor is assumed to be split evenly between the two stages as shown in equation (3.14) with no pressure drop across the intercooler as shown in equation (3.15).

$$P_7 - P_6 = P_9 - P_8 \quad (3.14)$$

$$P_8 = P_7 \quad (3.15)$$

The compressor is modeled as two separate stages with both intercooling and after-cooling capability. An

isentropic efficiency of $\varepsilon = 0.85$ is estimated for each stage. The equations for the first stage are implemented in EES as demonstrated in equations (3.16) through (3.19).

$$s_6 = entropy\left(Carbon\ Dioxide, P_6, h_6\right) \quad (3.16)$$

$$s_{7,isentropic} = s_6 \quad (3.17)$$

$$h_{7,isentropic} = enthalpy(Carbon\ Dioxide, P_7, s_{7,isentropic}) \quad (3.18)$$

Equation (3.19) is implicitly solved for h_7 in EES.

$$\varepsilon = \frac{h_{7,isentropic} - h_6}{h_7 - h_6} \quad (3.19)$$

The intercooling stage is modeled as demonstrated in equation (3.20) and (3.22).

$$dT \approx 10^{\circ} C \quad (3.20)$$

$$T_8 = T_{air} + dT \quad (3.21)$$

$$\dot{Q}_{intercooler} = \dot{m}_{compressor}\left(h_8 - h_7\right) \quad (3.22)$$

A second compressor stage is modeled similar to the first with equations (3.24) through (3.27) where the exit pressure returns to the inlet pressure as shown in equation (3.23).

$$P_9 = P_1 \quad (3.23)$$

$$s_8 = entropy(Carbon\ Dioxide, P_8, T_8) \quad (3.24)$$

$$s_{9,isentropic} = s_8 \quad (3.25)$$

$$h_{9,isentropic} = enthalpy\left(Carbon\ Dioxide, P_9, s_{9,isentropic}\right) \quad (3.26)$$

Again, equation (3.27) is implicitly solved for h_9.

$$\eta_{C,isentropic} = \frac{h_{9,isentropic} - h_8}{h_9 - h_8} \quad (3.27)$$

The compressor after-cooling stage is modeled similar to the intercooling stage between the two compression stages.

$$\dot{Q}^1_{intercooler} = \dot{Q}^2_{intercooler} \quad (3.28)$$

The flow splits at this point and is governed by the required flow rate through the test section. The mass balance governing this process was shown previously in (3.9) but shown here as (3.29) for reference.

$$\dot{m}_{compressor} = \dot{m}_{test-section} + \dot{m}_{excess} \quad (3.29)$$

The amount of cooling required to return to the inlet state P_1, ρ_1 is provided by equation (3.30).

$$\dot{Q}_{aftercooler} = \dot{m}_{test-section}\left(h_{10} - h_1\right) \quad (3.30)$$

The residual flow is cycled back through the excess loop and modeled as an isenthalpic throttling process with equation (3.31).

$$h_{10} = h_{11} \quad (3.31)$$

4.3.3 Extensive Cycle Estimates

The pressure drop due to form losses only was used as a baseline when designing this facility. The equipment needed to be of adequate size to accommodate the large density and pressure gradients in this test facility.

The most crucial aspect of this facility was making a preliminary estimate of the flow rate. Conceptually, **Figure 176** shows that the fluid starts off from an initially supercritical state and proceeds through a throttle to a two-phase region. These conditions ensure that the flow will cavitate and make modeling the flow particularly troublesome. The approach used in the development of this facility was to use the single phase isentropic expansion model described in Chapter 2 to estimate the mass flow rate through the geometry used at Sandia National Laboratories and compare it to the information reported in Wright et al (2009) as shown here in **Table 4-7**.

Table 4-7 Reported leakage flow rate estimates and measurements reported in Wright et al (2009) compared to single-phase isentropic flow model developed in Chapter 2

	Barber-Nichols and Sandia National Laboratory	
	Estimate A	Estimate B
Upstream Pressure	13.84 MPa	7.7 MPa
Input Temperature	325 K	325 K
Downstream Pressure	1.38 MPa	1.38 MPa
Diameter of Journal	13.97 mm	13.97 mm
Diametrical Clearance	76.2 μm	76.2 μm
Reported Mass Flow Rate	0.0882 kg/s	0.0326 kg/s
UW Mass Flow Rate	0.105 kg/s	0.0435 kg/s
% Difference	19.0%	33.4%

Estimate A represents the expected thermodynamic state the fluid will be in upon exiting the compressor expanded through the shaft seals to a downstream cavity pressure of 1.38 MPa. *Estimate B* is more indicative of a process where the compressor inlet thermodynamic state is allowed to expand through the shaft seals to a downstream cavity pressure of 1.38 MPa.

Table 4-7 compares the difference between the reported mass flow rate shown in Wright et al. (2009) and the UW model developed in Chapter 2. Note that the results of the UW model shown in **Table 4-7** do not consider two-dimensional effects as the discharge coefficient has been set to unity $C_d = 1$. A facility capable of replicating the working fluid pressures and upstream temperatures was conceived based on the UW methodology

used to model the mass flow rate shown in *Estimate A* of **Table 4-7**.

The next step was to determine the maximum clearance area the facility could support. This value was dictated by two key components: the coriolis mass flow meter and the compressor. The maximum expected flow rate could not exceed the capacity of the flow meter. Likewise, the capacity of the compressor had to support large flow rates delivered at high pressure.

The coriolis flow meter used in this experiment is a CMF010 Rosemount coriolis flow meter with a maximum capacity of 0.03 kg/s. As such, it was necessary to reduce the available flow area in order to decrease the maximum flow rate across the desired 12 MPa pressure drop. Mass flow rates on the order of 0.1 kg/s as estimated in **Table 4-7** were not possible with this flow meter.

The size of the compressor required to support flow rates on the order of 0.1 kg/s delivered at 13.8 MPa posed the largest limitation to this research. A simple analysis of the required volumetric flow rate at standard temperature and pressure conditions (STP) corresponding to a mass flow rate of 0.1 kg/s is presented below in equation (3.32). It shows that the required volumetric flow rate is about 115 scfm.

$$\begin{aligned}
&\dot{m}_{test-section} = 0.1\frac{kg}{s} \\
&\rho_{STP} = density\left(Carbon\ Dioxide, P = 101.325 kPa, T = 20\,^{\circ}C\right) = 1.84\frac{kg}{m^3} \\
&\dot{m}_{test-section} = \rho_{STP}\dot{V}_{STP} \\
&\dot{V}_{STP} = 0.054\frac{m^3}{s} = 115\,scfm
\end{aligned} \tag{3.32}$$

A compressor capable of delivering a capacity dictated by equation (3.32) at pressures of 13.8 MPa was not available at the time of this initial estimate. Delivery was also on the order of 24 weeks so the effort to test geometry similar to that at Sandia National Laboratories was left to a later date.

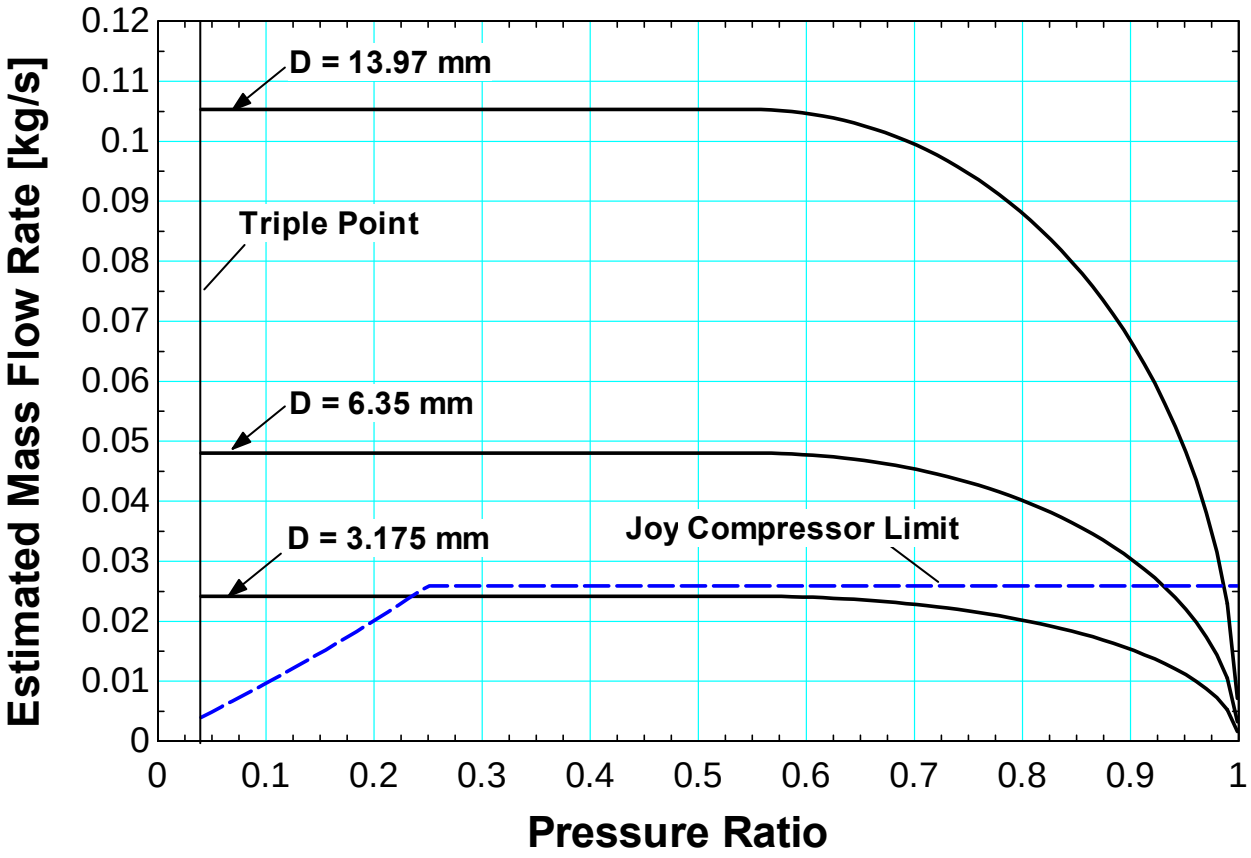

Figure 178 Estimate of mass flow rate for several different journal diameters at an inlet pressure of 13.8 MPa and temperature of 325 K. Compressor limit based on equation (3.34) through (3.40)

The flow area was reduced to accommodate a lower flow rate. **Figure 178** demonstrates the importance of reducing the diameter of the shaft journal in this test series. The reduction in area was accomplished by reducing the journal diameter size as demonstrated in **Figure 178**. The clearance area was kept at a prototypical level of 76.2 μm for each case. The final iteration showed that flow rates through shaft diameters on the order of $D = 3.175 mm$ could be tested with the available equipment. The estimated volumetric flow rate through the compressor based on a similar analysis exemplified in equation (3.32) is shown here as equation (3.33).

$$\dot{m}_{test-section} = 0.03 \frac{kg}{s}$$

$$\dot{V}_{STP} = 0.016 \frac{m^3}{s} = 34 \, scfm \qquad (3.33)$$

Notice that the mass flow rate through prototypical geometry identified in **Table 4-7** is shown to exceed the estimated capacity of the available Joy compressor. A photograph of this compressor is provided in **Figure 179** along with a specification sheet provided in **Table 4-8** Clearance area about shafts with diameters of $D = 13.97 mm$ and prototypical diametrical clearances of 76.2 μm were clearly unattainable. The following analysis demonstrates the estimated capacity of the Joy compressor shown here in equation (3.34) through (3.40) .

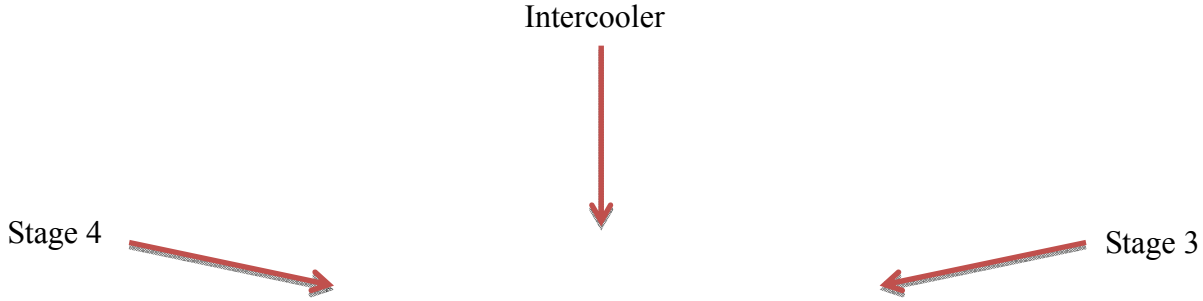

Figure 179 Four stage piston-type Joy compressor with the bottom two stages 1 and 2 not used in this experiment

Table 4-8 Measured Joy compressor parameters

PARAMETER	VARIABLE	RANGE
Third Stage		
Stroke	$S\|_{comp}^{3^{rd}}$	5.715 cm
Bore	$B\|_{comp}^{3^{rd}}$	2.680 cm
Volume	$V\|_{comp}^{3^{rd}}$	32.23 cm^3
Fourth Stage		
Stroke	$S\|_{comp}^{4^{th}}$	5.715 cm
Bore	$B\|_{comp}^{4^{th}}$	1.397 cm
Volume	$V\|_{comp}^{4^{th}}$	8.760 cm^3
Miscellaneous		
Frequency	f_{comp}	1540 rpm

The Joy compressor shown in **Figure 179** used in this research is an old 4-stage piston compressor shown in **Figure 179** where the bottom two low pressure stages could not be used in order to prevent the formation of solid carbon dioxide crystals from forming inside the compressor. The objective was to avoid pressures approaching the triple point of carbon dioxide at 518 kPa

The maximum pressure entering the compressor inlet was restricted to 3.45 MPa as demonstrated by equation (3.34). It was important to stay below this value for two reasons based on the hardware layout of this project. The major restriction was the compressor inlet stage itself. The compressor is old and little to no information

remains about the integrity of the system. At the onset of this project, the compressor was cycled with air and the natural inlet pressure to this stage was quantitatively found to be only slightly higher than 3.45 MPa. The second major restriction was based on the maximum outlet pressure of the regulator used in this project.

$$P_{\max-stage3} = 3.45MPa \quad (3.34)$$

The inlet pressure to the compressor could then be regulated anywhere below the value expressed in equation (3.34) as shown here in equation (3.35).

$$P_{comp-inlet} = \min\left(P_{outlet},\ P_{\max-stage3}\right) \quad (3.35)$$

The saturated vapor density $x = 1$ was determined based on the compressor inlet pressure shown in equation (3.36).

$$\rho_{comp-inlet} = density\left(CarbonDioxide, P = P_{comp-inlet}, x = 1\right) \quad (3.36)$$

The volumetric efficiency of both stages coupled together was approximated based on equation (3.37). Again the bottom two stages are not used to compress carbon dioxide so the cumulative effect of leakage from the high pressure stages into the low pressure stages is unknown. Equation (3.37) is by no means an exact measurement of the coupled-stage volumetric efficiency, but does provide at least a baseline of what one might expect in the system. The volumetric efficiency of each stage was estimated at $\eta\big|_{comp} = 0.65$. The compressor is old and prone to appreciable leakage from the high pressure stages into the low pressure stages (which are not used).

$$\frac{1}{\eta_{comp,two-stages}} \approx \frac{1}{\eta\big|_{comp}^{stage3}} + \frac{1}{\eta\big|_{comp}^{stage4}} \quad (3.37)$$

The volumetric flow rate through the compressor was approximated by measuring the frequency of the compressor f_{comp} and the volume of the cylinders inside the compressor shown here as $V\big|_{comp}^{3^{rd}}$ and $V\big|_{comp}^{4^{th}}$. The results were shown in **Table 4-8**. Note that a single stage does not support the required inlet to outlet compression ratio to reach testing pressures above 7.4 MPa.

The volumetric flow rate was estimated by equation (3.38) followed by the mass flow rate in equation (3.40).

$$\dot{V}_{comp} = f_{comp} V\big|_{comp}^{3^{rd}} \quad (3.38)$$

Finally, the mass flow rate through the compressor was approximated based on equation (3.40) with the result plotted in **Figure 178**. The referenced density corresponds to state 6 of the cycle shown here as equation (3.39).

$$\rho_{comp-inlet} = \rho_6 = density\left(CarbonDioxide, P_6, h_6\right) \quad (3.39)$$

$$\dot{m}_{compressor} = \eta_{comp,two-stages}\rho_{comp-inlet}\dot{V}_{comp} \quad (3.40)$$

The final mass flow estimate was determined as the difference between the compressor through flow to the

expected mass flow rate through the test section as demonstrated in equation (3.41).

$$\dot{m}_{excess} = \dot{m}_{compressor} - \dot{m}_{test-section} \quad (3.41)$$

Several valves were integrated into the test facility to accommodate the full range of flow rates and pressure gradients expected through the test section as illustrated for the 3.175 mm shaft detailed in **Figure 178**. The valve network is demonstrated in **Figure 180** with the test loop and excess loops highlighted.

The valves chosen for this facility were determined based on their maximum flow coefficients denoted in literature as C_v. The flow coefficient is effectively a standard measure of the flow conductance an object such as a valve, orifice, etc. imposes on the flow. **Figure 180** reports the maximum flow coefficient for each valve currently implemented in the facility. The valve detailed with a max flow coefficient of $C_v = 0.9$ will be replaced in the future as it is too big. Instead, it will be replaced with a much smaller valve on the order of C_v=0.04 as demonstrated in the excess loop.

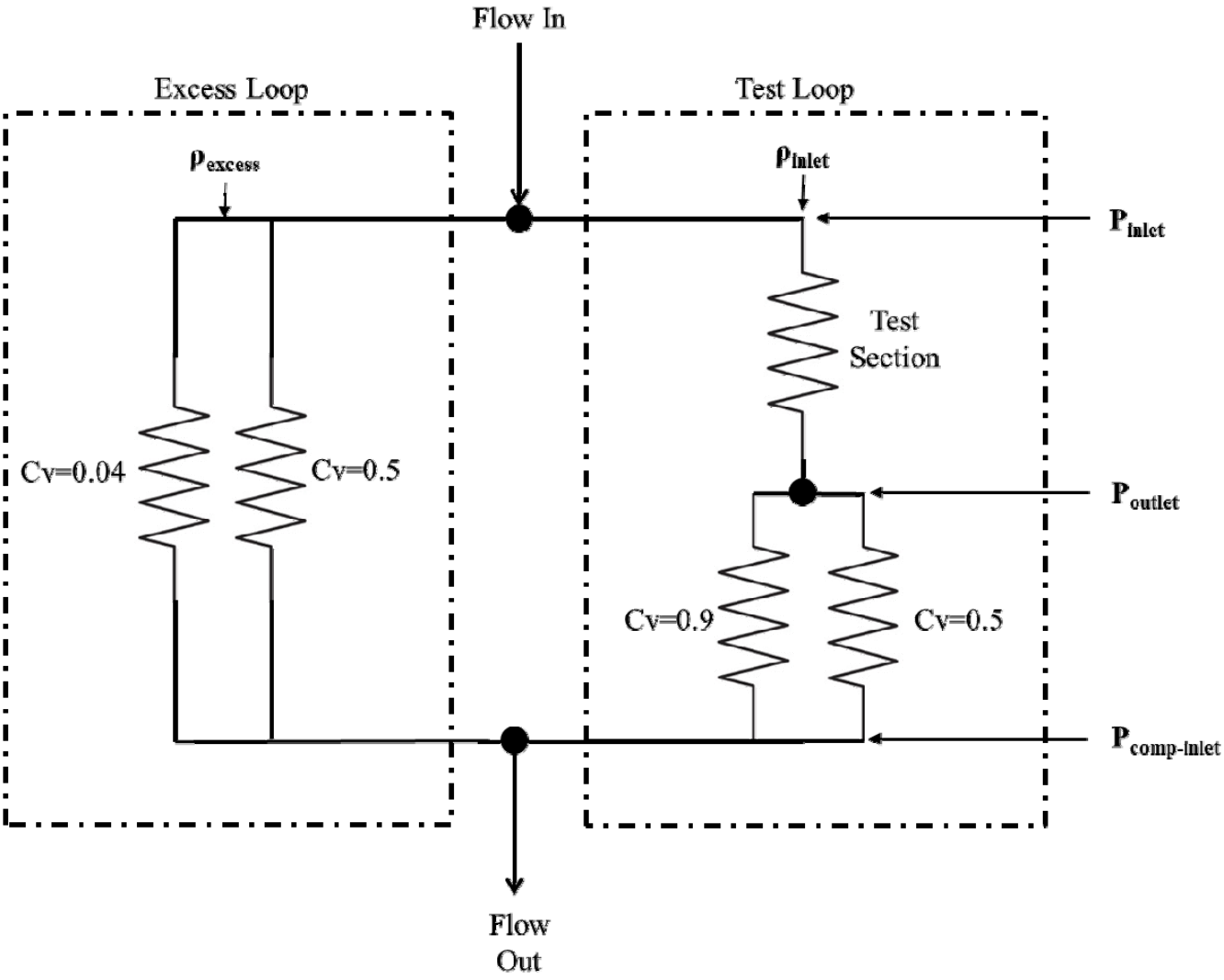

Figure 180 Valve network schematic where the max flow coefficient Cv for each valve is shown

The excess flow loop in the figure details a relatively large valve in parallel with a small valve. The idea here is

to effectively set the pressure differential from P_{inlet} to $P_{comp-inlet}$ with the larger valve and then have the smaller valve regulate the pressure by using a motorized mechanism to regulate the pressure differential controlled by a PID system. The objective of this system is to regulate the inlet pressure to the test loop by implementing small changes to the mass flow rate through the excess loop. Valve selection for this purpose was based on the following analysis.

The definition of the flow coefficient is quite often misinterpreted as simply equation (3.42). The problem is that equation (3.42) is not dimensionless and the definition provided here is strictly for incompressible flow through a flow restriction. The following documentation provides a simple overview from information attained via *swagelok.com* and *goreg.com.* Equations (3.42) through (3.45) were obtained from a *swagelok.com* technical bulletin entitled *Valve Sizing* (2007). Note that the published leading coefficient in equation (3.44), $coeff = \frac{1}{0.471}$, has been altered from its original form in *Valve Sizing* (2007) to be consistent with values obtained from *goreg.com*.

$$C_v = Q\sqrt{\frac{SG}{\Delta P}} \qquad Dimensional, Incompressible \tag{3.42}$$

Equation (3.43) is the measured industry standard for liquid service through a flow restriction. Q in this case represents the flow rate in US gallons per minute (not Imperial), GPM; SG_{liquid} is the specific gravity of the fluid relative to water at 60°F; and the pressure differential is measured in psi and denoted as ΔP. Note that since the equation only applies to incompressible fluids, no reference pressure for water is given and is assumed to be 1 atm. N_1 is a unit conversion variable where $N_1 = 1$ for the reference units provided here. Effects of temperature are commonly ignored for liquids.

$$Q_{liquid,STP} = N_1 C_v \sqrt{\frac{\Delta P}{SG_{liquid}}} \tag{3.43}$$

The simple formula shown for liquid service in (3.43) is severely contrasted with the definition required for gas service through a flow restriction shown here in equation (3.44) and (3.45). Q in this case represents the flow rate in standard cubic feet of air per minute, SCFM; SG_{gas} is the specific gravity of the fluid relative to air where both are determined at 60°F and 1 atm; the pressure differential is measured in psi and denoted as ΔP; P_{in} is the inlet pressure given in psia; and T_{in} is the inlet temperature in °R. $N_2 = 13.9$ for the reference units provided here.

Equation (3.44) is used for gas flow service above an assumed critical pressure ratio of 0.5. Note that the critical pressure of a substance is rarely exactly 0.5 as was demonstrated in **Figure 161** in chapter 2. However, this industry standard does seem to be a decent rule of thumb provided the aspect ratio of the flow restriction is kept at a minimum. Note that the critical pressure ratio of air is approximately 0.53.

$$Q_{gas,STP} = \frac{1}{0.471} C_v N_2 P_{in} \left[1 - \frac{2\Delta P}{3P_{in}}\right] \sqrt{\frac{\Delta P}{P_{in} T_{in} SG_{gas}}} \qquad PR > 0.5 \tag{3.44}$$

$$Q_{gas,STP} = C_v N_2 \frac{P_{in}}{\sqrt{T_{in} SG_{gas}}} \qquad PR \le 0.5 \tag{3.45}$$

The required size of the valve was estimated based on the following analysis using the definitions provided in equations (3.44) and (3.45) and desired values reported in **Table 4-9**.

Table 4-9 Parameters used in valve sizing estimate

PARAMETER	VARIABLE	VALUE
Inlet Temperature	T_{inlet}	325 K
Inlet Pressure	P_{inlet}	13.8 MPa
Outlet Pressure	P_{outlet}	1.4 MPa – 13.8 MPa
Expected Volumetric Flow Rate	$Q_{excess,STP}$	0 – 0.016 m^3/s

The expected values of pressures, temperatures, and flow rates identified in **Table 4-9** are those used to construct **Figure 178**. The additional volumetric flow rate was estimated based on equation (3.33).

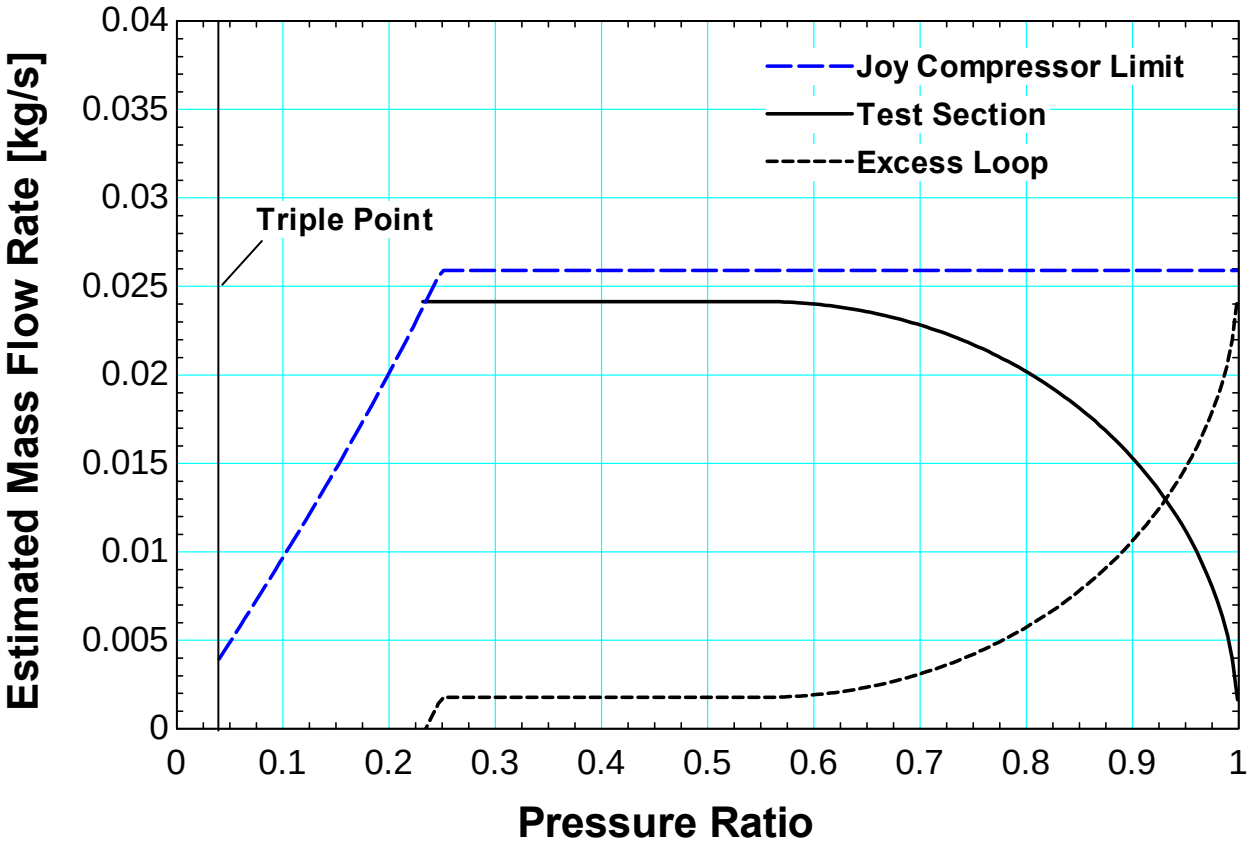

Figure 181 Expected flow rates in test facility from an initial inlet pressure of 13.8 MPa and an upstream temperature of 325 K

Figure 181 illustrates the estimated flow rates through the facility as a function of pressure ratio when throttling carbon dioxide with an upstream pressure of 13.8 MPa and an upstream temperature of 325 K. Notice that the flow rate through the compressor is fixed and is split between the test section and the excess loop as modeled in

equation (3.41).

With the flow rate through the excess loop fixed by equation (3.41), an estimation of the maximum required valve coefficient can be determined as illustrated in **Figure 182**. The methodology employed in this estimation is shown in equations (3.46) through (3.49).

The specific gravity $SG = 1.53$ for carbon dioxide at standard conditions is calculated in EES as shown in equation (3.46). Notice the reference values are consistent with those necessary to apply equations (3.44) and (3.45).

$$\rho_{CO_2-ref} = density\left(Carbon\ Dioxide, P = 1\,atm, T = 60^{\circ}F\right)$$
$$\rho_{Air-ref} = density\left(Air, P = 1\,atm, T = 60^{\circ}F\right)$$
$$SG = \frac{\rho_{CO_2-ref}}{\rho_{Air-ref}} = 1.53 \qquad (3.46)$$

The excess flow rate $\dot{m}_{excess}$ as calculated from equation (3.41) and illustrated in **Figure 181** is divided by the reference density to calculate the excess volumetric flow rate at 60°F and 1 atm as demonstrated in (3.47).

$$Q_{excess,STP} = \frac{\dot{m}_{excess}}{\rho_{CO_2-ref}} \qquad (3.47)$$

The pressure differential is obtained from equation (3.48) due to the pressure gradient experienced by the excess loop as was demonstrated in the resistance network highlighted in **Figure 180**.

$$\Delta P = P_{inlet} - P_{comp-inlet} \qquad (3.48)$$

Finally, the flow coefficient is determined using equations (3.44) and (3.45) in a function. The result is shown as a function of pressure ratio in **Figure 182**.

$$C_v = f\left(P_{inlet}, T_{inlet}, \Delta P, SG, Q_{excess,STP}\right) \qquad (3.49)$$

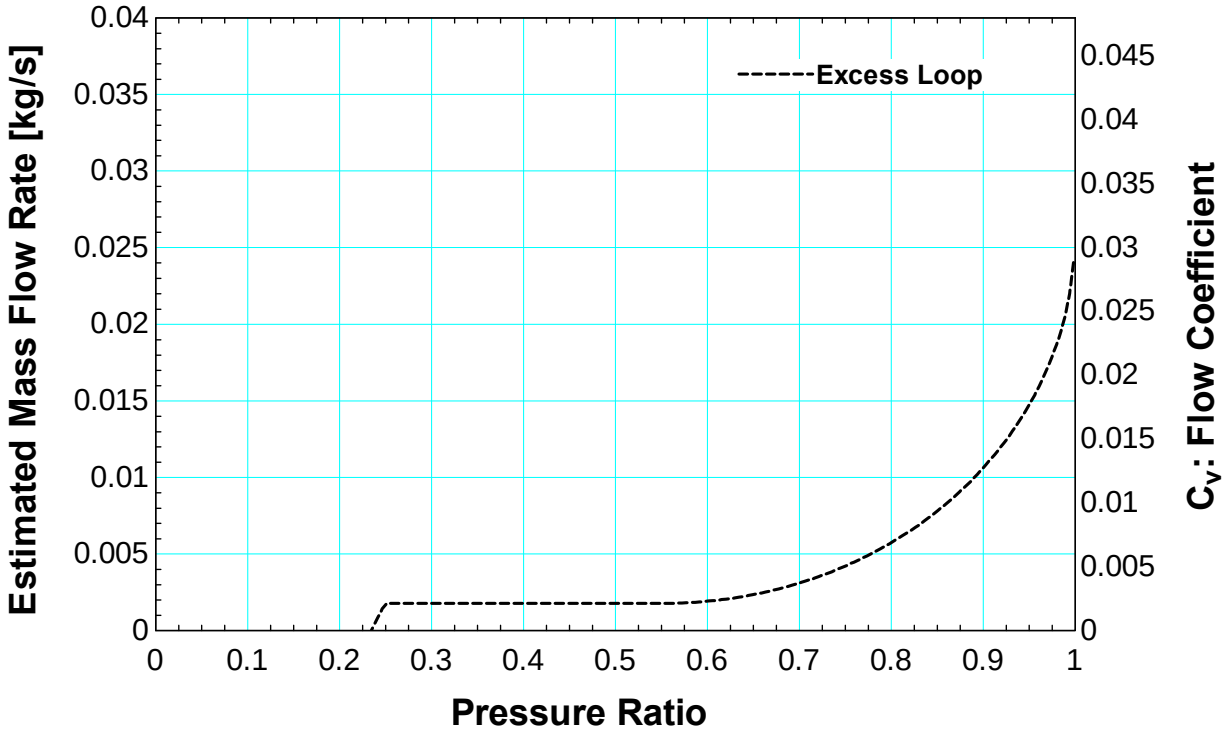

Figure 182 Excess flow loop valve coefficient estimation as a function of pressure ratio and estimated mass flow rate

Figure 182 shows that the maximum desired flow coefficient should be about $C_v = 0.03$; an SS-31RS4 valve from Swagelok was identified to meet the criteria specified. The flow coefficient as a function of the number of valve turns is detailed here as illustrated in **Figure 183**. Notice that the valve has particularly good flow coefficient resolution as a function of the number of turns at $\Delta C_v = \frac{0.0025}{turn}$. Furthermore, the maximum allowable pressure of the valve is 34.5 MPa which is well above the minimum 13.8 MPa requirement.

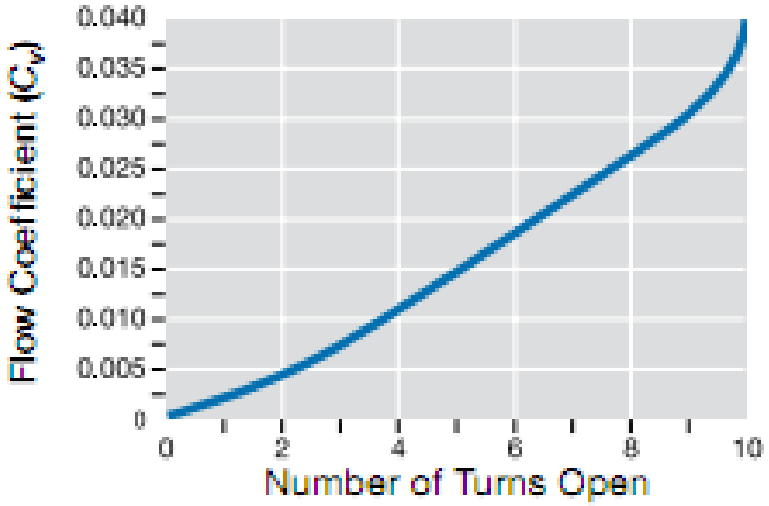

Figure 183 Flow coefficient for SS-31RS4 valve from Swagelok

4.3.4 Geometrical Parameters and Eccentricity Study

4.3.4.1 Geometrical Parameters

Section 4.3.3 illustrated that the desired pressure gradients investigated in this study coupled with the available compression equipment required that the flow conductance of the test section be reduced as much as possible. This meant that the flow had to be constricted by decreasing the effective available flow area to about $A_c = 0.3846 mm^2$. Conceptually, this meant that the flow coefficient C_v had to be of the same order as that used to size the excess loop valve detailed in **Figure 182**. Equation (3.50) provides an overview of the results obtained in that study.

$$O(C_v) \approx 0.03 \quad (3.50)$$

The effective flow area was minimized to acceptable levels by establishing maximum geometric values for each constrictive device chosen for investigation as detailed in **Table 4-10**. The natural annular orifices which occur between the outer diameter of various shafts and the inner diameter of various seals are used to simulate labyrinth seals.

Table 4-10 Components attributing to available flow area in test section

PARAMETER	VARIABLE	VALUE	UNCERTAINTY
ORIFICE			
Nominal orifice diameter	$D_{orifice}$	0.711 mm	12.7 μm
SEAL			
Nominal seal diameter	D_{seal}	3.183 mm	3.81 μm
Seal length	L_{seal}	0 – 7.62 mm	2.54 μm
Max seal roughness	e_{seal}	0.305 μm	
SHAFT			
Nominal shaft diameters	D_{shaft}	3.1 – 3.175 mm	0.762 μm
Shaft length	L_{shaft}	50.8 mm	
Max shaft roughness	E_{shaft}	0.051 μm	

4.3.4.2 Eccentricity Overview

Eccentricity is an important characteristic that must be controlled in devices which constrict fluid flow through an annular region in order to eliminate undesirable two dimensional effects. Eccentricity has been reported to increase the flow rate in many studies such as Piercy et al. (1933), Tao and Donovan (1955), and Gamal (2007). The change is flow rate due to eccentricity is conceptually described in this section. Note that in all instances identified, eccentricity is shown to increase the flow rate through an annular profile over the concentric counterpart.

The velocity profile in a concentric annular duct is reported in equation (3.53). This is an exact solution to the equations reported in (3.51) with boundary conditions identified in (3.52). Note that $r = a$ is the radial dimension of r at the outer radius and $r = b$ is the radial dimension of r at the inner radius. Furthermore, equations reported in (3.51) make the following assumptions:

- The flow is axisymmetric
- Fully developed incompressible flow
- Constant properties through the chamber
- Potential energy effects are negligible

$$\frac{\mu}{r}\frac{\partial}{\partial r}\left[r\frac{\partial u_x}{\partial r}\right]=\frac{\partial p}{\partial x}$$

$$\frac{\partial p}{\partial r}=0 \qquad (3.51)$$

$$u_x\big|_{r=a}=0 \qquad outer\ radius$$

$$u_x\big|_{r=b}=0 \qquad inner\ radius \qquad (3.52)$$

Note that the pressure differential $\frac{\partial p}{\partial x}$ in (3.53) has become the total differential $\frac{dp}{dx}$ as the pressure gradient with respect to *r* is shown to be negligible in (3.51).

$$u_x(r)=\frac{1}{4\mu}\left(\frac{dp}{dx}\right)\left[\left(r^2-b^2\right)-\left(a^2-b^2\right)\frac{\ln\frac{r}{b}}{\ln\frac{a}{b}}\right] \qquad (3.53)$$

Several velocity profiles based on equation (3.53) are plotted in **Figure 184** where $a=1$ and $0<\frac{b}{a}<1$. Also plotted is the location of the maximum velocity $u_{\max}$ through the annular channel for $0.001<\frac{b}{a}<1$. Notice that the location of the maximum velocity $u_{\max}$ seems to show the greatest sensitivity as $\frac{b}{a}\to 1$ (corresponding to a very small clearance annulus). For this reason, it would seem that the maximum velocity would show the greatest relative change to even minor deviations in eccentricity as $\frac{b}{a}\to 1$.

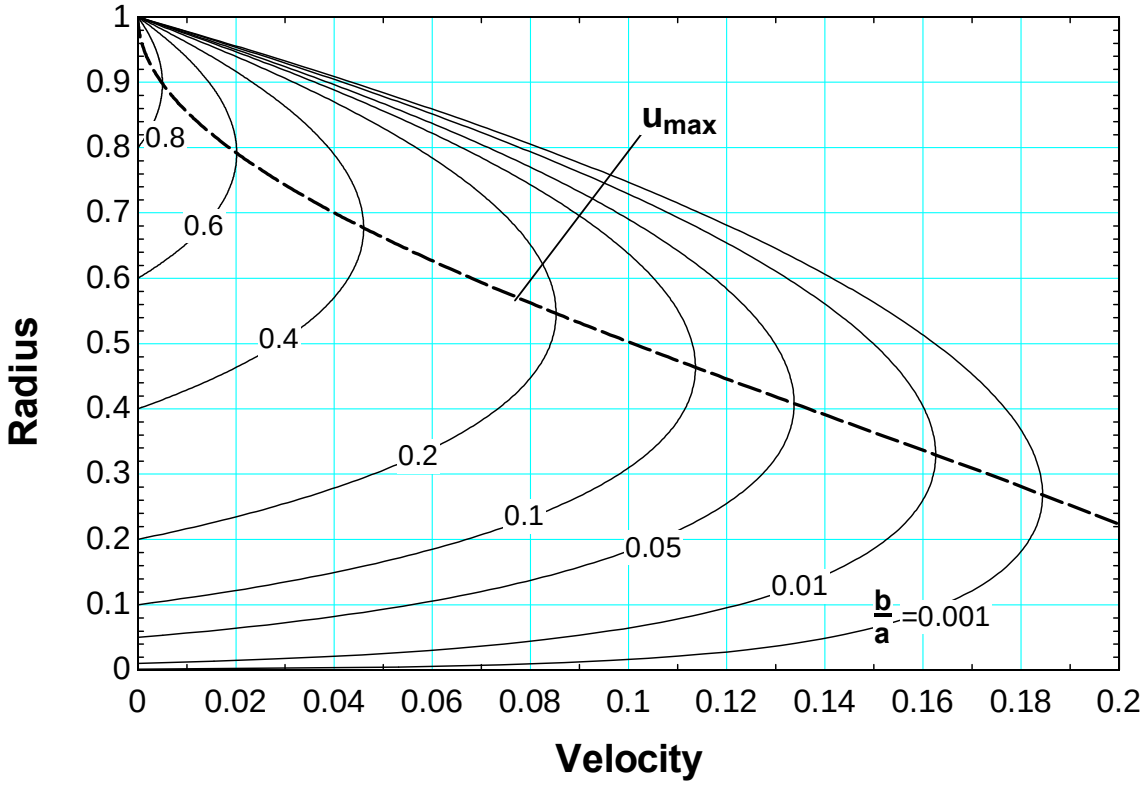

Figure 184 Velocity profiles through an annular region for a=1, 0<b/a<1

The flow rate through a concentric annular duct is derived by integrating equation (3.53) across the velocity profile to obtain equation (3.54).

$$Q_{concentric} = \frac{\pi}{8\mu}\left(-\frac{dp}{dx}\right)\left[a^4 - b^4 + \frac{\left(a^2 - b^2\right)^2}{\ln\frac{a}{b}}\right] \quad (3.54)$$

White (2006) reproduces the result obtained from Piercy et al. (1933) to evaluate the flow rates through eccentric channels. The result is shown here as equation (3.57) where the parameters used in the equation are demonstrated in equation (3.58). Equation (3.57) is an exact solution for laminar flow through eccentric annular channels; the result was obtained by considering a complex-variable method of the form demonstrated here as equations (3.55) and (3.56).

$$z' = M\tan\frac{\varsigma}{2} \quad (3.55)$$

where

$$z' = x + iy \;\; and \;\; \varsigma = \xi + i\eta \quad (3.56)$$

$$Q_{eccentric} = \frac{\pi}{8\mu}\left(-\frac{dp}{dx}\right)\left[a^4 - b^4 - \frac{4c^2M^2}{\beta-\alpha} - 8c^2M^2\sum_{n=1}^{\infty}\frac{ne^{-n(\beta+\alpha)}}{\sinh\left(n\beta - n\alpha\right)}\right] \quad (3.57)$$

$$F = \frac{a^2 - b^2 + c^2}{2c}$$

$$M = \left(F^2 - a^2\right)^{1/2}$$

$$\alpha = \frac{1}{2}\ln\frac{F + M}{F - M}$$

$$\beta = \frac{1}{2}\ln\frac{F - c + M}{F - c - M} \qquad (3.58)$$

Figure 185 illustrates the ratio between equations (3.57) to (3.54); that is, the ratio of the flow rate for an eccentric to a concentric annulus. The figure shows that the relative impact of eccentricity is substantial in laminar flow, especially in narrow gaps where $\frac{b}{a} \to 1$. In the worst case scenario, the flow rate will increase by a factor of 2.5 through a narrow gap at maximum eccentricity. This is the same result which is obtained from lubrication theory which applies to flow rates through a narrow annulus identified here as equation (3.59) and reproduced from White (2006); the result obtained from this equation is also plotted in the figure.

$$\frac{Q_{eccentric}}{Q_{concentric}} = 1 + \frac{3}{2}\left(\frac{c}{a-b}\right)^2 \quad Narrow\ Annulus,\ \frac{b}{a} = 1 \qquad (3.59)$$

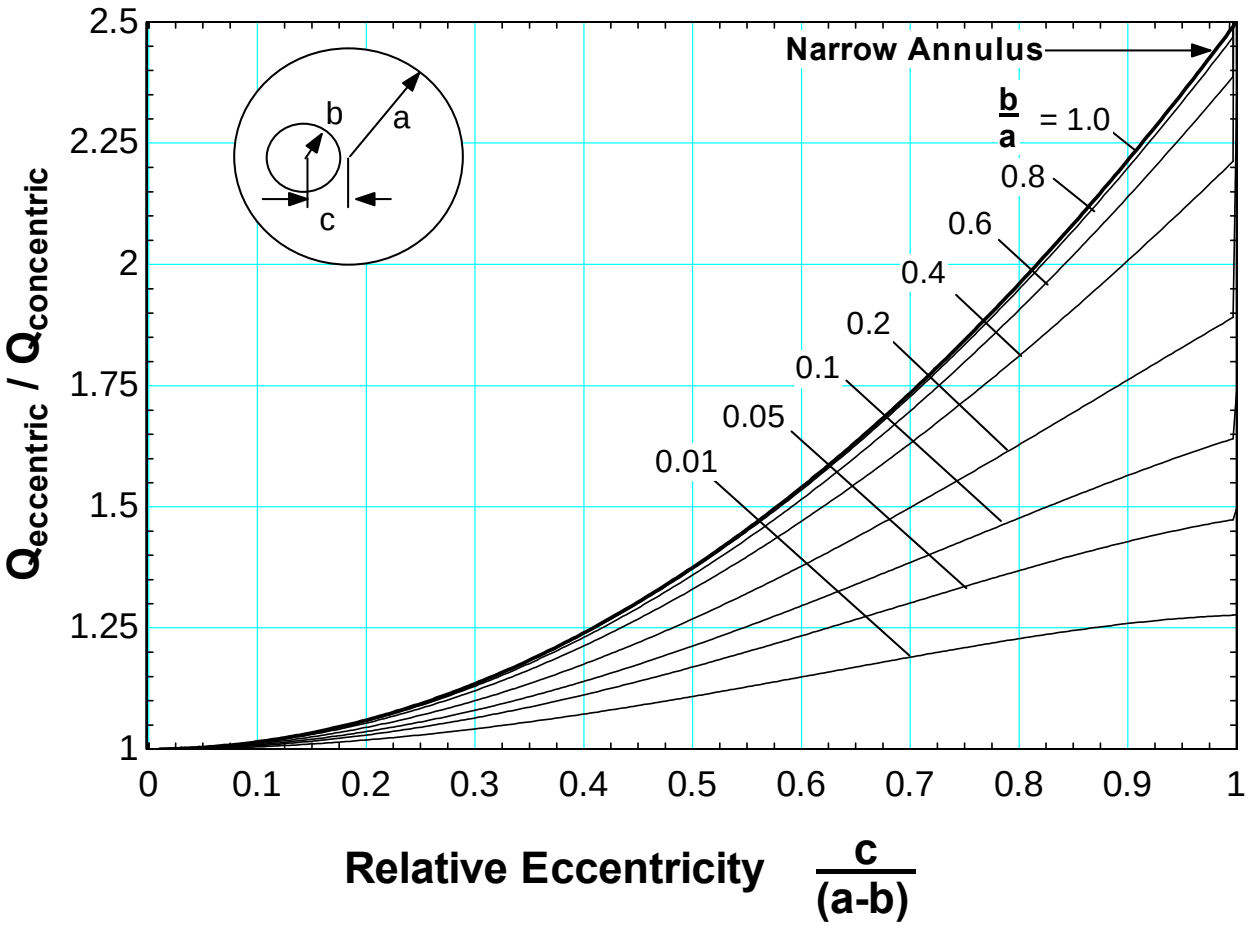

Figure 185 Flow rates through eccentric annular gaps relative to concentric annular gaps as a function of relative eccentricity. Also plotted is the relatively simple result lubrication theory.

Piercy et al. (1933) provides a contour plot of the velocity lines through an eccentric annulus where $\frac{b}{a}=\frac{c}{a}=\frac{1}{4}$. A swelling of the velocity profile biased towards the apogee of the seal is noticeable and is reproduced here as **Figure 186**.

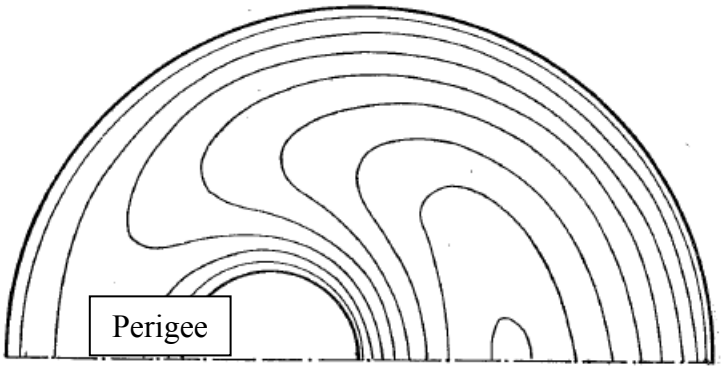

Figure 186 Contour plot of constant-velocity lines for an eccentric annulus where $\mathbf{b/a=c/a=1/4}$; [referenced from Piercy et al. (1933) and White (2006)]

A less rigorous study through narrow annular gaps only was conducted by Tao and Donovan (1955). The study assumes a frictional factor of the form illustrated in equation (3.60). The primary concern of the investigation was to detail the relative difference in flow rate between narrow eccentric and concentric annular gaps. The final relationship effectively shows that the value of $\frac{Q_{eccentric}}{Q_{concentric}}$ is independent of the constant D used in equation (3.60). Note that the actual value used for the coefficient D will be bounded by the values $D=64$ and $D=96$; these values correspond to flow through a circular channel and two infinite plates, respectively.

$$f=\frac{D}{\mathrm{Re}^n} \qquad (3.60)$$

The functional form for the expected flow increase over the concentric case due to eccentricity is reported here as equation (3.61).

$$\frac{Q_{eccentric}}{Q_{concentric}}=\frac{1}{\pi}\int_0^{\pi}\left(1+\left(\frac{c}{a-b}\right)\cos\theta\right)^{\frac{3}{2-n}}d\theta, \quad Narrow\ Annulus, \frac{b}{a}=1 \qquad (3.61)$$

The original study details specific techniques that can be used to solve equation (3.61) explicitly for both laminar and turbulent flow conditions. Indeed, in the case of laminar flow where $n=1$, the exact equation is simplified to a form consistent with equation (3.59). The result is more complicated for the turbulent case where the value $n=0.25$. The value $n=0.25$ is attributed to Blasius (1911), corresponding to turbulent flow through a smooth duct. A value of $D=0.316$ is noted, but not expressly used in equation (3.61). The explicit solution for turbulent flow results in a fairly complicated hypergeometric series. With the advent of modern computers, however, the results for both laminar and turbulent flow are easily obtained numerically in EES as demonstrated

in equation (3.62). The results are plotted in **Figure 187** along with the exact solution obtained for laminar flow by Piercy et al. (1933). Notice that the model developed by Tao and Donovan (1955) follows the trend developed by Piercy et al. (1933) exactly.

$$\frac{Q_{eccentric}}{Q_{concentric}} = \frac{1}{\pi}\text{integral}\left\{\left(\left(1+\left(\frac{c}{a-b}\right)\cos\theta\right)^{\frac{3}{2-n}}\right), \Delta\theta, \theta = 0, \theta = \pi\right\} \quad ...n = \begin{Bmatrix} 1 \rightarrow laminar \\ 0.25 \rightarrow turbulent \end{Bmatrix}$$

(3.62)

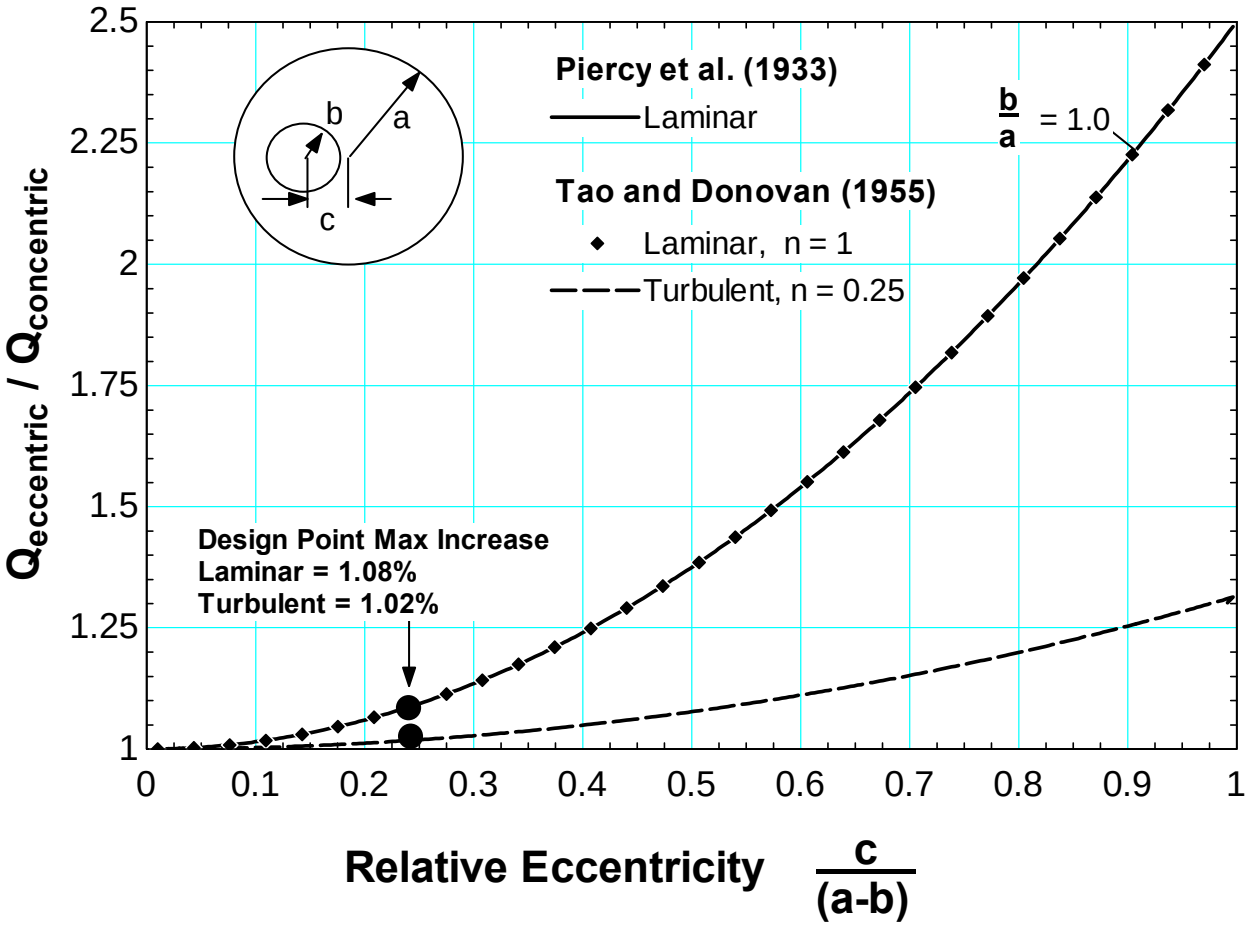

Figure 187 Flow rates through narrow eccentric annular gaps where $b/a = 1$ for both laminar and turbulent regimes; the results obtained from Piercy et al. (1933) and Tao and Donovan (1955) are reported.

Figure 187 establishes the clear objective that the effects of eccentricity must be minimized.

Three sources of error are specified in **Table 4-11** based on the tolerances of the components used to construct the test section. A great deal of effort has gone into the design of this test section to reduce systematic errors inherent with repeated assembly. Notice that an expected maximum relative eccentricity design point is specified in **Figure 187**. The actual test section design requires a careful assembly procedure in order to meet the specified design point illustrated above. The method is detailed in the next section where only the highlights are demonstrated here.

Table 4-11 Tolerances of components used to minimize eccentricity in the test section

PARAMETER	VARIABLE	VALUE	UNCERTAINTY

Nominal seal diameter	D_{seal}	3.175 mm	+ 2.54 µm
			+10.16 µm
Nominal assembly shaft diameter	$D_{shaft}\|_{assembly}$	3.099 mm	+0.000 µm
			+1.524 µm
Nominal alignment shaft diameter	$D_{shaft}\|_{alignment}$	3.175 mm	+0.000 µm
			+1.524 µm
PARAMETER	VARIABLE	UNCERTAINTY	
Collet total indicated runout	TIR_{collet}	Uncertainty @ Tip	1.016 µm
		Uncertainty @ $4 \cdot D_{shaft}$	3.048 µm

Table 4-11 identifies the tolerances of the components used to align the shaft within the seal to minimize the effects of eccentricity. The test section detailed here simulates a shaft-seal interface by holding a gauge-pin very precisely. The uncertainty due to eccentricity is a byproduct of two major contributing factors in the test section – uncertainty due to available cross-sectional area and uncertainty introduced as a byproduct of the total indicated runout of the collet system used to hold the shaft. Notice that the indicated runout of the collet used in this facility has two rated uncertainties – one at the tip of the collet and the other at 4 times the diameter of whatever it holding. A schematic is provided below in **Figure 188**. This section details the major sources of error in the cross-sectional area and that of the collet system.

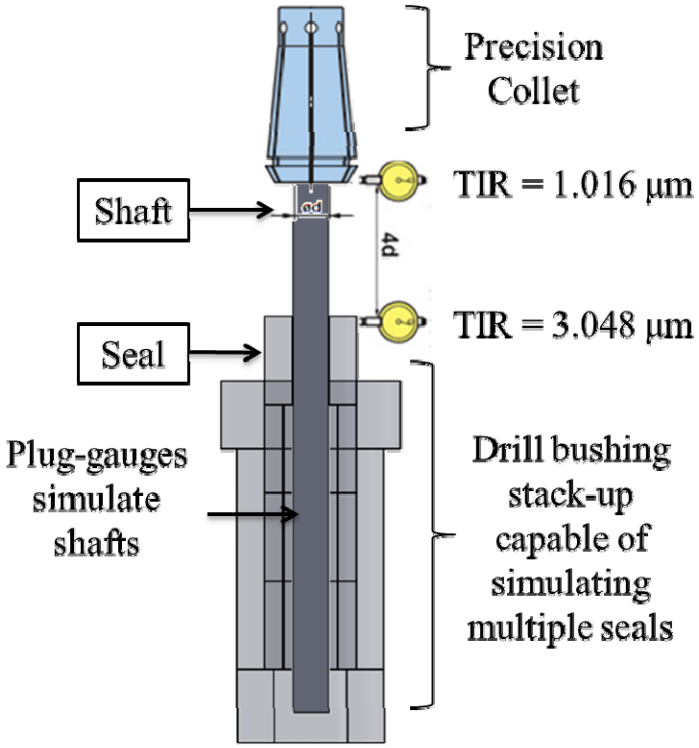

Figure 188 Schematic of components used in eccentricity tolerance calculation

4.3.4.3 Measurement Uncertainty in Cross-Sectional Area

Type X plug go-gauges are used in the facility to simulate the shaft as they have a maximum rated uncertainty on the order of +1.5 µm as noted in **Table 4-11**. A seal with a comparable rated uncertainty would be ideal; however, it was not possible to acquire such a precise seal at the geometry and tolerances desired. The best

available seal interface that could be fabricated was obtained by slicing apart drill bushings that have a maximum rated uncertainty of about +/- 4 μm. The relative impact on the uncertainty of the annular area is demonstrated below as an output from EES shown in **Figure 190**. It is clear that the uncertainty of the seal provides the largest relative error in the shaft-seal interface. Unfortunately, measurement of the inner diameter of the bushing proved to be just as inaccurate as the rated uncertainty from the manufacturer as demonstrated below in **Figure 190**. Said differently, the discrete nature of the computer pixilation went directly from 3178.4 μm to 3184.7 μm without allowing finer precision in the measurement. As it stands, the lens required to encompass the entire diameter of the seal inside the field of view of a microscope turned out to be just as inaccurate as the tolerance specified by the drill bushing manufacturer. Nevertheless, the uncertainty in the cross-sectional was reduced to about +/-5% based on the nominal conditions identified in **Figure 189**.

Variable±Uncertainty	Partial derivative	% of uncertainty
Ac = 0.4035±0.0194 [mm^2]		
seal = 3.181±0.00381 [mm]	∂Ac/∂ seal = 4.997	96.34 %
shaft = 3.1±0.000762 [mm]	∂Ac/∂ shaft = -4.869	3.66 %

No unit problems were detected.

Figure 189 Relative impact of shaft-seal uncertainty on annular area

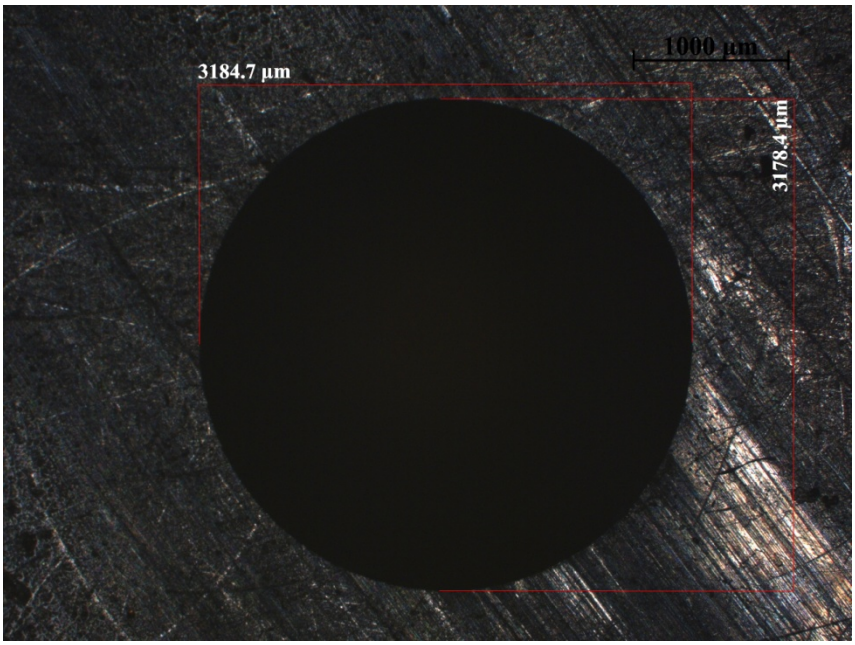

Figure 190 Measurements made of drill bushing with microscope proved to be just as inaccurate as manufacturer tolerances

4.3.4.4 Expected Eccentricity

The uncertainty in the diameter of the seal has the unfortunate effect of also contributing to uncertainty in the eccentricity. In a perfect assembly process, the seal would first be aligned with a shaft of the exact diameter of the seal. This alignment process was crucial in order to effectively "tare" the facility and reduce all other systematic errors in the facility. A degree of uncertainty is introduced in this process, however, as illustrated in **Figure 191**-A. The worst case alignment is demonstrated here, where the minimum shaft and maximum seal diameters based on the tolerances noted in **Table 4-11** are shown to result in a maximum eccentricity error of

$k_1 = 5.08\mu m$. The result is a worst-case assembly error of the same eccentricity using the smaller diameter shaft noted in **Figure 191**-B. The seal diameter would need to be toleranced more tightly in order to reduce this alignment eccentricity.

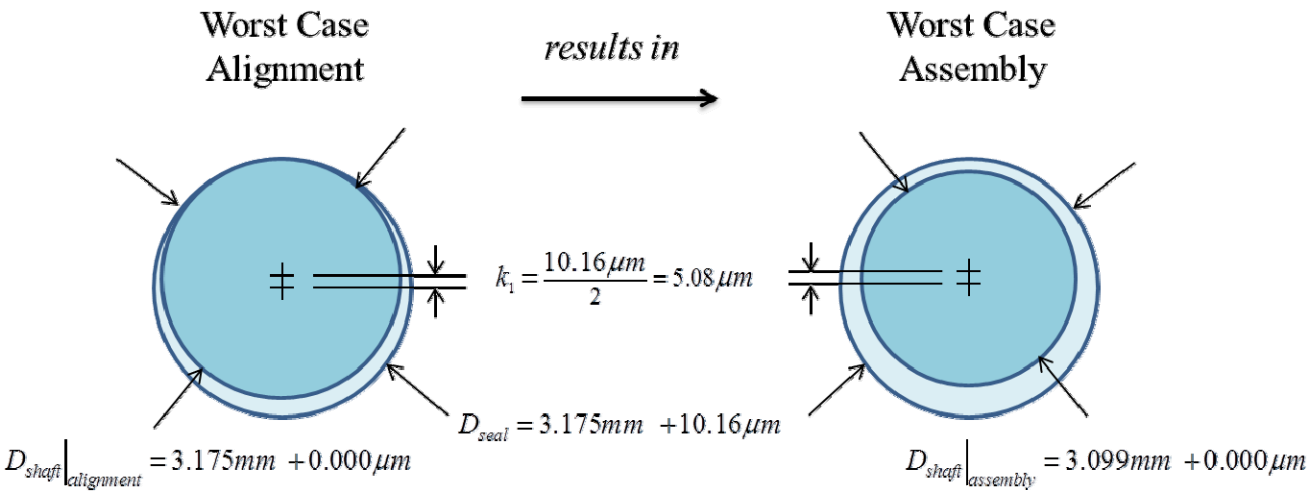

Figure 191 Shaft to seal alignment and final assembly process demonstrations; A – alignment pin used to center shaft and seal assembly; B – final assembled position of shaft and seal

The uncertainty in the eccentricity is compounded by alignment issues induced by the clamping mechanism used to hold the shaft in place. In order to align all components with the large shaft as demonstrated in **Figure 191**-A, a tool-holding mechanism had to be used that would allow the shaft in figure *A* to be replaced by the shaft shown in figure *B*. The problem was in locating or developing such a tool-holding mechanism that would hold the shaft as straight as it was when the facility was aligned. The concept is demonstrated in exaggerated fashion in **Figure 192**. Note the induced angular offset incurred when replacing shaft *A* by shaft *B*.

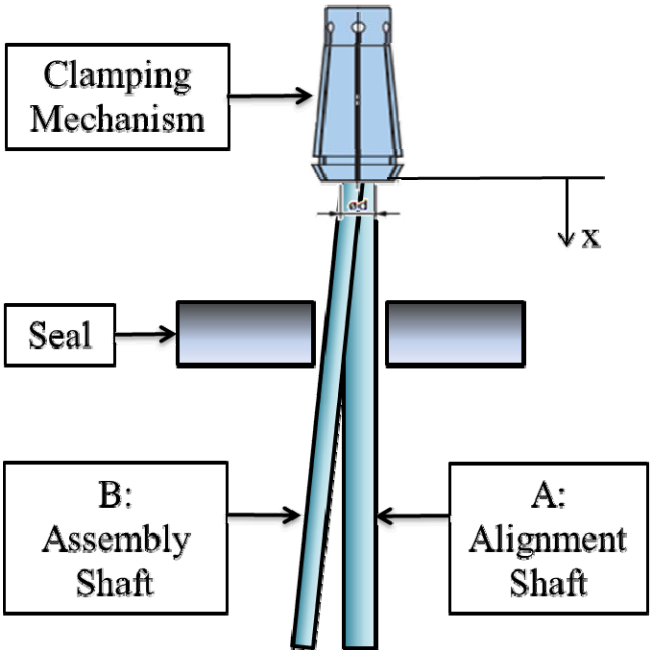

Figure 192 Alignment issues attributed to clamping mechanism error

A New Baby collet often used to hold end-mills in micro-machining was integrated into the test facility to limit the effects of this unavoidable error. The final tolerance on the assembly error is represented by the linear equation shown in equation (3.63) as a compilation of the shaft alignment error pictorially described in **Figure 191** and the clamping mechanism error illustrated in **Figure 192** respectively. The shaft straightness is regarded as exact, which is effectively true for a plug gauge.

$$\underbrace{c}_{\text{eccentricity}} = \underbrace{k_1}_{\substack{\text{shaft}\\ \text{alignment}}} + \underbrace{mx + k_2}_{\substack{\text{clamping}\\ \text{mechanism}}} \tag{3.63}$$

The final step was to estimate the eccentricity introduced as a function of the clamping mechanism. This step is demonstrated in equation (3.64) using the information provided in **Table 4-11** and conceptually illustrated in **Figure 188**. The final equation regarding the eccentricity at the nominal conditions listed in **Table 4-11** is shown in equation (3.65) and illustrated in **Figure 193**.

$$k_2 = TIR_{collet\,tip} = 1.016\mu m$$
$$m = \frac{TIR_{4\cdot D_{shaft}} - TIR_{collet\,tip}}{4\cdot D_{shaft} - 0} = \frac{3.048\mu m - 1.016\mu m}{4\left(3.099mm\right)} = 0.164\frac{\mu m}{mm} \tag{3.64}$$

$$\underbrace{c\big|_{D_{shaft}=3.099mm}}_{\text{eccentricity}} = \underbrace{5.08\mu m}_{\substack{\text{shaft}\\ \text{alignment}}} + \underbrace{0.164\frac{\mu m}{mm}\left(x_{shaft}\right) + 1.016\mu m}_{\substack{\text{clamping}\\ \text{mechanism}}} \tag{3.65}$$

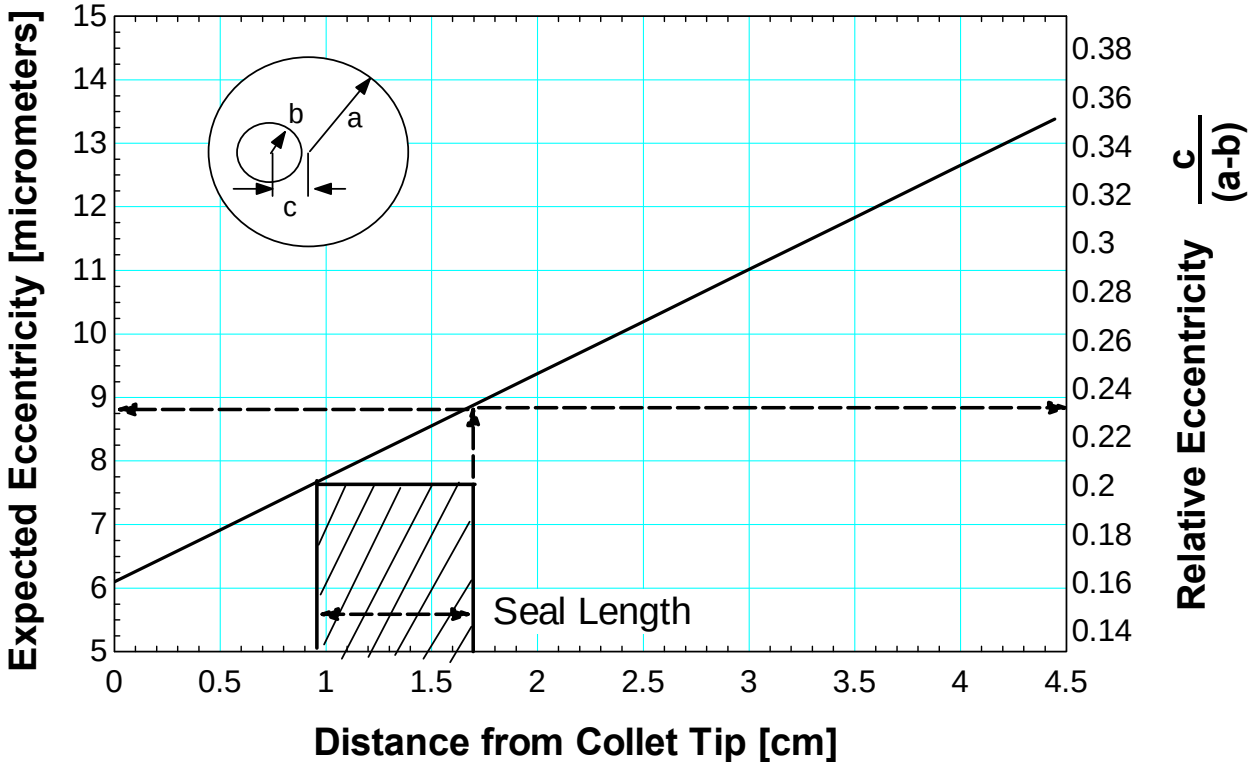

Figure 193 Expected eccentricity and relative eccentricity as a function of the distance from the collet tip.

Figure 193 illustrates the eccentricity as a function of the distance from the collet tip as defined by equation (3.65). The figure demonstrates the importance of positioning the seal as close as possible to the collet tip. The design specification calls for the seal to be positioned at a distance of about 1 cm from the collet tip. This

configuration results in a relatively small expected maximum eccentricity of about 9 μm at the end of the seal. The relative eccentricity, however, is as high as 0.24. The problem is that the annulus between the shaft and the seal is so small that $a-b=\frac{3.175mm}{2}-\frac{3.099mm}{2}=38\mu m$; this small gap facilitates the need for extremely tight tolerances on the equipment required to control the eccentricity. The final result was published in **Figure 187** where the ratio of $\frac{b}{a}=\frac{3.099mm/2}{3.175mm/2}=0.98$ is effectively unity.

4.3.4.5 Measured Eccentricity

The expected eccentricity detailed in the previous section was verified optically using the test setup presented in **Figure 194**. The test section was fastened to a fixture designed to clamp down to an optical table. A camera was outfitted with an external light source and a lens with a field of view that could verify the eccentricity in the as-assembled test condition. Alignment stages were outfitted to the camera fixture to provide adjustment of the field of view.

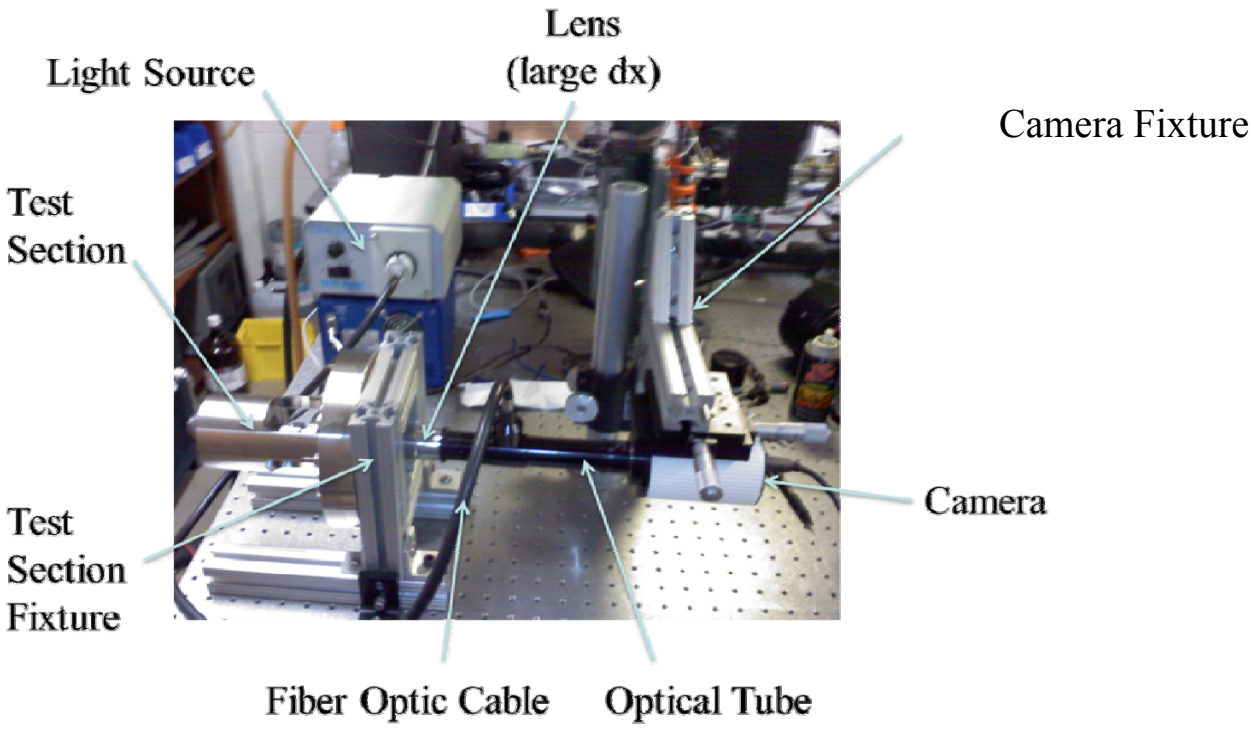

Figure 194 Optical setup used to verify the expected eccentricity

Pictures were taken about the shaft-seal interface as it was not possible to capture the entire structure in a single photograph. Several of these raw images are illustrated in **Figure 196**; the images have been aligned to a background image to provide a visual interpretation of what was desired from this test series.

It was not possible to record images with the shaft and seal significantly out of focus. The images illustrated in **Figure 196** were developed at the desired distance of $x_{shaft}\approx 1.8cm$ from the collet tip as shown in **Figure 193**, but the shaft had to be clamped farther into the collet tip – the concept is demonstrated in **Figure 195**.

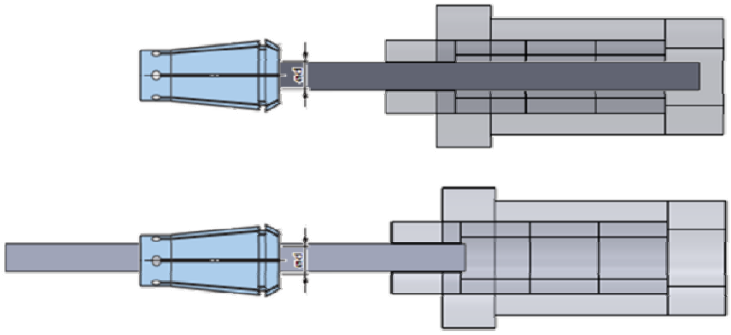

Figure 195 Focus solution which allowed imaging of shaft-seal interface at desired distance from collet tip

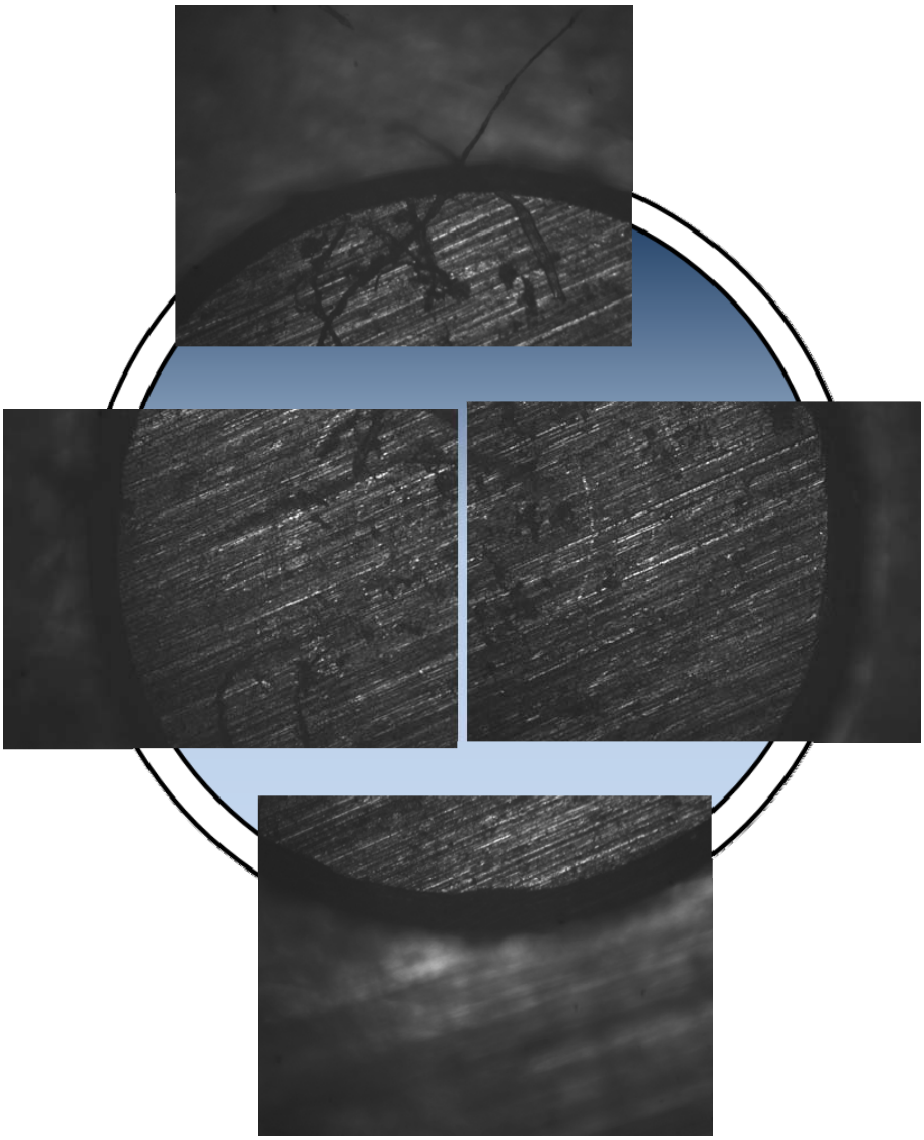

Figure 196 Raw images of assembled shaft-seal interface

The images obtained from the test series were difficult to interpret in raw form. The gradient across all the images made it difficult to state with any confidence that the distance from the shaft to the seal was being recorded comparatively. An imaging filter was developed in MATLAB for this process in order to bring the seal more in focus with the shaft and reduce background noise. The filtered images would then be used to deduce the

distance from the shaft to the seal at various points around the shaft across all images taken. The idea was that if the exact same process was applied to all images, the error introduced by the user recording the distance from the shaft to the seal would be the same for all measurements and therefore cancel from a measurement of the eccentricity. The program is conceptually illustrated in the flow chart detailed in **Figure 197** and recorded in **Error! Reference source not found.**.

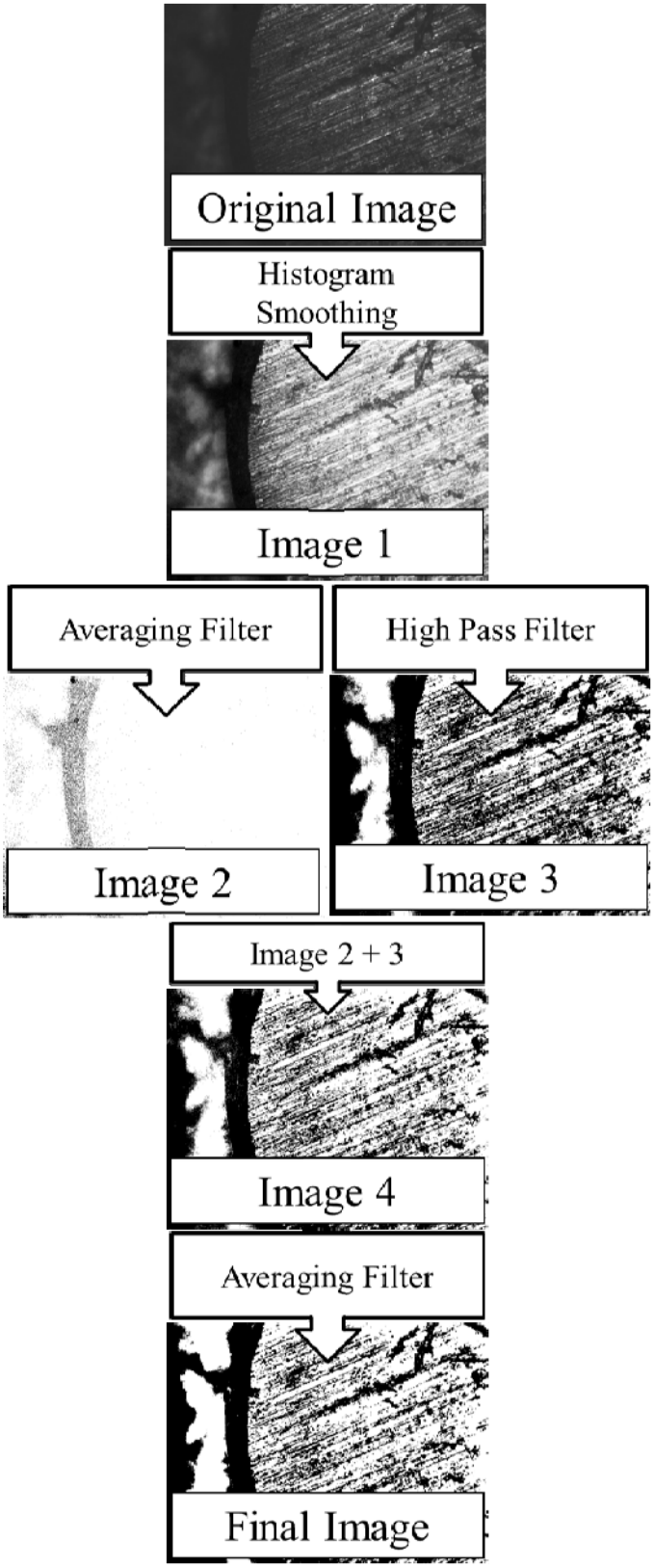

Figure 197 Flow chart of MATLAB image filtering program
The methodology used to develop the filtering program is as follows:

- A histogram smoothing technique is applied in order to extract the background image and increase the

contrast throughout. This image is stored as Image 1.

- A special 2-d digital averaging filter is applied to Image 1 to blur the image and save only the elements of the image with the highest contrast. This image is stored as Image 2.
- A high pass filter is applied to Image 1 by using the built in fast-fourier-transform tools in MATLAB.
    - The 2-d fast fourier transform of the image is taken and shifted such that image information in the frequency domain with zero-frequency components are shifted towards the center of the spectrum. This saved as sub-image A.
    - A meshgrid the size of the sub-image A is constructed with a value of 1. A circle made of all 0's is then deleted from the center portion of the meshgrid to construct a convolution image that will delete the zero-frequency components in sub-image A. The result of the operation is stored as sub-image B.
    - With the zero-frequency components deleted from sub-image B, an inverse fast-fourier shift is taken of the image. An inverse fast fourier transform is taken of the result to obtain the image in the frequency domain with all the zero-frequency components deleted. The overall result is a contrasted image in the spatial domain.
    - The final sub-image is saved as Image 3.
- A weighted sum of Image 2 and Image 3 is developed and stored as Image 4 to recover some of the less severely contrasted elements of the original image.
- The 2-d digital averaging filter is applied to Image 4 to highlight the contrast further and bring more of the background image into the forefront. The result is stored as the final image.

A pixel counting program was used on the final images to count the number of pixels from the shaft to the seal at various intervals around the shaft. A figure detailing the contrast of the raw images illustrated in **Figure 196** to the final images obtained from the filtering program is detailed in **Figure 198**.

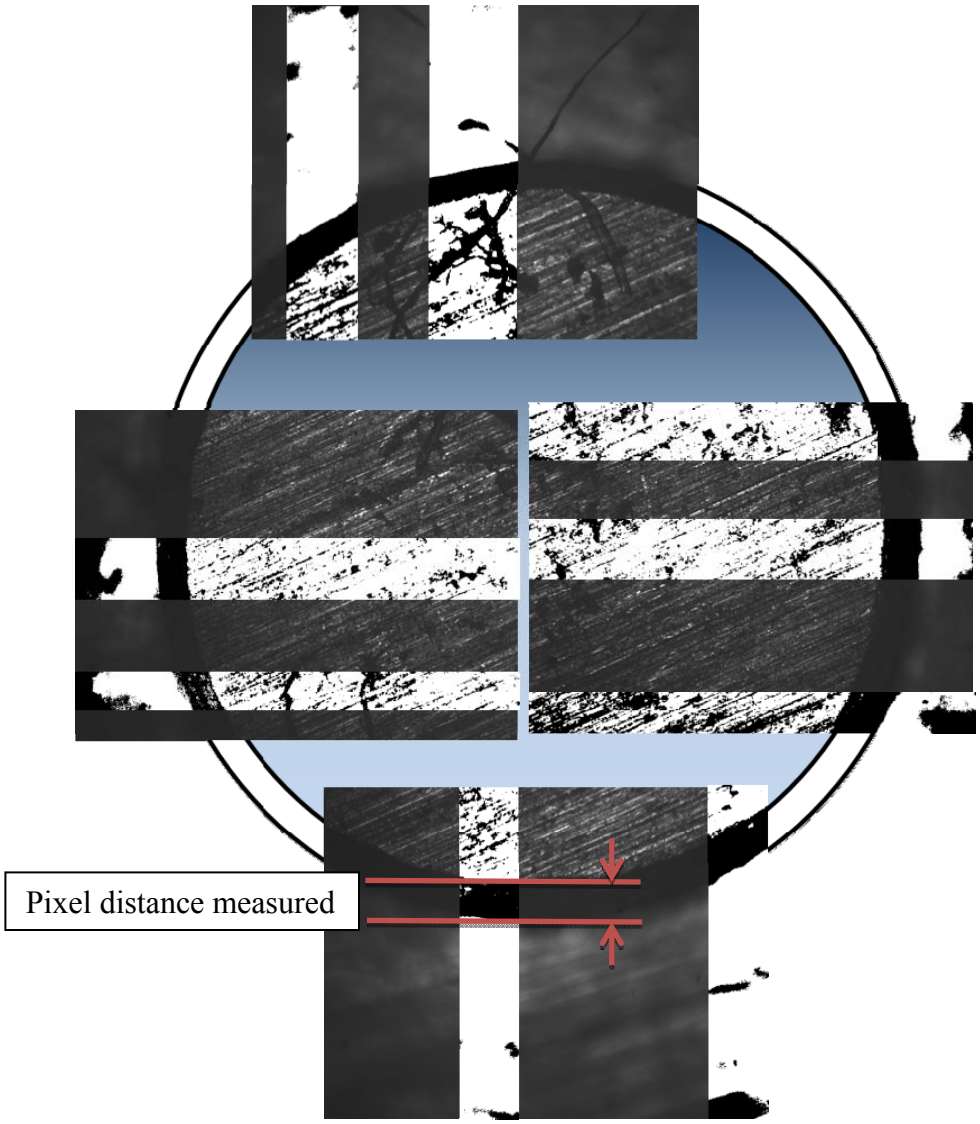

Figure 198 MATLAB filtered images placed over raw images of assembled shaft-seal interface

The results obtained from the pixel counting program are shown as a function of the pixel distance from the center shaft to the seal as conceptually demonstrated above in **Figure 198**. Pixel distances were measured at various locations around the shaft across all images taken. The results are shown in **Figure 199**. Two image results are presented in the figure where the seals and the shaft are in the image's focus, respectively. The data taken with the seals in focus, proved to be more consistent.

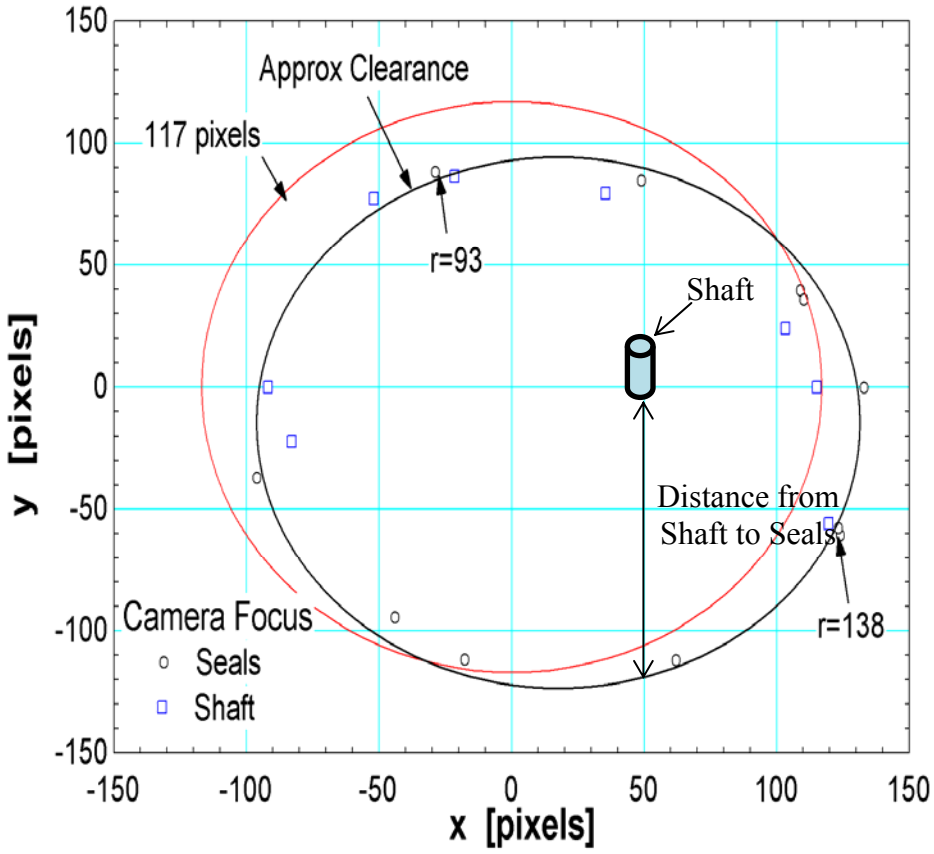

Figure 199 Results obtained from pixel counting program detailing the pixel distance from the center shaft to the seal.

An estimate of the relative eccentricity was determined based on the values provided in equation (3.66). Based on this analysis, the expected eccentricity detailed in **Figure 193** as specified by the manufacturer's tolerances is within the desired eccentricity in the assembled configuration.

Relative eccentricity

$$\frac{c}{a-b}=\frac{\max\left(abs\left(\max-avg\right)+abs\left(\min-avg\right)\right)}{avg}\approx\frac{\max\left(21+24\right)}{117}\approx 0.205 \tag{3.66}$$

4.3.5 Instrumentation Uncertainty and Facility Control

The instrumentation utilized in the design of this test facility was selected to minimize the uncertainty of key variables at test conditions. A description of each of the components selected for this experiment is provided in this section. The relative uncertainty attributed to each component at test conditions is provided in **Table 4-12**.

Table 4-12 Instrumentation uncertainty at nominal conditions

PARAMETER	VARIABLE	VALUE	UNCERTAINTY
Inlet Density	ρ_{inlet}	200 – 800 kg/m^3	0.2 kg/m^3
Inlet Pressure	P_{inlet}	7.33 – 14 MPa	30000 Pa

Outlet Pressure	P_{outlet}	1.4 – 14 MPa	30000 Pa
Mass Flow Rate	$\dot{m}_{test-section}$	0.01 – 0.03 kg/s	0.000015 kg/s

4.3.5.1 Pressure Transducers

Instrumentation Configuration

Siemens SITRANS P 7MF4332 pressure transducers are used in this experiment. The transducers are rated to a maximum 40 MPa but are calibrated with the NI 9216 computer DAQ card used in this experiment up 14 MPa. The relevant information for the pressure transducers is listed in **Table 4-13**.

Table 4-13 Pressure transducer configuration summary

PARAMETER	VALUE
Siemens Absolute Pressure Transducer	
Device Accuracy	0.075%
Full Span	40 MPa
Application Full Span	14 MPa
Sensor Output	1V to 5V
NI 9215 DAQ Card	
Bits	16
Range	-10V to 10V
NI MAX configuration	
Full Span	14 MPa
Limits	1V to 5V
Summary	
Transducer Uncertainty	30 kPa
Transducer Quantization (MAX conf.)	3.5 MPa/V
Least Significant Bit Change	305μV/bit
DAQ Card Limitation	1.07 kPa/bit

The information presented in **Table 4-13** shows that the uncertainty of the instrumentation is about 30 kPa. The National Instruments Measurement and Automation Explorer (MAX) is configured to read a voltage signal from 1V to 5V corresponding from 0 to 14 MPa respectively. This MAX configuration provides a 1.07 kPa/bit resolution compared to the transducer uncertainty of 30 kPa. Based on this information, the bit resolution of the NI 9215 DAQ card provides ample resolution for the pressure transducers used in this experiment.

Instrumentation Control

The facility is controlled by a LabView file which uses an integrated PI-controller to manipulate the inlet pressure into the facility. The pressure is manipulated by an actuated valve which controls the excess flow loop of the test facility. An NI MID-7602 motor controller drives an Oriental Motor PK246PDAR26 stepper motor. The instrumentation is shown in **Figure 200**.

A **B**

Figure 200 Components used to control test facility: A – NI MID-7602 motor controller; B – Oriental Motor PK246DAR26

The motor is attached to a SS-31RS4 valve – refer to **Figure 183** – with a MCS200506 flexible motor coupling. The layout of this system is provided in **Figure 201**. The valve stem is attached to the flexible motor coupling via a spline shaft which allows the valve stem to rise as a function of the number of turns. The valve-motor assembly sits on a platform which is welded together to form a solid base for the rest of the assembly.

A Labview VI was configured to read in the pressure output by the inlet pressure transducer and then update the location of the valve depending on the set point of the desired inlet pressure. It is important to note that this portion of the VI must only be turned on when the pressure is near the desired set point. The procedure for this sub-system dictates that the pressure be within +/- 150 kPa before it is turned on. The valve will then make fine adjustments to the excess flow loop allowing more or less mass to bypass the test section. Steady state does not last long with the current Joy compressor as a large amount of carbon dioxide is lost (i.e. the compressor was not designed for this application) during a single test run of about 15-20 minutes.

There are two valves which allow pressure to flow through the excess loop as was detailed in **Figure 180**. To reach system pressure, close both of these valves at the beginning of a test run and allow the pressure on the high pressure side to build up to the desired test section inlet pressure. Once the system has approximately reached the required test section inlet pressure, manually open the automated valve until the pressure levels off. *Make sure the output signal on the MID-7602 is suppressed or you will not be able to turn the valve!*

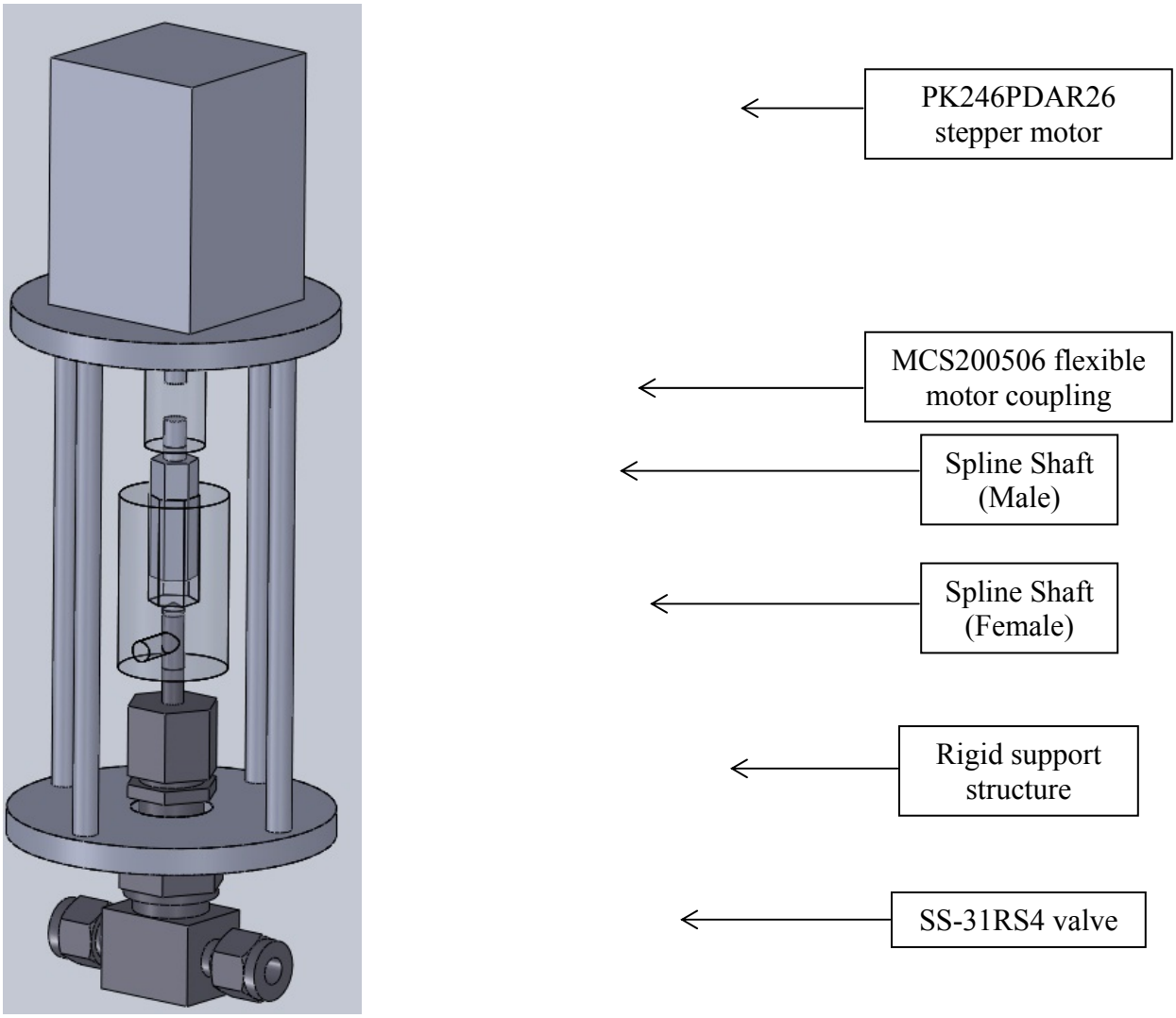

Figure 201 Automated valve which control test facility inlet pressure

4.3.5.2 Temperature

Instrumentation Configuration

Thermocouples are used to monitor and record the temperature at various locations in the facility. Type E thermocouples are used throughout the facility to monitor the temperature of the flow as they offer high resolution and work well at temperatures below 0°C. The pertinent information is summarized in **Table 4-14** and further illustrated in **Figure 202** which shows the expected error based on the manufacturer's data for Type E thermocouples.

The facility also uses Type K thermocouples to monitor the heater surface temperatures. The Labview VI monitors these temperatures and ensures that they do not become excessively high such that the heater wires start to melt. If the temperatures pass a certain threshold, the VI will shut them off automatically based on the maximum desired temperature specified by the user.

Table 4-14 Temperature sensor summary

PARAMETER	VALUE
Type-E Thermocouples	

Resolution	68µV/°C
Temperature range	-40 to 800°C
Type-K Thermocouples	
Resolution	41 µV/°C
Temperature range	0 to 1100°C
NI 9213	
Bits	24
Range	-78.125mV to 78.125mV
Expected Error (Type E)	0.8°C – **Figure 202**: Typ (High res)
Total Type-E Error	1°C

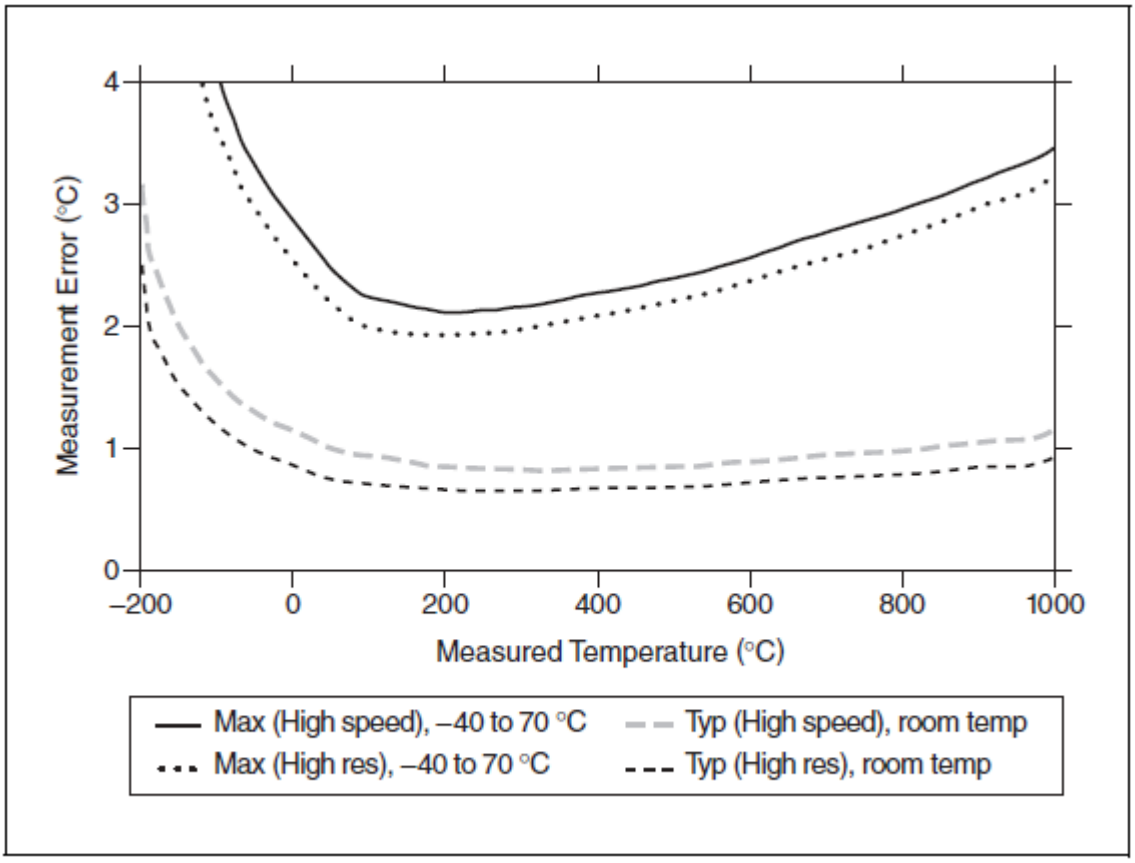

Figure 8. Thermocouple Types T and E Errors

Figure 202 NI 9213 Type E thermocouple measurement error illustrated to require high resolution input mode

The error in the temperature at the cold junction is shown to contribute greatly to the uncertainty of the thermocouples based on **Table 4-14**. There are 16 input channels and only one thermistor integrated into the NI 9213 card. National Instruments makes a note that nearby heat sources such as adjacent modules may cause errors in thermocouple measurements by creating a non-uniform temperature distribution across the reference terminal block. The temperature error will then increase as a function of the physical distance of the channel in question from the reference thermistor location. To decrease the severity of this effect, the NI CompactDAQ

was installed next to one of the Safety and Instrumentation Panel Box inlets shown at the bottom of **Figure 203** and **Figure 204**. Three 117 CFM axial fans were installed on the top of the box to draw high velocity cool air over the NI 9213 thermocouple module as well as to dissipate the heat generated by the 240V heater relays. The NI 9213 module was also installed away from the other modules used in the CompactDAQ housing. The entire system was calibrated with the fans turned on in order to ensure repeatability.

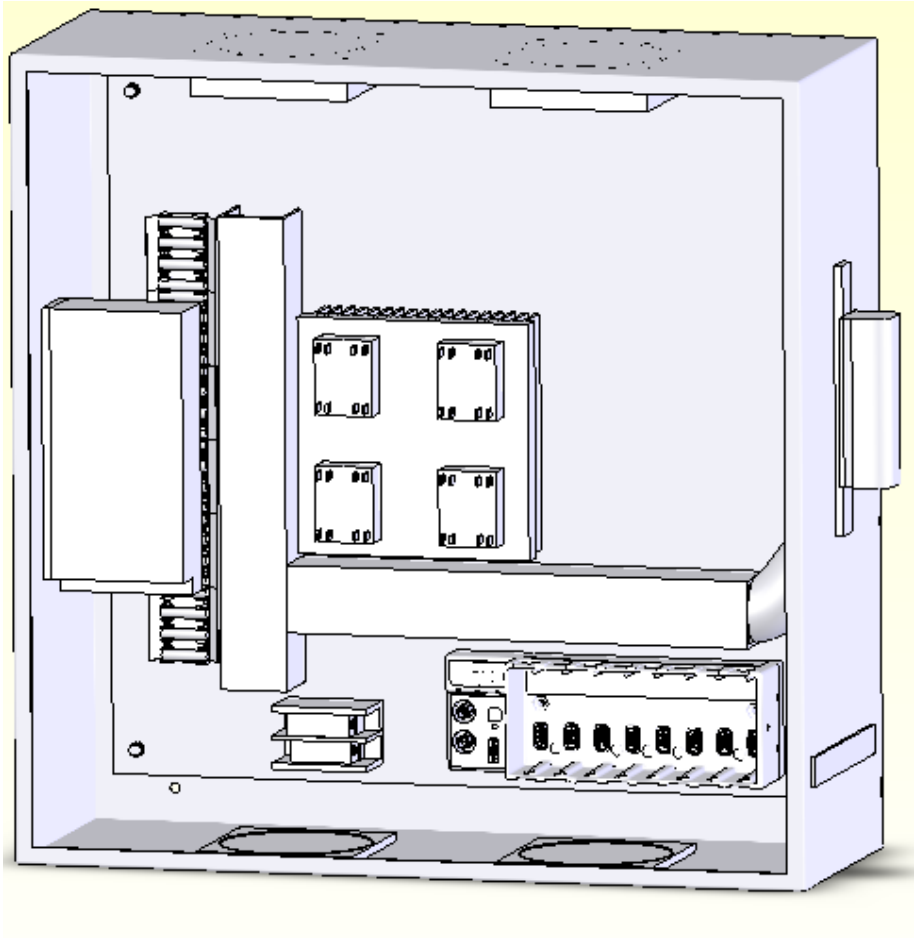

Figure 203 Layout of safety and instrumentation panel box

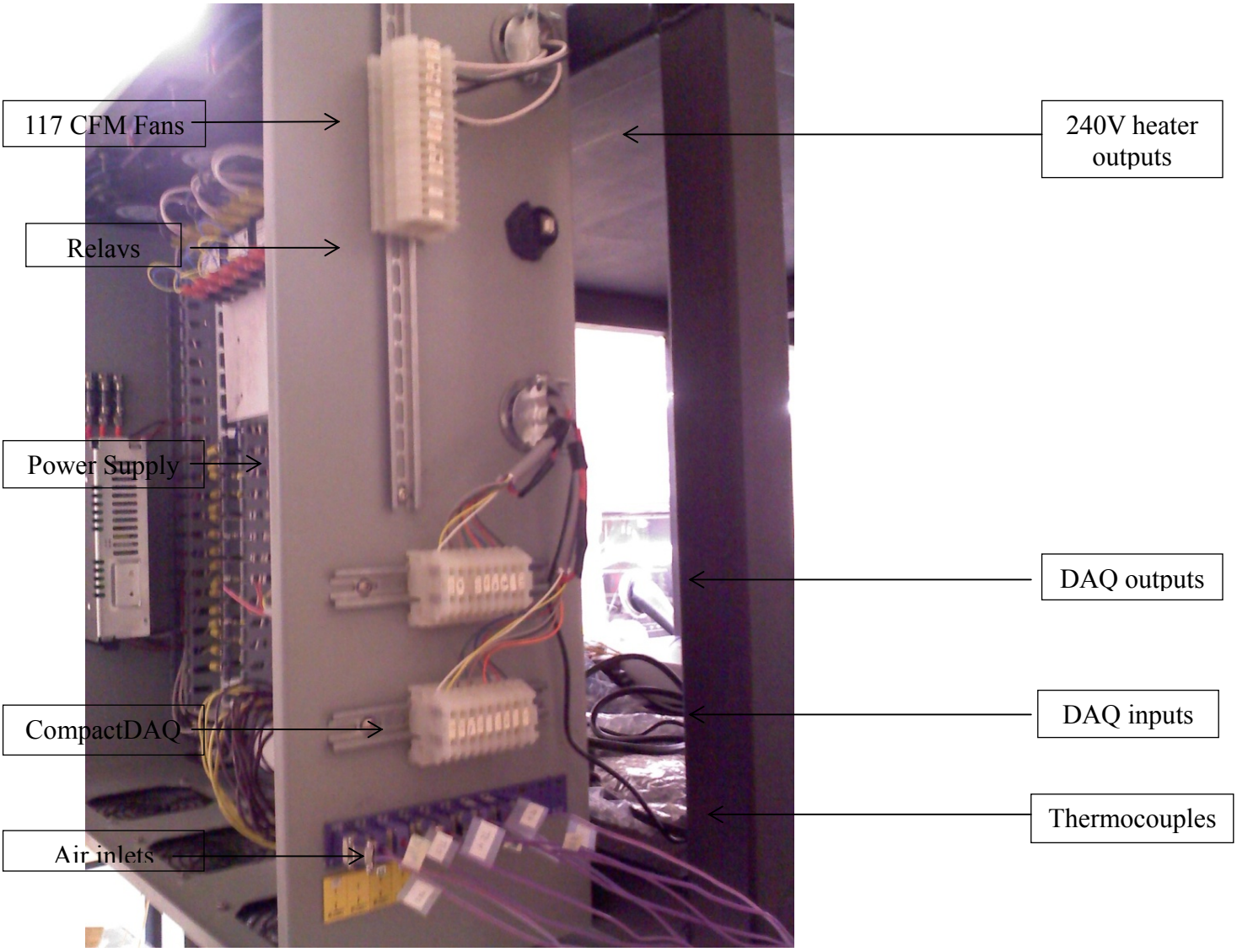

Figure 204 Safety and instrumentation panel box

The safety panel box was constructed to centralize the instrumentation and the 240V electrical lines which power the heaters.

Instrumentation Control

Temperature is regulated by two mechanisms in this facility. The first mechanism is the PID-controller implemented in Labview which continually monitors and adjusts the power sent to tube surface heaters implemented throughout the facility. The concept is explained in **Figure 205** and **Figure 206** where a wall output signal 240V, 60Hz signal is turned on and off by a computer controlled relay.

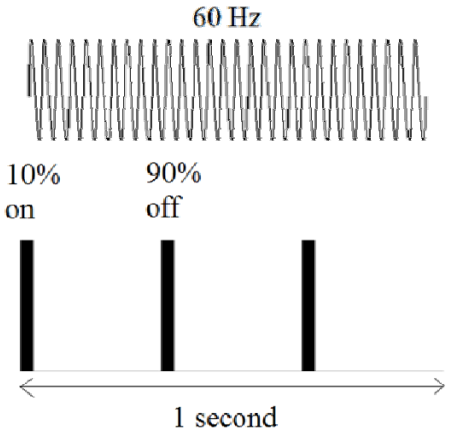

Figure 205 Relay controlled output signature of heaters

Figure 205 shows a 60Hz signal being continually cycled on and off over the course of 1 second. The energy output from the relay is on a total of 10% of the time and off 90% of the time in this example. The relay is not restricted to this limit however and by varying the ratio of the time the relay is on to the time the relay is off, one can adjust the integrated energy output dissipated by the heaters.

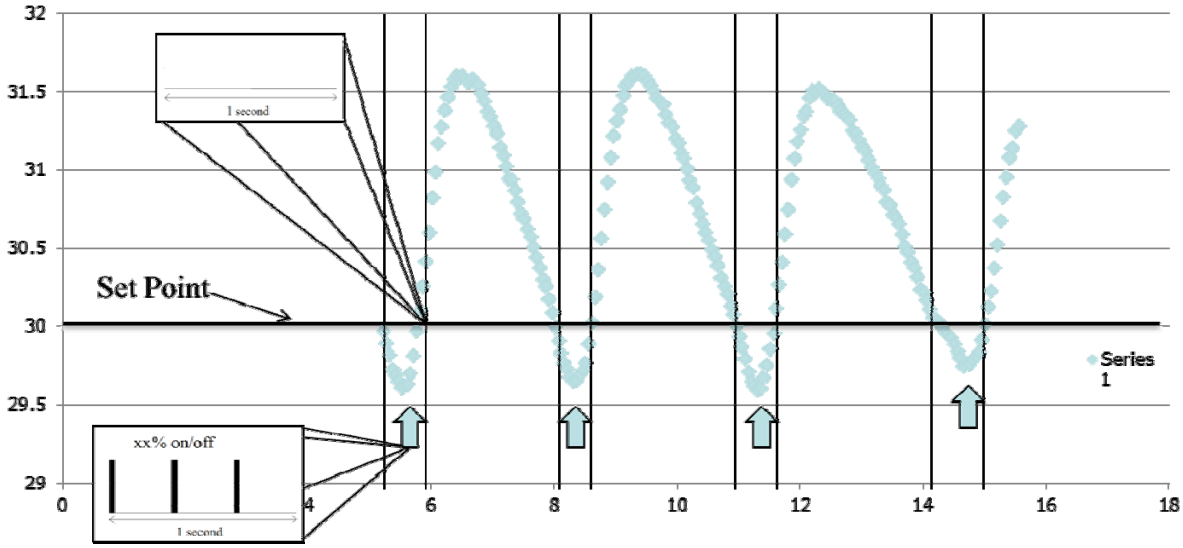

Figure 206 Description of PID operated heaters

Figure 206 shows a figure of a PID controller which has not been tuned for purposes of exaggerated demonstration. The set point in the figure indicated the desired temperature. At the point that the temperature falls below the set point, the total time the heaters are on quickly ramps up to a peak percentage which increases the temperature of the incoming stream. The power input into the stream is too great however and the flow overshoots the set point. The controller being insufficiently tuned quickly decreases in power output to effectively 0%. The incoming flow must then dissipate the thermal energy which has been stored in the stainless steel tubing. As times goes on, the energy content of the stainless steel tubing decreases and the flow again overshoots the set point. The heaters turn on again and the process repeats.

The problem discovered with this method was that the sampling time of the thermocouples interfered with the ability of the heater to respond quickly enough to flow temperature fluctuations. As was illustrated in **Figure 202**, the thermocouple temperature error increases with sampling rate (i.e. high speed vs. high resolution).

Figure 207 demonstrates that the timing modes if using all channels differ by a factor of 1 to 75 samples per second for high resolution and high speed respectively. The maximum sampling rate when operating in high resolution mode is 1 sample per second. It becomes exceedingly difficult to respond effectively to small temperature fluctuations in the flow when operating at such large time scales. The upstream heater was therefore decommissioned to only respond to large scale changes in temperature.

The heaters controlled in the two-phase region were unaffected by sampling time issues. Those heaters effectively need to operate at 100% duty cycle in order to cycle carbon dioxide continuously. The heaters are limited only by the melting point of the heating tape material rated to 480°C. The Labview VI will automatically decrease the power they dissipate if the surface temperature becomes too high.

Timing Mode	Conversion Time (Per Channel)	Sample Rate* (All Channels†)
High-resolution	55 ms	1 S/s
High-speed	740 µs	75 S/s

* If you are using fewer than all channels, the sample rate might be faster. The maximum sample rate = 1/(*Conversion Time* × *Number of Channels*), or 100 S/s, whichever is smaller. Sampling faster than the maximum sample rate may result in the degradation of accuracy.
† Including the autozero and cold-junction channels.

Figure 207 NI 9213 Timing mode disclaimer

4.3.5.3 Flow and Density

Instrumentation Configuration

Figure 208 shows the Rosemount CMF010 coriolis flow meter incorporated in the test loop. The coriolis flow meter offers exceptional independent resolution of the density and mass flow rate. A summary of the design configuration is provided in **Table 4-15**.

Figure 208 Rosemount CMF-010 Coriolis flow meter

Table 4-15 Coriolis flow meter summary

PARAMETER	VALUE
CMF010 Flow Meter with 2200 Transmitter	
Mass Flow Rate Accuracy	0.05%
Flow Rate Full Span	108 kg/hr
Density Accuracy	+/-0.2 kg/m^3
Density Full Span (MAX config)	1000 kg/m^3
Sensor Output	1V to 5V
NI 9215 DAQ Card	
Bits	16
Range	-10V to 10V
Least Significant Bit Change	305µV/bit
Summary	
Mass Flow Rate Uncertainty	0.054 kg/hr
Flow Rate Quantization	27 (kg/hr)/V
DAQ Card Limitation	0.008235 (kg/hr)/bit
Density Uncertainty	0.2 kg/m^3
Density Quantization	200 (kg/m^3)/V
DAQ Card Limitation	0.061 (kg/m^3)/bit

The uncertainty of the Coriolis flow meter is about 0.054 kg/hr and 0.2 kg/m^3 as reported in **Table 4-15**. The NI 9215 DAQ card quantization resolution is limited to 6.5 and 3.27 times the uncertainty of the input signals and provides adequate bit resolution.

4.3.5.4 Uncertainty of Isentropic Flow at Nominal Test Conditions

The uncertainty of the test loop where flow is expanded through an orifice from a nominal upstream condition of 7.6 MPa and 500 kg/m^3 is detailed in **Figure 209** and **Figure 210**. **Figure 209** seems to illustrate that the instrumentation uncertainty is small compared to the total uncertainty which takes into effect cross-sectional geometrical conditions. The problem with this figure is that it does not clearly illustrate how important uncertainty in the pressure ratio is to total uncertainty.

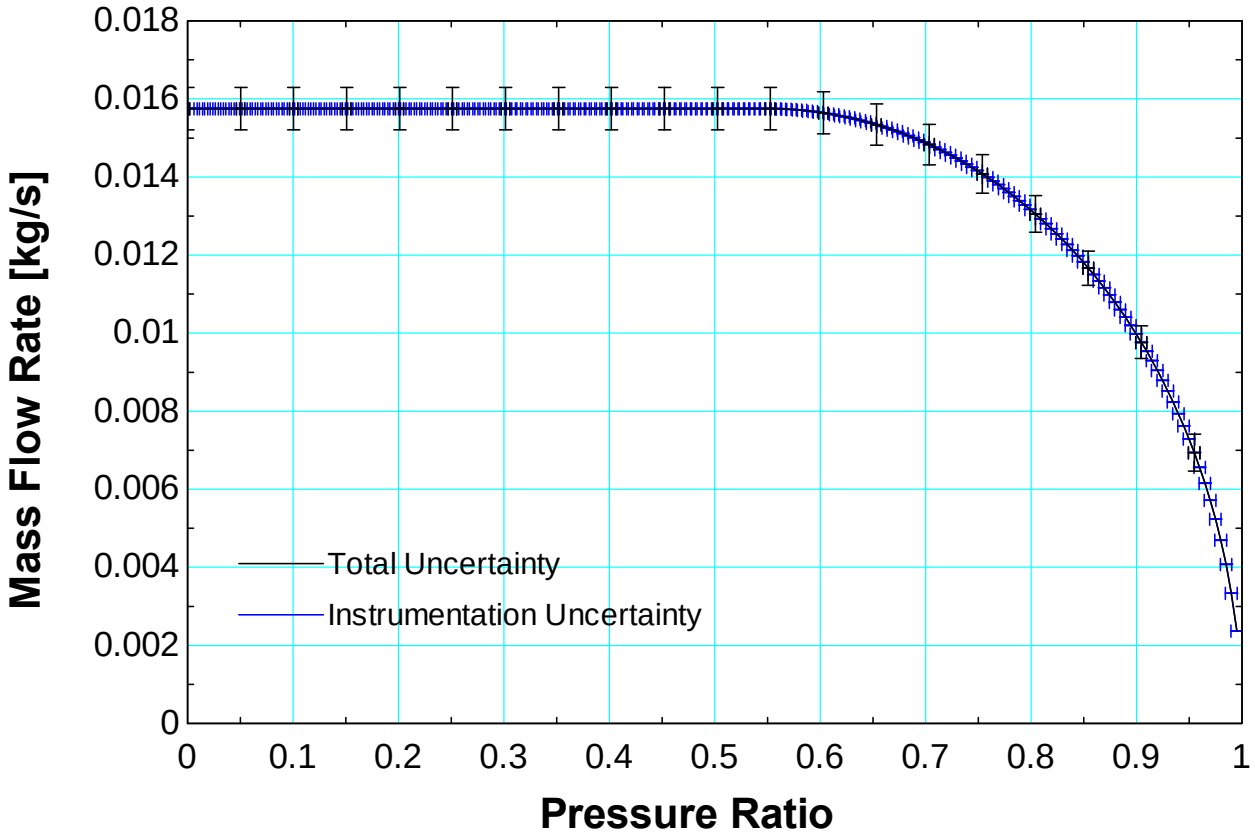

Figure 209 Uncertainty at nominal upstream test conditions of 7.6 MPa and 500 kg/m^3

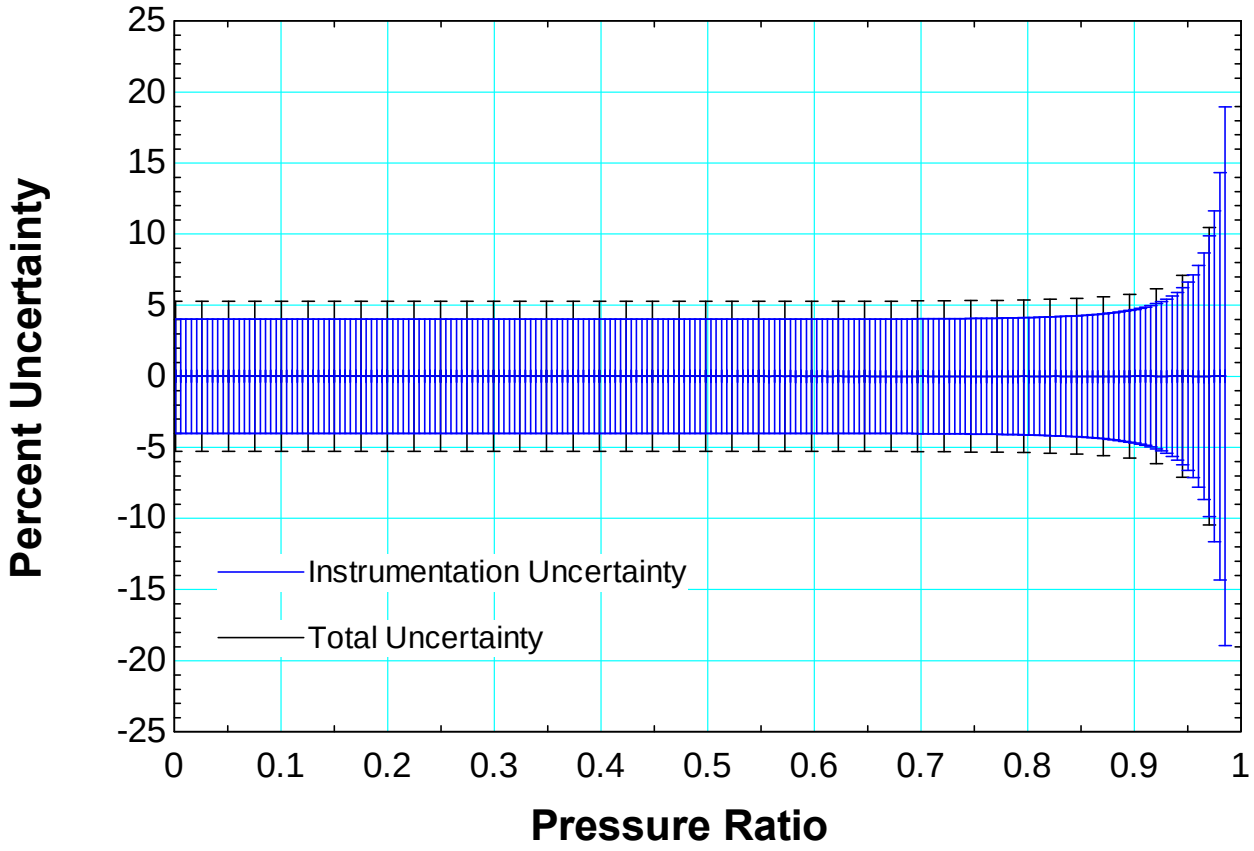

Figure 210 Percent uncertainty at nominal upstream test conditions of 7.6 MPa and 500 kg/m^3

A more interesting perspective of the facility uncertainty is illustrated in **Figure 210**. Notice that the facility maintains about +/-5% uncertainty throughout most of the range of pressure ratios desired when operating at a nominal upstream value of 7.6 MPa and 500 kg/m^3. Two regions are identified from the figure. In the first regime, both geometric and instrumentation uncertainty are important. The second regime is shown on the right hand side of **Figure 210** where instrumentation error becomes an issue. In this limit, the pressures measured by the pressure transducers begin to approach one another which facilitates higher relative uncertainty. The uncertainty attributed to the mass flow meter also begins to increase as the flow rate approaches a value of 0 kg/hr.

4.3.6 Test Facility Design

The test facility was designed to cycle carbon dioxide through the test section continuously. The following section highlights the unique design elements which were considered in the fabrication of this test facility.

Sections 4.3.6.1 and 4.3.6.2 document the analysis and construction methodology employed in the design of the test section. The ideas which facilitated this design were developed in Sections 4.3.2 through 4.3.4.

Sections 4.3.6.3 details the two-phase recovery system which was used to cycle gaseous carbon dioxide through the compressor.

4.3.6.1 Test section assembly procedure

Section 4.3.2 and 4.3.3 provided a basis for the properties the facility would need to support and in what

quantities. It was noted that the facility would need to accommodate high pressure gradients as well as large flow rates. This information was compounded by the ideas expressed in Section 4.3.4 where it was illustrated that limiting geometrical uncertainty was crucial to facility performance.

The goals outlined for the test section are provided below as well as noted in **Figure 211**.

- Accommodate high pressure gradients
- Support multiple seal configurations
- Limit uncertainty due to the design variable shown
- Encapsulate design in a pressure vessel shroud

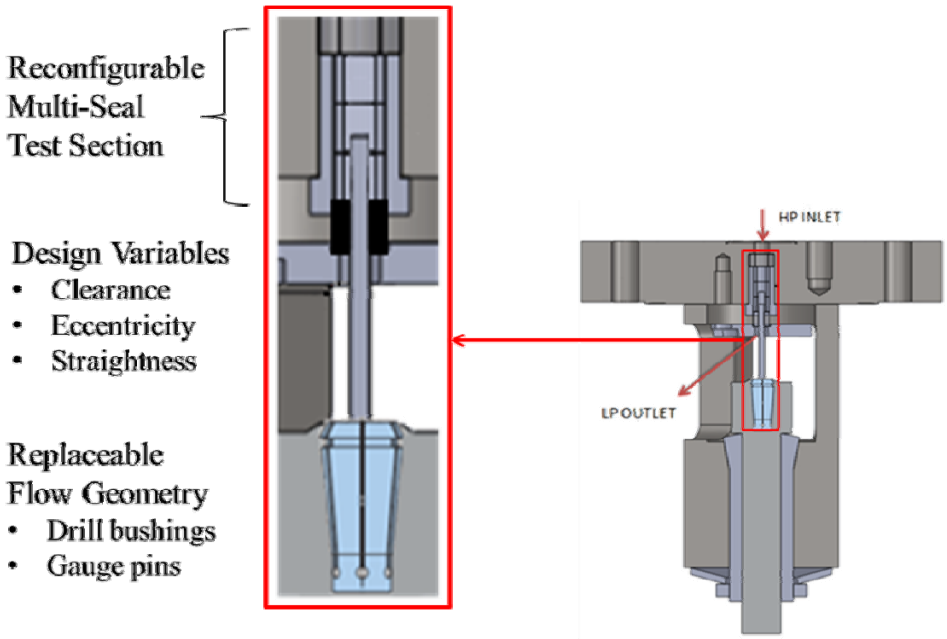

Figure 211 Design variables considered in the design of the test section

The alignment process used to simulate the shaft and seal interface is detailed here. The uncertainty in the eccentricity requires that the procedure detailed here be followed precisely in order to limit three-dimensional flow conditions.

Collet Holder Sub-Assembly

The Collet Holder Sub-Assembly is detailed in **Figure 212**. The design uses a multiple stage collet system in order to achieve proper alignment of the assembly gauge pin shown at the bottom. It is very important to use the assembly gauge pin with a diameter 3.175mm (0.125in) in this initial sub-assembly.

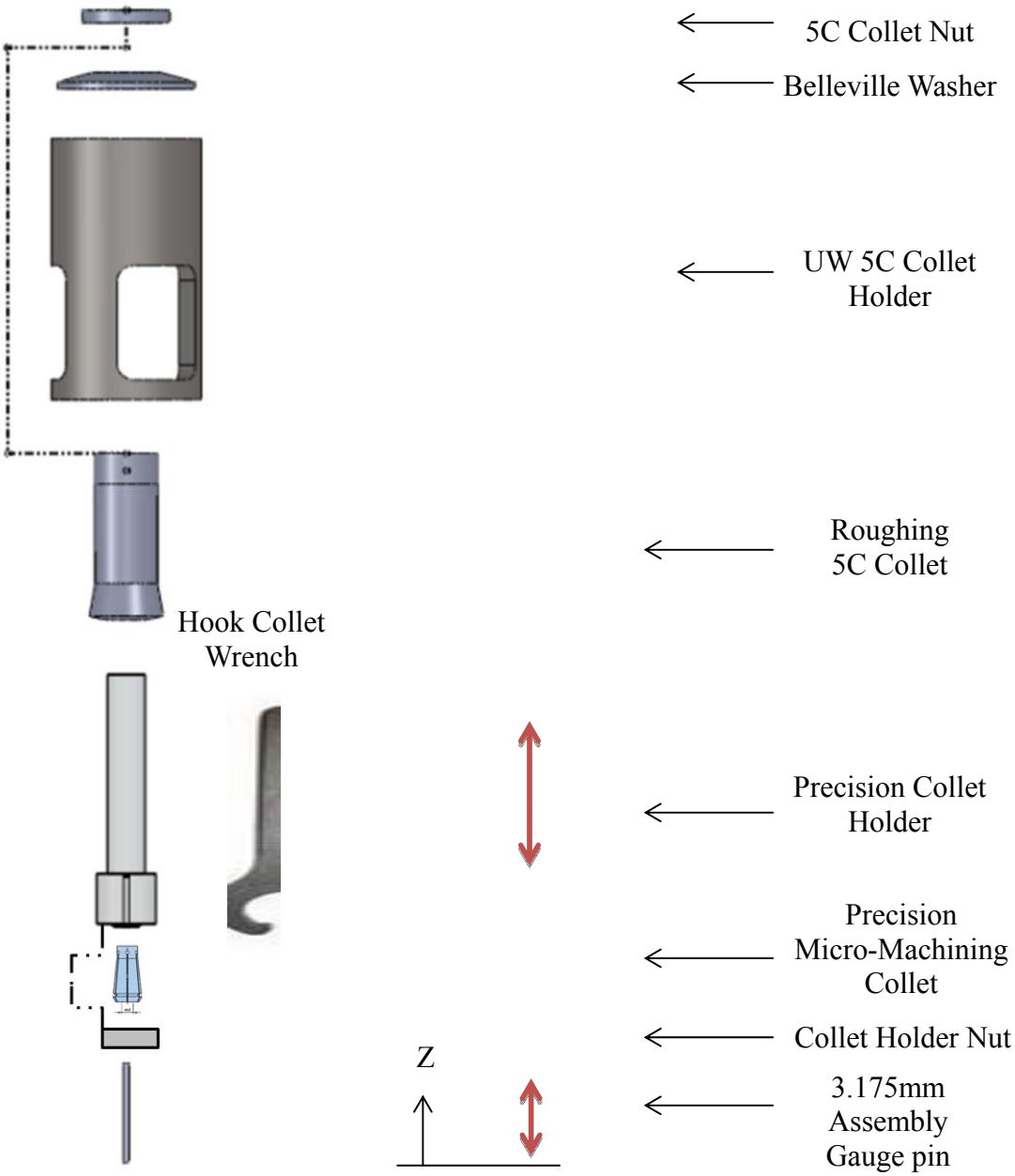

Figure 212 Assembly procedure of Collet Holder Sub-Assembly

The dashed lines in the figure represent the components which are screwed together in order to provide a clamping mechanism for dependent child components. Tightening the Collet Holder Nut requires the use of the Hook Collet Wrench also shown in the figure. The child components are illustrated in the figure with red up and down arrows noting the flexible parent-child interface in the axial Z-direction. The gauge pin and precision collet holder are free to move in the axial direction and allow the final assembly the ability to support multiple seal configurations. **Figure 213** illustrates one particular configuration of this sub-assembly.

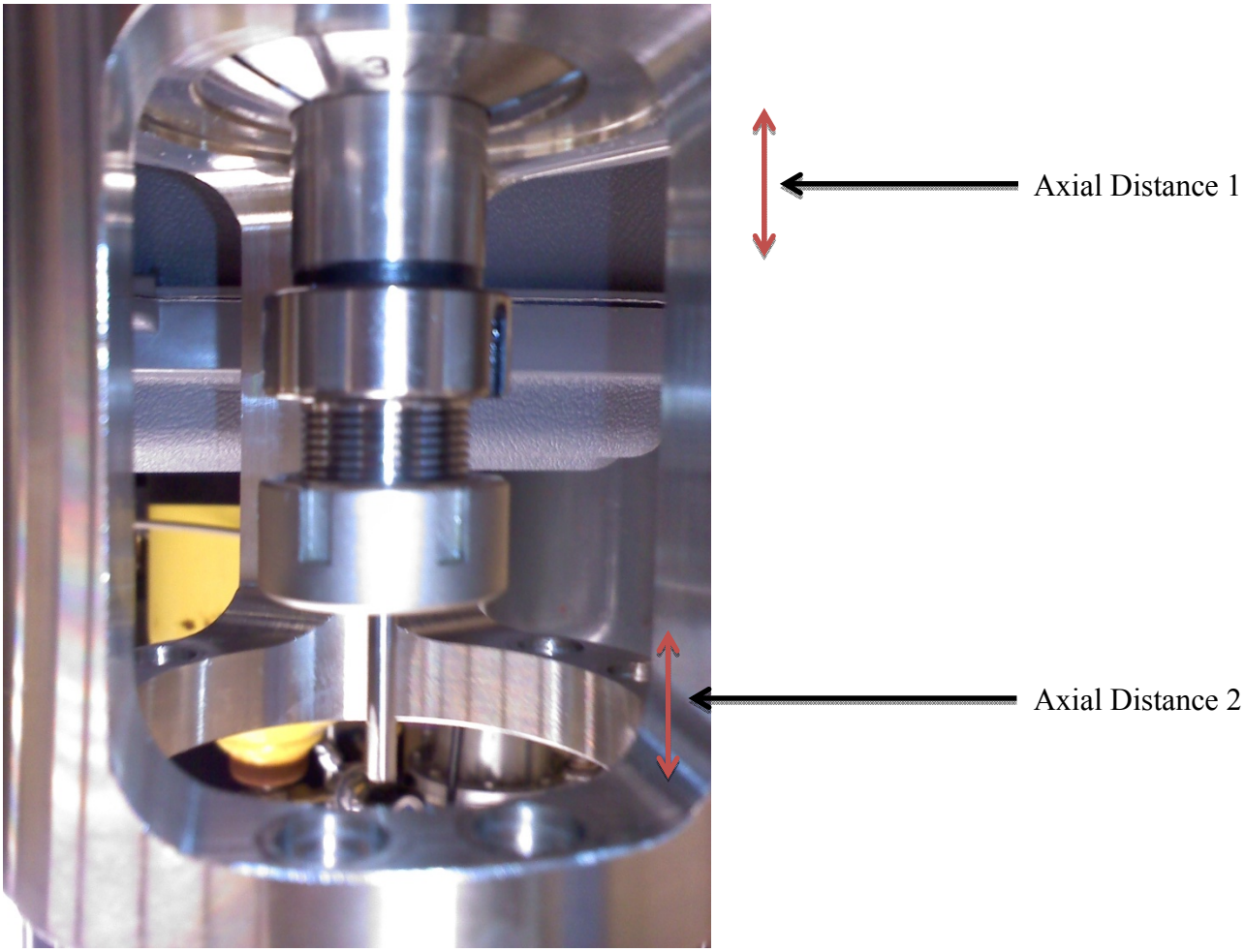

Figure 213 Collet holder sub-assembly shown in configured state with alignment gauge pin attached

Figure 213 illustrates the Collet Holder Sub-Assembly configured to support one seal. The red up and down arrows which were included in **Figure 212** are shown here to provide a visual aid of the flexible interfaces in the sub-assembly. Notice that the sub-assembly was designed to accommodate multiple seals by skewing the relative distances between the axial distances shown in the figure. Axial distance 1 may be reduced while simultaneously increasing axial distance 2 to provide up to 4 cm of axial depth available for seal stacking. The uncertainty in the annular area based on the axial depth was shown in **Figure 193**.

Shaft-Seal Sub-Assembly

The Shaft-Seal Sub-Assembly is illustrated in **Figure 214**. The Collet-Holder Sub-Assembly is combined with a stackup of drill bushings which simulate shaft seals. A seal clamp is used to bolt the seal-stackup to the Test Section Flange as shown in the figure.

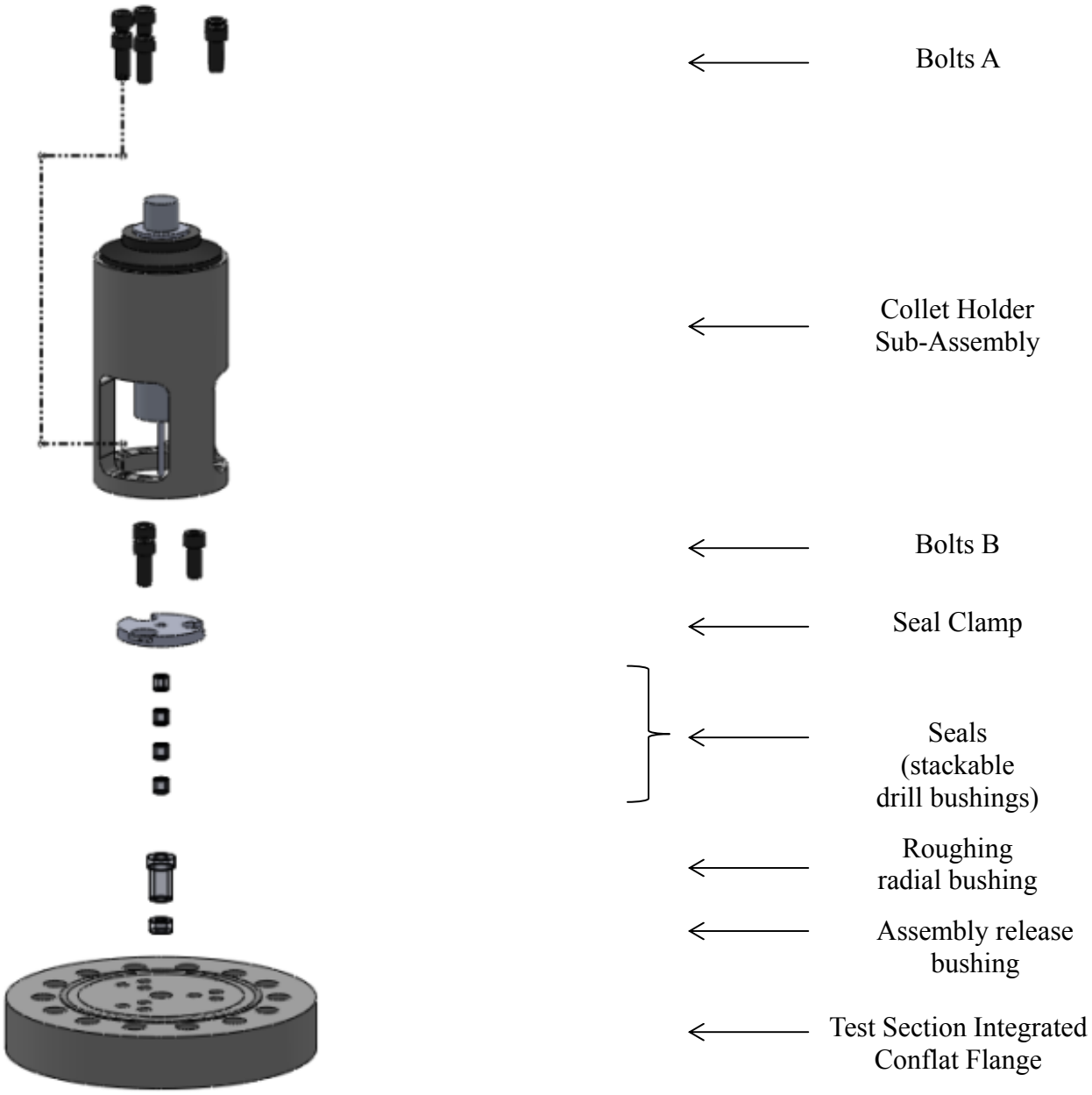

Figure 214 Assembly procedure of Shaft-Seal Sub-Assembly

Bolting the configuration in the proper order is crucial to limiting uncertainty in the final assembly. The inner bolt pattern is used to clamp the seal-stackup to the flange as demonstrated in **Figure 215**. The figure shows a stack-up of the assembly release bushing, roughing radial bushing, three 7.938mm ID seal spacers, one 3.175mm ID seal, and seal clamp mated to the test section flange. It is very important to leave this stack-up loosely bolted together (Bolts B in **Figure 214**) in this step in order to align all the seals with the 3.175mm gauge pin shown at the bottom of the Collet-Holder Sub-Assembly in **Figure 212** later. Use enough copper lubricant on Bolts A and B to prevent galling as shown in **Figure 214**.

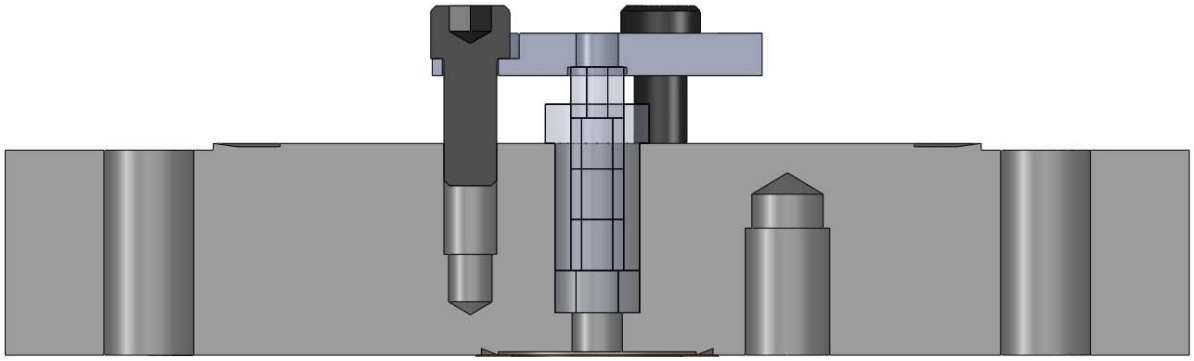

Figure 215 Conflat Flange seal-stackup bolting configuration

The Collet Holder Sub-Assembly from **Figure 212** is then bolted to the outer bolt pattern of the Test Section Flange as depicted in **Figure 216**. The outer diameter of the seal clamp and the inner diameter of the 5C Collet Holder from **Figure 212** should just clear with the gauge pin inserted into the center portion of the seal stack-up configuration. The final configuration of this assembly step is shown here as **Figure 216**. Notice that there is effectively zero clearance between the alignment gauge pin and the top seal shown in the figure; this alignment procedure is crucial to meeting the stringent uncertainty specifications referenced in Section 4.3.4.4 and illustrated in **Figure 191**-A.

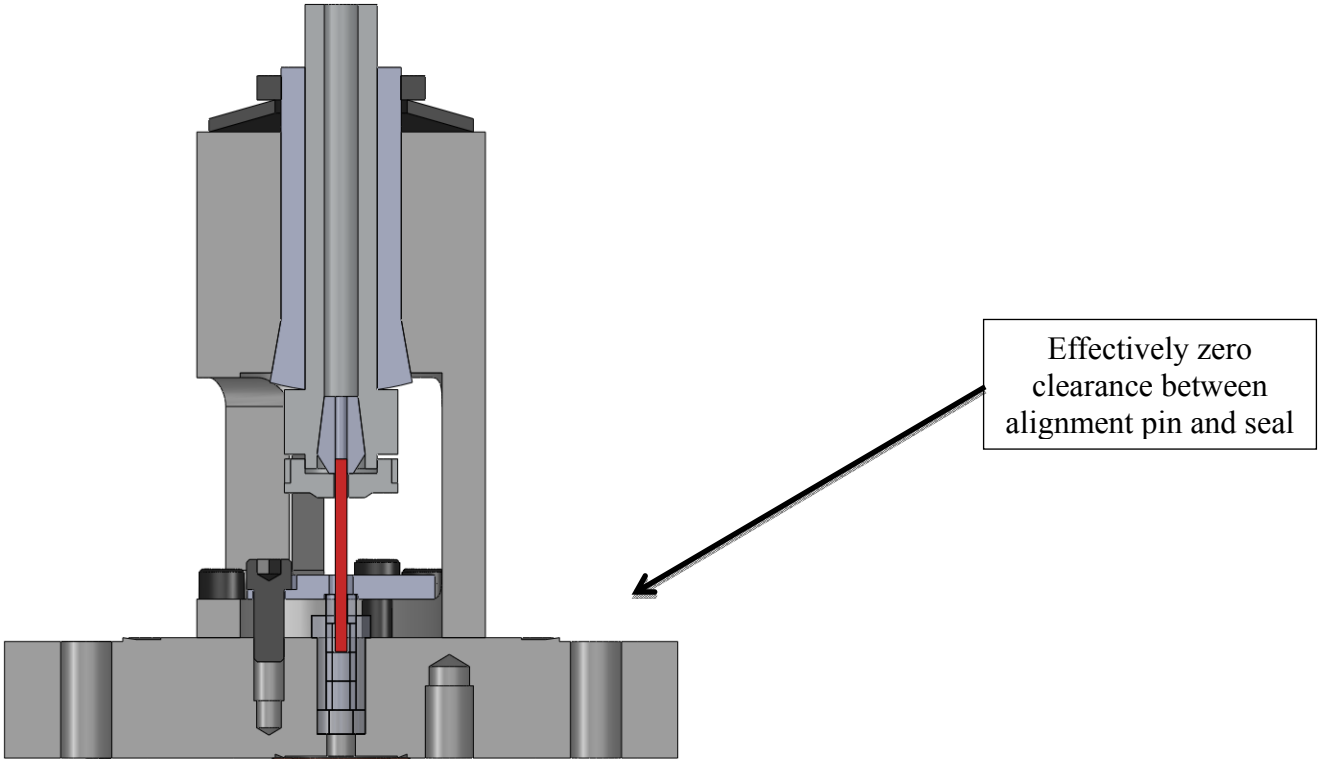

Figure 216 Shaft-Seal Sub-Assembly with 3.175mm gauge pin used to align multiple seals; shown here aligning only one seal

Once the Shaft-Seal Sub-Assembly shown in **Figure 216** has been loosely bolted together to form the configuration shown, tighten Bolts A as **Figure 214** to the flange while leaving Bolts B loose. In this fashion, the alignment pin will become a fixed reference centering point. The seals with then automatically align themselves to the centering pin. Tighten Bolts B to fix the seals in place about the alignment pin.

The next step requires considerable patience and is the most difficult step of the process. The objective is to

remove the alignment pin and replace it with a small diameter gauge pin in order to simulate the shaft-seal clearance.

The process requires the Hook Collet Wrench **Figure 212**, tweezers, and a hammer. Untighten the Collet Holder Nut from **Figure 212** with the Hook Collet to free the Precision Micro-Machinging Collet. The collet will stay stuck inside the Precision Collet Holder; stick the tweezers down the bore-hole of the Collet Holder to use as a hammer punch. Lightly tap on the tweezers with the hammer to completely free the collet. The alignment pin should be free to move inside the assembly at this point. It will be necessary, however, to use the tweezers, light hammering, and gravity to take the alignment pin out of the assembly completely.

Insert the desired shaft gauge pin into the assembly through the exposed hole on the backside of the Test Section Flange. Use the tweezers to position the shaft inside the collet. Finally, tighten the Collet Holder Nut with the Hook Collet. The final configuration of the Shaft-Seal Sub-Assembly is shown in **Figure 217**.

Figure 217 Shaft-Seal Sub-Assembly

Test Section Final Assembly

The final step in the test section assembly procedure is detailed in **Figure 218**. Note that the Pressure Vessel Shroud is fixed to the actual test facility. Copper gaskets are used to seal the enclosure together noted in the figure as Cu Gasket A and B. Grade 9 bolts are used in the facility detailed as Bolts C and D. A High Pressure Inlet Cap allows the Test Section Flange to interface with standard Swagelok connections.

Perhaps the most deceptive connection of the assembly is the Type-E Thermocouple which must be fastened to the assembly last. The thermocouple fits inside one of the windows of the 5C Collet Holder illustrated in **Figure 212**. *Be sure not to tighten Bolts D without first checking that the thermocouple will mate together with the assembly.* If the thermocouple does not go in completely, rotate the Shaft-Seal Sub-Assembly about its center axis until one of the windows in the 5C Collet Holder aligns with the thermocouple. The concept is demonstrated in **Figure 218**.

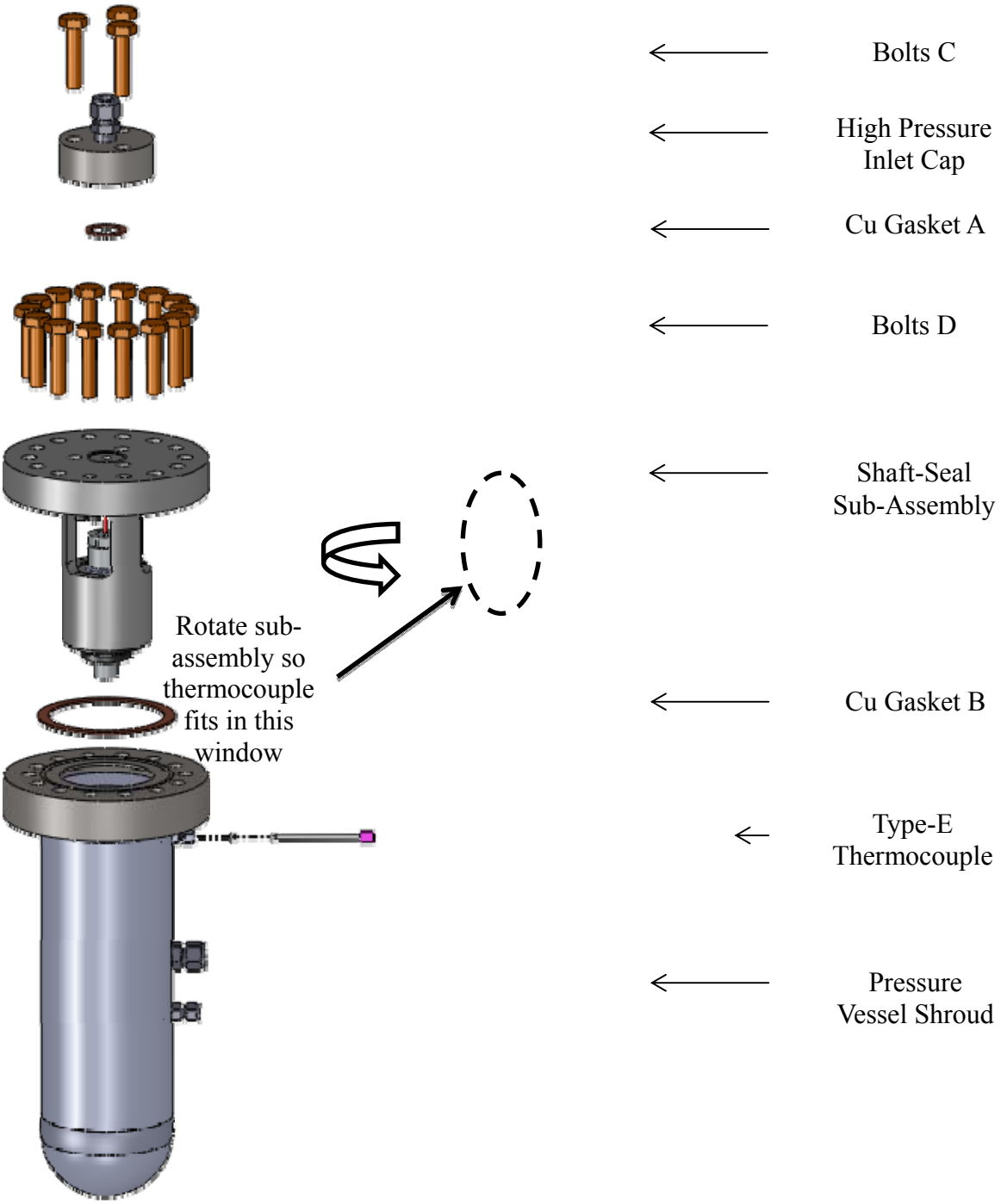

Figure 218 Final assembly procedure for configuring test section

The final configuration is illustrated as a section view in **Figure 219**. Again, the thermocouple must be the last item fastened to the test section during assembly and the first thing detached when disassembling. The orientation of the inlet and outlets is shown in the figure.

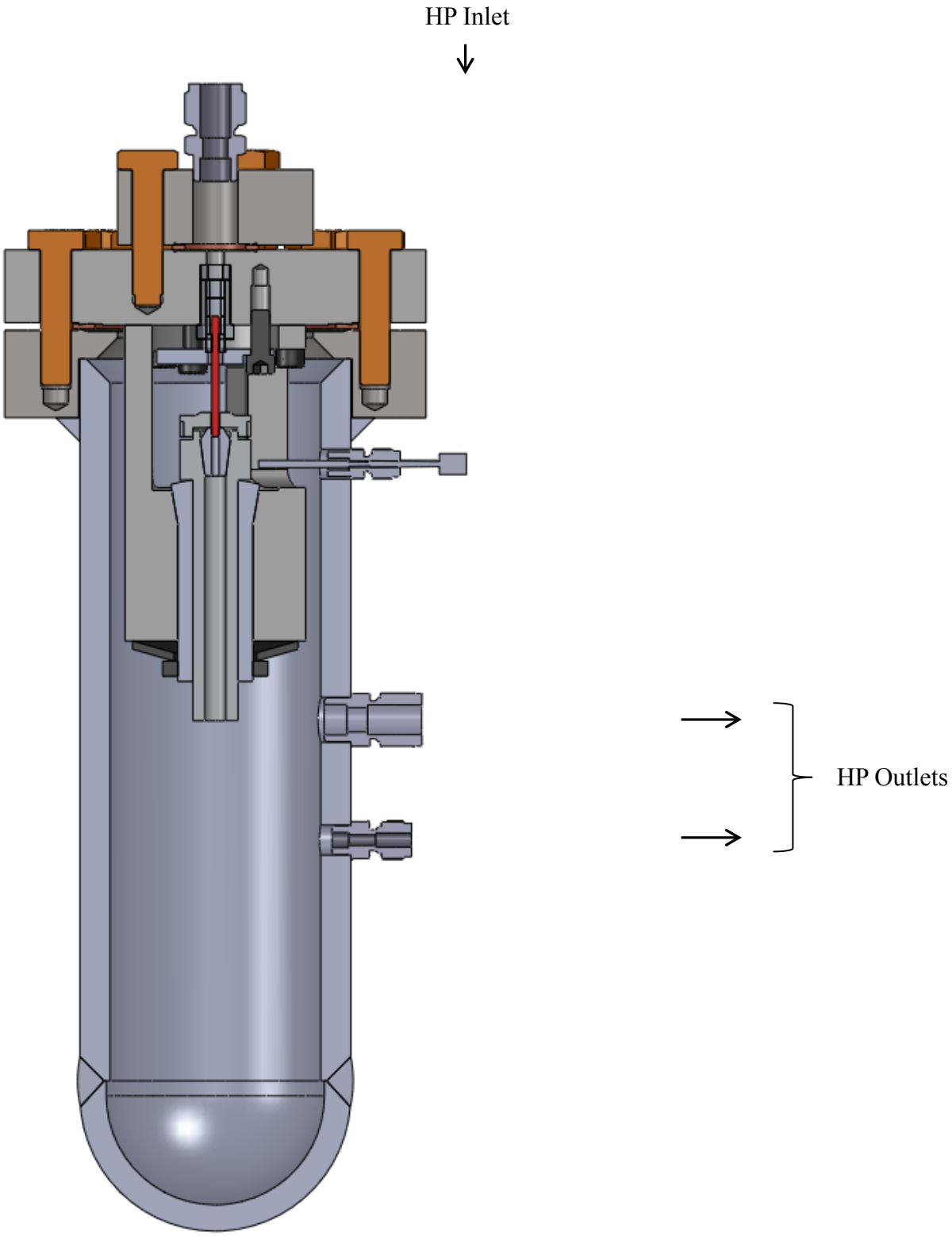

Figure 219 Detailed section view of test section

4.3.6.2 Pressure vessel design

The desired operating pressures of the test facility dictated that the test section needed to be encapsulated in a pressure vessel. The experimental test section was designed with this in mind based on the design methodology

outlined in the ASME Boiler and Pressure Vessel Code explained in the *Companion Guide to the ASME Boiler and Pressure Vessel Code* (hereafter referred to as the *Companion Guide*).

The flange was designed according to the 40.6 Flange-Design Methods section of the *Companion Guide* which is based on the design-by-formula approach of the ASME code, ASME Section VIII, Division 1, Appendix 2. The design philosophy shown is for a bolted-flange connection with ring-type gaskets.

The design criteria used in the design of this flange is shown in **Table 4-17**. The units are specified in English units as consistent with the *Companion Guide*. It is important to note that the design specifications outlined in Pressure Vessel Engineering Ltd. have been heavily referenced in this analysis.

Materials

The first step was to determine the design strength of the materials used in the facility. The materials used to construct the test section are itemized in **Table 4-16** along with the ambient strength, design strength, and maximum temperature supported by the facility. The design strength was ascertained at the temperature specified in equation (3.67).

$$T_{design} = 350^{\circ} F \qquad (3.67)$$

Table 4-16 Properties of materials used to construct pressure vessel housing

MATERIAL		AMBIENT STRENGTH (psi)	DESIGN STRENGTH (psi)	MAX TEMPERATURE (°F)
SA-312 304L	Sms. and Weld Pipe	16700	16250	1200
SA-240 316	Plate	20000	19650	1500

A linear interpolation between the ASME pressure vessel values at 300°F and 400°F was used for both materials.

Shell Housing

The shell housing was specified according to the parameters itemized in **Table 4-17**. The objective was to minimize the cost by minimizing the material required to construct the test section. A 4" nominal pipe size cylinder was used to create the shell of the pressure vessel. A detailed analysis is provided below.

Table 4-17 Straight shell design parameters

DESIGN PARAMETERS	VARIABLE	VALUE
STRAIGHT PIPE SHELL		
Nominal pipe size		4 in nps sch 160
Pipe material		SA-312 304L
Temperature		350°F
Pressure	P	3000 psi
Outside diameter	Do	4.5 in
Nominal wall thickness	t	0.531
Pipe length	L	12 in
Corrosion allowance	Corr	0.005 in
Allowable stress at design temp (350°F)	S_f	16250 psi
Long seam efficiency (hoop stress)	E_{long}	0.85
Circum. seam efficiency (long stress)	E_{circum}	0.70
Undertolerance allowance	UTP	12.5%

An undertolerance allowance *UTP* of 12.5% was specified to account for deviations in wall thickness which may occur during the extrusion process as shown in equation (3.68). The nominal thickness was then determined accounting for both the undertolerance as well as the corrosion allowance as demonstrated in equation (3.69). The corrected radius was determined from equation (3.70).

$$UT = t \cdot UTP \quad undertolerance\,allowance \tag{3.68}$$

$$nt = t - Corr - UT \quad nominal\,thickness \tag{3.69}$$

$$R_{inner} = \frac{D_o}{2} - nt \quad inner\,radius\,corrected\ \ for\,allowances \tag{3.70}$$

The required thickness based on the hoop stress and longitudinal stress as required by ASME is determined in equation (3.71).

$$\begin{aligned} &Required\,thickness\,parameters \\ &ta = \frac{P \cdot R_{inner}}{S \cdot E_{long} - 0.6 \cdot P} \qquad Required\,longitudinal\,thickness \\ &tb = \frac{P \cdot R_{inner}}{2 \cdot S \cdot E_{circum} + 0.4 \cdot P}\ Required\,circumferential\,thickness \end{aligned} \tag{3.71}$$

The thickness determined in equation (3.69) must be greater than both the longitudinal and circumferential thickness as shown in equations (3.72) and (3.73).

$$T_{required} = \max(ta, tb) + Corr \tag{3.72}$$

$$nt \geq T_{required} \quad Thickness\,requirement \tag{3.73}$$

The internal pressure supported longitudinally and circumferentially by the shell is demonstrated in equation (3.74).

$$\begin{aligned} &Maximum\,pressure \\ &P_{long,internal} = \frac{S \cdot E_{long} \cdot nt}{R_{inner} + 0.6 \cdot nt} \\ &P_{circum,internal} = \frac{2 \cdot S \cdot E_{circum} \cdot nt}{R_{inner} - 0.4 \cdot nt} \end{aligned} \tag{3.74}$$

The maximum internal pressure is determined by equation (3.75) where the design pressure must be lower than the maximum pressure as in (3.76).

$$P_{\max} = \min\left(P_{long,internal}, P_{circum,internal}\right) \tag{3.75}$$

$$P_{\max} \geq P \tag{3.76}$$

Weld-cap

The test section weld-cap was evaluated as an elliptical head to be conservative. The ideal shape for a head is a hemisphere which divides the pressure across the surface of the head equally. It is more common, however, to find elliptical heads available for purchase as this shape is oftentimes more economical. The elliptical head incurs a reduction in overall capacity as the radius of curvature is now a function rather than a fixed value.

The actual cap resembles a hemisphere more than an ellipse so the values listed here are purely conservative. Note that the test section cap was the least concerning aspect of this design from a maximum allowable working pressure point of view because the weld-cap could stand up to 2 or 3 times the factor of safety already built-in to the ASME Pressure Vessel Code.

Table 4-18 Elliptical head design parameters

DESIGN PARAMETERS	VARIABLE	VALUE
ELLIPTICAL HEAD		
Nominal pipe size		4 in nps sch 160
Pipe material		SA-312 304L
Temperature		350°F
Pressure	P	3000 psi
Outside diameter	Do	4.5 in
Thickness before forming	tb	0.531 in
Corrosion allowance	Corr	0.005 in
Straight skirt length	Skirt	1 in
Allowable stress at design temp (350°F)	S_f	16250 psi
Head longitudinal efficiency	E_{head}	0.85

The parameters used to evaluate the test section cap are listed in **Table 4-18**. A detailed analysis is provided in this section consistent with ASME specifications.

The thickness after forming was evaluated based on equation (3.77). The value obtained notes the thickness that can be expected once the metal has been stretched over a mold.

$$tf = \left\{ \begin{array}{l} tb - \frac{5}{8} in \rightarrow tb \le \frac{9}{16} in \\ 0.85 \cdot tb \rightarrow tb \le \frac{9}{16} in \end{array} \right\} \quad (3.77)$$

The nominal thickness is determined as a function of the form thickness minus the corrosion allowance by equation (3.78). The inner diameter is corrected based on the nominal thickness as demonstrated in equation (3.79).

$$nt = tf - Corr \quad nominal\ thickness \quad (3.78)$$

$$D = D_o - 2 \cdot nt \quad inner\ diameter\ corrected\ for\ allowances \quad (3.79)$$

The inside crown height is determined based on the corrected diameter as in (3.80). The outer crown height is determined from the bottom equation reported in (3.80).

$$h = \frac{D}{4} \qquad inner\ crown\ height$$

$$h_o = h + nt \quad outer\ crown\ height \quad (3.80)$$

These values obtained from equations (3.79) and (3.80) are used in equation (3.81) based on the reference tables listed for each equation as they have been reported by PV Engineering Ltd. EES was used to generate polynomial curve fits based on the lookup values as is demonstrated in **Figure 220** and **Figure 221**. The polynomial curve fits are reported here in equation (3.82) through (3.84). Notice the similarity between equations (3.83) and (3.84).

$$K = K\left(\frac{D}{2h}\right) \quad Table\ 1-4.1$$
$$K_1 = K_1\left(\frac{D}{2h}\right) \quad Table\ UG-37$$
$$K_0 = K_0\left(\frac{D_o}{2h_o}\right) \quad Table\ UG-33.1 \tag{3.81}$$

$$K = 0.337 - 0.0112\left(\frac{D}{2h}\right) + 0.174\left(\frac{D}{2h}\right)^2 - 0.00127\left(\frac{D}{2h}\right)^3 \tag{3.82}$$

$$K_1 = 0.253 + 0.140\left(\frac{D}{2h}\right) + 0.122\left(\frac{D}{2h}\right)^2 - 0.0153\left(\frac{D}{2h}\right)^3 \tag{3.83}$$

$$K_0 = 0.253 + 0.140\left(\frac{D_0}{2h_0}\right) + 0.122\left(\frac{D_0}{2h_0}\right)^2 - 0.0153\left(\frac{D_0}{2h_0}\right)^3 \tag{3.84}$$

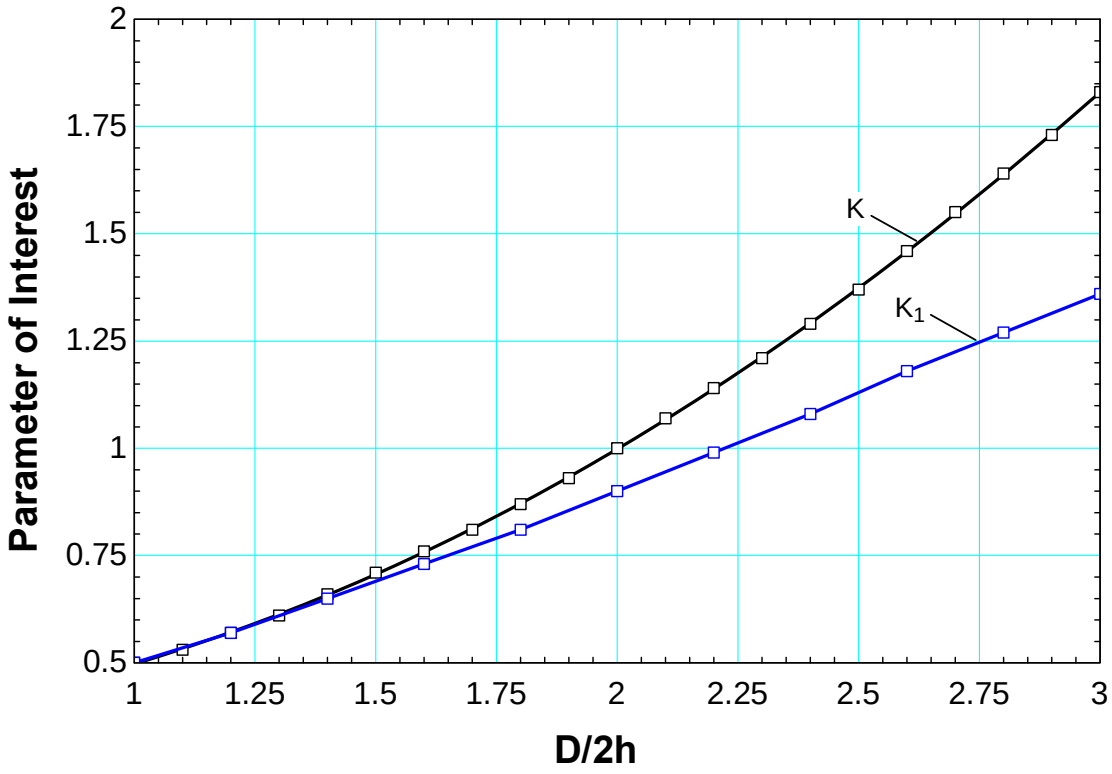

Figure 220 Parameters used to determine inner crown efficiency

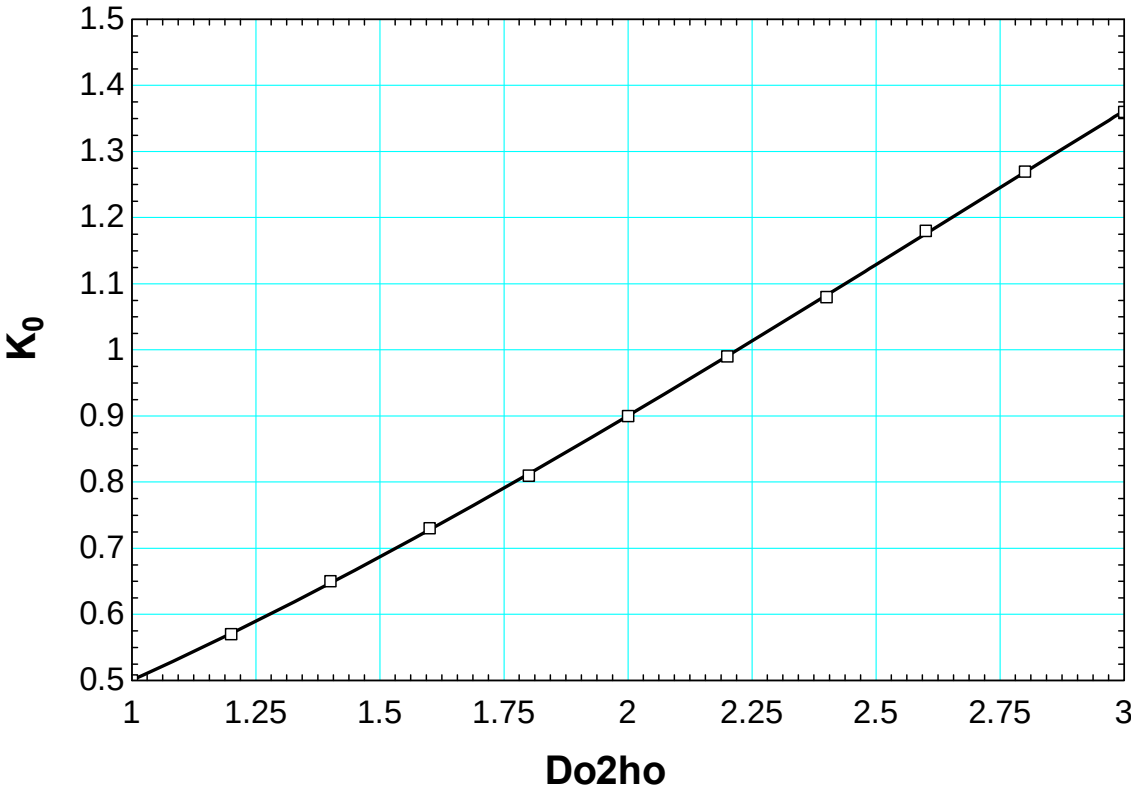

Figure 221 Parameters used to determine outer crown capacity

The parameters $K, K_1,$ and K_0 are effectively form factors that accommodate the deviations from the ideal hemispherical head. Elliptical "stunting" of the cap results in non-linear stress distributions which are a function of the cap's radius of curvature profile.

An effective outer radius is determined based on the outer crown parameter K_0 as demonstrated in equation (3.85).

$$R_o = K_0 D_o \qquad (3.85)$$

An analysis calculation is required if the parameter listed in equation (3.86) falls within the bounds specified in the first line. This is essentially a ratio of the forming thickness to the inner diameter multiplied by the inner crown parameter K_1. It is desirable to maintain as large of curvature as possible so that stress risers do not become excessive. In this case, the worse possible configuration corresponds to a flat surface.

$$App_{1\text{–}4}: \begin{cases} 0.0005 \le \dfrac{tf}{K_1 D} < 0.002 \rightarrow Calculation\ required \\ \dfrac{tf}{K_1 D} > 0.002 \rightarrow Calculation\ not\ required \end{cases} \qquad (3.86)$$

Calculation of this parameter was not required in the design of this pressure vessel as equation (3.86) was found to lie in acceptable bounds even in this conservative analysis.

The required thickness was determined based on equation (3.87) where the formed thickness was found to be

larger than that required as noted in equation (3.88).

$$t_{required} = \frac{P \cdot D \cdot K}{2 \cdot S \cdot E - 0.2 \cdot P} + Corr \quad (3.87)$$

$$tf \geq t_{required} \quad (3.88)$$

The max pressure was determined based on equation (3.89) where the design pressure is much less as shown in equation (3.90).

$$P_{\max} = \frac{2 \cdot S \cdot E \cdot nt}{K \cdot D + 0.2 \cdot nt} \quad (3.89)$$

$$P_{\max} \geq P \quad (3.90)$$

Again, the test section cap was by no means the limiting constraint in this test section design.

Flange Construction

The flange design was optimized to incorporate the test section as well as use the least amount of material as possible. The final configuration called for 6 kg loose-flange mated to a 9.5 kg blind flange. To put things into perspective, comparable standard class 1500 ASME flanges of this nature would have resulted in at 28.5 kg and 33.8 kg respective assembly. Standard ASME flanges are expensive and not easily modified. A graph of ASME flange specifications of pressure as a function of temperature has been provided in **Figure 222**. The minimum flange that meets the criteria for this test facility is highlighted as a class 1500 flange where the cost for a single class 1500 flange made of 316 stainless steel was determined to be in the thousands of dollars

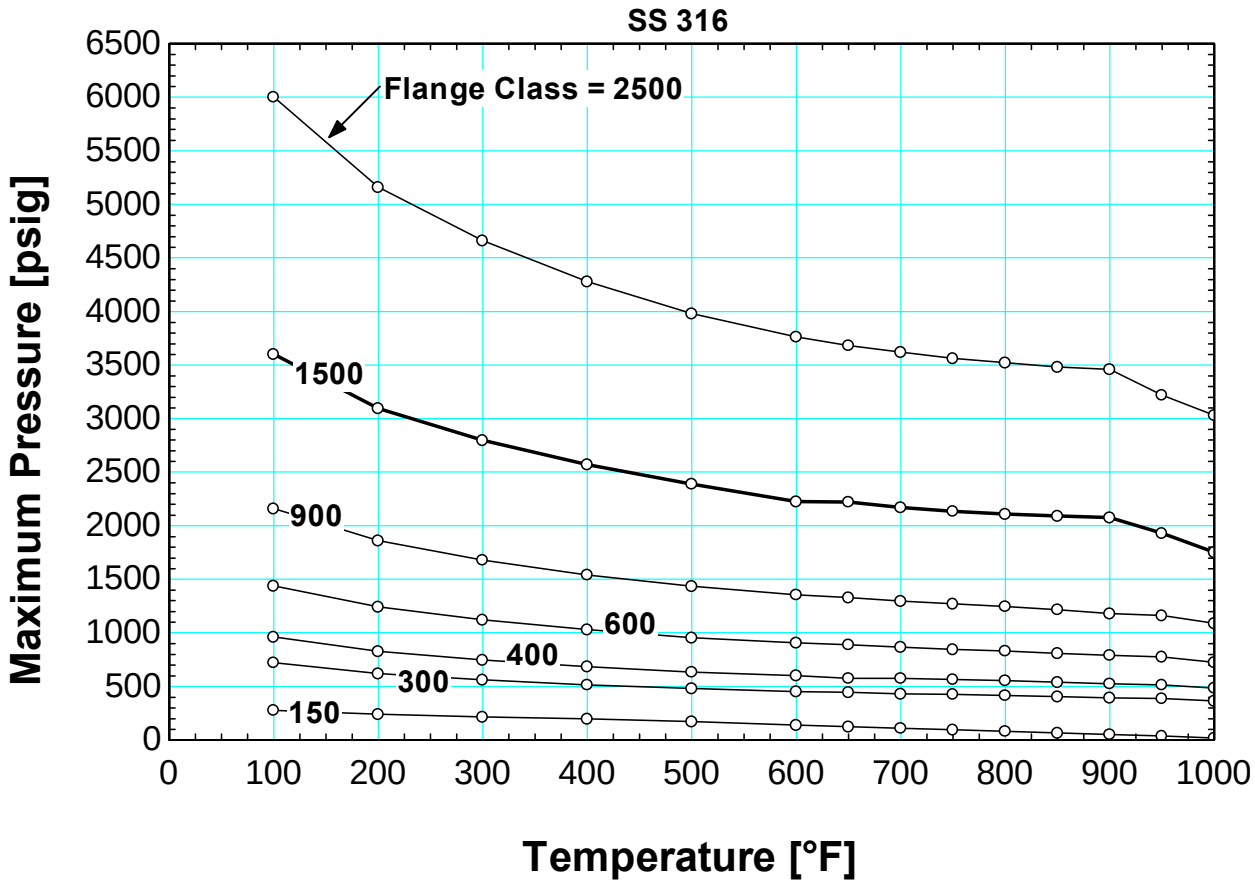

Figure 222 ASME SS 316 flange rating for different flange classes based on temperature

A list of the parameters used to design the flange for this pressure vessel is provided in **Table 4-19**. The flange analysis is for a loose-type flange without hubs. Notice that the parameters listed in **Table 4-19** document the flange, which was welded to the shell housing only.

The parameters listed in **Table 4-19** note a reduction in the desired operation pressure from $3000 psi$ to $2600 psi$. This reduction was necessary as the machine shop hired to construct this test section misread a print and did not include a knife-edge in the final product. The parts came back with an o-ring indentation and not a conflate-type surface. A reduction in the final working pressure was required to accommodate this change.

Table 4-19 Parameters used for loose type flange welded to accumulator tank

DESIGN PARAMETERS	VARIABLE	VALUE
FLANGE		
Flange material		SA-240 316
Temperature		350°F
Pressure	P	2600 psi
Outside diameter	A	7 in
Inside diameter	B	3.25 in
Flange thickness	t	1.48 in
Hubs	h	0.5 in
Allowable stress at assembly temp (70°F)	S_{fa}	20000 psi
Allowable stress at design temp (350°F)	S_{fo}	19600 psi

BOLTS		
Bolt material		SA 193 b7
Bolt size		½-13
Conservative torque bolt diameter	$D_{bolt,torque}$	0.5 in
Effective bolt area	$A_{bolt,eff}$	0.126 in^2
Tensile bolt area	A_t	0.142 in^2
Bolt circle	C	5.4 in
Number of bolts	Nbolts	14
Allowable stress at assembly temp (70°F)	S_a	80000 psi
Allowable stress at design temp (350°F)	S_b	80000 psi
Copper frictional bolt lubricant	k_{fric}	0.2
Number of threads per inch	n_{thread}	13
GASKET		
Gasket material		Soft copper
Gasket factor	m	4.75
Design seating stress	y	13000 psi
Outer diameter	$Gasket_{OD}$	4.743 in
Inner diameter	$Gasket_{ID}$	4.006 in
Knife-edge diameter	$D_{knife-edge}$	4.6 in
Gasket load reaction diameter	G	4.6 in
Effective seating width (estimated)	b	0.1 in

The methodology used in the final configuration met the design criteria by following the general rules of thumb shown below:

- Reduce the outer diameter to a form factor which is governed by the size of the bolt head and the outside diameter of the nominal pipe size.
- Limit the effective gasket seating width by incorporating a knife-edge.
- Increase the inner diameter to a value that is constrained by the inner pipe diameter.
- Use several smaller bolts instead of fewer larger bolts to limit the size of the bolt head.
- Constrain the gasket load reaction diameter with a knife-edge as close to the bolts as possible to maximize gasket seating stress to limit assembly stress.
- Use higher grade bolts to accommodate the larger stress concentrations which are observed with smaller bolts.

An illustration is shown here from Bickford and Nassar (1998) that demonstrates the critical parameters evaluated in this analysis. The definitions for each parameter identified in this section are largely expounded upon from the definitions provided by Bickford and Nassar (1998).

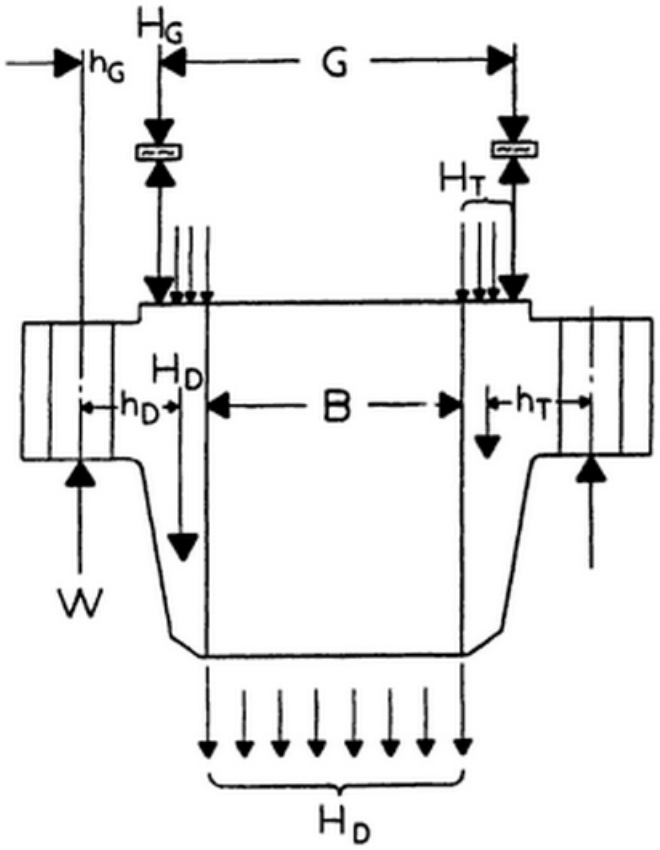

Figure 223 Illustration of critical parameters used to evaluate flanges by Bickford and Nassar (1998)

The *Companion Guide* requires the basic gasket contact width to be determined. This is just the radial displacement from the inner to the outer diameter of the gasket as demonstrated in equation (3.91). The result is used to calculate the basic gasket seating width which is assumed to be half the basic gasket contact width as shown in equation (3.92).

$$N = \frac{1}{2}\left(Gasket_{OD} - Gasket_{ID}\right) \quad Basic\ gasket\ contact\ width \tag{3.91}$$

$$b_o = \frac{N}{2} \quad Basic\ gasket\ seating\ width \tag{3.92}$$

The result of equation (3.92) is used to determine the effective gasket seating width shown here as equation (3.93). The results are plotted as a function of the basic gasket contact width N in **Figure 177**.

$$b = \begin{Bmatrix} b_o \rightarrow b_o \le 0.25in \\ \frac{1}{2}\sqrt{b_o} \rightarrow b_o > 0.25in \end{Bmatrix} \quad Effective\ gasket\ seating\ width \tag{3.93}$$

The problem with the definition of the effective gasket seating width demonstrated in equation (3.93) is that gaskets made of materials with higher yield strengths will not seat properly during assembly. The problem must then be overcome by using larger bolts to sustain the larger clamping forces required to properly seat the gasket. The form factor of the entire assembly will effectively double if not triple in size if this seemingly simple

concept is not kept in check.

Gaskets are typically made of polymer materials in order to avoid this issue. Polymer materials were avoided in this design in order to avoid solvent issues associated with S-CO_2. Kruizenga (2010) noted that Viton seals used to hold his test section together would show appreciable size deformation after each use.

Copper seals were incorporated into the design of this test facility as is commonly used to create exceptional sealing in vacuum technology. A conflate-type knife-edge was used to seat the gasket and an estimate of the effective gasket seating width was evaluated based on equation (3.94). The results from this estimate are also plotted in **Figure 224**.

$$b = \begin{Bmatrix} b_o \rightarrow b_o \leq 0.1in \\ 0.10in > 0.10in \end{Bmatrix} \quad Knife-edge\ effective\ gasket\ seating\ width \tag{3.94}$$

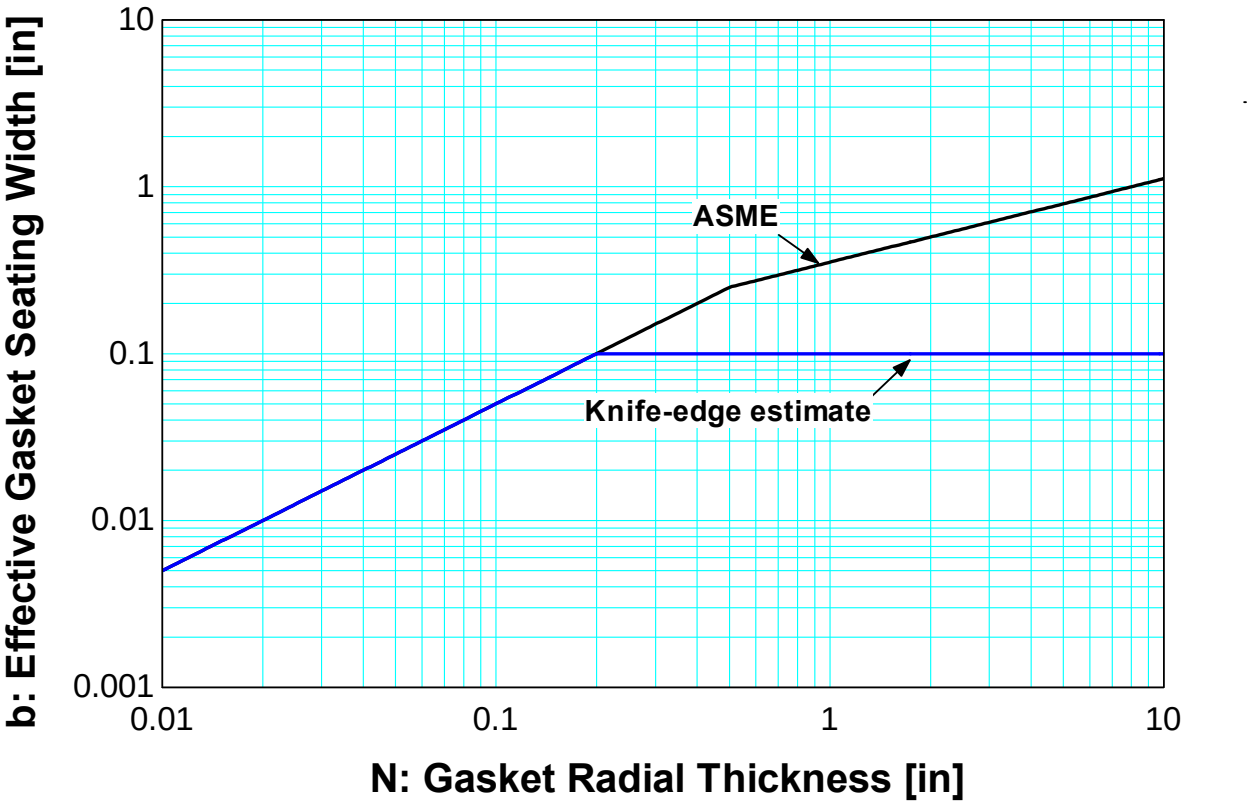

Figure 224 Effective gasket seating width based on ASME specification and new design shown with knife-edge estimate

The effective gasket load reaction location was another parameter that needed to be controlled. The definition based on ASME specification is shown in equation (3.95). The results are plotted as a function of

$$G = \begin{Bmatrix} \frac{1}{2}\left(Gasket_{OD} + Gasket_{ID}\right) \rightarrow b_o \leq 0.25in \\ Gasket_{OD} - 2b \rightarrow b_o > 0.25in \end{Bmatrix} \ Gasket\ load\ reaction\ location \tag{3.95}$$

The problem with this approach is that as the difference between the inner and outer diameter increases, the gasket load reaction location moves farther away from the bolt circle diameter. As the gasket load reaction

moves away from the bolt circle, the clamping force generated by the bolts becomes less effective at seating the gasket. The objective is to position the gasket load reaction location as close to bolts as possible.

The position of the knife-edge was fixed as close to the bolt-circle as possible and is set at a fixed value of 4.6 inches by equation (3.96). Copper gaskets from Nor-Cal were purchased for the facility. Note that the diameter of knife-edge was bounded by the dimensions of the gaskets available from Nor-Cal fixed at 4.743 inches and 4.006 inches.

$$G = D_{knife-edge} \quad (3.96)$$

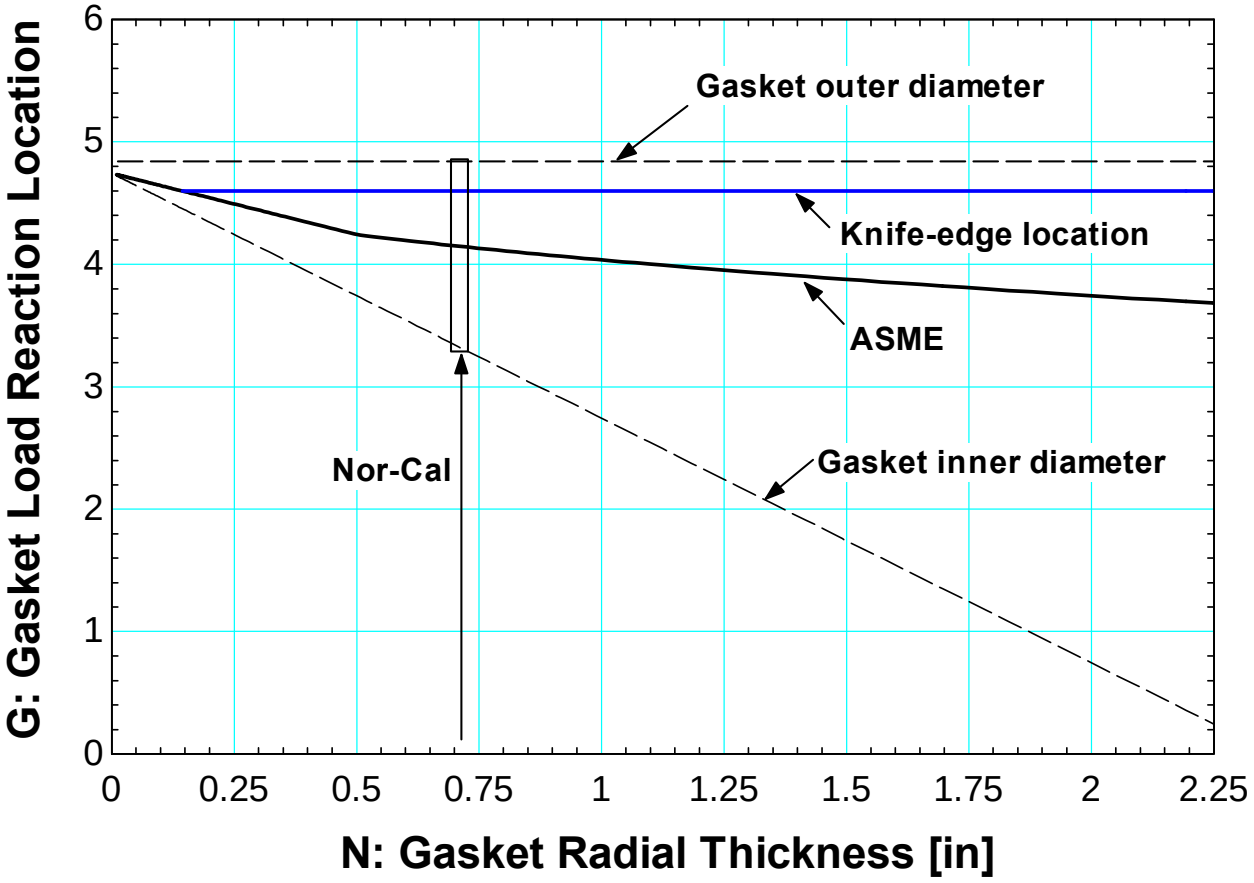

Figure 225 ASME equation-specified gasket load reaction location as a function of gasket thickness. Outer diameter of copper seal used in facility is specified with all other parameters varying according to the gasket thickness

Figure 225 demonstrates the importance of using a knife-edge with gaskets that have a larger radial thickness. If this location is not properly controlled, the effective gasket load reaction moves farther away from the outer diameter of the gasket and decreases the effectiveness of the clamping force generated by the bolts during assembly. Most polymer seals are very thin and the gasket load reaction occurs very close to the outside diameter of the gasket. For this reason, polymer seals can be located very close to the bolt-circle diameter where the clamping force generated by the bolts will be most effective.

There are benefits and consequences to positioning the gasket load reaction location so close to the gasket outer diameter. On one level, the hydrostatic load is increased as the cross-sectional area exposed to pressure is increased. This has the unfortunate consequence of increasing the normal stress that the bolts need to overcome

and attributes to the requirement for larger bolts. The benefit of course is that the load reactions get closer to the bolt-circle diameter which has the potential to lower the bending stresses throughout the pressure vessel. This concept is conceptually explained in the assessment that follows.

The total hydrostatic load is evaluated according to equation (3.97). Note that the cross-sectional area shown here represents the total area exposed to pressure.

$$H = \underbrace{\frac{\pi}{4}G^2}_{A_c} P \quad Total\ hydrostatic\ load \tag{3.97}$$

Note that a larger gasket load reaction location will lead to higher load concentration for H and H_T during operation as the effective area exposed to pressure increases as demonstrated in equation (3.97) and equation (3.99). This is an unfortunate byproduct of placing the gasket load reaction location as close to the bolt-circle diameter as possible. This issue also has drawbacks on the assembly stress however as is demonstrated in equation (3.98). The problem is mitigated however, as the effective gasket seating width b determined from equation (3.94) for a knife-edge is much smaller than that determined based on ASME specifications as was demonstrated in **Figure 224**. The variable m in this case notes the gasket factor which is relatively large for harder materials – i.e. copper has a gasket factor of $m = 4.75$ as was noted in **Table 4-19**.

$$H_P = 2m\underbrace{\pi bG}_{A_{gasket}} P \quad Required\ gasket\ load \tag{3.98}$$

The difference between the total hydrostatic end force and the hydrostatic end force acting on the area inside the flange is calculated from equation (3.99).

$$H_D = \frac{\pi}{4}B^2 P$$
$$H_T = \underbrace{\frac{\pi}{4}\left(G^2 - B^2\right)}_{A_{flange}} P = H - H_D \tag{3.99}$$

The minimum required bolt load during operation and assembly is calculated from equation (3.100). The gasket seating width b is also important here to limit the required seating area. The variable y is the design seating stress and has a required value of $y = 13000\,psi$ for copper.

$$W_{m1} = H + H_p \quad Minimum\ required\ bolt\ load\ during\ operation$$
$$W_{m2} = \underbrace{\pi bG}_{A_{gasket}} y \quad Minimum\ required\ bolt\ load\ for\ gasket\ seating \tag{3.100}$$

The minimum area required during operation and assembly are calculated from equation (3.101). The required bolt area is determined to be the greater of the two requirements as noted in equation (3.102).

$$A_{m1} = \frac{W_{m1}}{S_b} \quad \textit{Required bolt area during operation}$$

$$A_{m2} = \frac{W_{m2}}{S_a} \textit{Required bolt area for gasket seating} \tag{3.101}$$

$$A_m = \max\left(A_{m1}, A_{m2}\right) \quad \textit{Required bolt area} \tag{3.102}$$

The actual bolt area is determined based on the effective area of the bolts as found from ASME specifications and calculated from equation (3.103).

$$A_b = N_{bolts} A_{bolt,eff} \qquad \textit{Actual bolt area} \tag{3.103}$$

Note that the effective area is a reduced quantity from the nominal area of a standard bolt. The value published here is based on that shown in the *Companion Guide.* The idea is expressed in equation (3.104).

$$A_{bolt,eff}\left(bolt = \frac{1}{2} - 13\right) \neq A_{nom-bolt}\left(bolt = \frac{1}{2} - 13\right)$$

$$A_{nom-bolt} = \frac{\pi}{4}\left(\frac{1}{2}\right)^2 = 0.196\,in^2$$

$$A_{bolt,eff} = 0.126 in^2 \tag{3.104}$$

Finally, the criteria shown in equation (3.105) must be satisfied.

$$A_b \geq A_m \tag{3.105}$$

The required bolt load are demonstrated here in equation (3.106) is defined as the maximum of the operational and assembly bolt loads previously calculated in equation (3.100). The maximum available bolt load is taken as an average of the actual and required bolt areas multiplied by the allowable stress $S_a = 80000\,psi$ of the bolts at the assembly temperature of 70°F. Note that the values published in **Table 4-19** correspond to a standard grade 8 bolt rated at the proof load. The proof load of a bolt is a value which is marginally smaller than the yield strength of that bolt.

$$W_{required} = \max\left(W_{m1}, W_{m2}\right) \qquad \textit{Minimum bolt load required}$$

$$W_{possible} = \frac{1}{2}\left(A_m + A_b\right) S_a \qquad \textit{Maximum actual bolt load} \tag{3.106}$$

The requirement of course is that the bolt will not fail as demonstrated in equation (3.107).

$$W_{possible} > W_{required} \tag{3.107}$$

The bolts actually used in this facility were grade 9 rated to a proof load of $120000\,psi$ and were only slightly more expensive than bolts designated as grade 8. Nevertheless, the calculations were conservatively based on grade 8.

The load reaction locations are obtained from the definitions found in equation (3.108). Note that these definitions are only to be applied for loose-type flanges. Integral flanges require different definitions based on ASME specifications.

$$\begin{aligned}
&\textit{Load locations relative to bolt} - \textit{circle} \\
&h_D = \frac{1}{2}(C - B) && \textit{distance to inner flange diameter} \\
&h_G = \frac{1}{2}(C - G) && \textit{distance to gasket load reaction location} \\
&h_T = \frac{1}{2}(h_D + h_G) && \textit{averaged distance to load location of } H_T
\end{aligned} \tag{3.108}$$

The benefit previously mentioned regarding a reduction in bending stress is realized here as equation (3.109) where the increase in G always results in a reduction of the generated moment incurred during assembly. In contrast, the moment generated during operation may increase or decrease depending on the situation as is demonstrated for this pressure vessel illustrated in

$$\begin{aligned}
M_{o,assembly} &= \frac{1}{2} W_{m2}(C - G) && \textit{Moment generated during assembly} \\
M_{o,operating} &= h_D H_D + h_T H_T + h_G H_G && \textit{Moment generated during operation}
\end{aligned} \tag{3.109}$$

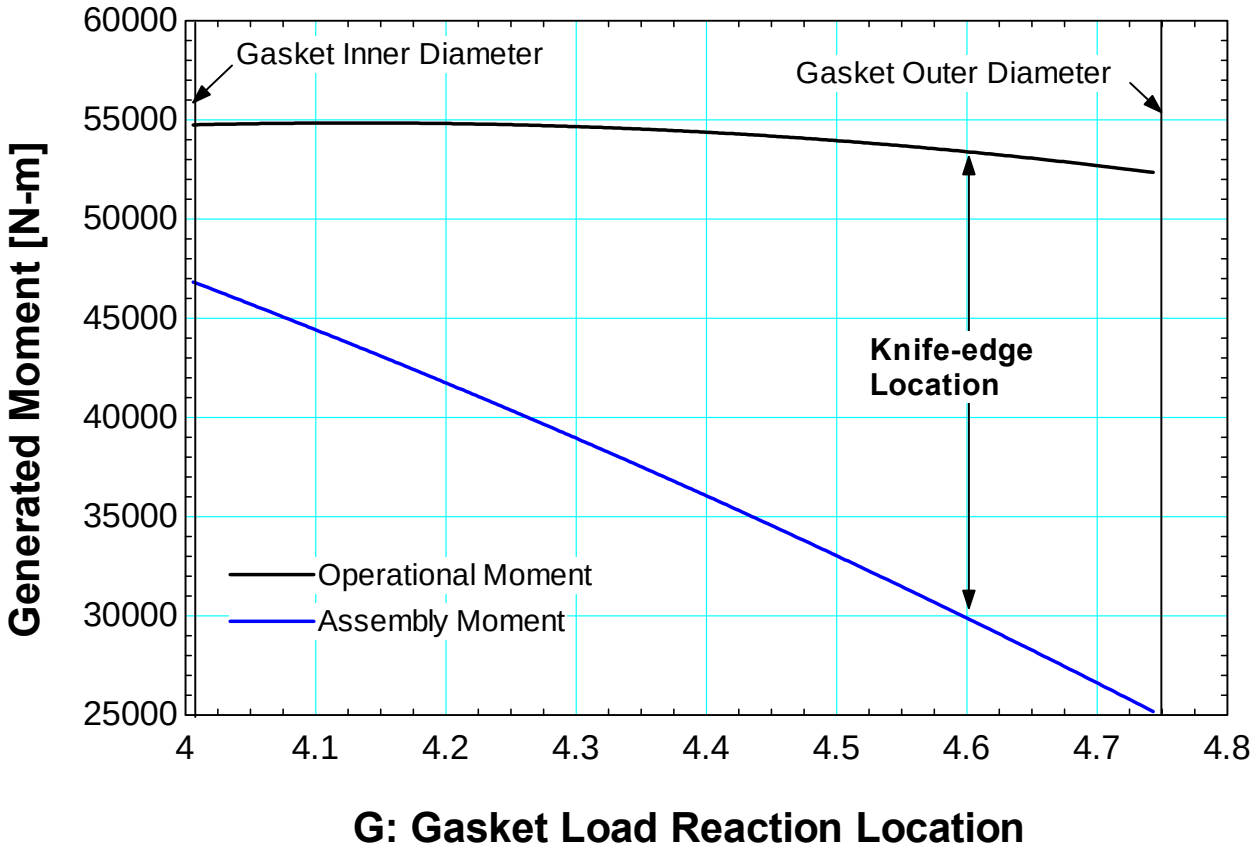

Figure 226 Assembly and operational moments generated as a function of gasket load reaction for the parameters listed in Table 4-19.

Curve-fit parameters have been developed to accommodate for other flange effects not expressly accounted for by the moments and normal forces previously expressed. The equations for the curve fit parameters $T, U, Y, \text{and } Z$ are based on the factor K which is effectively a ratio of the flange outer diameter $A = 7in$ to the flange inner diameter $B = 3.25in$ as identified in **Table 4-19**.

Parameters for flanges

$$K = \frac{A}{B}$$

$$T = \frac{K^2\left(1 + 8.55246\log_{10} K\right) - 1}{\left(1.04720 + 1.9448K^2\right)\left(K - 1\right)}$$

$$U = \frac{K^2\left(1 + 8.55246\log_{10} K\right) - 1}{1.36136\left(K^2 - 1\right)\left(K - 1\right)}$$

$$Y = \frac{1}{K - 1}\left(0.66845 + 5.7169\left(\frac{K^2\log_{10} K}{K^2 - 1}\right)\right)$$

$$Z = \frac{K^2 + 1}{K^2 - 1} \qquad (3.110)$$

The factor h_o is calculated from equation (3.111) where B is the flange inner diameter and g_o is the hub thickness. The hub thickness is effectively the stub height that adjoins the flange to the pipe wall. Note that this analysis considers a loose-type flange with no hubs, which is a conservative estimate that effectively assumes all bending stress acts through the flange itself and the pipe wall is not load bearing. The assumption is not the case as the pipe wall is 0.53 in thick 304L stainless steel.

$$h_o = \sqrt{B\,g_o} \qquad (3.111)$$

More flange factors for loose-type flanges are identified in equation (3.112) and (3.113). The factors identified by equation (3.112) were read from figures in the *Companion Guide*.

Loose – type flange factors

$$F_L = F_L\left(\frac{g_1}{g_o}, \frac{h}{\sqrt{B\,g_o}}\right) \; Fig. 2 - 7.4$$

$$V_L = V_L\left(\frac{g_1}{g_o}, \frac{h}{\sqrt{B\,g_o}}\right) \; Fig.\ 2 - 7.3 \qquad (3.112)$$

Note that $t = 1.48in$ notes the flange thickness in equation (3.113).

$$Loose-type\ flange\ factors\ 2$$

$$d = \frac{U}{V_L} h_o g_o^2$$

$$e = \frac{F_L}{h_o}$$

$$L = \frac{te+1}{T} + \frac{t^3}{d} \qquad (3.113)$$

Finally, the flange stresses are calculated as demonstrated in equation (3.114). Again, this analysis considers the conservative estimate for a loose-type flange with no hubs.

$$Loose\ flange\ without\ Hubs$$

$$S_T = \frac{YM_o}{t^2 B}$$

$$S_R = 0$$

$$S_H = 0 \qquad (3.114)$$

Two stress values are determined from the top line in equation (3.114). The operating and assembly stresses are calculated based on equation (3.115) respectively.

$$S_{T,operating} = \frac{YM_{o,operation}}{t^2 B} \quad Operating\ stress$$

$$S_{T,assembly} = \frac{YM_{o,assembly}}{t^2 B} \quad Assembly\ stress \qquad (3.115)$$

Finally, the requirements identified in equation (3.116) must be met. That is, the operating stress must be less than the allowable stress at the design temperature of 350°F and the assembly stress must be less than the allowable stress at the assembly temperature of 70°F. The final results are illustrated in **Figure 227**. Notice that even at the de-rated sustainable pressure of $2600\,psi$, the max operational stress is slightly exceeded based on the location of the knife-edge built into this facility.

$$S_{fo} \geq S_{T,operating}$$

$$S_{fa} \geq S_{T,assembly} \qquad (3.116)$$

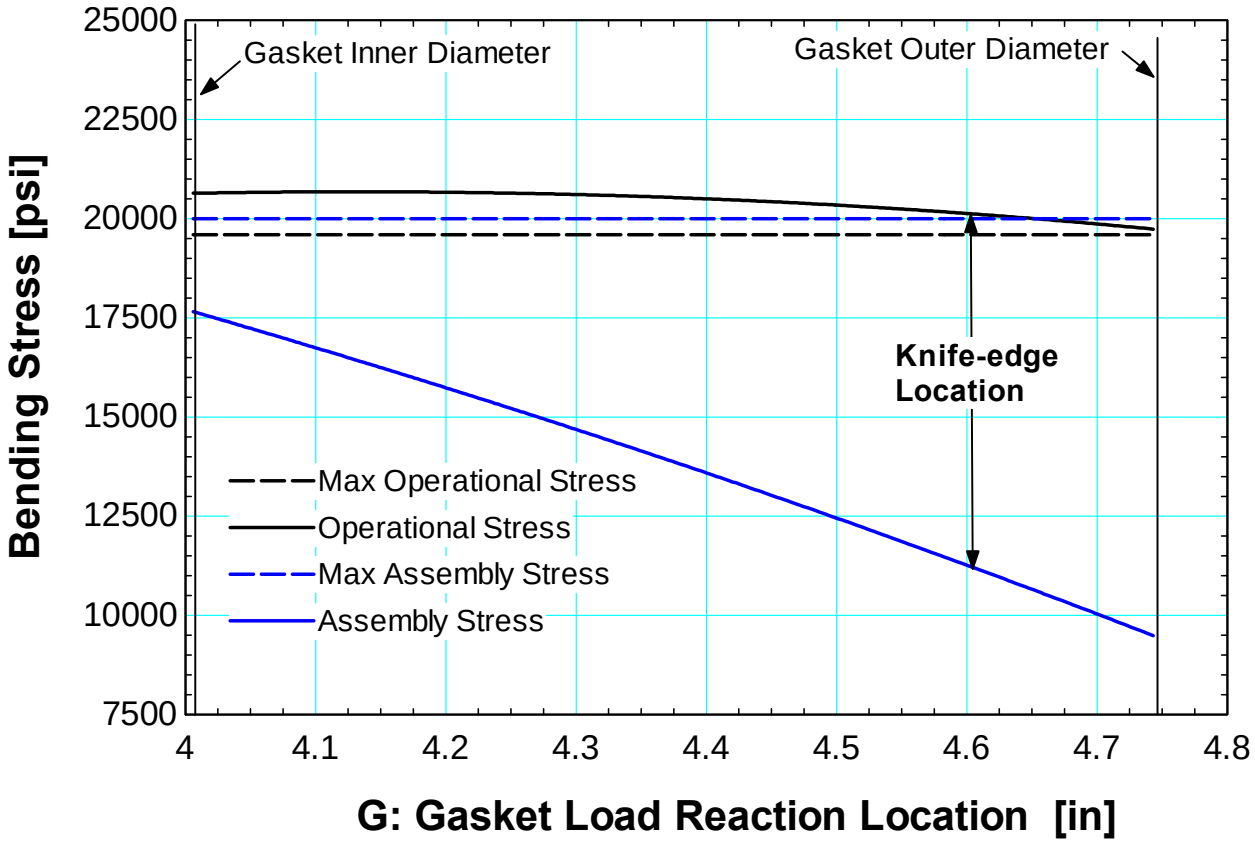

Figure 227 Assembly and operational stress as a function of gasket load reaction for the parameters listed in Table 4-19.

The proper preload for the assembly was determined based on equation (3.117) shown below. Effectively, the total of the hydrostatic load and the gasket load is divided among the bolts to determine the minimum required clamping force per bolt.

$$F_k = \frac{\overbrace{H}^{\text{hydrostatic load}} + \overbrace{mP\overbrace{(\pi Gb)}^{A_{gasket}}}^{\text{gasket load}}}{N_{bolts}} \quad \textit{Minimum required clamping force per bolt} \tag{3.117}$$

The minimum required bolt torque is calculated as demonstrated in equation (3.118). Notice that a lubricant frictional coefficient k_{fric} is necessary to prevent galling. The lubricant used is a copper-based paste rated at $k_{fric} = 0.2$ by the manufacturer. Furthermore, the bolt diameter $D_{bolt,torque} = 0.5in$ was evaluated conservatively so that the minimum required torque would generate more and not less clamping force than that required by (3.117). The required torque was determined to be about $\Gamma = 35lb - ft$.

$$\Gamma = k_{fric} D_{bolt,torque} F_k \quad \textit{Minimum required torque per bolt} \tag{3.118}$$

The assembly was hydrostatically tested to 2600 psi in July 2010.

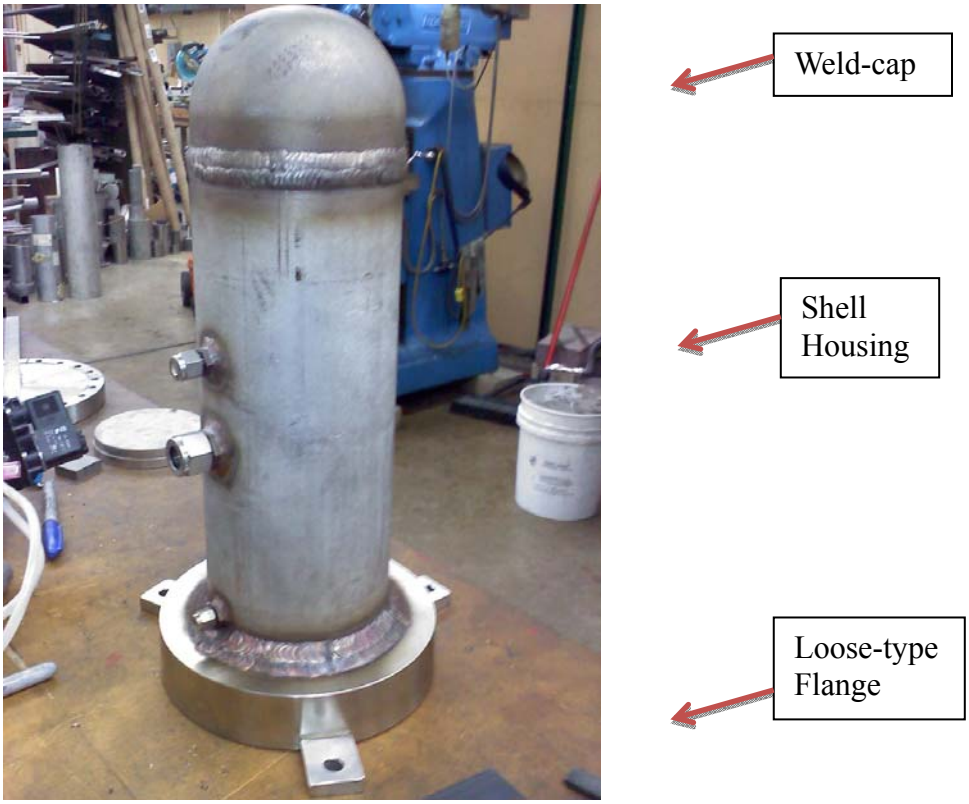

Figure 228 Final assembly of pressure vessel based on this analysis

The following analysis was calculated post-construction and concerns thread engagements. The analysis shows that the actual thread engagement is slightly lower than that determined by this design by formula methodology detailed here as equation (3.119) through (3.121).

The screw needs to fail before the threads strip. This is an especially critical parameter to calculate when the screw and hole are made of different materials as is the case in this facility. The shear area of the threaded feature is required to be 2 times the tensile stress area of the bolt as demonstrated in equation (3.119).

$$L_{engagement} = \frac{2A_t}{\frac{\pi}{2}\left[D_{major} - 0.64952\left(\frac{1}{n_{threads}}\right)\right]} \quad (3.119)$$

The thread engagement calculated from (3.119) is supplemented by a ratio of the tensile strength of the bolt compared the tensile strength of the hole. In this case, it was desirable that neither the screw nor the hole yield. A ratio of the bolt proof load was divided by the allowable operation stress as demonstrated here as equation (3.120) to approximate the parameter J.

$$J = \frac{\sigma_{tensile}(screw)}{\sigma_{tensile}(hole)} \rightarrow \frac{S_b}{S_{fo}} = \frac{80000\,psi}{19600\,psi} \quad (3.120)$$

The final length of engagement for this facility was determined to be about $1.6\,in$ based on equation (3.121). Unfortunately, the actual thread engagement is slightly lower at $1.3\,in$; the typical thread engagement

methodology of 2.5 times thread diameter of engagement was used in the initial construction as detailed in equation (3.122).

$$L_{engagement,final} = \max\left(L_{engagement}, J \cdot L_{engagement}\right) \quad (3.121)$$

$$L_{engagement,rough} = 2.5 \cdot D_{major} \quad (3.122)$$

4.3.6.3 Two-phase downstream recovery system

The fluid exiting the test section requires that the test facility accommodate a two-phase downstream recovery system. The fluid cavitates as it incurs the drastic pressure drops inherent in this test facility. The problem was mitigated by implementing a buffer tank after the test section which allows the two-phase exhaust to separate into liquid and gas components. Carbon dioxide as a saturated vapor is then pulled from the top of the tank into the compressor. The concept is demonstrated in **Figure 229**.

Figure 229-A shows that the fluid from the test section enters the tank as a two-phase mixture which is then exhausted through a long tube that runs all the way to the bottom of the gas cylinder shown in **Figure 229**-B. From there, the fluids separate into liquid and vapor counterparts in order to fill the volume of the gas cylinder entirely. An annular region which is slightly larger than the diameter of the inlet tube is used to extract carbon dioxide as a saturated vapor through the same entry hole in the gas cylinder. The vapor is then extracted through a pipe-tee so that it can be cycled through the compressor.

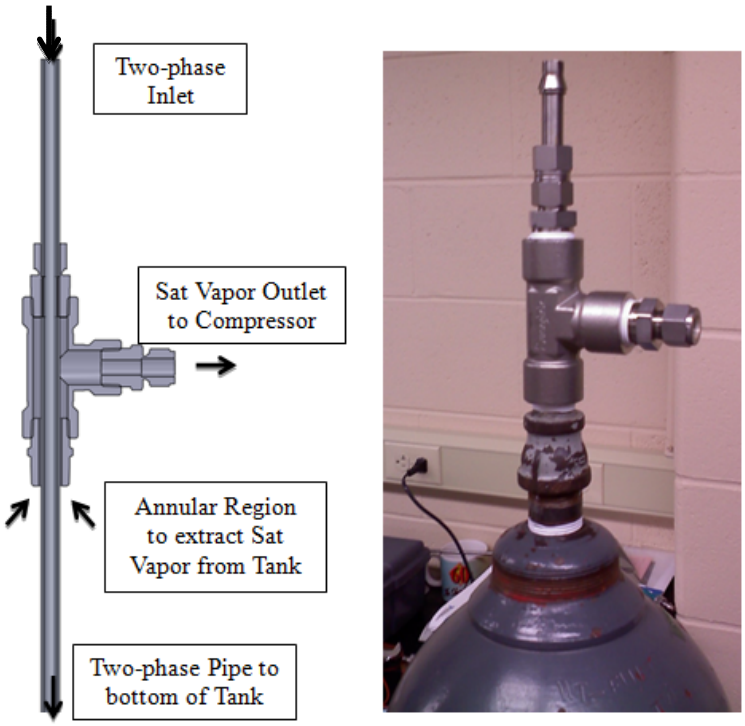

A **B**

Figure 229 Two-phase downstream recovery system; A – Two-phase separation system cross-section; B – As configured in actual test section

4.3.7 Test Facility Construction

A preliminary design was developed in SolidWorks and is shown in **Figure 230**. This initial model was used to design the facility base structure in order to integrate the test section, support equipment, and data acquisition system onto a single assembly. The secondary objective of this initial design was to determine the instrumentation layout as well as the number of high pressure fittings which would be required.

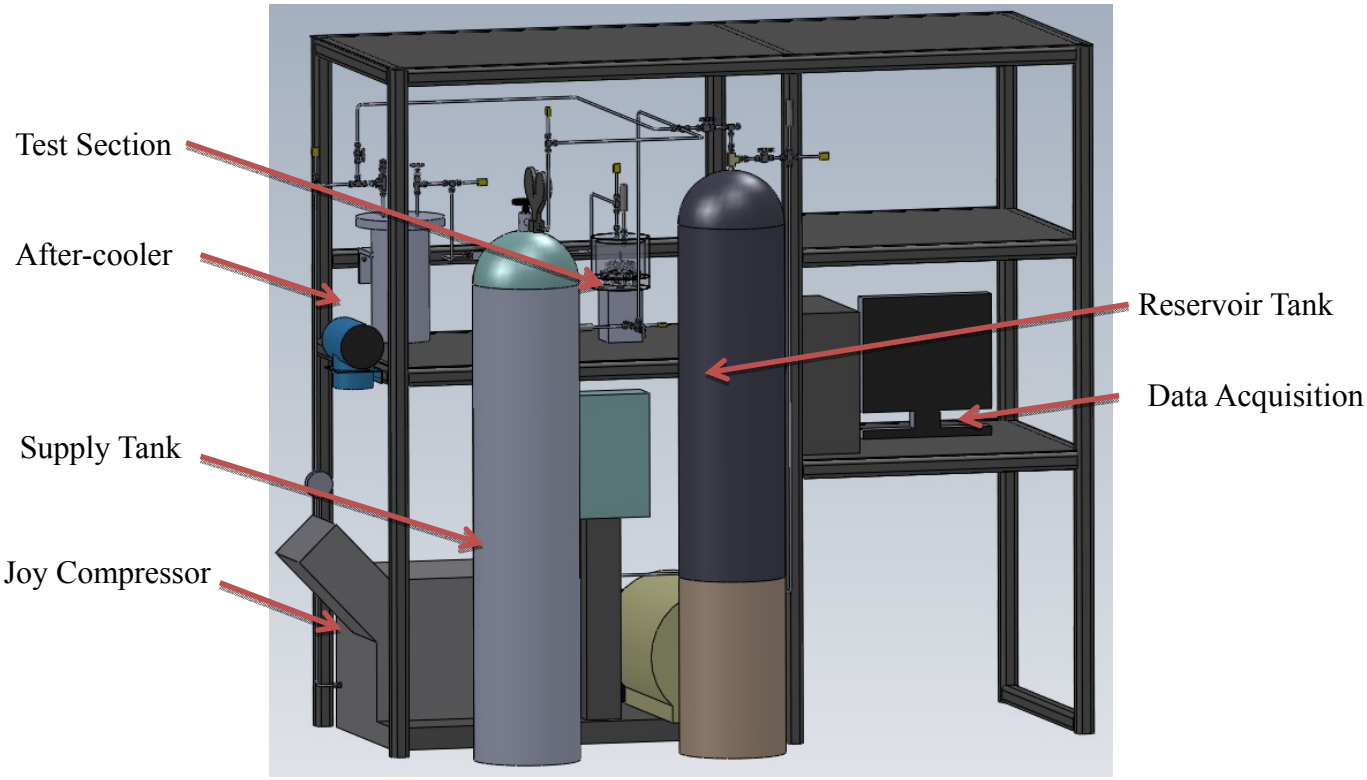

Figure 230 Initial SolidWorks representation of UW-Compression Loop facility

The components used in this initial rendering have since been heavily modified as is evident in the latest photographs of the facility illustrated in Figure 231 and Figure 232. Notice that the compressor and tanks have been rotated 90° from the original orientation shown in Figure 230 to allow less restrictive access to the test section.

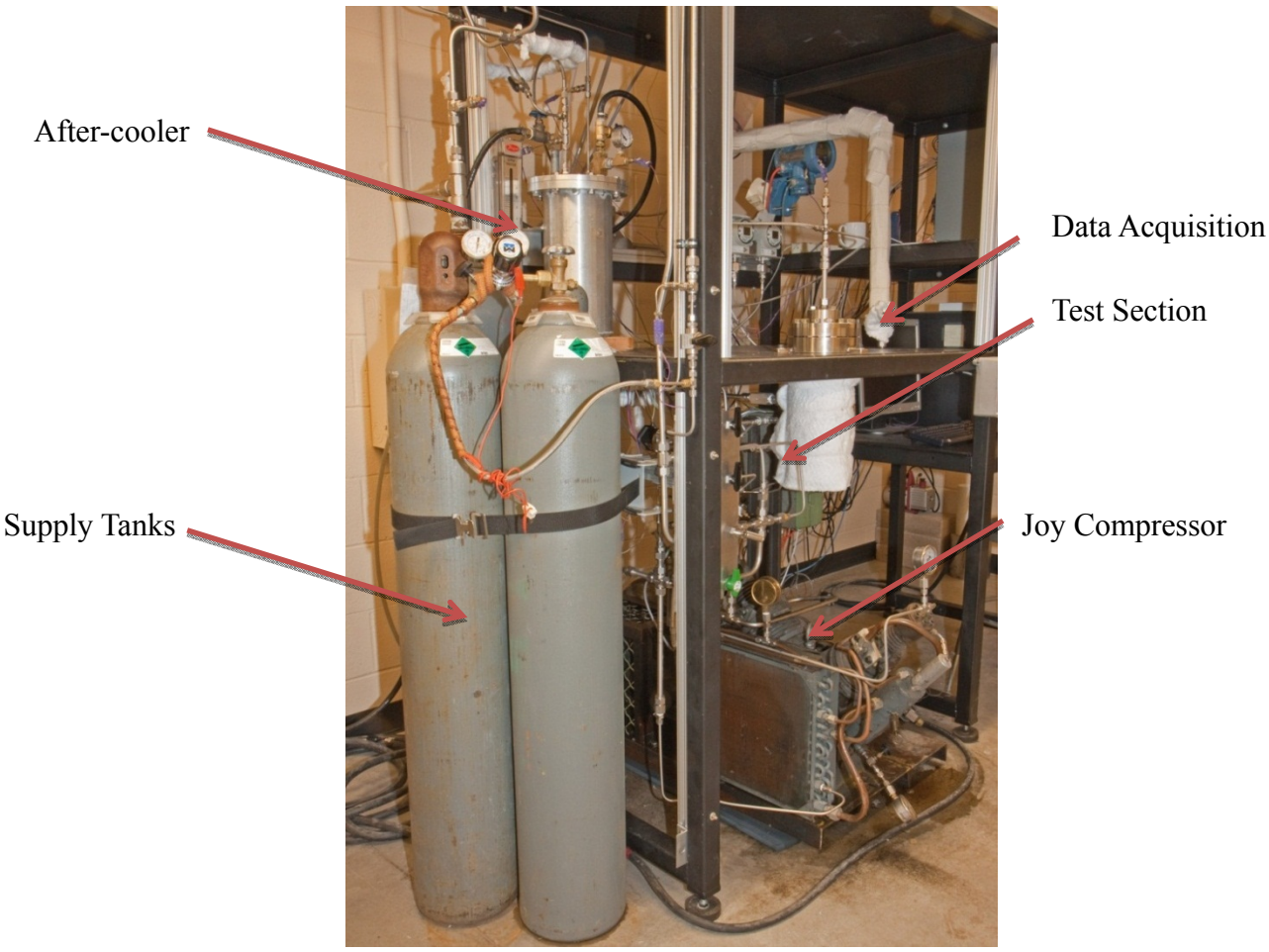

Figure 231 UW-Compression Loop facility (side view)

Figure 231 shows a side view of the test facility at the University of Wisconsin – Madison. The facility requires several supply tanks to charge the facility with sufficient working fluid as the facility is quite large. The Joy compressor shown at the bottom of the figure is a four stage air compressor with intercooling which has been modified to support carbon dioxide through the top two high pressure stages. The bottom stages cycle air from the environment. The exhaust from these two stages exits the compressor as a mixture of the inlet air plus some residual carbon dioxide which has leaked from the top two stages into the bottom stages. This exhaust is then evacuated to a building exhaust line on the opposite side of the room to prevent asphyxiation during testing.

The major problem with the current configuration is the Joy compressor. It was designed to leak to the environment and it has been particularly challenging to overcome this issue. When the facility is working, testing time is limited to about 15mins total.

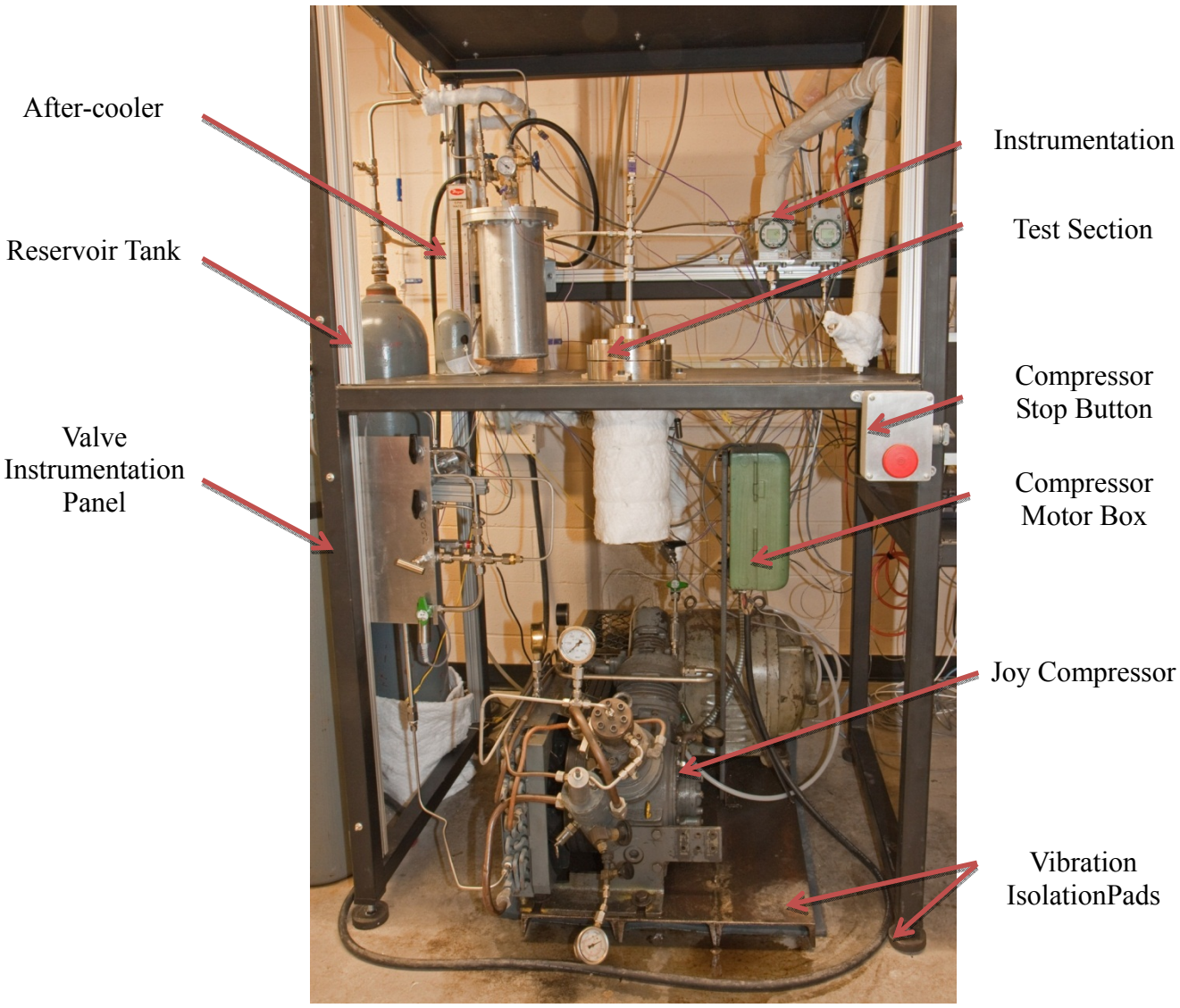

Figure 232 UW Compression-Loop facility (front view)

Figure 232 shows a front view of the UW Compression-Loop facility without the data acquisition system which is located further to the right. The valve instrument panel is located on the left hand side of the facility and centralizes system control. An emergency compressor stop button is also shown on the right hand side of the photograph.

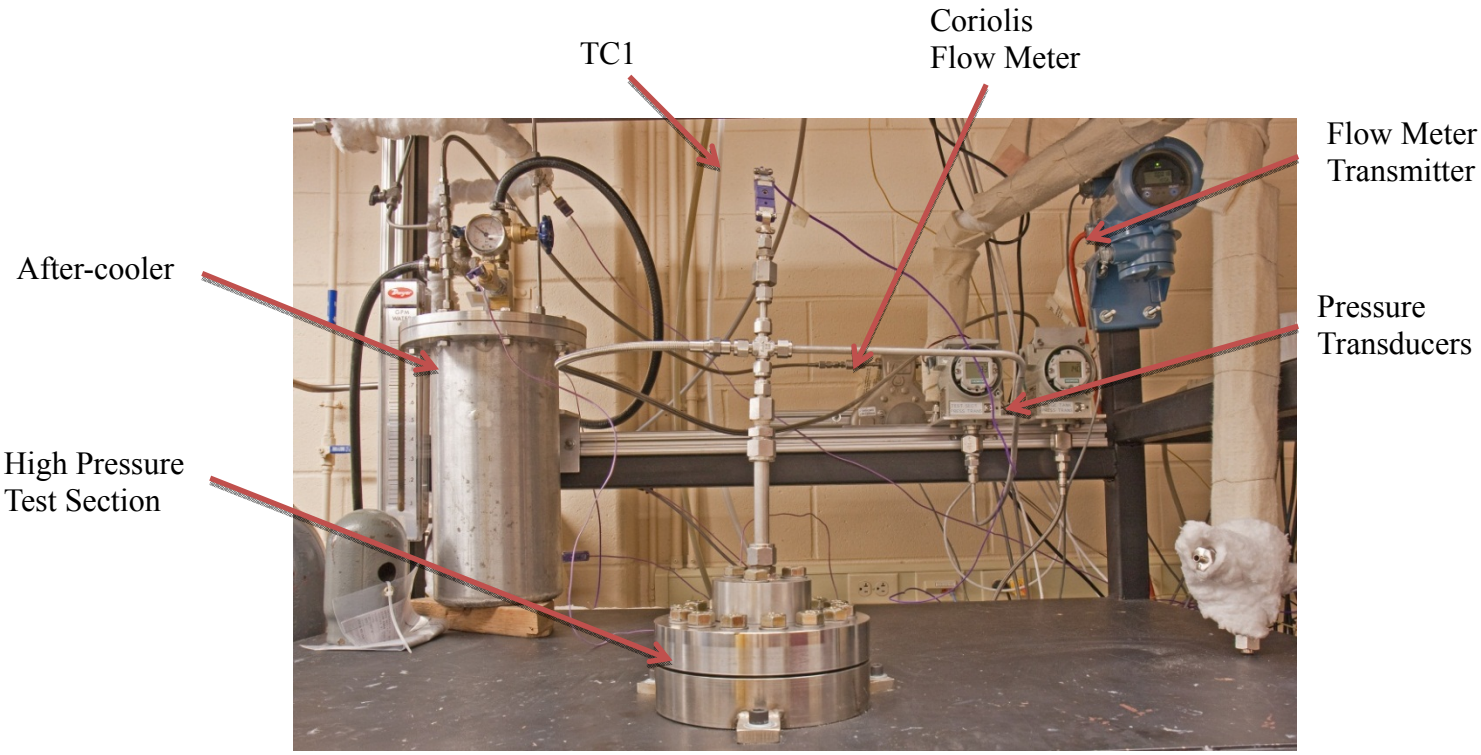

Figure 233 High pressure test section along with primary instrumentation

The pressure transducers, coriolis flow meter transmitter, and test section were integrated into the test stand as shown in **Figure 233**. Integration of the test section into the test housing was necessary in order to apply the necessary preload to the bolts used to fasten the test section together.

Notice that the Coriolis flow meter shown in **Figure 233** was moved away from the test facility. It was discovered that the compressor would vibrate with sufficient energy that the entire facility would shake despite the isolation pads placed at the base of the structure as well as a large vibration pad which was placed underneath the compressor – shown in **Figure 232**. The Coriolis flow meter was then mounted to the wall with additional vibration isolation equipment to overcome this issue.

References

Bickford, J.H. and Nassar, S., 1998, *Handbook of Bolts and Bolted Joints*, Marcel Dekker, Inc. New York.

Gamal, A.M., 2007, Ph.D. thesis. “Leakage and Rotordynamic Effects of Pocket Damper Seals and See-Through Labyrinth Seals.

Go Regulators, www.goreg.com 5 Mar. 2010.

Kruizenga, A., 2010, Ph.D. dissertation. “Heat Transfer and Pressure Drop Measurements in Prototypic Heat Exchangers for the Supercritical Carbon Dioxide Brayton Power Cycles”.

Piercy, N.A., Hooper, M.S., and Winny, H.F., 1933, “Viscous Flow through Pipes with Cores”, Philosophical magazine, Vol. 15, pp 647-676.

Pressure Vessel Engineering, 2010 www.pveng.com 6 Feb. 2010.

Rao, K.R., editor, 2002, *Companion Guide to the ASME Boiler and Pressure Vessel Code*, Vol 2. ASME Press: New York.

Swagelok Cv Flow Coefficient “Valve Sizing: Swagelok CV Flow Coefficient” Dec. 2007, R4 MS-06-84-E.

Tao, L.N., and Donovan, W.F., 1955, “Through-Flow in Concentric and Eccentric Annuli of Fine Clearance With and Without Relative Motion of the Boundaries”, Transactions of the ASME, Vol 77, pp. 1291-1299.

White, F.M., 2006, *Fluid Mechanics*. McGraw-Hill.

Wright et al. (2009)

4.4 Air Data Experimental Verification

The objective of this chapter is to provide a summary of tests conducted to provide validation of the instrumentation and capability of the supporting equipment. The focus of the study was to quantify the expected performance of the facility and establish a baseline to compare with carbon dioxide.

A series of air data tests were conducted to provide validation of the test facility. Tests were conducted with both a standard knife-edge orifice as well as through an annular region simulating a shaft-seal interface. Air flow through an orifice is a well-documented phenomenon with available literature and was presented in great detail in Chapter 2. Flow through an annular region represents a more complex flow scenario for which there is very little data, but the ideas expressed in this chapter seem to represent the data well.

4.4.1 Data taken through a Circular Orifice

Measurements were obtained with air as the working fluid at different inlet pressures to ensure that the facility was properly calibrated. A knife-edge orifice was used in order to compare the measurements to available literature summarized in Linfield (2000) and Ward-Smith (1979) as well as the manufacturer's suggested flow coefficient C_v. The results are presented here in **Figure 234** and **Figure 235**. Notice the larger uncertainty in the pressure ratio measurements for **Figure 234** compared to **Figure 235** is due to the relatively lower pressures measured during testing; the pressure transducers were selected based on their full scale and impose a larger relative uncertainty on the measurements obtained when operating at lower pressures.

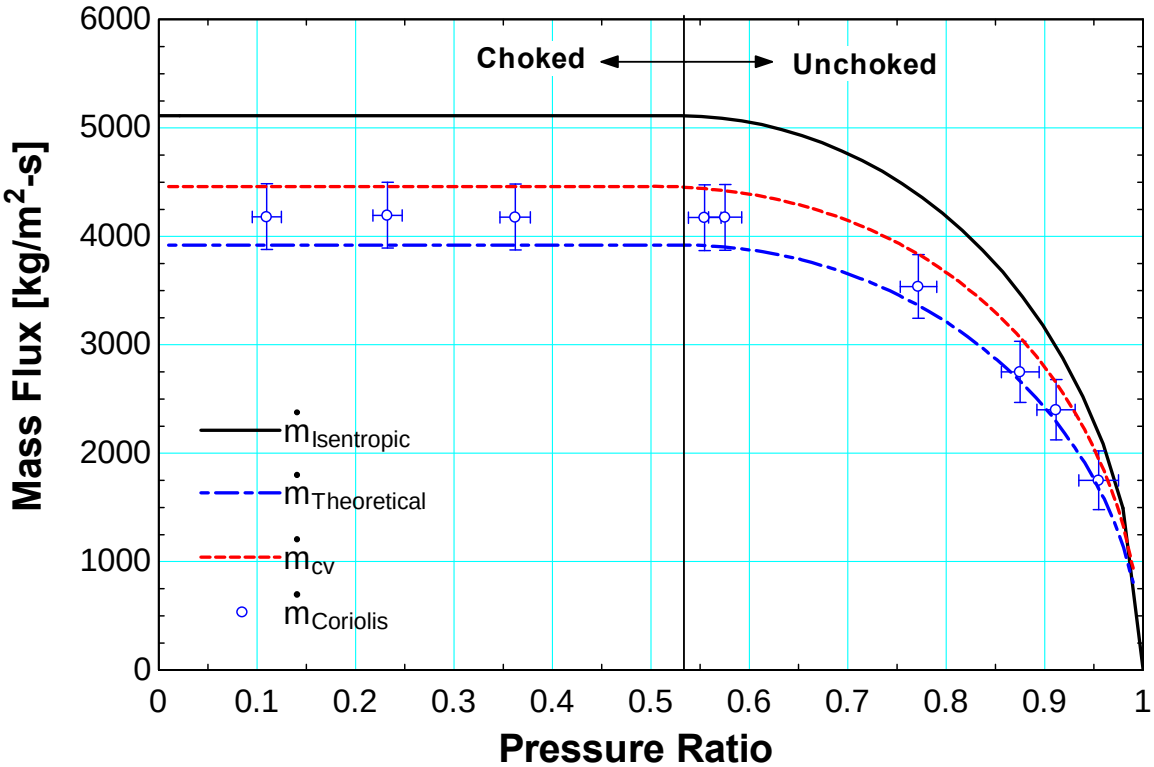

Figure 234 Measurements obtained with a knife-edge orifice at P_{inlet} = 2.068 MPa and ρ_{inlet} = 24 kg/m^3. Discharge coefficient evaluated at Cd = 0.84 for the data shown.

The measurements illustrated in **Figure 234** were taken with air at an upstream pressure of 2.068 MPa. Inlet density variation was negligible as density is a weak function of temperature at these conditions. Three models are illustrated in the figure. The top black-line depicts the isentropic model with a discharge coefficient C_d set to unity and serves as an upper bound on the flow. The next line shown in red depicts the manufacturer's suggested flow coefficient for this particular orifice; two values were quoted as illustrated in equation (4.1). The flow coefficient quoted for air was used to construct the red line in the figure.

$$\begin{aligned} Flow\big|_{air}^{\Delta P=40\,psi} &= 0.568\,scfm \rightarrow C_v\big|_{air} = 0.0170 \\ Flow\big|_{water}^{\Delta P=40\,psi} &= 0.114\,gpm \rightarrow C_v\big|_{water} = 0.0180 \end{aligned} \qquad (4.1)$$

The final blue line represents the isentropic model modified with a discharge coefficient of $C_d = 0.84$ as was nominally chosen based on the data presented in Ward-Smith (1979). The models presented in Chapter 2 reported in Linfield (2000) suggest a similar scenario where equation (4.2) summarizes the data presented in **Table 4-5**.

$$C_d\big|_{choked} : \; 0.81 < C_d\big|_{choked} < 0.86 \qquad (4.2)$$

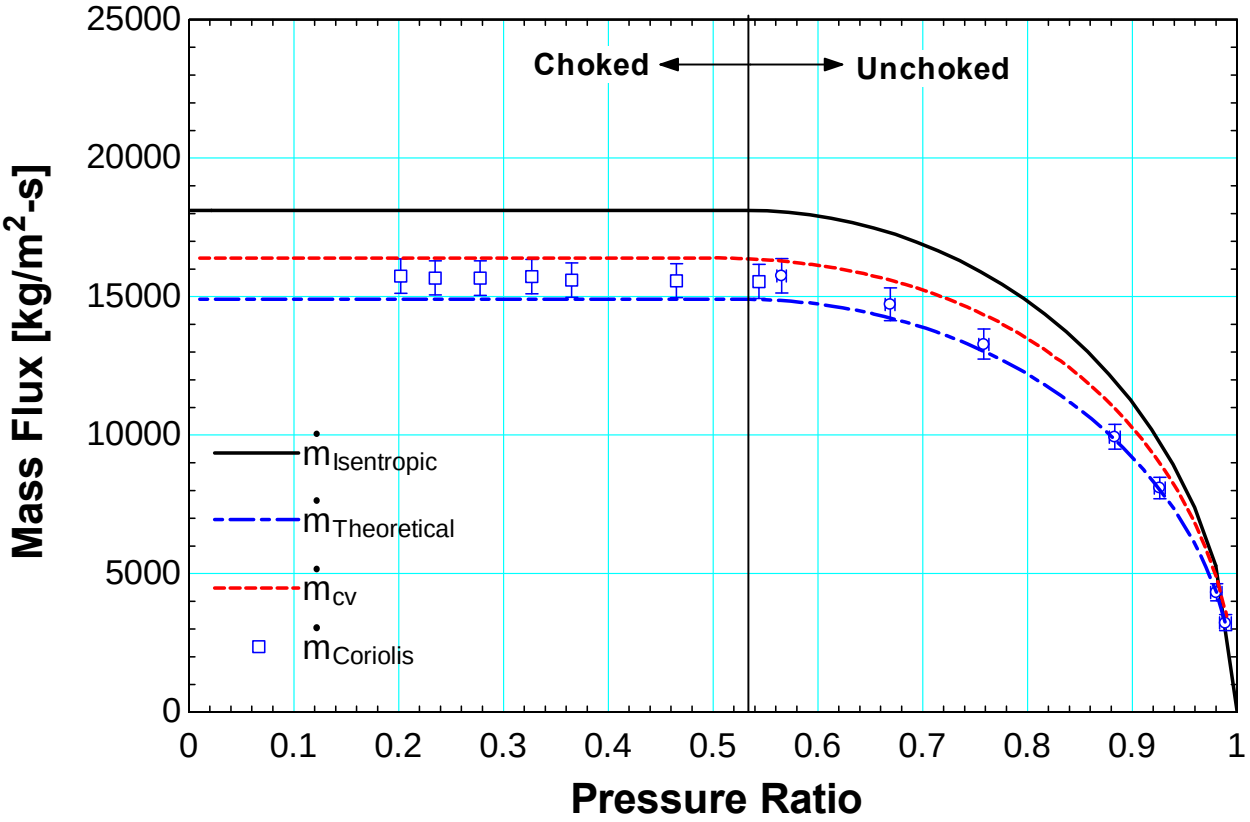

Figure 235 Measurements obtained with a knife-edge orifice at P_{inlet} = 7.67 MPa and ρ_{inlet} = 92 kg/m^3. Discharge coefficient evaluated at Cd = 0.84 for the data shown.

Figure 235 shows a similar trend to that developed in **Figure 234** with the exception that the measurements shown were taken at test section pressures and are less susceptible to minor deviations in the pressure ratio. A summary of both figures is shown below in **Figure 236** which illustrates the effect on the discharge coefficient as a function of pressure ratio for the measurements obtained with the facility.

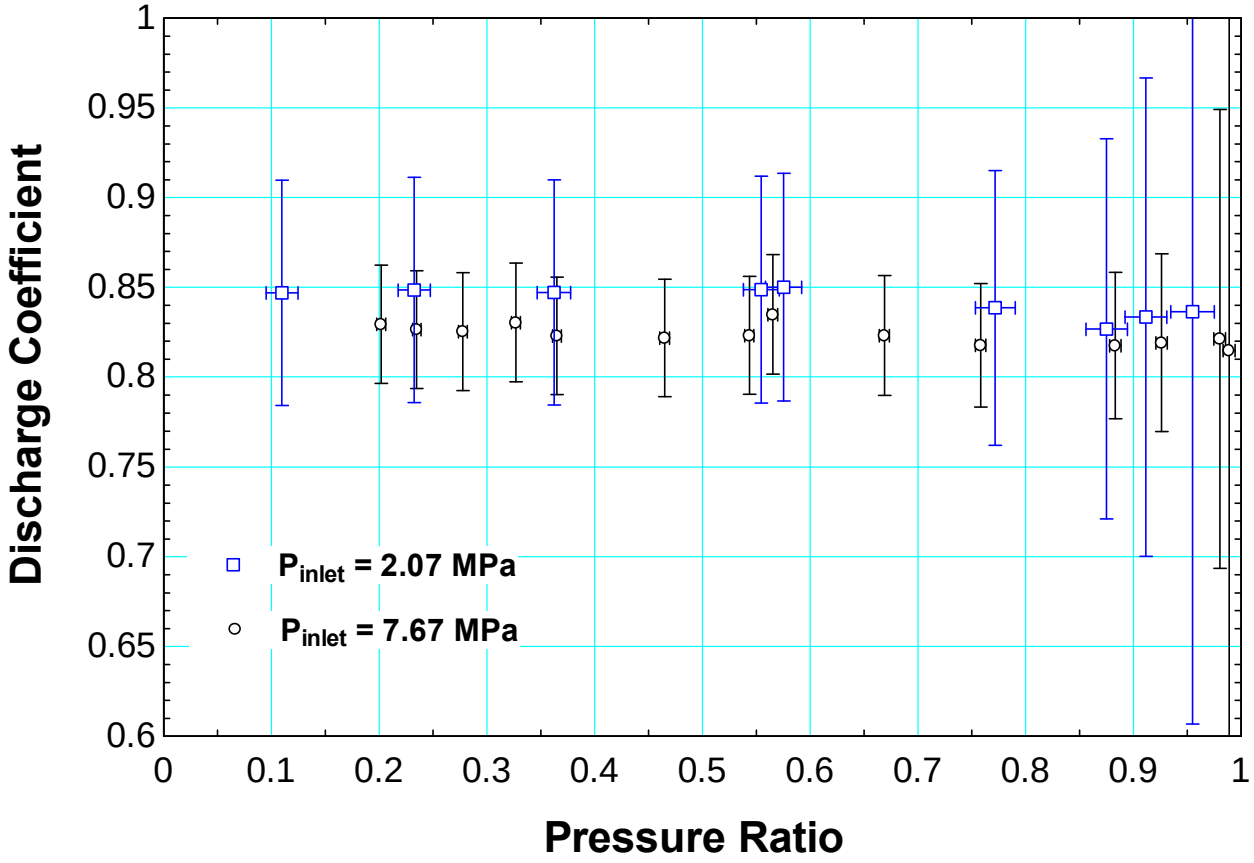

Figure 236 Discharge coefficient for measurements taken with an orifice at P_{inlet} = 2.07 MPa and P_{inlet} 7.67

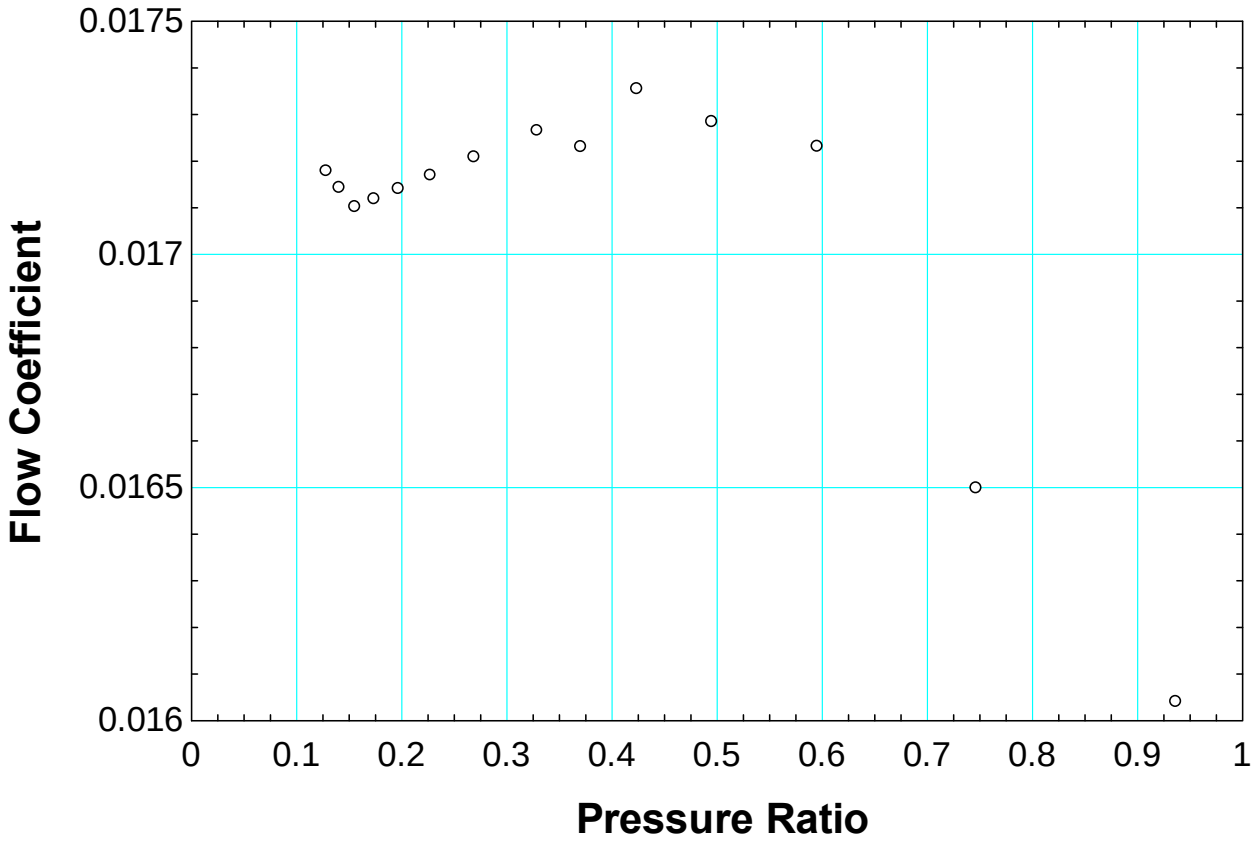

Figure 237 Manufacturer's Flow Coefficient Data – O'Keefe Controls Co. (www.okcc.com)

Data published on the O'Keefe's Controls Co. website was used to construct **Figure 237**. The figure shows that the actual flow coefficient varies with pressure ratio for pressure ratios greater than the critical pressure ratio. The flow coefficient then approaches a constant value of approximately $C_v \approx 0.01725$. This data was used to construct **Figure 238** which shows that the discharge coefficient nominally approaches a fixed value of $C_d \approx 0.91$ for $PR < 0.6$. The other major piece of information which can be extracted from **Figure 238** is that the discharge coefficient is particularly sensitive to even minor deviations in the available flow area at the conditions desired.

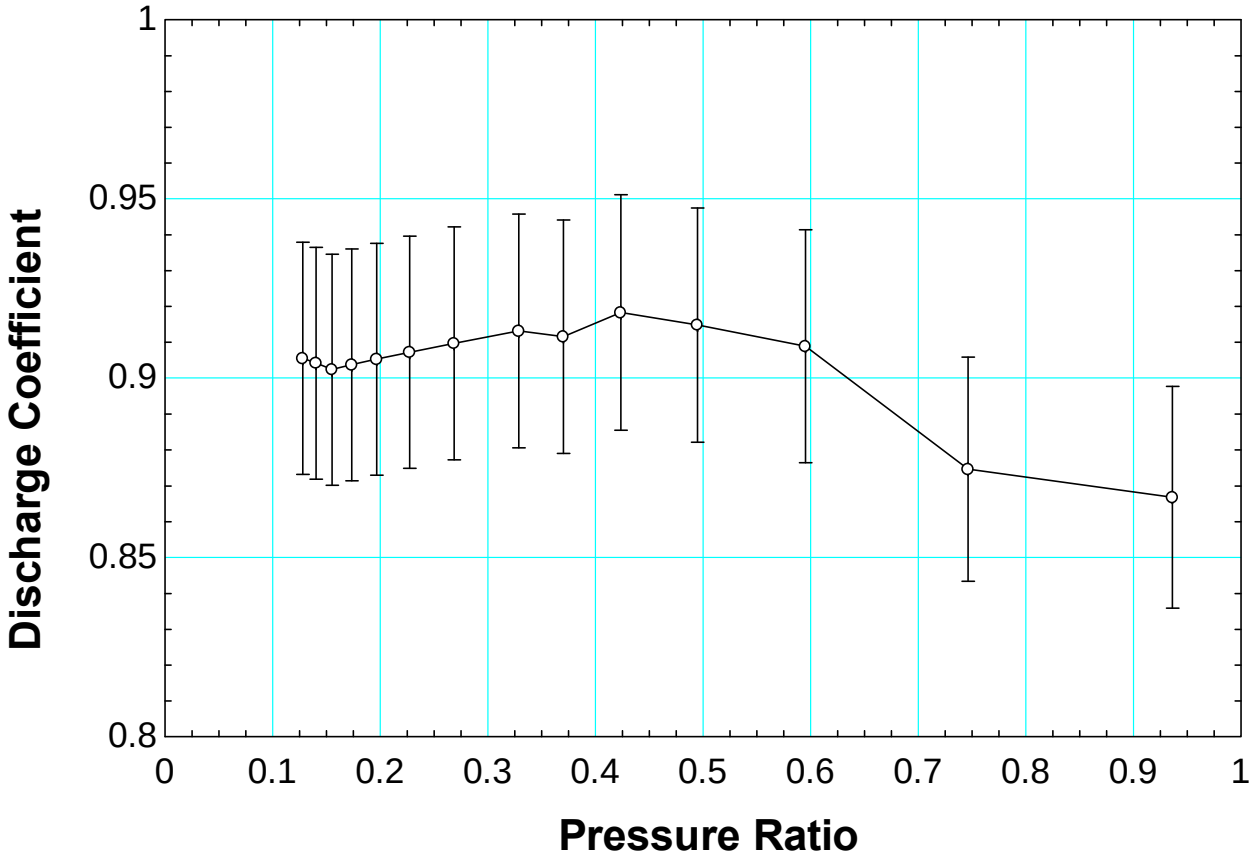

Figure 238 Manufacturer's Flow Coefficient Data in terms of Discharge Coefficient

It is important to note that **Figure 238** was constructed strictly based on the manufacturer's tolerance of the available flow area as demonstrated below in **Figure 239**. In general, the discharge coefficient for an orifice is a function of the flow area, the upstream and downstream pressures, inlet temperature, and flow rate; the latter information was not published so the uncertainty represented in the discharge coefficient shown in **Figure 238** should be considered a lower bound on the actual uncertainty. Nevertheless, the limited information obtained from the manufacturer does seem to match the data obtained with the facility.

Variable±Uncertainty	Partial derivative	% of uncertainty
Cdcheck = 0.9068±0.03239 [-]		
Deng = 0.028±0.0005 [in]	∂Cdcheck /∂ Deng = -64.78	100.00 %

Figure 239 Uncertainty in Discharge Coefficient strictly based on orifice diameter

4.4.2 Data taken through an Annular Orifice

Data taken through an annular orifice was more difficult to verify. Measurements were obtained with air as the working fluid at different inlet pressures. Essential geometrical information about this test series is summarized in **Table 4-20**. Measurements were compared to an empirical correlation of the incompressible discharge coefficient provided by Suryanarayanan (2009) who extended the work of Gamal et al. (2006, 2008). Two shafts were installed in the test facility for this test series. The results are presented in **Figure 240** prove to be consistent with the validation correlation in the limit that the pressure ratio approaches 1 – i.e. the flow is incompressible. This limiting condition is illustrated in **Figure 242** and **Figure 243**. Eccentricity effects also appear to be limited in this test facility as the results are consistent.

Table 4-20 Geometrical parameters used in annular orifice test series

PARAMETER	VARIABLE	VALUE	UNCERTAINTY
SEAL			
Diameter	D_{seal}	3.1814 mm	±3.81 μm
Length	L_{seal}	7.62 mm	±2.54 μm
Max seal roughness	e_{seal}	0.305 μm	
SHAFT			
Diameter 1	D_{shaft}	3.1021 mm	±0.762 μm
Diameter 2	D_{shaft}	3.1123 mm	±0.762 μm
Length	L_{shaft}	50.8 mm	
Max shaft roughness	E_{shaft}	0.051 μm	

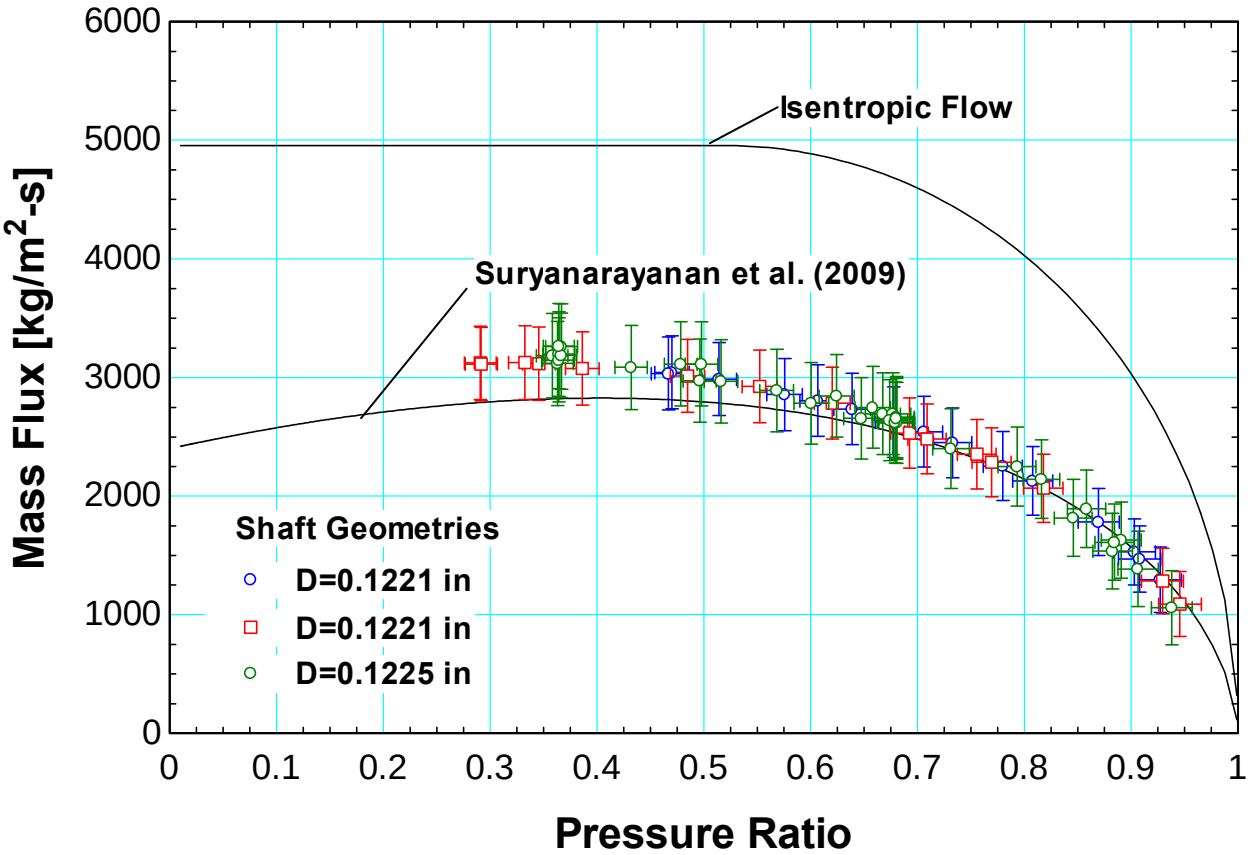

Figure 240 Measurements obtained through an annular orifice at P_{inlet} = 2.065 MPa and ρ_{inlet} = 24 kg/m^3. Mass flux is conserved as a function of pressure ratio for the geometry and working fluid conditions

shown.

The two shafts installed in the facility had a diametrical clearance of $D^1_{clear} = 79.3\,\mu m\ (0.00312\,in)$ and $D^2_{clear} = 69.1\,\mu m\ (0.00272\,in)$ respectively with the mass flow rates measured for the two cases differing by about 20% at lower pressure ratios. Again, the uncertainty of the Coriolis mass flow meter is $0.000015\frac{kg}{s}$ so the difference between the two mass flow rates should be significant enough for the flow meter to distinguish as demonstrated in equation (4.3).

$$\frac{\dot{m}_{0.1225}\left(PR \approx 0.5\right) - \dot{m}_{0.1221}\left(PR \approx 0.5\right)}{\dot{m}_{error}} = \frac{0.0012 - 0.001}{0.000015} = \frac{0.0002}{0.000015} = 13.3 \tag{4.3}$$

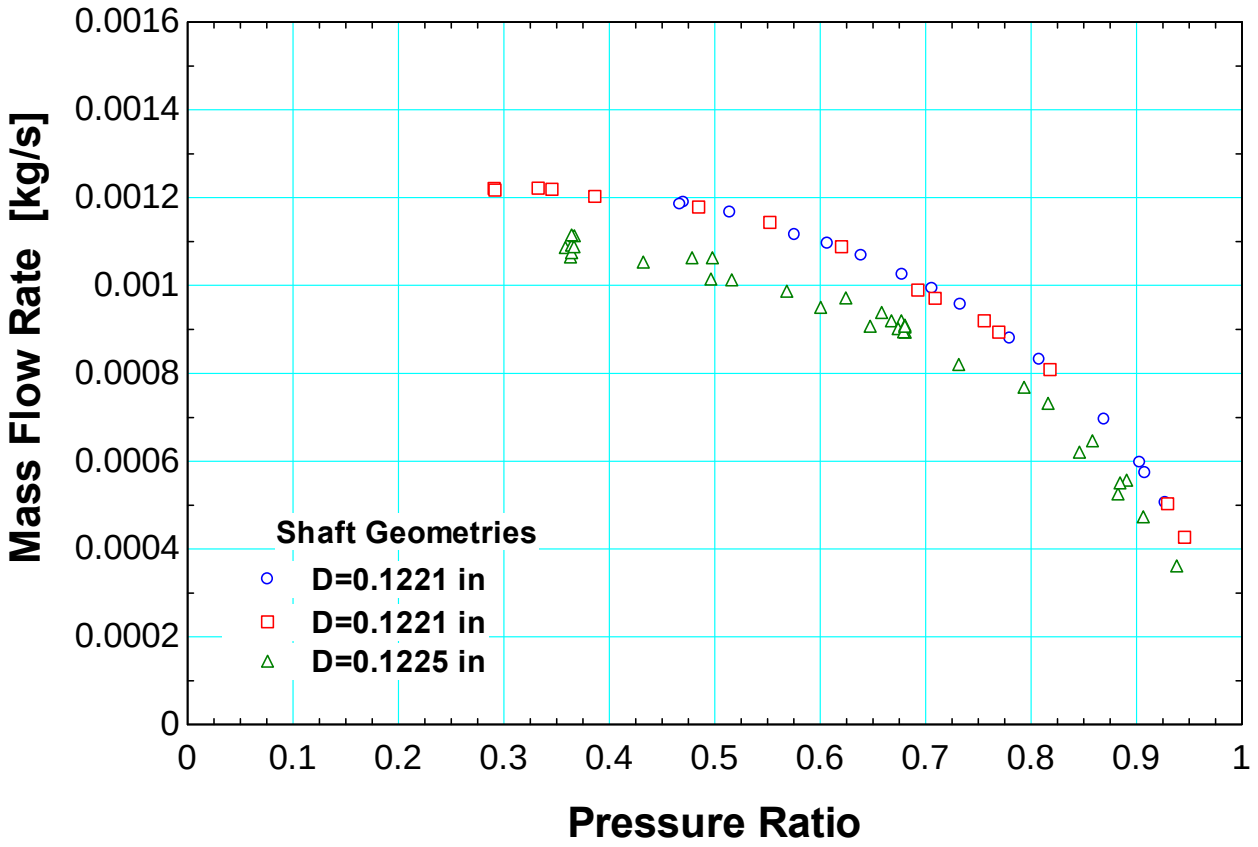

Figure 241 Raw data of measurements obtained with test facility at P_{inlet} = 2.065 MPa and ρ_{inlet} = 24 kg/m^3. Offset in mass flow rate clearly apparent for 10 µm difference in shaft diameter.

Figure 242 and **Figure 243** plot the discharge coefficient versus Reynolds number for the different geometrical inputs specified in **Table 4-20**. **Figure 242** illustrates the output of the empirical correlation by Suryanarayanan (2009) as a function of the Reynolds numbers encountered in this test facility. A word of caution must be interjected regarding the output from the correlation provided by Suryanarayanan (2009). Suryanarayanan (2009) states a dependency of his correlation of the variable $\frac{L}{c} = \frac{Length\ of\ seal}{Radial\ clearance}$. However, any and all attempts to plot the data obtained with this facility as a function of this parameter yielded unrealistic results. It is not clear if the author actually correlated the data from Gamal et al. (2008) as a function of $\frac{L}{D_h} = \frac{L}{2c} = \frac{Length\ of\ seal}{Hydraulic\ Diameter}$. However, if the correlation does applies to $\frac{L}{D_h}$ instead of $\frac{L}{c}$, the

following information is applicable.

Suryanarayanan (2009) specifies that the correlation is applicable to flows with $\mathrm{Re}_{D_h} < 15000$ at pressure ratios $PR \to 1$ but it is demonstrated here that the critical Reynolds number is also sensitive to the ratio of the labyrinth tooth thickness to the hydraulic diameter of the annulus, $\frac{L}{D_h}$. **Figure 242** and **Figure 243** illustrate that the applicability of the correlation drops from about 80% to 67% of the critical Reynolds number identified by Suryanarayanan (2009) for $\frac{L}{D_h}$ equal to 96.2 and 110.3 respectively. Again, the correlation has been highly tuned to predict discharge coefficients for incompressible flow. Discharge coefficient predictions where the correlation loses applicability are circled in **Figure 242** and **Figure 243**; in both cases, the correlation loses applicability for pressure ratios less than about $PR < 0.6$. This result was expected but it was also reassuring to verify that the facility was performing according to published trends in the limit that $PR \to 1$.

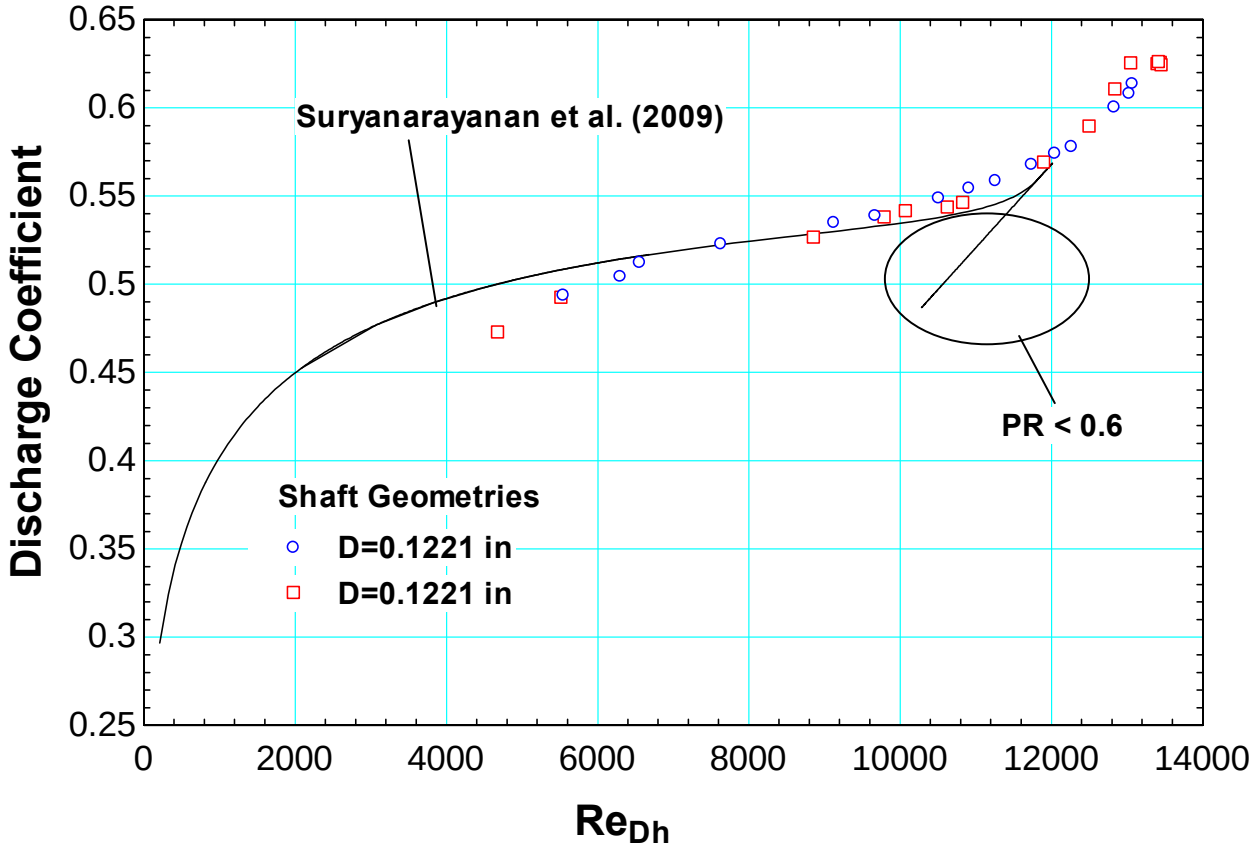

Figure 242 Discharge coefficient as a function of Re_D with compressibility effects included. Measurements demonstrated to deviate from empirical model at pressure ratios less than PR = 0.6 for length to hydraulic diameter ratios L/D_h = 96.2.

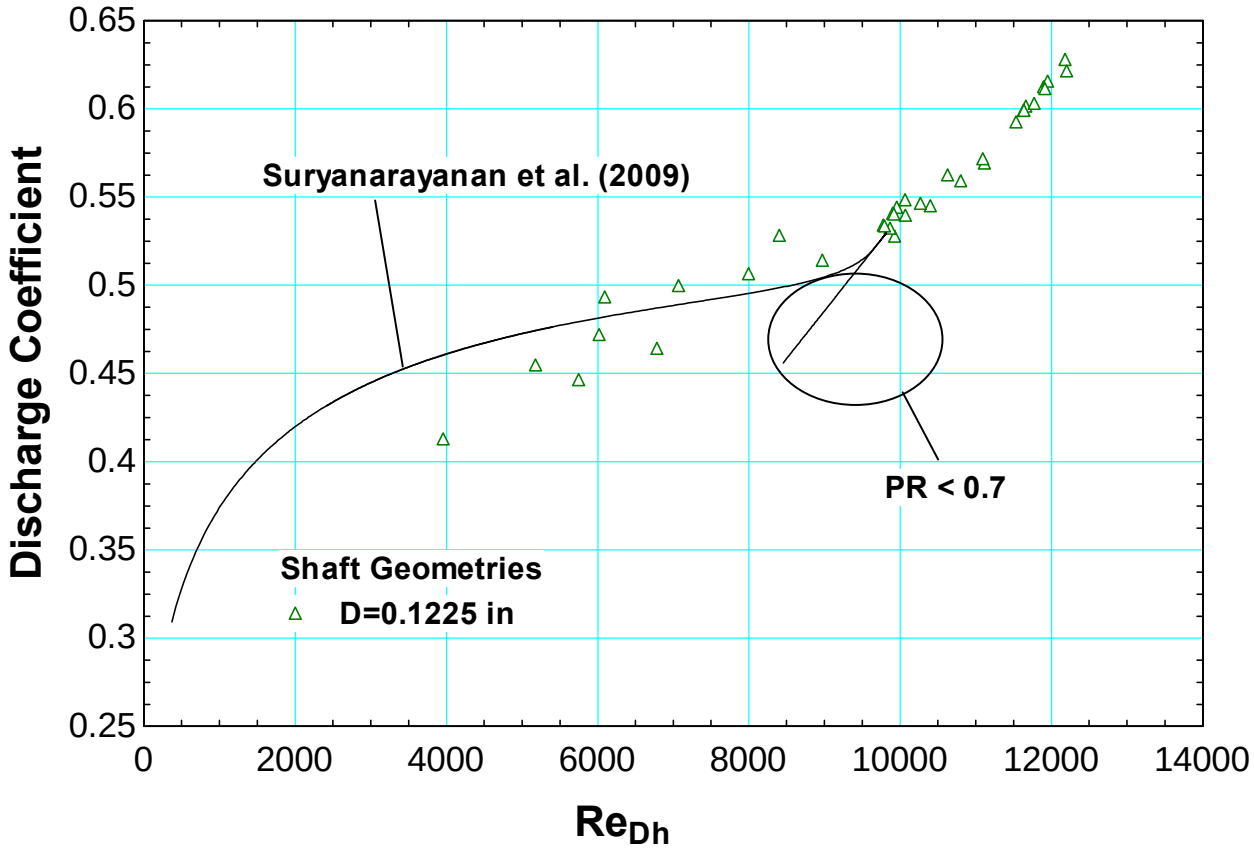

Figure 243 Discharge coefficient as a function of Re_D with compressibility effects included. Measurements demonstrated to deviate from empirical model at pressure ratios less than PR = 0.7 for length to hydraulic diameter ratios L/D_h = 110.3.

References

Gamal, A.M., Ertas, B.H., and Vance, J.M., High-pressure pocket damper seals: leakage rates and cavity pressures. Proceedings of GT2006 ASME Turbo Expo 2006: Power for Land, Sea, and Air, May 8-11, 2006, Barcelona, Spain.

Gamal, A.M., 2007, Ph.D. thesis. "Leakage and Rotordynamic Effects of Pocket Damper Seals and See-Through Labyrinth Seals", Texas A&M University, College Station.

Linfield, K.W., 2000, Ph.D. thesis, "A Study of the Discharge Coefficient of Jets from Angled Slots and Conical Orifices"

O'Keefe's Controls Co., 2000, www.okcc.com, 2 Oct, 2011.

Suryanarayanan, S., 2009, M.S. thesis, "Labyrinth Seal Leakage Equation", Texas A&M University, College Station.

Ward-Smith, A.J., 1979, "Critical Flowmetering: The Characteristics of Cylindrical Nozzles with Sharp Upstream Edges", Int. J. Heat & Fluid Flow, Vol. 1 No. 3 pp. 123-132.

4.5 Supercritical Carbon Dioxide Results

This chapter presents data obtained with the test facility using carbon dioxide as the working fluid. The working fluid was regulated on both the inlet and outlet states during data collection in an effort to obtain comparative results.

The most difficult aspect of the project was controlling the inlet state. Fluid properties vary dramatically in the vicinity of the critical point and even minor deviations in temperature on the order of ±0.8°C can lead to unacceptable differences in density on the order of ±230 kg/m^3 as was demonstrated in Section 4.3.1 and illustrated in **Figure 172**.

4.5.1 Data taken through a Circular Orifice

Data was taken with the same orifice used to conduct the test series outlined in Chapter 4.4 where air was used as the working fluid. The data shown in that test series illustrated that the measurements taken were consistent with previous results as well as within the experimental uncertainty detailed in Chapter 4.3.

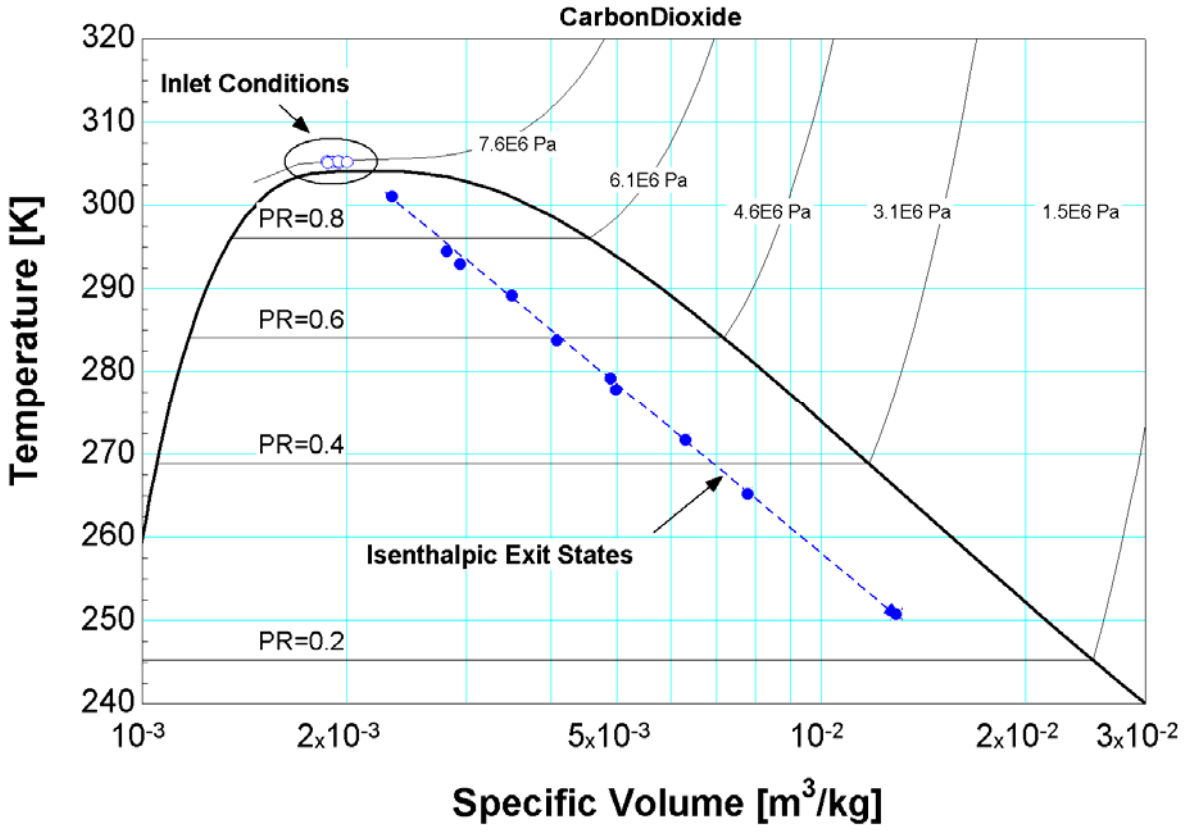

Figure 244 T-v diagram of data obtained with a sharp-lip orifice taken at P_{inlet}=7.6 MPa and ρ_{inlet} = 500 kg/m^3; isenthalpic reference points are provided to note the large pressure ratios achievable with the test facility.

Figure 244 shows a T-v diagram of a test series conducted at an inlet state of 7.6 MPa and 500 kg/m^3. For each measurement shown, the inlet state was fixed to within the capability of the facility while the exit pressure was

continuously adjusted to different pressure ratios denoted in the figure as *PR*. The figure shows that the facility is capable of achieving pressure ratios of 0.3 to 0.9 relative to the 7.6 MPa inlet condition. In each case, the facility was allowed to reach steady state so that the inlet and exhaust pressures, inlet density, and mass flow rate stabilized over a period of about 20 seconds. The results were then time-averaged over that period to evaluate the mass flow rate at a given pressure ratio where the concept is demonstrated by equation (5.1).

$$\dot{m}_{coriolis} = f\left(\overline{P_{inlet}(t)}\Big|_{20s}, \overline{\rho_{inlet}(t)}\Big|_{20s}, \overline{P_{outlet}(t)}\Big|_{20s}, geometry\right) \quad (5.1)$$

Figure 245 provides a close up view of the inlet conditions of the data set illustrated in **Figure 244**. **Figure 245** demonstrates the difficulty of maintaining an inlet condition in this region where density is a strong function of temperature along an isobar. Notice that the measurement uncertainty at test conditions is mostly due to the pressure transducers which have a relatively low uncertainty of about 0.075% with a full scale of 40 MPa. The density measurement has an uncertainty of about ±0.2 kg/m^3 and it was not possible to regulate the facility at this level of precision given that the temperature difference required would be on the order of ±0.0004°C.

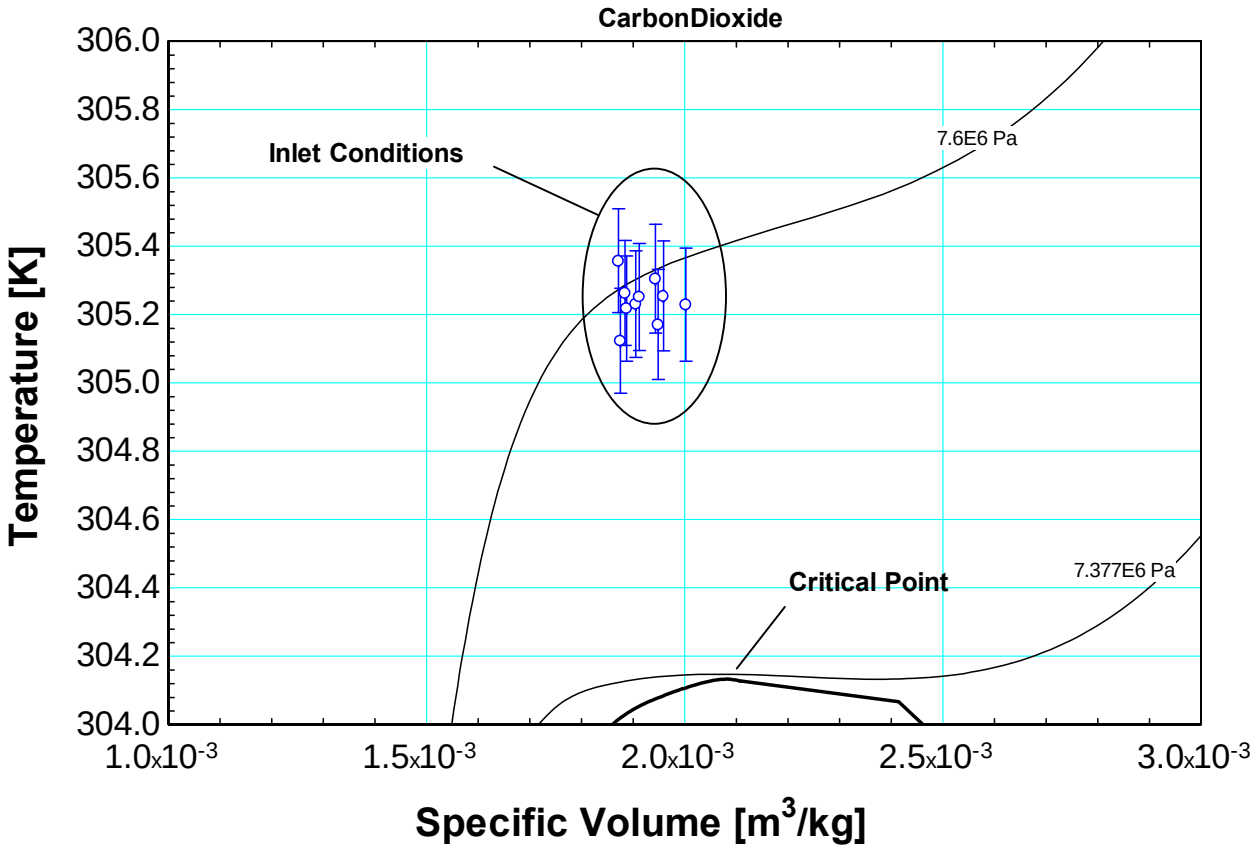

Figure 245 Measurement uncertainty of inlet conditions of data taken at P_{inlet}=7.58 MPa and ρ_{inlet} = 500 kg/m^3

Figure 246 demonstrates the extent of the problem outlined in **Figure 245**. Notice that if a Type-K thermocouple is used at these test conditions, the instrumentation error would account for a 46% error in inlet density and would render the data useless.

Variable±Uncertainty	Partial derivative	% of uncertainty
ρ = 500.8±230 [kg/m^3]		
P = 7.577E+06±30000 [Pa]	∂ρ/∂ P = 0.002664	12.07 %
T = 32.09±0.8 [C]	∂ρ/∂ T = -269.6	87.93 %

No unit problems were detected.

Figure 246 Measurement uncertainty using Type-K thermocouples facilitates the use of a coriolis flow meter at test conditions

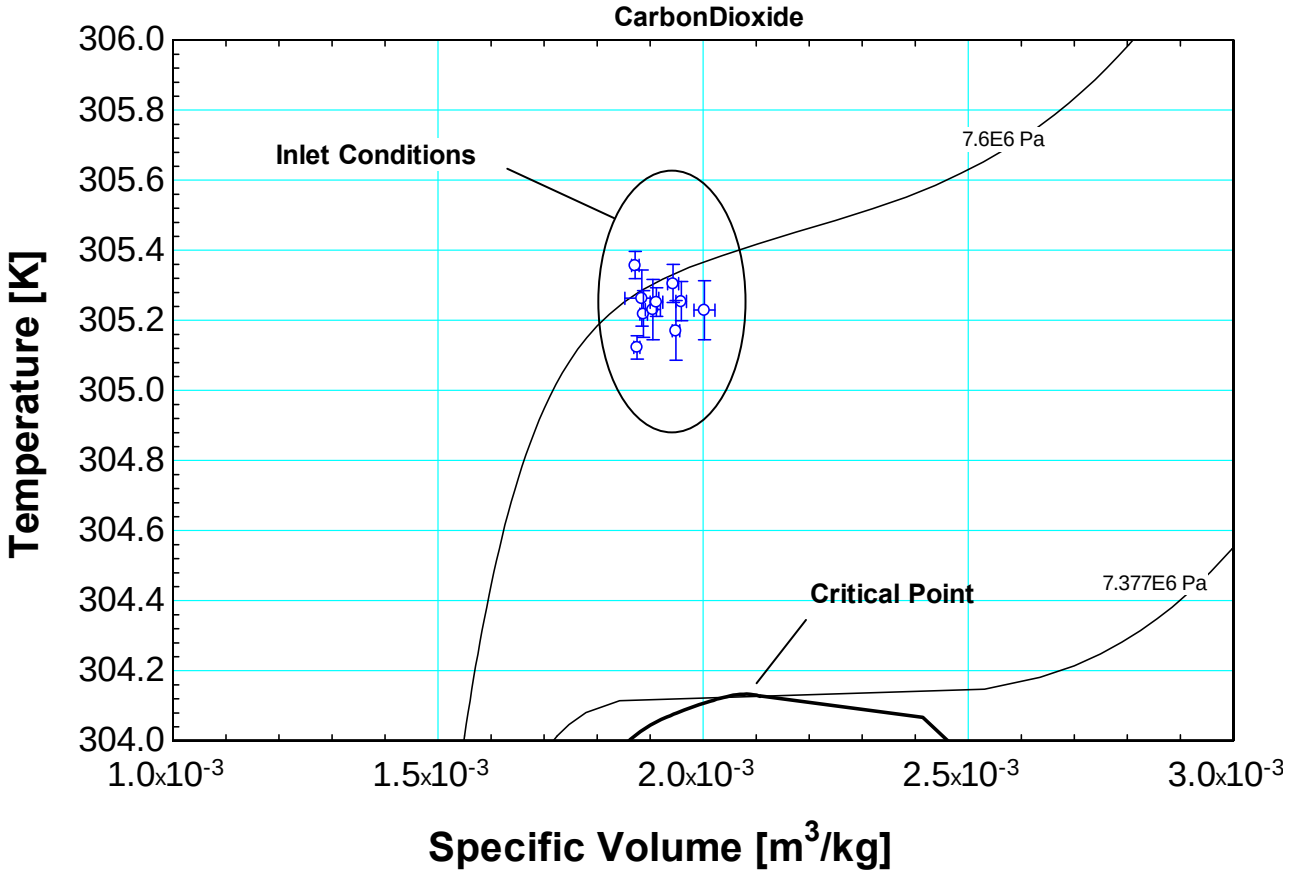

Figure 247 Standard deviation of measurements taken at P_{inlet}=7.58 MPa and ρ_{inlet} = 500 kg/m^3

Figure 247 shows the standard deviation in inlet thermodynamic state for each steady state point taken at these conditions. Notice that the temperature deviation shown on the y-axis is much smaller than the y-axis measurement uncertainty illustrated in **Figure 245**; this effectively shows that the inlet pressure was controlled to within the uncertainty of the pressure transducers. The pressure transducers were regulated to within ±25 kPa. Again, it was not possible to regulate the density within the uncertainty of the coriolis flow meter. At quasi-steady state, the density fluctuated about ±25 kg/m^3 from each nominal condition measured. This was considered acceptable based on the difficulty in obtaining these flow conditions and measurements.

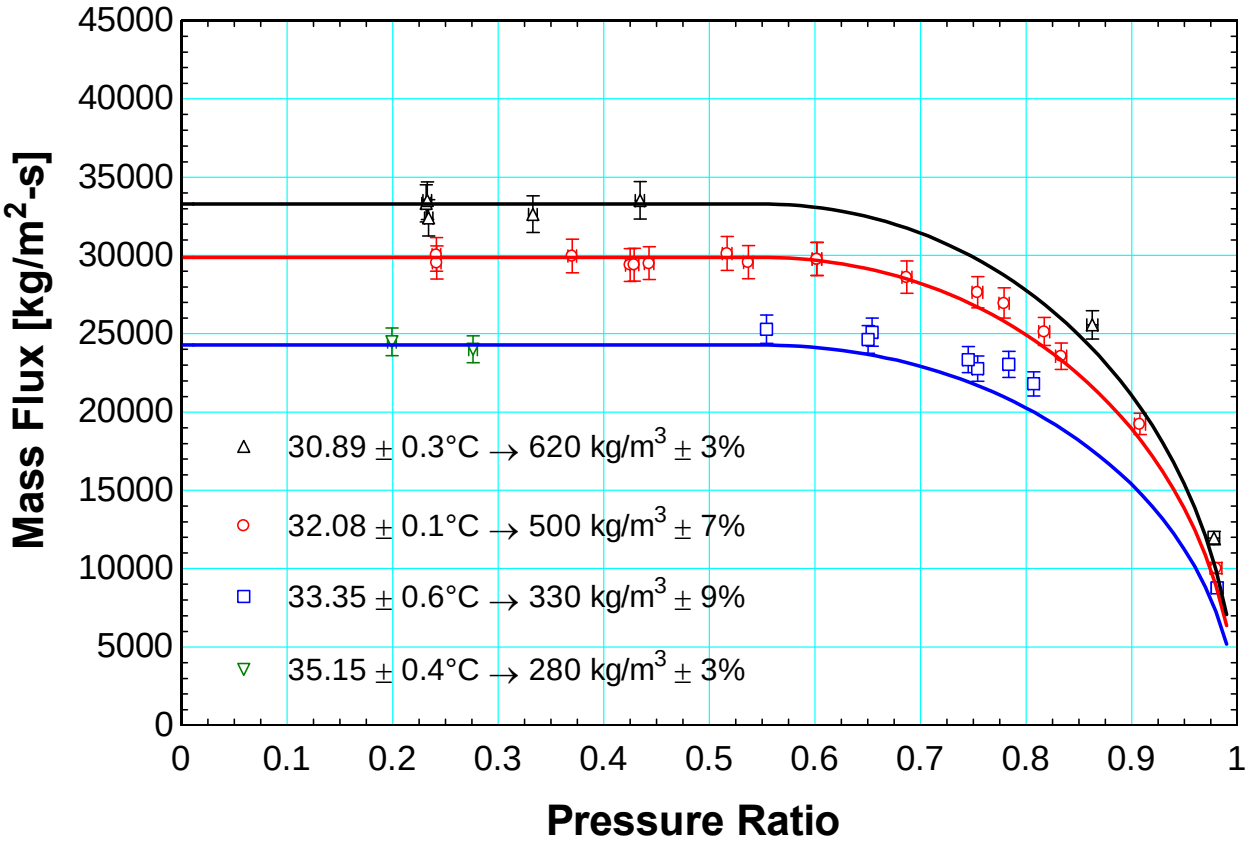

Figure 248 Mass flux versus pressure ratio for measurements taken at P_{inlet}=7.58 MPa and different inlet densities. Discharge coefficient of 0.75 fit to data.

Figure 248 shows the mass flux versus pressure ratio for data taken at an upstream pressure of 7.58 MPa and several inlet densities. A discharge coefficient of C_d = 0.75 was fit to the data for the measurements obtained using a modified version of the isentropic model from Chapter 2 shown here as equation (5.2). The density was held fixed to within 10% of the nominal value desired for all data illustrated in the graph. The data shown in red corresponding to 500 kg/m^3 is representative of the data elaborated upon in **Figure 244**, **Figure 245** and **Figure 247**.

$$\frac{\dot{m}}{A_c} = C_d \sqrt{\frac{P_{in}\rho_{in}\left(\frac{2k_{ideal}}{k_{ideal}-1}\right)\left[(PR)^{\frac{2}{k_{ideal}}} - (PR)^{\frac{k_{ideal}+1}{k_{ideal}}}\right]}{1-\left\{(AR)^2 (PR)^{\frac{2}{k_{ideal}}}\right\}}}$$

$$PR = \frac{\max(P_{out}, P_{crit})}{P_{in}};\ AR = \frac{A_{c,out}}{A_{c,in}};\ C_d\big|_{data-fit} = 0.75 \qquad (5.2)$$

The flow through an orifice is well studied and the general trends which apply in ideal gas flow seem to hold true for the present situation with the exception of the flow oscillations observed during testing. The large pressure gradients and relative location to the vapor dome dictate that the flow will cavitate through the restriction imposed by the orifice. Inside this restriction, the flow will separate into liquid and vapor components. The oscillatory motion with identifiable amplitude and frequency observed during testing is postulated to occur as a byproduct of a process where the liquid and vapor phases continuously exchange occupancy of the core of the flow.

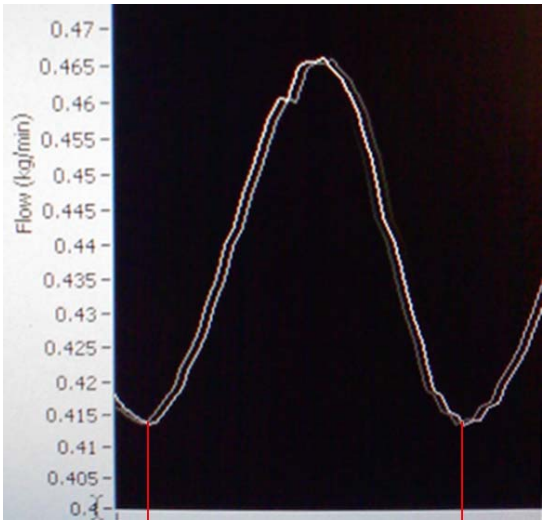

Figure 249 Oscillatory motion of the flow observed during testing

4.6 Conclusions

This study was conducted to gain a better understanding of flow through seal geometry subject to supercritical inlet conditions and two-phase outlet conditions. An experimental test facility was constructed to quantify the mass flux of carbon dioxide near its critical point. Tests were executed with both orifices and rotor-stator configurations. A detailed uncertainty analysis was applied to the investigation to identify parameters which could be modified in the future to create a more effective sealing mechanism.

This preliminary investigation focuses on the development of the test facility constructed to aid in this study. A continuous system capable of cycling supercritical carbon dioxide was constructed at the University of Wisconsin – Madison. The system is expandable and supports multiple seal-shaft configurations.

4.6.1 Experimental Facility

The experimental test facility was designed to withstand system pressures as high as 14 MPa and produce pressure drops on the order of 12 MPa. The facility supports densities from 100 kg/m^3 to 1000 kg/m^3. The compressor is currently undersized for the experiment but is capable of continuous duty at about 7.6 MPa. The test section supports multiple seal configurations with limited uncertainty in the eccentricity.

The experimental facility was verified by comparing the measurements taken to the manufacturer's data as well as literature available from Ward-Smith (1979) and Linfield (2000).

4.6.2 Flow near the critical point through a knife-edge orifice

Test conducted with carbon dioxide at 7.58 MPa showed that the isentropic model of flow through an orifice provided a good baseline in capturing the physics of the flow. A knife-edge orifice was used for in this preliminary testing in order to avoid reattachment of the flow inside the orifice. The measurements obtained showed that the flow would choke at pressure ratios of about $PR = 0.6$. Measurements collapsed nicely in the unchoked region to the isentropic model when using a discharge coefficient of about $C_d = 0.75$ and an ideal gas specific heat ratio at the fluid temperatures provided $k = \frac{C_p(T_{inlet})}{C_v(T_{inlet})}$.

An oscillatory motion of the flow was observed to occur during testing when the downstream pressure was regulated inside the vapor dome. This phenomenon is believed to be cavitation driven with the two-phase separation occurring inside the very narrow opening. The oscillatory motion is not random but periodic with identifiable amplitude and frequency. One explanation which is offered to account for this unexpected result was presented in Chapter 4.5.

4.6.3 Future Work

The test facility is prone to appreciable leaking through the compressor and severely limits the amount of testing time at the large pressure drops desired. A new compressor is shown in **Figure 250** and will be installed in the fall of 2010. The new compressor is a 40hp driven assembly capable of delivering 107 scfm at inlet pressures between 200-1500 psi and outlet pressures of 2400 psi as shown in the instruction manual – Hydro-Pac (2011).

The new compressor will allow larger more prototypical shaft geometries to be tested. The compressor also allows the speed to be regulated which will be incorporated into a PID control system implemented in LabView to compliment the current automated valve detailed in Section 4.3.5.

Figure 250 Hydro-Pac compressor to be installed Fall 2011

The other major design change will be to implement a recuperator in the system as detailed in **Error! Reference source not found.**. The recuperator will provide the additional heating and cooling to allow the loop to operate at steady state with the larger compressor. Additional facility regulation will be accomplished by using the bypass valve shown at the top of the figure to divert the inlet flow into two streams according to the desired inlet density. Mixing will occur in the vicinity of thermocouple 4 labeled accordingly in the figure.

Cited Sources:

[i] Incoloy Alloy 800H & 800HT, Technical Bulletin, Special Metals Publication SMC-047, March 2004. Available from: http://www.specialmetals.com.

[ii] AL-6XN Alloy, Allegheny Ludlum Corporation, 2002. Available from: http://www.alleghenyludlum.com.

[iii] J.F. Grubb, Elevated temperature stability of a 6% Mo superaustenitic stainless steel, NACE Corrosion 96 Conference, Denver, CO, NACE International, Paper No. 426, 1996.

[iv] R.L. Klueh, D.R. Harries, Development of high (7-12%) chromium maretnsitic steels. In: High-Chromium Ferritic and Martensitic Steels for Nuclear Applications, ASTM International, 2001.

[v] R. Viswanathan, W.T. Bakker, Materials for boilers in ultra supercritical power plants. In: Proceedings of 2000 International Joint Power Generation Conference (IJPGC2000-15049), Miami Beach, Florida, July 23-26, 2000.

[vi] E.M. Russick, G.A. Poulter, C.L.J. Adkins, N.R. Sorensen, Corrosive effects of supercritical carbon dioxide and cosolvents on metals, The Journal of Supercritical Fluids 9 (1996) 43-50.

[vii] L. Tan, Y. Yang, T.R. Allen, Oxidation behavior of iron-based alloy HCM12A exposed in supercritical water, Corrosion Science 48 (2006) 3123-3138.

[viii] B.L. Henke, E.M. Gullikson, J.C. Davis, X-ray interactions: photoabsorption, scattering, transmission, and reflection at E=50-30000 eV, Z=1-92, Atomic Data and Nuclear Data Tables 54 (1993) 181-342.

[ix] NIST X-ray Photoelectron Spectroscopy Database, Version 3.5 (National Institute of Standards and Technology, Gaithersburg, 2003); http://srdata.nist.gov/xps/.

[x] M.J. Bennett, M.R. Houlton, J.W. McMillan, C.F. Knights, R.W.M. Hawes, F.C.W. Pummery, The oxidation behavior of the Nimonic alloy PE16 in carbon dioxide at 700-800°C, Oxidation of Metals 15 (1981) 231-249.